Trace elements in ore minerals as indicators of hydrothermal fluid evolution in the Au-rich porphyry system of Iron Cap, British Columbia, Canada

Hugh Graham

Submitted in accordance with the requirements for the degree of Doctor of Philosophy

The University of Leeds
School of Earth and Environment

June 2022

Declaration

The candidate confirms that the work submitted is his own and that appropriate credit has been given where reference has been made to the work of others.

Acknowledgements

First and foremost, I would like to extend my sincerest thanks to my supervisors, Dan Morgan, Rob Chapman, and David Banks, for all their efforts in supporting and guiding me through this process, and ensuring not only my academic development, but also my personal well-being throughout, for which I am especially grateful. Thank you.

I wish also to express my gratitude to Seabridge Gold, for granting and arranging access to Iron Cap, and also for the logistical support provided during two periods of fieldwork at KSM. Specific thanks are extended to Mike Savell, Michelle Campbell, and Marcus Adam, who all also educated me on various aspects of the deposit.

Thanks are also extended to Sean McClenaghan, Foteini Drakou, and Maurice Brodbeck of the Raw Materials Characterisation Laboratory of Trinity College Dublin, for their generous assistance in facilitating LA-ICP-MS analyses, and also reducing the raw data.

From the University of Leeds, Harri Wyn Williams is thanked for his excellent work in preparing the numerous thin sections analysed during this project. Similarly, my gratitude is expressed to Richard Walshaw for his assistance with the extensive SEM, CL and EMPA analyses completed during this project.

My PhD experience has been defined by the people who I shared it with. For making it as enjoyable an experience as possible, my thanks go to Georgian Manuc, James Shaw, Carl Spence-Jones, and Lucia Savastano, and also to others of the Ores and Mineralisation Group, and the Earth and Environment PhD group.

Finally, I want to thank my family, for their unerring support with anything that I choose to do. And Claire, who's brightened my life with her presence, and sustained me through the last few years.

Abstract

Trace elements in ore minerals are increasingly utilised to illuminate genetic processes, and improve mineral exploration and processing approaches. However, the ore minerals of porphyry deposits have received limited study, despite the need to better understand the nature of hydrothermal fluid evolution in porphyry systems. In this thesis, the trace element contents of the ore mineral assemblages of successive vein generations are examined to investigate variations in hydrothermal fluid characteristics throughout formation of the Au-rich porphyry deposit of Iron Cap, British Columbia, Canada.

Detailed petrographic analyses have led to the classification of eight vein generations at Iron Cap. Trace element analyses by LA-ICP-MS reveal that different vein generations exhibit unique geochemical signatures. Both Se and Ag display consistent ore mineral partitioning trends between vein generations, but their concentrations vary systematically. This suggests that these elements record specific changes in hydrothermal fluid characteristics between vein generations, such as temperature, pH, and/or salinity.

A lattice strain model for pyrite has been developed, which shows that Co and Ni are lattice-hosted, and actually exhibit higher partition coefficients for pyrite than Fe does. This means that Co/Ni ratios in pyrite (0.2 to 186.6) directly record Co/Ni ratios in the hydrothermal fluids. Fluctuations in Co/Ni ratios in pyrite growth zones revealed by trace element mapping illustrate that the characteristics of the hydrothermal fluids precipitating the pyrite at Iron Cap are regularly oscillating, which can only be explained by the influx of multiple different fluids during vein formation.

This research shows that trace elements in porphyry ore minerals have the potential to elucidate genetic processes. In particular, hydrothermal fluid evolution in porphyry systems is shown to be inherently chaotic and complex on both the local and deposit scale, with specific veins necessarily formed by numerous episodes of fluid pulsing, fluid mixing, and/or vein re-opening.

Contents

List of tables

List of figures

Abbreviations

apfu	Atoms per formula unit
BC	British Columbia
BSE	Back-Scattered Electron
CL	Cathodoluminescence
D_o	Strain-compensated partition coefficient
EDX	Energy Dispersive X-ray
E	Young's modulus
E_{M}	Young's modulus of a lattice site
EMPA	Electron Microprobe Analysis
FMQ	Fayalite-Magnetite-Quartz
fO_2	Oxygen fugacity
HS	High-Sulphidation
ICF	Iron Cap Fault
IOCG	Iron-Oxide-Copper-Gold
IS	Intermediate-Sulphidation
IQR	Interquartile range
JF	Johnstone Fault
K	Bulk modulus
K_D	Partition coefficient
K_p	Polyhedral bulk modulus
KSM	Kerr-Sulphurets-Mitchell
LA-ICP-MS	Laser Ablation Inductively Coupled Plasma Mass Spectrometry
LS	Low-Sulphidation
MORB	Mid-Ocean Ridge Basalt
MSS	Monosulphide Solid Solution
MTF	Mitchell Thrust Fault
ppb	Parts per billion
ppm	Parts per million
r	Correlation coefficient
r^2	Coefficient of determination
r_a	Covalency-adjusted ionic radius
r_c	Covalent radius
r_e	Effective ionic radius
r_i	Radius of an ion

r_o	Optimum ionic radius for a lattice site
SCLM	Sub-Continental Lithospheric Mantle
SEM	Scanning Electron Microscopy
SFTB	Skeena Fold-and-Thrust Belt
STF	Sulphurets Thrust Fault
T	Temperature
TAG	Trans-Atlantic Geotraverse
VMS	Volcanogenic Massive Sulphide

Mineral abbreviations and formulas

Where possible, mineral abbreviations follow the format recommended by Whitney and Evans (2010). Selected mineral formulas are from Mindat.org.

Act	Actinolite
Alt	Altaite (PbTe)
Alu	Alunite
Anh	Anhydrite
Ank	Ankerite
Ap	Apatite
Apy	Arsenopyrite (FeAsS)
Au	Native gold (including Au-Ag alloys)
Bn	Bornite (Cu_5FeS_4)
Brt	Barite ($BaSO_4$)
Bst	Bastnäsite ((Ce/Nd/Y/REE)(CO_3)F)
Bt	Biotite
Cal	Calcite
Cb	Carbonate mineral
Ccp	Chalcopyrite ($CuFeS_2$)
Cct	Chalcocite (Cu_2S)
Chl	Chlorite
Col	Coloradoite (HgTe)
Cv	Covellite (CuS)
Dg	Digenite (Cu_9S_5)
Dol	Dolomite
Dsp	Diaspore
Eng	Enargite (Cu_3AsS_4)
FeO	Iron oxide mineral
Fl	Fluorite
Fsp	Feldspar
Gn	Galena (PbS)
Hes	Hessite (Ag_2Te)
Ilt	Illite
Ksp	K-feldspar
Mag	Magnetite (Fe_3O_4)

Mol	Molybdenite (MoS_2)
Mrc	Marcasite (FeS_2)
Pl	Plagioclase feldspar
Ptz	Petzite (Ag_3AuTe_2)
Py	Pyrite (FeS_2)
Qz	Quartz
Rt	Rutile
Sd	Siderite
Ser	Sericite
Sp	Sphalerite (ZnS)
Thr	Thorite ($Th(SiO_2)$)
Tnt	Tennantite ($Cu_6(Cu_4[Fe, Zn]_2)As_4S_{12}S$)
Ttr	Tetrahedrite ($Cu_6(Cu_4[Fe, Zn]_2)Sb_4S_{12}S$)

1 Introduction

1.1 Rationale

Porphyry-style mineral deposits are major sources of Cu, Au, and Mo, with by-products of Ag, Pd, Te, Se, Bi, Re, Zn, Sn, Pb, and W (Sillitoe, 2010; Sun et al., 2015). They have relatively low metal grades (averaging 0.5-1.5% Cu, 0-1.5 g/t Au, and 0-0.04% Mo) in comparison to other mineral deposit styles, such as epithermal (averaging 1-3 g/t Au), or volcanogenic massive sulphide (VMS) deposits (averaging 0.6-1.8% Cu, 0.6-1.4 g/t Au, 0.8-4.4% Zn, and 0.02-1.14% Pb), yet are still economically attractive because of their huge size (km^3 scale; Sillitoe, 1972, 2010; Hannington et al., 2014). They tend to be sought after for their considerable Cu contents, the extraction of which makes up around 75% of global Cu production (Sillitoe, 2010). However, they also account for 15% of global Au endowment (based on past production, reserves, and resources), with only orogenic and paleoplacer deposits accounting for more (Lipson, 2014). The importance of porphyry deposits as a source of Au on the world stage is expected to increase, as production from, and exploration for, other deposit styles wanes (Lipson, 2014). Not all porphyry deposits contain Au to exploitable levels (e.g., Cu-Mo deposits), thus large, Au-rich, porphyry Cu deposits are of particular interest to exploration geologists owing to their greater economic potential and feasibility (Sillitoe, 2000; Lipson, 2014). Elucidating the genesis of specific deposits may aid in their exploration and development, and also have similar implications for other deposits elsewhere. More porphyry deposits need to be developed to supply the resources required for the green energy transition. The current, and expected, increase in demand for metals like Cu, and critical elements such as Co and Te, is largely driven by green energy technologies (e.g., electric cars, wind turbines, photovoltaic cells; BEIS, 2022). Porphyry deposits host many the required resources, and as such, will be essential in supplying the vast quantities required over the coming years.

Porphyry deposits (discussed in depth in Chapter 2) are characterised by hydrothermal features, such as veins and alteration assemblages, situated in and around porphyritic intrusions of intermediate to felsic compositions (Figure 1.1; e.g., Sillitoe, 1972; Hedenquist and Lowenstern, 1994; Seedorff et al., 2005; Sillitoe, 2010). The deposits typically form at 2-4 km depth in volcanoplutonic magmatic arcs above active subduction zones, from mineralising (i.e., metal-concentrating and/or metal-enriched) magmatic-hydrothermal systems (e.g., Sillitoe, 2010). The association with magmatic arcs is due to a necessary control arising from the oxidation and fluid conditions present in the magma source region (e.g., Park et al., 2021). Subduction of an oceanic plate initiates melting at

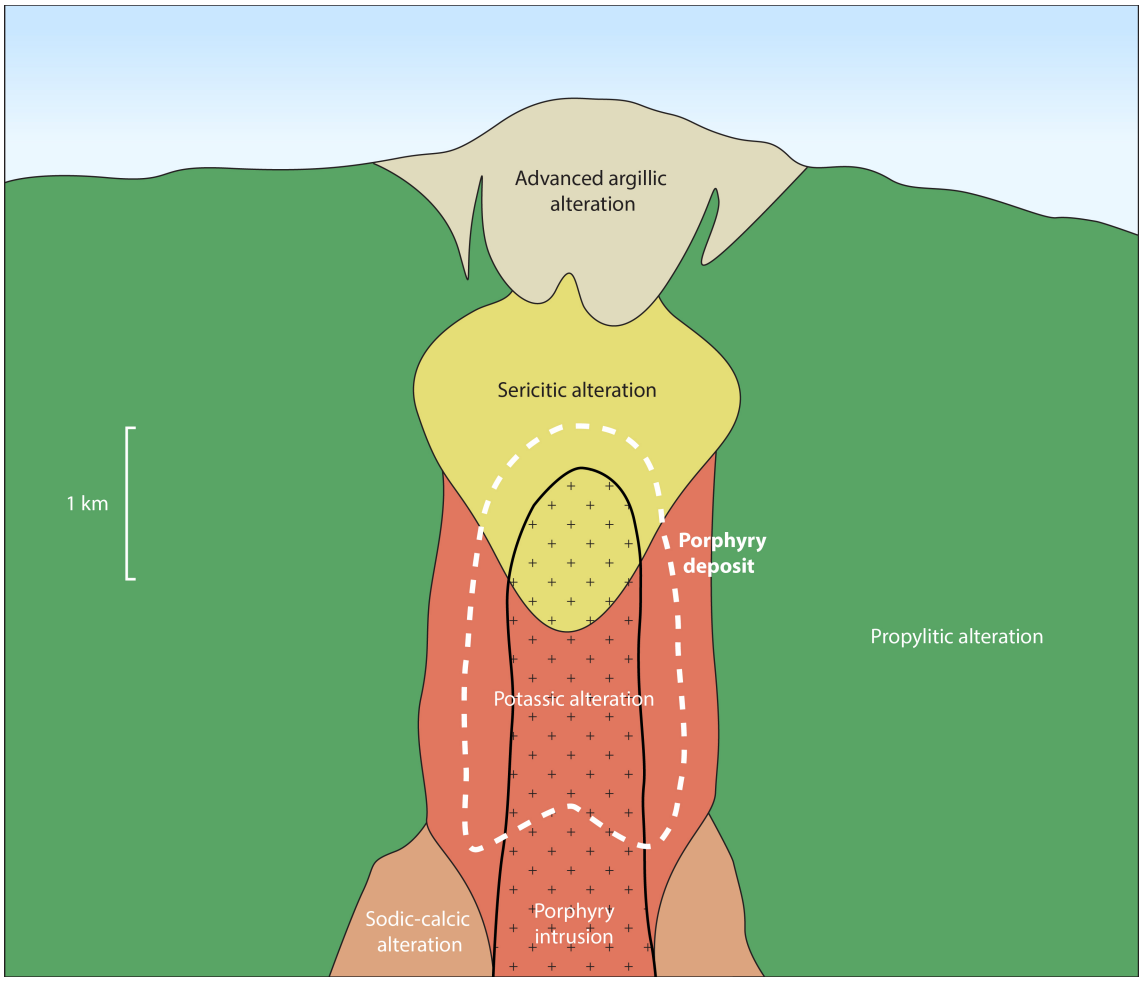

Figure 1.1. Schematic illustration of a porphyry deposit, principally showing the generalised distribution of common alteration assemblages with respect to the porphyry ore (i.e., exploitable concentrations of Cu, Au and/or Mo) and intrusion (modified from Sillitoe, 2010). Note that the potassic and sericitic alteration assemblages are typically the main hosts for ore.

depth in the mantle wedge, producing hydrous, relatively oxidising magmas that may ultimately ascend to upper crustal levels (e.g., Best, 2003). Not all arc magmas are capable of generating porphyry deposits, but those that are are thought to have undergone an array of processes as they migrate (e.g., Park et al., 2021). In essence, intrusion and associated cooling of a suitable magma in the upper crust causes hydrothermal fluids to exsolve from the magmatic body (e.g., Richards, 2011). These fluids extract metals from the associated magma, then transport and concentrate the metals into a smaller rock volume to form an enriched deposit (e.g., Wilkinson, 2013).

The hydrothermal fluids evolve (i.e., change characteristics) through space (e.g., as an individual fluid migrates away from the point of exsolution), and through time (e.g., as the hydrothermal system receeds downwards due to cooling of the source intrusion; Einaudi et al., 2003; Heinrich, 2005). This is often clearly exemplified by the distribution and overprinting relationships of alteration assemblages both within and around the source

intrusion. For example, potassic alteration usually occurs at higher temperatures early in the formation of the deposit, while sericitic alteration may overprint the potassic assemblage as it often occurs later, when the system has cooled and evolved through time (e.g., Seedorff et al., 2005; Sillitoe, 2010).

Ore minerals are precipitated at various stages during the evolution of hydrothermal fluids, when the ore mineral constituents become stable as the solid phase, rather than remaining in the fluid (e.g., Reed and Palandri, 2006). Changes in the characteristics of the fluids may be induced by processes such as cooling, phase separation, and fluid-rock interaction (e.g., Seedorff et al., 2005). Despite this fundamental understanding, the specific characteristics of the hydrothermal fluids, and the nature of fluid evolution in porphyry systems, remain poorly constrained (e.g., Heinrich, 2005; Kouzmanov and Pokrovski, 2012; Hurtig et al., 2021), because the hydrothermal systems responsible for ore deposition cannot be empirically observed when active. Furthermore, experimental and modelling studies are limited by their constrained nature (e.g., Reed et al., 2013; Zajacz et al., 2017), because natural hydrothermal systems are inherently complex (e.g., Kouzmanov and Pokrovski, 2012). There also remain drawbacks to fluid inclusion studies, which are commonly employed to determine fluid characteristics – most significantly that the fluids trapped in inclusions may not be representative of the fluids precipitating the ore minerals, as fluid inclusion studies are principally conducted on quartz (e.g., Mernagh et al., 2020); additional drawbacks are discussed in Section 2.5.2.

Mineralisation in porphyry deposits is found in veins and in the host rock as disseminations, with common sulphide minerals of chalcopyrite, bornite, molybdenite and pyrite (Sillitoe, 2010). Native Au, sulphosalt minerals (e.g., tennantite), and other base metal sulphides (e.g., sphalerite, galena) may also be present (Sillitoe, 2010). Each deposit hosts a complex array of multiple veins, with early-formed veins frequently cross-cut by later-formed veins (e.g., Gustafson and Hunt, 1975); these veins represent pathways of greatest hydrothermal fluid flow during the formation of a deposit (Seedorff et al., 2005). Interpretation of vein characteristics often leads to veins being classified into generations, with each successive generation defined by having different characteristics than its predecessor; the most significant differences are usually in the mineral assemblages (e.g., Gustafson and Hunt, 1975; Sillitoe, 2010). The differing mineral assemblages between vein generations show that the characteristics of the hydrothermal fluids have changed, because different mineral assemblages precipitate under different conditions (e.g., Reed and Palandri, 2006; Seward et al., 2014; Maydagán et al., 2015). Successive vein generations therefore record different stages in the evolution of the hydrothermal fluids.

The ore minerals contained within these veins commonly host trace amounts of a

variety of elements (e.g., Sykora et al., 2018). Their presence in ore minerals has been documented by numerous workers in a range of mineral deposits, such as orogenic gold deposits (e.g., Large et al., 2016; Augustin and Gaboury, 2019), volcanogenic massive sulphide deposits (e.g., Grant et al., 2018; Martin et al., 2019), and porphyry and epithermal deposits (e.g., Franchini et al., 2015; Sykora et al., 2018; Keith et al., 2020). It is likely that the characteristics of hydrothermal fluids play a key role in determining the trace element contents of an ore mineral, much as they control the mineral assemblage (e.g., Frenzel et al., 2016; Keith et al., 2018). Yet despite the increasingly large amount of trace element data acquired, it remains poorly understood how changes in hydrothermal fluid characteristics influence the concentration of specific trace elements in certain ore minerals. Hence, there is an opportunity to improve this understanding.

To address the aforementioned topics, the trace element compositions of the ore mineral assemblages of successive vein generations in a large, Au-rich, porphyry Cu deposit were studied, specifically to investigate variations in hydrothermal fluid characteristics throughout formation of the deposit. Previous studies have investigated fluid evolution between vein generations (e.g., Maydagán et al., 2015; Monecke et al., 2018), the trace element content of a single ore mineral at different stages of mineralisation (e.g., Reich et al., 2013; Sykora et al., 2018), and the partitioning of trace elements between different ore minerals (e.g., George et al., 2016; Grant et al., 2018). However, this research project aimed to combine and build upon these approaches to generate an improved understanding of fluid evolution, and the deportment of trace elements in the ore minerals of a porphyry system.

1.2 The Iron Cap deposit

The case study deposit selected for this research is Iron Cap, which is situated in the Kerr-Sulphurets-Mitchell (KSM) district, northwestern British Columbia (BC), Canada (Figure 1.2). It is one of four porphyry Cu-Au deposits within the KSM district; the remaining three – Kerr, Sulphurets, and Mitchell – giving the KSM district its name. Iron Cap is not included in the acronym because it was only discovered to be of economic importance in 2017, while the district as a whole has a long history of exploration – back to the late 1890s (Seabridge Gold, 2020a). Seabridge Gold are currently exploring and developing the district, and have been in full ownership since 2006 (Seabridge Gold, 2020a).

The latest reserve and resource estimates for the KSM deposits are presented in Table 1.1, showing that Iron Cap has proven and probable mineral reserves of 224 Mt at 0.49 g/t Au, and inferred resources of 1899 Mt at 0.45 g/t Au (Threlkeld et al., 2020). It can therefore be classified as a Au-rich porphyry deposit, following the definition of Sillitoe (1979),

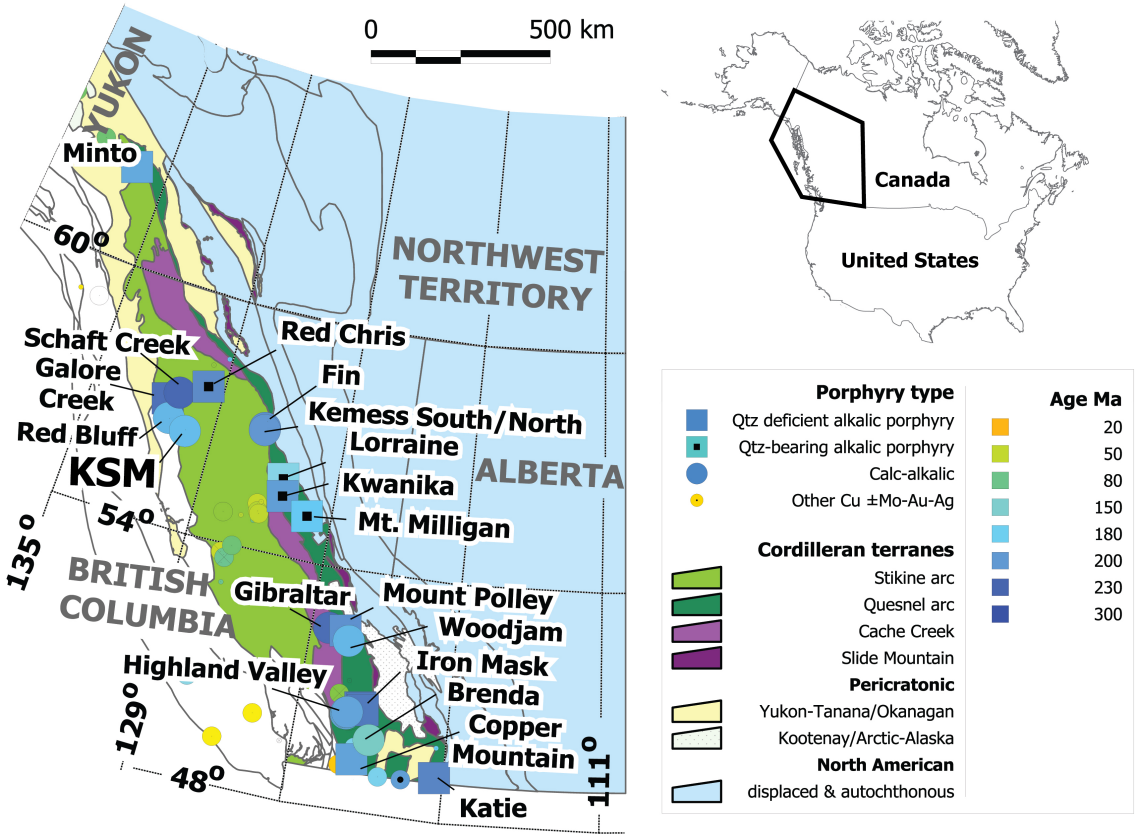

Figure 1.2. Location of the KSM district in British Columbia (adapted from Logan and Mihalynuk, 2014). Other porphyry deposits of the Canadian Cordillera are also shown, with porphyry type represented by symbol shape, and the age of deposits depicted by colouration.

with >0.4 g/t Au. Similarly, the inferred resource estimate of 27.5 Moz Au puts Iron Cap in contention for one of the most Au-endowed deposits in the world (cf. MINING.com, 2021). Furthermore, the combined quantity of resources in the KSM district as a whole makes it one of the largest undeveloped Cu-Au prospects in the world (MINING.com, 2021), and thus of regional and global importance.

Selection of Iron Cap as a study site was informed by discussions with Seabridge Gold geologists, who recognised that Iron Cap may contain features of both porphyry and epithermal environments (M. Adam, pers. comm., 2018). The working hypothesis of Seabridge Gold is that the surface exposure of the deposit may be epithermal in nature, overlying a deeper porphyry deposit (Seabridge Gold, 2020a). Deep drilling in 2017 confirmed the presence of significant porphyry-style mineralisation beneath the exposed cap, providing evidence to support the latter part of the Seabridge Gold hypothesis (Seabridge Gold, 2020a). However, concrete evidence for the presence of epithermal mineralisation is not available, but inferred largely from the presence of overprinting sericite-quartz-clay alteration associated with increases in sulphosalt minerals (M. Adam, pers. comm., 2018; Seabridge Gold, 2020b). The presence of both deep and shallow (i.e., early and late)

Table 1.1
Mineral reserve and resource estimates for the deposits of the KSM district, from Threlkeld et al. (2020). Note that only the Mitchell deposit has proven reserve estimates.

		Average grades				Contained metal			
Deposit	Size (Mt)	Au (g/t)	Cu (%)	Ag (g/t)	Mo (ppm)	Au (Moz)	Cu (Mlb)	Ag (Moz)	Mo (Mlb)
Proven and probable mineral reserves									
Kerr	276	0.22	0.43	1	3.4	2	2586	9	2
Sulphurets	304	0.59	0.22	0.8	51.6	5.8	1495	8	35
Mitchell (prov.)	460	0.68	0.17	3.1	59.2	10.1	1767	45	60
Mitchell (prob.)	934	0.58	0.16	3.1	50.2	17.4	3325	95	104
Iron Cap	224	0.49	0.2	3.6	13	3.5	983	26	6
Total	2198	0.55	0.21	2.6	42.6	38.8	10156	183	207
Inferred resources									
Kerr	1999	0.31	0.4	1.8	23	19.8	17720	114	103
Sulphurets	223	0.44	0.13	1.3	30	3.1	639	9.3	15
Mitchell	478	0.42	0.12	3.2	52	6.4	1230	48.7	55
Iron Cap	1899	0.45	0.3	2.6	30	27.5	12556	158.7	126
Total	4599	0.38	0.32	2.2	29	56.8	32145	331.1	299

porphyry-style features is beneficial for this research, as it allows the study of trace elements in ore minerals throughout successive fluid phases (veins), from early to late in the evolution of the hydrothermal system. The suitability of Iron Cap as the case study deposit was based primarily upon the presence of these features, and the availability of extensive drill core (62 km by 2019; Threlkeld et al., 2020) from both deep and shallow environments.

The amount of previous work undertaken on the KSM deposits was also considered. Upon commencement of this research project in 2017, Iron Cap had undergone no prior detailed study, with the extent of knowledge limited to that of Seabridge Gold geologists, and researchers focussed on other deposits, or other areas in the region (e.g., Kirkham and Margolis, 1995; Nelson and Kyba, 2014; Febbo et al., 2015). This provides an additional benefit to the project, whereby improved understanding of Iron Cap features and ore-forming processes may aid Seabridge Gold in optimising their development strategies for Iron Cap.

During the later stages of this research project, the first study of Iron Cap was published by Campbell et al. (2020). Their work describes the features of the Iron Cap deposit, including the geology, alteration, mineralisation, and vein sequences, and presents a simple genetic model for the formation of the deposit. The study of Campbell et al. (2020) is a major step forward for the understanding of deposit features, but does not address many of the aspects that this thesis aims to shed light on. In particular, many of the observations and interpretations of Campbell et al. (2020) are based on macro-scale

features, necessary to meet their research aims of describing deposit characteristics. Contrastingly, however, this thesis aims to utilise a raft of micro-scale analytical techniques in addition to hand specimen observation, to provide a more detailed understanding of the vein petrography and ore mineral chemistry, and in turn reveal insights to the nature of hydrothermal fluid evolution during deposit formation.

Another point to note is that, as the study of Campbell et al. (2020) is the first to provide a geological description of the deposit, it stands to reason that the detailed characteristics and genetic history of the deposit are yet to be fully realised. Ore deposits in general often require numerous studies before these aspects are understood to a satisfactory level, through consolidation of previous work, and the focus of subsequent works on different aspects of the deposit. Finally, given that the study of Campbell et al. (2020) was carried out roughly in parallel with this research project, there are naturally some similarities and discrepancies between the two studies. However, the study of Campbell et al. (2020) did not influence the observations and interpretations made in this thesis. Chapter 3 contains further discussion of the Campbell et al. (2020) study.

1.3 Aims

The aims of this research project are to:

- Establish the mineralogy of Iron Cap, in terms of the ore and gangue minerals present, with a particular focus on Au-bearing minerals.
- Characterise the vein generations of Iron Cap, and establish a paragenetic sequence of veins and minerals.
- Investigate the processes that may have been involved in the formation of different vein generations, and different ore minerals within vein generations.
- Characterise the concentration and distribution of trace elements in the ore mineral assemblage of different vein generations.
- Investigate the controls on the partitioning of trace elements between ore minerals and hydrothermal fluids.
- Understand the implications of trace element deportment for the characteristics of the hydrothermal fluids that formed different vein generations.
- Develop a model that describes the evolution of hydrothermal fluids at Iron Cap, both between and within vein generations.

- Assess the implications of the research, both locally for Iron Cap, and in the broader context of porphyry deposits in general.

2 Porphyry deposits and magmatic-hydrothermal systems

2.1 Introduction

This chapter reviews the current understanding of porphyry deposits, and the magmatic-hydrothermal systems from which they form. Porphyry deposits are rare worldwide (e.g., Wilkinson, 2013), and yet there is a crucial need for their development, as the demand for resources – particularly Cu and critical elements such as Co and Te – is expected to increase owing to the transition to green energy technologies (Park et al., 2021; BEIS, 2022). Therefore, it is necessary to understand what makes porphyry deposit formation possible, in terms of processes involved, and the characteristics of both the magmatic intrusions, and the hydrothermal fluids.

The current understanding of hydrothermal fluid characteristics throughout the evolution of a mineralising magmatic-hydrothermal system is of particular importance to this thesis, because of the aim to elucidate the characteristics and evolution of the hydrothermal fluids that formed the Iron Cap deposit. Moreover, knowledge of typical porphyry vein generations, and their implications for fluid characteristics and evolution, is essential prior to the analysis and interpretation of vein generations at the Iron Cap deposit, so that empirical observations made during data analysis can be compared to those previously described in the literature. Fundamentally, it is critical to first build a base of knowledge covering typical porphyry deposit characteristics and genetic process, prior to commencing the study of a specific porphyry deposit. This not only allows the recognition of common or indicative features, but also enables prediction of expected characteristics and processes, and comparison with features and process described elsewhere.

Firstly, the tectonic settings of porphyry deposits are considered in Section 2.2, to identify the global-scale controls on their distribution. Magmatism involved in porphyry deposit formation is then discussed in Section 2.3. The causes of certain magma characteristics, and the resulting impacts on the formation of mineralising magmatic-hydrothermal systems, remains a key topic of debate. A current understanding of this debate is necessary to shed light upon the important processes involved in porphyry deposit formation. Following this, Section 2.4 presents the classification criteria for porphyry deposits (and associated deposits), and emphasises the associations between different deposit types and certain magmatic processes. The characteristics and evolution of hydrothermal fluids are then discussed in Section 2.5, in the context of vein formation. Finally, a review of mineral characteristics that can be utilised to illuminate fluid

characteristics is presented in Section 2.6.

2.2 Tectonic setting of porphyry deposits

Most porphyry deposits form in volcanoplutonic magmatic arcs above active subduction zones, as shown in Figure 2.1 (Sillitoe, 1972; Corbett and Leach, 1998; Seedorff et al., 2005; Sillitoe, 2010). Continental arcs more commonly host porphyry deposits than island arcs, which is thought to be a product of the thickness of the overlying crust during subduction, as thicker crust may encourage the production of evolved magmas suitable for porphyry deposit generation (Section 2.3; Chiaradia, 2014; Lee and Tang, 2020). Furthermore, the higher preservation potential at continental arcs relative to island arcs (e.g., Spencer et al., 2017) must play a part in the number of deposits found in each setting. Preservation bias also impacts on the age of discovered deposits, with the majority being Mesozoic and Cenozoic in age, and the remainder Palaeozoic to Archean in age; older deposits are more likely to have been eroded (Seedorff et al., 2005; Singer et al., 2008).

A minority of porphyry deposits are of an age, or situated in a location, thought to be incompatible with arc magmatism (e.g., some porphyry deposits in Tibet; Richards, 2009, 2011; Hou et al., 2015; Park et al., 2021). Such deposits may be found as isolated clusters,

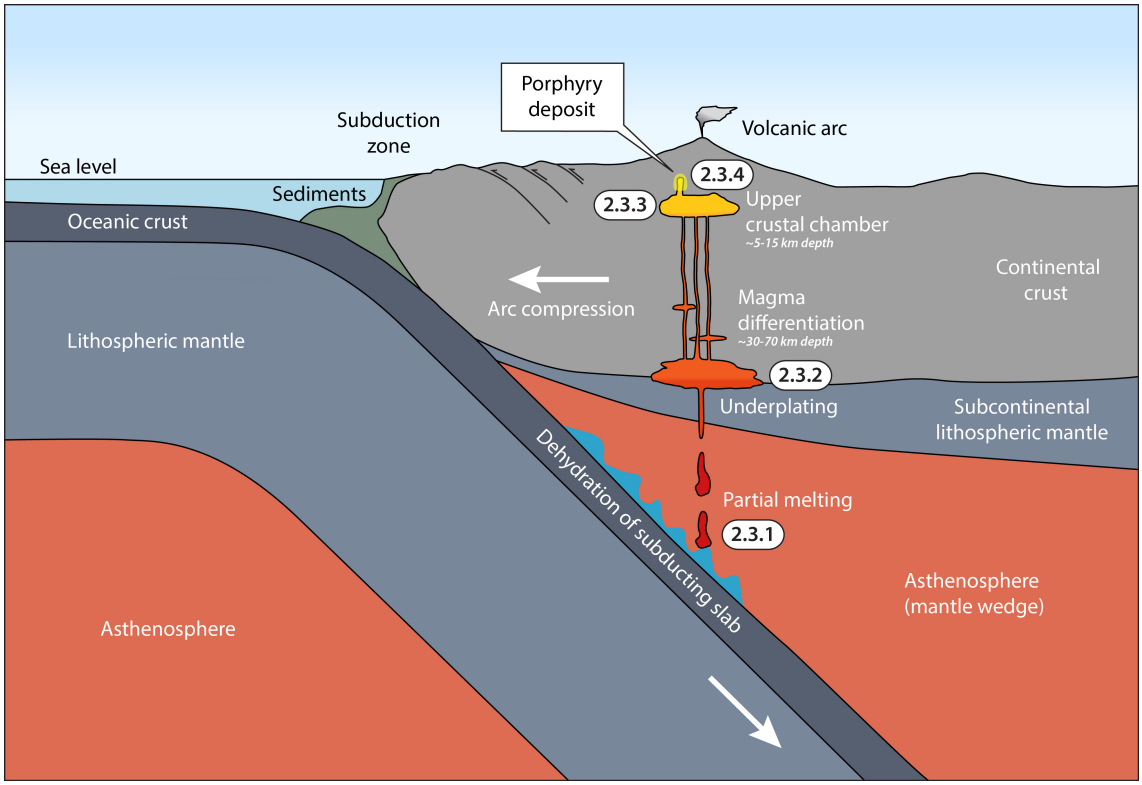

Figure 2.1. Schematic overview of an oceanic-continental subduction zone setting for the formation of porphyry deposits (modified from Wilkinson, 2013; Lee and Tang, 2020). Porphyry deposits typically form in and around intrusions at 2-4 km depth (Sillitoe, 2010). Numbered boxes refer to relevant sections in the text.

or stand-alone deposits, instead of the more characteristic linear belts associated with arc magmatism (Sillitoe, 2000; Richards, 2009; Logan and Mihalynuk, 2014). Richards (2009) proposes that post-subduction tectonic processes are responsible, whereby arc extension or arc collision initiates magma generation after subduction ceases. More recent research has corroborated the recognition of post-subduction porphyry deposits (Richards, 2011; Hou et al., 2015; Holwell et al., 2019; Park et al., 2021), but they nonetheless remain scarce in comparison to subduction-related deposits, and as such, will not be considered in detail here.

2.3 Magmatism

2.3.1 Primary magma generation

The upper crustal magmas that exsolve hydrothermal fluids to form porphyry deposits originate in the mantle (Figure 2.1). As an oceanic plate and its surface sediments are subducted, the increasing pressures initiate metamorphism, which releases fluids from the subducting slab, forming anhydrous eclogite (Best, 2003; Richards, 2011). The fluids are derived from the destabilisation of hydrous minerals in the seafloor-altered basaltic oceanic crust (i.e., micas and amphiboles; Best, 2003; Richards, 2015). Infiltration of these fluids into the overlying mantle wedge causes metasomatism, and lowers the solidus temperature, leading to partial melting of the mantle wedge, which generates primary basaltic arc magmas (Best, 2003). This conventional understanding of the generation of primary arc magmas is complicated when considering the source of specific melt components, of which there are two: the mantle wedge, and the subducting slab (e.g., Mungall, 2002; Lee et al., 2012). Here, the source of primary arc magma characteristics that might be essential for porphyry ore formation are considered. An overview is provided in Figure 2.2.

Porphyry deposits are associated with relatively oxidised intrusions (e.g., Sillitoe, 2010), but there is discussion over whether this characteristic is acquired in the magma during primary melting, or during later processes. An oxidised nature is argued to be likely during primary magma generation (e.g., Mungall, 2002), as this increases the ability of the magma to concentrate Cu and Au from the outset. Enrichments of Cu and Au in primary magmas are deemed critical by some for the formation of porphyry deposits (Mungall, 2002; Park et al., 2019). As chalcophile (S-loving) elements, Cu and Au are strongly linked to the behaviour of S (e.g., Sun et al., 2017). In oxidising mafic silicate magmas with oxygen fugacities (fO_2) >1.5 log units above the fayalite-magnetite-quartz fO_2 buffer (>ΔFMQ +1.5), S is largely present as highly soluble sulphate, rather than the

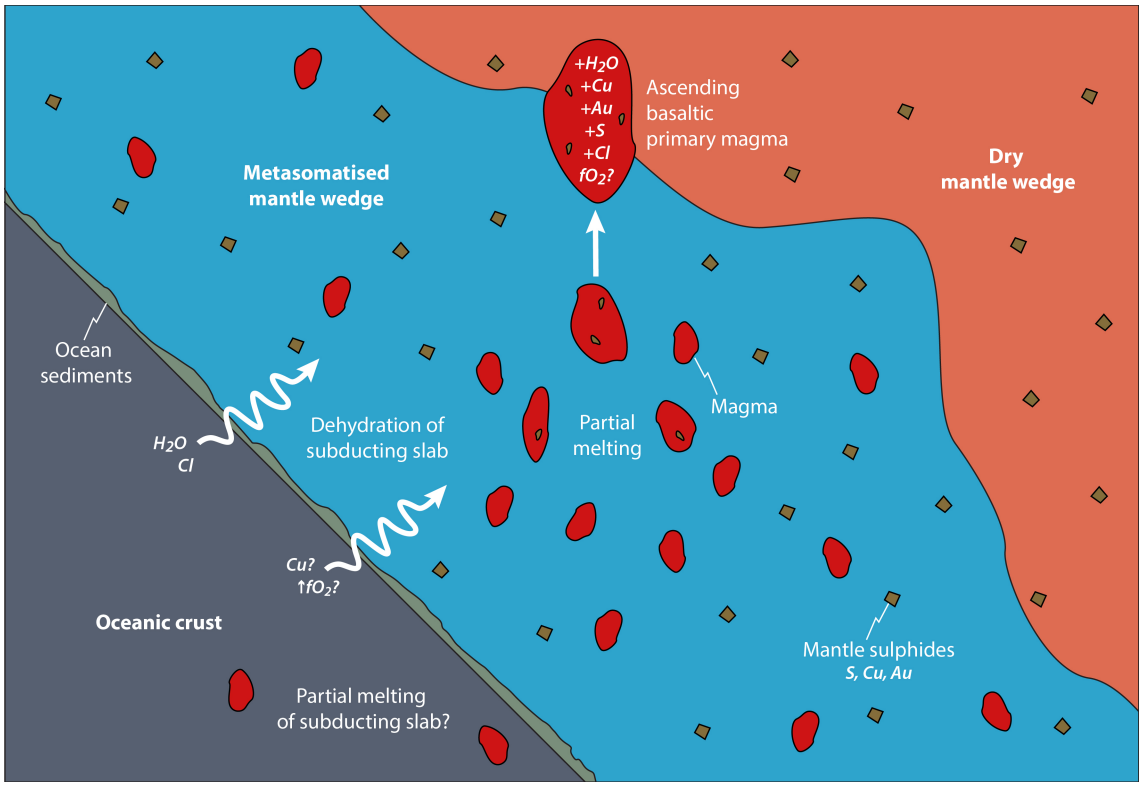

Figure 2.2. The generation of primary magmas capable of forming porphyry deposits, and the potential source of magma components. This field of view is situated around the 2.3.1 label in Figure 2.1.

less-soluble sulphide (Jugo et al., 2010). Magmas with a high fO_2 can also accumulate more S; for example, an oxidising magma with an fO_2 of ΔFMQ +1.5 can incorporate >1 wt.% more S before saturation, predominantly as sulphate, than a magma with an fO_2 of ΔFMQ +1, which may only incorporate ∼0.3 wt.% S before becoming saturated (Jugo et al., 2010). Accordingly, an oxidising magma should be able to accumulate higher concentrations of Cu and Au, because more S phases containing Cu and Au can be dissolved in the magma before sulphide saturation occurs (discussed further below). Nevertheless, some researchers have demonstrated that significant metal enrichment at the primary magma stage is not necessary, but it would still increase the probability of forming a deposit (Cline and Bodnar, 1991; Chelle-Michou et al., 2017). The abundance of relatively oxidised intrusives in magmatic arcs, in comparison to the scarcity of porphyry deposits, further shows that oxidation is not the only controlling factor for the formation of porphyry deposits (Sun et al., 2017), yet the timing of oxidation may still be important. It remains to be proven if the primary arc magmas that ultimately give rise to porphyry deposits are relatively oxidising or not; however, they become relatively oxidising at some point in their journey to the upper crust. This is necessary in order to accumulate and transport sufficient quantities of S, Cu and Au to generate an enriched deposit.

If primary arc magmas are oxidising, the subducting slab is likely involved, because

it is thought to be the only source of oxidising components in the subduction environment (Mungall, 2002). Slab partial melts are argued to be more capable of producing primary magmas with high oxidation states than the primary magmas produced solely from melting of the mantle wedge metasomatised by slab fluids, as the relative abundance of oxidised Fe (Fe^{3+}, as Fe_2O_3) in slab melts compared to fluids acts as a highly effective oxidising agent (Mungall, 2002). However, the generation of slab melts likely requires unconventional subduction scenarios, such as the subduction of a young, hot slab, which could perhaps help to explain the rarity of porphyry deposits in magmatic arcs (Mungall, 2002; Richards, 2015; Sun et al., 2017). Moreover, it has been suggested that slab partial melts can contribute higher quantities of Cu to primary magmas than partial melting of the mantle wedge alone (Sun et al., 2011), and even that this is required for primary magmas to achieve high enough concentrations of Cu to form a porphyry deposit (Sun et al., 2017). The involvement of slab melts could be corroborated by the recognition that porphyry intrusions frequently exhibit high Sr/Y ratios relative to unmineralised arc intrusions (Loucks, 2014), as this signature can be acquired by partial melting of the slab, with amphibole or garnet as residual phases in the slab, sequestering Y (Defant and Drummond, 1990). However, high Sr/Y ratios may also arise during later magma differentiation, when garnet or amphibole fractionate from the melt and plagioclase crystallisation is delayed due to high melt water contents, leading to discussions over the source of this geochemical signature (Section 2.3.2; e.g., Lee and Tang, 2020).

Notwithstanding the involvement of slab melts, it is widely agreed that water released from the slab during subduction metasomatises the mantle wedge, and that this aqueous fluid effects partial melting of mantle peridotite to produce hydrous basalts, typically with 2-6 wt.% H_2O (e.g., Best, 2003; Richards, 2015, and references therein). It therefore stands to reason that water-soluble components in the slab should be transferred to the mantle wedge, and therefore also to resulting partial melts (e.g., Kelley and Cottrell, 2009). Water itself is not thought to be the main oxidising agent in the subduction environment, instead dissolved (whether in fluid or melt) Fe- and Mn-oxides, sulphates, and carbonates are deduced to be the main carriers of O (e.g., Mungall, 2002; Kelley and Cottrell, 2009; Richards, 2015, and references therein). Therefore, if primary magmas are oxidising and lack the involvement of slab melts, then these components must be transported by the aqueous fluids, with some researchers proposing the involvement of supercritical liquids (Bureau and Keppler, 1999; Kessel et al., 2005). Other water-soluble components that may be transferred from the slab (aside from Fe^{3+}, Mn^{4+}, S^{6+}, and C^{4+}; Richards, 2015, and references therein), include Be, B, Rb, Cs, Sr, Ba, light rare earth elements (LREE; e.g., Ce, La, Nd), Pb, Th and U (Kessel et al., 2005). Chlorine is another key

water-soluble component – particularly affecting metal transport in hydrothermal fluids (Section 2.5) – and is relatively enriched in primary arc magmas (compared to mid-ocean ridge basalts; MORB) owing to contributions from the subducting slab (Wallace, 2005).

In contrast to the evidence supporting the involvement of slab components, it has been shown that the Cu in primary arc basalts and MORB – produced by decompression melting of the mantle, in the absence of fluids – are identical, suggesting that they share similar oxidation states (Lee et al., 2012). This, and other geochemical evidence (Zn/Fe systematics of primary arc basalts, which are also identical to MORB signatures; Lee et al., 2010), has led some researchers to propose that primary magmas are not particularly oxidised, or enriched in Cu, with the implication being that the subducting slab does not supply oxidising components, or Cu, to primary arc magmas (Lee et al., 2010, 2012). Despite this, 'normal' primary arc basalts may have different characteristics to the primary magmas that eventually end up forming porphyry deposits, the latter, as outlined above, possibly requiring a high oxidation state to incorporate larger quantities of metals, which would help to account for their scarcity (Park et al., 2021).

If there is little involvement of subducting slab components during primary magma generation, then the essential ore-forming components, S, Cu, and Au, must largely come from the mantle wedge. Indeed, mantle sulphide phases are overwhelmingly proposed to be the dominant source of S, Cu, and Au in primary arc magmas, regardless of slab involvement (e.g., Audetat and Simon, 2012). These phases may be sulphide liquids, or crystalline sulphides (largely monosulphide solid solution, MSS; Audetat and Simon, 2012). Experimental studies of metal partitioning between sulphide liquid, MSS, and primary silicate melts at conditions representative of mantle partial melting have found that Cu and Au both partition strongly into sulphide liquid and MSS relative to silicate melts (Li and Audétat, 2012; Botcharnikov et al., 2013). However, Au is modelled to have a $\sim$10 times lower partition coefficient for MSS over sulphide liquid compared to Cu, indicating that when mantle sulphides are dominantly MSS, the primary magmas dissolving these will have lower Cu/Au ratios than the primary magmas produced by the melting of mantle with sulphide liquid as the dominant sulphide phase, because Au is more easily liberated from the melting of MSS compared to sulphide liquid (Li and Audétat, 2012; Botcharnikov et al., 2013).

Similarly low Cu/Au ratios may still be achieved from the melting of a sulphide liquid-dominated mantle, but only when all the sulphide liquid is dissolved, because the last fraction of sulphide liquid will be highly enriched in Au (Botcharnikov et al., 2013). With increasing degrees of partial melting of MSS-dominated mantle, primary magmas will attain higher Cu/Au ratios because more Cu is liberated from MSS relative

to Au, suggesting that Au-rich primary magmas may be achieved by low degrees of partial melting of MSS-dominated mantle (Li and Audétat, 2012; Botcharnikov et al., 2013). Meanwhile, Au-Cu-rich primary magmas may require a high degree of partial melting to completely exhaust mantle sulphide reserves, or, if the magma is sufficiently oxidising, and thus able to accumulate higher concentrations of S, low-degree partial melts could be similarly effective (Botcharnikov et al., 2013; Sun et al., 2017). However, experimental studies have indicated that Au concentrations in the magma depend on the amount of dissolved sulphide, as Au is predominantly dissolved in the melt as a sulphide species, whereas Cu is predominantly dissolved as an oxide species (Botcharnikov et al., 2011; Zajacz et al., 2012). Accordingly, the solubility of Au in a magma at a high fO_2 (e.g., $>\Delta$FMQ +2), when most of the S is present as sulphate, may be markedly reduced when compared to a moderately oxidised magma (e.g., $\sim\Delta$FMQ +1; Botcharnikov et al., 2011). A high fO_2 ($>\Delta$FMQ +2) might therefore be considered optimal during primary magma generation for the production of Cu-rich porphyry deposits (Sun et al., 2015), whereas Au-rich deposits may be unlikely to form from highly oxidised magmas where sulphate dominates, instead requiring moderately oxidising conditions ($\sim\Delta$FMQ +1) under which the highest concentrations of dissolved sulphide can accumulate in the melt (Botcharnikov et al., 2011; Li et al., 2019). The oxidation state of the magma, and the nature and abundance of mantle sulphide phases, are thus critical factors affecting the Cu and Au endowment and Cu/Au ratios of primary magmas, but it is not clear if primary magmas achieve metal enrichment, and if the metal endowments and ratios acquired at this stage are transferred to related porphyry deposits.

In summary, debate continues over both the nature of primary arc magmas associated with porphyry deposits – highly oxidised, metal-rich, or not? – and also the source of magma components, i.e., does the subducting slab contribute magma components, and if so, by melts, fluids, or supercritical liquids? Nevertheless, understanding the possible generation mechanisms and the source of components for primary magmas is valuable as this is the ultimate start point for porphyry deposit generation. If deposit components or characteristics are not acquired at this stage in magmatic-hydrothermal system evolution, then they must be acquired at later stages. Furthermore, primary magma components must be effectively transported from the mantle to the upper crust, such that they eventually reside in a porphyry deposit.

2.3.2 Magmatic differentiation

Following partial melting, the relatively buoyant primary arc magmas rise towards the crust. Ascension typically stalls as the magmas approach neutral buoyancy around the

crust-mantle boundary, because the crustal rocks are more dense than the mantle melts (e.g., Thybo and Artemieva, 2013). This stalling is known as underplating, and may be overcome by magma differentiation (Figure 2.1; Thybo and Artemieva, 2013). Primary magmas may alternatively intrude into the lower to mid crust before stalling, if the tectonic environment permits (Annen et al., 2006). Traditional models propose that repeated injections of mantle-derived basaltic magmas may recharge magma chambers, and that fractional crystallisation of stable mineral phases occurs; elements compatible in these minerals are preferentially extracted from the magma, potentially reducing their abundance, while incompatible elements remain in the residual melt and may become relatively enriched (Hildreth and Moorbath, 1988; Hedenquist and Lowenstern, 1994; Annen et al., 2006). Meanwhile, the progressive assimilation and partial melting of crustal rocks, followed by the mixing of crustal and residual mantle melts, produces more evolved, hydrous, and silica-rich (commonly andesitic) magmas that periodically discharge from the magma chambers to rise through the crust (Hildreth and Moorbath, 1988; Annen et al., 2006). These evolved magmas experience further differentiation during their ascent – particularly if they stall again – and there is the possibility of multiple magma chambers experiencing differentiation at different levels in the crust (Annen et al., 2006). Vertically extensive magmatic systems that span the depth of the crust (i.e., trans-crustal) have also recently been proposed, in contrast to the traditional models that support magma chamber formation in the lower to mid-crust (Cashman et al., 2017). The impact of the trans-crustal model on the porphyry ore potential during magmatic differentiation is not yet understood, although there are implications for later magmatic-hydrothermal processes (Section 2.5; Blundy et al., 2021). For ease of discussion in this section, differentiation is assumed to take place in magma chambers as per traditional models. Numerous factors can affect the porphyry ore potential at the differentiation stage in magma evolution, and these are discussed here. Some of the key processes outlined above, and discussed below, are illustrated in Figure 2.3.

The oxidation state of magmas undergoing differentiation is a key consideration, given the effect fO_2 has on the behaviour of S, Cu, and Au (Section 2.3.1). As previously discussed, it is not yet clear whether the primary magmas involved in differentation are particularly oxidised, though a high fO_2 in primary magmas (ΔFMQ +1 to +2) would likely be more favourable for the formation of porphyry deposits, and the magmatic intrusions intrinsic to porphyry deposit formation are known to be characteristically oxidised (Sillitoe, 2010; Sun et al., 2015). Differentiation processes can elevate the oxidation state of the magma to the necessary levels, as seen in geochemical data from arc igneous rocks (Lee et al., 2010; Richards, 2015). This may be achieved through the fractionation

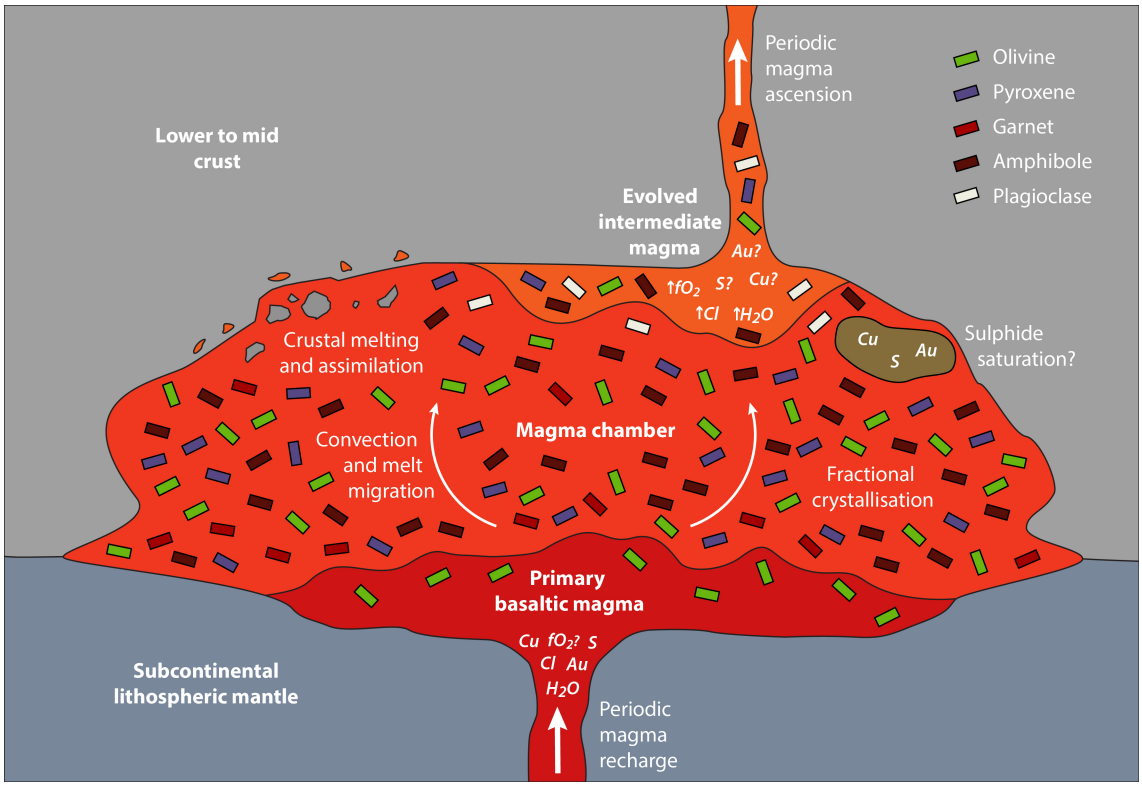

Figure 2.3. Schematic diagram of magmatic differentiation processes that affect the porphyry ore potential of magmas (modified after Wilkinson, 2013; Blundy et al., 2021). This field of view is situated around the 2.3.2 label in Figure 2.1.

of stable mineral phases (e.g., olivine) that increase the relative abundance of oxidising agents (e.g., Fe^{3+}) in the magma, the assimilation of oxidised crustal rocks, and/or devolatilisation processes; although the latter are more impactful at shallower depths (i.e., later stages; Lee et al., 2010; Richards, 2015; Sun et al., 2015). Equally, arc magmas may become more reduced during differentiation, through the fractionation of stable mineral phases that sequester oxidising agents (e.g., magnetite; Jenner et al., 2010), and the assimilation of reduced crustal rocks (e.g., graphitic rocks; Sun et al., 2015); although such magmas are unlikely to ever to porphyry deposits. Suffice to say that oxidation during differentiation must occur in porphyry-forming magmas if they were not previously oxidised to appropriate levels (i.e., ΔFMQ +1 to +2).

It has recently been proposed that an overarching control on the nature and genesis of porphyry deposits is the thickness of the crust (Park et al., 2021), building on previous research that identified associations between crustal thickness and porphyry deposit abundance (Cooke et al., 2005; Sillitoe, 2010), and the characteristics and evolution of porphyry-forming magmas (e.g., Chiaradia, 2014; Chiaradia and Caricchi, 2017; Lee and Tang, 2020). This is because crustal thickness directly or indirectly affects: the depth of differentiation; the duration of magmatic activity in the differentiation zone; the water content of the magma; the timing, likelihood, and scale of sulphide saturation in the

Table 2.1
Differences in magma differentiation and magma characteristics between magmas evolving under thick and thin crust. Note that most variables are stated as relative differences between thick and thin crust. See text for discussion.

Variable	Thick crust (>40 km)	Thin crust (<40 km)
Tectonic setting	Continental arc, active subduction, compression	Island arc, post-subduction, extension
Depth of differentiation	Deep	Shallow
Duration of differentiation	Long-lived	Short-lived
Volume of magma	High	Low
Fractionation	Amphibole ± garnet-dominant	Plagioclase and amphibole-dominant
Sulphide saturation	Early	Late
Fe-depletion	Early	Late
Magma metal enrichment	Moderate Cu, Au-poor	High Cu and Au
Magma water content	High	Low
Magma Sr/Y ratio	High (∼40-160)	Moderate (∼30-80)

magma; the mineral phases that fractionate from the magma; its Cu and Au endowment; as well as the emplacement depth of shallow-level porphyry intrusions (Section 2.3.3), and later hydrothermal processes (Section 2.5; Chiaradia, 2014; Chiaradia and Caricchi, 2017; Lee and Tang, 2020; Park et al., 2021). These factors are clearly interlinked to varying degrees. A summary of the key differences in magma differentiation and magma characteristics between magmas evolving under thick (>40 km) and thin (<40 km) crust is shown in Table 2.1.

The depth at which differentiation takes place should vary according to crustal thickness, with primary magmas at the base of thick crust experiencing differentiation at greater depths than those at the base of thin crust; however, differentiation depth also depends on whether primary magmas stall at the base of the crust, or intrude into the lower to mid crust (Annen et al., 2006; Lee and Tang, 2020; Park et al., 2021). Nevertheless, thick crust encourages deeper differentiation depths, even if primary magmas intrude into the lower to mid crust. This can be seen in geochemical data from arc igneous rocks, which show that a generally greater and more rapid Fe-depletion occurs during the differentiation of magmas under thick crust relative to thin crust, owing to the earlier crystallisation of amphibole, garnet, and/or magnetite, and the later crystallisation of plagioclase; a result of the higher pressures at greater depths (Chiaradia, 2014; Loucks, 2014; Lee and Tang, 2020). The degree of differentiation in arc igneous rocks is represented by MgO

contents, because MgO is most compatible in the early-fractionating minerals that are then retained in the lower to mid crust as cumulates, and so more evolved magmas will exhibit lower MgO concentrations (e.g., Richards, 2015).

Iron-depletion not only influences the geochemical signature of the magma (producing a calc-alkaline trend), but also decreases the solubility of S (O'Neill and Mavrogenes, 2002; Zimmer et al., 2010). While the behaviour of S in silicate melts is primarily a function of fO_2 (e.g., Jugo et al., 2010), the variability of magma differentiation compared to partial melting in the mantle means that additional parameters must also be considered. Temperature, pressure, and the composition of the silicate melt can additionally influence the solubility of S, with S solubility decreasing with decreasing temperature, increasing pressure, and decreasing Fe content (O'Neill and Mavrogenes, 2002). Experimental work shows that Fe content could have a dominant control on the solubility of S (O'Neill and Mavrogenes, 2002), thus the timing and extent of Fe-depletion would become a crucial factor for the porphyry ore potential. Indeed, Park et al. (2021) propose that the earlier Fe-depletion under thick crust causes earlier sulphide saturation, resulting in more signficiant S and chalcophile metal depletion in magmas differentiating under thick crust compared to thin crust.

A key question that arises is whether amphibole-, garnet-, or magnetite-dominant crystallisation is responsible for Fe-depletion in arc igneous rocks, because each would have a different effect on the magma characteristics, and by extension, the porphyry ore potential. Combined with the suppression of plagioclase crystallisation, early amphibole-dominant fractionation is frequently proposed to account for the enhanced Fe-depletion in porphyry-forming magmas, because the high water contents and fO_2 of differentiating arc magmas stabilises amphibole (e.g., Zimmer et al., 2010; Loucks, 2014). Magnetite-dominant fractionation may also account for Fe-depletion in arc rocks, but it has been suggested that magnetite fractionation also coincides with abrupt sulphide saturation and chalcophile metal depletion, caused by reduction of the magma via the preferential incorporation of Fe^{3+} over Fe^{2+} in magnetite (Jenner et al., 2010). However, others have noted that arc magmas tend to become more oxidised during differentiation, and evolve to higher Fe^{3+}/Fe^{2+} ratios, and that "pure" magnetite occurs relatively late in the crystallisation sequence (Richards, 2015; Lee and Tang, 2020). This throws the influence of magnetite fractionation on Fe content into uncertainty.

Alternatively, Lee and Tang (2020) propose garnet-dominant fractionation as a key process for porphyry formation in magmas differentiating under thick crust where garnet is stable, because garnet crystallisation causes Fe-depletion. This promotes sulphide saturation and chalcophile metal depletion, but this effect is then counteracted by auto-

oxidation; where garnet crystallisation increases the Fe^{3+}/Fe^{2+} ratio of the magma – increasing the fO_2 – and allows more S and chalcophile metals to be dissolved in the magma (Lee and Tang, 2020). In summary, Fe-depletion during differentiation is most likely caused by amphibole-dominant fractionation, while garnet fractionation could feasibly be involved under thick crust, leading to more oxidised and fertile magmas; however, further investigation is needed.

Another geochemical signature, Sr/Y ratio, is attributed to the differential fractionation of amphibole and/or garnet, and plagioclase, because the former sequester Y, and the latter Sr (Loucks, 2014). Therefore, the thick crust crystallisation sequence outlined above can also account for the high Sr/Y ratios (>35) characteristic of porphyry intrusions (Loucks, 2014); indeed, a correlation between the highest Sr/Y ratios and intrusions formed under thick crust has been recognised (Lee and Tang, 2020; Park et al., 2021). However, porphyry intrusions formed under thin crust also exhibit moderately elevated Sr/Y ratios compared to barren intrusions (Loucks, 2014; Park et al., 2021), which requires a different explanation. Elevated Sr/Y ratios may also arise during primary magma generation, as a result of delayed plagioclase crystallisation owing to high melt water contents (Section 2.3.1; Williamson et al., 2016), and so it remains unclear whether this geochemical signature truly records differentiation processes.

The magma chambers where differentiation takes place are more likely to be longer-lived under thick crust, because the higher temperature of the surrounding rock at greater depths slows the cooling process (Annen et al., 2006; Loucks, 2014; Chiaradia and Caricchi, 2017). Deep and long-lived magma chambers are able to accumulate higher water contents than shallow and short-lived chambers, owing to greater water solubility at higher pressures (greater depths) in a silicate melt (Burnham, 1979), and an overall more voluminous input of mantle-derived magma into a long-lived compared to a short-lived magma chamber (Chiaradia and Caricchi, 2017). Fractional crystallisation of the primary mantle-derived magma enriches the residual melt in water, even when hydrous minerals (e.g., amphibole) crystallise (Annen et al., 2006); therefore, a greater overall input of primary magma allows for greater water enrichment in the evolved magmas, up to the point at which they become saturated, which as already noted, is higher in deep magma chambers (Lee et al., 2014). Water enrichment in porphyry-forming magmas is necessary because water is an essential component of the hydrothermal fluids that exsolve from the magma during emplacement in the upper crust, where the fluids transport and deposit metals to form porphyry deposits (Section 2.5). Petrological and geochemical modelling has shown that more water in an evolved magma allows for a greater flux of hydrothermal fluids in the upper crust (i.e., longer-lived hydrothermal systems), corresponding

to the formation of larger porphyry deposits (higher Cu tonnages), when assuming an adequate supply of Cu from the magma (Chiaradia and Caricchi, 2017). Consequently, while water enrichment occurs to some degree during primary magma generation (with water originating from the subducting slab), it is at the differentiation stage that evolved magmas can become particularly hydrous, which contributes to an increased porphyry ore potential.

The deep, long-lived magma chambers that are more likely under thick crust should also have a greater potential to accumulate Cu and Au – which are incompatible in the fractionating minerals – owing to a greater overall input of primary magma (e.g., Lee et al., 2014). However, a well-known conundrum is that arc magmas become relatively depleted in Cu during differentiation, with the Cu contents of arc rocks largely decreasing in line with decreasing MgO contents (e.g., Lee et al., 2012; Chiaradia, 2014). Depletion in Cu is attributed to the onset of sulphide saturation, where sulphide phases separate from the magma and eventually form cumulates rich in Cu (Lee et al., 2012). Some researchers suggest that these Cu-rich cumulates must be remelted by later S-undersaturated magmas in order for porphyry-forming magmas to accumulate enough Cu to form a deposit (Lee et al., 2012; Chiaradia, 2014). Conflictingly, others have suggested that the reworking of Cu-rich cumulates is not a critical step (Richards, 2015; Lee and Tang, 2020; Park et al., 2021), not least because it has been shown that particularly Cu-rich magmas are not required to form porphyry deposits (Cline and Bodnar, 1991; Chelle-Michou et al., 2017), but also because the Cu-rich cumulates are likely to delaminate into the mantle (Chen et al., 2020), contrary to the proposals of re-melting by later magmas. Alternative models instead highlight the importance of the duration of the magmatic-hydrothermal system (Chiaradia and Caricchi, 2017; Chiaradia, 2020; Park et al., 2021), rather than the concentration of Cu in the magma and whether or not sulphide saturation occurs. Nevertheless, it is clear that sulphide saturation plays a role in the enrichment of Cu in the differentiating magma, and more Cu-enriched magmas should be more likely to form porphyry deposits.

The behaviour of Au is expected to be largely similar to that of Cu in a magma that does not experience sulphide saturation; both metals are retained in the magma, and will increase in concentration with increasing S content if sulphide phases remain dissolved. This scenario should be most favourable for the formation of porphyry deposits. Conversely, extensive sulphide saturation is catastrophic for the Cu and Au fertility of the magma, making it unlikely to be suitable for porphyry ore formation. When limited sulphide saturation occurs, the differential partitioning of Cu and Au between the magma and precipitating sulphide phases affects the Cu/Au ratio of the magma. Again,

crustal thickness is influential. Modelling based on the experimental study of chalcophile element partitioning between MSS, sulphide liquid, and hydrous silicate melt at conditions representative of magmatic differentiation suggests that, under thick continental crust (>30 km), precipitating sulphides are dominantly MSS (>80 %), while under thinner island arcs (<20 km), precipitating sulphides are liquid-dominated (50-90%; Li et al., 2021). This would generally indicate that sulphide saturation under thick crust promotes a lower Cu/Au ratio, because Cu more strongly partitions into MSS over silicate melt than Au, while sulphide saturation under thin crust results in a higher Cu/Au ratio, given that Au more strongly partitions into sulphide liquid over silicate melt compared to Cu (Li et al., 2021). However, this does not take into account the timing of sulphide saturation.

Magmas emplaced under thick crust experience earlier sulphide saturation compared to those emplaced under thin crust, recognised from the Cu depletion trends in arc rocks during differentiation (MgO contents), because S solubility is reduced at the higher pressures and lower Fe contents of magmas under thick crust (Chiaradia, 2014; Lee and Tang, 2020; Park et al., 2021). Consequently, magmas that differentiate under thick crust should have lower concentrations of Cu and Au, evolving to higher Cu/Au ratios, because the earlier saturation of sulphide (largely as MSS) allows for a greater extraction of metals, with Au becoming more depleted because it is present in the magma at much lower concentrations than Cu (Li et al., 2021), but only has a slightly lower partition coefficient for MSS over silicate melt compared to Cu. Meanwhile, the late sulphide saturation under thin crust would mean that minimal Au and Cu would be lost to the sulphide liquid-dominated precipitates, with the majority of metals retained in the magma. The Cu/Au ratio of a magma differentiating under thin crust would thus be relatively unaffected by late sulphide saturation, although Au would more strongly partition into the sulphide liquid than Cu if significant sulphide saturation did occur. Some researchers hence propose that the timing of sulphide saturation ultimately accounts for the differences in metal endowment between Cu-rich (early sulphide saturation) and Au-Cu-rich (late sulphide saturation) porphyry deposits (Park et al., 2021). The latter would also be produced if no sulphide saturation occurred prior to ore formation.

In summary, the processes of magma differentiation exert fundamental controls on both the potential for porphyry ore formation, and the geochemical characteristics of a resultant porphyry deposit and related intrusive(s). Magmas become more felsic, hydrous and oxidised (if not already so), during differentiation. Furthermore, differences are evident between magmas differentiating under thick crust relative to thin crust, as highlighted in the model of Park et al. (2021). Thick crust differentiation results in deeper,

longer-lived magma chambers that experience a greater input of primary magma, allowing for greater accumulations of dissolved water, chalcophile metals, and S, with Fe-depletion and sulphide saturation occurring earlier, resulting in large volumes of Au-depleted and moderately Cu-enriched magmas rising through the crust. The fractionation of garnet under thick crust may be crucial for allowing magmas to transport adequate quantities of Cu for the formation of large, Cu-rich porphyry deposits (Lee and Tang, 2020). Conversely, thin crust differentiation results in shallower, shorter-lived magma chambers that experience a lower input of primary magma, meaning that dissolved water, chalcophile metals, and S are present at lower concentrations. However, because Fe-depletion and sulphide saturation occur later in magmas differentiating under thin crust, the concentrations of Cu and Au are largely retained, allowing for the formation of smaller, Au-Cu-rich porphyry deposits if later magmatic-hydrothermal processes are favourable.

2.3.3 Magma emplacement in the upper crust

Evolved arc magmas rise to shallower levels, where they accumulate in upper crustal chambers at depths of 5-15 km (Figure 2.1; Sillitoe, 2010). For a porphyry deposit to form, magmas must then intrude into the roof of the chamber and generate a finger-like stock, typically extending to depths of 2-4 km, into and around which the metals contained within the magma may be extracted and deposited by hydrothermal fluids to form an ore deposit (Sillitoe, 2010; Richards, 2011). These final steps in the formation of a porphyry deposit, from a magmatic perspective, depend on multiple factors and processes, which are discussed here, and illustrated in Figure 2.4. The hydrothermal processes, while relevant to this discussion, are considered in detail in Section 2.5.

Large-scale arc-parallel or arc-transverse fault systems or lineaments that pre-exist or are coincident with magmatism are thought to play an important role in the ascent and localisation of magmas associated with porphyry deposits, acting as conduits for the magmas to exploit and ascend (Corbett and Leach, 1998; Sillitoe, 2010). Specifically, intersections between arc-parallel and arc-transverse structures are proposed to be an important localiser, with these dilational structural settings encouraging magma ascent (e.g., Richards et al., 2001). While structural features offer clear pathways for magma ascent, not all porphyry deposits show a close association to major structures, and in these cases there may not even be proximity to minor structures (Sillitoe, 2000). More generally for arc magmatic systems, it has been proposed that the principal control on distribution is the stress regime affecting the overriding plate during subduction, based on a spatial analysis of volcano distribution in the Mariana Arc (Andikagumi et al., 2020). Pre-

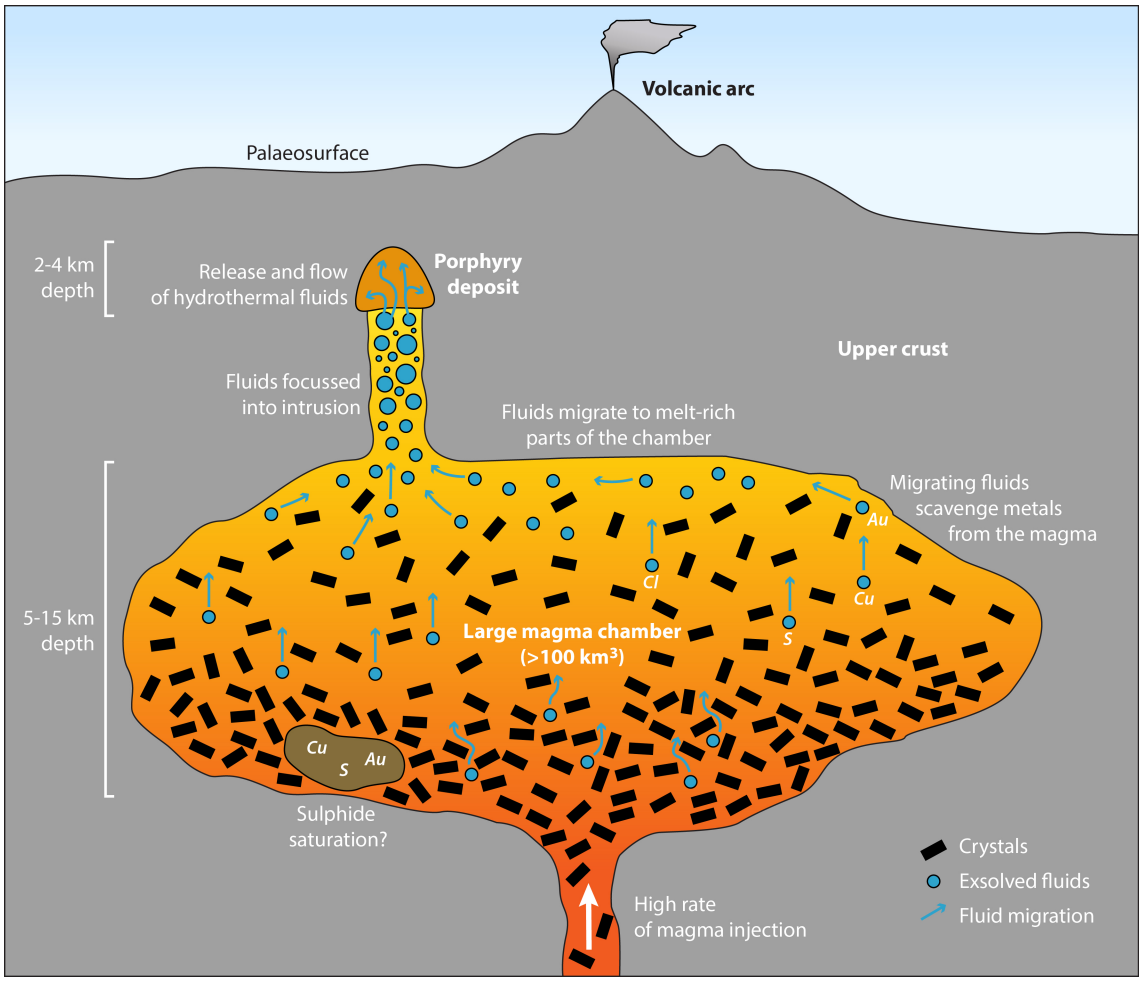

Figure 2.4. Schematic diagram of a shallow magma chamber generating a porphyry deposit (modified after Wilkinson, 2013; Edmonds and Woods, 2018; Blundy et al., 2021). See text for discussion. This field of view is situated around the 2.3.3 label in Figure 2.1.

existing structures may play a role where present, but the key suggestion is that tensile stress in the deep upper plate during subduction is the primary mechanism that controls volcano distribution, by generating the pathways for magma ascent (Andikagumi et al., 2020). This theory may also be applied to magma ascension related to porphyry deposit formation, as porphyry deposits can be considered as failed volcanic eruptions, owing to the comparable volumes of magma and injection rates involved in the formation of both shallow magma chambers associated with porphyry deposits and those associated with volcanic eruptions (Chiaradia and Caricchi, 2022). Therefore, it is possible that pathways generated in the deep upper plate dominantly control the distribution of porphyry intrusions, and these pathways may or may not be expressed or preserved as structures at surface.

One of the most critical changes for evolved, porphyry-forming magmas ascending to upper crustal chambers is a reduction in pressure. Water solubility is strongly controlled by pressure, reducing at lower pressures, thus magmas will become saturated in water

at shallower depths and exsolve a water-rich fluid – termed "first boiling" (Burnham, 1979). Crystallisation of a magma may also induce water saturation and fluid exsolution – termed "second boiling" – owing to temperature reductions, which progresses the fractional crystallisation of water-poor minerals (Burnham, 1979). The vast majority of hydrothermal fluids in porphyry systems are generated by first and second boiling processes; meteoric waters may have minor involvement in some cases (Section 2.5).

Hydrothermal fluid exsolution additionally depends on the composition of the magma and assimilated crustal rocks (in particular the amount of contained water in both), the crystal-melt ratio of the magma, the magma emplacement rate, and the volume of magma, because these factors affect the first and second boiling processes (Chiaradia and Caricchi, 2017). It is a requirement that porphyry-forming magmas contain enough water (e.g., 2-6 wt.% H_2O; Richards, 2015) to exsolve sufficient quantities of fluids to form an ore deposit. Magmas close to water-saturation prior to emplacement will require less change than magmas more undersaturated in water to exsolve a water-rich fluid, for example, a minor reduction in pressure may suffice for the former, whereas the latter would require a greater pressure reduction, leading to fluid exsolution (first boiling) at shallower depths. The crystallinity of the magma is also of importance, because magmas with higher melt-crystal ratios may dissolve more water before saturation than magmas with lower melt-crystal ratios, depending on their composition. The last two factors – magma emplacement rate and magma volume – are particularly important in controlling fluid exsolution related to porphyry deposit formation; multiple studies propose that these factors may be linked to the size of a porphyry deposit, and ultimately control whether or not a deposit forms at all (Chiaradia and Caricchi, 2017; Chelle-Michou et al., 2017; Schöpa et al., 2017; Chiaradia and Caricchi, 2022).

High rates of emplacement are considered necessary for the generation of porphyry-forming upper crustal chambers, in contrast to the lower rates of emplacement linked to the formation of unmineralised plutons (Schöpa et al., 2017). A key reason high emplacement rates are required is because higher temperatures may be maintained for longer when compared to slower rates of emplacement, assuming the magma and crustal rock characteristics are the same. Magma volume is clearly involved too, with large volumes of magma (1000s km^3; Schöpa et al., 2017) able to sustain higher temperatures compared to smaller volumes. The most favourable scenario would therefore involve large magma volumes at high rates of emplacement (Chiaradia and Caricchi, 2022). Higher temperatures preserve the molten state of the magma for longer. This is important, because the current model of porphyry formation necessitates the interaction of exsolved hydrothermal fluids with large volumes of magma (i.e., in the upper crustal chamber), in order

to extract adequate quantities of metals (e.g., Sillitoe, 2010). Fluids are thought to be exsolved as bubbles, which then migrate upwards towards the chamber roof – accumulating metals as they go – owing to their affinity for melt-rich parts of the chamber, and their efficient migration through the crystal-rich parts (e.g., Parmigiani et al., 2016). Importantly, exsolved fluids must then be focussed into the finger-like stock in the chamber roof, which acts as an "exhaust valve" to the magma chamber, otherwise ore deposition will be dispersed over a large region (Sillitoe, 2010; Richards, 2018). It therefore stands to reason that a porphyry deposit cannot form if there is an insufficient volume of magma available for exsolved fluids to interact with.

If small volumes of magma are emplaced at slow rates, the magma is likely to cool and crystallise before a magma chamber can form, or at least when the volumes of magma in a chamber are relatively small (Schöpa et al., 2017). This means that fluid exsolution will occur almost entirely during the emplacement process, with fluid fluxes relatively low because the volumes of magma emplaced at any one time are low (Chelle-Michou et al., 2017; Schöpa et al., 2017). The porphyry ore potential here would accordingly be low, because there is only a small magma volume for the fluids to extract metals from. It is additionally possible that the fluids would not be focussed into a finger-like stock, instead dispersing into the cooled intrusion or crustal rocks, because there is no continuously present "exhaust valve", owing to the lack of a significant magma chamber (Schöpa et al., 2017). If large volumes of magma are emplaced at high rates, fluid exsolution would again occur during emplacement, but the flux of fluids would be higher because the volumes of magma involved are higher (Chelle-Michou et al., 2017; Schöpa et al., 2017). Furthermore, there would be increasing volumes of magma available for the exsolved fluids to interact with during the formation of a large magma chamber, and fluid exsolution would continue after emplacement has ceased owing to the time required for cooling and crystallisation of the large chamber (Chelle-Michou et al., 2017; Schöpa et al., 2017). Large magma volumes produced in the deeper crust during differentiation (linked to differentiation under thick crust; Section 2.3.2) are considered essential for both sourcing enough magma to produce large magma chambers in the shallow crust, and preventing the eruption of the magma that could be expected for rapid rates of magma emplacement in the shallow crust; eruptions are detrimental to porphyry ore formation (Chiaradia and Caricchi, 2022). Thus, it appears likely that porphyry deposits preferably form from large upper crustal magma chambers generated by high rates of magma emplacement.

Sulphide saturation may be an important process in porphyry-forming upper crustal magma chambers. While separation of sulphide phases has previously been shown to be detrimental, but not necessarily inhibiting, to porphyry ore formation during magma dif-

ferentiation, it is conversely possible that sulphide saturation in an upper crustal chamber could be influential in generating a porphyry deposit (e.g., Wilkinson, 2013). This is because separated sulphide phases in an upper crustal chamber could be available for interaction with exsolved hydrothermal fluids (Nadeau et al., 2010; Wilkinson, 2013), unlike the sulphides sequestered in the lower crust during differentiation. Evidence for sulphide liquid and hydrothermal fluid interaction comes from the observation of variably dissolved sulphide melt inclusions in contact with bubbles previously containing hydrothermal fluid, in samples of scoria from Merapi Volcano, Indonesia (Nadeau et al., 2010). Furthermore, the particularly high metal contents of ore-forming fluids in some porphyry deposits have been proposed to result from interaction with sulphide liquids (Wilkinson, 2013). If interaction does occur, the pre-enrichment of metals and S in the separated sulphides should also negate the need for exsolved fluids to interact with large volumes of magma, hence sulphide saturation could be particularly influential where magma volumes are low during fluid exsolution, such as when magma emplacement rates are slow. Alternatively, a sudden trigger, such as the injection of a sulphide-saturated mafic magma into an upper crustal chamber comprised of an oxidised felsic magma may initiate the interaction of sulphide liquid and exsolved hydrothermal fluid, as is proposed at Merapi Volcano (Nadeau et al., 2010). Nevertheless, evidence for upper crustal sulphide saturation is limited at present, and particularly so for the formation of porphyry deposits; hence, further study is required.

In summary, the location of arc magma emplacement in the upper crust principally depends on the structural setting of the crust, likely derived from the stress regime affecting the upper plate during subduction. Meanwhile, the formation of an upper crustal magma chamber favourable for porphyry deposit formation requires the emplacement of large volumes of evolved, water-rich magma, at high rates of injection. Exsolution of hydrothermal fluids from the magma takes place principally owing to pressure reductions (i.e., during emplacement), and temperature reductions that cause increased fractional crystallisation (i.e., during incubation). The fluids migrate up through the chamber and extract metals from the magma. It is not yet clear whether sulphide saturation is an important process in this environment. A porphyry intrusion, rising from the roof of the magma chamber, must form to channel the exsolved metal-bearing fluids to shallower levels where they can precipitate their metals as ore.

2.3.4 Magmatic characteristics of porphyry deposits

Porphyry deposits are intrinsically derived from porphyritic intrusions with intermediate to felsic compositions, with mineralisation located in and around the magmatic bodies

(Sillitoe, 2010). The porphyritic rocks have abundant phenocrysts of between 35-55% in terms of volume, and fine-grained groundmass textures (Seedorff et al., 2005). Aplitic textures are often reported (Seedorff et al., 2005), indicating rapid, decompression-induced crystallisation took place, which some authors relate to sudden events, such as the collapse of a volcanic edifice (Richards, 2018). Phenocrysts of plagioclase, hornblende, biotite, K-feldspar, and quartz are frequently observed, with mineral proportions dependent on the rock composition (Seedorff et al., 2005). As previously mentioned, the intrusions are typically emplaced at depths of 2-4 km, but in some cases may have reached depth extremes of 1 km (e.g., Kisladag, Turkey; Baker et al., 2016) and 9 km (e.g., Butte, Montana, USA; Rusk et al., 2004). Intrusion depth may be linked to the thickness of the crust under which the magmas evolved, with magmas evolving under thicker crust generating deeper intrusions, and vice versa for magmas evolving under thin crust (Section 2.3.2; Chiaradia, 2020). In particular, long-lasting periods of compression (i.e., lacking extensional interludes from slab rollback, for example) are proposed to generate porphyry intrusions at greater depths (Park et al., 2021).

Intrusions vary considerably in form, from stocks (e.g., Bingham Canyon, Utah, USA; Porter et al., 2012) to dyke swarms (e.g., Cadia East, New South Wales, Australia; Wilson, 2003), and size (e.g., a 2 km^2 exposure at Bingham Canyon, and dyke widths reaching up to $\sim$50 m in drill core at Cadia East). The distribution – but not the volume – of mineralisation varies according to intrusion morphology, owing to the flow dynamics of exsolved hydrothermal fluids (Section 2.5; Sillitoe, 2010). Furthermore, porphyry deposits are characterised by multiple intrusive phases, only some of which may be synchronous with, and thus likely causative to, the mineralisation (i.e., syn-mineralisation; Sillitoe, 2010). For example, the intrusive suite at the Altar porphyry deposit, Argentina, consists of one pre-mineralisation porphyry, three syn-mineralisation porphyries, and two post-mineralisation intrusions (Maydagán et al., 2014). The episodic emplacement of variably mineralised intrusions shows that upper crustal magma chambers are active before and after mineralising events, and the age of intrusions provides constraints to the lifespan of shallow magmatism sourced from the magma chamber, and specifically to the duration of the ore-forming magmatic-hydrothermal system. Using the Altar example, all intrusions were emplaced over a period of $\sim$2.85 m.y., with the syn-mineralisation intrusions emplaced within $\sim$0.7 to 1.3 m.y. (from U-Pb ages in zircons; Maydagán et al., 2014). This is in line with the findings of a review of geochronological studies of porphyry systems, where it is stressed that the likely duration of hydrothermal systems initiated by porphyry intrusions is 10's k.y., but that multiple syn-mineralisation intrusions may extend the overall duration of the mineralising systems up to $\sim$2 m.y. (Chiaradia et al., 2013).

Breccia bodies up to 100's m in diameter are often observed in and around porphyry deposits, and may be ore-bearing to varying degrees (Sillitoe, 2010). Multiple classification schemes exist to define breccias in porphyry deposits (e.g., Sillitoe, 1985; Jebrak, 1997; Corbett and Leach, 1998; Sillitoe, 2010), although none adequately account for the wide range of breccia characteristics; indeed, deposit-scale studies typically assign their own classification schemes (e.g., Micko et al., 2014; Wang et al., 2020). Perhaps this is not surprising, given that breccia characteristics to consider include: position in the system, size, morphology, clast characteristics (i.e., composition, size, morphology), matrix (and/or cement) characteristics (i.e., composition, grain size), proportion of clast to matrix, alteration, and mineralisation. Moreover, Sillitoe (1985) notes that there is inherent ambiguity in breccia classification, because a continuum exists between different types of breccia.

Nevertheless, the most recent and widely-used classification scheme of Sillitoe (2010) (derived from that of Sillitoe, 1985) will be considered here. Three broad categories are defined, based on the inferred formation processes: magmatic-hydrothermal, phreatic, and phreatomagmatic. Magmatic-hydrothermal breccias are the most common in porphyry deposits, and are thought to form as a result of explosive hydrothermal fluid exsolution, typically from the apex of a porphyry intrusion, hence they are spatially associated with the intrusive phases and are contained in the sub-surface (Sillitoe, 1985; Corbett and Leach, 1998; Richards, 2018). Importantly, these breccias frequently host ore, with mineralisation interpreted to occur immediately after emplacement, in line with breccia formation from magmas exsolving hydrothermal fluids (Sillitoe, 1985). For fluid exsolution to be explosive, sudden depressurisation events (e.g., volcanic edifice collapse, mega-earthquakes, or movement on a controlling structure) or agitation of a primed magma chamber are thought to be required (Corbett and Leach, 1998; Richards, 2018). In addition, the size and abundance of magmatic-hydrothermal breccias may depend on the extent and abundance of dilational structural environments in the overlying crust; for example, mineralisation in the Huangtun porphyry deposit, China, is predominantly hosted in a up-to-200 m thick breccia pipe, generated at the intersection of two pre-existing faults (Wang et al., 2020).

Phreatomagmatic and phreatic breccias tend to be late relative to porphyry ore formation, and are likely to have extended to the palaeosurface (Corbett and Leach, 1998; Sillitoe, 2010). The former are generated by mixing of hydrothermal fluids and cooler meteoric waters, and the latter by depressurisation of geothermal waters (Corbett and Leach, 1998), hence their lateness. Both breccia types typically generate upward-flaring pipe-like geometries, with phreatomagmatic breccias constituting diatremes that com-

monly extend up to 2 km in depth (Sillitoe, 1985). Distinguishing between the three breccia types depends on a detailed analysis of the breccia characteristics outlined above, although Sillitoe (2010) highlights that magmatic-hydrothermal breccias lack tuffaceous material, unlike phreatomagmatic breccias, and phreatic breccias commonly form pebble dykes (i.e., polymict clasts set in a rock-flour matrix). Ultimately, the extent and distribution of alteration and mineralisation in all breccia types are of particular importance to recognise, as these features provide constraints to the timing of breccia formation relative to ore formation, and allows an assessment of whether breccias may be an important host for ore in a given deposit.

Porphyry deposits may be found as stand-alone occurrences, or be localised in a district; for example, five porphyry deposits are situated along a $\sim$6 km trend in the Cadia district, New South Wales, Australia (Wilson, 2003). Moreover, deposits tend to be regionally aligned in belts (e.g., the $>$1000 km long porphyry trend of the Andes, extending northwards from Santiago, Chile), clearly reflecting the geometry of the magmatic arcs from which they formed (Sillitoe, 2010). Within a district, geochronological studies have shown that mineralisation is confined to one or more ore-forming events that occur within constrained time periods, with a maximum time period for district formation of $\sim$18 m.y. for the deposits in the Cadia district (Wilson et al., 2007). This has led some researchers to suggest that a single upper crustal magma chamber may be capable of forming multiple porphyry deposits in different locations over time (Sillitoe, 2010). Similarly in a belt, porphyry deposits tend to be formed within mineralising epochs, such as that of the Canadian Cordillera, where many porphyry deposits preferentially formed during a $\sim$15 m.y. time period (Sillitoe, 2010; Logan and Mihalynuk, 2014). The time-constrained formation of multiple porphyry deposits in districts and belts indicates that arc magmatism was particularly favourable for porphyry deposit formation at certain points in time and space, although some researchers alternatively suggest that prospective areas mainly correspond to optimal erosional levels (Chelle-Michou et al., 2017).

2.4 Classification of porphyry deposits

There are multiple classification schemes used for porphyry deposits, and also different mineral deposit styles that may be related to porphyry intrusions. When investigating the formation of a porphyry deposit, it is essential to consider both because fundamental differences between deposits point toward differences in formation processes. Therefore, a given porphyry deposit should be considered in the context of different classification schemes, such that the results and conclusions of an investigation can be appropriately applied elsewhere; for example, an orogenic Au deposit study cannot be easily com-

pared to a volcanogenic massive sulphide deposit study, although certain aspects may be comparable. This section outlines the different schemes used to classify porphyry deposits, and the implications for formation processes. Mineral deposit styles associated with porphyry intrusions are also covered, such that they can be identified if present in conjunction with porphyry mineralisation.

2.4.1 Classification by metal enrichment

Copper, Au, and Mo are the main resources contained within porphyry deposits, and constitute the primary classification scheme from an economic perspective. One or more of these metals may be present to define the dominant resource and by-product (e.g., Cu-Au, Cu-Mo, Cu-Mo-Au; Sillitoe, 2010). As noted in Section 1, this research focusses primarily on the Au-rich deposit of Iron Cap. Gold-rich porphyry deposits also contain Cu as a by-product or as the dominant resource, but most usually lack significant amounts of Mo (Sillitoe, 2000), indicating that Mo-bearing deposits have a different formation history. Indeed, there appears to be no consensus for the source of Mo in porphyry deposits, with arguments for both a crustal source and a mantle origin seeming plausible, although mantle source theories often rely on post-subduction processes (Richards, 2011). This implies that the magmas forming the most Au-rich porphyry deposits either lack extensive crustal contamination, and/or are generated during active subduction.

Section 2.3 has highlighted numerous variables and magmatic processes that are influential in controlling the Cu and Au endowment of porphyry deposits. Hydrothermal activity additionally exerts controls on Cu and Au transport and deposit endowments, discussed in Section 2.5, below. In conjunction with these specific variables, various models and simulations have been developed in efforts to understand the overarching controls on Cu and Au endowments in porphyry deposits, which are considered below.

Figure 2.5 illustrates that the metal endowments of Cu-Au porphyry deposits define two discrete trends, based on whether a deposit is Cu-rich (Au/Cu ratio of $\sim$4 x 10^{-6}) or Au-rich (Au/Cu ratio of $\sim$80 x 10^{-6}; Chiaradia, 2020). Monte Carlo simulations, supported by geochronological data from Cu-Au porphyry deposits, show that Cu-endowment appears to be principally linked to the duration of the ore-forming process (Chiaradia and Caricchi, 2017; Chelle-Michou et al., 2017; Chiaradia, 2020). The emphasis on duration indicates that the impact of other variables, such as the Cu-endowment of the magmas, and the efficiency of Cu precipitation (i.e., the characteristics of the hydrothermal fluids), are of secondary importance; indeed, it has been shown that porphyry Cu deposits can form from a typical calc-alkaline arc magma with $\sim$50 ppm Cu, precipitated at 50% efficiency (i.e., 50% of the contained Cu in the magma ends up in the deposit; Cline

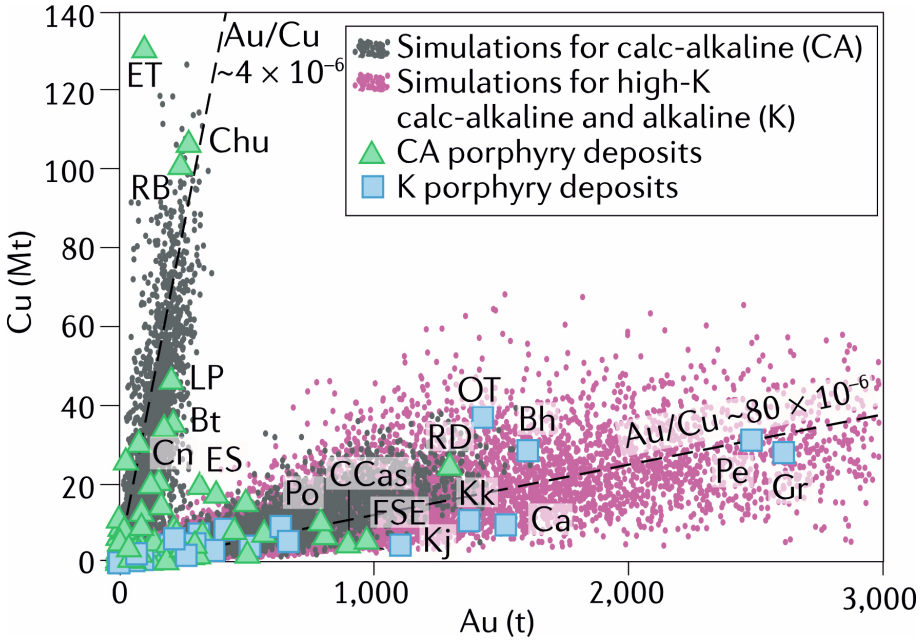

Figure 2.5. The metal endowments of Cu-Au porphyry deposits, showing two distinct trends that define Cu-rich and Au-rich deposits (Park et al., 2021, adapted from Chiaradia, 2020). Monte Carlo simulations that reproduce the Au-rich trend are differentiated from the Cu-rich trend by a higher Au precipitation efficiency; 12 times higher for the simulations of calc-alkaline (CA) systems, and 5 times higher for the simulations of high-K calc-alkaline and alkaline (K) systems. The Monte Carlo simulation parameters are described by Chiaradia (2020). Porphyry deposit abbreviations: Bh, Bingham; Bt, Butte; Ca, Cadia; CCas, Cerro Casale; Chu, Chuquicamata; Cn, Cananea; ES, El Salvador; ET, El Teniente; FSE, Far Southeast-Lepanto; Gr, Grasberg; Kj, Kadjaran; Kk, Kalmakyr; LP, Los Pelambres; OT, Oyu Tolgoi; Pe, Pebble; Po, Potrerillos; RB, Rio Blanco; RD, Reko Diq.

and Bodnar, 1991; Chelle-Michou et al., 2017; Chiaradia, 2020). Furthermore, Cu endowments of porphyry deposits appear to increase in line with the duration of ore formation, suggesting that the other variables (i.e., Cu precipitation efficiency and magma Cu content) are relatively consistent between different porphyry systems (Chiaradia, 2020). Following this logic, the most Cu-rich porphyry deposits (e.g., El Teniente, Chile) are principally the product of a long-lived magmatic-hydrothermal system. As discussed in Section 2.3.2, the duration of magmatic-hydrothermal activity is enhanced under thicker crust owing to the accumulation of greater volumes of magma and water, thus Cu-rich deposits should be more likely to form under thicker crust.

Comparatively, Au-endowment is thought to be dominantly controlled by precipitation efficiency, with a lesser influence from the duration of the ore-forming process, and the Au content of the magma (Murakami et al., 2010; Chiaradia, 2020). This is because the most Au-rich deposits are geochronologically determined to have a shorter ore-forming process (<0.5 M.y.) compared to the most Cu-rich deposits (<2 M.y.), yet can contain over five times more Au than the most Cu-rich deposits (Chiaradia, 2020). Variables such

as the Au-content of the magma and the partition coefficient of Au between fluid and melt cannot explain this discrepancy because arc magmas are thought to contain enough Au (e.g., 6-32 ppb) to form the most Au-rich deposits, and partition coefficients for Au between fluid and melt would have to be particularly low (i.e., <1) to generate Au-poor fluids to form the Cu-rich deposits (Chiaradia, 2020). Instead, Au is suggested to precipitate ∼5-12 times more efficiently in Au-rich deposits, which likely relates to differing characteristics and evolution of the hydrothermal fluids in Au-rich and Cu-rich deposits (Chiaradia, 2020). One cause for an increased Au precipitation efficiency may be the shallower average depth of formation for Au-rich deposits (2.1 km) compared to Au-poor deposits (3.7 km; Murakami et al., 2010), possibly enforced by magma evolution under thinner crust (Section 2.3.2). That the decoupling of Cu and Au in Au-rich and Cu-rich deposits cannot alone be explained by magmatic processes highlights the importance of understanding the characteristics and evolution of porphyry-forming hydrothermal fluids, and particularly those forming Au-rich deposits. Section 2.5 reviews porphyry-forming hydrothermal systems, and highlights potential differences in the formation of Au-rich porphyry deposits.

2.4.2 Classification by magmatic association

The association of porphyry deposits with calc-alkaline or alkaline igneous rocks is another common classification criteria (Cooke et al., 2014), yielding the nomenclature of calc-alkaline and alkaline deposits. Porphyry deposits are often described in this way as the metal endowments and deposit characteristics tend to differ depending on the magmatic association, because the two magma types require different generation mechanisms and therefore have different characteristics when emplaced in the shallow crust, impacting on the nature of resultant porphyry deposits. Most arc magmas related to porphyry deposits evolve to become calc-alkaline, while fewer become alkaline; the latter may be differentiated from the former by having higher proportions of Na_2O + K_2O relative to SiO_2, though other classification mechanisms also exist (e.g., Lang et al., 1995b; Seedorff et al., 2005; Sillitoe, 2010; Marks et al., 2011; Bissig and Cooke, 2014; Dostal, 2017). Rocks from calc-alkaline intrusions are most commonly in the compositional range of diorites, quartz diorites, quartz monzodiorites, granodiorites, and granites, while alkaline intrusions tend more toward quartz monzonites and monzodiorites, and rarely syenites (Seedorff et al., 2005). Alkaline intrusions have higher concentrations of magnetite than their calc-alkaline counterparts, and may be further subdivided into quartz-saturated (i.e., granites) or -undersaturated (i.e., syenites), with the latter feldspathoid-bearing (Lang et al., 1995b; Marks et al., 2011). Figure 2.5 illustrates that the most Cu-rich porphyry

deposits are calc-alkaline, while the most Au-rich deposits are alkaline.

Calc-alkaline magmas are derived from slab-dehydration-induced partial melting of the mantle during subduction, and experience Fe-depletion during differentiation, as discussed in Section 2.3. Alkaline magmas, meanwhile, require different generation mechanisms to account for the greater enrichment of $Na_2O + K_2O$ relative to SiO_2. Indeed, there is general agreement that alkaline magmas are produced by partial melting of the subcontinental lithospheric mantle (SCLM), which was metasomatised by slab-dehydration fluids during subduction (Figure 2.1; e.g., Best, 2003; Richards, 2009; Holwell et al., 2019). In particular, low-degree partial melting of the SCLM is deemed necessary for the generation of porphyry-forming alkaline magmas, because this enriches the magma with the alkali metals, and may enrich oxidised magmas in Cu and Au, contributing to the Au-rich nature of many alkaline porphyry deposits (e.g., Logan and Mihalynuk, 2014; Grondahl and Zajacz, 2017). Relatively short-lived, low-degree partial melting may also account for the smaller volume of alkaline intrusions and alkaline porphyry deposits compared to their calc-alkaline equivalents (Richards, 2009). Gold-enrichment in alkaline deposits may be encouraged by the nature of mantle sulphides in the SCLM; if the SCLM is saturated in MSS rather than sulphide liquid, Au would be more easily liberated than if mantle sulphides were dominated by sulphide liquid (Li and Audétat, 2012). On a similar note, if porphyry deposit Au-enrichment is principally a product of Au precipitation efficiency (Section 2.4.1), the characteristics of the hydrothermal fluids exsolved from alkaline intrusions, and the conditions of exsolution (i.e., depth), compared to calc-alkaline intrusions, could be the key factors in optimising Au transport and precipitation in alkaline porphyry deposits.

The tectonic settings that can initiate partial melting of the metasomatised SCLM to generate alkaline porphyry deposits are not well understood. Extensional settings are traditionally associated with more alkaline magmas (e.g., Best, 2003). However, extension does not comply with the conventional model of porphyry formation during active subduction, as described in Section 2.3. This has led to the proposition that more complex tectonic settings generate alkaline magmas in magmatic arcs, in particular those that involve the cessation of active subduction, on a temporary or permanent basis (e.g., Lang et al., 1995a; Richards, 2009; Logan and Mihalynuk, 2014; Bissig and Cooke, 2014; Holwell et al., 2019). Changes in subduction polarity, and slab rollback (subduction reversal), stalling and tearing are commonly proposed, with partial melting of the SCLM induced by resultant extension, compression, and/or mantle upwelling (e.g., Richards, 2009; Bissig and Cooke, 2014; Logan and Mihalynuk, 2014). Theories change depending on the local tectonic setting; British Columbia, Canada, and the Southwest Pacific (Australia

and Papua New Guinea) are two of the most prospective regions for alkaline porphyry deposits (Bissig and Cooke, 2014).

In addition to the above, the hydrothermal characteristics of alkaline porphyry deposits differ from those of calc-alkaline deposits, and are discussed in Section 2.5.

2.4.3 Associated deposits

When porphyry intrusions exsolve metal-rich hydrothermal fluids, different styles of mineralisation have the potential to form. Porphyry-style mineralisation is generated when the fluids deposit their metals in and around the parent intrusion; however, the fluids may also be transported away from the intrusion, and/or interact with reactive wall rocks, to develop alternative styles of mineralisation. The most prevalent of these porphyry-associated mineralisation styles are summarised in Figure 2.6. Empirical observations suggest that it is uncommon to find multiple mineralisation styles related to a parent intrusion(s) (e.g., Table 3 of Sillitoe, 2010), yet this does not preclude their formation. Nevertheless, it is generally thought that the metal endowments of a porphyry deposit, and its associated deposits, are intertwined (e.g., Murakami et al., 2010), suggesting that if there is an abundance of associated mineralisation developed in relation to a porphyry deposit, the metal endowment of the porphyry deposit is likely to be lower, compared to when a porphyry deposit is formed in isolation and the majority of available metals are deposited in the porphyry orebody.

The most significant of the porphyry-related mineralisation styles are epithermal deposits. These deposits are smaller-volume, higher-grade deposits, and form at shallower depths (<1.5 km) compared to porphyry deposits (Simmons et al., 2005). Their characteristics differ depending on the type of deposit, with classification based on the sulphidation state (i.e., S fugacity and temperature at formation) of the mineral assemblage, with the nomenclature high-sulphidation (HS), intermediate-sulphidation (IS), and low-sulphidation (LS) epithermal deposits (Einaudi et al., 2003). Many porphyry deposits have no evidence of associated epithermal mineralisation, at least in part because of the shallower formation depth of epithermal deposits; epithermal deposits may be completely destroyed during exhumation, because the exposure of a porphyry deposit at surface invariably requires erosion of the overlying rock package. A post-depositional tectonic rearrangement is required to ensure that both deposits are preserved near-surface. Alternatively, epithermal mineralisation may overprint and rework a porphyry orebody if the environment where porphyry deposition occurred changes to become cooler and shallower, in a process called telescoping (Sillitoe, 2010). Telescoped deposits contain both mineralisation styles, and represent the evolution of a hydrothermal system from

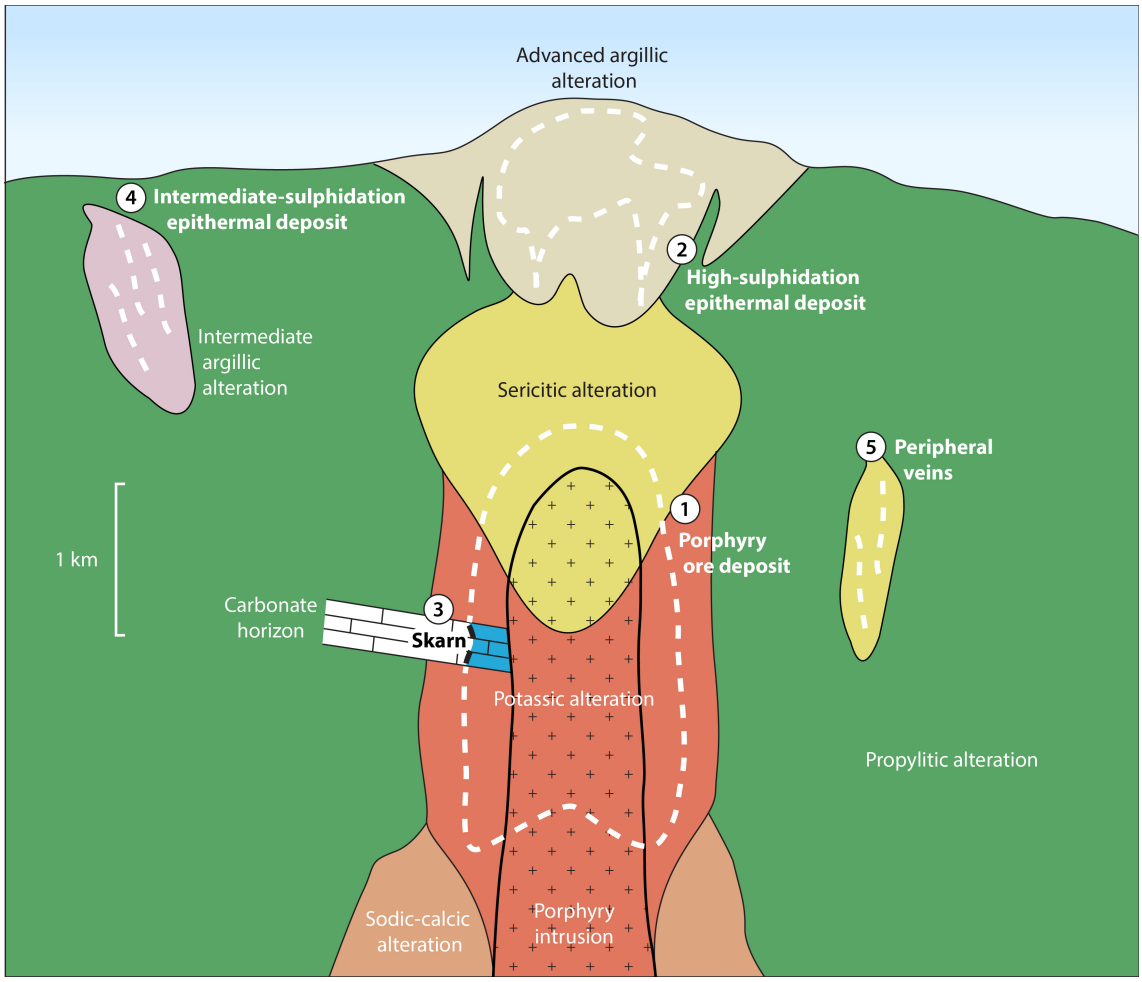

Figure 2.6. Mineralisation associated with a porphyry intrusion (modified from Sillitoe, 2010). Orebodies are denoted by thick dashed lines: 1) Porphyry deposit with an orebody containing Cu ± Au ± Mo in veins and as disseminations, principally in the potassic and sericitic alteration zones; 2) High-sulphidation epithermal mineralisation within advanced argillic alteration (see text for sub-classes), vein-hosted at depth, and disseminated in the main orebody, hosting Cu-Au ± Ag; 3) Skarn (carbonate-reactive) deposits, both proximal (Cu ± Au) and distal (Au and/or Zn-Pb); 4) Intermediate-sulphidation epithermal mineralisation, vein-hosted Au-Ag within intermediate argillic alteration (i.e., smectite, illite, kaolinite); and 5) Peripheral, sub-epithermal veins, situated in sericitic alteration and hosting Zn-Cu-Pb-Ag ± Au.

porphyry to epithermal environments (e.g., Maydagán et al., 2015; Sykora et al., 2018). Epithermal mineralisation found overprinting porphyry mineralisation due to telescoping is exclusively of the high-sulphidation (HS) type (Sillitoe, 2010; Cooke et al., 2014). However, intermediate-sulphidation (IS) epithermal mineralisation may be found distally to a HS epithermal-porphyry system (Figure 2.6; Sillitoe, 2010).

Key characteristics of HS epithermal mineralisation are the metal endowments (particularly high Au grades – locally up to percent levels), the largely disseminated nature of the ore minerals (open space-filling), and distinctive zoned alteration assemblages – collectively classified as advanced argillic – derived from hot, acidic fluids (including vuggy silica, pyrophyllite-diaspore, and alunite-kaolinite; Corbett, 2002). Veins may be present,

but are usually located toward the base of the advanced argillic alteration zone, associated with fissures or dilatant structures, and are typically much wider than those formed in the porphyry environment (i.e., metre-scale; Corbett, 2002; Sillitoe, 2010). Common ore minerals include pyrite, enargite, covellite, and native Au, and less frequent tennantite-tetrahedrite, chalcopyrite, galena and sphalerite, with gangue minerals including barite and native S (Corbett, 2002; Saunders et al., 2014). While the presence of these minerals in the porphyry environment may be indicative of later HS epithermal mineralisation, they should be considered in the context of the other features of HS epithermal mineralisation noted above.

2.5 Hydrothermal activity

2.5.1 Introduction

The previously-covered magmatic processes (Section 2.3) only provide the first part of the story of porphyry deposit formation. The second part involves the hydrothermal system generated by a shallow magma chamber and associated intrusive bodies. The hydrothermal aspect is arguably more important in an economic and exploration sense, because it is the nature of the hydrothermal system that primarily controls the distribution of hydrothermal characteristics (i.e., ore minerals, veins, and alteration) in a deposit. Therefore, understanding the characteristics of the hydrothermal system enables us to better constrain and predict the distribution of mineralisation within porphyry deposits.

Hydrothermal fluids have consequently been a focus of research for decades, and although significant advancements have been made, they remain a poorly-constrained aspect of porphyry deposit formation (e.g., Roedder, 1971; Henley and McNabb, 1978; Hedenquist and Lowenstern, 1994; Heinrich, 2005; Sillitoe, 2010; Kouzmanov and Pokrovski, 2012; Reed et al., 2013; Zajacz et al., 2017; Mernagh et al., 2020; Hurtig et al., 2021). The complexity arises not only from the array of parameters to consider for a given fluid (i.e., pressure, temperature, phase, salinity, sulphidation and oxidation state, and the concentration of key components – metals, for example) but also its cryptic spatio-temporal and physico-chemical evolution, and variable interaction with external influences (i.e., wall rocks and external fluids). Further complications are that the nature of the starting fluids can vary (e.g., exsolved from different intrusions) and/or fluids can be at different points in their evolution, particularly later fluids with different characteristics, which can pass through the same rocks as preceding fluids, potentially obliterating, overprinting, or obscuring the geological record of earlier fluids.

Considering in detail the vast array of possible fluids and evolutionary processes is

outside the scope of this research project. This section therefore focuses primarily on the fluids that generate different mineralised veins in porphyry deposits. Veins are themselves a record of hydrothermal fluid flow, with different veins formed by fluids with different characteristics. Overprinting relationships between veins in porphyry deposits is a key piece of evidence that shows the relative timing of vein formation, and related fluid flow, providing time- and sequence-constraints to the activity of specific hydrothermal fluids. Meanwhile, the spatial distribution of veins, and their relationship to other hydrothermal features (i.e., alteration), informs the evolution of the hydrothermal system through space.

This section is structured to first provide a summary of key hydrothermal fluid characteristics in porphyry deposits (Section 2.5.2), and common processes involved in their evolution (Section 2.5.3). Next, typical vein types in porphyry deposits, and their classification schemes (Section 2.5.4), are covered to provide a basis for the discussion of fluid characteristics and evolution related to the formation of each successive vein type (Section 2.5.5-2.5.8).

2.5.2 Hydrothermal fluid characteristics

The hydrothermal fluids that exsolve from a shallow magma body to form a porphyry deposit must derive their characteristics from the magma. As such, fluid flow begins at magmatic temperatures (e.g., >800°C), and under lithostatic pressures dependent on the intrusion depth of the magma. The effective partitioning of components from the magma into the fluids is required for the fluids to be suitable for porphyry deposit formation (e.g., Richards, 2011). The fluids that form porphyry deposits are largely composed of water (owing to the hydrous nature of the magma), with lesser amounts of CO_2, SO_2, H_2S, and variable concentrations of dissolved components – particularly chloride salts (e.g., NaCl, KCl, $FeCl_2$), metals, and other trace elements (Williams-Jones and Heinrich, 2005; Bodnar et al., 2013).

Owing to the extensive variety in composition, but ubiquitous presence of chloride salts (∼2-13 wt.% NaCl equivalent; Richards, 2011), magmatic-hydrothermal fluids are often simplistically considered in terms of the H_2O-NaCl system (Figure 2.7). In this system, temperature, pressure and salinity conditions in an aqueous fluid determine phase stability relationships – particularly the boundary between a single-phase fluid (with a higher and liquid-like, or lower and vapour-like density, and variable salinity) and a low-salinity vapour, co-existing with a high-salinity liquid (also called hypersaline liquid, or brine, when salinities exceed the solubility of halite at room temperature – 26% wt.% NaCl; Heinrich, 2005). The phase state of a fluid has implications not only for the

behaviour of the fluid (e.g., low-density fluids should ascend more rapidly than high-density fluids), but also for the ability of the fluid to transport metals and other key components throughout the hydrothermal system. In particular, metal partitioning between co-existing liquid and vapour phases has been a particular focus of research in recent years, providing evidence to support theories that ore-forming fluids can be low-salinity vapours (e.g., Heinrich et al., 1992; Williams-Jones and Heinrich, 2005; Lerchbaumer and

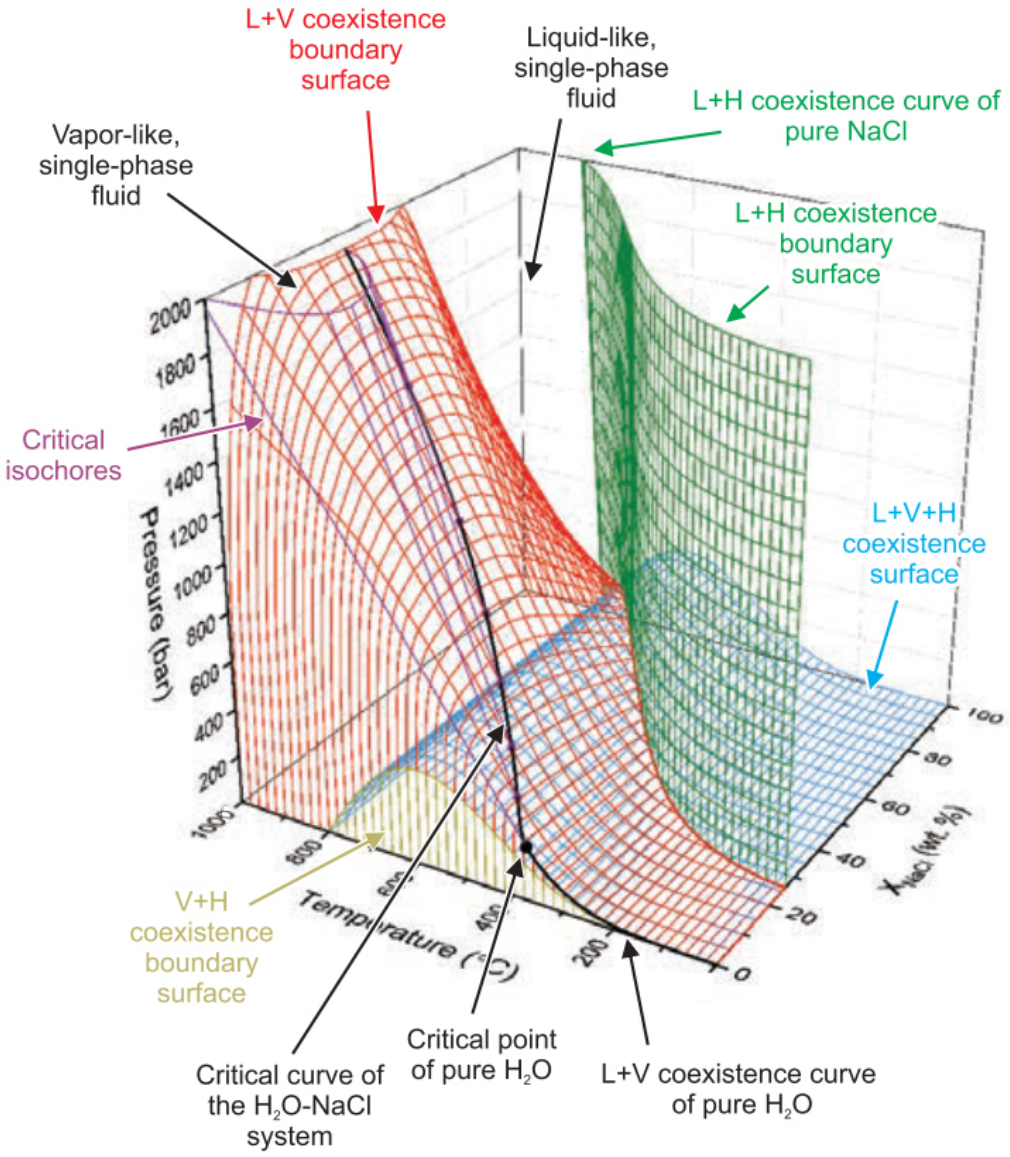

Figure 2.7. Phase relationships in the H_2O-NaCl system (Monecke et al., 2018). A key feature of this system is that a vapour and liquid can co-exist at much higher temperatures and pressures than for pure water. Abbreviations: L, liquid; V, vapour; H, halite. Given that single-phase fluids exsolving from a magma are thought to contain ~2-13 wt.% NaCl equivalent, be at magmatic temperatures (e.g., >800°C), and at typical depths of 2-4 km (~700-1300 bar; see text), the L+V coexistence boundary surface (red) is of most importance to consider when determining phase relationships in porphyry fluids. The critical isochores (purple) mark a region above the L+V coexistence boundary surface where a single-phase fluid exhibits vapour-like behaviour, as opposed to liquid-like behaviour.

Audétat, 2012; Zajacz et al., 2017), as well as the traditionally assumed hypersaline liquids (e.g., Roedder, 1971). Single-phase fluids may also be related to ore formation in some deposits (e.g., Rusk et al., 2004).

Given that hydrothermal fluids in porphyry systems cannot be empirically observed when active, there remains a great deal of uncertainty around specific fluid characteristics. Studies of fluid characteristics in porphyry systems are commonly either experimental (e.g., Zajacz et al., 2011; Hurtig and Williams-Jones, 2014), modelling-based (e.g., Heinrich, 2005; Reed et al., 2013; Hurtig et al., 2021), or analytical, based on fluid inclusions in quartz (e.g., Landtwing et al., 2010; Mernagh et al., 2020). Fluid inclusions are one of the only direct sources of information enabling observation and analysis of the hydrothermal fluids. While they provide a valuable insight to the nature of fluids active in hydrothermal systems, there are caveats to their interpretation – chiefly that, because they are identified and analysed in quartz (and less commonly in other transparent gangue minerals), they may not be directly related to the fluids that precipitated the ore minerals. As such, fluid inclusions require rigorous petrographic and textural work to determine their relationships to ore (e.g., cathodoluminesce, SEM imaging), particularly when considering a specific ore stage (i.e., within a single vein generation), and indeed their relationship to the host quartz (i.e., trapped during growth as a primary inclusion, or a secondary inclusion trapped on a fracture plane). In a review of fluid inclusions in hydrothermal ore deposits, Bodnar et al. (2013) notes that throughout the literature there are many different approaches and levels of care given to data collection and interpretation, which emphasises that there is a need to appraise the quality of fluid inclusion data.

With particular relevance to fluid inclusions in porphyry deposits, most fluid inclusion stages have, until recently, been limited to temperatures of 600°C or 700°C, handicapping the identification of high temperature fluids (Bodnar et al., 2013). It has now been shown that fluid inclusions from porphyry deposits can record temperatures in excess of 1300°C, which are paradoxical because they exceed solidus temperatures for typical porphyry magmas (Mernagh et al., 2020). Furthermore, estimates of pressure and thus depth from fluid inclusions tend to be much higher than those based on geological data, sometimes leading to erroneous interpretations of fluid evolution and the conditions of ore deposition (Mernagh et al., 2020). These extreme estimates of depth and temperature are interpreted to arise because of the heterogeneous entrapment of fluid inclusions during fracture opening and re-sealing cycles; the extreme pressures are likely to represent local conditions rather than depth, and extreme temperature may be erroneous due the differential entrapment of liquids, vapours, and/or solids (Mernagh et al., 2020).

In terms of the partitioning of Cu between a co-existing hypersaline liquid and low-salinity vapour, the analysis of fluid inclusions by LA-ICP-MS had previously shown that Cu partitions preferentially into the vapour phase (e.g., Williams-Jones and Heinrich, 2005). However, experimental research has now shown that these studies are based on incorrect data, because fluid inclusions of vapour can gain Cu post-entrapment by volume diffusion through quartz, and thus exhibit higher concentrations of Cu than were present in the vapour during entrapment (Lerchbaumer and Audétat, 2012). Despite the limitations involved with the analysis of fluid inclusions, and the lack of better alternatives, fluid inclusion studies remain the most common way to determine fluid characteristics in a given deposit, and much of what we know about porphyry fluids comes from their analysis.

2.5.3 Fluid evolution

Fluid evolution in porphyry systems occurs through both space and time, and can be considered both in terms of the evolution of a specific hydrothermal fluid and the evolution of the hydrothermal system as a whole (Figure 2.8). A specific hydrothermal fluid originates in the magma, and travels away from the point of exsolution, rising through the intrusion and out into the surrounding wall rock, depending on the extent of the hydrothermal system. The main processes that can affect the specific fluid are:

1. Cooling, as the fluid travels away from the intrusive heat source, and loses heat to cooler wall rocks.

2. Decompression, as the fluid ascends, and the pressure regime changes from lithostatic to hydrostatic.

3. Changes in phase state (e.g., single-phase, liquid, vapour) owing to changes in the temperature-pressure conditions.

4. Fluid-rock interaction, where the fluid equilibrates with the surrounding rock, generating hydrothermal alteration and changing the fluid composition by removal and/or addition of components; pH is a key parameter affected by fluid-rock interaction.

5. Mineral precipitation, as the previous processes occur to allow mineral components in the fluid to become more stable in a solid state.

In contrast, the hydrothermal system consists of an array of different hydrothermal fluids at any one time, depending on their individual evolutionary paths. The main processes that can affect the hydrothermal system are:

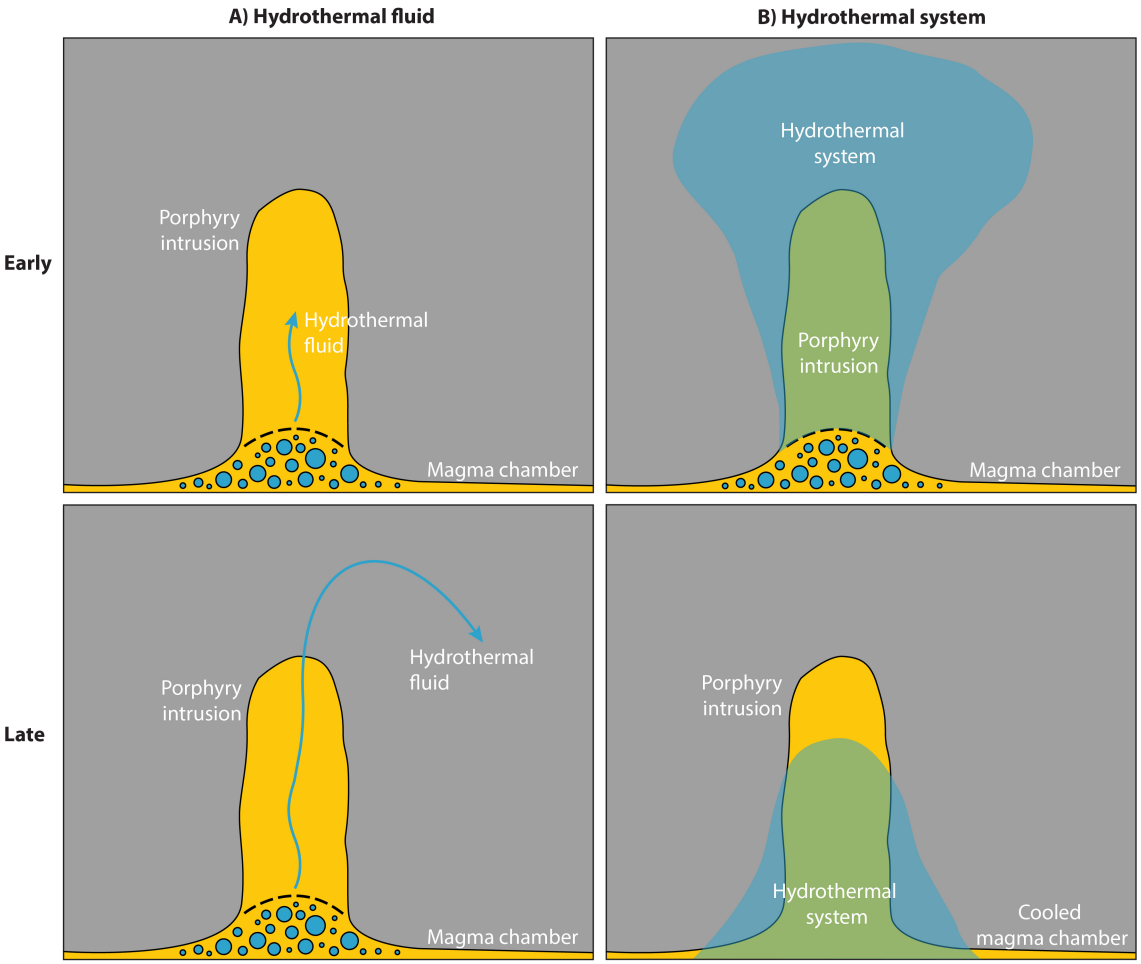

Figure 2.8. Schematic illustrations of hydrothermal fluid evolution through space and time in a porphyry system. A) A possible path taken by a specific hydrothermal fluid evolving as it travels through the intrusion (early), out into the surrounding wall rock (late); and B) The hydrothermal system expanding out from the intrusion as fluid flow commences (early), and then retraction of the hydrothermal system as the intrusion cools (late). In this illustration, the timeframe over which a specific hydrothermal fluid evolves is much shorter than the timeframe over which the hydrothermal system evolves.

1. Exsolution of more fluids with the same characteristics, expanding the active hydrothermal system (e.g., from the intrusion margins out into the surrounding wall rocks), and re-opening previously used fluid pathways (i.e., veins), or generating new fluid pathways.

2. Cooling of the intrusion, causing the hydrothermal system to retract downwards in line with isotherm retraction. Rocks previously at the core of the hydrothermal system will transition toward the periphery, and overprinting of core hydrothermal features (e.g., potassic alteration) by more peripheral hydrothermal features (e.g., sericitic alteration) will occur.

3. Exsolution of different starting fluids, either as the intrusion cools and receeds to

depth (changing the partition coefficients of components between melt and fluid), or with the emplacement of a second intrusion of a different composition. The latter scenario could also change the temperature of the hydrothermal system (causing it to progress upwards again, for example) and change the fluid flow dynamics owing to multiple heat sources. Overprinting of previous hydrothermal fluid features in the rocks (e.g., alteration) would invariably occur.

These processes are considered in the context of vein formation below, but firstly, the vein types commonly present in porphyry deposits must be discussed.

2.5.4 Vein classifications

Gustafson and Hunt (1975) were the first to lay out a framework for the classification of porphyry veins, based on the study of the El Salvador Cu-Mo porphyry deposit, Chile. Subsequent work by Gustafson and Quiroga (1995) on the same deposit enhanced this initial classification. These studies defined a distinctive series of veins inferred to reflect the evolution of the porphyry system, from early to late, with the nomenclature A-, B-, C-, and D-veins (Table 2.2). The earliest, A-veins, are described as finely equigranular, with assemblages dominated by quartz, and ore minerals of chalcopyrite $\pm$ bornite. They are primarily found in association with potassic alteration, and often show little to no distinguishable alteration halo. Next are B-veins, containing quartz and chalcopyrite-molybdenite as the characteristic assemblage. These veins are often symmetrical, with coarser, more euhedral mineral forms than A-veins, and the ore minerals tend to be contained in a central suture, or in cracks perpendicular to the vein walls. Alteration halos are uncommon. The C-veins follow, composed largely of pyrite-chalcopyrite, often lacking quartz and commonly associated with chlorite alteration in the wall rock. Lastly are D-veins, which are composed of minor quartz $\pm$ carbonate and abundant sulphides, dominated by pyrite, and including one or more of chalcopyrite, bornite, tennantite, enargite, sphalerite and galena. Intense, feldspar-destructive (often sericitic) alteration halos are common around D-veins.

The A-, B-, C-, and D-veins of Gustafson and Hunt (1975) and Gustafson and Quiroga (1995) remain the most frequently-referenced vein classification scheme used in porphyry deposit studies, regardless of deposit classification, but there are clearly variations on this sequence in other porphyry deposits. This highlights a limitation of the original studies by Gustafson and Hunt (1975) and Gustafson and Quiroga (1995), which were based on

Table 2.2
(next page) Common vein type classifications used in porphyry deposit studies.

Vein type	Common ore minerals	Common gangue minerals	Alteration halo	Associated wall rock alteration	Textures	Morphology
Group 1 – Early qz- and sulphide-free veins[1]						
M[3]	Mag	Act	None, or fsp	Potassic	Arrays of individual mag grains; locally generating sheeted vein structure	Discontinuous; wavy margins, but relatively planar; generally <30 mm
EB[2]	None, or mag and sulphides	Bt, fsp, ksp, ser, anh, act	None, or fsp	Potassic	Variable; bt may be finely disseminated in ksp, or coarse-grained	Thin; generally <10 mm in width
Group 2 – Granular qz veins with sulphide[1]						
A[4]	Ccp, bn	Qz, ksp, anh	Potassic	Potassic	Fine, equigranular qz with disseminated sulphides; ksp may be banded	Discontinuous; wavy margins, some straighter; up to 25 mm in width
Banded[5]	Mag, Au, py	Qz, chl, ksp, ilt	None	Potassic	Banded; dark grey bands occur as symmetrical pairs near vein walls	Continuous; wavy margins; <20 mm in width
B[4]	Mol, ccp	Qz, anh	None	Potassic	Coarse qz with sulphides in central suture or cracks perpendicular to vein	Continuous; straight; up to 50 mm in width
Group 3 – Late qz-sulphide veins with fsp-destructive alteration halos[1]						
C[2]	Py, ccp, bn	Ser, bt, anh, rare qz	Ksp, ser, chl	None described	Sulphide-dominated	Continuous; straight; up to 10 mm in width
D[4]	Py, ccp, bn, eng, tnt, sp, gn	Anh, qz, cb	Ser	Chl	Py usually dominant; anh forms coarse masses, or is banded with sulphides; qz euhedral where present	Continuous; locally irregular, occupying fractures; up to 75 mm in width
E[7]	Py, bn, ccp, tnt, eng	Qz	Qz, alu, dsp	Ser, advanced argillic	Massive sulphide	Continuous; straight; cm to m in width

References: [1] Sillitoe (2010), [2] Gustafson and Quiroga (1995), [3] Arancibia and Clark (1996), [4] Gustafson and Hunt (1975), [5] Muntean and Einaudi (2000), [7] Masterman et al. (2005).

a single Cu-Mo deposit. Indeed, pre-A-vein M(magnetite)-veins (Arancibia and Clark, 1996) and EB(early biotite)-veins (Gustafson and Quiroga, 1995), and the post-D-vein E(polymetallic massive sulphide)-veins (Masterman et al., 2005) are some of the more common additions to the A-D sequence implemented by authors of later studies (Table 2.2).

In an effort to acknowledge the general similarities between the numerous veins recognised in deposits worldwide, Sillitoe (2010) collated and divided vein sequences into three groups: 1) early veins, lacking quartz and sulphides; 2) granular quartz veins with sulphide; and 3) late quartz-sulphide veins with feldspar-destructive alteration halos (Table 2.2). Group 1 veins tend to be associated with potassic alteration and include one or more of actinolite, magnetite, biotite, and K-feldspar (e.g., M- and EB-veins). Group 2 veins constitute the A- and B-veins described above, also potassic-related, and typically account for the majority of vein-hosted metals in porphyry deposits. Group 3 veins may also account for a portion of deposit metal endowment, and are stated to include D-veins, but E-veins should also be included; C-veins may be transitional between groups 2 and 3. Owing to their later emplacement, Group 3 veins are more often associated with sericitic alteration, but are also found with overprinting advanced argillic alteration, where present.

With particular relevance to this research project, the work of Sillitoe (2000, 2010) highlights that Au-rich porphyry deposits tend to show some differences in their vein generations from the A-D veins classified in Cu-Mo deposits. Firstly, they tend to lack B-veins and have a lower abundance of D-veins. Instead, early M-veins, main stage A-veins, and late chlorite-pyrite $\pm$ quartz $\pm$ chalcopyrite veins with chlorite alteration halos dominate (C-vein variation). The M-veins may transition into A-veins, in that the traditional A-vein assemblage of quartz-chalcopyrite can contain additional magnetite, and where both are present, magnetite-bearing A-veins pre-date magnetite-free A-veins. Also unique to Au-rich deposits are banded quartz veins, with layers of both dark gray and translucent quartz (Table 2.2; Muntean and Einaudi, 2000). They contain similar ore minerals to A-veins, and are thought to closely post-date them, or be their shallower expressions (Muntean and Einaudi, 2000). A significant observation in Au-rich deposits, and less so in other porphyry deposits, is that there tends to be a correlation between metal content and quartz vein intensity (Sillitoe, 2000), implying that vein formation has a greater control on ore deposition in Au-rich deposits.

Differences in veins between deposits classified as calc-alkaline and alkaline are also evident. Most significantly, alkaline deposits tend to lack the abundance of veins seen in calc-alkaline deposits (Lang et al., 1995b; Sillitoe, 2000).

The difficulty in defining a strict classification for porphyry vein sequences arises from the fact that each porphyry deposit shows some differences in its veins to that of another deposit, as implied above. For example, in comparison to the A-D veins described by Gustafson and Hunt (1975) and Gustafson and Quiroga (1995) at El Salvador, Maydagán et al. (2015) defined 11 porphyry vein generations (including sub-classes) at the Altar Cu-(Au-Mo) deposit, Argentina. Herein lies an issue with conforming to accepted vein classifications, because Maydagán et al. (2015) assign veins to the types of EB, A, B, C, D, and E, but types A, D, and particularly E, have multiple sub-classes, and some of the characteristics of their veins differ from those of the original classifications (e.g., sulphide-free C-veins). The presence of additional vein types, and also multiple subclasses, shows that there is a much greater complexity to the hydrothermal system at the Altar deposit, than at the El Salvador deposit, and drawing comparisons between two radically different deposits (not only in veins, but also in contained metals) by assigning similar (but not exactly the same) vein types, may not appropriate. This is because the evolution of the hydrothermal systems is clearly different, and the fluids forming, A-veins at Altar and A-veins at El Salvador are probably different, although there is likely some similarities, while the fluids forming C-veins at Altar are markedly different from the fluids forming C-veins at El Salvador.

Further complications arise as vein sequences may be repeated at a significantly later time following the emplacement of a later intrusion (most frequent with early, Group 1 veins; Sillitoe, 2010). Veins may also be re-opened during later hydrothermal activity (e.g., Redmond et al., 2004), and conversely, the metal contents of mineralised veins may be reduced by later hydrothermal activity, and post-depositional processes (e.g., metamorphism) may also alter vein features, via, for example, recrystallisation or alteration (Sillitoe, 2010). Therefore, depending on the criteria used for classification, one could define any number of vein sequences in a porphyry deposit, which may or may not comply with the accepted nomenclature. Nevertheless, the classifications described above do have value, in that similarities between veins in two different deposits suggests a similarity of formation process, and thus similarity in the chracteristics of the hydrothermal fluids.

The following discussion on fluid evolution related to vein formation is divided into three sections, based on the overarching vein groupings by Sillitoe (2010), above. This is in an effort to acknowledge the key fluid characteristics and evolutionary processes involved during vein formation in porphyry deposits, from early in the lifetime of the hydrothermal system, through the main stage of fluid flow, and to late-stage hydrothermal activity as the system wanes. While individual vein types and their key characteristics

are discussed – particularly those found in Au-rich deposits – the intricacies of vein characteristics specific to individual deposits will be avoided, owing to the variety in vein classifications discussed above.

2.5.5 Group 1 veins

As described above, the hydrothermal fluids exsolved from a magmatic intrusion will initially experience pressures primarily dependent on the intrusion depth of the magma. Owing to the lack of quartz in Group 1 veins, classic fluid inclusion studies (i.e., on quartz) cannot be used to determine the phase state of the vein-forming fluids. Nevertheless, fluid inclusion studies of porphyry systems as a whole indicate that the most common fluid phase evolution path is where a single-phase fluid of intermediate salinity (e.g., ∼2-13 wt.% NaCl equivalent; Richards, 2011) exsolves from a magma, and then cools and/or decompresses below the two-phase surface to separate into a co-existing low-salinity vapour and high-salinity liquid (e.g., Landtwing et al., 2010; Mernagh et al., 2020). However, Figure 2.7 also shows that direct exsolution of co-existing vapour and liquid from a magma is likely to have occurred in deposits formed at shallower depths (i.e., lower pressures), and this is indeed confirmed by various modelling studies (e.g., Heinrich, 2005; Monecke et al., 2018). Hence the first fluids active in a porphyry hydrothermal system, and those forming the earliest veins (Group 1), are likely to be single-phase fluids in deeply-formed deposits (e.g., >6 km depth), and co-existing liquid and vapour in more shallowly-formed deposits.

Group 1 veins characteristically lack quartz and sulphide minerals, suggesting that the constituents of these minerals have a high solubility in the vein-forming fluids, and that conditions do not change sufficiently to bring these phases into saturation. In a single-phase intermediate-density fluid with 10 wt.% NaCl eq., modelling shows that the solubility of common porphyry sulphide minerals (i.e., chalcopyrite, pyrite, and molybdenite, among others) increases with increasing temperature and pressure (Kouzmanov and Pokrovski, 2012). A similar correlation is evident in quartz solubility calculations, where the same fluid under the highest pressures and temperatures can transport the most quartz (Monecke et al., 2018). This indicates that fluids exsolved from a magma in deeper-formed porphyry deposits should transport quartz and sulphide mineral components during the initial stages of fluid flow, when fluids are at near-magmatic temperatures and under high pressures, and thus generate veins that lack both. Initial empirical evidence of relatively high temperatures in Group 1 veins comes from vein morphology; wavy margins indicate deposition under a ductile regime (i.e., >350-500°C; Sillitoe, 2010; Fournier, 1999; Monecke et al., 2018).

A more complex scenario exists for the co-existing liquid and vapour exsolving from a shallowly-emplaced intrusion. The lower pressure invariably results in a lower bulk solubility of quartz and sulphides in the fluid (liquid + vapour) compared to a deeply-exsolved single-phase fluid, and the partitioning of the mineral components between liquid and vapour phases leads to variations in solubility in each phase. Nevertheless, a sufficient drop in quartz and sulphide solubility is required for mineral deposition to occur. If Group 1 veins are present in shallow-formed deposits, this suggests that such a drop does not occur, likely owing to the high temperature of early fluids in proximity to the magma; cooling is thought to be a major ore deposition mechanism (e.g., Kouzmanov and Pokrovski, 2012).

The mineralogy of Group 1 veins also supports formation under high temperatures. The magnetite-actinolite assemblage of M-veins draws similarities to Fe-oxide-Cu-Au (IOCG) deposits, where such minerals are common (e.g., Del Real et al., 2021). These deposits share many similarities with porphyry deposits, but are S-poor and Fe-oxide-rich (Richards, 2013). Particularly high temperatures, and a lack of S in IOCG-forming fluids relative to porphyry-forming fluids are proposed to account for the key differences between deposit types (Richards, 2013). The dominance of magnetite in porphyry M-veins, coupled with the lack of sulphides (which require reduced S species, i.e., H_2S), indicates a similarity in formation conditions to IOCG deposits, and may thus indicate that the fluids forming these veins experience particularly high temperatures – reasonable, given that they are the earliest-formed veins – and that they contain a lack of reduced S, accounted for by the dominance of SO_2 at high temperatures ($\sim$>400°C, depending on pH; Kouzmanov and Pokrovski, 2012). Indeed, high precipitation temperatures of $\sim$800-675°C are reported for the magnetite-actinolite assemblage at the Candelaria IOCG deposit, Chile, based on actinolite geochemistry (Del Real et al., 2021). Similarly in a porphyry single-phase fluid with 10 wt.% NaCl eq., pH-buffered by an assemblage of quartz-muscovite/andalusite-K-feldspar, the dependence of S species on temperature suggests that magnetite precipitates at 500-600°C, below which pyrite and chalcopyrite are preferred (Kouzmanov and Pokrovski, 2012).

Group 1 veins are associated with potassic alteration (Table 2.2), where K-feldspar $\pm$ biotite are the key minerals (Sillitoe, 2010). Hydrothermal alteration is principally a product of fluid-rock interaction, with the alteration assemblage primarily recording the temperature and pH of the fluids. A fluid will attempt to equilibrate with the rock it passes through, thus modelling studies tend to assume equilibrium conditions (e.g., Reed et al., 2013). The fluid-rock ratio becomes important in this regard, as a fluid-dominated system will develop an alteration assemblage in the wall rock representative of the fluid

temperature and pH, while a rock-dominated system will develop an alteration assemblage representative of the wall rock temperature and pH. In order to form potassic alteration in an igneous intrusion, a high temperature (∼350-600+°C) and a near-neutral pH (∼5) are required so that amphibole and plagioclase in the intrusive rock can be altered to biotite and K-feldspar, respectively (Seedorff et al., 2005; Reed et al., 2013). Fluids exsolved from an intrusion are thought to have a near-neutral pH because the H^+ ions are associated at high temperatures (e.g., as HCl; Kouzmanov and Pokrovski, 2012), thus a fluid-dominated system can generate potassic alteration at high temperatures (>600°C). A rock-dominated system may also generate potassic alteration down to ∼350°C, assuming the pH of the rock is near-neutral (Reed et al., 2013). The main takeaway here is that potassic alteration is indicative of high temperatures, therefore aligning with the previous lines of evidence to suggest a high formation temperature for Group 1 veins, supressing the deposition of sulphide minerals and quartz.

2.5.6 Group 2 veins

Similarly to Group 1 veins, Group 2 veins are associated with potassic alteration, and the earliest veins exhibit wavy margins indicating deposition under ductile conditions. Both these features indicate relatively high temperatures of formation (at least ∼350°C), as discussed above. However, there is a distinct change in mineralogy in Group 2 veins – the presence of quartz and sulphide minerals (Table 2.2). After formation of Group 1 veins, the evolved fluid must at some point deposit its load of quartz, metal and sulphide. As the earliest sulphide-bearing quartz veins, Group 2 veins likely represent this first stage of ore deposition from the initial fluid that formed Group 1 veins, but there are complications (see below).

Fluid inclusion assemblages in Group 2 veins are either intermediate-density single-phase fluids, co-existing low-salinity vapour and high-salinity liquid, or vapour-rich with rare liquid (Monecke et al., 2018). This suggests that in deeply-formed deposits, a single-phase fluid exsolved from a magma generates Group 1 veins, and may then remain in the single-phase field to form Group 2 veins (Figure 2.7). Alternatively, a single-phase fluid may form Group 1 veins and then fall below the two-phase surface owing to pressure reductions, generating Group 2 veins from co-existing liquid and vapour. Comparatively in shallow deposits, there may be no change in phase state between Group 1 and 2 veins, with both forming from co-existing liquid and vapour, or the co-existing liquid and vapour could cool and/or decompress below the vapour and halite co-existence boundary.

These differences in phase state may help explain the formation of some Group 2

veins. For example, banded veins (Table 2.2) are recognised in numerous Au-rich deposits, and contain an abundance of vapour-rich inclusions and micrometre-sized crystals of magnetite in dark grey bands of quartz near the vein walls (Muntean and Einaudi, 2000; Koděra et al., 2014). Combined with the analysis of quartz textures that suggest recrystallisation from a silica gel, the abundance of vapour-rich inclusions are interpreted to indicate that the dark grey quartz bands formed due to episodes of rapid decompression, when pressures changed from lithostatic to hydrostatic at high temperatures (∼600-700°C) and shallow depths (∼1 km; Muntean and Einaudi, 2000). The co-existing liquid and vapour would therefore have transitioned into the vapour and halite co-existence field, where the vapour rapidly expanded along the fluid pathway to deposit the silica gel containing magnetite and inclusions of vapour (Muntean and Einaudi, 2000). Gold is enriched in banded veins (Table 2.2), suggesting transport by, and precipitation from, the vapour phase. However, more recent petrographical work by Tsuruoka (2017) proposes that the Au was introduced at a later stage, from later fluids that formed cross-cutting veins containing Au.

Another study of banded veins in the shallow-formed, Au-rich, but unusually Cu-Mo-sulphide-poor Biely Vrch porphyry deposit, Slovakia, identified co-existing vapour and salt melt inclusions, again showing that fluids entered the vapour and halite (or salt melt) co-existence field (Koděra et al., 2014). Analysis of the fluid inclusions by LA-ICP-MS shows that Au was present in the salt melt as well as the vapour, implying that Au-deposition was synchronous with banded vein formation, but this phenomenon may be restricted to deposits formed by the intrusion of magmas capable of generating salt melts at shallow depths (e.g., Fe-rich dioritic magmas; Koděra et al., 2014). Nevertheless, these studies show that banded veins likely form as a consequence of fluids evolving at low pressures (shallow depths) into the vapour and halite co-existence field. The common presence of banded veins in Au-rich deposits further suggests that shallow depths favour Au-enrichment, perhaps owing to the enhanced precipitation of Au from fluids in the co-existing vapour and halite field (cf. Section 2.4.1), however the timing of Au introduction in banded veins requires clarification.

Quartz in the remaining Group 2 veins – A- and B-veins – contains fluid inclusions of either intermediate-density single-phase fluids, or co-existing low-salinity vapour and high-salinity liquid (e.g., Redmond et al., 2004; Pudack et al., 2009; Landtwing et al., 2010). However, textural evidence suggests that the quartz may not be related to the introduction of the ore minerals (e.g., Landtwing et al., 2005; Monecke et al., 2018). This is most clearly seen in B veins, where ore minerals typically occupy a central suture, or cracks perpendicular to the vein walls, indicating that they were introduced later than

the quartz (Table 2.2). However, B-veins are generally quite scarce in porphyry deposits worldwide, particularly Au-rich deposits (Sillitoe, 2010). In some deposits, it is alternatively recognised that veins exhibiting B-vein-like quartz- and ore-filled sutures or cracks are in fact re-opened A-veins, owing to the differences in the quartz between A-veins (granular, anhedral) and B-veins (coarse, euhedral; e.g., Redmond et al., 2004; Maydagán et al., 2015; Tsuruoka, 2017). Cathodoluminesce (CL) of quartz from these A-veins confirms that re-opening occurred, as there are clear differences in the luminescence of the early quartz, and later quartz infill (e.g., Redmond et al., 2004; Landtwing et al., 2010). Even in A-veins with disseminated sulphides, the relationship between quartz and ore is tenuous – ore minerals commonly occur along fractures and microfractures in the quartz (Monecke et al., 2018). These textures suggest that A- and B-veins are formed by multiple different fluids, with the bulk of the quartz, and the ore minerals, deposited at different points in time in the evolution of the hydrothermal system.

The lack of a clear relationship between quartz and ore in Group 2 veins complicates the understanding of fluid evolution. Cross-cutting relationships place Group 2 veins between those of Groups 1 and 3, but vein re-opening means that the fluid precipitating the ore minerals in Group 2 veins could feasibly post-date Group 2 vein quartz formation, and indeed, be synchronous with Group 3 vein formation. According to quartz solubility calculations, precipitation of Group 2 vein quartz may be facilitated by cooling of the ascending high temperature fluids that previously formed Group 1 veins, to temperatures no less than 500°C (Monecke et al., 2018). If ore minerals are not synchronous with the quartz, their solubility in the quartz-precipitating fluid must remain high. Therefore, as temperature, pressure, and fluid-rock interaction exert a dominant control on ore deposition (e.g., Kouzmanov and Pokrovski, 2012; Hurtig et al., 2021), cooling and decompression must be relatively minor, and fluid-rock interaction limited. Given that Group 2 veins are situated in the potassic alteration zone, and are dominantly found within porphyry intrusions, it is reasonable to suggest that the vein-forming fluids retained high temperatures and experienced relatively high pressures commensurate with the depth of the intrusion. The association with potassic alteration suggests that the effects of fluid-rock interaction were also limited, because potassic alteration is dominantly a product of alkali exchange between fluid and rock (e.g., Na for K; Seedorff et al., 2005), which should have little effect on the metal-transporting capacity of the fluid.

The precipitation of ore minerals in Group 2 veins requires particular consideration, because the abundance of these veins often positively correlates with the highest metal grades in a deposit, implying that they host the majority of ore (Sillitoe, 2010). The timing and cause of ore mineral deposition in porphyry systems remains a contentious topic,

not least because questions remain around the phase state of the ore-forming fluids (i.e., liquid vs. vapour), and by extension the hydrothermal system processes that occur to facilitate ore deposition from fluids with different phase states (e.g., Sillitoe, 2010; Weis et al., 2012; Blundy et al., 2015; Zajacz et al., 2017; Monecke et al., 2018; Mernagh et al., 2020; Hurtig et al., 2021). As described above, fluid inclusion studies provide an indication of the phase state of fluids that were active in a porphyry hydrothermal system, but there remains a lack of certainty that the ore-forming fluids were liquid (e.g., Sillitoe, 2010; Kouzmanov and Pokrovski, 2012), vapour (e.g., Henley and McNabb, 1978; Weis et al., 2012), or otherwise (e.g., Koděra et al., 2014). Experimental studies show that the transport of the main economic metals (Cu and Au) in the liquid phase should occur mainly as chloride complexes at high temperatures, with S complexes becoming more dominant for Au at lower temperatures (below $\sim$350°C; Williams-Jones et al., 2009). Meanwhile, transport of Au and Cu in the vapour phase likely occurs as solvated (e.g., by HCl and H_2O) or hydrated species (with H_2O), with Au-Cl and Au-S complexes facilitating Au solubility, and Cu-Cl complexes facilitating Cu solubility, although Cu-S species have not yet been evaluated (Hurtig et al., 2021).

Increasingly it is proposed that vapours are dominantly responsible for metal transport and ore deposition. Analysis of co-existing hypersaline liquid and vapour fluid inclusions from porphyry deposits has shown that Cu, Fe, Pb, Zn, Na, and K are more concentrated in the liquid phase, while S, Au, and As are more concentrated in the vapour (e.g., Heinrich et al., 1992; Seo et al., 2009; Lerchbaumer and Audétat, 2012; Kouzmanov and Pokrovski, 2012). However, experimental studies conducted at high temperatures (>650°C) show that both Cu and Au preferentially partition into the liquid phase, but a key finding is that reductions in temperature also reduce the partition coefficients of Cu and Au between liquid and vapour (Zajacz et al., 2017). Therefore, lower temperatures allow increasingly more Cu and Au to be transported by the vapour phase, even if they are preferentially partitioned into the liquid. The proportion of liquid to vapour then becomes important, as this determines the bulk metal budget of each phase. Pressure, temperature and salinity control the proportions, thus they are not constant, and are likely to change as the fluid and system evolve (Landtwing et al., 2010; Mernagh et al., 2020). Mass balance calculations at the Alumbrera deposit, Argentina, indicate that vapour/brine mass ratios were between 4-9 (equivalent to 96-98% volume proportion of vapour; Lerchbaumer and Audétat, 2012; Hurtig et al., 2021), while calculations of phase proportions at the Grasberg deposit, Indonesia, shows that the vapour phase accounts for 93 wt.% of the overall fluid, equivalent to a 98% volume fraction (Mernagh et al., 2020). This illustrates that the vapour may proportionally dominate over the liquid, and thus

be able to supply the bulk of metals to sites of ore deposition – a conclusion backed up by modelling of metal transport in vapours (Hurtig et al., 2021). Nevertheless, it remains that many researchers advocate for single-phase or high-salinity liquids as ore-forming fluids in porphyry systems, either in conjunction with, or in isolation of, vapours (e.g., Sillitoe, 2010; Kouzmanov and Pokrovski, 2012; Lerchbaumer and Audétat, 2012; Reed et al., 2013; Monecke et al., 2018; Jensen et al., 2022).

Ore deposition from liquid and vapour phases is largely similar, in that reductions in temperature and pressure, and increased fluid-rock interaction favours mineral precipitation, although cooling and fluid-rock interaction are thought to be dominant for ore deposition from the liquid phase, and vapour expansion (i.e., pressure reduction) is thought to be dominant for ore deposition from the vapour phase (Kouzmanov and Pokrovski, 2012; Hurtig et al., 2021). Group 2 vein ore mineral assemblages (A- and B-veins in particular) are dominated by chalcopyrite, bornite and molybdenite (Table 2.2). Deposition of these minerals requires reduced S species not previously available in the fluid. Disproportionation of SO_2 to H_2S and sulphuric acid below ∼400°C is thought to be a key process, which also lowers fluid pH if interaction with neutralising wall rocks is limited (Kouzmanov and Pokrovski, 2012). A reduction in pH is not favourable for the deposition of Cu and Fe from a liquid phase in this temperature range (Kouzmanov and Pokrovski, 2012), thus it is likely that Group 2 ore minerals were deposited at the beginning of this transition to reduced S, where the drop in fluid pH was minor, remaining near-neutral to generate potassic alteration, while also providing enough reduced S to form chalcopyrite, bornite and/or molybdenite as an intermediate-high sulphidation assemblage (Einaudi et al., 2003). Thus, a decrease in temperature is likely to be a key driver for ore deposition.

Further evidence for temperature reductions comes from the morphology of B-veins, and some later A-veins; margins change from wavy to planar, in line with changes from ductile to brittle conditions, over the temperature range of ∼350-500°C (Fournier, 1999; Monecke et al., 2018). This suggests that the ductile-brittle transition occurred roughly between the formation of A- and B-vein quartz, and if the ore minerals in Group 2 veins post-date the quartz, then the transition likely occurred before ore depositon. Furthermore, if re-opening of Group 2 veins was facilitated by the dissolution of vein quartz as the fluid followed a path of retrograde quartz solubility, this could place temperature constraints in the region of ∼375-450°C (Monecke et al., 2018). Meanwhile, the presence of Au in banded veins – if synchronous with the quartz and deposited by a vapour – suggests that ore deposition probably occurred at lower temperatures than that of A- and B-veins, because Au solubility in the vapour phase is determined to reach a high

between 340-510°C (Hurtig et al., 2021).

In summary, Group 2 veins likely form at lower temperatures and pressures than Group 1 veins, as the fluids migrate further away from the intrusion, and the hydrothermal system expands. Quartz deposition occurs due to cooling and decompression, from single-phase fluids, co-existing liquid and vapour, or vapour alone (sometimes co-existing with salt melts). The association with potassic alteration suggests a similar fluid pH (i.e., near-neutral) to Group 1 veins, and that the influence of fluid-rock interaction was minor. Vein textures indicate that ore deposition occurred after the quartz precipitated, when veins were re-opened by later fluids that were even cooler (∼400°C) and may have been liquids and/or vapours.

2.5.7 Group 3 veins

During the formation of Group 2 veins in the potassic-altered core of the hydrothermal system, alteration of the surrounding wall rocks simultaneously occurs due to heating of external ground waters; propylitic alteration is produced, the mineral assemblage of which is typically zoned outward due to temperature gradients (e.g., Cooke et al., 2014). This is important to acknowledge, because some Group 3 veins are associated with propylitic alteration (i.e., chloritic; Table 2.2), but may not be synchronous with the development of the wall rock alteration. One of the main characteristic features of Group 3 veins is the presence of feldspar-destructive alteration haloes (i.e., sericitic, advanced argillic), and as such, the alteration halo – rather than the wall rock alteration assemblage – provides a clearer insight to the nature of the vein-forming fluids. Nevertheless, some Group 3 veins (e.g., E-veins) have associations with sericitic and advanced argillic wall rock alteration, and in these cases it is likely that the wall rock alteration is associated with vein formation, because there is synchronicity of vein alteration haloes and wall rock alteration, suggesting formation by fluids of similar characteristics.

Sericitic and advanced argillic alteration assemblages are feldspar-destructive, and are principally a product of the hydrothermal fluids becoming more acidic as temperatures fall (Seedorff et al., 2005; Reed et al., 2013). Sericitic alteration is the higher temperature and less acidic variant, where K-feldspar is altered to sericite and quartz, while advanced argillic is lower temperature and more acidic, characterised by the formation of koalinite, pyrophyllite or andalusite (Seedorff et al., 2005). This is the first line of evidence to suggest that Group 3 veins form at lower temperatures from fluids with a lower pH than those that form Group 2 veins. Incidentally, the reduction in the temperature of the fluids is thought to account for the change in pH; as mentioned above, the disproportionation of SO_2 to H_2S and sulphuric acid occurs below ∼400°C (Richards, 2011;

Kouzmanov and Pokrovski, 2012; Reed et al., 2013). Furthermore, the degree of fluid-rock interaction (i.e., fluid-rock ratio) and the nature of the wall rocks also influences whether the pH will progress to highly acidic (e.g., fluid-dominated system) as SO_2 disproportionation occurs, or be neutralised to remain near-neutral (e.g., rock-dominated system; Reed et al., 2013).

Low temperatures are also indicated by the mineralogy of some Group 3 veins. In particular, C-veins are conspicuous, because they often lack quartz (Table 2.2). However, this can be explained by retrograde quartz solubility at temperatures of ∼375-450°C, as mentioned for the deposition of ore minerals in Group 2 veins (Monecke et al., 2018). The D- and E-veins are quartz-bearing, and post-date C-veins, thus are likely to have formed at temperatures below ∼375°C (Monecke et al., 2018).

Group 3 vein-forming fluids at temperatures of ∼400°C may be in the single-phase field or co-existing liquid and vapour field (Figure 2.7). However, owing to the lower temperatures compared to Group 1 and 2 vein-forming fluids, there is a higher likelihood that fluids will exist in the single-phase field, particularly for porphyry systems at greater depth. Indeed, fluids that were previously below the liquid + vapour co-existence surface during the formation of Group 1 and/or Group 2 veins may now move into the single-phase field owing to temperature reductions. A fluid phase not previously considered are vapours that have separated from a more dense hypersaline liquid and condensed to a low-salinity single-phase liquid (Heinrich, 2005; Williams-Jones and Heinrich, 2005). Fluid inclusion studies suggest that liquid-rich assemblages are more common in Group 3 veins, but these tend to have variable salinities, illustrating the variance in the source of the fluids; they may be either single-phase fluids (i.e., continuously evolved in the single-phase field since exsolution), hypersaline liquids, or contracted vapours (Pudack et al., 2009; Landtwing et al., 2010; Monecke et al., 2018).

Group 3 veins are sulphide-rich, showing that vein formation coincides with conditions favourable for sulphide precipitation. The abundance of pyrite and Cu-bearing ore minerals in Group 3 veins indicates that the solubility increase of Cu and Fe in a liquid phase owing to a pH reduction is strongly negated by other factors. In particular, cooling is thought to have a dominant effect on Cu solubility, with fluid inclusions at the Bingham deposit, Utah, found to exhibit a significant drop in Cu concentrations in the temperature range of 425-350°C (Landtwing et al., 2005). Thermodynamic modelling also shows that pyrite and chalcopyrite solubility decreases as temperatures fall below 400°C (Kouzmanov and Pokrovski, 2012). Cooling has a similar effect on the solubility of Cu in a vapour phase, if any is present, while vapour expansion (decompression) is a more potent way to reduce Cu solubility (Hurtig et al., 2021).

The fluids forming Group 3 veins are likely to experience lower pressures than Group 2 veins, not least because of the change from ductile to brittle conditions (illustrated by the straight margins of the veins), and the coincident change from lithostatic to hydrostatic pressures as temperatures fall between 500-350°C (Fournier, 1999; Sillitoe, 2010; Monecke et al., 2018). Group 3 veins also exhibit progressively greater vein widths (Table 2.2), and often occupy the upper portions of the porphyry orebody (e.g., Sillitoe, 2010), illustrating the vertical expansion of the hydrothermal system to shallower depths and lower pressures.

The presence of galena and sphalerite in D-veins is likely due to the progressive cooling of the acidic fluid, possibly augmented by fluid-rock interaction; their absence in earlier vein generations may also be partly due to the low concentrations of Pb and Zn in porphyry fluids (Reed et al., 2013). The solubility of galena and sphalerite in acidic fluids is higher than that of pyrite and chalcopyrite, thus greater cooling of the fluid to lower temperatures, or acid neutralisation by fluid-rock interaction at higher temperatures, is required to allow precipitation (Kouzmanov and Pokrovski, 2012). The sulphosalt minerals present in D- and E-veins may also inform the sulphidation state of the fluids, where a pyrite-bornite-enargite assemblage describes a high sulphidation state, and a pyrite-chalcopyrite-tennantite assemblage describes an intermediate-sulphidation assemblage; for a given temperature the high sulphidation assemblage describes a higher S fugacity, and vice versa for the intermediate-sulphidation assemblage (Einaudi et al., 2003).

In summary, Group 3 veins are formed at lower temperatures (i.e.,$<$400°C) and from more acidic fluids than Group 1 and Group 2 veins. They are generated in the brittle regime where hydrostatic pressures dominate, and may be formed at shallower depths than the preceeding veins. The abundance of ore minerals in Group 3 veins further shows that the solubility of most metals is greatly reduced in the vein-forming fluids.

2.5.8 Vein formation in an evolving hydrothermal system

The preceeding discussion of fluid evolution related to vein formation principally focusses on the evolution of a single starting fluid as it cools, decompresses and experiences increasing fluid-rock interaction. This is because the features of porphyry vein sequences often indicate that later veins formed under cooler temperatures, lower pressures, and from more compositionally evolved fluids than earlier veins (e.g., Reed et al., 2013; Maydagán et al., 2015; Monecke et al., 2018). However, vein and alteration overprinting relationships show that the hydrothermal system must also evolve through space and time, as summarised in Figure 2.8. Integrating the evolution of a single fluid with hydrothermal system evolution allows a generalised model of vein formation to be as-

sembled, illustrating porphyry deposit formation through time (Figure 2.9).

The influence of external fluids (i.e., ground waters) in the formation of porphyry deposits is one aspect of the model not yet discussed. Originally, it was thought that mixing of magma-derived hydrothermal fluids and ground waters was a central process, resposible for ore deposition and particularly the development of sericitic alteration (Sillitoe, 2010, and references therein). The recognised importance of ground waters has been lessened following O isotope studies (e.g., Fekete et al., 2016), although porphyry systems may still experience their incursion at later stages (Sillitoe, 2010), and in the epithermal environment at shallower depths, the mixing of magmatic-derived fluids with ground waters is a more important process (e.g., Hedenquist et al., 1998; Heinrich, 2005). It is now thought that the principal effect of ground waters on porphyry systems is that their convection acts as an efficient means by which to cool the magmatic intrusions (Fekete et al., 2016). Ascending magmatic-derived hydrothermal fluids must clearly interact with the external waters, but hydrological models suggest that in most cases this interaction principally forms a heat exchange interface between the lithostatically-pressured hydrothermal fluids, and hydrostatically-pressured ground waters (Weis et al., 2012). However, the cooling effect of the ground waters may also be a key driver for ore deposition from the hydrothermal fluids, with models proposing the existence of an ore deposition front near the hydrothermal fluid-ground water interface (Weis et al., 2012; Fekete et al., 2016).

With regards to the formation of Au-rich porphyry deposits, there are some additional hydrothermal factors to consider, over and above those discussed in Section 2.4.1. The differences in vein types in Au-rich deposits compared to Cu-Mo deposits (Section

Figure 2.9. *(next page)* Schematic illustrations depicting the formation of a porphyry deposit as the hydrothermal fluids and the hydrothermal system evolve through space and time (constructed from discussions in the text, and modified from the illustrations of Heinrich, 2005; Sillitoe, 2010; Richards, 2011). This scenario considers the formation of an intermediate-depth porphyry deposit (∼3-5 km). Initially, magma is intruded into relatively cool wall rocks, where it begins to crystallise and exsolve an intermediate-density single-phase fluid. The fluid evolves to a co-existing hypersaline liquid and low-salinity vapour as it ascends. The vapour ascends more rapidly than the liquid, eventually contracting to a single-phase fluid at lower temperatures. Meanwhile, the hypersaline liquid is constrained to greater depths owing to its higher density. The intrusion cools over time as heat is diffused into the wall rocks, encouraged by circulating ground waters that generate propylitic alteration. Isotherms retract to depth as the magma crystallises. Veins and alteration assemblages are produced by the magmatic-derived hydrothermal fluids, with earlier vein generations and alteration assemblages successively overprinted by later variants as the system cools. One possibility not shown in the model is the emplacement of later intrusions, which could perturb the typical sequence of veining, and generate later veins from hotter fluids, possibly with different compositions.

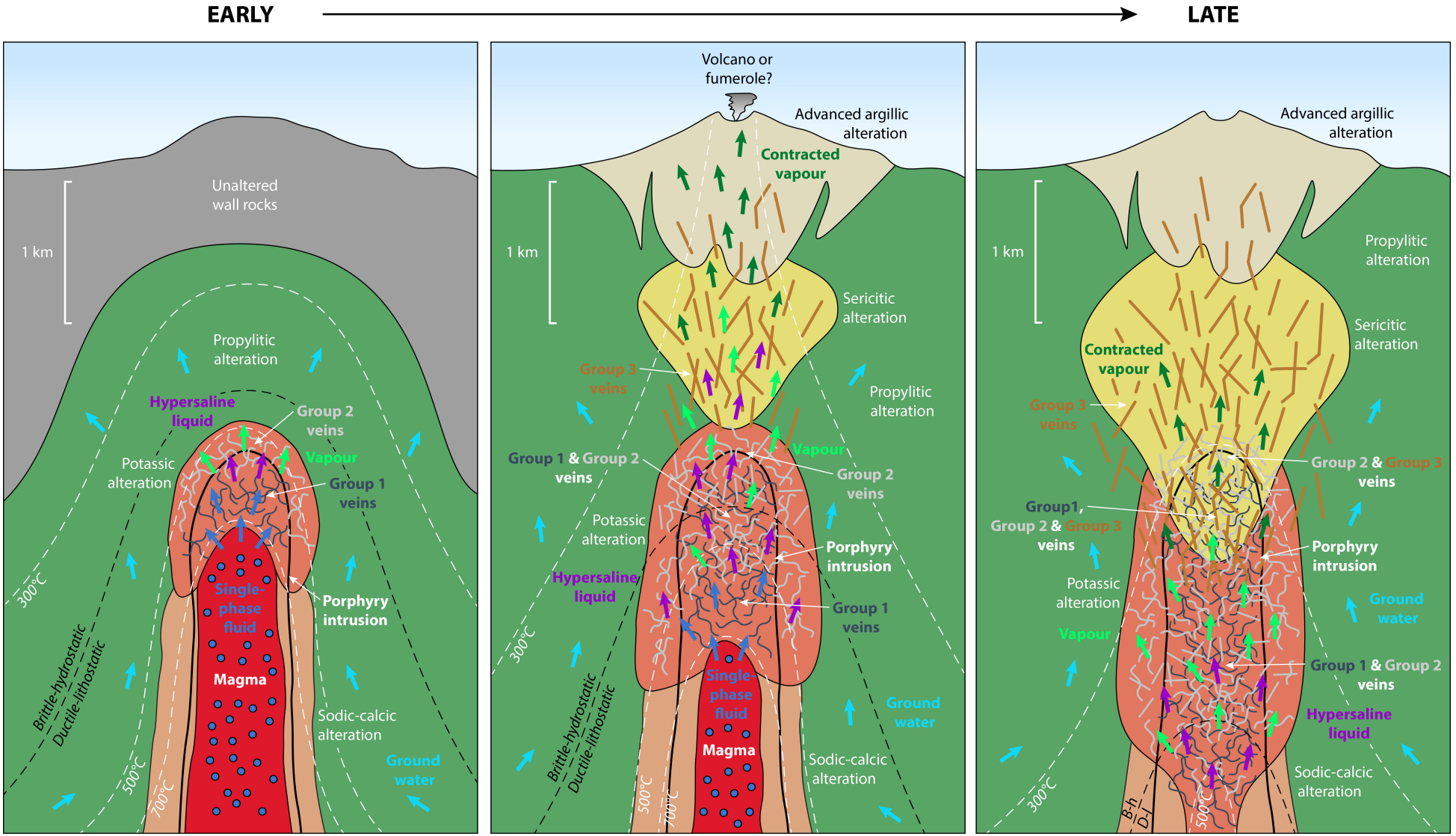
EARLY
LATE
Unaltered wall rocks
1 km
Propylitic alteration
Hypersaline liquid
Group 2 veins
Vapour
Potassic alteration
Group 1 veins
Single-phase fluid
Porphyry intrusion
Magma
Sodic-calcic alteration
Ground water
300°C
500°C
700°C
Brittle-hydrostatic
Ductile-lithostatic
Volcano or fumerole?
Advanced argillic alteration
Contracted vapour
Sericitic alteration
Group 3 veins
Group 1 & Group 2 veins
Group 1, Group 2 & Group 3 veins
B-h
D-l

2.5.4) indicates that most of the ore deposition occurs in the high temperature environment of Group 1 and 2 veins. Moreover, the presence of banded veins, likely formed by fluids in the vapour + halite field, suggests that the hydrothermal systems are active at shallow depths, coinciding with the recognised shallower depths of formation for Au-rich deposits (Murakami et al., 2010). The correlation between quartz vein intensity and metal content (Sillitoe, 2000), and the general association of Au and Cu grades in Au-rich deposits (Sillitoe, 2010), further suggests that the physical process of vein formation (i.e., fracturing and decompression) is primarily responsible for the deposition of both Au and Cu.

This evidence indicates that ore deposition in veins in Au-rich deposits likely occurs from vapour-phase fluids at high temperatures, primarily driven by decompression and coincident vapour expansion, lowering the solubility of Au and Cu in the fluid at shallow depths. This agrees well with the conclusions of Murakami et al. (2010) and Chiaradia (2020), who also suggest that Au-poor deposits are generated because Au and Cu are decoupled in the fluid at greater depths, where Cu is deposited from a single-phase fluid or relatively dense vapour, while Au remains in solution to low temperatures and may be transported to the epithermal environment. Ore deposition from a vapour in shallow porphyry deposits may account for the greater precipitation efficiency of Au purported to be required for the generation of Au-rich deposits (Section 2.4.1).

On another note, a review of large hydrothermal Au deposits by Meffre et al. (2016) indicates that the related hydrothermal systems show a more complex evolution compared to regular Au, or Au-poor, deposits. In particular, Au-rich deposits seem to require multiple stages of mineralisation, which act as small cumulative enrichment steps, rather than a single, large enrichment event. Meffre et al. (2016) suggest that multi-stage enrichments in the porphyry environment are most likely to be facilitated by multiple intrusions, leading to the generation of multiple, or long-lived, hydrothermal systems that rework earlier mineralisation and/or add to existing ores. This could be indicated where the ore and vein paragenesis is particularly complex, with evidence for high temperature fluids forming veins that overprint vein generations formed at a lower temperature.

There are also differences in the hydrothermal systems of calc-alkaline and alkaline porphyry deposits. The model illustrated in Figure 2.9 is of a calc-alkaline deposit. Alkaline porphyry deposits exhibit different patterns of alteration from those in calc-alkaline deposits, with calcic-potassic (calc-silicate and K-feldspar dominated), sodic (albite dominated), and sodic-calcic (albite-actinolite dominated) alteration assemblages observed to be more common and widespread (Lang et al., 1995b; Seedorff et al., 2005; Sillitoe, 2010). Sericitic alteration is also absent, or present in smaller volumes, than is common in calc-

alkaline deposits, while pyrite is lacking (Lang et al., 1995b; Bissig and Cooke, 2014). This means that the calc-alkaline alteration patterns illustrated in Figure 2.9 are not applicable to alkaline deposits, which instead typically exhibit a calcic-potassic altered core, zoned outward to potassic alteration and then propylitic alteration (Bissig and Cooke, 2014). Furthermore, sodic and sodic-calcic alteration may characterise the shallow and deep parts of the system, respectively, with sodic-calcic alteration distal to potassic alteration (Bissig and Cooke, 2014).

These differences in alteration may be primarily due to the greater abundance of Ca in the hydrothermal fluids associated with alkaline intrusions (Lang et al., 1995b; Bissig and Cooke, 2014), while the scarcity of sericitic alteration and pyrite shows that the amount of sulphide in the fluids is also lower in alkaline systems, with less SO_2 available to provide reduced S for pyrite deposition, and sulphuric acid to lower the fluid pH and generate sericitic alteration. This could align with a low-degree partial melt of a SCLM source for alkaline magmas, where only a fraction of the sequestered mantle sulphide phases are incorporated into the relatively low-volume partial melt (Section 2.4.2), compared to the sulphide-saturated, voluminous calc-alkaline magmas generated during active subduction. Indeed, sulphides in general are observed to be less abundant in alkaline compared to calc-alkaline deposits (Bissig and Cooke, 2014). A lower abundance of veins in general in alkaline deposits is also likely owing to the composition of alkaline magmas, which are commonly quartz-undersaturated (Lang et al., 1995b; Sillitoe, 2000), meaning that less quartz is available to the hydrothermal fluids for vein formation.

As alkaline deposits are commonly Au-rich, hydrothermal processes that are favourable for Au transport and deposition are likely to contribute to deposit formation. One of the most significant contributors may be a relative deficiency of reduced S in the fluids compared to calc-alkaline systems, meaning that Au is primarily transported as a chloride complex, and therefore unlikely to be transported as a sulphide complex to lower temperatures and potentially lost to the epithermal environment. Shallower depths of formation for Au-rich deposits may also correlate to the shallower depths of emplacement for alkaline intrusions, perhaps owing to their generation in tectonic environments not associated with active subduction (e.g., slab rollback; Section 2.4.2). As previously mentioned, shallower depths of formation are thought to promote the deposition of both Au and Cu from hydrothermal fluids in the porphyry environment, rather than the decoupling and loss of Au to the epithermal environment.

2.6 Mineral characteristics

The characteristics of different minerals located in and around porphyry deposits can be used to elucidate genetic processes, and/or aid in deposit discovery. This section principally considers two aspects relevant to the aims of the thesis: mineral growth zoning, and the development of porphyry indicator minerals.

2.6.1 Growth zoning

Minerals precipitate from a melt or fluid over given periods of time, meaning that a given mineral grain is often composed of material precipitated at different points in time. Some minerals preserve this growth history as compositionally and/or texturally-distinct zonations – commonly as concentric (or oscillatory) zones (i.e., layers), or sector zones (e.g., Shore and Fowler, 1996; Chouinard et al., 2005a; Wu et al., 2019; Steadman et al., 2021). In the case of ore minerals relevant to porphyry deposits, pyrite, tennantite-tetrahedrite, galena, and sphalerite have all been observed to exhibit zonations (Shore and Fowler, 1996). The study of growth zoning in porphyry ore minerals thus has the potential to elucidate changes in the hydrothermal fluid conditions over time. This section chiefly reviews the potential causes and implications of zoning in pyrite, given that this thesis investigates the characteristics of pyrite in detail via trace element maps (Chapter 6).

Pyrite is commonly studied in a wide range of ore deposits, owing to its ubiquity. Studies have highlighted that pyrite can exhibit oscillatory and/or sector zoning (e.g., Chouinard et al., 2005b; Large et al., 2009; Reich et al., 2013; Wu et al., 2019, 2021). In particular, trace element maps (typically via LA-ICP-MS) show that changes in the trace elements contents in pyrite tend to characterise different zones (e.g., Chouinard et al., 2005a; Large et al., 2009; Reich et al., 2013; Wu et al., 2019, 2021). However, textural changes, such as the presence or absence of porosity or inclusions, may also characterise different zones (e.g., Roman et al., 2019).

Concentric zoning in pyrite is often attributed to changes in the conditions of crystallisation (i.e., temperature, pressure, and/or the composition of the hydrothermal fluid) during mineral growth (e.g., Deditius et al., 2009; Reich et al., 2013; Tardani et al., 2017; Sykora et al., 2018; Steadman et al., 2021). For example, Tardani et al. (2017) identified fluctuations in Cu/As ratios across pyrite zones from the Tolhuaca Geothermal System, Chile, and compared this with chemical data of fluid inclusions to show that changes in hydrothermal fluid characteristics (Cu/As ratios) directly corresponded to the changes across pyrite zones. Elsewhere, Sykora et al. (2018) investigated pyrite compositions at the Lihir porphyry-epithermal deposit, Papua New Guinea, showing that early (higher

temperature), porphyry-stage pyrite had a distinct trace element signature compared to later (lower temperature), epithermal-stage pyrite. They identified some pyrite crystals with zonations that corresponded to a porphyry-stage core and epithermal-stage rim; it was interpreted that changes in the conditions of crystallisation during mineral growth were responsible for the formation of these composite pyrite crystals.

In efforts to better understand the controls on the formation of growth zoning in pyrite, Wu et al. (2019) combined nanoscale secondary ion mass spectrometry and atom probe tomography. They found that, at the micron-scale, concentric zoning of pyrite was indeed controlled by changes in fluid composition, in agreement with the findings of the studies noted above. However, they also showed that, at the nano-scale, incorporation of Au, As, and Cu into pyrite was affected by kinetic processes, including self-organisation at the crystal-fluid interface, and variations in the structure of the crystal surface (Wu et al., 2019). Growth rate, another kinetic process, is also thought to affect the development of zonations in pyrite; Roman et al. (2019) analysed pyrite geochemistry and microtextural features to show that rapid pyrite crystallisation during fluid boiling preserves porosity and inclusions in pyrite, coupled with enrichments of As, Cu, Pb, Ag, and Au in the pyrite crystal. In contrast, slower rates of crystallisation were linked to pristine pyrite crystals with elevated concentrations of Co and Ni (Roman et al., 2019). These studies show that while external factors (i.e., fluid characteristics) tend to have a dominant control on the formation of zonations in pyrite, there are also contributions from internal factors (i.e., crystal-based controls).

In the case of sector zoning in pyrite, it is thought that internal factors have a dominant influence. In particular, differences in the structure of pyrite crystal surfaces (i.e., different crystal faces) leads to variations in trace element incorporation (Chouinard et al., 2005a). If the growth rate is rapid enough that it exceeds the rates of near-surface diffusion and lattice diffusion, then sector zoning can be preserved (Wu et al., 2019).

In summary, zoning in pyrite has the potential to elucidate the genetic history of a crystal. That growth zones may record changes in the characteristics of hydrothermal fluids over time has great relevance to the aims of this thesis, and is explored further in Chapter 6 and 8.

2.6.2 Porphyry indicator minerals

Indicator minerals are mineral species, or minerals with a specific chemicstry, that indicate the presence of porphyry mineralisation; they are primarily used in exploration to locate and evaluate deposits (e.g., in terms of ore potential, or level of exposure), and vector in on mineralisation (Kelley et al., 2011; Cooke et al., 2020). A wide range of min-

erals have been studied to assess their use as indicator minerals, including igneous zircon, apatite, plagioclase, and magnetite; and hydrothermal epidote, chlorite, and alunite (Cooke et al., 2020). Such minerals were first applied in an exploration sense by assessing their presence or abundance in relation to porphyry mineralisation (e.g., Kelley et al., 2011). More recently, however, indicator minerals are increasingly studied in terms of their composition, to assess how mineral chemistry changes in relation to genetic processes and/or proximity to mineralisation (e.g., Wilkinson et al., 2015; Williamson et al., 2016; Cooke et al., 2020).

Study of magmatic plagioclase compositions from a range of porphyry-associated and barren intrusions worldwide has highlighted that plagioclase from porphyry-associated intrusions contains excess Al compared to plagioclase from barren intrusions (Williamson et al., 2016). This relationship has been confirmed in a case study of the La Paloma and Los Sulfatos porphyry systems in Chile, which further highlights that excess Al in plagioclase is variable within systems and likely a result of magmatic processes (Williamson et al., 2016). Investigation of plagioclase compositions in igneous rocks could thus be used to assess the fertiliy of intrusive suites for porphyry mineralisation.

In terms of hydrothermal minerals, it is those of propylitic alteration assemblage that have garnered most attention (Wilkinson et al., 2015; Cooke et al., 2020). This is principally owing to the comparatively large footprint of propylitic alteration in porphyry systems. Wilkinson et al. (2015) initially investigated the composition of chlorite from the Batu Hijau porphyry deposit, Indonesia, using EMPA. They found that a range of elements vary systematically in relation to the core of the deposit; in particular, the concentration of Ti, V, and Mg in chlorite exponentially decreases outwards, while the remainder of analysed elements increase (Wilkinson et al., 2015). This relationship was used to develop an equation for a given chlorite analysis that describes the distance of the chlorite from the porphyry centre; constituting a new vectoring tool (Wilkinson et al., 2015). Additionally, porphyry-related hydrothermal chlorite was shown to be compositionally distinct from local metamorphic chlorite (Wilkinson et al., 2015). More recently, Cooke et al. (2020) undertook a case study of the Resolution porphyry deposit, USA, to determine whether the chemistry of propylitic minerals could help reveal concealed deposits. Their LA-ICP-MS analyses showed that both epidote and chlorite have use in this regard; epidote exhibits a subdued As-Sb response when co-existing with pyrite, compatible with an epidote origin of between 0.7-1.5 km from the porphyry core, while temperature-sensitive trace elements in chlorite depicted spatial zonations that indicated the location of the heat source (Cooke et al., 2020).

Ore minerals have not been the focus of many studies that aim to develop indicator

minerals, as their presence is generally restricted to the deposits themselves, and thus their use is limited to vectoring in on enriched zones, or paragenetic events, within deposits, rather than discovering deposits in the first instance. It is for this reason that developing an indicator mineral from an ore mineral is not one of the primary aims of this study. However, the composition of ore minerals in porphyry deposits has been investigated, as explored in Chapter 4, and there remains some potential to develop an indicator mineral approach for ore minerals that are more widespread, such as pyrite. Furthermore, if the research of this thesis reveals links between genetic processes and the composition of ore minerals, this could constitute an initial step to developing an ore indicator mineral for porphyry deposit exploration.

2.7 Summary

This chapter has outlined the fundamental characteristics of porphyry deposits, and the genetic processes critical to their formation. It is apparent that many aspects of deposit formation are poorly constrained – particularly those related to the production of different vein generations, and the associated fluid characteristics and evolutionary processes.

The following chapters of this thesis will attempt to improve this understanding, using the Iron Cap deposit as a case study. The detailed petrographic study of vein samples in hand specimen and thin section, using an array of analytical techniques (i.e., microscopy, SEM, SEM-CL), was first carried out (Chapter 5) to identify the different vein generations present at Iron Cap. While published classification schemes provided invaluable context (Table 2.2), it was decided to classify vein generations based on empirical observations to avoid bias. Each vein generation assigned should relate to a different stage in the evolution of the hydrothermal fluids and/or the hydrothermal system. This vein-by-vein approach aims to provide a more in-depth picture of deposit formation by hydrothermal fluids, and elucidate the key stages of fluid and system evolution.

Once the veins had been characterised, the nature of the hydrothermal fluids forming different vein generations was assessed. Fluid inclusion studies have not previously been carried out at Iron Cap, and most studies investigating fluid characteristics employ fluid inclusion analyses; however, as previously mentioned, these can be fraught with complications and uncertainties. In efforts to directly assess the nature of the fluids precipitating the ore minerals, the trace element contents of ore minerals was determined by LA-ICP-MS. While this analytical approach has been applied in other mineral deposit studies to elucidate general conditions of formation, it has yet to be extensively applied to porphyry deposits in a sequential way (i.e., through the analysis of ore minerals in successive vein generations). Further discussion of this aspect of the study can be found

in Chapter 4.

The following chapter reviews the Iron Cap deposit, to provide background knowledge prior to sample analysis. It will therefore be possible to assess the characteristics of the deposit in the context of this review of porphyry deposit characteristics and genetic processes, to determine which features previously described here are also present at Iron Cap, and what this means for the understanding of the deposit.

3 Iron Cap and the KSM district

3.1 Introduction

Prior to commencement of this research project, a critical analysis of previous work on Iron Cap and KSM was required to assess the amount of study that the deposit and district have been subject to, and recognise the extent to which they are understood – in terms of their characteristics and genetic processes. Moreover, it was necessary to ensure that the aims of this research project (Section 1.3) are appropriate and achievable when using Iron Cap as a case study deposit, and to identify any particular features of the deposit that may affect the research and/or warrant further investigation. This chapter focusses on addressing these points.

Firstly, the regional and local geological setting of the KSM district is reviewed to provide a wider geological context for the Iron Cap deposit in terms of its tectonic setting, associated magmatic activity, and post-mineralisation modification (Section 3.2 and 3.3). The specific characteristics of Iron Cap are then considered on a local scale, with a focus on the lithologies, structure, alteration, mineralisation, veins, and post-mineralisation modification (Section 3.4). The characteristics described in the literature are scrutinised to provide background knowledge of the deposit, and provide a basis for comparison with the results of this research project. The characteristics of Iron Cap are then compared to those of other porphyry deposits, to assess whether there are similarities in features (Section 3.5). There is then a discussion of the genetic model of the Iron Cap deposit (Section 3.6), based on features of the deposit described in the literature, and in the context of the review of porphyry deposits and magmatic-hydrothermal systems (Chapter 2). Lastly, the implications of previous work on the aims of this thesis are assessed, to highlight the differences between the current understanding of the Iron Cap deposit, and the level of understanding required to complete this research project (Section 3.7).

3.2 Regional geological setting

British Columbia (BC) is well-endowed with both calc-alkaline and alkaline porphyry deposits (Figure 1.2; Table 3.1). The deposits are predominantly found in the accreted arc terranes of Stikine and Quesnel, where most mineralising activity is thought to have occurred during a short ∼15 m.y. period at the Triassic–Jurassic boundary (∼210-195 Ma; Logan and Mihalynuk, 2014; Febbo et al., 2015). These accreted island arc terranes are the most prolific for alkaline porphyry deposits worldwide (Bissig and Cooke, 2014). The deposits of the KSM district collectively have the highest metal endowments, and

Table 3.1
Comparison of porphyry deposits in British Columbia (from Logan and Mihalynuk, 2014, and references therein). Iron Cap and KSM data are from Febbo et al. (2015, and references therein), Campbell and Dilles (2017) and Threlkeld et al. (2020). Deposit locations are shown in Figure 1.2.

Name	Magmatic association	Terrane	Age (Ma)	Cu (Mt)	Au (t)	Values reported
This study						
Iron Cap	Calc-alkaline	ST	195	5.71	779.61	4
KSM district	Calc-alkaline	ST	190-197	14.56	1610.25	4
Other porphyry deposits in British Columbia						
Brenda	Calc-alkaline	QN	195	0.27	2.28	1
Copper Mountain	Alkaline	QN	204	1.53	n.d.	1 + 2
Galore Creek	Alkaline	ST	210-208; 205	4.08	227.8	3
Gibraltar	Calc-alkaline	CC	210	3.51	n.d.	1 + 2
Highland Valley	Calc-alkaline	QN	210; 208-206	6.12	n.d.	1 + 2
Kemess South	Calc-alkaline	ST	199	0.4	92.3	1 + 2
Kwanika	Calc-alkaline	QN	200	0.53	51.1	3
Lorraine	Alkaline	QN	178	0.21	8.29	4
Mount Polley	Alkaline	QN	205	0.48	50.1	1 + 2
Mt. Milligan	Alkaline	QN	185	0.96	187.24	2
Red Chris	Alkaline	ST	204	3.5	360.4	3
Schaft Creek	Alkaline	ST	222	3.14	209.7	3
Woodjam	Calc-alkaline	QN	197	0.48	n.d.	5

Terrane abbreviations: ST, Stikine; QN, Quesnel; CC, Cache Creek. Values reported: 1, Metal produced; 2, Proven and probable reserves; 3, Measured and indicated resources; 4, Inferred resources; 5, Initial resource. n.d., no data.

Iron Cap alone is the most Au-enriched (Table 3.1), making both the KSM district and the Iron Cap deposit of particular economic and geological significance for the region.

Iron Cap and the KSM district are situated in the Stikine terrane – a long-lived arc terrane that developed over 200 m.y. from the Late Devonian until the Early Jurassic, and now forms part of the Intermontane belt of the Canadian Cordillera (Figure 1.2; Nelson and Kyba, 2014; Febbo et al., 2019). The Intermontane belt is comprised of the oceanic rocks of the Cache Creek terrane, sandwiched between the volcanosedimentary rocks of the Quesnel and Stikine arc terranes (Logan and Mihalynuk, 2014). There is strong stratigraphic, magmatic, and metallogenic evidence to suggest a similar genetic history for the Stikine and Quesnel terranes (Logan and Mihalynuk, 2014), leading to proposals that the present-day arrangement may have arisen due to oroclinal enclosure of the oceanic Cache Creek rocks by island arc segments representing the Stikine and Quesnel terranes (e.g., Nelson et al., 2013). However, debate continues over the exact geodynamic mechanisms reponsible (Logan and Mihalynuk, 2014).

The Stikine terrane is made up of three, unconformity-bounded, island arc successions of volcanosedimentary strata (Febbo et al., 2015). The Early Jurassic Hazelton

Group unconformably overlies the Late Triassic Stuhini Group, and represents the waning of island arc magmatism prior to accretion of the terrane to the Laurentian Margin (North American Craton) in the Middle Jurassic (Nelson and Colpron, 2007; Nelson and Kyba, 2014). The sequences of the Hazelton Group are the dominant hosts for mineralisation within the Stikine terrane (Nelson and Kyba, 2014), suggesting that porphyry deposits in the Stikine terrane are largely associated with the later stages of island arc activity prior to accretion. Indeed, Logan and Mihalynuk (2014) explain that, following an early period of porphyry-forming arc magmatism in the Late Triassic (∼208-202 Ma), the locus of magmatism migrated toward the back-arc, leading to the generation of progressively younger porphyry deposits in the Late Triassic and Early Jurassic.

In contrast to conventional theories of magma generation in subduction settings (Section 2.3), Logan and Mihalynuk (2014) propose a model whereby Late Triassic-Early Jurassic magmas were generated during stalling and tearing of the subducting slab, which critically induced partial melting of the overlying mantle wedge by incursion of hot sub-slab mantle through the slab tear. This is thought to have initially produced a high degree of partial melting (i.e., calc-alkaline magmas and porphyry deposits), but as the thermal spike receded and the tear widened, a low degree of partial melting occurred across a wider area, generating later alkaline magmas and associated porphyry deposits (Logan and Mihalynuk, 2014). Moreover, magmatism migration toward the back-arc may reflect migration of the slab gap (Logan and Mihalynuk, 2014). Geochemical evidence for this theory comes largely from studies of Late Triassic arc rocks, which show a lack of crustal assimilation in the magmas and retention of a primary mantle source signature that is thought to signify the absence of significant storage and evolution in a lower-mid crustal chamber (Logan and Mihalynuk, 2014, and references therein).

3.3 KSM district geology

The four porphyry deposits of the KSM district are centered on a series of diorite to syenite intrusions, part of the Texas Creek intrusive suite, with adjacent wall rocks comprising the units of the Stuhini Group and Hazelton Group (Figure 3.1; Alldrick, 1993). The Texas Creek suite was emplaced in the Early Jurassic, and is coeval and cogenetic with the volcanosedimentary units of the Hazelton Group (Nelson et al., 2018). On a local scale, radiometric dating (U-Pb zircon) suggests that the KSM intrusions, and hence the associated mineralisation, were emplaced in the Early Jurassic between 197 and 189.6 Ma (Febbo et al., 2015, and references therein).

The KSM deposits are classified as calc-alkaline, exhibiting an abundance of quartz veins, pyrite, and sercitic alteration (cf. Section 2.4.2; Campbell and Dilles, 2017). How-

ever, an earlier overview of alkaline porphyry deposits by Bissig and Cooke (2014) incorrectly classifies the KSM deposits as alkaline. This discrepancy is possibly due to the differing magmatic classification of the two Texas Creek intrusive suites present in the district, with the Sulphurets suite classified as calc-alkaline, and the Premier suite as alkaline (Febbo et al., 2015). The calc-alkaline Sulphurets plutons are composed of diorite, monzodiorite, granodiorite, and monzonite, while the roughly contemporaneous alkaline Premier plutons, sills and dykes are monzonite to syenite in composition (Febbo et al., 2015; Campbell et al., 2020). Mineralisation in the KSM district is largely related to the Sulphurets intrusions, which are pre-, syn-, and post-mineralisation (Febbo et al., 2015). One exception is the Sulphurets *deposit*, whose mineralisation is dominantly wall rock-hosted and not clearly linked to an intrusive suite (Campbell et al., 2020). Mineralisation can also be found on the margins of some of the Premier intrusions, though this is low grade (Campbell et al., 2020).

The KSM district forms part of a 60 km-long trend of magmatic related mineral deposits, including porphyry, epithermal, and VMS, which stretches N-NW from the town of Stewart to the mining district around KSM (Figure 1.2; Logan and Mihalynuk, 2014; Febbo et al., 2015). Geological mapping, and the spatial association of mineral deposits to regional lineaments, lead Nelson and Kyba (2014) to hypothesise a structural control to this trend. They suggested a model in which a large-scale basin-bounding fault, formed by the extensional or transtensional tectonics dominant in the Early Jurassic, acted as a conduit for the magmas to ascend and form associated mineral deposits (Nelson and Kyba, 2014). While this hypothesis explains deposit alignments, empirical evidence for such a large-scale fault is yet to be acquired.

In contrast, post-mineralisation tectonic activity in the KSM district is clearly evident. The Stikine terrane as a whole was deformed in the mid-Cretaceous by sinistral transpression that produced the Skeena Fold-and-Thrust Belt (SFTB), an extensive NE-verging zone of shortening that resulted in N-NW-trending structures (Nelson and Kyba, 2014). A N-trending structural culmination associated with this tectonic activity, the McTagg anticlinorium, now hosts KSM on its eastern limb (Febbo et al., 2015). Locally, the KSM deposits are mostly situated within the footwall of the E-verging Sulphurets Thrust Fault

Figure 3.1. *(next page)* Geology of the KSM district, showing company licence areas at the present time (Campbell et al., 2020, adapted from Febbo et al., 2015). Mineral deposits in the adjacent licence area include Snowfield; purported to be the displaced cap of the Mitchell deposit, and Brucejack (collectively "West zone" and the "Valley of the Kings"), a high-grade epithermal-Au deposit (Savell and Threlkeld, 2013).

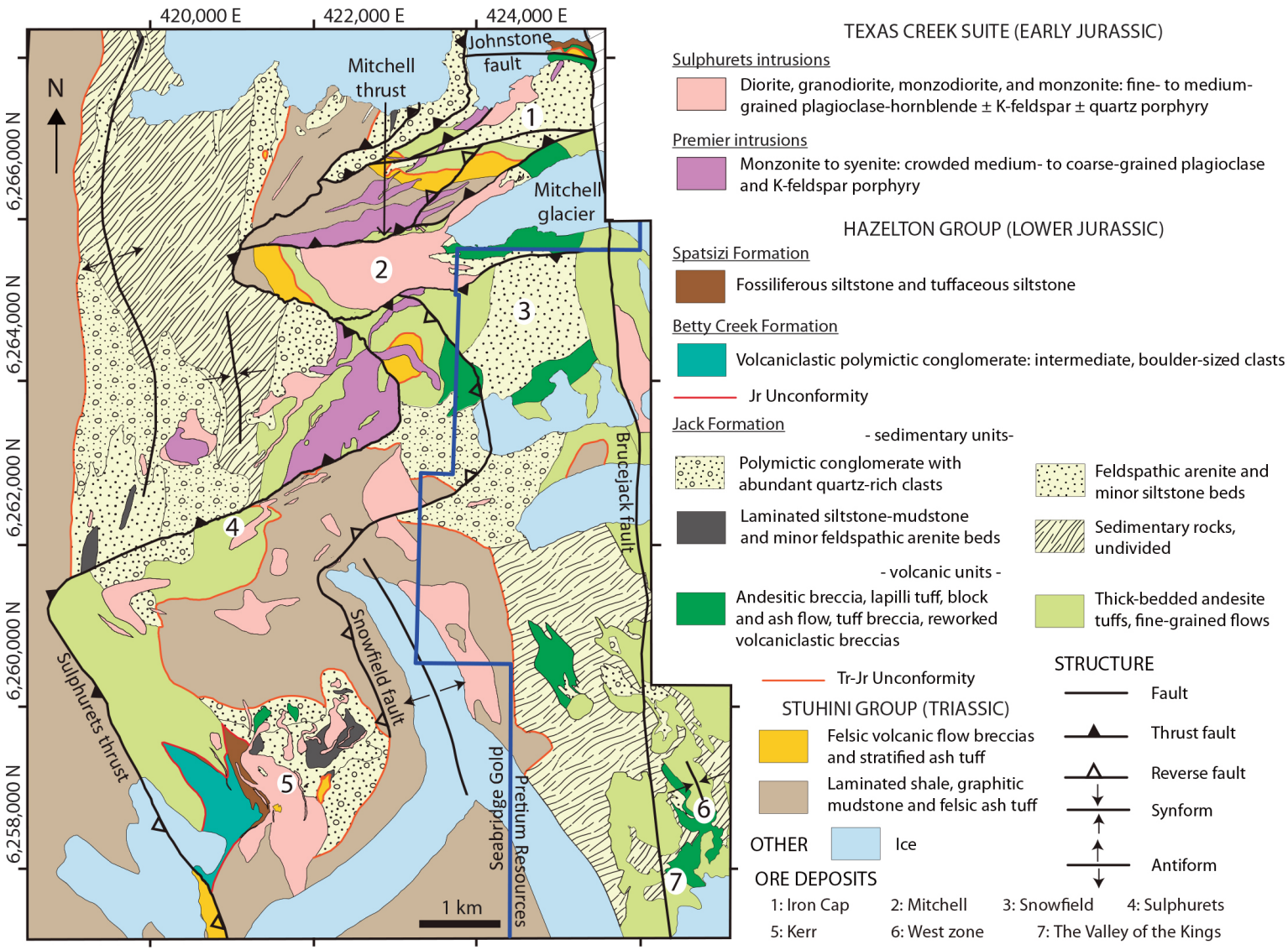
420,000 E
422,000 E
424,000 E
6,266,000 N
6,264,000 N
6,262,000 N
6,260,000 N
6,258,000 N
N
Johnstone fault
Mitchell thrust
Mitchell glacier
Brucejack fault
Snowfield fault
Sulphurets thrust
Seabridge Gold
Pretium Resources
1 km
1
2
3
4
5
6
7
TEXAS CREEK SUITE (EARLY JURASSIC)
Sulphurets intrusions
Diorite, granodiorite, monzodiorite, and monzonite: fine- to medium-grained plagioclase-hornblende ± K-feldspar ± quartz porphyry
Premier intrusions
Monzonite to syenite: crowded medium- to coarse-grained plagioclase and K-feldspar porphyry
HAZELTON GROUP (LOWER JURASSIC)
Spatsizi Formation
Fossiliferous siltstone and tuffaceous siltstone
Betty Creek Formation
Volcaniclastic polymictic conglomerate: intermediate, boulder-sized clasts
Jr Unconformity
Jack Formation
- sedimentary units-
Polymictic conglomerate with abundant quartz-rich clasts
Laminated siltstone-mudstone and minor feldspathic arenite beds
Feldspathic arenite and minor siltstone beds
Sedimentary rocks, undivided
- volcanic units -
Andesitic breccia, lapilli tuff, block and ash flow, tuff breccia, reworked volcaniclastic breccias
Thick-bedded andesite tuffs, fine-grained flows
Tr-Jr Unconformity
STUHINI GROUP (TRIASSIC)
Felsic volcanic flow breccias and stratified ash tuff
Laminated shale, graphitic mudstone and felsic ash tuff
OTHER
Ice
ORE DEPOSITS
1: Iron Cap
2: Mitchell
3: Snowfield
4: Sulphurets
5: Kerr
6: West zone
7: The Valley of the Kings
STRUCTURE
Fault
Thrust fault
Reverse fault
Synform
Antiform

(STF), which is linked to the SFTB (Figure 3.1; Kirkham and Margolis, 1995; Febbo et al., 2015). A splay of the STF, the Mitchell Thrust Fault (MTF), also separates the Iron Cap and Mitchell deposits at the northern end of the district (Febbo et al., 2015). It is *not* thought that Iron Cap and Mitchell were once one deposit; rather, a deposit in the adjacent licence area (Snowfield) is thought to be the displaced cap of the Mitchell deposit (Figure 3.1; Savell and Threlkeld, 2013). The Brucejack deposit is a high-grade epithermal Au deposit also situated in the adjacent license area, hosted by younger host rocks than the KSM deposits (U-Pb zircon dates of 188-184 Ma; cf. Table 3.1), and structurally separated from the district by the oblique dextral and reverse Brucejack Fault, which is interpreted to have been active after epithermal mineralisation (Tombe et al., 2018). The alkaline Premier intrusions and associated mineralisation are largely confined to the hanging walls of the STF and MTF (Campbell et al., 2020), thus are spatially and structurally separated from the main ore zones.

Lower greenschist facies metamorphism likely coincided with tectonic activity in the mid-Cretaceous (Alldrick, 1993). This is purportedly represented by the mineral assemblage of chlorite-carbonate-sericite-pyrite-epidote identified in volcaniclastic rocks of the KSM district (Alldrick, 1993). However, this mineral assemblage can also characterise hydrothermal propylitic alteration (Seedorff et al., 2005). Alldrick (1993) suggests that distinction between greenschist facies metamorphism and hydrothermal propylitic alteration is possible by comparison, where propylitic rocks have a greener colour, host coarser pyrite, and have a greater calcite content than metamorphically-altered rocks. Further mineralogical evidence to indicate the coincidence of metamorphism with tectonic activity in the mid-Cretaceous is provided by pyrite pressure shadows infilled by chlorite, or quartz and minor sericite, and the curving of quartz and chlorite crystals during mineral growth, both of which exemplify syn-deformational mineral growth (Alldrick, 1993). Alldrick (1993) suggests that peak metamorphic conditions were 280$\pm$20°C and 4.5$\pm$1.5 kbar, evidenced by the mineral assemblage phase transitions, and the resetting of K-Ar dates from biotite, sericite and feldspar, the latter of which also indicates that the thermal peak occurred 110$\pm$10 Ma – in alignment with the occurrence of tectonic activity in the mid-Cretaceous.

3.4 Iron Cap deposit geology

3.4.1 Introduction

The Iron Cap deposit stretches NE for $\sim$1.5 km at the northern end of the KSM district, and is so named owing to the distinctive Fe-oxide stained exposure on the ridge line

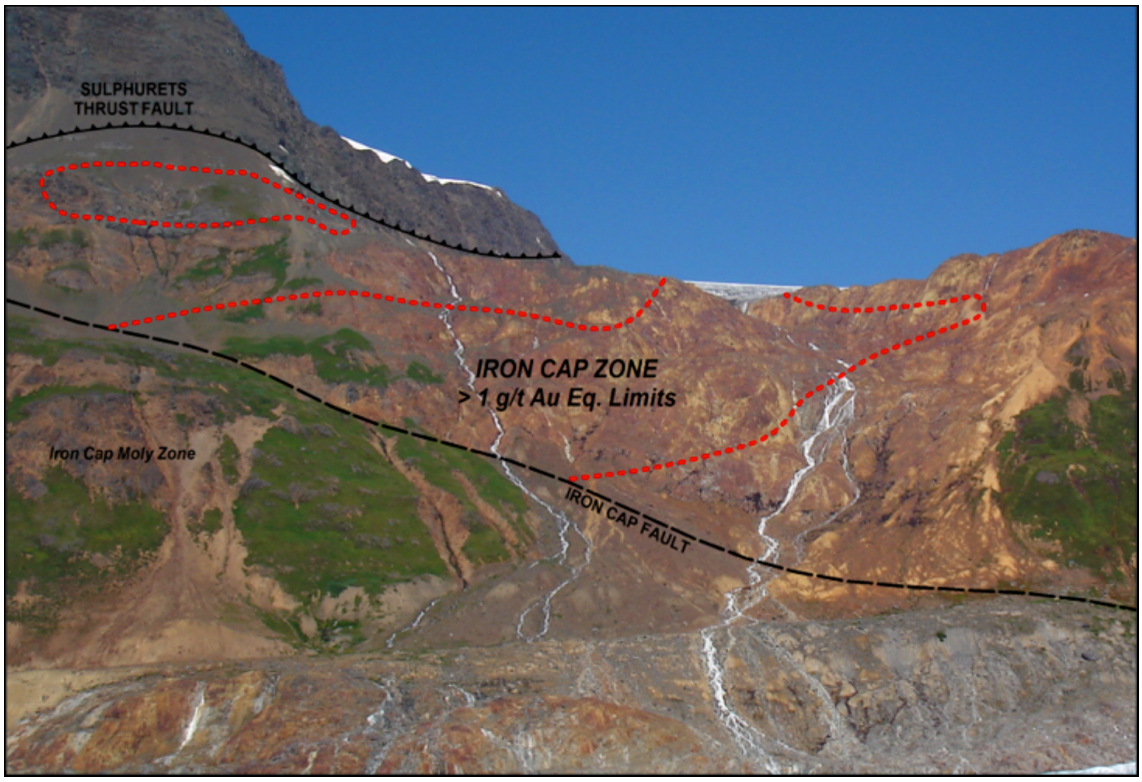

Figure 3.2. View of the Iron Cap deposit exposure from the eastern end of the Mitchell deposit, looking northwards (Savell and Threlkeld, 2013). This photograph was taken from approximately 1 km southwards of the middle of the bottom edge of the map in Figure 3.3. The zone limits shown here are outdated; current demarkations are shown in plan view in Figure 3.3.

opposite the Mitchell deposit (Figure 3.2; Seabridge Gold, 2020a). The roughly cylindrical orebody attains thicknesses of up to 800 m, and plunges ∼60° to the W-NW, extending down to at least 1.5 km below surface (Threlkeld et al., 2020). Iron Cap can be classified as both a Au-rich porphyry deposit (Section 1.2), and a giant Cu-Au porphyry deposit in terms of total contained metal, significantly exceeding the benchmark of giant deposits defined by Singer (1995) of 2 Mt Cu and 3.2 Moz Au (equivalent to ∼90 t Au; Table 3.1).

The following sections outline the key lithologies, structure, alteration, mineralisation and vein sequences related to Iron Cap, as reported by Campbell et al. (2020) – the only in-depth study of the deposit to date.

3.4.2 Lithologies

Intrusives of the Texas Creek suite form the central ore zone of the Iron Cap deposit (Figure 3.3, 3.4a, and 3.5a). These are classified as the pre-mineralisation P2 East diorite, syn-mineralisation P2 West diorite, P3 East and P3 West monzonites, and the post-mineralisation P4 monzodiorite (Figure 3.6; Campbell et al., 2020). Syn-mineralisation hydrothermal breccias and the surrounding wall rocks of the Hazelton Group also host mineralisation, while rare, barren post-mineralisation mafic dykes also occur (Campbell

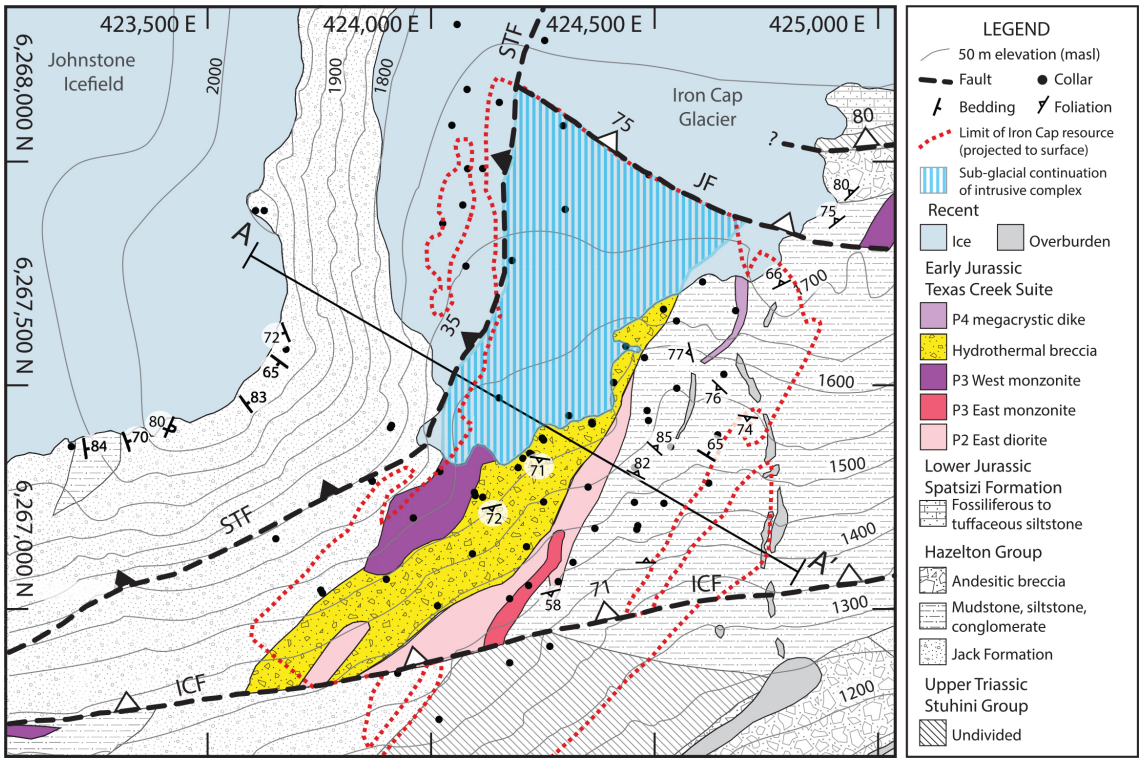

Figure 3.3. Geology of the Iron Cap deposit (Campbell et al., 2020). Three faults are seen at surface: the Iron Cap fault (ICF), the STF, and the Johnstone Fault (JF).

et al., 2020).

3.4.2.1 P2 diorites

As the intrusive equivalent of andesites, diorites are dominated by plagioclase, with lower proportions of dark-coloured minerals, such as hornblende and biotite (Best, 2003). The diorites classified as P2 at Iron Cap are plagioclase- and hornblende-phyric, with a fine-grained groundmass (Figure 3.6c; Campbell et al., 2020). They are divided into the pre-mineralisation P2 East diorite and the syn-mineralisation P2 West diorite, although the only petrographical distinction between the two is the slight difference in the size of phenocrysts; those in P2 East diorites are 1-5 mm long, while those in P2 West diorites are 1-3 mm long (Campbell et al., 2020). This difference is minor enough that it would be difficult to distinguishing between P2 East and P2 West diorites on petrography alone. Indeed, it appears that Campbell et al. (2020) recognise that the key distinction between P2 East and P2 West diorites is the location of the intrusive bodies, and their relationship to hydrothermal features; the P2 West intrusion is reported to host significant volumes of A-veins (below) and some of the highest Au and Cu grades, while the P2 East intrusion is comparatively quartz vein- and metal-poor. However, Figure 3.4 and 3.5 show that the P2 East diorite still hosts modest Au grades and patchy concentrations of quartz veins. In general, these maps also show that there is a poor correlation between lithol-

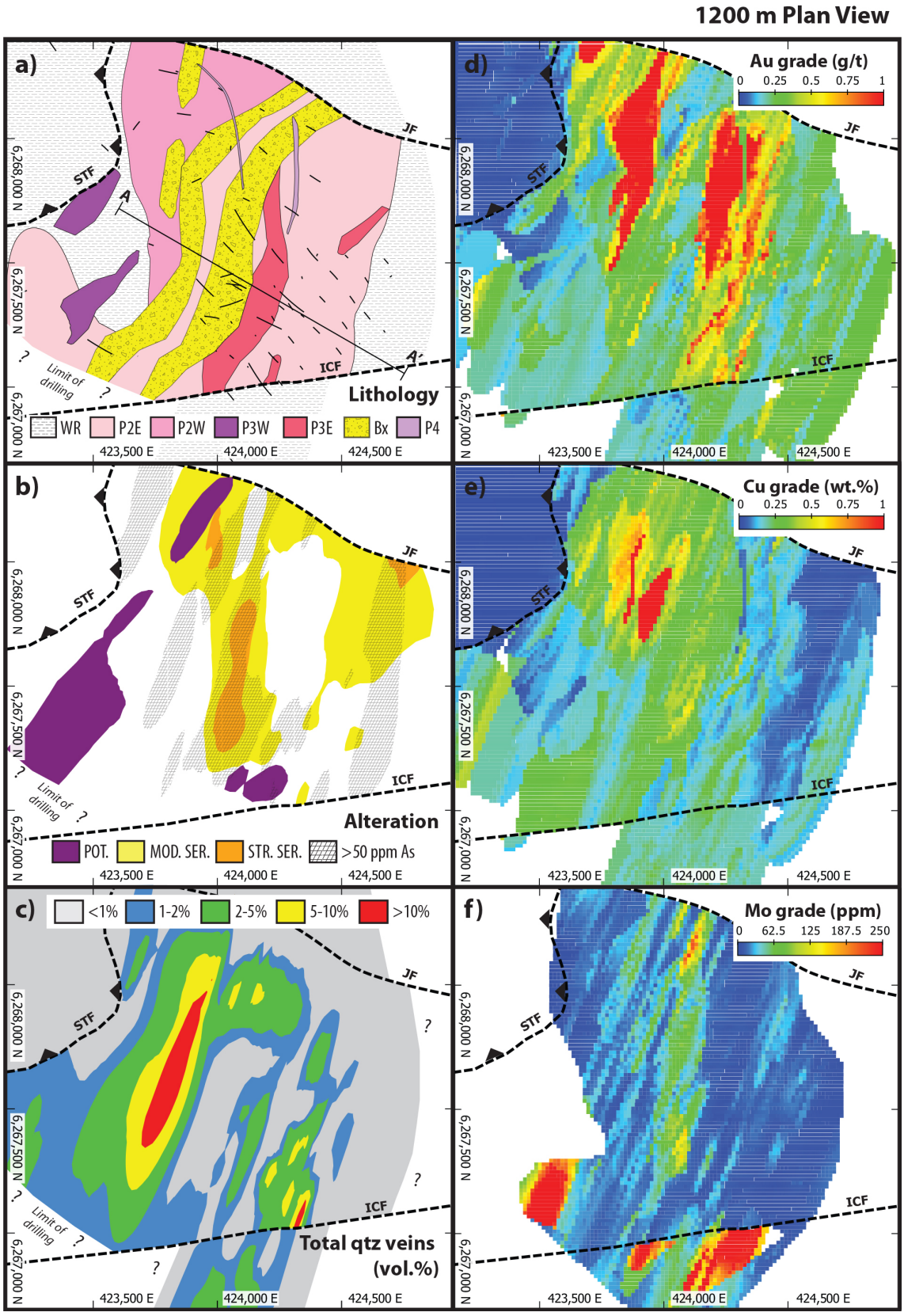

Figure 3.4. Plan view of the Iron Cap deposit at 1200 m elevation, showing: a) Lithologies, where P2E-P4 are intrusives described in the text, WR = undifferentiated wall rock, Bx = hydrothermal breccias, and black lines are drill holes within 100 m of the section; b) Hydrothermal alteration zones, where POT. = potassic, MOD. SER. = moderate sericitic, STR. SER. = strong sericitic; c) Volume of quartz veins; d) Au grade; e) Cu grade; f) Mo grade (Campbell et al., 2020).

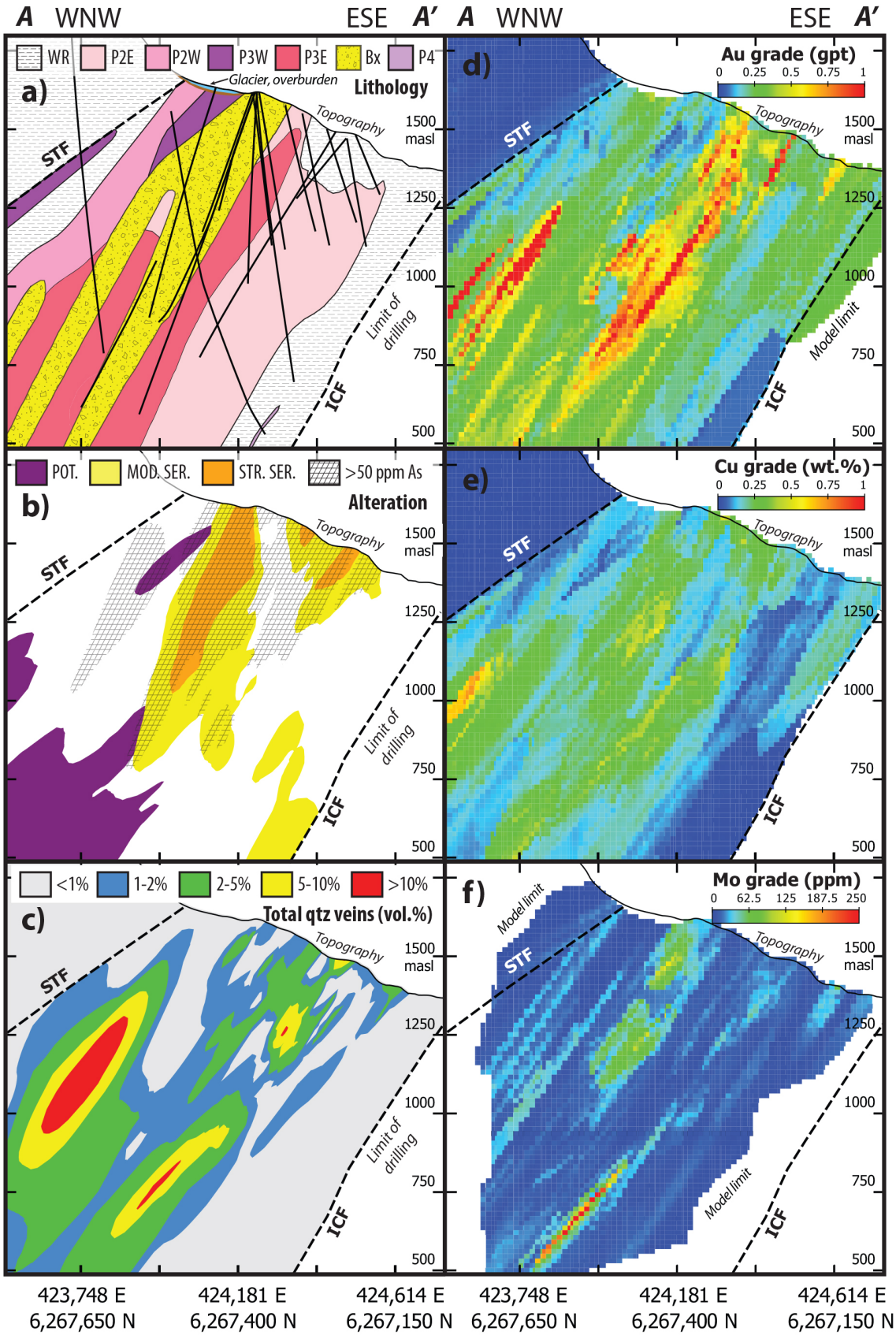

Figure 3.5. Cross section through the Iron Cap deposit along the A-A′ section line shown in Figure 3.3 and 3.4a, and looking N-NE (Campbell et al., 2020). The cross section shows: a) Lithologies, with drill holes within 100 m of the section shown as black lines; b) Hydrothermal alteration zones; c) Volume of quartz veins; d) Au grade; e) Cu grade; f) Mo grade. Abbreviations are the same as in Figure 3.4.

ogy, quartz vein volume, and metal grades, meaning that intrusion classification based on hydrothermal features is not conclusive.

The distribution of quartz veins and metals in the P2 diorites is also the criteria used to assign a pre-mineralisation timing for emplacement of the P2 East diorite, and syn-mineralisation timing for emplacement of the P2 West diorite (Campbell et al., 2020). No cross-cutting relationships are observed between any of the P2 diorites and P3 monzonites (Campbell et al., 2020), although the distribution of the P3 East intrusion in Figure 3.5a suggests that it post-dates the P2 diorites, and Campbell et al. (2020) note that hydrothermal breccias that contain clasts of P2 East diorite are cut by P3 intrusions, implying that P3 intrusions post-date the P2 East diorite. Nevertheless, because both the P2 East and P2 West intrusions host veins, metals, and are hydrothermally altered (Figure 3.4 and 3.5), they must have been emplaced either pre- or syn-mineralisation. As above, the volume and distribution of hydrothermal features within intrusions is not a conclusive indication of genetic difference, thus the relative emplacement timing of the P2 diorites is open to interpretation.

Diorites with near-identical characteristics to P2 diorites are also central to the nearby Mitchell deposit, where they are classified as a single pre- to syn-mineralisation intrusive phase, and show a similar widespead distribution in the ore zone as observed at

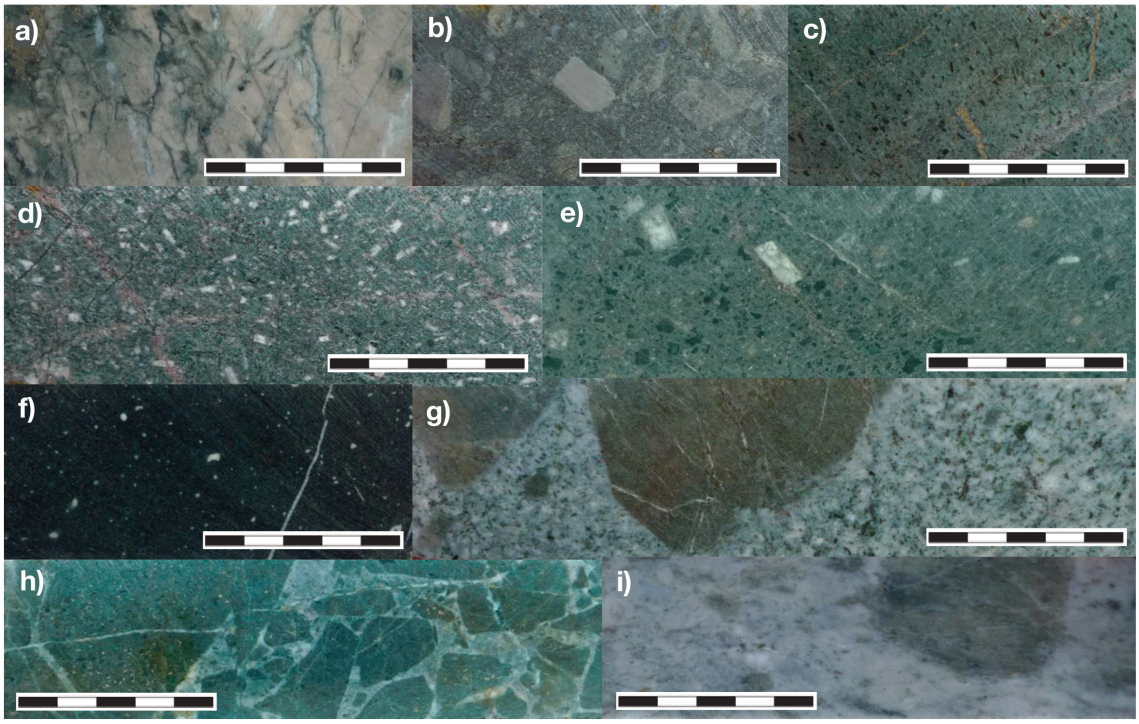

Figure 3.6. Lithologies of the Iron Cap deposit: a) Hazelton Group mudstone hornfels; b) Jack Formation conglomerate; c) P2 East diorite; d) P3 East monzonite; e) P4 monzodiorite; f) mafic dyke; g) P3 East monzonite intrusion breccia with wall rock clasts; h) hydrothermal breccia with P2 East clasts; i) strongly altered hydrothermal breccia (5 cm scale; Campbell et al., 2020).

Iron Cap (Febbo et al., 2019). The Mitchell deposit diorites are distinguished as pre-mineralisation when veins hosted by the intrusions have relatively sharp margins, and as syn-mineralisation when veins are wavy, disarticulated, and irregular; the latter thought to imply incomplete diorite crystallisation (Febbo et al., 2015). This classification may be flawed, because vein formation in a ductile regime (associated with the emplacement of a later intrusion, for example) may also generate wavy, disarticulated, and irregular veins (Sillitoe, 2010), hence this feature does not necessarily imply incomplete crystallisation of a magma body. Therefore, the diorites at Mitchell also do not exhibit definitive evidence to be classed as either pre- or syn-mineralisation, but they are classed as pre- *to* syn-mineralisation (Febbo et al., 2019).

Overall, the limited petrographical distinction between the P2 East and P2 West diorites, the inconclusive discrimination based on location and hydrothermal features, and comparisons with Mitchell diorites, suggests that the P2 diorites at Iron Cap may constitute a single intrusive phase. The higher volumes of quartz veining and higher metal grades in the P2 West diorite relative to the P2 East diorite could be attributed to differing degrees of hydrothermal activity, rather than a difference in the timing of intrusion emplacement. For example, as discussed in Section 2.3.3, magma emplacement rate and magma volume appear to be particularly important in controlling the hydrothermal fluid flux during porphyry deposit formation. Therefore, the P2 West diorite may have been emplaced more rapidly and/or in greater volumes than the P2 East diorite, to allow a greater flux of fluids and the potential for higher volumes of quartz veining and greater metal endowments (e.g., Chelle-Michou et al., 2017; Schöpa et al., 2017; Chiaradia and Caricchi, 2022).

3.4.2.2 P3 monzonites

The key difference between diorites and monzonites is the greater abundance of K-feldspar in the monzonites, combined with a lower proportion of plagioclase (Best, 2003). Intrusions classified as monzonite at Iron Cap have a seriate texture, with phenocrysts of plagioclase, K-feldspar, and hornblende (and quartz) up to 6 mm in size (Figure 3.6d; Campbell et al., 2020). As with the P2 East and West diorites, there is limited petrographical distinction between P3 East and West monzonites; the P3 West monzonites are typically coarser-grained than P3 East monzonites (Campbell et al., 2020). Location relative to the deposit is the key distinction between the P3 monzonite intrusions, with P3 East constituting thin dykes and a singular ∼100 m thick, west-dipping (∼60°), tabular instrusive that strikes roughly north through the centre of Iron Cap, while P3 West intrusions are observed in the western half of the deposit and are not morphologically defined (Figure

3.4a and 3.5a; Campbell et al., 2020). From the data presented, it is possible that the P3 East and P3 West monzonites collectively constitute a single intrusive phase, and thus, similarly to the P2 diorites, do not necessitate discrete classification.

Nevertheless, Campbell et al. (2020) note that metals are more concentrated in the P3 East monzonites, relative to the poorly-mineralised P3 West monzonites. This can be observed to some degree in Figure 3.4 and 3.5, although there is generally a poor correlation between lithology and metal contents. As noted above, hydrothermal breccias that contain clasts of P2 East diorite are cut by P3 intrusions (Campbell et al., 2020), implying that P3 monzonites post-date P2 diorites. The P3 monzonites must therefore have been emplaced syn-mineralisation, because these are the youngest intrusions that host mineralisation. Radiometric U-Pb zircon dating of the P3 East monzonite returned an age of 194.4 ± 2.1 Ma (Campbell and Dilles, 2017) – the only absolute age for magmatism at Iron Cap, which probably coincides with the timing of mineralisation.

3.4.2.3 Hydrothermal breccias

Volumetrically significant hydrothermal breccias are present in the centre of the Iron Cap ore zone (Figure 3.3; Campbell et al., 2020). Two types are recognised; the first occurs in 10-250 m wide, N-striking zones that are tabular and steeply-dipping (Figure 3.4a and 3.5a; Campbell et al., 2020). This breccia type exhibits matrix-supported, poorly sorted, sub-angular clasts that can often be identified as P3 monzonite in areas where hydrothermal alteration has not destroyed the original rock texture (Figure 3.6i; Campbell et al., 2020). Together with the cross-cutting of the P3 East intrusion by the hydrothermal breccia (Bx) in Figure 3.4a and 3.5a, the nature of the clasts implies syn- or post-P3 formation. This breccia type is therefore syn-mineralisation, as indeed interpreted by Campbell et al. (2020), in line with the syn-mineralisation timing of the P3 intrusions.

The second breccia type is common on the margins of the P2 East intrusion, exhibiting a jigsaw pattern texture, and containing sub-angular to angular clasts of P2 East diorite in a fine-grained and hydrothermally-altered matrix (Figure 3.6h; Campbell et al., 2020). This breccia type must have formed syn- or post-P2 East emplacement, and is therefore pre- or syn-mineralisation, in line with the timing of the P2 intrusions.

Separate to the hydrothermal breccias, small intrusion breccias are common at the margins of P3 intrusives, and can be distinguished by their coherent monzonite matrix, with poorly sorted, sub-angular wall rock clasts (Figure 3.6g; Campbell et al., 2020). The formation of these breccias coincides with the emplacement of the P3 intrusions, given that the matrix is composed of the same rock as the P3 intrusives.

Although not categorised by Campbell et al. (2020), the hydrothermal breccias appear

to fall into the class of magmatic-hydrothermal breccias (as defined by Sillitoe, 2010), as opposed to phreatic or phreatomagmatic breccias (cf. Section 2.3.4). An implication of this is that hydrothermal breccia formation is synchronous with early and/or main-stage, deep-seated hydrothermal activity, and not related to later and/or shallower hydrothermal activity (cf. Section 2.3.4). This coincides with the timing of hydrothermal breccia emplacement informed by clast analysis as syn-mineralisation (first breccia type), and pre- or syn-mineralisation (second breccia type).

3.4.2.4 P4 monzodiorites

Monzodiorites sit compositionally between diorites and monzonites, with a higher proportion of K-feldspar than diorites, and a lower proportion than monzonites (Best, 2003). The post-mineralisation P4 monzodiorites at Iron Cap are plagioclase-K-feldspar-hornblende-phyric, with phenocrysts of plagioclase and hornblende up to 8 mm, and K-feldspar up to 2 cm (Figure 3.6e). This intrusive phase occurs as thin dykes restricted to the northern half of the deposit (Figure 3.4a; Campbell et al., 2020), and clearly cuts the P2 diorites and hydrothermal breccias, providing relative timing constraints. It is not implicitly stated by Campbell et al. (2020) why the P4 monzodiorites are interpreted as post-mineralisation, other than that they are comparable to post-mineralisation dykes at the nearby Kerr deposit, and that this dyke suite is collectively thought to have been formed during the waning stages of the porphyry magmatic system.

Conflictingly, Figure 3.4 shows that the two P4 occurrences at 1200 m elevation exhibit different metal endowments. The eastern P4 dyke post-dates the mineralisation, observed as a low-grade strip in the Au and Cu grade maps. Meanwhile, the western P4 dyke does not appear to cut the mineralisation in the same way, and is not visible on the Au and Cu grade maps. However, this may be an artefact of the model, with the cell size for metal grades exceeding the width of the dyke, thus its low metal content is not represented. Regardless, the P4 dykes are relatively rare, and do not appear to be volumetrically significant.

3.4.2.5 Mafic dykes

A series of mafic to ultramafic dykes are also present at Iron Cap, exhibiting dark green to black colours, aphanitic textures, and metre-scale thicknesses (Figure 3.6f; Campbell et al., 2020). They are rare at Iron Cap, although common throughout the KSM district as a whole, and are thought have been emplaced in the Cretaceous during post-mineralisation tectonic activity (Campbell et al., 2020).

3.4.2.6 Wall rocks

The wall rock immediately surrounding the intrusive complex is composed of Jack Formation – a basal unit of the Hazelton Group – mudstones, sandstones, and polymictic pebble conglomerates (Figure 3.3 and 3.6b; Nelson and Kyba, 2014; Campbell et al., 2020). The sedimentary rocks are altered to hornfels (Figure 3.6a; Campbell et al., 2020), although the extent of this alteration is not defined. The presence of hornfels implies contact metamorphism at high temperatures (>700°C) took place around the intrusions (Best, 2003); however, the mineralogy of the hornfels is not reported, hence the exact grade of contact metamorphism cannot be defined.

3.4.3 Structure

The mid-Cretaceous SFTB that affected the Stikine terrane also produced localised features around Iron Cap. The deposit is bounded by four faults: the ICF to the south, the STF to the west and above, the JF to the north, and the MTF at depth (Figure 3.1, 3.3, and 3.4a; Campbell et al., 2020). The imbricate, E-verging STF, and associated MTF splay, are interpreted to have formed as a direct result of the shortening that occurred to produce the SFTB (Febbo et al., 2015). The STF is shallow- to moderately-dipping, and strikes to the north, while the MTF strikes roughly to the east (Campbell et al., 2020).

The origin of the ICF is less clear, lacking observed kinematic indicators (Campbell et al., 2020). Given the steep northerly dip and E-W strike, Campbell et al. (2020) suggest either a dip-slip motion, or a strike-slip tear relating to the SFTB. The JF has a similar orientation, striking E-W and with a subvertical dip, though the origin is again uncertain – Campbell et al. (2020) suggest a strike-slip step-over motion, parallel to the shortening direction of the SFTB. Comparatively, Febbo et al. (2019) propose that the JF was active during the Early Jurassic, and that movement is consistent with a south-side-down normal fault. This is purportedly evidenced by differences in lithology; north of the JF a <100 m thick section of the Hazelton Group unconformably overlies the Stuhini Group, while south of the fault, a thick sequence of Jack Formation is present. However, these changes in lithology are not evident in Figure 3.3.

Section 3.4.7 contains further discussion of deposit modification by post-mineralisation tectonic activity.

3.4.4 Alteration

Alteration associated with hydrothermal activity is present throughout Iron Cap, with potassic and sericitic assemblages the most prolific (Figure 3.4b and 3.5b). Campbell

et al. (2020) state that the only unaltered areas of the deposit are located to the north of the JF, in the hanging wall of the STF, and the mafic to ultramafic dykes. However, Figure 3.4b and 3.5b show blank (white) areas in the central ore zone. It is unclear whether these areas are altered or not; propylitic alteration may occur here, given that it is recognised as a peripheral assemblage at Iron Cap by Campbell et al. (2020). The extent of propylitic alteration is generally not well recorded, but Campbell et al. (2020) state that an assemblage of chlorite-epidote-carbonate $\pm$ hematite $\pm$ magnetite extends out in to the distal wall rock. As mentioned previously, this assemblage can also represent greenschist facies metamorphism (Section 3.3), thus difficulty distinguishing between propylitic and greenschist facies metamorphism assemblages likely explains the absence of propylitic alteration in Figure 3.4b and 3.5b, and its undefined distribution.

Potassic alteration consists of a K-feldspar-magnetite $\pm$ biotite (chloritised) assemblage, and is mostly located at depth in and around the P2 West, and P3 East and West intrusions, their associated hydrothermal breccias, and adjacent wall rock (Campbell et al., 2020). The distribution of potassic alteration is another criteria used by Campbell et al. (2020) to assign a syn-mineralisation timing for these intrusions, but there is not a stong correlation of potassic alteration with intrusion type in Figure 3.4b and 3.5b. The P3 East intrusion has perhaps the strongest association with potassic alteration at depth (Figure 3.5b), grading into sericitic alteration near-surface, consistent with the inferred syn-mineralisation timing. However, the P2 West and P3 West intrusions (and indeed some regions of the P3 East intrusions) exhibit inconsistent alteration in Figure 3.4b and 3.5b, with regions of unaltered rock, and a poor correlation with potassic and sericitic alteration.

Biotite is rarely present in the potassic alteration zones, which is interpreted by Campbell et al. (2020) to be due to later overprinting by sericitic alteration or the lower greenschist facies metamorphism proposed by Alldrick (1993) to have affected the KSM district. Although the extent of biotite replacement in potassic assemblages by sericitic alteration is not stated, it is reasonable to assume that areas of potassic alteration overprinted by sericitic alteration are included in the sericitic zones in Figure 3.4b and 3.5b. Conversely, the potassic alteration zones depicted in Figure 3.4b and 3.5b probably constitute the areas of potassic alteration where biotite is chloritised in absence of sericitic alteration (see assemblage below), thus inferred to be affected by metamorphism.

An assemblage of fine-grained muscovite or illite-quartz-pyrite characterises sericitic alteration at Iron Cap, with varying degrees of intensity defined by the extent of mineral replacement; from full replacement of felsic minerals, to the partial replacement of mafic minerals, to the complete and texturally destructive replacement of both felsic and mafic

minerals (Campbell et al., 2020). Strong sericitic alteration is generally located in shallow and central parts of the deposit, particularly in the large hydrothermal breccias, with decreasing intensity outwards from these areas (Figure 3.4b and 3.5b). The intrusions and wall rocks are also affected, and pre-existing potassic assemblages are overprinted where the two alteration zones interact (Campbell et al., 2020).

3.4.5 Mineralisation

Gold and Cu are the primary resources at Iron Cap, but Campbell et al. (2020) note that they are not strongly associated, with differences in their spatial relations throughout the deposit. Indeed, Figure 3.4d, e and 3.5d, e show that, while Au and Cu are present throughout most of the deposit, the highest Au grades do not correlate to the highest Cu grades, and neither metal consistently correlates to lithology, alteration, or quartz vein volume. Locally, however, it appears that high Au grades sometimes correlate to high volumes of quartz veins (red zones in Figure 3.5c and d), implying that certain veins are key contributors to the Au endowment of the deposit (Section 3.4.6). Furthermore, Campbell et al. (2020) state that the P2 West and P3 East intrusions host most of the Au-Cu mineralisation at Iron Cap, with some of the highest Au and Cu grades recorded in the P2 West intrusion. However, this is not apparent in Figure 3.4 and 3.5, where the hydrothermal breccias appear to contain a greater proportion of high Au and Cu grades than both the P2 West and P3 East intrusions.

The overall distribution of metals also does not follow a simple concentric zoning pattern, contrary to observations at some other calc-alkaline porphyry deposits (e.g., Mitchell; Campbell et al., 2020), implying that the hydrothermal system at Iron Cap experienced a more complex evolution than some other porphyry systems. Although it is not clear which zoning pattern Campbell et al. (2020) refer to (i.e., high grade to low grade, or, for example, central Cu-Au to more peripheral Ag-Pb-Zn; Sillitoe, 2010), both Figure 3.4d-f and 3.5d-f, and the lack of zonation in Pb and Zn grades recognised by Campbell et al. (2020), confirms the absence of zonations in metal grade or type.

Chalcopyrite is the primary Cu-bearing ore mineral and is the second most abundant sulphide, behind pyrite (Campbell et al., 2020). Most economic mineralisation is of the low- to intermediate-sulphidation assemblage of pyrite-chalcopyrite $\pm$ tennantite $\pm$ tetrahedrite (Campbell et al., 2020). Less common high-sulphidation assemblages also occur, such as pyrite-bornite (Figure 3.7e; Campbell et al., 2020). Tennantite and tetrahedrite are most abundant in the shallower regions of the deposit, geochemically represented by the zone limits of $>$50 ppm As in Figure 3.4b and 3.5b (Campbell et al., 2020); these regions also partly co-occur with sericitic alteration and below average Au concentrations.

Given that tennantite-tetrahedrite occurs in late syn-mineralisation veins associated with sericitic alteration, or post-mineralisation veins (Section 3.4.6), the low Au concentrations in the >50 ppm As zones may result from the tennantite-tetrahedrite-bearing vein generations being Au-poor.

Molybdenite is also present to a lesser degree, its distribution represented by Mo grade in Figure 3.4f and 3.5f. The higher Mo grade regions in the central areas of Figure 3.4f and 3.5f appear to roughly correlate to sericitic-altered hydrothermal breccia. A zone of enriched Mo is shown to the south of the ICF, where molybdenite is most abundant and commonly hosted in the matrices of hydrothermal breccias (Figure 3.7f; Campbell et al., 2020). This zone could be an offset section of the Iron Cap deposit, or part of a separate mineralising system altogether (Campbell et al., 2020).

Campbell et al. (2020) do not extensively discuss the hosting of the Au at Iron Cap. The early work conducted for this thesis was presented at AME Roundup 2019, and Campbell et al. (2020) use that presentation as their source of information for the hosting of the Au. As the hosting of the Au at Iron Cap is one area this thesis aims to shed light on, the findings of the early work are updated and presented in full later in the thesis (Chapter 5).

3.4.6 Veins

The veins at Iron Cap are of particular importance to this research project, because vein samples will be used as the main source of information on the nature and evolution of the hydrothermal fluids that formed the deposit. Furthermore, the ore minerals contained within the veins were analysed to determine their trace element compositions; it is hoped that this information may elucidate hydrothermal fluid characteristics, and the behaviour of trace elements during the evolution of the system. Owing to the importance of veins in this study, a thorough review of the veins described and defined by Campbell et al. (2020) at Iron Cap is necessary to pin subsequent refinements to understanding. To this end, this section considers the work of Campbell et al. (2020) in isolation. Later discussion of vein classifications at Iron Cap is primarily located in Chapter 5, where the vein classifications of Campbell et al. (2020) are considered in the context of the results of this research project.

Campbell et al. (2020) defined a series of seven vein generations at Iron Cap, shown in Table 3.2. Where applicable, these definitions are stated to relate to the porphyry vein classifications of Gustafson and Hunt (1975) (i.e., A-, B- and D-veins; Section 2.5.4). However, the specific criteria used to define different vein generations is not presented. Furthermore, vein cross-cutting relationships are uncommonly observed at Iron Cap; only

Table 3.2
Vein generations at Iron Cap, as defined by Campbell et al. (2020).

Vein	Mineralogy	Associated alteration	Timing
A-vein	Qz-ccp ± mag	Potassic	Early syn-mineralisation
Magnetite	Mag ± ccp	Potassic	Early syn-mineralisation
B-vein	Qz-ccp ± mol ± py	Potassic	Early syn-mineralisation
Molybdenite	Mol ± qz ± ccp ± py	Potassic?	Early syn-mineralisation?
Polymetallic	Qz-py ± tnt ± ttr (± ccp ± sp)	Sericitic	Late syn-mineralisation
D-vein	Py	Sericitic	Late syn-mineralisation
Post-mineral	Qz-cb ± chl ± sp ± gn ± ccp ± tnt ± ttr	None	Post-mineralisation

two of the seven vein generations (polymetallic and post-mineral) are observed to cross-cut other vein generations (Campbell et al., 2020). This means that the relative timing of the vein generations is largely inferred.

Apart from the vein classifications presented in Table 3.2, Campbell et al. (2020) additionally report narrow, structurally-controlled, Au-bearing and As-rich pyrite veins in the hanging wall of the STF, but these were not time-constrained or of sufficient significance to be classes as a separate vein generation. Indeed, given that there is a lack of hydrothermal alteration in the hanging wall of the STF, and displacement along the STF occurred post-mineralisation, in the Cretaceous, it is possible that this mineralisation is not genetically related to the porphyry system, and may instead represent a minor orogenic Au occurrence.

3.4.6.1 A-veins

The first veins emplaced are interpreted to be quartz-chalcopyrite ± magnetite A-veins, forming either stockworks or sheets, some of which show a thin alteration halo of K-feldspar ± magnetite (Figure 3.7a-c; Campbell et al., 2020). Sheeted A-veins are particularly concentrated in some narrow (up to ∼50 m thick) zones in the P2 West and P3 East intrusions, represented by high quartz vein volumes (>10 vol.%) in Figure 3.4c and 3.5c (Campbell et al., 2020). As noted above, these zones sometimes correlate to elevated Au grades, and Campbell et al. (2020) additionally state that these zones also correspond to elevated Cu grades, and in some cases more intense potassic alteration, although these associations are not clearly observed in Figure 3.4 and 3.5. Nevertheless, the recognised correlation of A-veins with elevated metal grades suggests that these veins provide an important contribution to the metal endowment of the deposit.

The A-veins of Campbell et al. (2020) appear to have a more variable texture and

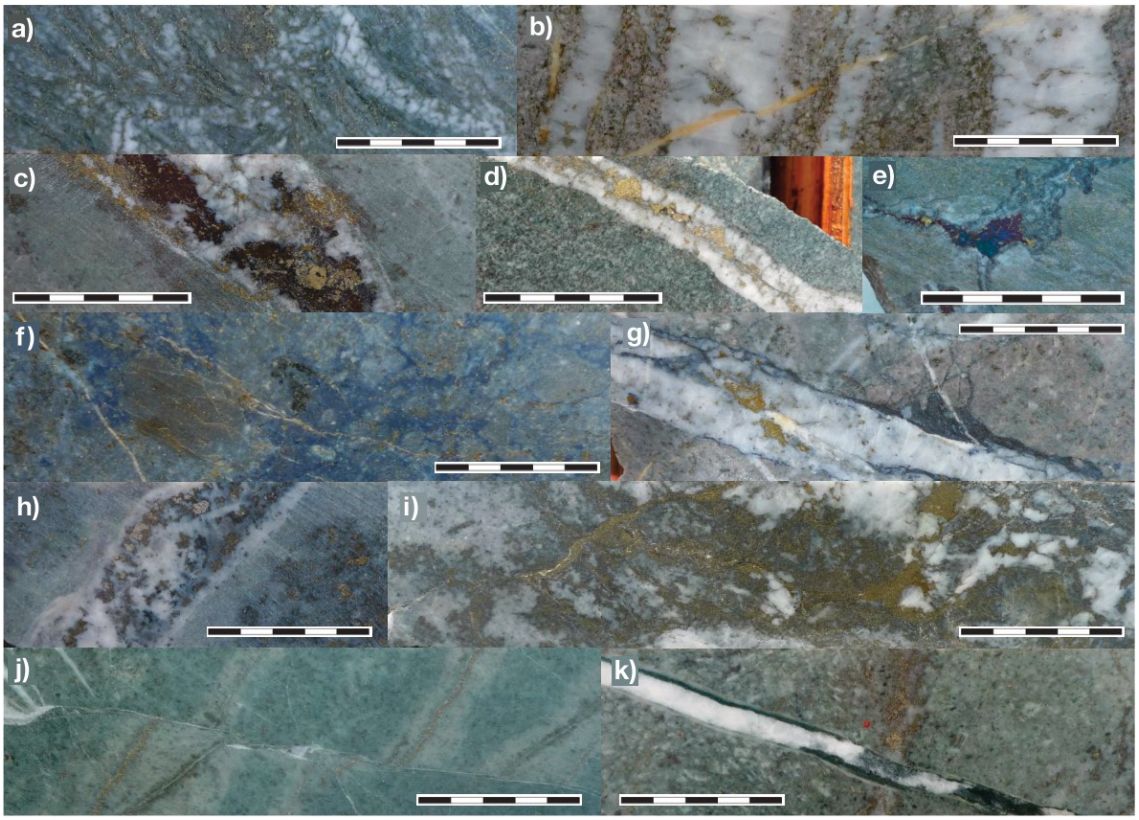

Figure 3.7. Veins and mineralisation styles of the Iron Cap deposit, described by Campbell et al. (2020): a) coalesced A-veins; b) sheeted A-veins; c) A-vein with significant magnetite; d) B-vein; e) bornite-chalcopyrite clot; f) molybdenite in the matrix of a hydrothermal breccia; g) quartz-molybdenite-chalcopyrite vein; h) polymetallic vein; i) polymetallic vein with diffuse margins; j) D-veins; k) post-mineral vein (5 cm scale).

morphology (Figure 3.7a-c) in comparison to the A-vein classification of Gustafson and Hunt (1975) described in Section 2.5.4. In particular, the A-veins of Campbell et al. (2020) exhibit widths of up to at least 50 mm (Figure 3.7c) and contain sulphides as isolated crystals (Figure 3.7b), coarse masses (Figure 3.7c), and in fracture-like networks ("crackled" texture; Figure 3.7a) in quartz. This is in contrast to the disseminated sulphide A-veins of Gustafson and Hunt (1975), which reach widths of up to 25 mm. These textural differences imply that A-veins at Iron Cap may have formed by different processes, or under different conditions, than the traditional A-veins of Gustafson and Hunt (1975), and that the A-vein classification may not be wholly applicable. Furthermore, the inconsistent presence of magnetite in the A-veins at Iron Cap (Campbell et al., 2020) suggests that there may be multiple sub-classes present; generally in Au-rich porphyry deposits, magnetite-bearing A-veins are thought to pre-date magnetite-free A-veins (Section 2.5.4; Muntean and Einaudi, 2000). A-veins are discussed further in Section 3.4.6.3.

3.4.6.2 *Magnetite veins*

Magnetite-chalcopyrite veins are reportedly coincident with A-veins (Campbell et al., 2020), with the presence (A-veins) or absence (magnetite) of quartz assumed to be the key distinction between the two. No crosscutting relationships between A-veins and magnetite veins are observed, and only the mineralogy of the magnetite veins is recorded (Campbell et al., 2020). Given the lack of quartz in the magnetite veins, it could be interpreted that these veins pre-date A-veins, based on the vein groupings of Sillitoe (2010), discussed in Section 2.5.4. These veins may represent a transition between Group 1 and 2 veins, where chalcopyrite reaches saturation during vein formation, but quartz did not. When also considering that the presence of magnetite in A-veins implies an earlier formation than magnetite-free A-veins (above), it is reasonable to suggest that the magnetite veins may pre-date the A-veins.

3.4.6.3 *B-veins*

B-veins at Iron Cap host sulphides of chalcopyrite $\pm$ molybdenite $\pm$ pyrite along a central suture, surrounded by quartz, and are thought to post-date A-veins and magnetite veins (Campbell et al., 2020). The B-vein occurrence shown in Figure 3.7d appears similar in morphology and sulphide texture to some of the A-veins (Figure 3.7a, b), with the only difference being that the sulphide minerals are preferentially (but not wholly) hosted in a central suture. This does comply with the textural description of B-veins by Gustafson and Hunt (1975), but the textural similarities to some of the A-veins suggests that there may be genetic similarities. The difference in ore mineralogy in B-veins (chalcopyrite $\pm$ molybdenite $\pm$ pyrite), compared to A-veins (chalcopyrite $\pm$ magnetite) may be a more reliable discriminator. However, only chalcopyrite is always present in both veins, meaning that chalcopyrite-only A-veins and chalcopyrite-only B-veins may occur; such veins would exhibit similarities in morphology, texture and mineralogy. Furthermore, the absence of cross-cutting relationships observed between A-veins and B-veins (Campbell et al., 2020) adds to the uncertainty around whether there are genetic links between the two vein generations.

The emplacement of A-veins, magnetite $\pm$ chalcopyrite veins, and B-veins is reported to be synchronous with significant Au and Cu introduction, and early potassic alteration, leading Campbell et al. (2020) to collectively interpret them as early syn-mineral veins. However, empirical evidence to support causative links between vein formation, metal introduction, and alteration is not presented. Furthermore, Figure 3.4 and 3.5 show that, overall, there is a poor correlation between metal grade, quartz vein volume, and potassic

alteration, meaning that the relationships noted by Campbell et al. (2020) may not be consistent throughout Iron Cap. The poor correlation between metal grade and quartz vein volume could be explained by differences in the timing of ore and quartz precipitation; textural analysis of A- and B-veins in other porphyry deposits shows that the sulphides were introduced later than the quartz (Section 2.5.6; e.g., Monecke et al., 2018). Therefore, quartz and ore formation in the A- and B-veins at Iron Cap may have been decoupled in time and not genetically related, with ore distributions unconstrained by quartz veining.

3.4.6.4 Molybdenite veins

Molybdenite ± quartz ± chalcopyrite ± pyrite veins were identified by Campbell et al. (2020), and appear to be pictured in Figure 3.7g. In the vein occurrence shown, molybdenite (blue-black) appears largely on the margins of the vein, sometimes penetrating into the centre, and clasts of quartz are hosted by the molybdenite, suggesting that molybdenite was introducted by later fluids that infiltrated the earlier quartz. Chalcopyrite appears to be hosted by the quartz, and not related to the molybdenite. If this interpretation is correct, molybdenite could be unrelated to the quartz ± chalcopyrite ± pyrite veins in which it is found. Indeed, the fact that only molybdenite is always present, while quartz, chalcopyrite, and pyrite are variable, suggests that molybdenite-only veins may occur elsewhere. Therefore, the molybdenite ± quartz ± chalcopyrite ± pyrite vein generation may be a product of at least two stages of fluid flow, the first forming quartz ± chalcopyrite ± pyrite veins (possibly A- or B-veins), with the later introduction of molybdenite. Alternatively, these veins may be different occurrences of B-veins, owing to their identical mineralogy (Table 3.2), although they are texturally different. Nevertheless, the molybdenite veins are only occasionally observed (Campbell et al., 2020), indicating that they are not an abundant host of metals.

3.4.6.5 Polymetallic veins

Polymetallic veins are mineralogically defined by grey quartz and a variable assemblage of pyrite ± tennantite ± tetrahedrite ± chalcopyrite ± sphalerite (Campbell et al., 2020). Figure 3.7h and 3.7i show that they are sulphide-rich, and can be >10 cm in width with diffuse margins defined by sulphides (Figure 3.7i), or ∼25 mm in width with more linear margins defined by quartz (Figure 3.7h). The veins are primarily concentrated in areas of sericitic alteration, but are also found throughout the rest of the deposit (Campbell et al., 2020). This association with sericitic alteration, combined with observations that they crosscut A- and B-veins, and the central hydrothermal breccias lead to the interpretation that the polymetallic veins were emplaced during the later stages of mineralisation

(Campbell et al., 2020). One caveat is that the polymetallic veins exhibit very similar characteristics to the D-veins of Gustafson and Hunt (1975) (cf. Section 2.5.4), yet they are not categorised as such in the study of Campbell et al. (2020), where a different vein type is classified as D-veins (below).

3.4.6.6 D-veins

The D-veins at Iron Cap only host pyrite, and are interpreted as late syn-mineralisation due to an association with sericitic alteration; no crosscutting relationships between the previous veins are observed, although the D-veins are observed to cut the hydrothermal breccias (Campbell et al., 2020). Figure 3.7j shows that D-veins are characterised by thin widths (<5 mm), and exhibit cm-scale sericitic alteration halos. The D-veins of Campbell et al. (2020) do not closely resemble the D-vein classification of Gustafson and Hunt (1975), apart from exhibiting pyrite as the dominant ore mineral. Polymetallic veins appear more comparable to this classification (above). The thin and straight morphology of the D-veins of Campbell et al. (2020), combined with the lack of quartz and the dominance of sulphides, suggests that the veins are more comparable to the C-veins of Gustafson and Quiroga (1995), rather than the D-veins of Gustafson and Hunt (1975). This could lead to the suggestion that the D-veins of Campbell et al. (2020) pre-date the polymetallic veins, when taking the typical sequence of porphyry veining outlined in Section 2.5.4 into consideration. Nevertheless, empirical evidence of timing relations between D-veins and polymetallic veins is lacking.

3.4.6.7 Post-mineral veins

Post-mineral veins, characterised by an assemblage of quartz-carbonate ± chlorite ± sphalerite ± galena ± chalcopyrite ± tennantite ± tetrahedrite, are reported to cross-cut all preceeding veins (Figure 3.7k; Campbell et al., 2020). Key distinctions from the polymetallic veins are that post-mineral veins have milky-white quartz, host carbonate, and exhibit ore minerals in the form of coarse clots (Campbell et al., 2020). However, some of the quartz shown in the polymetallic vein of Figure 3.7i appears very similar in colour to the white mineral (quartz and/or carbonate) of the post-mineral vein in Figure 3.7k; therefore, it is not clear if apparent differences in quartz colour are a reliable discriminating criteria. When comparing Figure 3.7h, i, and k, it is evident that the mineral proportions of polymetallic veins and post-mineral veins are very different; post-mineral veins are sparsely populated with sulphides, compared to the sulphide-abundant polymetallic veins. Furthermore, the post-mineral veins are thin (∼10 mm width), and exhibit straight margins unlike some of polymetallic veins. The mineralogy of the post-mineral veins is

suggestive of lower temperatures, and comparable to that of late porphyry D- or E-veins (e.g., Section 2.5.4; Masterman et al., 2005; Sillitoe, 2010; Kouzmanov and Pokrovski, 2012; Maydagán et al., 2015).

Campbell et al. (2020) state that the post-mineral veins are observed throughout the KSM district, and suggest that the veins are associated with deformation and metamorphism during activity of the SFTB, as the veins are not deformed in deformed areas of the district. At Kerr, Ditson et al. (1995) previously recognised "post-deformation" veins of quartz-carbonate-chlorite-chalcopyrite, which are comparable to the post-mineral veins of Campbell et al. (2020). Ditson et al. (1995) state that their post-deformation veins either overprint, or are proximal to, the crackled quartz stockwork (comparable to A-veins at Iron Cap); this implies a post-stockwork/A-vein formation, but not necessarily a post-mineralisation formation. Indeed, Ditson et al. (1995) also note that they did not carry out a detailed study of vein characteristics or paragenesis, and their interpretation of a post-deformation timing for the veins of quartz-carbonate-chlorite-chalcopyrite appears to be solely based on the cross-cutting of crackled A-veins, where the sulphides in the crackle-texture were interpreted to be introduced after deformation and fracturing of the quartz. However, Campbell et al. (2020) report that the syn-mineralisation polymetallic veins crosscut crackled A-veins at Iron Cap, meaning that the crackled texture is not imparted during later deformation, but is instead a syn-mineralisation texture. Meanwhile, at Mitchell, Febbo et al. (2015) did not record any post-mineralisation veins, meaning that the post-mineral veins present at Iron Cap may not be as widespread throughout the district as stated. It could therefore be suggested that the post-mineral veins at Iron Cap may be related to porphyry mineralising activity.

To align with their interpreted post-mineralisation timing of post-mineral veins, Campbell et al. (2020) suggest that the veins formed by remobilisation of local porphyry mineralisation, because the veins contain minerals that reflect the metals present in adjacent wall rocks. However, most veins formed during magmatic-hydrothermal activity in porphyry deposits contain ore minerals that are also commonly present as disseminations in the surrounding wall rock (e.g., Seedorff et al., 2005; Sillitoe, 2010), meaning that similarities in mineralogy between a vein and the surrounding wall rock is not necessarily an indication that remobilisation has occurred. Furthermore, remobilisation is not restricted to a post-mineralisation timing; numerous studies of different ore deposits recognise syn-mineralisation remobilisation (e.g., of Au; Sillitoe, 2010; Fougerouse et al., 2016b; Hastie et al., 2020; Hurtig et al., 2021). This means that if post-mineral veins are a product of remobilisation, it is equally possible that they formed during magmatic-hydrothermal activity.

In summary, the post-mineral veins of Campbell et al. (2020) are the youngest vein generation recognised, given that they are observed to crosscut all other vein types. However, further evidence is required to support the interpretation that they were formed during deformation, after cessation of porphyry mineralising activity. Alternatively, the post-mineral veins may have formed during the later stages of porphyry mineralisation.

3.4.7 Post-mineralisation modification

Tectonic activity that took place in the Cretaceous, related to development of the SFTB, is proposed to be the main post-mineralistion modification event affecting Iron Cap (Campbell et al., 2020), and the other deposits of the KSM district (Ditson et al., 1995; Febbo et al., 2019). While the development of structures has already been discussed (Section 3.4.3), the local effects of this tectonic activity on the porphyry orebodies in the KSM district is yet to be addressed.

At Iron Cap, Campbell et al. (2020) suggest that post-mineralisation modification occurred due to the development of the post-mineral veins (discussed above), and the SEM analyses of pyrite, which shows ore minerals of chalcopyrite, arsenopyrite, Ag-bearing galena, and freibergite (Ag-bearing sulphosalt) in vugs and microfractures in the pyrite crystals. The interpretation is that the pyrite crystals were formed during porphyry mineralisation, and that these microfractures and vugs developed during SFTB activity in the Cretaceous (Campbell et al., 2020); however, the latter could equally have formed during later porphyry mineralisation, as similar pyrite textures are commonly recognised in other porphyry deposits unaffected by post-mineralisation modification (e.g., Altar, Argentina; Lihir, Papua New Guinea; Maydagán et al., 2013; Sykora et al., 2018). Furthermore, Campbell et al. (2020) state that the pyrite crystals analysed are from the KSM district, and thus may not be from Iron Cap specifically. If the pyrite crystals originated from elsewhere in the KSM district, the conclusions drawn from the analyses are not directly applicable to Iron Cap. Overall, further evidence is required to confirm that post-mineralisation modification or remobilisation occurred at Iron Cap, but this does not preclude the possibility.

Assuming Iron Cap originally formed at a vertical orientation, as would be expected for most porphyry deposits (e.g., Figure 2.9), the current steep dip to the W-NW suggests that rotation of the deposit has occurred (Campbell et al., 2020), probably during Cretaceous tectonic activity. Meanwhile, ductile deformation at Iron Cap is observed to be minimal; deformation fabrics related to the SFTB are only poorly developed (Campbell et al., 2020), particularly in comparison to the other KSM deposits (e.g., Mitchell; Febbo et al., 2015, 2019). The lack of ductile deformation implies that Iron Cap was situ-

ated above the ductile-brittle transition (i.e., <350-500°C; Fournier, 1999; Monecke et al., 2018), experiencing cooler temperatures during the Cretaceous deformation than elsewhere in the KSM district. Furthermore, the fact that Iron Cap appears to have experienced weaker deformation than the other KSM deposits suggests that direct similarities cannot be drawn between Iron Cap and the other KSM deposits in terms of post-mineral modification (e.g., in terms of pyrite textures, above).

Nevertheless, the study of Cretaceous deformation at Mitchell by Febbo et al. (2019) highlights the presence of some features that would be important to recognise if present at Iron Cap. In particular, Febbo et al. (2019) note a relationship between strain partitioning and alteration assemblage, where the most incompetent assemblages (i.e., sericitic) accomodate the most strain, and are therefore intensely foliated, while the most competent assemblages (i.e., potassic) generally lack cleavage. At the same time, veins hosted within zones of sericitic alteration are intensely folded (owing to the difference in compentency between the more-competent veins and the less-competent sericitic-altered wall rock), while veins hosted in zones of potassic alteration are undeformed (Febbo et al., 2019). While Campbell et al. (2020) note that deformation fabrics, even in zones of sericitic alteration, are poorly developed, it is important to be aware of these local features, because the veins hosted in sericitic alteration may have experienced minor folding. This means that they could appear to exhibit wavy margins – a feature usually indicative of early, syn-mineralisation vein formation under ductile conditions, rather than post-mineralisation modification under ductile conditions.

In sericitic-altered zones at Mitchell, Febbo et al. (2019) also highlight that strain is partitioned between sulphide minerals. Pyrite crystals are more competent and are therefore brittlely-fractured, and sometimes exhibit pressure shadows, while chalcopyrite and molybdenite are less competent and thus accomodate strain, resulting in mechanical reshaping into elongated geometries parallel to the earliest cleavage (Febbo et al., 2019). Furthermore, sericitic-altered zones are estimated to have experienced flattening of between 10-70%, effected by the removal of quartz via pressure solution and the development of pressure solution cleavage, which also passively enriched the flattening domains in sulphide minerals (Febbo et al., 2019). Observation of these micro-scale textures at Iron Cap may indicate that similar post-mineralisation processes have taken place.

3.5 Other porphyry deposits with comparable features

Iron Cap is distinct from the other deposits of the KSM district, but Campbell et al. (2020) recognise that it is most comparable to the Kerr deposit, when considering metal distribution and deposit morphology. This is based on the similarly irregular Au and Cu

distribution along strike, together with the comparable orientation of narrow, steeply W-dipping and N-striking intrusions (Ditson et al., 1995). Principally, of course, the host intrusions for both deposits are of the same Sulphurets intrusive suite (Figure 3.1; Febbo et al., 2015).

Outside of the KSM district, Iron Cap is not directly comparable to other Au-rich porphyry deposits in BC in terms of deposit classification, because most of the Au-rich deposits in BC are alkaline, while Iron Cap is calc-alkaline. Nevertheless, the alkaline Galore Creek deposit shows similarities to Iron Cap in terms of its metal proportions, and its hosting within the island arc Stikine terrane (Table 3.1). Furthermore, Galore Creek also hosts monzonites comparable to the P3 monzonites at Iron Cap, although the Galore Creek intrusions are $\sim$10 m.y. older than those at Iron Cap (Micko et al., 2014). The Galore Creek orebodies also host hydrothermal breccias; however, most of the hydrothermal features of Galore Creek are not comparable to Iron Cap, owing to its alkaline nature; the deposit exhibits typical alkaline alteration assemblages (e.g., calcic), lacks sericitic alteration, and quartz veining is sparse (Micko et al., 2014).

In comparison to other Au-rich and calc-alkaline porphyry deposits worldwide in terms of metal endowment, Iron Cap shows similarities to Cerro Casale, Chile, and Potrerillos, Chile (cf. Table 3.1, Figure 2.5). However, these deposits were emplaced in continental arc settings (Vila et al., 1991), unlike Iron Cap. Nevertheless, Cerro Casale is largely hosted by syn-mineralisation diorite intrusions, comparable to the P2 intrusions at Iron Cap, and hydrothermal breccias are observed in the centre of the ore zone (Palacios et al., 2001). The Cerro Casale deposit also exhibits similar alteration patterns to Iron Cap (i.e., early potassic and later sericitic overprint, with peripheral propylitic), and abundant quartz veining is characterised by A-veins in the potassic zone, and D-veins in the sericitic zone (Palacios et al., 2001), as at Iron Cap.

3.6 Iron Cap genetic model

The simple genetic model of Iron Cap described by Campbell et al. (2020) largely focusses on magmatism and post-mineralisation deformation, commensurate with the aims of their study. In summary, it is proposed that intrusion emplacement began with the pre-mineralisation P2 East diorite, followed by emplacement of the syn-mineralisation P2 West diorite, and P3 monzonites, with hydrothermal breccias developed synchronously with the P2 and P3 intrusions (Campbell et al., 2020). The P2 West and P3 East intrusions are intepreted to have driven the hydrothermal system and associated mineralisation (Campbell et al., 2020). Post-mineralisation modification is thought to have occurred in the Cretaceous, where local foliation was developed, faulting occurred, and greenschist

facies metamorphism affected the region (Campbell et al., 2020). This model does not consider the vein generations, as the work of Campbell et al. (2020) primarily constitutes a description of the geological features of Iron Cap. Nevertheless, based on the previous discussions in this chapter, and consideration of Chapter 2, an alternative and expanded genetic model can be constructed.

Given that the Iron Cap deposit is situated in an island arc terrane that is also prolific for alkaline porphyry deposits, the magmas that generated the Iron Cap intrusions may have evolved under a relatively thin crust; this is also suggested by the Au-rich nature of the deposit (Chapter 2). Furthermore, the moderate Cu-endowment of the deposit (cf. Table 3.1, Figure 2.5) suggests that the magmatic-hydrothermal system was not long-lived, commensurate with evolution under thinner crust (Chapter 2). Emplacement of the porphyry intrusions at Iron Cap may have been facilitated by a NE-trending structure generated under a NW-SE extensional regime, as Figure 3.4a shows that the intrusions and breccias are elongated in a NE-SW orientation. The hydrothermal features (quartz vein volume, alteration) and metal grades also reflect the orientation of the intrusions, implying the hydrothermal system developed under the same regime. This agrees with the theory of Nelson and Kyba (2014), who suggested that a large-scale basin-bounding fault localised the KSM intrusions in the Early Jurassic under a extensional-transtensional regime. Febbo et al. (2019) also propose a similar theory, but infer that the KSM deposits were emplaced in a pre-existing framework of N-trending lineaments, with subsidiary E-trending lineaments accounting for the differences in orientation between Kerr (N-S), Sulphurets (NE-SW), and Mitchell (E-W), with maximum extension ranging from N-S, through NE-SW, to E-W, depending on the local structure.

Intrusive activity at Iron Cap began with the emplacement of the P2 diorites, which appear to constitute a single intrusive phase owing their near-identical characteristics. They may have been emplaced pre- or syn-mineralisation, but probably pre-date the P3 monzonites because hydrothermal breccias hosting clasts of P2 diorite are cut by the P3 intrusions. P3 monzonites also constitute a single intrusive phase owing to their lack of differentiation, and are the youngest intrusions hosting mineralisation; they were therefore emplaced syn-mineralisation. The P3 intrusions probably provided the bulk of the hydrothermal fluids, because of their syn-mineralisation timing, and the observation that voluminous hydrothermal breccias are developed from them (e.g., Figure 3.5a). Intrusion breccias are also synchronous with the emplacement of the P3 intrusions, given that their matrices are P3 monzonite.

Hydrothermal fluids first developed potassic alteration in the intrusions and wall rock (cf. Chapter 2). Magnetite veining likely occurred at high temperatures, probably

in conjunction with potassic alteration. As the fluids cooled, magnetite veins may have transitioned into A-veins, although the quartz of A-veins was probably emplaced prior to the introduction of magnetite and chalcopyrite (cf. Chapter 2), particularly in crackle-textured A-veins, where the sulphides must have been introduced later than the quartz. Sheeted A-veins, if oriented NE-SW, may provide evidence for deposit formation in a NW-SE extensional regime.

High concentrations of A-veins sometimes correlate to elevated Au contents, suggesting that A-veins may be causative to local Au-enrichment. B-veins may be synchronous with A-veins as no cross-cutting relationships are observed, and, much like the A-veins, the quartz of B-veins was probably emplaced prior to the introduction of ore minerals (cf. Chapter 2). Molybdenite veins may be a variation on A- and/or B-veins, with post-quartz molybdenite introduction similar to the post-quartz ore mineral introduction of A- and B-veins. Potassic alteration of the intrusions and wall rock probably continued during the formation of A- and B-vein quartz (cf. Chapter 2), although the post-quartz ore mineral introduction might not be associated with fluids generating potassic alteration. Proximally, propylitic alteration of the surrounding wall rock likely occurred due to heating of circulating ground waters by the intrusions (Chapter 2).

Hydrothermal breccias are synchronous with mineralisation because they host clasts of P2 and/or P3 intrusions, are potassic-altered (at depth) and sericitic-altered (near-surface), and host elevated metal concentrations; however, they likely formed after the magnetite, A- and B-veins, because they are cross-cut by later D-veins and polymetallic veins. It is likely that the late hydrothermal fluid flow (i.e., post-B-vein) was preferentially channelled through the high permeability breccias, rather than the surrounding rock. This may be exemplified by the distribution of sericitic alteration, which is late in the evolution, and appears to be preferentially concentrated in the hydrothermal breccias (Figure 3.4a, b and 3.5a, b). Furthermore, Mo is preferentially concentrated in the hydrothermal breccias, implying that it was introduced relatively late in the evolution of the hydrothermal system, and in particular, after the early Cu and Au introduction associated with the formation of A- and B-veins. This agrees well with the relatively late timing of Mo introduction typical of Au-rich porphyry deposits (e.g., Sillitoe, 2010).

The hydrothermal breccias at Iron Cap may also be partly responsible for the lack of zonations in metal grade or type that are sometimes observed in other porphyry deposits, because the breccias are voluminous and brecciate the central ore zone, meaning that some of pre-existing mineralisation was entrained by the hydrothermal breccias, and later mineralisation precipitated in the breccia matrix, or in cross-cutting veins, leading to mixing and overprinting of early and late mineralisation, obscuring metal zonations.

In particular, the concentration of Mo in hydrothermal breccias at Iron Cap suggests a perturbation of typical metal zonations, because later fluids were probably channelled through the hydrothermal breccias, rather than ascending concentrically upwards and outwards from the central ore zone, as would be expected in deposits that exhibit metal zonations. The abundance of hydrothermal breccias at Iron Cap provides additional evidence to support the theory that the magmatic-hydrothermal system was developed along a structure in an extensional or transtensional regime, because breccia formation requires fluid exsolution to be explosive, and movement on a controlling structure is one way to achieve this (Chapter 2).

Polymetallic and D-veins are observed to cut the hydrothermal breccias, meaning that they were emplaced post-brecciation. It is possible that the D-veins formed prior to the polymetallic veins, because they exhibit more similar characteristics to C-veins than D-veins (cf. Gustafson and Hunt, 1975; Gustafson and Quiroga, 1995). Furthermore, polymetallic veins exhibit a base metal-rich mineralogy more likely to be associated with lower temperatures, and thus the later stages of hydrothermal system evolution (assuming a hot-to-cold thermal evolution; Chapter 2). Both polymetallic and D-veins are associated with sericitic alteration, with the latter exhibiting a sericitic halo, indicating that these veins were formed during the later stages of hydrothermal activity, when the fluids were cooler and more acidic, owing to the disproportionation of SO_2 to H_2S and sulphuric acid below $\sim$400°C (Chapter 2).

The overall poor correlation between Cu and Au, and quartz vein volume and metal content (e.g., Figure 3.4 and 3.5), at Iron Cap implies that the metals were not introduced at the same time by the same fluids, or concentrated in the same vein generations. Alternatively, remobilisation may have occurred to re-distribute the metals. Either way, this suggests that the evolution of hydrothermal system is more complex than other Au-rich porphyry deposits that exhibit metal grade and type zonations, and correlations between vein intensity and metal grade (cf. Chapter 2). However, the Au-rich nature of Iron Cap may suggest that the precipitation of Au was more efficient than in Au-poor porphyry deposits, possibly owing to deposition from vapour-phase fluids (Chapter 2). The inferred magma evolution under thin crust suggests that the porphyry intrusions could have been emplaced at relatively shallow depths (e.g., $<$2 km), which would correlate to the dominance of metal deposition by vapour-phase fluids (Chapter 2).

Post-mineral veins exhibit a low-temperature sulphide assemblage, and cross-cut all other veins. They may have been emplaced during the later stages of porphyry mineralisation, or during post-mineralisation tectonic activity. After cessation of mineralising activity, P4 monzodiorite dykes were emplaced, cross-cutting the mineralisation and pre-

ceeding intrusions. Post-mineralisation modification of the Iron Cap deposit occurred in the Cretaceous, during tectonic activity related to the development of the SFTB. The mafic to ultramafic dykes are thought to have been emplaced during this tectonic activity. The deposit was bounded by four faults, while ductile deformation fabrics were poorly developed, and probably only in areas of sericitic alteration where strain was preferentially accomodated. Synchronous greenschist facies metamophism particularly affected biotite in potassic assemblages, altering it to chlorite, while the surrounding wall rocks were altered to a greenschist assemblage, obscuring the extent of propylitic alteration.

3.7 Implications for this research project

The study of Campbell et al. (2020) provides a crucial framework for the understanding of deposit features. However, given that their research is the first to be completed on Iron Cap, and the remit of their study was to provide a geological desciption of the deposit, it is inevitable that there are features of Iron Cap that require a more detailed understanding. With particular relevance to this thesis, the vein generations at Iron Cap require further study, and have the potential to be refined. In particular, micro-scale mineral occurrences and textures, such as those observed under reflected or transmitted light, or by SEM, are yet to be investigated. The relative timing of ore mineral precipitation within veins, and the relationship of ore minerals to each other, also remains to be determined. Furthermore, the proportions of individual ore minerals within the veins have not yet been quantified. Any variation in the ore mineralogy within a vein generation must also be highlighted. Study of the veins by SEM-CL has not yet been undertaken, leaving an opportunity to acquire empirical evidence of different quartz generations that could help to distinguish the veins further, and establish whether each vein formed by a single hydrothermal fluid event, or multiple events. Variability in characteristics between veins of the same generations must also be accounted for.

The deportment of trace elements at Iron Cap has not been specifically addressed, although it is evident that whole rock geochemistry for parts of the deposit has been acquired, at least in the case of the economic metals, and As and Sb (e.g., Figure 3.4 and 3.5; Campbell et al., 2020). It is thought that elevated As and Sb concentrations correlate to the distribution of tennantite-tetrahedrite within Iron Cap (Campbell et al., 2020), but micro-scale petrography and trace element analysis by LA-ICP-MS may highlight other causes. Discussions with Seabridge Gold geologists have also revealed that there are particularly elevated concentrations of Se throughout the deposit (M. Savell, pers. comm., 2018). This provides an opportunity for this research project to characterise and understand the deportment of trace elements at Iron Cap, which is useful not only for in-

vestigating the characteristics and evolution of the hydrothermal fluids, but also from an economic perspective. For example, Se, like As, can incur smelter penalties (e.g., Salomon de Friedberg and Robinson, 2015), but could also be economically attractive to recover as a by-product to reduce smelter penalties (Jenkin et al., 2019), and because Se demand is likely to increase in the future owing to the transition to renewable energy sources; Se is used in thin film photovoltaic solar cells (USGS, 2022).

Lastly, the genetic model of Iron Cap outlined above provides a theory of formation that can be tested over the course of this thesis to improve the understanding of hydrothermal fluid characteristics and evolution.

3.8 Summary

This chapter provides background knowledge for the Iron Cap deposit. The regional geology is important for the understanding of large-scale geological features and processes that may have affected the nature and formation of porphyry mineralisation at the district scale (i.e., host rocks, tectonic activity, and magmatic events). At the local scale, similar factors are still of importance (host lithologies, the timing and nature of intrusive events), as these again likely contributed to the unique array of circumstances that generated the deposit. Most relevant for this thesis is that previous research shows that there are multiple vein generations present within Iron Cap (Campbell et al., 2020). These vein generation have been classified, largely in terms of their mineralogy, but require further study to determine their detailed characteristics and trace element geochemistry, which could elucidate genetic processes. Accordingly, the genetic model of Iron Cap is early in its development, and the hydrothermal processes remain to be addressed.

4 Trace elements in ore minerals

4.1 Introduction

This chapter lays the groundwork to use trace elements in ore minerals as a means by which to investigate the evolution of the hydrothermal fluids that formed Au-rich porphyry deposits, and the Iron Cap deposit in particular. To this end, trace elements will first be characterised (Section 4.2), and their typical concentrations in relevant ore minerals will be reviewed (Section 4.3). The current understanding of trace element incorporation in ore minerals will then be assessed (Section 4.4), in order to lead into the controls on ore mineral composition (Section 4.5). Lastly, the composition of ore minerals during the formation of Iron Cap will be discussed (Section 4.6), to provide a theoretical model of trace element deportment that can be compared to the ore mineral compositional data collected from Iron Cap (Chapter 6).

4.2 Trace elements in porphyry deposits

Trace elements are defined here as any element present in an ore mineral that departs from the ideal mineral formula; for example, any element other than Fe and S in pyrite (FeS_2) would be classed as a trace element when discussing pyrite. In general, trace elements in ore minerals are measured at ppm levels, but some may attain weight percent levels (and thus could be classified as minor or major elements), depending on the element, mineral, and occurrence in question.

The different trace elements that can be found in the ore minerals of porphyry deposits are numerous, and include precious metals (e.g., Au, Ag), semimetals (e.g., As, Sb, Se, Te, Ge) and heavy metals (e.g., Cu, Co, Ni, Zn, Hg, Pb, Bi, Cd; Reich et al., 2013; Franchini et al., 2015). This thesis specifically considers a wide range of trace elements: V, Mn, Fe, Co, Ni, Cu, Zn, Ga, Ge, As, Se, Mo, Ag, Cd, In, Sb, Sn, Te, W, Au, Hg, Tl, Pb, and Bi. This trace element suite is chosen because these elements are often found in the ore minerals of porphyry deposits (Section 4.3). Furthermore, it is necessary to consider a wide range of trace elements to highlight any changes in the composition of the ore minerals, as only some of these elements are likely to be present at any one time in a given ore mineral.

The presence of certain trace elements in the ore minerals of a porphyry deposit indicates that these elements were present in the hydrothermal fluids that precipitated them, while a lack of certain trace elements suggests that these elements were either not present in the fluids, or were retained in the fluid during the deposition of the ore minerals.

Meanwhile, variations in the concentration of trace elements throughout an individual deposit implies that there was a change in the conditions of mineral precipitation, such that more or less of the trace element in question was incorporated into the ore minerals than at a previous point in time and/or space.

Currently, from an economic standpoint, finding elevated concentrations of trace elements that are not the principal products (i.e., Cu, Au, Mo) in a porphyry deposit is likely to result in reduced economic feasibility or net profit, because many trace elements (e.g. As, Se, Bi, Sb, Hg) incur smelter penalties (e.g., Salomon de Friedberg and Robinson, 2015). However, some trace elements, such as Ag, can be recovered as by-products during smelting and refining processes (Ayres et al., 2003), and therefore contribute to economic recoveries. Additionally, technologies are being developed to make the by-product recovery of trace elements more economically attractive, particularly for elements that are usually deleterious during processing, or are discarded in tailings (e.g., Jenkin et al., 2019). Combined with an increase in the demand of certain trace elements owing to the transition to green technologies (e.g., Se, Te, Co, Ga, In; Schulz et al., 2017), improvements in by-product recovery could make the deportment of trace elements in porphyry deposits highly desirable information for mineral exploration and mining companies. Regardless, the distribution of trace elements in and around porphyry deposits still remains economically important at present, because this knowledge allows mining companies to enhance their exploration programs with the use of pathfinder elements (e.g., Wilkinson et al., 2015), tailor their processing methodologies appropriately to reduce smelter penalties (e.g., Salomon de Friedberg and Robinson, 2015), and address concerns over the toxicity of mine tailings and weathering products (e.g., Savage et al., 2000).

Despite the advantages of characterising trace element deportment, there have only been a limited number of studies that consider ore mineral compositions in porphyry deposits, as summarised in Table 4.1. It is likely that the relatively recent development of trace element studies of ore minerals plays a part in the limited number of trace element studies undertaken on porphyry deposits. For reference, one of the earliest studies of trace element (Au) concentrations in ore minerals is just over three decades old (Cook and Chryssoulis, 1990), while the first comprehensive trace element study of ore minerals (pyrite) from a porphyry deposit is less than a decade old (Reich et al., 2013). The scarcity of trace element studies means that the deportment of trace elements in the ore minerals of porphyry deposits is poorly constrained, and there is much more yet to be learned. In particular, there is a level of understanding not yet achieved; many of the present studies of trace elements in porphyry deposits focus on differentiating between porphyry-stage and later epithermal-stage trace element signatures in ore minerals (e.g., Franchini et al.,

2015; Sykora et al., 2018; Steadman et al., 2021), and/or do not distinguish ore mineral compositions by porphyry paragenetic stage (i.e, vein generation). This leaves an opportunity for this thesis to build upon the understanding of trace element deportment throughout the evolution of a porphyry hydrothermal system.

There are an increasing number of trace element studies of ore minerals from other mineral deposits, such as epithermal (e.g., Chouinard et al., 2005b; Deditius et al., 2009), orogenic gold (e.g., Large et al., 2007, 2009), Carlin-type (e.g., Large et al., 2009; Muntean et al., 2011), VMS (e.g., Maslennikov et al., 2009; Sharman et al., 2015; Martin et al., 2019; Mishra et al., 2021), and modern seafloor massive sulphide deposits (e.g., Grant et al., 2018), as well as active hydrothermal systems (e.g., Keith et al., 2016; Simmons et al., 2016; Tardani et al., 2017; Keith et al., 2021). The particular focus of ore mineral trace element studies on active hydrothermal systems is primarily due to the fact that the fluids at these sites can be directly sampled and analysed, allowing correlations to be made between ore mineral compositions and hydrothermal fluid characteristics (e.g., Tardani et al., 2017; Keith et al., 2021). Nevertheless, all these studies are useful to consider in the context of this thesis, because they provide comparative data sets of ore mineral compositions (Section 4.3), and have also improved the fundamental understanding of trace element incorporation (Section 4.4) and deportment (Section 4.5), all of which are relevant to the trace element study of ore minerals in porphyry deposits.

4.3 Ore mineral compositions

Different ore minerals can host different trace elements at varying concentrations. As such, the trace element concentrations of each ore mineral must first be considered in isolation. The ore minerals that will be investigated in this thesis are pyrite, chalcopyrite, tennantite-tetrahedrite, galena, sphalerite, and arsenopyrite. These ore minerals are chosen owing to their presence in the vein generations of the Iron Cap deposit (Chapter 5), and similarly their common occurrence in porphyry deposits in general (Chapter 2), which will allow comparisons to be made. Pyrite and chalcopyrite in particular are the most widespread ore minerals at Iron Cap and in porphyry deposits in general, and are therefore the main focus of this thesis.

4.3.1 Pyrite

Pyrite is ubiquitous in most mineral deposits, and particularly porphyry deposits (e.g., Seedorff et al., 2005; Sillitoe, 2010). It is the most common sulphide at Iron Cap (Chapter 3), and present in most of the vein generations (Chapter 5). Pyrite is therefore an essential mineral to study in terms of trace element deportment, because changes in the compo-

Table 4.1

A summary of studies that investigate trace elements in ore minerals, which include data from porphyry deposits.

Reference	Study approach	Porphyry deposit(s)	Ore minerals studied	Elements studied	Main findings
Cook et al. (2011)	Analysis of bn and cct from different mineral deposits	Elatsite, Bulgaria	Bn, cct, ccp	Ag, As, Au, Bi, Cd, Co, Ga, Ge, In, Mo, Ni, Pb, Sb, Se, Sn, Te, Tl, U	Bn consistently contains elevated concentrations of Ag and Bi, and less so Se and Te, but is a poor host for Au; cct hosts more Au than bn
Reich et al. (2013)	Analysis of py from a porphyry deposit	Dexing, China	Py	Ag, As, Au, Bi, Co, Cu, Hg, Ni, Pb, Sb, Se, Te, Zn	First database of py compositions from a porphyry deposit, and elemental maps of py show Au-As-Cu variations that may reflect changes in hydrothermal fluid conditions
Maydagán et al. (2013)	Analysis of ore minerals hosted in porphyry and epithermal alteration	Altar, Argentina	Py, ccp, tnt, ttr, eng, bn, sp, gn, dg, cv	Ag, As, Au, Bi, Cd, Co, Cu, Fe, Ge, Mn, Mo, Ni, Pb, Sb, Sn, Te, Zn	Potassic-hosted ccp and py is trace element-poor, apart from elevated Zn, Sn, and Ag (ccp), and Co and Ni (py); later sericitic-hosted ccp and py show inclusions of native Au (Ag) and sulphosalts with Ag, As, V, Zn, Sn, Bi, and Sb
Gregory et al. (2013)	Case study of metal deportment	Pebble, USA	Py, ccp, bn-dg-cv	Ag, As, Au, Co, Cu, Ni	Identified multiple py generations based on trace element deportment, and recognised py as an important host of Au
Cioacă et al. (2014)	Regional-scale analysis of ore minerals	Six deposits in the Metaliferi Mountains, Romania	Py, ccp, bn, gn	Ag, As, Au, Bi, Co, Cu, Ge, Ni, Sb, Se, Te	Wide variation of trace element concentrations in the same minerals, even in the same sample, but particularly elevated concentrations of Au, Ag, and Te are recorded
Deditius et al. (2014)	Review and analysis of py from different mineral deposits	Butte, USA and Ok Tedi, Papua New Guinea, plus literature data	Py	As, Au	Au and As concentrations in py increase with decreasing temperature, and the Au/As ratio of py may record the Au/As ratio of the hydrothermal fluids

(continued on next page)

(continued)

Reference	Study approach	Porphyry deposit(s)	Ore minerals studied	Elements studied	Main findings
George et al. (2015)	Analysis of gn from different mineral deposits	Elatsite, Bulgaria	Gn	Ag, As, Au, Bi, Cd, Co, Cr, Cu, Fe, Ga, Hg, In, Mn, Mo, Ni, Sb, Se, Sn, Te, Tl, W, Zn	Gn can host elevated concentrations of more elements than previously thought, particularly Ag, Bi, Sb, Tl, Se, Te; gn crystals may also be zoned, while Cr, Mn, Fe, Co, Ni, Zn, Ga, As, Mo, and W are absent from all analyses
Franchini et al. (2015)	Comparison of porphyry and epithermal py	Agua Rica, Argentina	Py, mrc	Ag, As, Au, Bi, Cd, Co, Cu, Ge, Hg, Mn, Mo, Ni, Pb, Sb, Sn, Te, V, Zn	Porphyry py is trace element-poor, apart from elevated Co and Ni; epithermal py varies in composition with depth, becoming most enriched in Pb, Cu, Zn, Ag, Au, Bi, and Te in the ore zone
Pašava et al. (2016)	Analysis of mol from different mineral deposits	Kalmakyr, Uzbekistan	Mol	Ag, As, Au, Bi, Co, Cu, Nb, Ni, Pb, Re, Sb, Se, Sn, Te, W, Zn, Zr	Mol composition indicative of mineralisation type; porphyry mol contains the highest Re values, and Se and W are homogeneously distributed
Sykora et al. (2018)	Comparison of porphyry and epithermal py	Lihir, Papua New Guinea	Py	Ag, As, Au, Bi, Cd, Co, Cu, Fe, Mn, Mo, Ni, Pb, Sb, Se, Sn, Te, Tl, Zn	Porphyry py is trace element-poor, apart from elevated Co, Ni and Se; epithermal py is enriched in trace elements, particularly As, Mo, Ag, Sb, Au and Tl
Steadman et al. (2021)	Analysis of py from different mineral deposits	Five porphyry or porphyry-epithermal deposits, Australia	Py	Ag, As, Au, Bi, Cd, Co, Cu, Ga, Hg, Mn, Mo, Ni, Pb, Pt, Re, Sb, Se, Sn, Te, Tl, U, V, W, Zn	Porphyry py hosts high Co, and lower and variable Ni, As, and Se; these four elements define zonation patterns; epithermal py hosts high As, plus generally high Au and Ag, and variable Te and Sb

sition of pyrite crystals within or between vein generations at Iron Cap may highlight changes in the hydrothermal fluid throughout the lifetime of the hydrothermal system.

Pyrite is commonly studied as a trace element host because of its ubiquity, and the fact that it can contain a wide range of trace elements, as exemplified by the porphyry pyrite compositions reported in Table 4.2. This compositional data shows that pyrite from porphyry deposits tends to host elevated concentrations of Co, Ni, Cu, As, and Se, while the remaining trace elements analysed are variably present, and generally at low concentrations. This is in line with the findings of multiple studies reviewed in Table 4.1, which recognise a Co-Ni-Se signature in early-stage porphyry pyrite, and elevated As and other variable trace elements (e.g., Cu, Au, Ag, Sb, Te, Bi, Pb, Zn) in late-stage porphyry pyrite, or epithermal pyrite. Pyrite may also be an important host for Au in some porphyry deposits (e.g., Gregory et al., 2013; Cioacă et al., 2014; Crespo et al., 2020), highlighting the relevance of studying pyrite trace element compositions to gain insights into the genetic processes of Au-rich porphyry deposits, and to better constrain Au deportment.

Analytical trace elements maps of pyrite from porphyry deposits have illustrated that pyrite crystals are often heterogeneous, and composed of multiple compositionally-distinct zones (e.g., Gregory et al., 2013; Sykora et al., 2018; Steadman et al., 2021). These maps have been utilised to distinguish different generations of pyrite within a single crystal, based on compositional differences, and morphological differences highlighted by changes in composition (e.g., Gregory et al., 2013; Sykora et al., 2018). These studies illustrate that spot analyses of pyrite are not necessarily representative of the bulk composition of each crystal, and that each crystal may be composed of multiple pyrite generations with different compositions. Interrogation of these maps may therefore allow insights to be gained into subtle changes in the hydrothermal fluids that cannot be observed macroscopically. Indeed, in a review of pyrite compositions, Steadman et al. (2021) stress the importance of trace element mapping as a means by which to elucidate growth history, define mineral paragenesis, and illuminate genetic processes.

4.3.2 Chalcopyrite

Chalcopyrite is the main Cu ore mineral at Iron Cap (Chapter 3), and most other porphyry deposits (e.g., Sillitoe, 2010). As with pyrite, chalcopyrite is widespread throughout the Iron Cap vein generations (Chapter 5), and identifying and understanding the trace element deportment of chalcopyrite has similar implications to pyrite (above). However, chalcopyrite compositions are more likely than pyrite compositions to directly reflect the characteristics of the ore-forming fluids that precipitated the bulk of the Cu, because the two minerals may not be co-precipitated. Furthermore, as chalcopyrite is the

Table 4.2
Trace element concentrations in pyrite from porphyry deposits.

Deposit	Dexing, China	Altar, Argentina	Pebble, USA	Colnic, Romania	Agua Rica, Argentina	Lihir, Papua New Guinea
Deposit type	Porphyry Cu-Mo-Au	Porphyry-epithermal Cu-(Au)	Porphyry Cu-Au-Mo	Porphyry Cu-Au	Porphyry-epithermal Cu-(Mo-Au)	Porphyry-epithermal Au
Analysis	SIMS	LA-ICP-MS	LA-ICP-MS	EMPA	LA-ICP-MS	LA-ICP-MS
Values reported	Py from deep sericitic alteration (n. 1)	Mean of potassic py from one sample (n. 4)	Mean of earliest py gen. (n. 4)	Mean of deposit py (n. 41)	Mean of porphyry py from one sample (n. 5)	Geometric mean of porphyry py, from maps (n. ?)
Reference	Reich et al. (2013)	Maydagán et al. (2013)	Gregory et al. (2013)	Cioacă et al. (2014)	Franchini et al. (2015)	Sykora et al. (2018)
Trace elements in ppm						
V	–	0.11	–	–	0.02	–
Mn	–	1.82	–	–	–	–
Co	119	603	168	1950	165.08	131
Ni	–	32.2	329	50	9.4	163
Cu	9.3	–	877	338	26.92	52.1
Zn	–	1.07	–	–	0.39	6.01
Ge	–	0.83	–	<10	1.25	–
As	19	0.12	136	502	2.25	169
Se	10.7	–	–	45	–	125
Mo	–	n.d.	–	–	0.01	0.71
Ag	12.4	0.02	2.2	69	0.01	1.77
Cd	–	0.01	–	–	0.02	–
Sb	12.1	n.d.	–	75	0.02	2.08
Sn	–	0.21	–	–	0.02	–
Te	12.3	0.1	–	174	0.02	11.6
Au	0.19	0.001	0.37	256	0.01	0.54
Tl	–	–	–	–	–	0.2
Pb	–	0.07	–	–	0.19	29.8
Bi	–	0.11	–	–	0.16	–

Abbreviations: SIMS, Secondary-Ion Mass Spectrometry; LA-ICP-MS, Laser Ablation-Inductively Coupled Plasma-Mass Spectrometry; EMPA, Electron Microprobe Analysis; –, not analysed; n.d., not detected.

primary Cu ore mineral at Iron Cap, it is especially important to recognise economically advantageous and deleterious trace elements, because mine concentrates will necessarily contain high proportions of chalcopyrite.

Table 4.3 shows compositional data for chalcopyrite from different porphyry deposits. Elevated concentrations of Ni, Zn, As, Se, and Ag are most evident, although only Zn and Se are consistently elevated in all datasets where they are analysed. Differences are

Table 4.3
Trace element concentrations in chalcopyrite from porphyry deposits.

Deposit	Altar, Argentina	Pebble, USA	Colnic, Romania	Rio Blanco, Chile	Chuquicamata, Chile
Deposit type	Porphyry-epithermal Cu-(Au)	Porphyry Cu-Au-Mo	Porphyry Cu-Au	Porphyry Cu-Mo	Porphyry Cu-Mo
Analysis	LA-ICP-MS	LA-ICP-MS	EMPA	LA-ICP-MS	LA-ICP-MS
Values reported	Mean of potassic ccp from one sample (n. 6)	Mean of deposit ccp (n. 118)	Mean of deposit ccp (n. 19)	Mean of deposit ccp (n. 148)	Median of deposit ccp (n. 173)
Reference	Maydagán et al. (2013)	Gregory et al. (2013)	Cioacă et al. (2014)	Crespo et al. (2020)	Rivas-Romero et al. (2021)
Trace elements in ppm					
V	0.54	–	–	–	n.d.
Mn	8.77	–	–	32.3	6.3
Co	2.56	0.27	–	96.43	3.7
Ni	5.9	9.6	–	1229.55	21.15
Zn	127	–	–	366.32	126.5
Ga	–	–	–	3.27	19
Ge	1.14	–	<10	20.91	60
As	1.05	18	168	2850.23	20
Se	–	–	49	257.78	275
Mo	0.03	–	–	1.53	8.5
Ag	9.01	57	151	16.44	8.9
Cd	0.27	–	–	3.93	3
In	–	–	–	4.3	5.9
Sb	0.08	–	106	74.05	7
Sn	107	–	–	8.58	25.3
Te	0.56	–	185	3.65	2.4
W	–	–	–	–	0.24
Au	0.18	0.13	283	0.03	0.25
Hg	–	–	–	3.53	3.25
Tl	–	–	–	3.97	0.19
Pb	15.9	–	–	20.8	4.4
Bi	0.32	–	–	14.16	1.86

–, not analysed; n.d., not detected.

noted by Maydagán et al. (2013) between chalcopyrite from potassic-altered zones of the Altar deposit, Argentina, and sericitic-altered zones of the deposit, where chalcopyrite is enriched in Zn, Sn and Ag in the former (but otherwise trace element-poor), and is generally enriched in trace elements in the latter, as observed in trace element maps. At Colnic, Romania, chalcopyrite is enriched in nearly all the elements analysed: As, Se, Ag, Sb, Te, and Au (Table 4.3; Cioacă et al., 2014). However, the data of Cioacă et al. (2014) is collected by EMPA, which is hindered by comparatively high limits of detection when compared to LA-ICP-MS; detection limits of 10 ppm, 10 ppm, 20 ppm and 30 ppm are reported for Ag, As, Au, and Te, respectively. It is likely that this contributes to

the elevated mean concentrations of these trace elements in chalcopyrite, because below detection limit concentrations of these elements will not have been included in the mean values.

In a review of trace elements in chalcopyrite, George et al. (2018a) provide a comprehensive dataset of chalcopyrite compositions from 15 different mineral deposits. In general, their work shows that chalcopyrite may contain elevated concentrations of a range of elements, particularly Zn, Ag, Sn, Se, In, which may reach concentrations of 1000s ppm; this agrees with the data from porphyry deposits in Table 4.3. The other elements that George et al. (2018a) detected are Mn, Co, Ga, Cd, Sb, Hg, Tl, Pb, Bi. They concluded that chalcopyrite is generally a poor host for deleterious (i.e., harmful or unwanted) trace elements, apart from Se and Hg. It is important to consider that the elevated concentrations of Se at Iron Cap may be partly hosted by chalcopyrite. This will be investigated in Chapter 6.

4.3.3 Tennantite-tetrahedrite

Tennanite and tetrahedrite form part of a solid solution series, with tennantite the As-rich end member (ideal formula $Cu_6[Cu_4(Fe,Zn)_2]As_4S_{13}$), and tetrahedrite the Sb-rich end member (ideal formula $Cu_6[Cu_4(Fe,Zn)_2]Sb_4S_{13}$; George et al., 2017). However, a range of elements are noted to be present in other minerals of the tetrahedrite isotypic series, such as Ag, Hg, Te, and Se; these may therefore reside in tennantite and tetrahedrite (George et al., 2017). Tennantite and tetrahedrite are considered collectively in this thesis owing to the variance in composition that can only be determined after geochemical analysis. Tennantite-tetrahedrite is variably present in porphyry deposits, and tends to be associated with the later stages of hydrothermal activity where sericitic alteration is developed (e.g., Sillitoe, 2010). However, it is found in the majority of vein generations at Iron Cap (Chapter 5), and is a major phase in some; it may therefore constitute an important host of trace elements.

There are very few published data on tennantite-tetrahedrite compositions from porphyry deposits. Crespo et al. (2020) report tennantite-tetrahedrite trace element compositions from the Rio Blanco Cu-Mo deposit, Chile. Their data shows that, in order of most enriched to least enriched, Ag, Bi, Cd, Hg, Co, Pb, Se, Te, In, Tl, are present in tennantite-tetrahedrite, with Ag reaching concentrations of 11980 ppm, and Tl reaching concentrations of $\sim$10 ppm. Futhermore, Crespo et al. (2020) identify an association whereby higher Ag contents are correlated to higher Sb contents and lower As, indicating that Ag is more compatible in the tetrahedrite end member of tetrahedrite-tennantite. Maydagán et al. (2013) also report tennantite(-tetrahedrite) compositions from the Altar

porphyry-epithermal Cu-Au deposit, Argentina; their data shows elevated mean concentrations of Te (1300 ppm), Ag (295), Bi (133 ppm), Cd (107), Mn (102 ppm), and Pb (30 ppm).

A review of the tennantite-tetrahedrite compositions from different mineral deposits by George et al. (2017) agrees largely with the element suite in tennantite-tetrahedrite defined above, although these authors note that Sn, Ni, Ga, Mo, and Au may also be concentrated in tennantite-tetrahedrite, and they recognise that tennantite-tetrahedrite may exhibit compositional zoning. George et al. (2017) also group elements by the concentrations they can reach in tennantite-tetrahedrite, with Ag, Hg and Pb recognised to be the most abundant (wt. % levels), followed by Cd, Co, Mn, and Bi (>1000 ppm), Se (<1000 ppm), Sn (<100 ppm), and the remaining trace elements of Ni, Ga, Mo, In, Au, and Tl (<10 ppm). Conspicuously, George et al. (2017) note that Te is rarely found above 1 ppm, in contrast to the findings from porphyry deposits above.

4.3.4 Galena

Galena is commonly considered as part of a peripheral, low temperature assemblage in porphyry deposits, associated with propylitic alteration (e.g. Sillitoe, 2010; Reed et al., 2013). Although typically not abundant in the main ore zone of porphyry deposits, galena is present throughout all the vein generations at Iron Cap (commonly as a minor phase; Chapter 5). This means that galena could be an important repository for certain trace elements, and has the potential to illuminate changes in the hydrothermal fluids between vein generations. Therefore, it is necessary to consider galena as part of the ore mineral assemblage to be analysed for trace elements.

Much like tennantite-tetrahedrite, there are few reports of galena compositions from porphyry deposits, although galena is recognised as an inclusion phase during the analysis of other ore minerals (e.g. Steadman et al., 2021). Cioacă et al. (2014) report galena compositions in terms of Ag, Au, Te, Se, Sb, and Ge from porphyry deposits of the Metaliferi Mountains, Romania; they find that galena hosts particularly elevated concentrations of Se (average values approaching 2 wt.%) and Ag (average values approaching 0.3 wt.%), with lower concentrations of Ge (average values approaching 0.1 wt.%) and Te (average values approaching 500 ppm; Cioacă et al., 2014). Antimony was rarely present above lower limits of detection, while Au was always below lower detection limits (Cioacă et al., 2014).

In a review of galena compositions from different deposit types, George et al. (2015) include the analysis of galena samples from the Elatsite porphyry deposit, Bulgaria. The trace elements with the highest mean concentrations in galena from Elatsite are Bi (1388

ppm) and Ag (618 ppm), with lower mean concentrations for Se (146 ppm), Te (143 ppm), Cd (29 ppm), and Sb (13 ppm), and mean concentrations of <10 ppm for In, Au, and Tl, while Cu, Sn, and Hg are below minimum detection limits. The concentrations of Se in galena from Elatsite are greater than two orders of magnitude lower than the concentrations of Se in galena from the Metaliferi Mountains, while the concentrations of Ag, Te, Sb, and Au are fairly comparable between the two sites.

As well as reporting galena compositions from Elatsite, George et al. (2015) also summarise their findings of galena compositions from mineral deposits in general. In addition to the trace elements above, they show that galena can also be an important host of Tl and Hg, and they recognise the presence of compositional zoning in some galena crystals (from epithermal deposits; George et al., 2015).

Even though galena is commonly present as a minor phase in the vein generations of Iron Cap (Chapter 5), its ability to host high concentrations of Se could contribute to the Se-rich nature of the deposit. This will be investigated in Chapter 6.

4.3.5 Sphalerite

Along with galena, sphalerite is often part of a low temperature, peripheral mineral assemblage in porphyry deposits, although it can be found in sericitic-altered zones (e.g., Sillitoe, 2010). Sphalerite is less widespread at Iron Cap than the previous ore minerals described, but is nevertheless present as a major, minor, or trace phase in the mineral assemblage of multiple vein generations (Chapter 5). It is important to consider sphalerite in this thesis because it may contribute specific trace elements (below) to the geochemical signature of vein generations where it is present.

Again, sphalerite compositions are rarely reported from porphyry deposits. Maydagán et al. (2013) do not study sphalerite from the Altar porphyry-epithermal Cu-Au deposit in-depth, only noting that the sphalerite in late porphyry veins contains Cd (0.16-0.24 wt.%), Mn (<0.16 wt.%), Pb (0.12 wt.%) and Fe (<0.1 wt.%). Reviews of sphalerite compositions from different mineral deposits (including epithermal and skarn deposits, but not porphyry) show that sphalerite can contain variable elevated concentrations (wt.% levels) of Fe, Cd, Co, Cu, Ga, Ge, In, Mn, Sn, As, and Tl, while Ag, Pb, Sb, and Bi are uncommonly recognised above lower detection limits (Cook et al., 2009; Frenzel et al., 2016). As the closest relations to porphyry deposits, skarn and epithermal deposits are noted to host sphalerite with higher concentrations of most trace elements, compared to other deposit types (Cook et al., 2009).

The largely unknown nature of trace elements in sphalerite from porphyry deposits means that there is potential to shed light on this over the course of this thesis. Similar-

ities or differences between the compositional data of sphalerite reported from different deposit types in the literature, and that from Iron Cap may also be recognised, which could help to elucidate the characteristics of the hydrothermal fluids that precipitated the sphalerite at Iron Cap.

4.3.6 Arsenopyrite

Arsenopyrite is not common or widespread in porphyry deposits, and tends not to be reported in deposit overviews (e.g., Sillitoe, 2010). It is noted as a rare occurrence in the veins of some porphyry deposits (e.g., Gustafson and Hunt, 1975), although it largely appears to be attributed to peripheral mineralisation (e.g., Corbett and Leach, 1998), or superjacent epithermal mineralisation (e.g., Kouhestani et al., 2017; Zhang et al., 2017). However, as will be shown in Chapter 5, it is present in the V7 vein generation at Iron Cap as a major phase (Section 5.4.7). Arsenopyrite is therefore considered in this thesis because of its occurrence in the V7 vein generation, and because it may be an important host of Au; arsenopyrite statistically hosts more Au than pyrite in a variety of ore deposits (Deditius et al., 2014), and is generally recognised to be able to host high concentrations of gold (up to ∼2 wt.%; Reich et al., 2005). Compositional data of arsenopyrite from porphyry deposits is not available, nor are data of arsenopyrite from other deposit types, aside from where studies report the Au content of arsenopyrite (e.g., Cook and Chryssoulis, 1990). This leaves an opportunity to characterise the trace elements, other than Au, that may be detected in arsenopyrite.

4.4 Trace element incorporation

There are two main ways in which trace elements can be incorporated into ore minerals: as lattice substitutions, or as discrete inclusions of minerals, native metals, or fluids (e.g., Bethke and Barton, 1971; Reich et al., 2005; Cook et al., 2009; George et al., 2015, 2017, 2018a; Frenzel et al., 2020). Lattice substitutions depend on multiple factors, as summarised by Blundy and Wood (2003), who review lattice strain models and the development of understanding of trace element incorporation into ionic structures since the seminal work of Goldschmidt (1937). The most important variables governing trace element incorporation as lattice substitutions are recognised as the charge and size of the trace ion, relative to the charge and size of the lattice site in the ore mineral, and the Young's modulus of the lattice site (effectively how "stiff" the bonds are; Blundy and Wood, 2003). Ion charge and size decides the "fit" of the trace ion into the crystal lattice; trace ions that most closely match the charge and size of the lattice site will produce the least strain on the crystal lattice and therefore be preferentially accommodated (i.e.,

have the highest partition coefficient) into the crystal structure, over trace ions that are poorly matched in terms of charge and size (Blundy and Wood, 2003). However, the Young's modulus of the lattice site is also influential, because lattice sites that have more elastic bonds (i.e., a lower Young's modulus) respond to lower degrees of stress, and can therefore more easily accomodate trace ions that are less well-matched to the lattice site, compared to sites with stiffer bonds (i.e., a higher Young's modulus; Blundy and Wood, 2003).

Some complications to lattice strain models come about when the composition of the ore mineral changes, as the lattice site properties (i.e., optimum radius, Young's modulus) may be affected when other ions in the crystal lattice depart from the ideal, that is, are smaller or larger and/or have a weaker or greater charge than the ore mineral ions (Blundy and Wood, 2003). Compositional changes to the crystal may then allow different trace elements that were not previously compatible to be substituted into the crystal lattice. Examples of this are coupled substitutions, whereby two trace ions that are alone not well matched to a lattice site in terms of charge and size can together be incorporated into the crystal lattice in the place of two ore mineral ions (e.g., Grant et al., 2018). For example, two trace ions, A^{+} and B^{3+}, with a radius of 0.5 Å and 1.5 Å, respectively, could feasibly substitute for two of the same ore mineral ions, C^{2+}, that each have a radius of 1 Å, assuming that the lattice sites can accommodate the strain induced by the incorporation of the smaller and larger trace ions. The theoretical understanding of trace element incorporation by lattice substitution outlined above allows a prediction of expected substitutions in ore minerals; this topic will be explored in greater detail in Chapter 7.

Studies of trace elements in ore minerals often consider lattice substitutions to have occurred based on the homogeneous distribution of a given trace element within an ore mineral (e.g., Cook et al., 2011; George et al., 2015; Grant et al., 2018; Rivas-Romero et al., 2021). In particular, these studies analyse the signal intensities of LA-ICP-MS spots or maps (common named ablation profiles or traces) as a means by which to infer lattice incorporation of a trace element. A smooth ablation profile for an element over the analytical time period (e.g., 30s) is interpreted to represent the lattice incorporation of the element; the homogeneous distribution of an element in a map or zone is similarly interpreted as lattice incorporations. In contrast, fluctuating (i.e.,"spiky") ablation profiles that are often matched with the spiky profiles of other elements are interpreted to represent the inclusion of discrete mineral phases, with the high points (i.e., the spikes) recording the inclusions; heterogeneous distribution of an element in a map or zone is often similarly interpreted. One difficulty of this method is distinguishing between lattice-hosted elements and elements hosted in micro- or nano-inclusions in an ore mineral.

Both may produce a smooth profile, or homogeneous distribution in a map or zone; the latter because the inclusions are too small to detect individually, and may be relatively evenly distributed within the crystal to be ablated such that they mirror the smooth ablation profile of a lattice-hosted element. Determination of trace element incorporation by interrogation of LA-ICP-MS profiles is discussed further in Chapter 6.

Inclusions of discrete minerals or native metals may form prior to, during, or after ore mineral growth (e.g., Putnis, 2009; Roman et al., 2019). If formed prior to, or during, ore mineral growth, the inclusion phase may be incorporated as the ore mineral grows, or continues to grow, around it (e.g., Roman et al., 2019). Alternatively, inclusions may form after ore mineral growth, for example, via exsolution (e.g., Bente and Doering, 1993; Putnis, 2009), recrystallisation (e.g., Roman et al., 2019), or dissolution-reprecipitation processes (e.g., Putnis, 2009; Hastie et al., 2020, 2021). Distinguishing between these processes may be difficult, particularly in cases where inclusions are invisible to microscopic study. Nevertheless, if the origin of inclusions can be determined, the inclusions (and their composition) may help to elucidate the conditions and processes of ore formation (pre- or syn-ore mineral growth inclusions), and/or the original composition of the ore mineral, or the nature of post-ore mineral modification processes (post-ore mineral growth inclusions). Fluid inclusions within an ore mineral that contain trace elements may be primary (i.e., trapped during mineral growth) or secondary (i.e., trapped during later fluid activity, as the mineral is fractured, for example), meaning that, as above, their composition may or may not represent the original ore-forming fluid (e.g., Wilkinson, 2001).

In addition to lattice substitution and inclusions, adsorption onto ore mineral surfaces may also be an important incorporation mechanism for some trace elements (e.g., Au, Mn, V, U; Fougerouse et al., 2016b; Grant et al., 2018), as could the non-substitutional incorporation of trace elements into lattice defects or vacancies in the ore mineral crystal structure (e.g., Au in pyrite; Reich et al., 2005). However, these incorporation mechanisms are unlikely to constitute a major incorporation process for most trace elements considered in this thesis, and determining that these processes have occurred (as opposed to lattice substitutions or inclusions) often requires atom-scale analyses (e.g., Fougerouse et al., 2016b, 2021; Wu et al., 2019, 2021), the like of which are not utilised in this thesis. Nevertheless, these processes may be inferred to explain trace element incorporation that cannot be clearly attributed to lattice substitutions or inclusions.

4.5 Controls on ore mineral composition

There are numerous controls on the composition of ore minerals, which are intrinsically linked to the incorporation mechanisms of trace elements (Section 4.4). The main aim of this thesis is to utilise the study of trace elements in ore minerals to help constrain hydrothermal fluid conditions during ore genesis. There will therefore be a focus on considering trace elements incorporated into ore minerals as lattice substitutions, because lattice substitutions are the most well-constrained and predictable of the trace element incorporation mechanisms, and have a greater potential to elucidate the characteristics of the hydrothermal fluids, as discussed below, and further in Chapter 7.

The primary control on variations in ore mineral compositions owing to lattice substitutions are the characteristics of the hydrothermal fluids (e.g., Deditius et al., 2009; van Hinsberg et al., 2010; Reich et al., 2013; Deditius et al., 2014; George et al., 2016; Grant et al., 2018; Wu et al., 2019; Frenzel et al., 2020; Steadman et al., 2021). The composition of a hydrothermal fluid is a fundamental control on ore mineral composition, because if a trace element is not present within a hydrothermal fluid, it cannot be incorporated into an ore mineral. This basic understanding was utilised to explain the decoupling of Cu and As in LA-ICP-MS trace element maps of pyrite at the Dexing porphyry deposit, China (Reich et al., 2013). In this case, it was proposed that the pyrite-forming fluids were mixed with high temperature (∼600-700 °C), As-rich vapours, alternating with low temperature (∼300 °C), Cu-rich vapours that intermittently invaded the main hydrothermal system (Reich et al., 2013); the presence or absence of Cu and As in the fluids was thought to be a key control.

When present in a fluid, a trace element should be preferentially incorporated into a crystallising ore mineral if the partition coefficient of the trace element between the ore mineral and an aqueous fluid phase is greater than 1, in favour of the ore mineral (e.g., Blundy and Wood, 2003). The partition coefficient thus depends on the solubility of the trace element in an aqueous fluid phase (itself largely dependent on pressure, temperature, and fluid composition; e.g., Archibald et al., 2001; Stefánsson and Seward, 2003), and the compatibility of the trace element in the ore mineral (largely dependent on the lattice substitution constraints introduced in Section 4.4, and temperature). Temperature is an important variable because increases in temperature marginally lower the Young's modulus of a mineral (lattice bonds become more "elastic" as temperature increases), thus increasing the likelihood of substitution and accordingly increasing the partition coefficient of a trace element (cf. Section 4.4; Blundy and Wood, 1994); this is illustrated further in Chapter 7. In a review of pyrite compositons from magmatic-hydrothermal deposits,

Steadman et al. (2021) inferred that the absence of Cu and Au in early porphyry pyrite was due to the pre-Cu-Au ore timing of pyrite crystallisation, implying that Cu and Au remained soluble in the fluid during the precipitation of pyrite, and/or that the partition coefficients for Cu and Au ions into pyrite were low. On the other hand, Deditius et al. (2014) showed that the Au/As ratios of pyrite crystals from similar deposits were primarily dependent on the crystal properties of pyrite, with Au and As in pyrite from porphyry and epithermal deposits directly recording the Au/As ratio of the hydrothermal fluids.

The nature of the co-crystallising ore mineral assemblage also comes into play when considering trace element deportment, because a trace element will have a partition coefficient between an aqueous fluid phase and each ore mineral crystallising from the fluid. Therefore, the ore mineral with the highest partition coefficient for a given trace element between its aqueous fluid phase will preferentially incorporate that trace element. This primarily depends on the compatibility of the trace element in each of the ore mineral crystal lattices (Section 4.4), with the trace element being preferentially incorporated into the ore mineral in which it has the best fit; however, there may be overlaps in the compatibility of a given trace element in different ore minerals.

The relative order of partition coefficients can be determined empirically from compositional data; for example, George et al. (2016) studied the partitioning of trace elements between co-crystallised chalcopyrite, sphalerite and galena in a range of hydrothermal deposits. From their LA-ICP-MS analyses they found that in ore samples unaffected by recrystallisation, galena was always the preferred host of Se, Ag, Sb, Te, Tl, and Bi, while sphalerite was always the preferred host of Mn, Fe, and Cd, and chalcopyrite was not the preferred host of any trace elements (apart from Zn, but Zn is preferentially incorporated into sphalerite; George et al., 2016). The findings of George et al. (2016) show that certain ore mineral compositions can identify the availability of a certain trace element in a fluid, with, for example, the presence or absence of Se in galena indicating that Se was likely present or absent in the fluid, respectively. Meanwhile, the absence of Se in sphalerite co-crystallised with galena would not necessarily mean that Se was absent in the fluid, because Se would be preferentially incorporated into galena, and may not be incorporated into sphalerite at detectable concentrations if the partition coefficient for Se into sphalerite was sufficiently low. The work of George et al. (2016) also found that the preferred host of some elements (e.g., Co and Hg) is not always predictable, meaning that there are variations on the partitioning trend, possibly caused by similarities in the compatibility of these trace elements between different ore minerals. Nevertheless, the study of (George et al., 2016) emphasises the importance of studying the composition of an ore mineral assemblage, rather than individual ore minerals, to help explain the

concentrations of trace elements in ore minerals.

While partitioning trends are essential to consider, the maximum concentration of an element an ore mineral can accommodate also plays a role in determining ore mineral compositions. This is dependent on temperature, and the amount of strain the lattice can accommodate as more of the trace element is incorporated (e.g., Blundy and Wood, 2003; Reich et al., 2005; Deditius et al., 2014). The maximum concentration of a given trace element an ore mineral can host as lattice substitutions is therefore variable, particularly when other trace elements are incorporated into the lattice. For example, Reich et al. (2005) determined the solubility limit for Au in As-bearing pyrite, which varies according to As content and temperature, where As acts to neutralise the strain exerted on the pyrite lattice by incorporation of the Au, therefore allowing greater Au concentrations to be hosted in increasingly As-bearing pyrite, compared to As-poor pyrite. Reich et al. (2005) also deduced that the speciation of Au could be determined by its concentration in As-bearing pyrite, whereby Au concentrations below the solubility limit were present as lattice substitutions of Au^{1+}, while Au concentrations above the solubility limit necessitated the contribution of inclusions of nanoparticulate Au^0. In turn, these findings are able to imply that As-bearing pyrite containing concentrations of Au above the solubility limit was precipitated from hydrothermal fluids that were saturated with respect to Au^{1+} in an aqueous complex, and Au was also transported in nanoparticulate form (Au^0) in the fluid.

In summary, trace elements are not ubiquitous to all occurrences of a specific ore mineral, meaning that the presence or absence of a trace element, and/or the concentration of a trace element in an ore mineral can be used to investigate changes in the conditions of ore mineral precipitation from hydrothermal fluids, to build a picture of hydrothermal fluid evolution through space and time. These topics will be discussed further in Chapter 7 and 8.

4.6 Expected ore mineral compositions at Iron Cap

Combining the genetic model of Iron Cap and an understanding of trace elements in ore minerals allows a general prediction to be made of ore mineral compositons at Iron Cap, as summarised in Table 4.4. This has been constructed based on predicted hydrothermal fluid conditions forming each vein generation (Section 3.6), and the changes in the composition of different ore minerals, outlined above. Such a prediction is useful because it can be tested over the course of this thesis, allowing similarities and differences to be recognised, which may help to elucidate the characteristics and evolution of the hydrothermal fluids at Iron Cap.

Table 4.4
Predicted presence of trace elements in the ore minerals of the Iron Cap vein generations defined by Campbell et al. (2020)

Vein	Py	Ccp	Tnt-ttr	Gn	Sp
A-vein	–	Zn, Sn, Ag, Se	–	–	–
Magnetite	–	Zn, Sn, Ag, Se	–	–	–
B-vein	Co, Ni ± Se	Zn, Sn, Ag ± Se	–	–	–
Molybdenite	Co, Ni ± Se	Zn, Sn, Ag ± Se	–	–	–
Polymetallic	As, Cu, Au, Ag, Sb, Te, Bi, Pb	± Se, Sn, Zn	Te, Hg, Pb, Bi ± Se, Ag, Cd, Mn, Co	–	In, Ga ± Se, Sn, Cd, Mn, Co, Fe
D-vein	As, Cu, Au, Ag, Sb, Te, Bi, Pb	–	–	–	–
Post-mineral	–	± Se, Sn, Zn	± Te, Hg, Bi Se, Ag, Cd, Mn, Co	Se, Ge, Tl ± Te, Hg, Bi, Ag	In, Ga ± Se, Sn, Cd, Mn, Co, Fe

4.7 Summary

Background information has now been provided for porphyry deposits and magmatic-hydrothermal systems, the Iron Cap deposit and the KSM district, and trace elements in ore minerals. These reviews have culminated in a genetic model for Iron Cap (Section 3.6), and a prediction of the deportment of trace elements at Iron Cap (Section 4.6). Comparisons with these models aim to improve the understanding of hydrothermal fluid evolution at Iron Cap, and assess the applicability of using trace elements in ore minerals to identify and characterise hydrothermal fluid evolution throughout formation of a Au-rich porphyry deposit.

5 Petrography of vein generations

5.1 Introduction

To begin investigating trace element deportment and hydrothermal fluid evolution at Iron Cap, 70 samples of drill core were collected from the deposit. The sample selection criteria, and the full sample list is provided in Appendix A. The drill core samples were first analysed as hand specimens, and most (n. 52) were then made into polished thin sections, where the majority were analysed using transmitted and reflected light microscopy, Scanning Electron Microscopy (SEM), and Cathodoluminesence (CL). These analytical procedures are described in Appendix A, where a record of the analytical work undertaken on each sample is also presented. This chapter summarises the analytical work undertaken, introduces the mineralogy of Iron Cap, characterises the vein generations present within the deposit, and proposes a paragenetic sequence of vein formation and ore mineral precipitation.

The petrographic data presented here forms the fundamental basis of the thesis, in that the interpretation of the trace element analysis of ore minerals is constrained by the characteristics of the vein generations in which the ore minerals are present. Both defining vein generations and constructing a paragenetic sequence are additionally useful in the context of this thesis, because this information is essential to allow investigation of the evolution of the hydrothermal system at Iron Cap.

This chapter is structured to first describe the rock types hosting the veins at Iron Cap. Then, the criteria used to classify the vein generations at Iron Cap are outlined. Next, the characteristics of each vein generation are described, including their ore and gangue mineralogy, textures, and morphology. The topic of vein classifications is then revisited in the context of the paragenesis, where the relative timing of each vein generation is justified using the previously presented data. Following this, the new vein classifications and the paragenesis are critically evaulated in the context of previously published work. The implications of the petrographical study for the understanding of Iron Cap are then discussed. Finally, a suite of vein samples were selected for trace element analysis by LA-ICP-MS. The rationale used to make these selections is defined, to justify, and lead into, the trace element analyses presented in Chapter 6.

5.2 Host rocks

The host rock type of vein samples from Iron Cap is difficult to discern in the majority of cases, owing to the abundance and intensity of hydrothermal alteration, which obscures

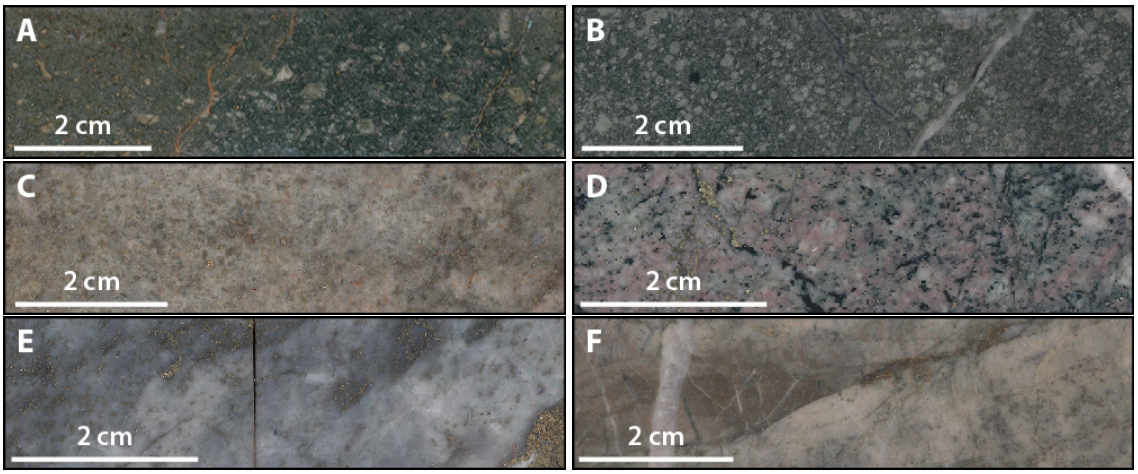

Figure 5.1. Representative host rock types of the Iron Cap vein samples, from samples IC01-054 (A), IC66-084 (B), IC37-038 (C), IC72-821 (D), IC73-518 (E), IC01-109 (F).

original rock textures and primary mineralogy. Campbell et al. (2020) also noted this as an issue in identifying and classifying the host rocks during their study of Iron Cap (Chapter 3). Figure 5.1 illustrates the variety in preservation and type of host rock constituting the vein samples.

Phenocrysts are preserved in some samples (e.g., Figure 5.1A, B), recording the porphyritic nature of the host rock, although the phenocrysts are altered to quartz and sericite. The groundmass of these samples is composed largely of quartz, sericite, and pyrite, with minor rutile, apatite, monazite, calcite, and K-feldspar. The mineralogy principally illustrates sericitic alteration; however, the abundace of mafic replacement minerals (quartz, sericite, pyrite), the occasional presence of K-feldpsar and plagioclase, and the accessory mineralogy (rutile, apatite, monazite), suggests that the protolith was in the compositional field of monzonite. This complies with the classifications of Campbell et al. (2020), where Figure 5.1A and B bear similarities to the monzonites illustrated in Figure 3.6.

Variable degrees and types of alteration are observed in the host rocks; Figure 5.1C illustrates intense sericitic alteration, while Figure 5.1D illustrates intesne potassic alteration. Such samples regularly exhibit a lack of textural preservation, and the mineralogy is dominated the by the alteration assemblage, leading to difficulties identifying protolith lithologies. Some samples have host rocks dominated by quartz (Figure 5.1E), suggesting that a pre-vein phase of silicification may have occurred to obliterate the original host rock mineralogy and texture. In two samples, the host rocks appear to be hornfels (e.g., Figure 5.1F), evidenced by the textural preservation of sedimentary structures, the lack of igneous textures (e.g., phenocrysts), and the dominance of quartz.

It is difficult to decypher whether certain host rocks are the source of the vein-forming

fluids in the sample suite, owing to the limited distribution of core samples, which hinders the understanding of vein and alteration distribution. However, degrees of alteration could be used to indicate that some host rocks are more likely to be the source of hydrothermal fluids than others. For example, those that exhibit intense alteration and veining may be more likely to be the source, or proximal to the source, of hydrothermal fluids, whereas samples that lack intense alteration and veining, and exhibit original host rock textures, are more likely to be distal to the fluid source. This is based on the idea that rocks closer to the fluid source should experience a greater fluid flux, and a high fluid:rock ratio.

5.3 Vein classification criteria

Each vein generation in the drill core samples from Iron Cap is primarily classified based on differences in vein characteristics. The characteristics considered are mineralogy (ore and gangue), texture, morphology, alteration halo, and wall rock alteration. Similar approaches to vein classification are applied in other porphyry deposit studies (e.g., Sillitoe, 2010; Maydagán et al., 2015; Jensen et al., 2022). The vein samples have been analysed by SEM to identify the characteristics of the vein generations that cannot be observed macroscopically; these specific characteristics are elaborated upon in Section 5.4.

Vein mineralogy is an important classification criteria, because a change in mineralogy signifies a change in the characteristics of the hydrothermal fluids. A change in the major (>10% in terms of volume) and minor (2-10%) minerals present is considered to account for the primary differences in vein mineralogy. The trace minerals (<2%) identified contribute to the classification of a vein generation, but are of secondary consideration owing to their rare, and often variable, occurrence. Mineral proportions can change within a vein generation, but slight changes are not sufficient to classify a discrete vein generation, as long as other vein characteristics remain compatible.

Vein texture and morphology are also considered, because these characteristics also indicate genetic processes, and changes in these characteristics can suggest that different veins formed in different ways, or under different conditions. For example, typical porphyry B-veins contain a central suture of ore minerals within quartz, whereas C-veins are dominated by ore minerals with a massive texture (Section 2.5.4), indicating that these veins formed by different processes. Similarly, sinuous, mm-cm scale A-veins are attributed to formation under hotter, ductile conditions, whereas linear, structurally-controlled, cm-m scale E-veins are ascribed to formation under cooler, brittle conditions (Sillitoe, 2010). These examples illustrate that texture and morphology are vital to consider in the context of this thesis.

Alteration associated with vein occurrences is identified and characterised to assess whether there are genetic relationships between the veins and alteration, and whether this is characteristic of a vein generation. Alteration halos are the clearest evidence of a relationship between a vein and alteration, whereby the alteration halo is directly associated with the vein-forming hydrothermal fluids. Wall rock alteration is also recorded, but cannot be directly linked to the veins hosted within it.

Cross-cutting relationships provide key information on the relative timing of different veins, allowing different vein generations, and stages of hydrothermal fluid flow, to be defined. However, Campbell et al. (2020) found the lack of cross-cutting relationships at Iron Cap challenging when developing a vein sequence, and the same issues are encountered in the present study. Nevertheless, cross-cutting relationships are utilised, where present. There are further paragenetic constraints (e.g., sample location) that inform the classification of certain veins; these are discussed in Section 5.5, after the petrographic data has been presented.

It is important to note that the vein classifications of this thesis are limited by the nature of the sample suite; in particular, the number of samples containing each vein generation. This is because vein generation characteristics can vary between samples, and recognising the extent of variations is dependent upon multiple vein occurrences being observed. It is therefore possible that the characteristics recorded here for vein generations that are rarely observed in the sample suite may not be wholly representative of the vein generations within the Iron Cap deposit. Similarly, there may be additional vein generations that are absent from the sample suite, but present within Iron Cap, leading to their absence in the vein generations classified here.

Differences in the number of samples containing each vein generation may have been affected by the sampling method, as there was a sampling bias for core from certain drill holes and from shallower depths, owing to availability (Appendix A). In particular, only 3 samples are taken from drill core that reached depths greater than 900 m. Therefore, there may be an under-representation of some vein generations in the sample suite due to sampling bias. Equally, however, differences between vein generations in terms of abundance in the sample suite may be representative of relative vein generation abundances within Iron Cap. Another limitation of the sample suite is that most samples are derived from quarter-core (some are from half-core), and are typically $\sim$2 cm in width, varying in length from 9-40 cm. Therefore, vein continuity cannot be reliably assessed in most cases, and vein thickness measurements represent minimums where only one vein margin is observed.

5.4 Vein generations at Iron Cap

Eight vein generations are classified at Iron Cap. Their ore and gangue mineralogy, texture and morphology are summarised in Table 5.4. The vein generations are named according to relative timing, with V1 interpreted to be the earliest-formed vein generation, and V8 the latest-formed vein generation; the vein paragenesis is discussed in detail in Section 5.5. Samples of drill core from Iron Cap are named according to the format: IC11-222, where "IC" stands for Iron Cap, "11" represents the drill hole number, and "222" records the depth the drill core sample was taken from. For example, sample IC72-798 was collected from the drill core of drill hole number 72, and from a depth of 798 m.

This section reports the characteristics of the vein generations at Iron Cap. There is a particular focus on the ore mineralogy of the veins, and the paragenetic relationships of the ore and gangue minerals, to determine whether specific assemblages are coeval.

5.4.1 V1

Only one occurrence of V1 was observed in the sample suite from Iron Cap. The vein is contained within drill core from a depth of 970 m, and is characterised by a magnetite-dominated mineral assemblage (Figure 5.2). The vein is discontinuous, with diffuse and asymmetrical boundaries, and an irregular form. A massive texture is defined by the roughly equant crystals of magnetite, which reach up to $\sim$50 µm in size, and are often annealed to form larger masses. Magnetite is sometimes interspersed with similarly-sized crystals of magnetite-rutile intergrowths (Figure 5.3). Gangue minerals of thorite, K-feldspar, plagioclase, sericite, and chlorite are also present within the vein margins, but are not interpreted to be part of the V1 mineral assemblage, as discussed in Chapter 8. The V1 vein is situated within a potassic-altered groundmass, characterised by K-feldspar, plagioclase, and quartz; however, sericite is often present and most concentrated where magnetite is brecciated and of smaller grain sizes (Figure 5.3), such as at the vein margins (Figure 5.4)

Chalcopyrite and galena are present in the vein, but are associated with the formation of later, cross-cutting V4 veins, which have a chalcopyrite-galena ore mineral assemblage (Figure 5.2; Section 5.4.4). Additional textural evidence is apparent in Figure 5.5, where chalcopyrite is grown around the magnetite crystals, and chalcopyrite and galena inclusions are present within both magnetite and thorite.

Table 5.1

Characteristics of the vein generations at Iron Cap. Major minerals constitute >10% of a vein in terms of volume, minor minerals 2-10%, and trace minerals <2%.

	Ore minerals			Gangue minerals				
Vein	Major	Minor	Trace	Major	Minor	Trace	Textures	Morphology
V1	mag				rt		Massive mag	Discontinuous, with diffuse, asymmetrical boundaries and irregular forms; widths may exceed 20 mm
V2		ccp, py ± tnt-ttr	gn ± Au ± hes ± ptz ± sp ± bn ± mol ± alt ± col	qz	± ser ± rt ± ap ± brt ± cal	± chl ± ksp ± fl ± bst ± ank	Crackled texture and/or central suture within qz, defined by ore minerals	Continuous, with sinuous to linear forms, and wavy to straight margins; widths from ∼10 mm to >8 cm
V3	py	ccp	gn ± tnt-ttr ± Au ± sp ± alt ± hes ± ptz ± BiTe ± bn	qz, ser	rt, ap ± fl	± brt ± bst	Massive py	Continuous, with wavy margins, and sinuous to relatively linear forms; widths from 1 mm to >12 cm
V4		ccp	± gn ± Au ± mag	qz ± chl	± cal	± sd ± ksp ± rt ± ser ± ap	Massive black chl is distinctive where present; qz-rich veins host coarse masses of ccp and/or chl	Continuous, with wavy to straight margins, and sinuous to linear forms; multiple veins often found in the same sample; widths from 1-18 mm

(continued on next page)

Table 5.1
(continued)

	Ore minerals			Gangue minerals				
Vein	Major	Minor	Trace	Major	Minor	Trace	Textures	Morphology
V5	tnt-ttr	± ccp	gn ± AgHg ± hes ± bn ± sp ± col	qz ± brt	± cal ± ank ± ksp		Tnt-ttr often occurs as clots in the vein centre or at the margins	Continuous, with relatively straight margins; multiple oriented veins within a sample; widths from 5-18 mm
V6	sp, ccp, py	gn ± tnt-ttr	± hes ± ptz ± Au ± BiTe ± apy	qz	cal ± dol ± ank ± sd ± chl ± ser ± ap ± brt	± FeO	Massive sulphide, with qz-cb; alteration halos (usually sericitic) often observed	Straight, linear forms; widths from 5 mm to >20 cm
V7	py, apy		Au ± gn ± ccp ± sp	qz	cal, ser ± ank		Sulphide-dominated; black colour due to fine-grained apy	Continuous, with relatively straight margins; widths from 1-20 mm
V8				± cal ± ank ± dol ± sd ± qz	± brt ± fl		Barren carbonate ± qz	Elongate, sinuous or straight; widths up to 20 mm

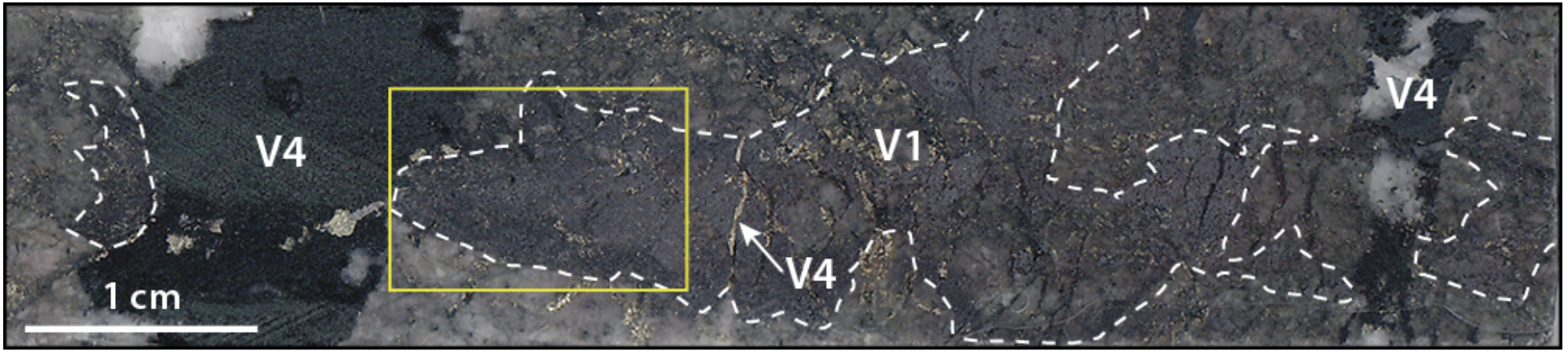

Figure 5.2. Occurrence of V1 in sample IC71-970, with the diffuse margins roughly outlined by white dashed lines. The steel-grey magnetite is cross-cut by V4 veins, which are characterised by dark green-black chlorite, quartz and chalcopyrite. Chalcopyrite-rich veinlets of V4 can also be observed cross-cutting V1, and the disseminated chalcopyrite within V1 is associated with V4. The yellow box marks the location of the BSE image in Figure 5.4.

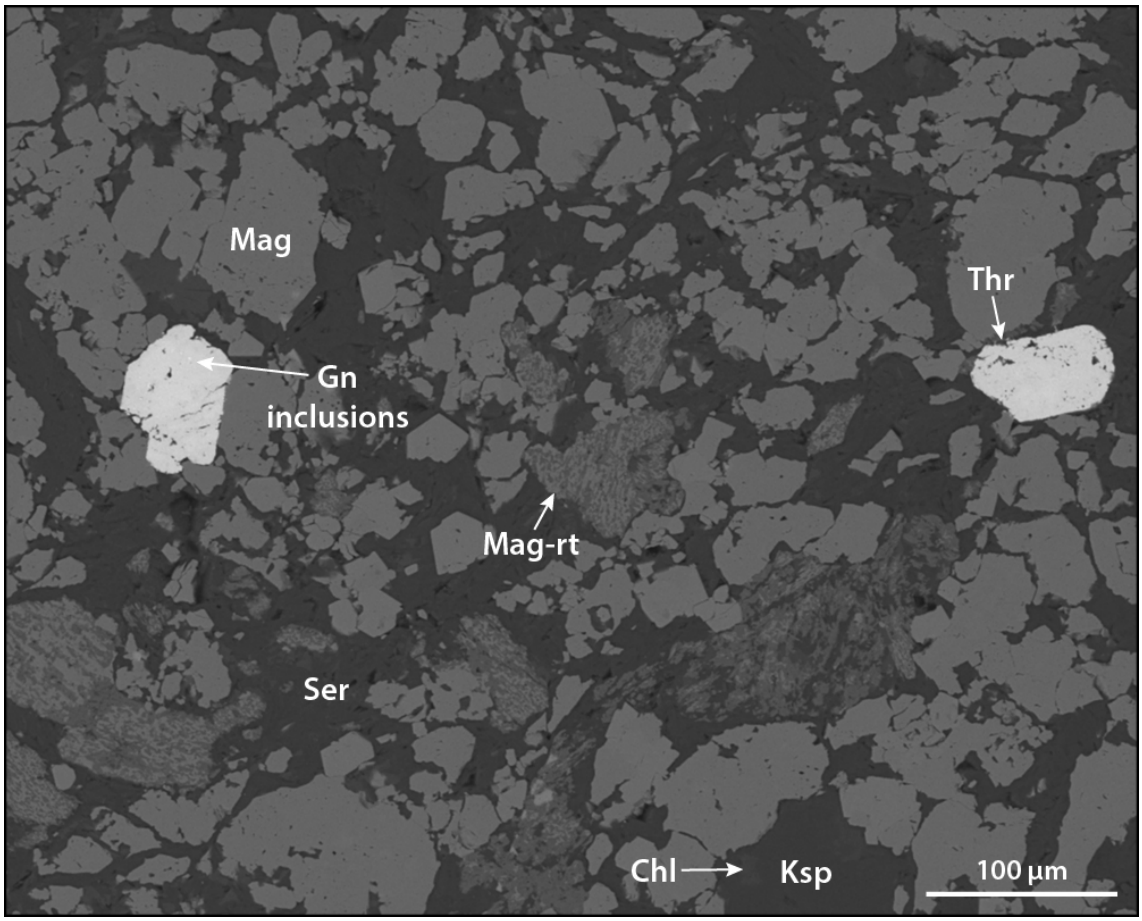

Figure 5.3. Mineral occurrences and textures in V1, imaged by SEM (BSE mode). Most of the gangue in this field of view is sericite; only minor K-feldspar and chlorite are present.

5.4.2 V2

The V2 vein generation at Iron Cap is principally characterised by quartz-rich veins that exhibit a crackled texture and/or a central suture occupied by ore minerals (Figure 5.6). Vein width varies from ∼10 mm (e.g., Figure 5.6A) to >8 cm (e.g., Figure 5.6G). Morphology is also variable, with some V2 veins relatively linear, with straight-boundaries (e.g., Figure 5.6A, B), while others exhibit more sinuous forms, with wavy boundaries (e.g., Figure 5.6C, E). Symmetry between vein margins is occasionally observed, but is not ubiquitous, tending to be associated with the more linear and straight V2 vein occurrences. V2 veins are observed at different locations within the deposit, as evidenced by the varying depth of the samples in Figure 5.6, and shown further in Section 5.7. Wall rock alteration in V2 vein samples is predominantly sericitic, evidenced by the widespread presence of sericite, quartz and pyrite in the groundmass. Other wall rock gangue minerals commonly observed are rutile, apatite, and monazite. Some samples contain minor K-feldspar in the wall rock groundmass, indicating that sericitic alteration has overprinted pre-existing potassic alteration.

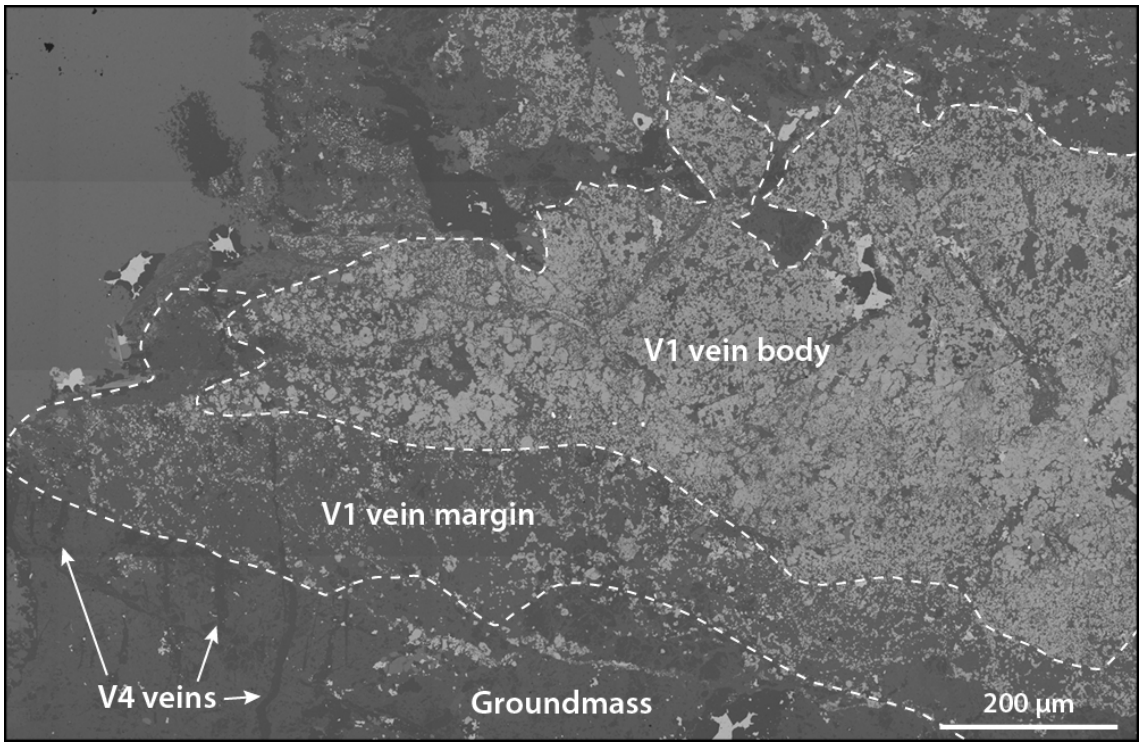

Figure 5.4. V1 vein structure imaged by SEM (BSE mode). This field of view is marked by the yellow box in Figure 5.4. The vein body is dominated by magnetite, where crystal sizes are larger (up to ∼50 µm) than at the vein margin, where post-V1 sericite introduction has disseminated and brecciated the magnetite. In the groundmass, potassic alteration is largely preserved, although sericite does occur. V4 quartz veins present in the groundmass are truncated or overprinted by the sericite-rich V1 vein margin.

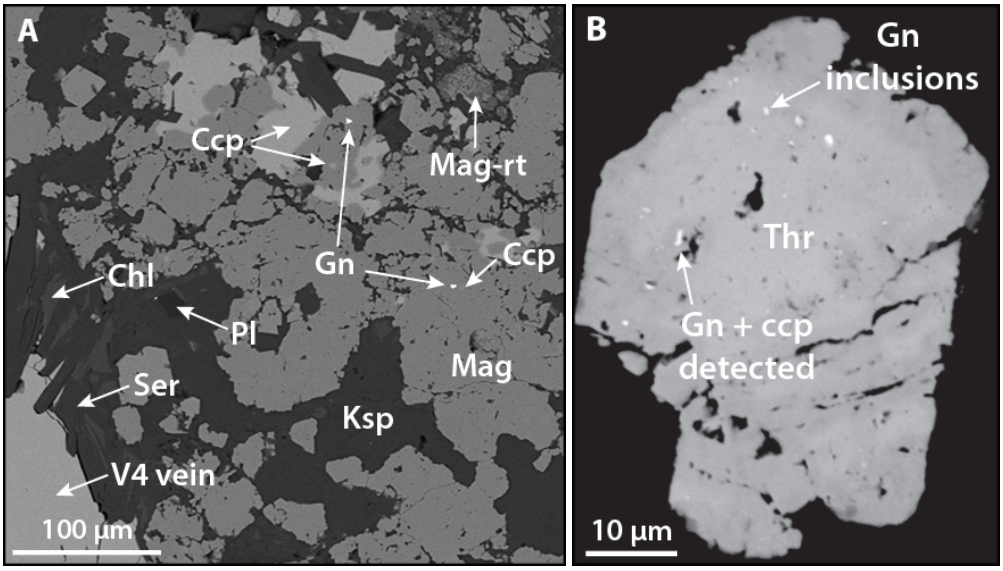

Figure 5.5. Occurrence of V4-associated chalcopyrite and galena in the V1 vein, imaged by SEM (BSE mode). A shows a V4 vein (bottom left) cross-cutting V1, with associated chalcopyrite and galena as inclusions in the magnetite of V1, and chalcopyrite grown around V1 magnetite. B shows a porous thorite crystal with inclusions of galena and chalcopyrite.

The texture of V2 veins varies within the constraints of the crackled and/or central suture description. Some V2 veins exhibit purely crackled textures, with no apparent cen-

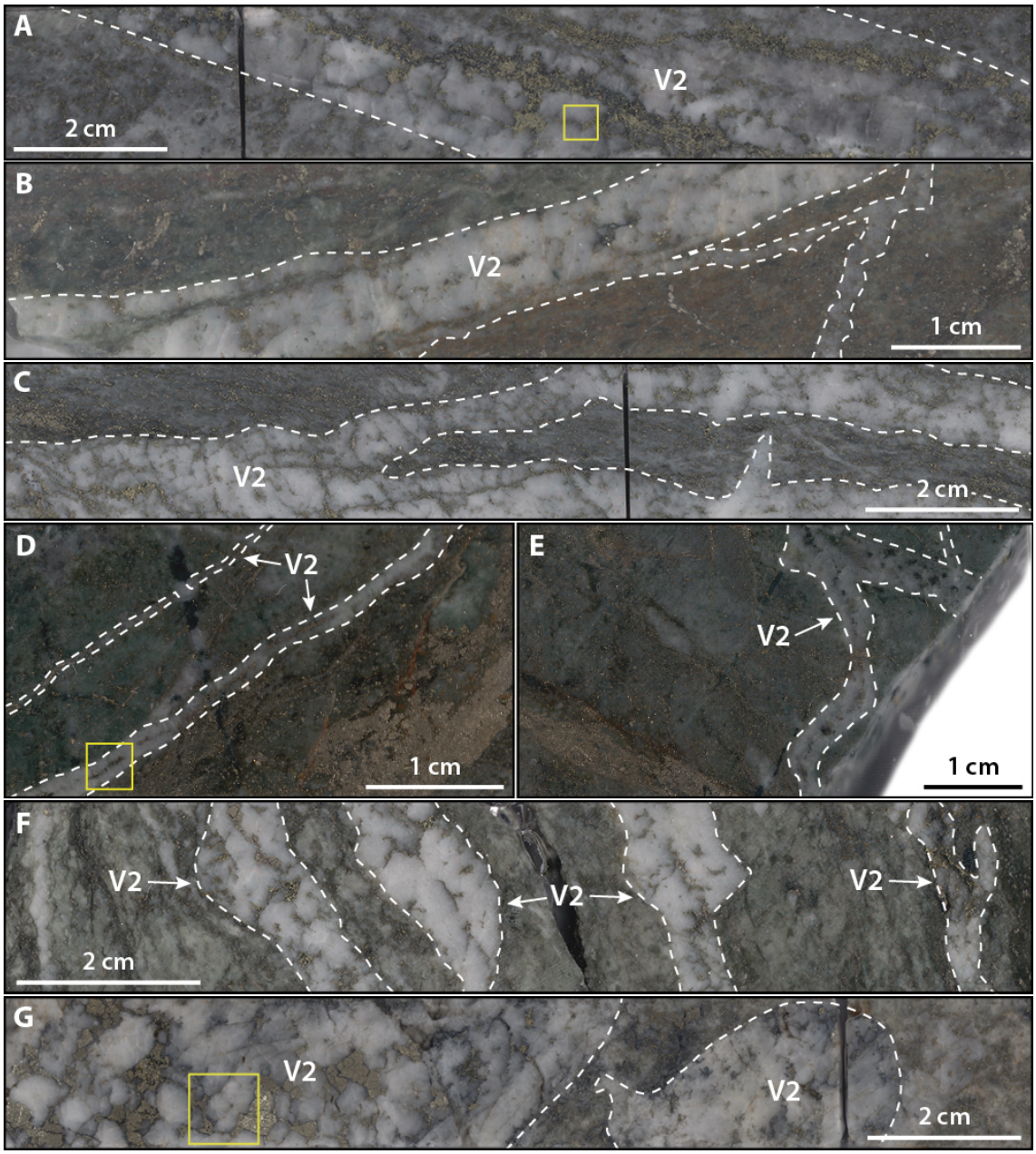

Figure 5.6. Representative V2 vein occurrences, from samples IC72-798 (A), IC71-570 (B), IC70-402 (C), IC65-430 (D, E), IC64-156 (F), IC37-038 (G). The characteristic crackled texture and/or central suture, marked by the ore minerals within the quartz, is clearly observed. Yellow boxes outline the approximate location of CL images in Figure 5.7.

tral suture (e.g., Figure 5.6C, G), while others show only a central suture, and no crackled texture (e.g., Figure 5.6D, E). Variations between these two end member classifications are also apparent, where a crackled texture is present, but ore minerals are preferentially concentrated within a central suture (e.g., Figure 5.6A, B, F). The ore mineral-filled cracks or sutures are generally <1 mm in width, apart from where ore minerals are particularly concentrated (e.g., Figure 5.6A), and where crystal sizes are larger (e.g., Figure 5.6G, where pyrite is up to 40 mm in size).

Cathodoluminescence of V2 veins shows that two generations of quartz (Q1: bright

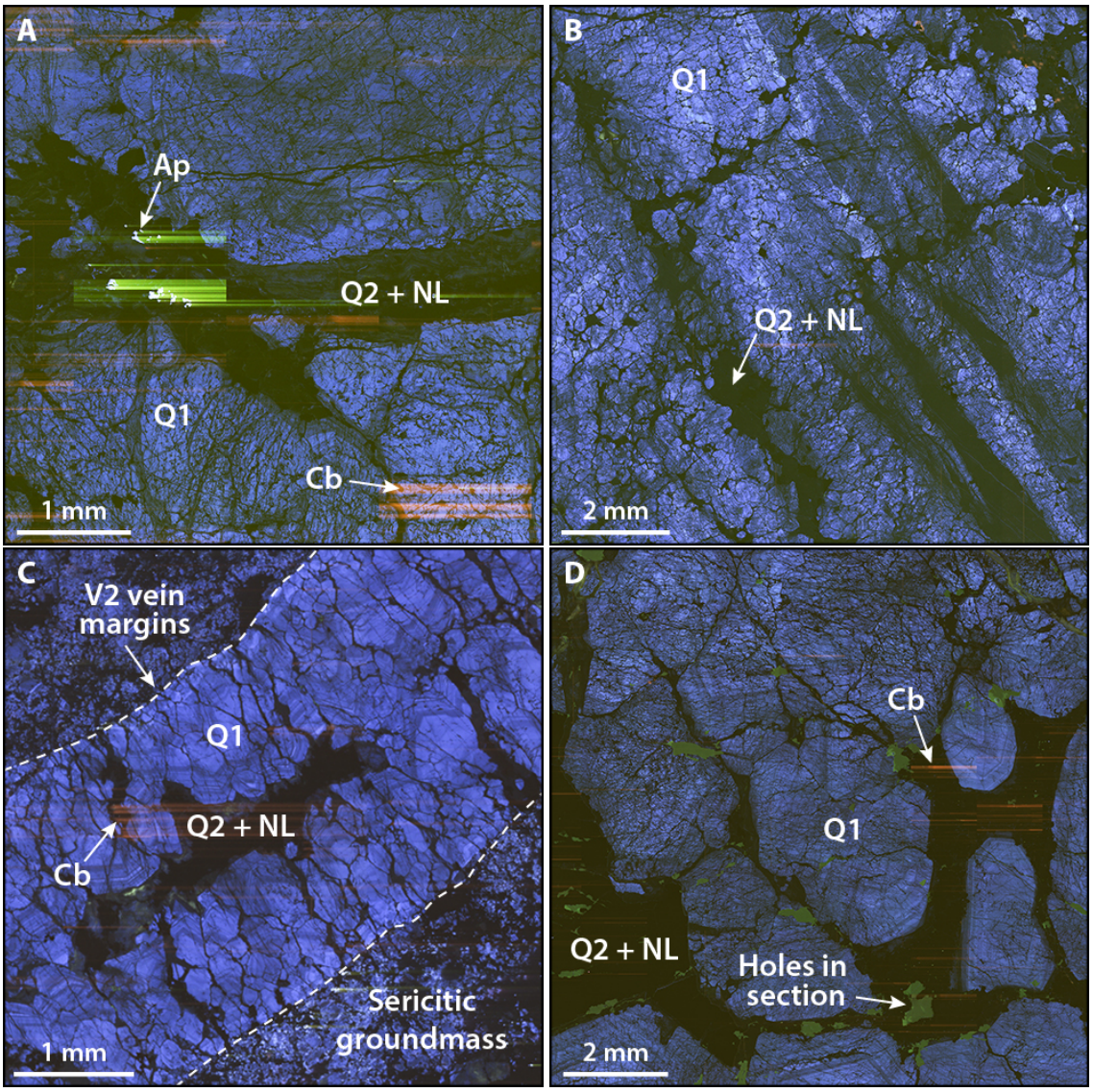

Figure 5.7. V2 vein quartz imaged by CL, from samples IC72-798 (A), IC70-429 (B), IC65-430 (C), and IC37-038 (D). The approximate location of CL images A, C, and D are marked by yellow boxes in Figure 5.6. Two generations of quartz (Q1 and Q2) are classified in all V2 vein occurrences. Q1 is bright-blue luminescent, and often exhibits zonations that mark original crystal forms and boundaries. Q2 is weakly luminescent, with dark blue-green to black colours, making it difficult to discern crystal shapes or sizes. Q2 quartz is precipitated along Q1 grain boundaries, cuts through Q1 crystals as veinlets, and brecciates and entrains Q1 crystals. The non-luminescent (NL) minerals, which appear black, and are predominantly ore minerals, are associated with Q2. The distinction between ore minerals and Q2 is illustrated in Figure 5.8.

blue luminescece, and Q2: dark blue-green to black luminescence) are present within each vein occurrence (Figure 5.7). Ore minerals are associated with the Q2 quartz generation (Figure 5.8), and both ore minerals and Q2 are distributed along Q1 grain boundaries, or are present in veinlets cutting Q1, which sometimes entrain brecciated clasts of Q1. This distribution of ore minerals and Q2 has created the crackled texture and/or central suture that characterises the V2 vein generation. A suite of other minor gangue minerals are also variably present in V2 veins (Table 5.1); they are also associated with ore

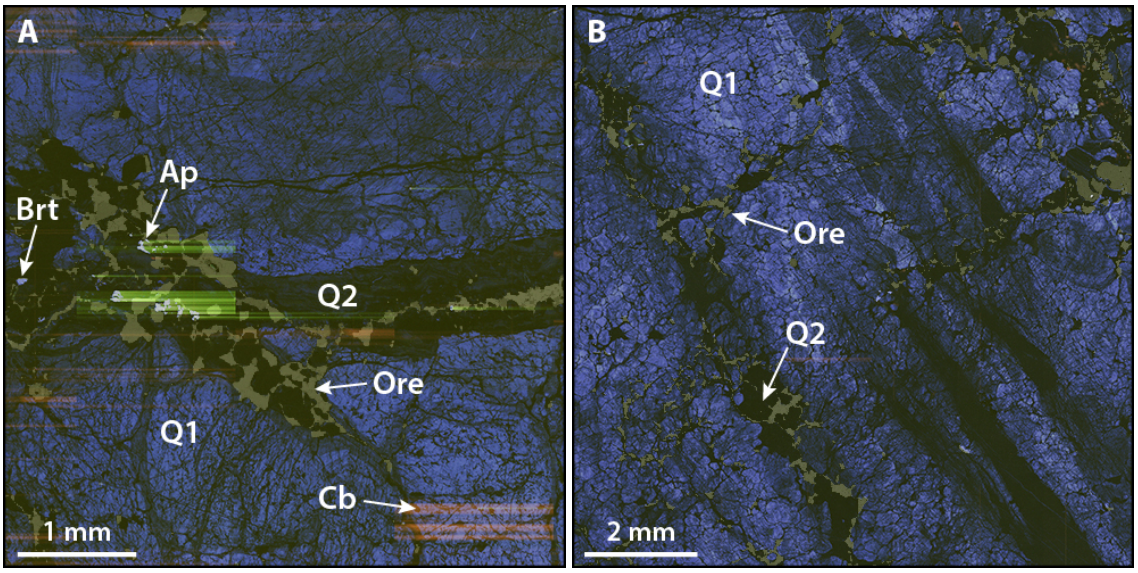

Figure 5.8. Composite CL-BSE images of V2 veins, from samples IC72-798 (A), and IC70-429 (B). The approximate location of image A is marked by a yellow box in Figure 5.6A. Ore minerals (pale brown) are concentrated within Q2 (dark blue-green to black), while the remainder are situated within cracks in Q1 (bright blue). The ore minerals are sometimes grown around Q2 quartz crystals, highlighting their shape. This is particularly evident in A, where the ore minerals largely occupy a central suture in Q2 quartz on the right side of the image. However, some of the ore minerals are also observed within the Q2 quartz on either side of the suture.

minerals and Q2 quartz, and also characterise the crackled texture and/or central suture.

V2 veins predominantly host ore minerals of chalcopyrite, pyrite, and trace amounts of galena, with the variable minor presence of tennantite-tetrahedrite; other trace minerals are also variably present (Table 5.1). The ore mineral textures observed in V2 veins are summarised in Figure 5.9. Chalcopyrite occurs within quartz, in cracks in pyrite, or grown around pyrite, with galena (with detectable Se by SEM-EDX) and tennantite-tetrahedrite, where these are present. Pyrite often forms discrete crystals, or is annealed into larger masses. Elongate inclusions of chalcopyrite, tennantite-tetrahedrite, galena, and other trace minerals are also common (Figure 5.9B, C, F). Pyrite also sometimes exhibits more rounded and poorly-defined crystal boundaries, and contains rounded inclusions of chalcopyrite (Figure 5.9D, F). All ore minerals are situated within cracks or sutures in Q1 quartz, associated with Q2; however, Q2 quartz sometimes grows around pyrite, infills cracks in pyrite, and/or forms ~120° grain boundaries with two of pyrite, chalcopyrite, tennantite-tetrahedrite, and galena (Figure 5.9B-D, F). When three of these ore minerals are adjacent without quartz, they also form 120° grain boundaries, although this relationship doesn't always hold true when pyrite is one of the three (Figure 5.9D).

Gold is observed in two V2 vein samples as <5 µm crystals of native Au or petzite. Figure 5.10 shows the Au occurrences in sample IC72-798, where Au is either present in native form as inclusions in pyrite, or in native form in petzite (also Au-bearing), in

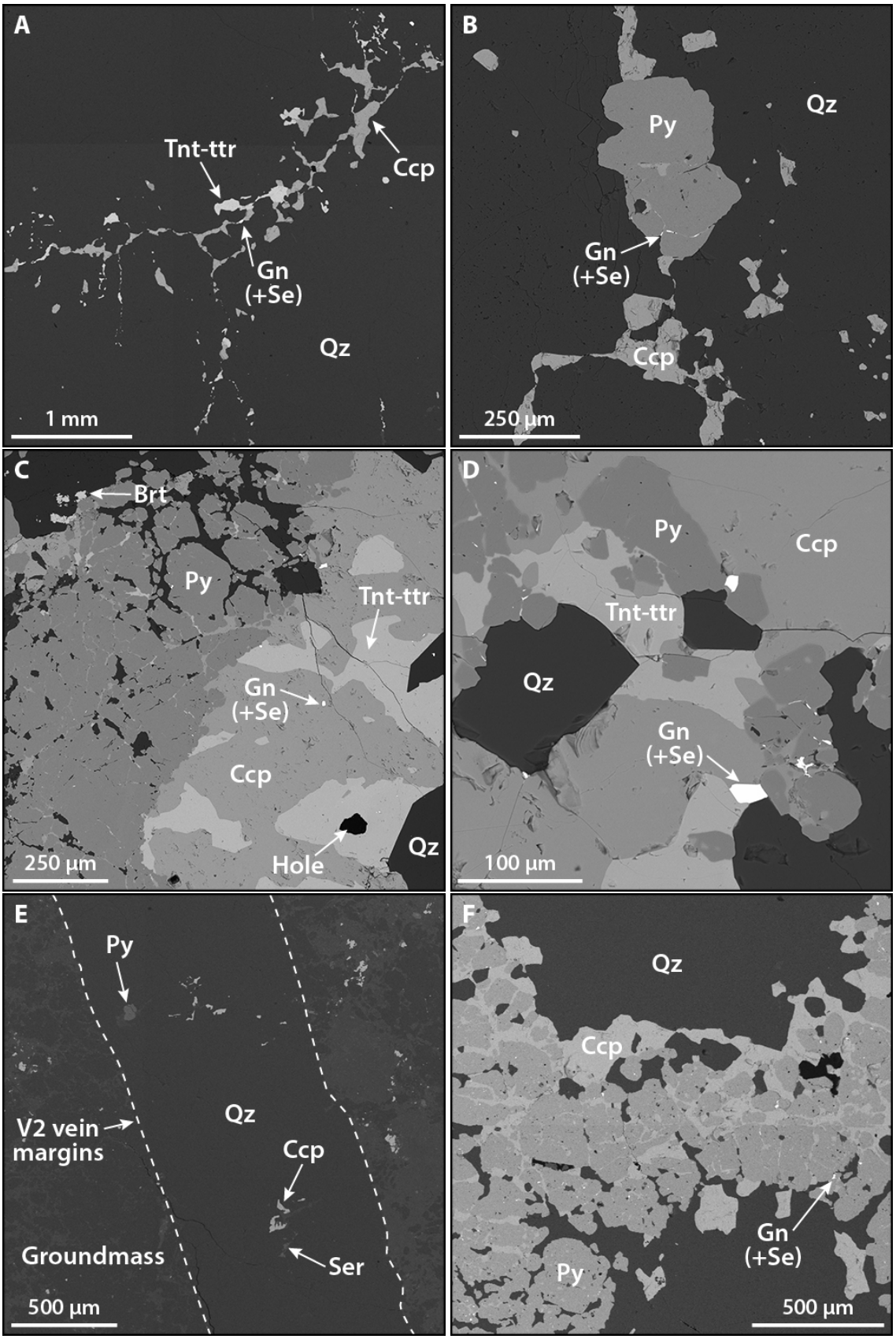

Figure 5.9. Representative V2 ore mineral textures, imaged by SEM (BSE mode), from samples IC72-798 (A), IC70-429 (B), IC70-402 (C, D), IC65-430 (E), and IC37-038 (F).

hessite. Native Au is also observed in sample IC70-402, where it is present as <1 µm crystals in holes in Q2 quartz.

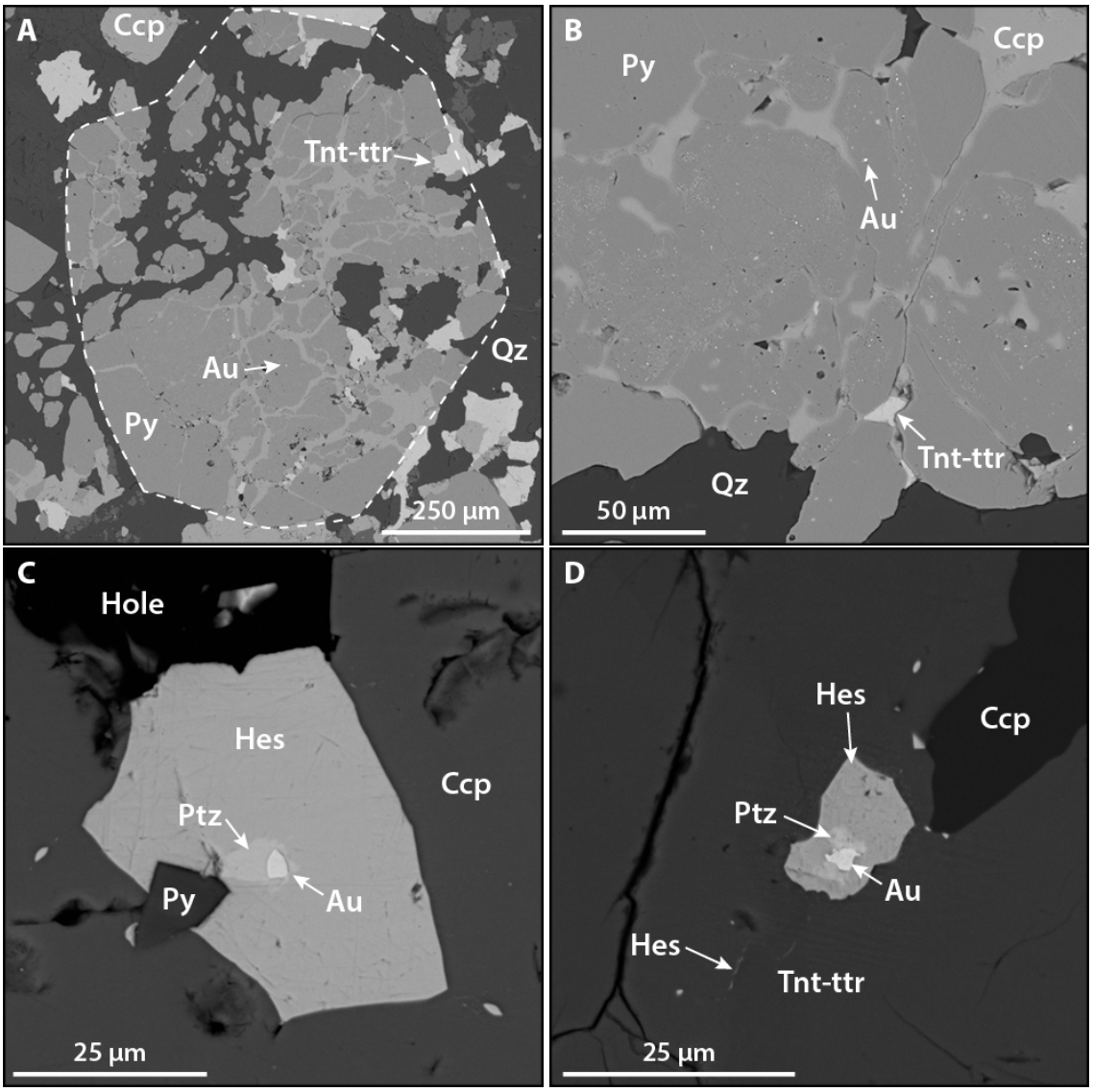

Figure 5.10. Gold observed in sample IC72-798, imaged by SEM (BSE mode). A, Native Au inclusions in pyrite (white dashed line highlights original pyrite grain boundary); B, Numerous native Au inclusions in pyrite; C, Native Au hosted within petzite, hosted within hessite, hosted within chalcopyrite, and surrounding pyrite; and D, same as C, but hessite is hosted within tennantite-tetrahedrite.

5.4.3 V3

V3 veins are pyrite-dominated and exhibit low quartz volumes, particularly in comparison to the V2 vein generation; massive pyrite textures are commonly observed (Figure 5.11). Vein textures vary where there is a higher proportion of gangue (quartz and/or sericite), with ore minerals more disseminated and unevenly distributed where sericite is more abundant (e.g., Figure 5.11C, D), and where quartz is more abundant, ore minerals tend to be fairly evenly distributed within the quartz (e.g., Figure 5.11F). V3 veins regularly exhibit asymmetrical wavy margins, with vein forms varying between sinuous and relatively straight. Vein width varies from 1 mm (e.g., Figure 5.11E) to >12 cm (e.g., Fig-

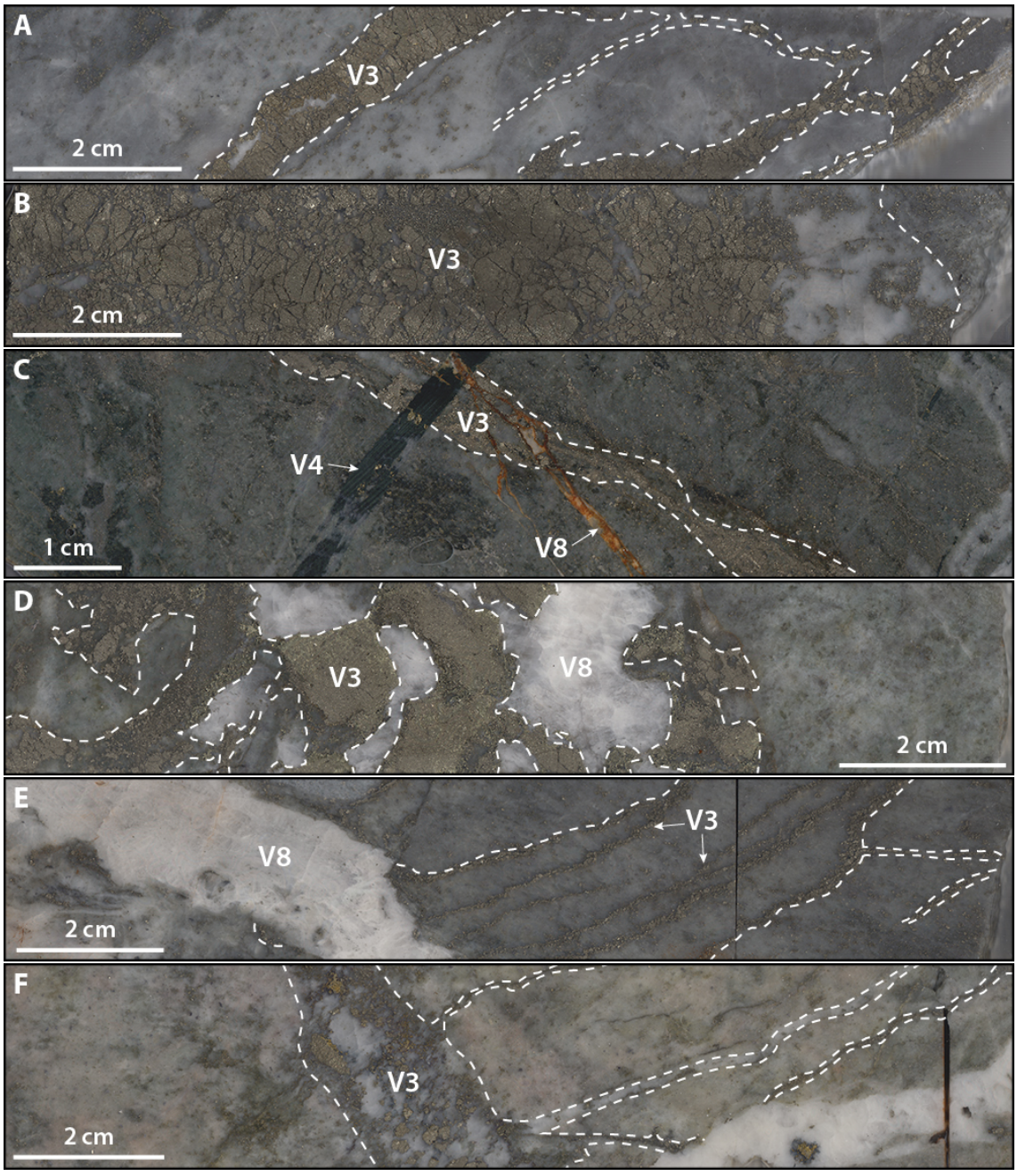

Figure 5.11. Representative V3 vein occurrences, from samples IC73-518 (A), IC70-560 (B), IC65-430 (C), IC67-350 (D), IC59-060 (E), and IC59-033 (F). The pyrite-rich, quartz-poor nature of V3 veins is particularly evident. Some V3 occurrences contain greater quantities of quartz (e.g., F), but do not exhibit the crackled texture and/or central suture observed in V2 veins. V3 veins are also often crosscut by barren V8 veins (e.g., C, D, E), and rarely V4 veins (C).

ure 5.11B). V3 is the vein generation most commonly observed in the drill core samples collected from Iron Cap, and is present in drill core from shallow to deep depths (Section 5.7). The majority of samples that contain V3 veins exhibit sericitic wall rock alteration, characterised by an assemblage of sericite, quartz, and pyrite, and the variable presence of trace gangue minerals, which often include rutile, apatite, and monazite. In contrast, a minority of V3 vein samples exhibit potassic alteration characterised by K-feldspar, pla-

gioclase, chlorite, and trace apatite and rutile, indicating that V3 veins are not exclusively associated with sericitic alteration.

Most V3 veins are not particularly suited to study by CL, owing to the low quartz abundance, but images have been collected where possible. Dark blue-green colours are sometimes faintly visible, but more often, V3 quartz appears black and is indistinguishable from ore minerals under CL. The CL attributes of V3 quartz are comparable to the Q2 quartz of the V2 vein generation.

Pyrite dominates the ore mineralogy of V3 veins (Table 5.1). Chalcopyrite is most often present as a minor mineral (2-10% in terms of volume), although its abundance does vary by occurrence, where it can alternatively be present as a major (>10%) or trace (<2%) component; however, pyrite is the dominant mineral in all cases. Galena is always present as a trace mineral, while other trace ore minerals are also variably present (Table 5.1).

The ore mineral textures of V3 veins are summarised in Figure 5.12. Pyrite is hosted in quartz and/or sericite, where discrete pyrite crystals are sometimes observed, but more often, pyrite crystals are annealed into larger masses. Multiple pyrite generations are also evidenced by compositional differences (e.g., As-rich pyrite in Figure 5.12A, F) or the hosting of different minerals in discrete regions (e.g., in Figure 5.12C, where a pyrite core is surrounded by chalcopyrite, which is surrounded by galena inclusion-rich pyrite with Cu, and finally surrounded by regular pyrite). Pyrite sometimes exhibits more rounded and poorly-defined crystal boundaries when in contact with chalcopyrite (Figure 5.9D, F). Chalcopyrite and galena (and other trace ore minerals) are found in cracks in pyrite (Figure 5.12B, D, F), as inclusions in pyrite (Figure 5.12A-C, F), surrounding pyrite crystals (Figure 5.12B, D-F), within discrete pyrite generations (Figure 5.12A, C), and/or with/within quartz (Figure 5.12B, E, F).

Gold is present in the V3 vein generation, predominantly as native Au, but also as petzite (Figure 5.13). Native Au occurs in vein quartz, as inclusions in pyrite, or in cracks in pyrite with chalcopyrite. Petzite is also observed intimately associated with hessite, the whole forming an inclusion in pyrite.

5.4.4 V4

The V4 vein generation is characterised by a quartz, chalcopyrite ± chlorite mineral assemblage (Figure 5.14). V4 veins are relatively thin, from 1 mm to 18 mm in width, and vary from relatively straight with linear, symmetrical margins (e.g., Figure 5.14D, F), to sinuous with wavy margins (e.g., Figure 5.14A, B, E, G). The veins are continuous, and regularly occur more than once in the same sample, sometimes forming interconnected

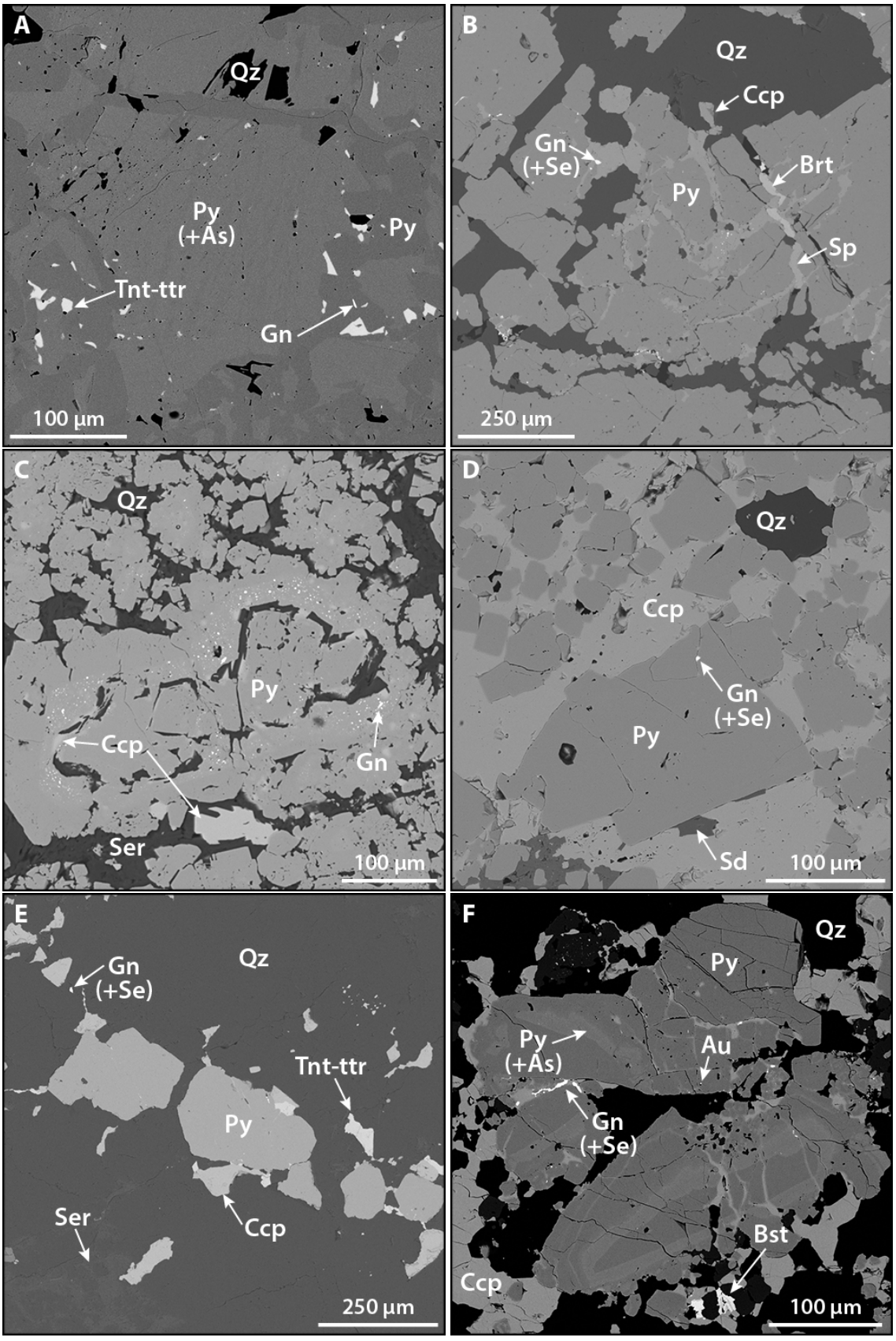

Figure 5.12. Representative V3 ore mineral textures, imaged by SEM (BSE mode), from samples IC73-518 (A), IC70-560 (B), IC65-430 (C), IC67-350 (D), IC59-060 (E), and IC59-033 (F).

networks (e.g., Figure 5.14B, C, E). They are observed in both potassic-altered rocks (e.g., Figure 5.14A-C) and rocks dominated by sericitic alteration (e.g., Figure 5.14D-G), most

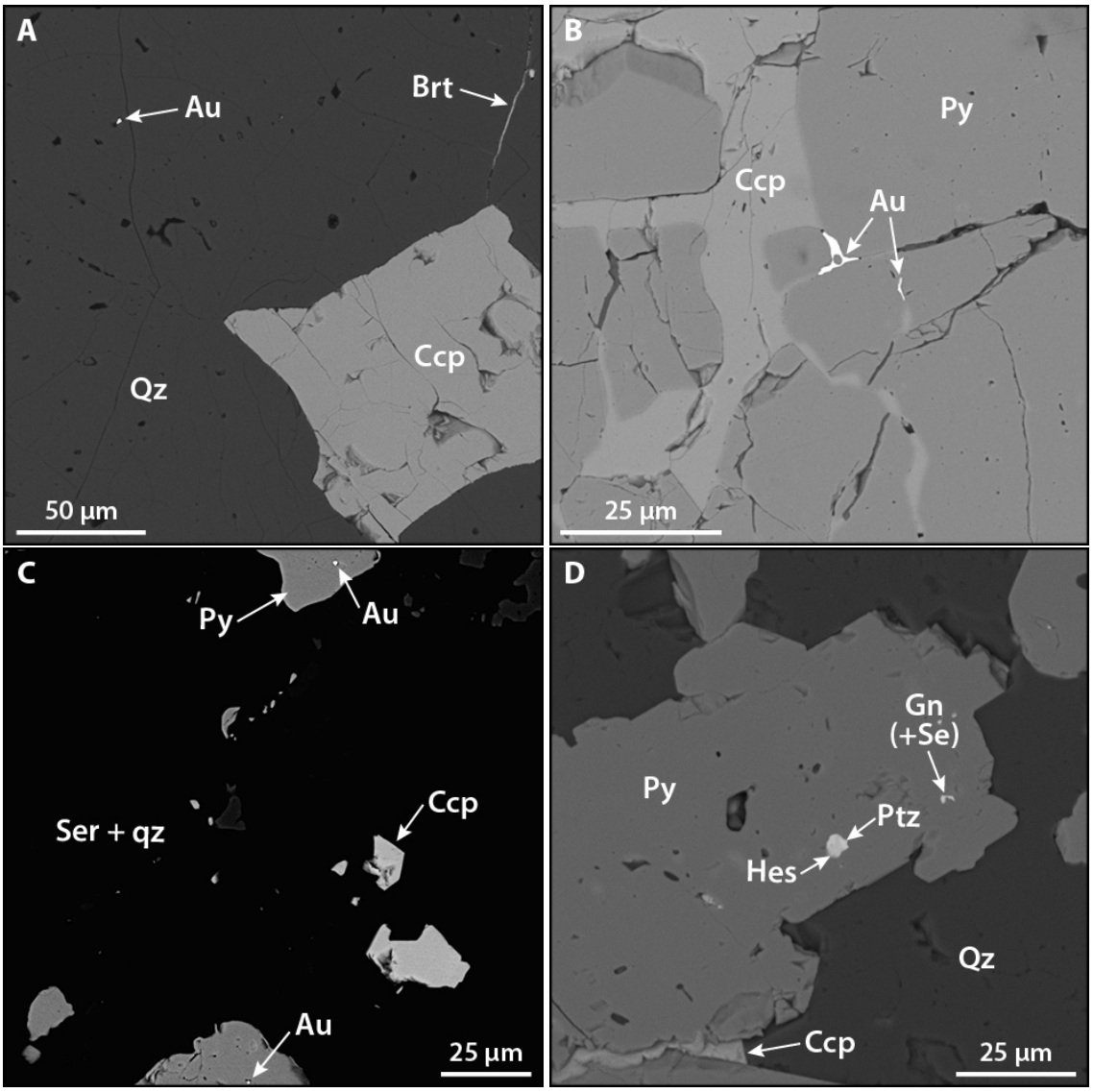

Figure 5.13. Gold observed in V3 veins, imaged by SEM (BSE mode), from samples IC59-033 (A), IC67-350 (B), IC65-532 (C), and IC69-598 (D). Native Au is observed in vein quartz (A), in cracks in pyrite with chalcopyrite (B), and as inclusions in pyrite (C). Petzite is present as inclusions in pyrite, with hessite (D).

of which retain evidence of previous potassic alteration. V4 veins are present across the entire range of sampled depths, from 48 m to 1252 m – the deepest sample looked at in this project. The three-dimensional distribution of V4 veins is illustrated in Section 5.7.

Variations in V4 vein mineralogy are clearly observed in Figure 5.14, where V4 veins can be dominated by chlorite, with minor quartz and chalcopyrite (e.g., Figure 5.14A, B, D, G), host minor chlorite with increased volumes of chalcopyrite (e.g., Figure 5.14C), or lack chlorite altogether (e.g., Figure 5.14E). Despite this, V4 veins can be defined by their mineralogy; they always host quartz, with one or both of chalcopyrite and black chlorite visible in hand specimen. The lack of ore minerals apart from chalcopyrite is also indicative of V4 in hand specimen, although other ore minerals do occur in trace quantities, identifiable at the micro-scale (Table 5.1). Cross-cutting relationships with

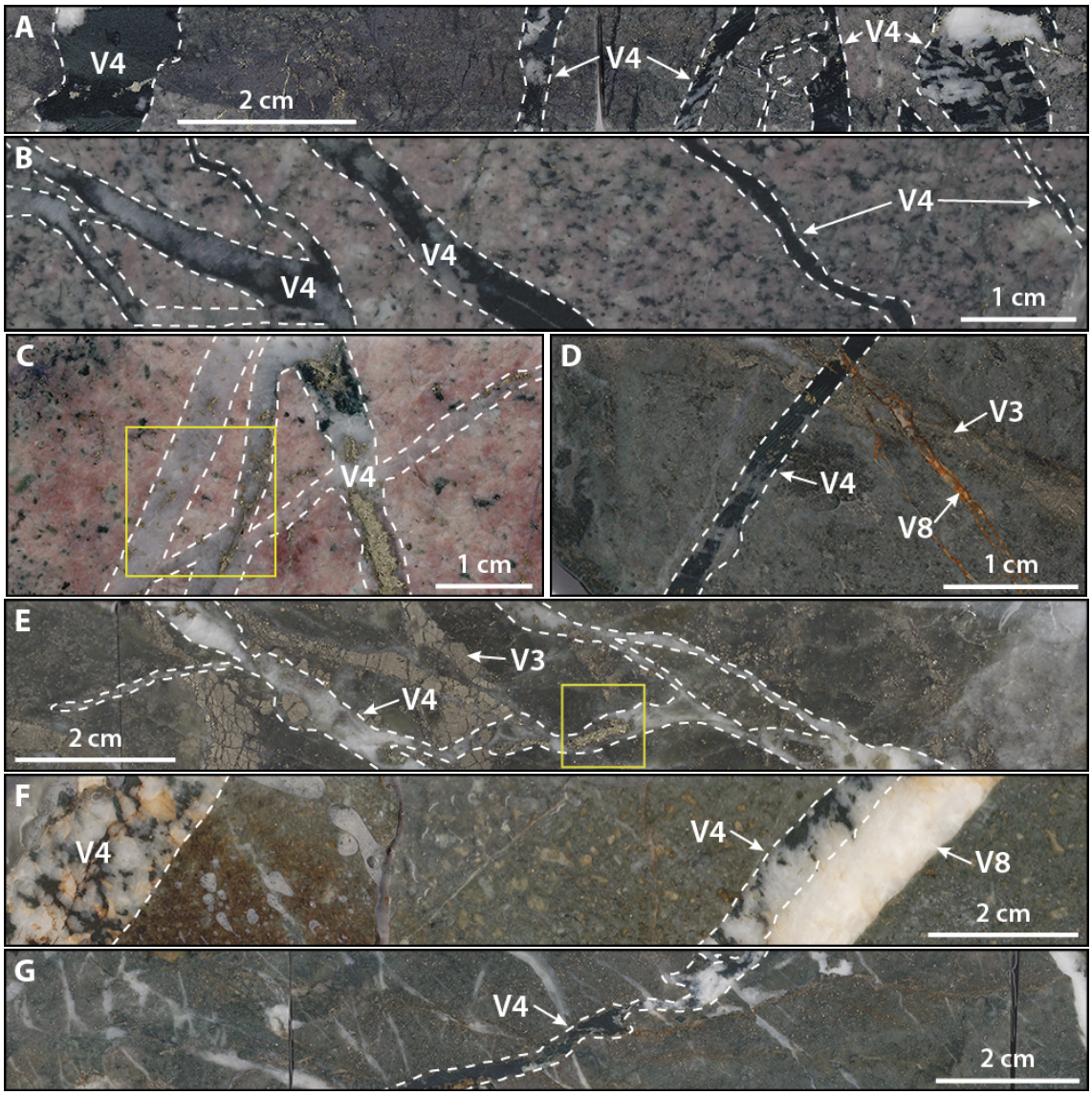

Figure 5.14. Representative V4 vein occurrences, from samples IC71-970 (A), IC72-821 (B), IC71-784 (C), IC65-430 (D), IC59-123 (E), IC01-054 (F), and IC01-048 (G). Chalcopyrite is typically more abundant in V4 veins where quartz dominates, and less abundant in V4 veins where black chlorite dominates; this implies that quartz and chalcopyrite and genetically related. The V4 vein in E contains clasts of the groundmass, and vein quartz crosscuts and surrounds V3 pyrite; in F, V8 carbonate (white-orange) re-opens the V4 veins, while the orange-red colour is Fe-staining resulting from long-term storage of drill core outdoors. Yellow boxes outline the approximate location of CL images in Figure 5.15.

other vein generations (i.e., V3; Figure 5.14D, E) also aid in classification.

Cathodoluminesce of V4 vein quartz highlights differences between samples, in line with mineralogy. For example, in samples IC71-970 and IC65-430 (Figure 5.14A and D, respectively), where chlorite is a major vein constituent, V4 vein quartz is non-luminescent and appears black. Meanwhile, in samples IC71-784 and IC59-123 (Figure 5.14C and E, respectively), where chlorite is less abundant or absent, V4 vein quartz is bright blue-luminescent (Figure 5.15A), similar to the Q1 quartz of V2 veins, or is faintly visible with

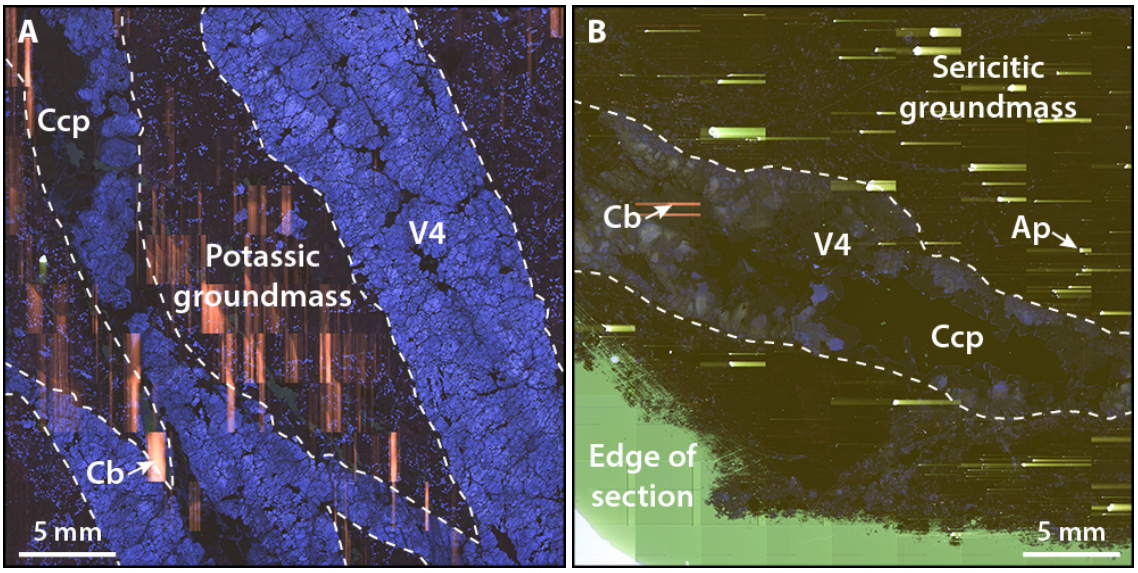

Figure 5.15. V4 vein quartz imaged by CL, from samples IC71-784 (A) and IC59-123 (B). The approximate location of CL images A and B are marked by yellow boxes in Figure 5.14C and E, respectively.

dark blue-green luminesence, similar to the Q2 quartz of V2 veins (Figure 5.15B).

The ore mineral textures of V4 veins are relatively consistent between samples, as shown in Figure 5.16; only chalcopyrite is present as a major, or sometimes minor, ore mineral. Chalcopyrite is commonly hosted by quartz, where it fills space between quartz crystals (Figure 5.16A-C, E, F), and/or is in contact with the surrounding chlorite (Figure 5.16A, C, D). Galena is sometimes present as a trace ore mineral, where it is found as inclusions in chalcopyrite, or free within vein quartz (Figure 5.16B, E).

Calcite is variably present as a minor mineral in V4 veins, where it occurs next to chlorite (Figure 5.16A), is found within quartz (with or without chalcopyrite; Figure 5.16B, E), and cross-cuts quartz (Figure 5.16F). Other minor or trace minerals sometimes occur with chalcopyrite, many of which were likely entrained from the groundmass. For example, clasts of sericitic-altered groundmass are entrained within V4 chlorite in Figure 5.16C, but cut by V4 quartz-chalcopyrite.

Native Au is observed in four V4 vein occurrences; usually as free crystals within vein quartz, but also less commonly as inclusions within chalcopyrite (Figure 5.17). It is difficult to observe owing to its small crystal size (<10 µm), which may account for the lack of observations in other V4 samples.

5.4.5 V5

The V5 vein generation at Iron Cap is characterised by an ore mineral assemblage dominated by tennantite-tetrahedrite, hosted within a quartz-rich gangue (Figure 5.18). V5 veins are generally continuous and exhibit widths from 5-18 mm, with slightly wavy,

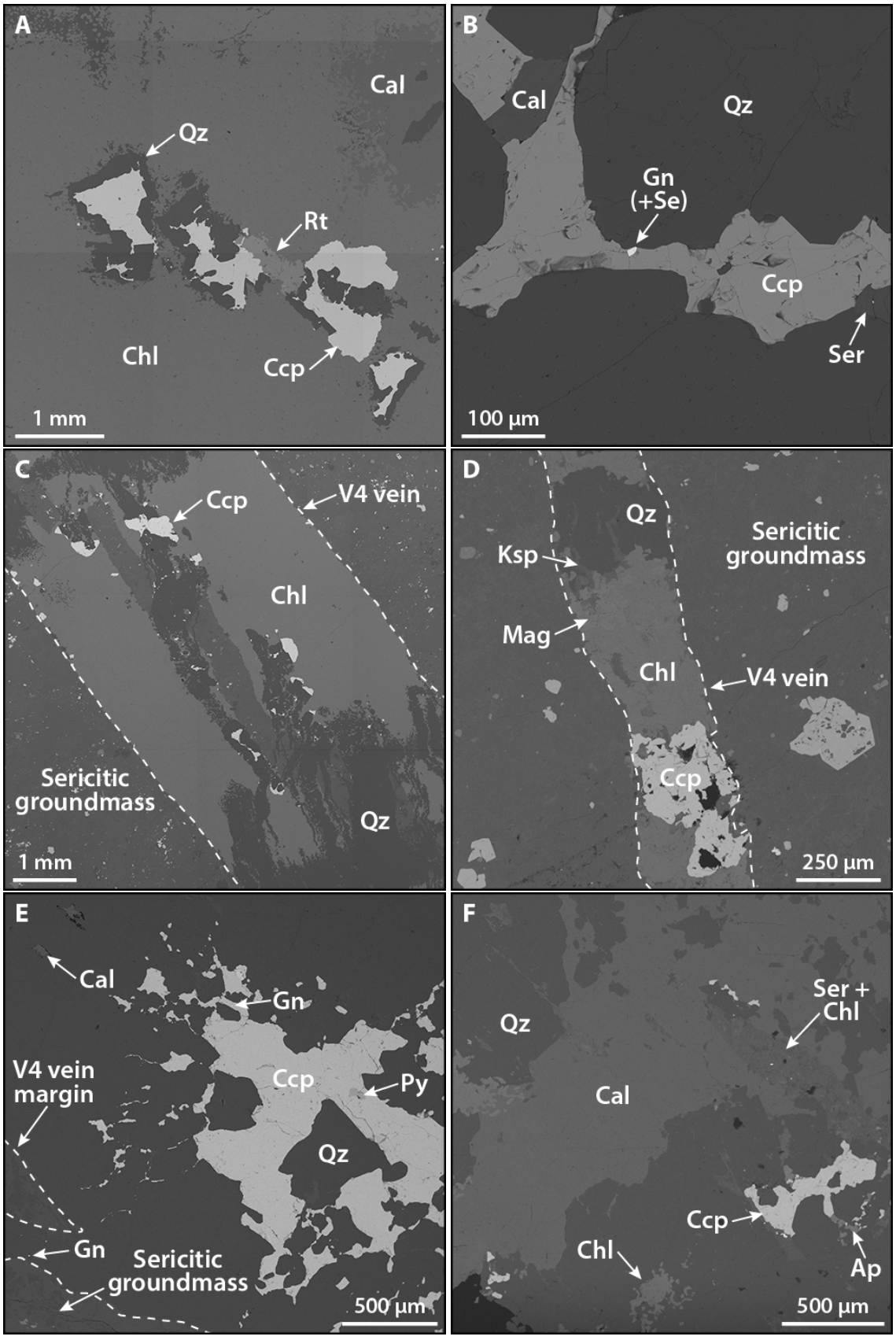

Figure 5.16. Representative V4 ore mineral textures, imaged by SEM (BSE mode), from samples IC71-970 (A), IC71-784 (B), IC65-430 (C, D), IC59-123 (E), and IC01-054 (F). The holes (black) in chalcopyrite in D are likely due to the location of this crystal on the edge of the thin section.

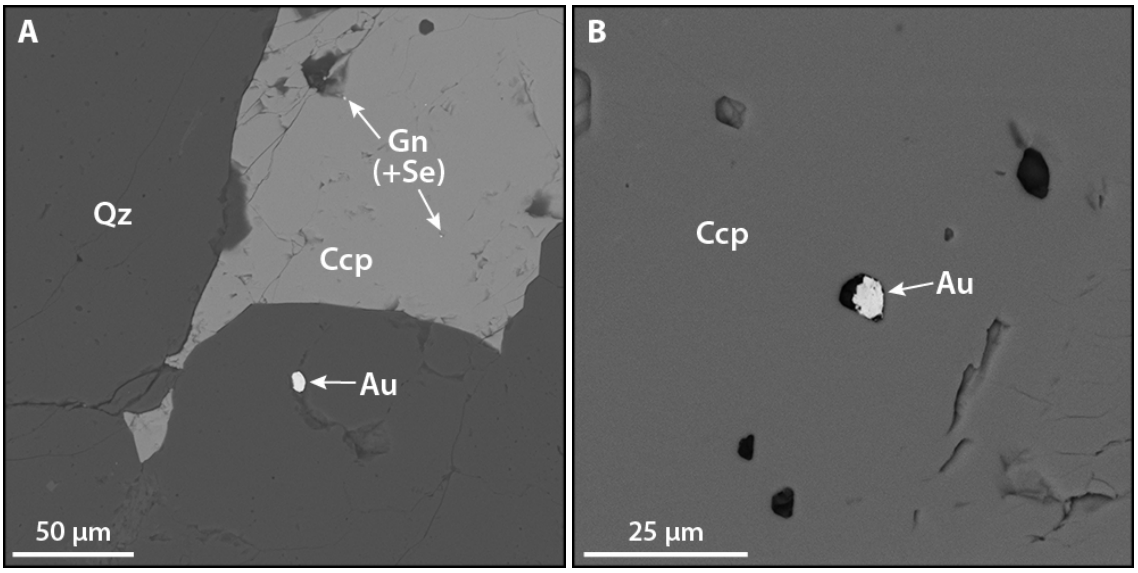

Figure 5.17. Gold observed in V4 veins, imaged by SEM (BSE mode), from samples IC71-784 (A) and IC64-156 (B). Gold is most often present within quartz (A), but is also observed as inclusions in chalcopyrite (B). These are some of the largest Au crystals observed in V4 veins, at ∼7 µm in size; Au is commonly <1 µm in size.

but relatively straight margins. They are not observed as isolated occurrences in the sample suite, rather as arrays of multiple veins that tend to exhibit similar orientations within the same sample. Only the four samples shown in Figure 5.18 contain V5 veins;

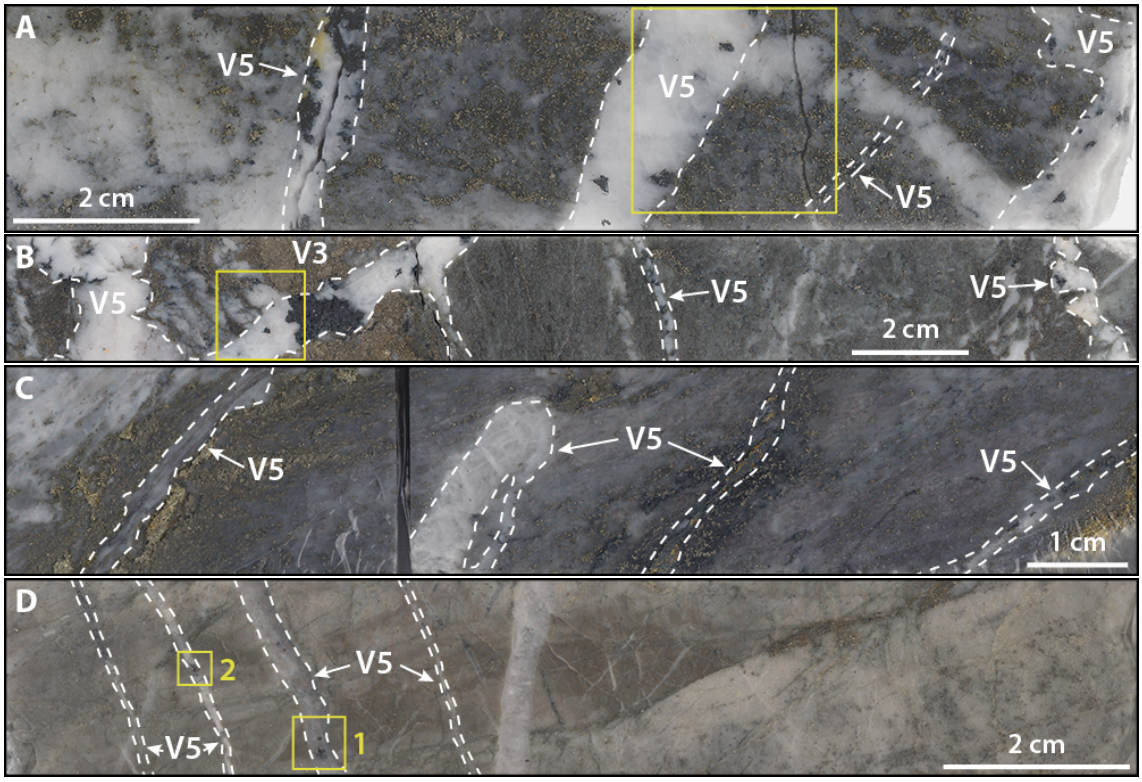

Figure 5.18. V5 vein occurrences, from samples IC63-791 (A), IC69-598 (B), IC63-421 (C), and IC01-109 (D). Tennantite-tetrahedrite is present as clots within the quartz gangue. The wall rock in D is hornfels. Yellow boxes outline the approximate location of CL images in Figure 5.19.

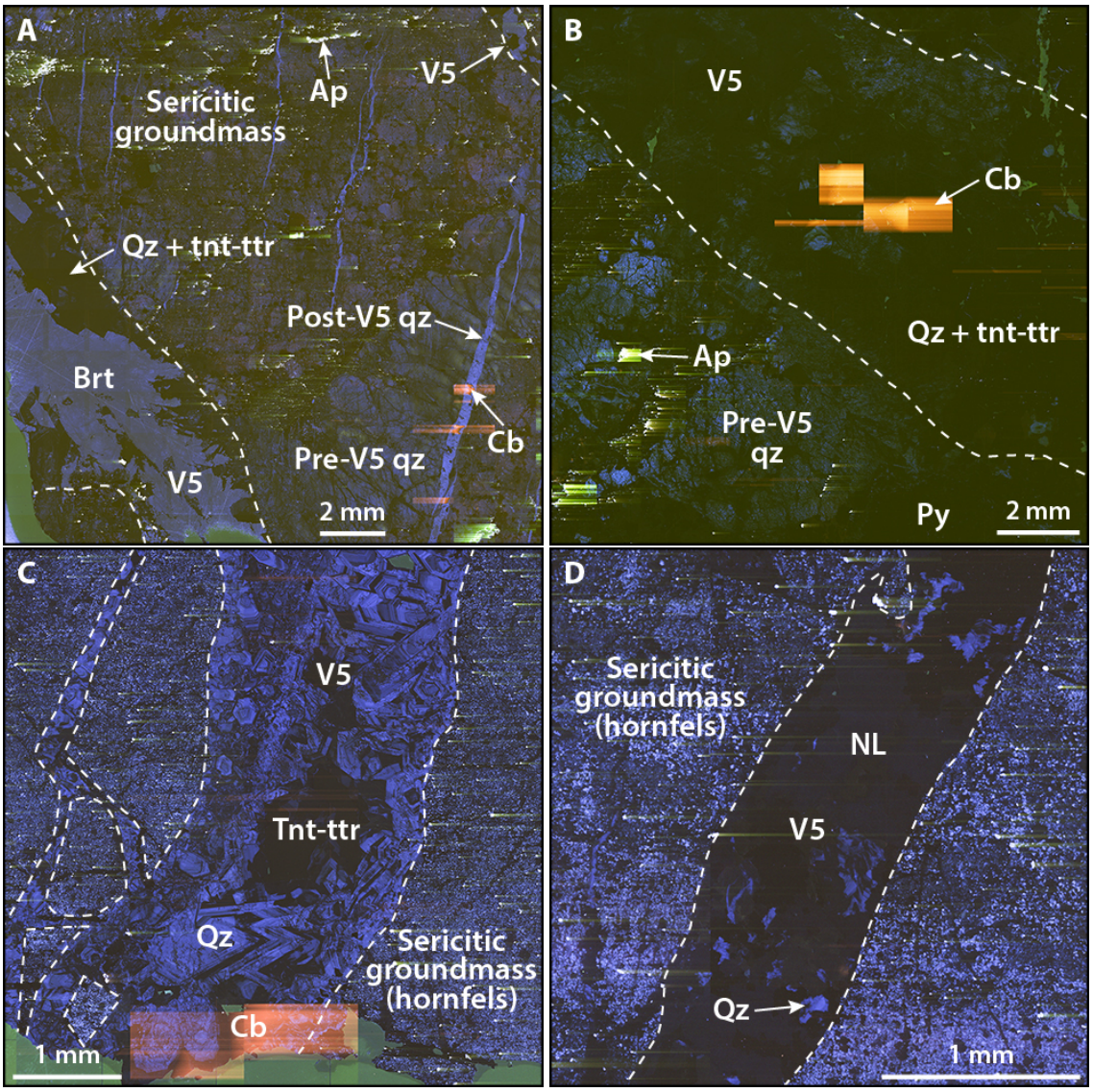

Figure 5.19. V5 vein quartz imaged by CL, from samples IC63-791 (A), IC69-598 (B), and IC01-109 (C, D). The approximate location of the CL images are marked by yellow boxes in Figure 5.18; box 1 in Figure 5.18D is image C, while box 2 is image D. The distinction between ore minerals and quartz is illustrated in Figure 5.20. Non-luminescent minerals (NL) in D are K-feldspar, quartz, ankerite, tennantite-tetrahedrite, and chalcopyrite.

therefore, this vein generation does not appear to be common at Iron Cap, although sampling limitations may contribute to their apparent scarcity. Nevertheless, V5 veins constitute a discrete generation, because they exhibit a distinct ore mineral assemblage (i.e., tennantite-tetrahedrite-dominated), and are differentiated from earlier quartz-rich veins because they exhibit different textures (i.e., clots of tennantite-tetrahedrite), and cross-cut V3 veins (e.g., Figure 5.18B). All V5 veins in the sample suite are hosted by sericitic-altered rocks; one V5 vein is hosted by hornfels (sample IC01-109), and contains K-feldspar and ankerite in the groundmass, with a sericitic assemblage also present. The wall rock in Figure 5.18C exhibits metamorphic fabrics; metamorphism may have affected the V5 veins in this sample.

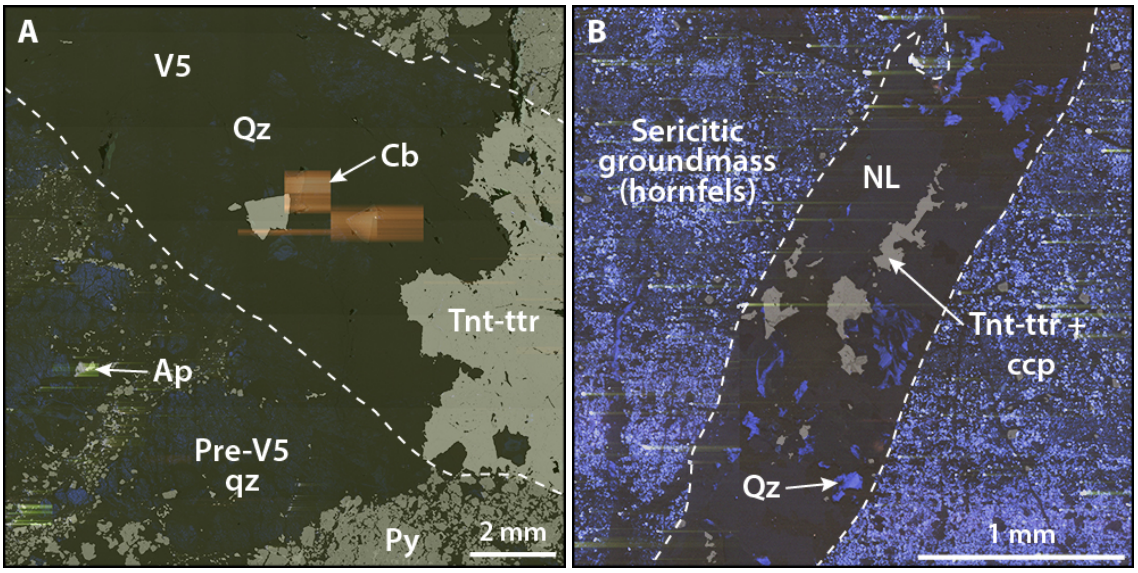

Figure 5.20. Composite CL-BSE images of V5 veins, from samples IC69-598 (A), and IC01-109 (B). The approximate location of image A is marked by a yellow box in Figure 5.18B; image B is box 2 in Figure 5.18D.

Cathodoluminesce of V5 vein quartz shows that quartz is commonly non-luminescent (i.e., black; Figure 5.19), comparable to the non-luminescent quartz of preceeding vein generations. One V5 vein sample differs in that it contains blue-black-luminescent zoned quartz (Figure 5.19C, D); this is the V5 vein hosted by hornfels (sample IC01-109). Quartz and tennantite-tetrahedrite dominate the V5 vein in Figure 5.20A, as is typical of most V5 veins. The hornfels-hosted V5 vein in Figure 5.20B contains quartz, tennantite-tetrahedrite, and chalcopyrite, with non-luminescent gangue minerals (K-feldspar, quartz, and ankerite) also present; these gangue minerals are also found in the host rock groundmass.

Tennantite-tetrahedrite is the dominant ore mineral in V5 veins, while chalcopyrite is sometimes present as a minor phase; V5 veins lack pyrite. Typical V5 ore mineral textures are illustrated in Figure 5.21. Tennantite-tetrahedrite occasionally exhibits zones (Figure 5.21C); lighter zones have a higher Sb:As ratio, whereas darker zones have a lower Sb:As ratio (analysed by SEM-EDX). Trace ore minerals are also variably present in V5 veins (Table 5.1). This is illustrated in Figure 5.21C and D, where galena (with Se), hessite, and AgHg alloy are included in tennantite-tetrahedrite. Ore minerals often demarkate quartz crystal boundaries (e.g., Figure 5.21E, F), and contain inclusions of quartz (e.g., Figure 5.21C, D). No Au-bearing minerals are identified within V5 veins, although a AgHg alloy is recognised in the V5 vein of sample IC69-598 (Figure 5.21D).

5.4.6 V6

The V6 vein generation is enriched in a base metal sulphide assemblage of sphalerite, chalcopyrite and pyrite, with minor galena (Figure 5.22). Massive sulphide textures are

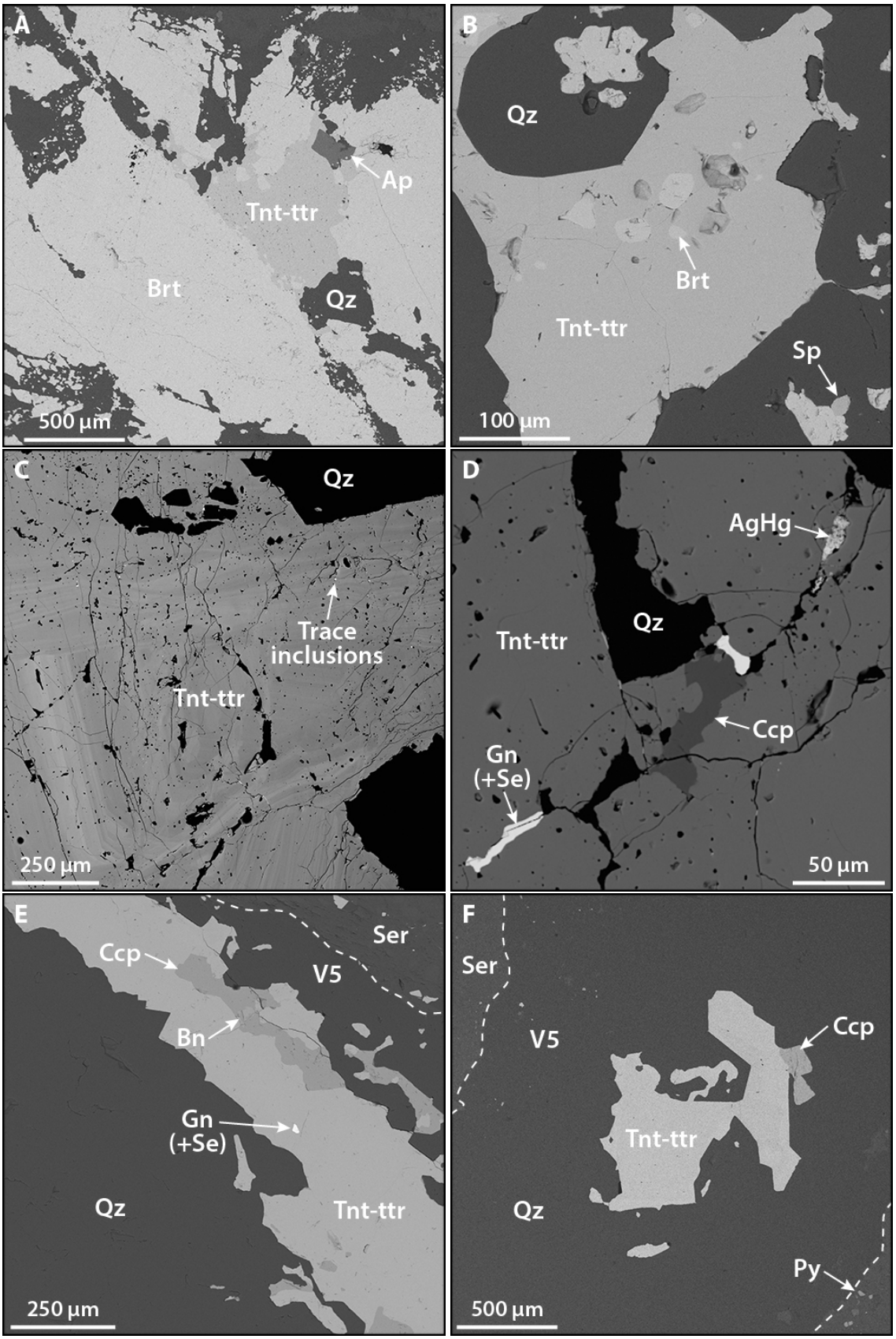

Figure 5.21. Representative V5 ore mineral textures, imaged by SEM (BSE mode), from samples IC63-791 (A, B), IC69-598 (C, D), IC63-421 (E), and IC01-109 (F). Image D is close-up view of ore minerals included in the same tennantite-tetrahedrite crystal as in C.

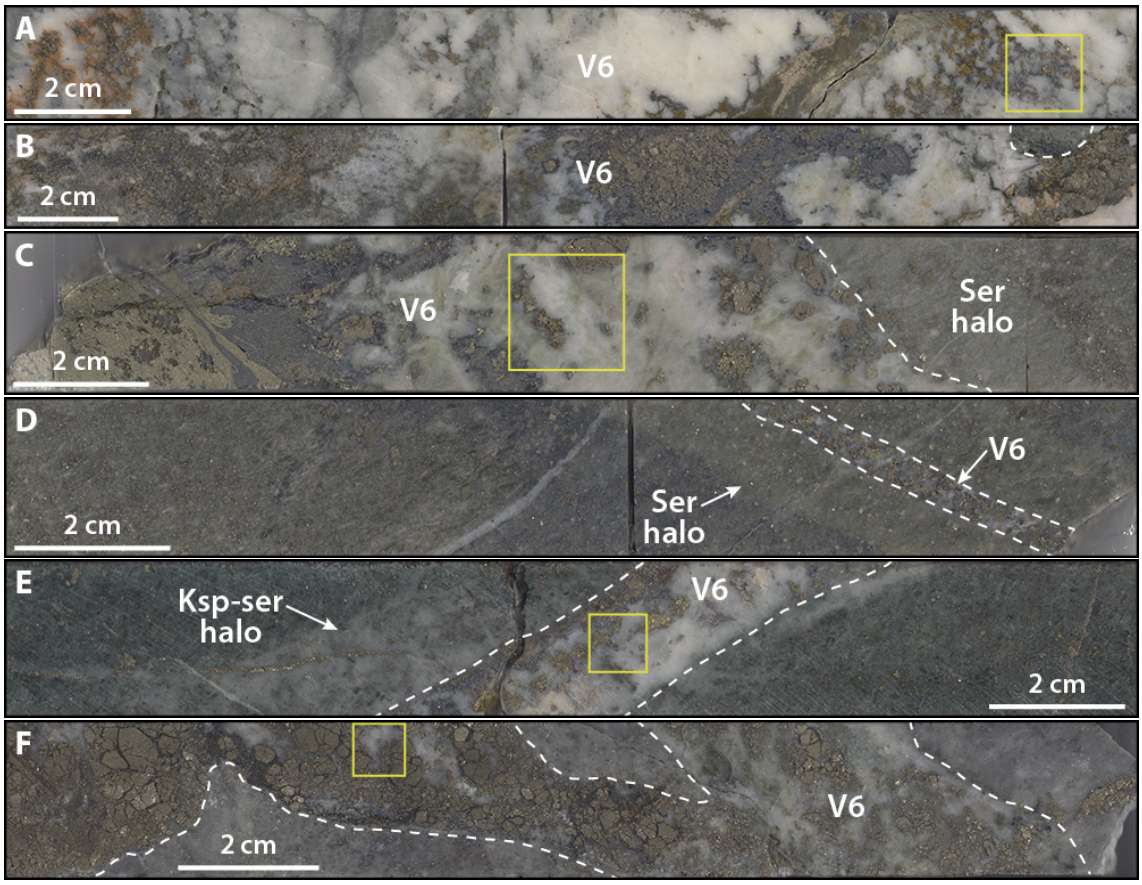

Figure 5.22. Representative V6 vein occurrences, from samples IC43-224 (A), IC37-218 (B), IC37-157 (C, D), IC01-052 (E) and IC33-030 (D). Sphalerite, chalcopyrite and pyrite dominate the ore mineral assemblage, with gangue minerals of quartz and carbonate. V6 veins make up most of the sample in A and B. Yellow boxes outline the approximate location of CL images in Figure 5.23.

often observed (e.g., Figure 5.22A-C), with a quartz-carbonate gangue. Most V6 veins exhibit widths of at least 20 cm (e.g., Figure 5.22A-C), but some occurrences are as thin as 0.5 cm (e.g., Figure 5.22D). Where V6 vein margins are observed, they tend to appear straight and linear (e.g., Figure 5.22C-E), with some exceptions, where they appear slightly wavy (e.g., Figure 5.22F). Eight samples contain V6 veins, all of which are from shallow depths (up to 224 m). Section 5.7 illustrates the three-dimensional distribution of V6 veins.

Host rock alteration in samples containing V6 veins is dominantly sericitic, although previous potassic alteration (K-feldspar) is also present. More intense alteration is often localised around V6 veins in the form of sericitic halos (e.g., Figure 5.22C-E), which are up to 8 cm wide (receeding in intensity outwards from the vein). One sample (IC01-052) contrastingly exhibits a white K-feldspar halo (Figure 5.22E), with sericitic alteration only affecting wall rock clasts in the halo. This vein sample also exhibits more prominent potassic alteration in the host rock than other V6 vein samples, and is laterally separated (i.e., from a different drill hole) from V6 veins that exhibit sericitic halos.

Quartz in V6 veins exhibits distinctive characteristics when imaged by CL, as illus-

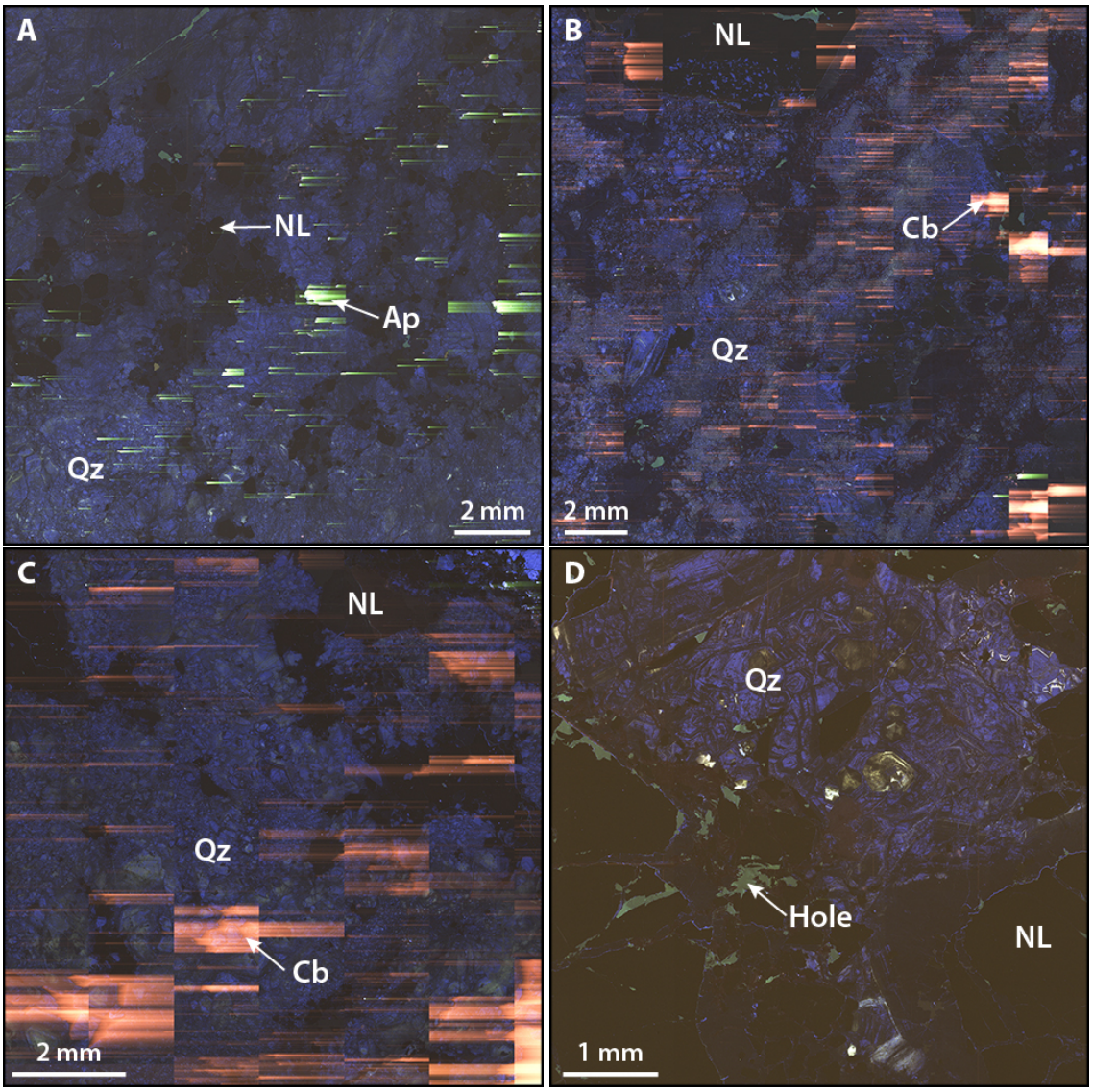

Figure 5.23. V6 vein quartz imaged by CL, from samples IC43-224 (A), IC37-157 (B), IC01-052 (C), and IC33-030 (D). The approximate location of the CL images are marked by yellow boxes in Figure 5.22. V6 quartz luminesces in dark blue-green colours. Non-luminescent minerals (NL) consist primarily of ore minerals, and in some cases (i.e., B) non-luminescent carbonates, such as dolomite.

trated in Figure 5.23. Dark blue-green luminescent quartz makes up the majority of the veins, with quartz of the darkest blue luminescence (almost black) typically hosting the ore minerals. The more luminescent quartz crystals are commonly brecciated, with the brecciated fragments exhibiting zonations; textures are not visible in the darkest blue-luminescent quartz. Crystal sizes are smaller (micron-scale) where quartz is more brecciated, although some crystals are larger, retaining relatively euhedral shapes and mm-scale sizes.

The ore mineral textures observed in V6 veins are summarised in Figure 5.24. Sphalerite, chalcopyrite, galena, tennantite-tetrahedrite and hessite regularly exhibit 120° grain boundaries when three of these minerals are in contact (Figure 5.24A, C, D, F). Chalcopy-

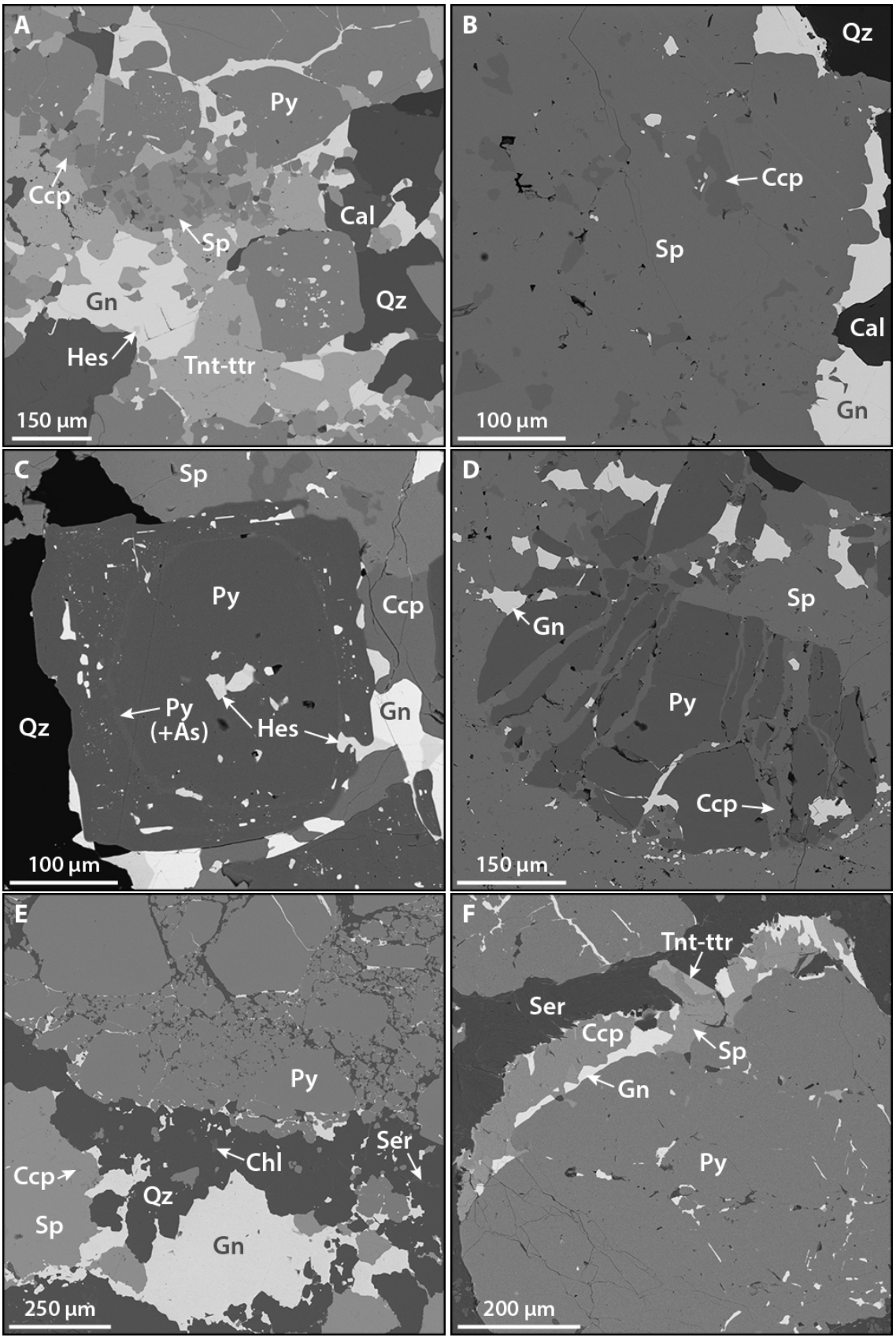

Figure 5.24. Representative V6 ore mineral textures, imaged by SEM (BSE mode), from samples IC37-218 (A), IC37-157 (B-D), IC01-052 (E), and IC33-030 (F).

rite (and galena) "disease" in sphalerite is also observed (Figure 5.24B). Pyrite exhibits many different forms and textures in V6 veins, with grain sizes varying from micron-

scale to mm-scale (e.g., Figure 5.24A, F). It can be found as relatively euhedral crystals, with few inclusions, and also as more anhedral crystals with many inclusions of other ore minerals and quartz (Figure 5.24A, C-F). Inclusions can be angular, or rounded, and are sometimes localised in discrete regions in a pyrite crystal (e.g., Figure 5.24C, where inclusions are principally found in the core, and near the rim, where some inclusions are oriented roughly parallel to the grain boundaries). Pyrite may also form 120° triple junction grain boundaries with other ore minerals and quartz (Figure 5.24A). Furthermore, fracture-filling of pyrite by other ore minerals is common (Figure 5.24A, D-F), while some pyrite crystals exhibit compositional heterogeneity (e.g., the As-rich zone in the pyrite crystal in Figure 5.24C). Annealing of pyrite crystals into larger masses is also observed (Figure 5.24E).

Gold is present in two V6 vein samples (Figure 5.25). Petzite and native Au are observed as inclusions in pyrite, commonly co-occurring with hessite. Petzite-only inclusions, and inclusions of petzite or native Au with other V6 minerals are also observed. The inclusions containing petzite or native Au are only found in relatively inclusion-poor pyrite (compared to other V6 pyrite; e.g., Figure 5.24A, C). Indeed, Figure 5.25B shows a boundary between relatively clean and massive pyrite containing a Au-hessite inclusion, and pyrite containing abundant angular inclusions of quartz (top half of the image).

Carbonate minerals (dominantly calcite, but dolomite is abundant in sample IC37-157) are variably present in V6 veins, typically infilling around and between quartz and pyrite crystals (e.g., Figure 5.24A). Ore minerals (apart from pyrite) are sometimes hosted by carbonates.

5.4.7 V7

The V7 vein generation is characterised by a pyrite and arsenopyrite ore mineral assemblage, hosted by a quartz and carbonate gangue (Figure 5.26). Only two samples host V7 veins, but the mineralogy of these veins is sufficiently distinctive to justify the classification of a discrete vein generation. Vein width varies from 1-20 mm, although the widest V7 vein (Figure 5.26B) hosts quartz generations and clasts of the wall rock. V7 veins are relatively straight, with the thinner occurrences exhibiting slightly sinuous forms (Figure 5.26A). The thinner V7 veins also tend to form interconnected networks. The two samples that host V7 veins are from the same drill hole, and similar shallow depths (i.e., 73 and 97 m). The wall rock surrounding V7 veins in both samples is affected by sericitic alteration.

Cathodoluminesence of V7 quartz is mostly obscured by the abundant carbonate minerals, but where the veins are relatively carbonate-free, the vein quartz is observed to be

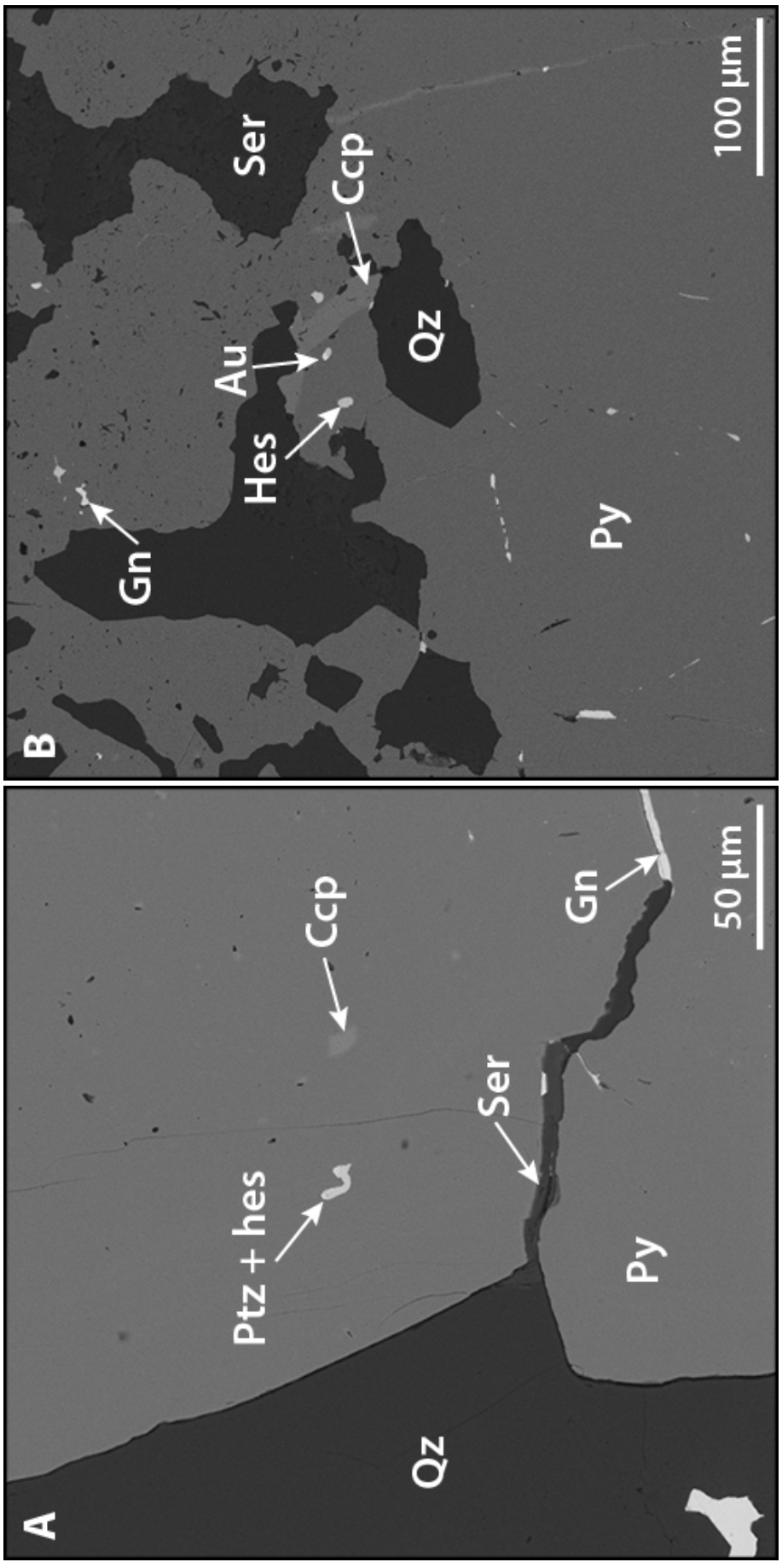

Figure 5.25. Gold observed in V6 veins, imaged by SEM (BSE mode), from samples IC37-157 (A, B) and IC11-026 (C, D). *(continued on next page)*

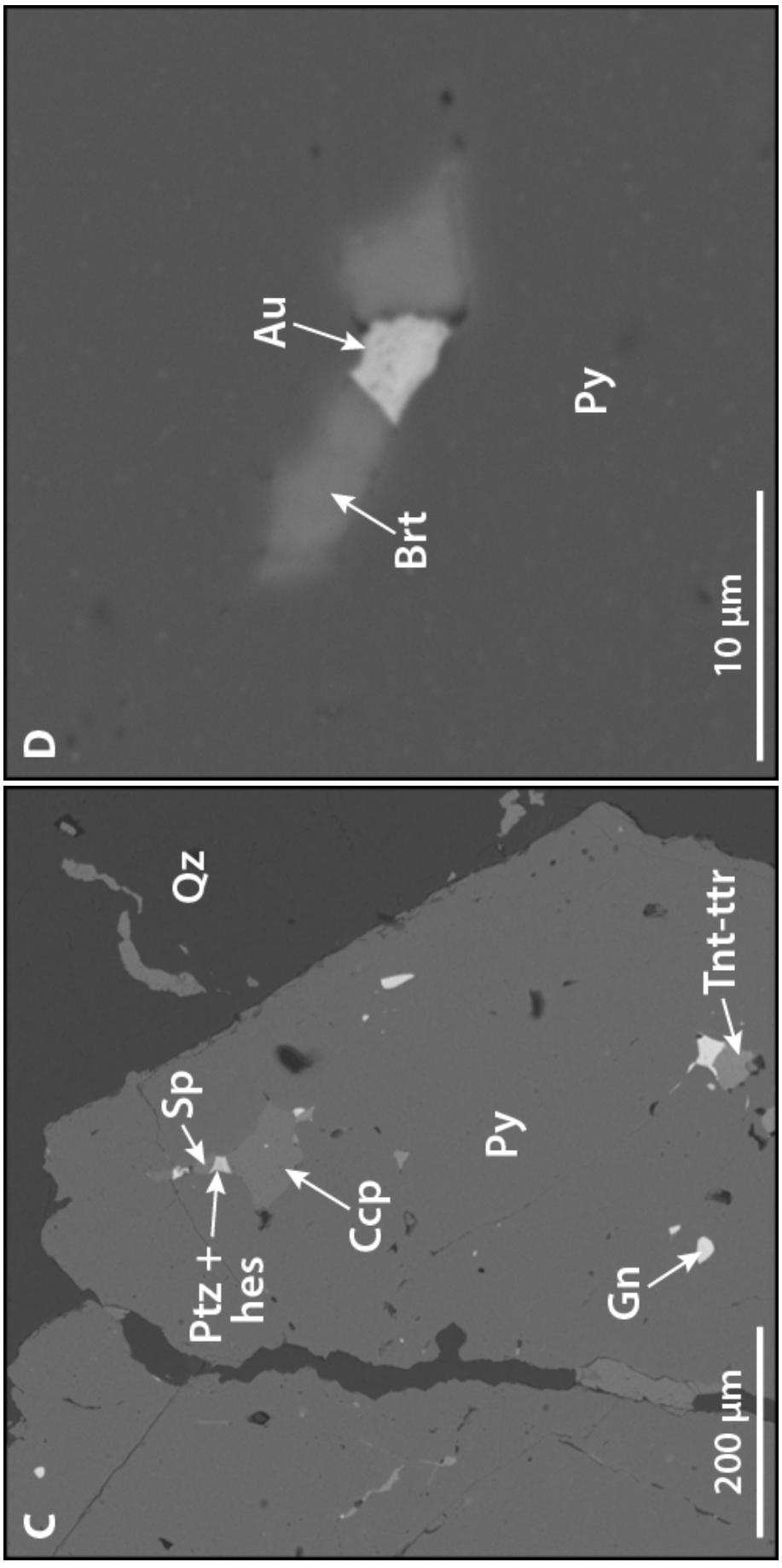

Figure 5.25. *(continued)*

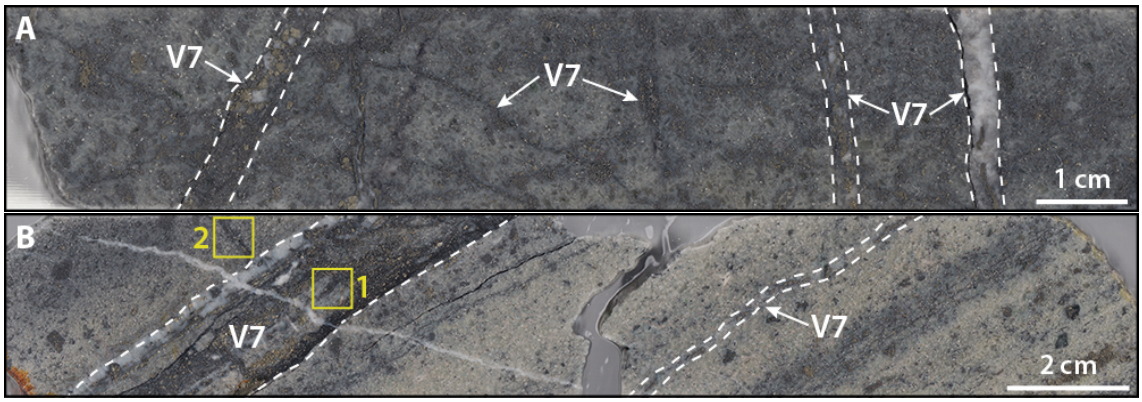

Figure 5.26. V7 vein occurrences, from samples IC66-097 (A) and IC66-073 (B). Arsenopyrite is responsible for the black colour of the veins. A network of mm-width V7 veins is present in A. Clasts of the sericitic groundmass are entrained in the large V7 vein in B. Yellow boxes outline the approximate location of CL images in Figure 5.27.

poorly luminescent, exhibiting dark blue-green to black colours (Figure 5.27). This is similar to the quartz of other vein generations (i.e., V2 Q2, V3, V4, V5). The common presence of carbonate minerals that are observed in CL images appears to be more indicative of V7 veins than the CL characteristics of the quartz.

The ore mineral textures observed in V7 veins are illustrated in Figure 5.28. Two types of pyrite are observed. The first pyrite type is either found as larger crystals (up to mm-scale; Figure 5.28A) characterised by a porous texture and the presence of elongate, linear inclusions of arsenopyrite; as smaller, isolated, elongate crystals overgrown by arsenopyrite (Figure 5.28B); or as masses of smaller crystals linearly intergrown with arsenopyrite

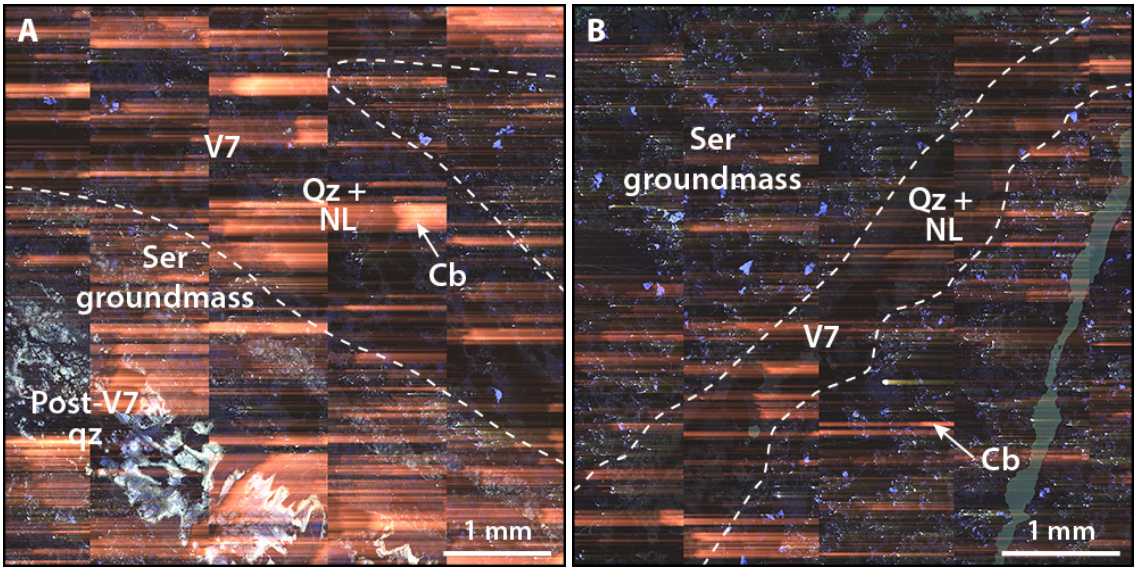

Figure 5.27. V7 vein quartz imaged by CL, from sample IC66-073. The approximate location of the CL images A and B are marked by yellow boxes 1 and 2, respectively, in Figure 5.26B. Non-luminescent minerals (i.e., pyrite and arsenopyrite) appear black. A post-V7 quartz generation that is bright green-blue luminescent is observed in A.

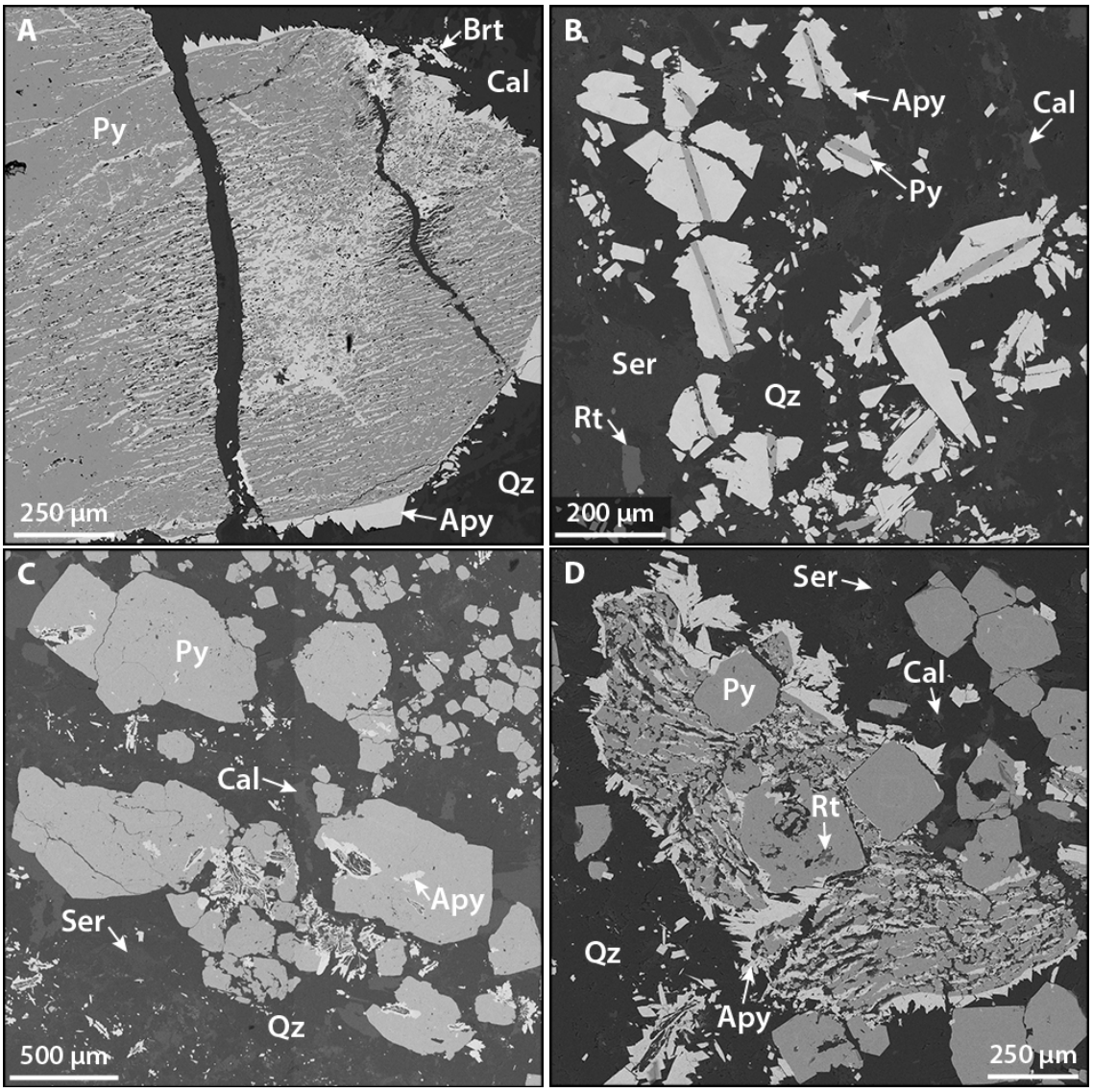

Figure 5.28. Representative V7 ore mineral textures, imaged by SEM (BSE mode), from samples IC66-097 (A, B) and IC66-073 (C, D).

(Figure 5.28D). Arsenopyrite grows around this first pyrite type. The second pyrite type tends to form more euhedral crystals than the first pyrite type, and is relatively clean, although it occassionally exhibits minor porosity, and hosts angular inclusions of arsenopyrite (Figure 5.28C, D). Arsenopyrite is rarely observed to grow around this pyrite type, but arsenopyrite is also observed unassociated with pyrite, usually hosted as brecciated crystal fragments in quartz or sericite (Figure 5.28B, C). Calcite in V7 veins rarely hosts ore minerals, and is observed to infill around quartz, pyrite and arsenopyrite, and fill cracks in pyrite (Figure 5.28A). Quartz is the dominant host for the ore minerals.

Native Au is observed in both V7 vein samples, most commonly hosted in arsenopyrite, but also as inclusions in the first pyrite type, or free in sericite or quartz (Figure 5.29). Arsenopyrite sometimes exhibits compositional zones, with Au observed in a specific zone (Figure 5.29A).

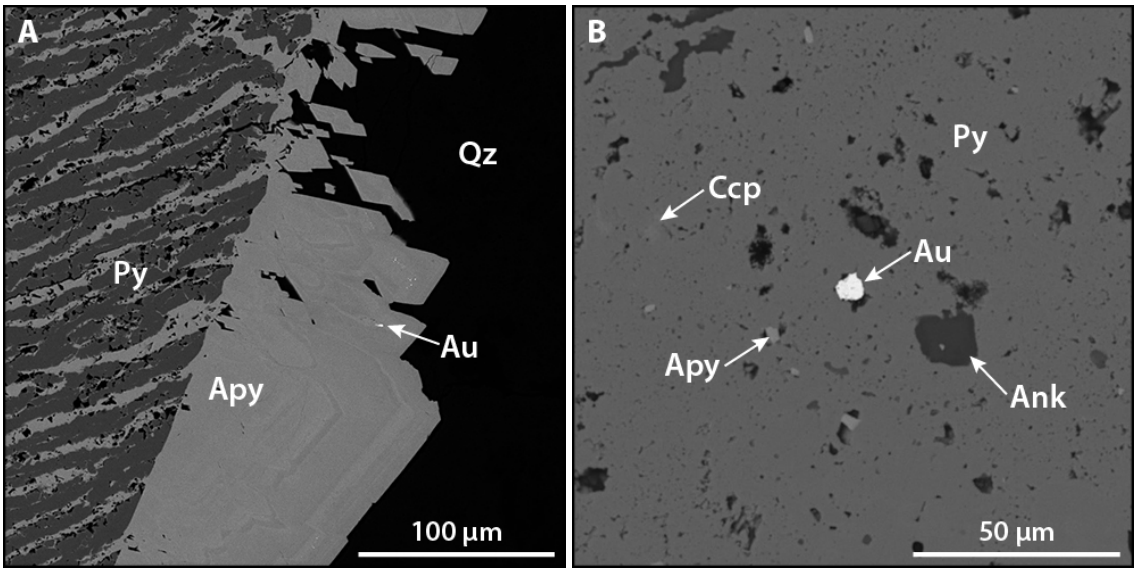

Figure 5.29. Gold observed in V7 veins, imaged by SEM (BSE mode), from sample IC66-097. Native Au is often observed in arsenopyrite (A), or less commonly as inclusions in pyrite (B).

5.4.8 V8

The V8 vein generation at Iron Cap is barren, with a gangue mineralogy dominated by carbonate minerals and quartz (Table 5.1). V8 veins are observed in a range of samples, and throughout the depth of the sample suite. They often appear white-coloured owing to their mineralogy. Some examples are shown in Figure 5.11C-E, Figure 5.14D (orange-coloured) and F, Figure 5.22D, and Figure 5.26B, where they cross-cut the mineralised veins.

5.5 Relative timing of vein emplacement

The vein generations described above have been placed in a paragenetic sequence that constrains their relative timing of emplacement, as illustrated in Figure 5.30. Cross-cutting relationships provide the clearest empirical evidence of the relative timing of vein formation; however, when cross-cutting relationships are not observed, other information has been used to construct the paragenetic sequence, as explained below. A more detailed paragenetic sequence that accounts for the mineralogy of each vein generation is presented and discussed in Chapter 8, to elucidate vein and ore formation processes.

Figure 5.30. *(next page)* Schematic illustration of the vertical distribution and cross-cutting relationships of the mineralised vein generations at Iron Cap. Depth roughly corresponds to the depth of the drill core that vein samples are contained within; the horizontal scale is unconstrained and arbitrary. The pink background colour represents a potassic-dominant alteration assemblage, while the yellow background colour represents a sericitic-dominant alteration assemblage.

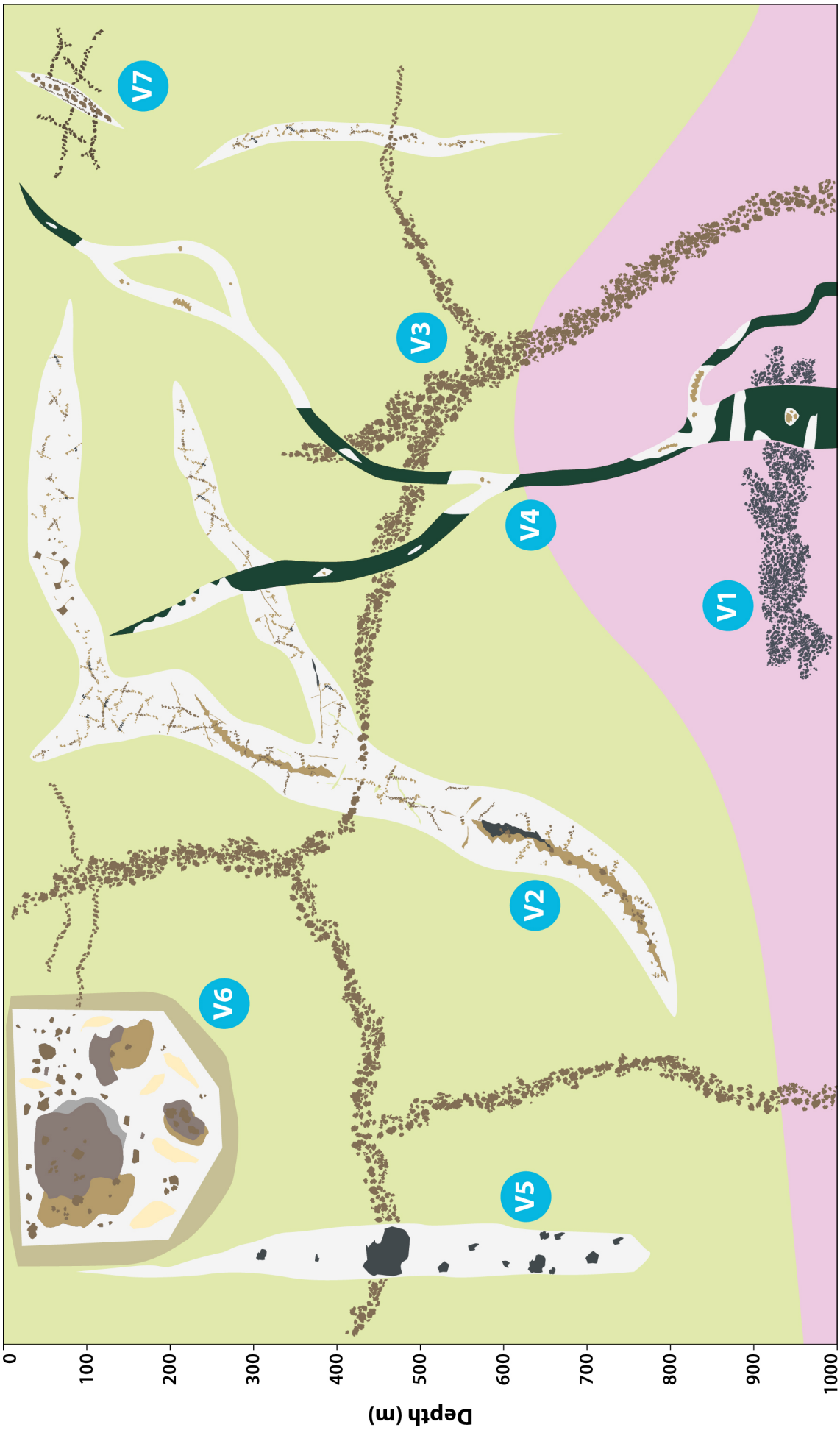
V7
V3
V4
V1
V2
V6
V5
0
100
200
300
400
500
600
700
800
900
1000
Depth (m)

The location of the samples that the vein generation is contained in is considered to be particularly relevant, in conjunction with wall rock alteration. As described by Campbell et al. (2020), and shown in Figure 3.5, the Iron Cap deposit tends to exhibit potassic alteration at depth, and sericitic alteration at shallower levels. This is similar to typical porphyry models (e.g., Figure 2.9; Sillitoe, 2010), although Iron Cap has been tilted so that it now dips steeply to the NW (Campbell et al., 2020). This suggests that drill core from ∼750 m or more below surface is more likely to exhibit potassic alteration, and host veins more representative of the earlier stages of hydrothermal fluid flow. Conversely, drill core samples from less than ∼750 m below surface are more likely to exhibit sericitic alteration, and host veins more representative of the later stages of hydrothermal fluid flow. However, the samples from less than ∼750 m are also likely to host veins representative of the earlier stages of hydrothermal fluid flow, which may or may not have been affected by later stage hydrothermal activity (i.e., potassic alteration overprinted by sericitic). Nevertheless, sample depth alone does not necessarily imply timing; therefore, other features considered are vein mineralogy, texture, morphology, abundance, and alteration halos, as outlined in Section 5.3. These characteristics are compared with porphyry veins described in the literature (Section 2.5.4) to infer relative timings.

The V1 vein generation is only present in one sample, but is cross-cut by V4 veins, meaning that it must pre-date V4 (Figure 5.2). The timing of V1 relative to V2 and V3 cannot be conclusively determined owing to a lack of observed cross-cutting relationships. However, as the V1 vein occurrence is only found in a potassic-altered sample from a depth of 970 m, and was present prior to sericitic alteration, it is interpreted that the V1 vein generation formed during the early stages of hydrothermal system evolution (e.g., the early panel in Figure 2.9). In comparison, V2 and V3 are present throughout Iron Cap, and are not constrained to depth. An early timing for the V1 vein occurrence is also indicated by its close similarity to the M-veins of Arancibia and Clark (1996); it also meets the criteria for the Group 1 vein classification of Sillitoe (2010) (i.e., a lack of sulphide minerals and quartz; Table 2.2). As discussed in Section 2.5.5, these classifications are consistent with vein formation occurring during the early stages of hydrothermal system evolution; therefore, V1 veins are likely to have formed early at Iron Cap.

The V2 vein generation is cross-cut by V3 and V4 veins (Figure 5.31); V2 veins therefore pre-date V3 and V4 veins. Similarly, the V3 vein generation is cross-cut by V4 veins (Figure 5.31B), meaning that V3 veins pre-date V4 veins. On the other hand, no cross-cutting relationships are observed between V4, V5, V6, or V7 veins. Barren V8 veins are observed to cross-cut and/or re-open V3, V4, V6, and V7 veins, indicating that they were the most recently-formed vein generation.

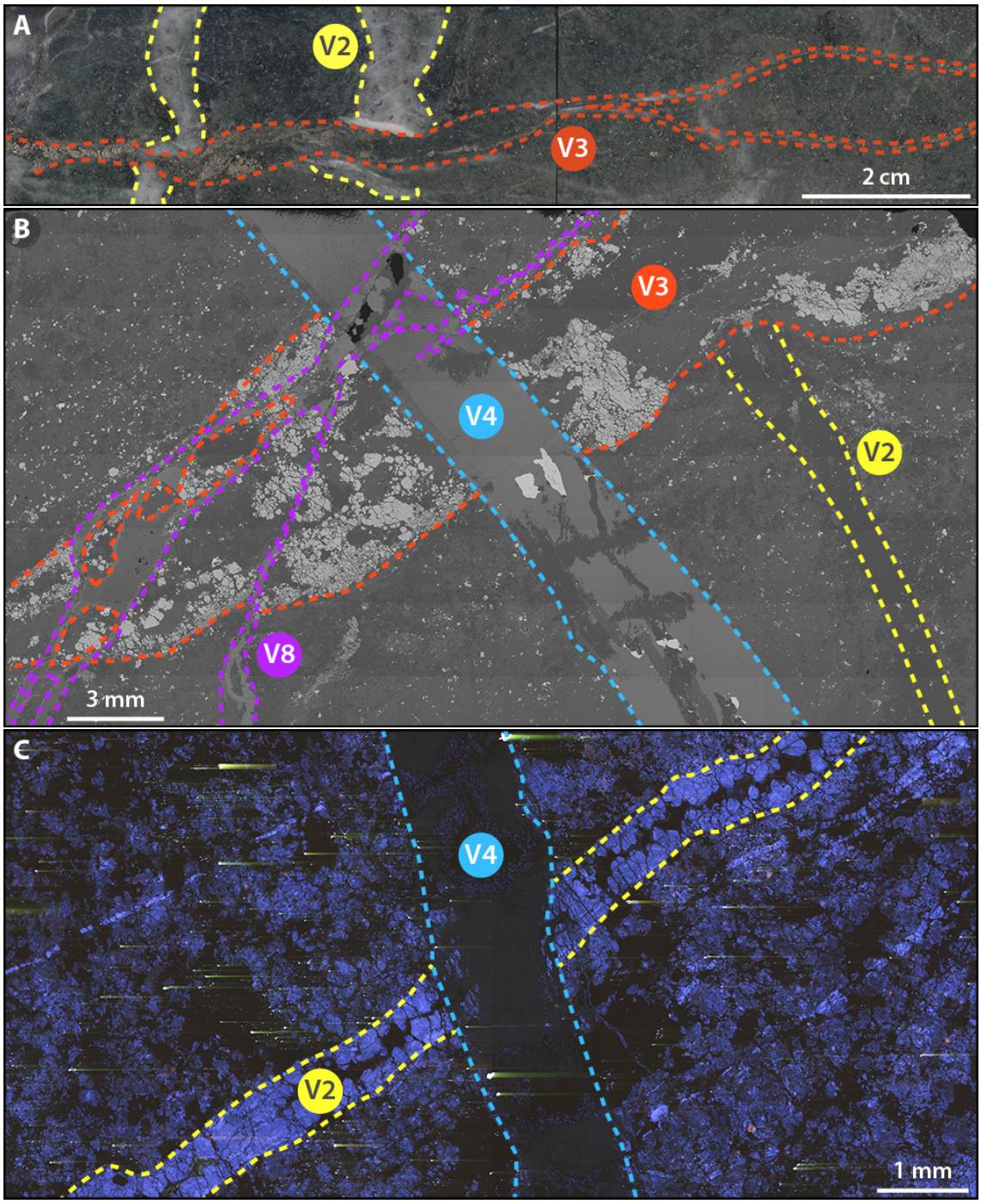

Figure 5.31. V2 vein cross-cutting relationships, from sample IC65-532 (A) and IC65-430 (B, C). A shows a V2 vein cut by a V3 vein. B is imaged by SEM (BSE mode), and shows a V2 vein cut by V3, which is cut by V4; V8 cuts V3 and V4. C is a CL image, showing a V2 vein cut by a V4 vein.

The only other cross-cutting relationships observed are between V3 veins, and V5 and V6 veins. The left side of Figure 5.18B shows a V5 vein cross-cutting a V3 pyrite vein, indicating that V5 veins post-date V3 veins. The sample in Figure 5.22F is interpreted to be a V3 vein re-opened by V6 base metal sulphides and quartz. Vein re-opening is often recorded in porphyry systems (e.g., Sillitoe, 2010; Landtwing et al., 2010; Maydagán et al., 2015; Monecke et al., 2018), and has also been identified in the KSM district, at the Kerr

deposit (Rosset, 2017). Re-opening of this vein (Figure 5.22F) is interpreted because the vein shows slightly dissimilar characteristics to other V3 and V6 veins (Figure 5.22). The vein is comparatively pyrite-rich and base metal sulphide-poor, whereas other V6 veins contain higher proportions of the base metal sulphides compared to pyrite. However, the volume of base metal sulphides is still significant enough to distinguish this vein from other V3 veins. These differences in mineralogy indicate that the conditions of vein formation may have been different to other V3 and V6 veins.

The morphology of this vein is also relatively sinuous, with wavy margins evident, comparable to the morphology of V3 veins (Figure 5.11); other V6 veins tend to have more linear vein margins, where observed (e.g., Figure 5.22C-E), suggesting that the conditions of vein formation were different. Veins with wavy and linear morphologies can be interpreted to have formed under ductile and brittle conditions, respectively (Sillitoe, 2010). Therefore, it is interpreted that a sinuous V3 vein was utilised as a fluid flow path by V6-precipitating fluids. The CL characteristics of this re-opened vein are compatible with other V6 veins (Figure 5.23D), luminescing with dark blue-green colours, and indicating that the quartz was introduced by fluids similar to those that introduced quartz into other V6 veins. Finally, the base metal sulphides in this vein grow around pyrite, or in pyrite fractures, and are particularly concentrated at the vein margins; pyrite also appears to be have been heavily brecciated and fractured, consistent with the interpretation that later fluid infiltration occurred. These relationships indicate that V6 veins post-date V3 veins.

The lack of further cross-cutting relationships observed in the sample suite means that the V4-V7 vein generations are paragenetically constrained by other lines of evidence. V4 veins are interpreted to be the earliest of the remaining vein generations, because they are present throughout the sample suite, and are particularly present in samples from depth that exhibit potassic alteration. In addition, a unique characteristic of V4 veins is the presence (and often abundance) of chlorite, which also characterises C-veins from the Altar deposit, Argentina (Maydagán et al., 2015). Although different in mineralogy to the C-vein classification of Arancibia and Clark (1996), they are interpreted by Maydagán et al. (2015) to have a similar timing (i.e., post A-B-vein, pre-D-E vein; Table 2.2), which suggests that chlorite-bearing veins can form relatively early in the evolution of some porphyry deposits.

Many V4 veins also exhibit sinuous forms and wavy margins (Figure 5.14) that could be attributed to emplacement in a ductile regime, and thus at relatively high temperatures (i.e., >350-500°C; Fournier, 1999; Sillitoe, 2010; Monecke et al., 2018). The lack of base metal-bearing ore minerals apart from chalcopyrite (± trace galena), may also indi-

cate that V4 veins formed at relatively high temperatures, where sphalerite and galena are not precipitated in great quantities owing to their higher solubility (Kouzmanov and Pokrovski, 2012). The association of higher temperatures with earlier vein formation inherently assumes a thermal evolution of the system from hot to cold as would be expected for hydrothermal fluid flow related to cooling of a causative intrusion (Seedorff et al., 2005). However, this may not be accurate, as additional intrusions can perturb a typical hot-to-cold evolution, and produce veins related to higher temperatures after veins related to cooler temperatures (Seedorff et al., 2005). Nevertheless, a thermal evolution from hot to cold is assumed at this stage to enable construction of a paragenetic sequence for veins from the V4-V7 generations; this will be discussed further in Chapter 8.

The V5 vein generation is interpreted to post-date the V4 vein generation, because it is observed in samples from intermediate to shallow depths (compared to V4, which is observed in samples from the entire depth range sampled), is associated with sericitic alteration, and hosts tennantite-tetrahedrite instead of chalcopyrite as a major ore mineral. The association of V5 veins with sericitic alteration implies that they were formed later than those associated with potassic alteration (including some V4 veins), because sericitic alteration overprints potassic alteration and is commonly situated at shallower depths than potassic alteration, showing that sericitic alteraton is a later-stage product of the hydrothermal system (e.g., Seedorff et al., 2005; Sillitoe, 2010). Furthermore, tennantite-tetrahedrite is more often observed as a major ore mineral in later-stage veins in porphyry deposits (e.g., Table 2.2; Gustafson and Hunt, 1975; Masterman et al., 2005; Maydagán et al., 2015), compared to chalcopyrite, which can be present throughout (e.g., Gustafson and Hunt, 1975; Gustafson and Quiroga, 1995; Sillitoe, 2010; Maydagán et al., 2015), indicating that V5 veins are likely to be later than V4 veins.

The V6 vein generation is interpreted to have formed later than V4 and V5, because V6 veins are only observed in samples from shallow depths, contain a base metal-rich massive sulphide assemblage, have linear forms and straight margins, and have wide vein widths that also often exhibit sericitic alteration halos (Figure 5.22). In contrast to V6, both V4 and V5 also lack pyrite, which is more common for earlier-formed porphyry veins (Table 2.2; Gustafson and Hunt, 1975), despite the fact that both V2 and V3 host pyrite. The enrichment in base metals in V6 indicates that the solubility of sphalerite and galena was greatly reduced during the formation of V6, in comparison to previous veins; this is attributable to a reduction in temperature (Kouzmanov and Pokrovski, 2012). The linear forms and straight margins of V6 veins also suggest that V6 veins formed in a brittle regime, at lower temperatures than veins with wavy forms that can be associated

with formation in a ductile regime (Sillitoe, 2010). When assuming a hot-to-cold thermal evolution, this evidence indicates that V6 veins formed later than V4 and V5 veins.

The shallow depth of V6 veins also complies with formation during the later stages of hydrothermal system evolution, where fluids may have migrated further away from the magma body (e.g., the middle panel in Figure 2.9; Sillitoe, 2010; Richards, 2011). The decimeter-scale widths and linear forms of V6 veins draws similarities to porphyry E-veins, which are often interpreted to have formed in linear structures late in the evolution of porphyry hydrothermal systems (Masterman et al., 2005; Maydagán et al., 2015). The quartz brecciation textures in V6 CL images (Figure 5.23) could support the interpretation that V6 veins formed in linear structures, later than the thinner arrays of V4 and V5 veins, as Masterman et al. (2005) also recognise breccia textures in their late E-veins. Finally, the alteration halos often observed around V6 veins are a characteristic feature of veins classified as late-stage in other porphyry deposits (e.g., Table 2.2; Gustafson and Hunt, 1975; Gustafson and Quiroga, 1995), again indicating that V6 veins formed later than V4 and V5 veins, which lack alteration halos.

The apparent scarcity and localisation of V7 veins to a specific region at very shallow depths indicates that these veins may be a local product of late, shallow fluid flow. This may also be suggested owing to the presence of arsenopyrite as a major mineral. Arsenopyrite is rarely observed in porphyry deposits, but is sometimes recognised in peripheral mineralisation (e.g., Corbett and Leach, 1998), implying that V7 veins may be peripheral. There is also an association of V7 veins with strong sericitic alteration, indicating that V7 veins may have formed relatively late in system evolution (e.g., Seedorff et al., 2005; Sillitoe, 2010). The V7 vein generation is interpreted to have formed later than V4-V6 veins, although there is a particular lack of evidence to constrain timings, owing to the few occurrences observed in the sample suite, and the lack of similarity between V7 veins and veins common in porphyry systems in general (e.g., Table 2.2). The relative timing of vein generations and the conditions of vein formation are discussed further in Chapter 8.

5.6 Comparison to the vein generations of Campbell et al. (2020)

The vein generations described by Campbell et al. (2020) show some similarities and differences to the vein generations described here (Table 5.2). The A- and B-veins described by Campbell et al. (2020) are collectively comparable to the V2 vein generation, and show the same crackled-texture and/or central suture. However, in this thesis, it is not thought that the differences in texture (i.e., crackled texture in A-veins vs. central suture in B-veins) represent different vein generations, rather that there is a continuum

Table 5.2

Comparison of vein generation classifications for the Iron Cap deposit. Arrows indicate similarities in vein characteristics between the classifications, as discussed in the text. The mineralogy listed for the vein classifications of this thesis only includes major and minor ore minerals, and major gangue (cf. Table 5.1).

Previous vein classifications, Campbell et al. (2020)			Current vein classifications, this thesis		
Key characteristics	Mineralogy	Vein	Vein	Mineralogy	Key characteristics
Stockworks or sheeted sets, sometimes exhibit potassic halo	Qz-ccp ± mag	A-vein	V1	Mag	Massive mag, discontinuous
Sometimes exhibit potassic halo	Mag ± ccp	Magnetite	V2	Qz, ccp, py ± tnt-ttr	Ore minerals define crackled texture and/or central suture within qz
Sulphide-bearing central suture surrounded by qz	Qz-ccp ± mol ± py	B-vein	V3	Py, ccp, qz, ser	Massive py, wavy margins
No description	Mol ± qz ± ccp ± py	Molybdenite	V4	Qz, ccp ± chl	Thin veins where ccp is the only sulphide; black chl is distinctive
Variable sulphide-sulphosalt assemblage with grey qz	Qz-py ± tnt ± ttr (± ccp ± sp)	Polymetallic	V5	Qz, tnt-ttr ± ccp	Qz-rich with isolated tnt-ttr crystals
Py-rich veinlets with sericitic halos	Py	D-vein	V6	Qz, sp, ccp, py, gn ± tnt-ttr	Wide veins with massive base metal sulphides and sericitic halos
Coarse clots of ore minerals in milky qz	Qz-cb ± chl ± sp ± gn ± ccp ± tnt ± ttr	Post-mineral	V7	Py, apy, qz	Py-apy-rich, black colour due to fine-grained apy
			V8	Cb ± qz	Barren cb

between the two. Similar conclusions were reached by Gustafson and Hunt (1975) at the El Salvador deposit, Chile, where veins with sulphides in a central suture or in cracks perpendicular to the vein were classified as B-veins.

Campbell et al. (2020) also identify the variable presence of magnetite in their A-veins and molybdenite in their B-veins, whereas these minerals are not present as major or minor minerals in the V2 vein generation; molybdenite is only rarely observed as a trace mineral. Similarly, the drill core sample suite collected for this thesis does not contain the molybdenite vein generation of Campbell et al. (2020). The molybdenite veins may be constrained to other parts of the deposit, be relatively uncommon within the deposit, or simply not contained within the samples collected, owing to the limitations of the sampling method, and the number of samples that were feasible to collect and study (Section 5.3).

The V1 vein generation is comparable to the magnetite vein generation of Campbell et al. (2020), although Campbell et al. (2020) include chalcopyrite in their vein mineralogy, and place their magnetite vein generation after A-veins in their paragenesis. As in this study, Campbell et al. (2020) do not observe cross-cutting relationships between magnetite veins and other vein generations. In this study, V1 veins (i.e., magnetite) lack chalcopyrite (although are cross-cut by chalcopyrite-bearing V4 veins), and appear to be the earliest-formed, followed by V2 veins (i.e., A- and B-veins). As discussed in Section 2.5.4, quartz-free magnetite veins in porphyry systems are often attributed to earlier stages of system evolution than quartz-chalcopyrite veins (e.g., Sillitoe, 2010), because quartz has a higher solubility in hydrothermal fluids at higher temperatures and pressures (Monecke et al., 2018). This means that the magnetite veins of Campbell et al. (2020) may pre-date their A-veins, as noted in Section 3.4.6.2, which would then conform to the interpreted timing of V1 and V2 veins in this thesis. A caveat of the interpretations of V1 veins is that only one occurrence is observed in the sample suite, meaning that a more conclusive understanding of their characteristics and timing is yet to be acheived. Meanwhile, Campbell et al. (2020) may have recognised multiple occurrences of their magnetite veins that provided more information to constrain their characteristics and timing. Nevertheless, both studies recognise the early timing of these vein generations, although the specific timings are interpreted differently.

The polymetallic veins of Campbell et al. (2020) appear to be comparable to the V6 vein generation, and have a similar late timing, although chalcopyrite and sphalerite are recognised to be dominant in V6 veins, while they are variably present in the polymetallic veins of Campbell et al. (2020). The D-veins of Campbell et al. (2020) also comply with the classification of V3, but Campbell et al. (2020) recognise sericitic halos surrounding

these veins, which are not present around the V3 veins described in this thesis; rather, they are present around V6 veins. The interpreted vein timings are also different, with Campbell et al. (2020) proposing that their D-veins (i.e., V3) post-date the polymetallic veins (i.e,. V6), although there are no cross-cutting relationships observed between the D-veins and other vein generations. Meanwhile, V3 veins are observed to cross-cut V2 veins, and be cross-cut and/or re-opened by V4, V5, V6, and V8 veins, meaning that their timing is fairly well-constrained.

The V4, V5, V7, and V8 vein generations are not directly comparable to any of the vein generations described by Campbell et al. (2020), but they may be included in some classifications. The post-mineral veins of Campbell et al. (2020) have a variable ore mineralogy, and could feasibly include V4, V5, and V8 veins, owing to the ubiquitous presence of quartz and carbonate (V8), and the variable presence of chlorite and chalcopyrite (V4), and tennantite-tetrahedrite (V5). Furthermore, Campbell et al. (2020) note that ore minerals in post-mineral veins occur as coarse clots, which is sometimes observed for chalcopyrite in V4 veins (Figure 5.14C), and tennantite-tetrahedrite in V5 veins (Figure 5.18B). The image of a post-mineral vein in the Campbell et al. (2020) study (Figure 3.7k) does appear similar to a V4 vein, although there are no ore minerals present. Nevetheless, it is difficult to be certain whether V4, V5, and V8 veins were observed and collectively classified as post-mineral veins by Campbell et al. (2020), or whether a discrete vein generation was observed, which is not present in the sample suite of this thesis.

As described above, V4, V5, and V8 necessitate discrete classification in this thesis owing to their differing characteristics, which has implications for their relative timing. Campbell et al. (2020) state that their post-mineral veins cross-cut all preceeding veins, but if their post-mineral veins include V4, V5, and V8 veins, then it is difficult to be sure which veins are cutting which. Regardless, the relatively late timing of V4, V5, and V8 veins, at least in comparison to V2 and V3 veins, is a similarity between this thesis and the study of Campbell et al. (2020).

The nature of the wall rock alteration assemblage that appears to be associated with each vein generation is a difference between this thesis and the study of Campbell et al. (2020). It should however be noted (as in Section 5.3) that wall rock alteration may not be coincident with vein formation (e.g., Sillitoe, 2010), and may therefore not have direct genetic implications. Association with wall rock alteration is therefore simply an observation of the alteration assemblage that affects the wall rock that each vein generation is hosted within; genetic associations are implied but not proven.

Nevertheless, while Campbell et al. (2020) report that magnetite veins (i.e., V1), A- and B-veins (i.e., V2), and potentially molybdenite veins are associated with potassic

alteration, this thesis only recognises that V1 veins are associated with potassic alteration, although only one occurrence of V1 is observed in the sample suite. Furthermore, Campbell et al. (2020) record that their polymetallic veins and D-veins are associated with sericitic alteration, while post-mineral veins show no association. In this thesis, veins classified as V2, V5, V6, and V7 are observed in samples that exhibit sericitic alteration alone, or potassic alteration overprinted by a dominantly sericitic assemblage, implying an association with sericitic alteration. Meanwhile, V3, V4, and V8 are present in samples that exhibit potassic alteration, sericitic alteration, or potassic overprinted by sericitic, implying that they are associated with potassic alteration, or not associated with any alteration assemblage. However, sericitic alteration alone does not necessarily preclude the presence of pre-existing potassic alteration, rather that all the K-feldspar has been replaced so that no record of potassic alteration remains (e.g., Seedorff et al., 2005).

The lack of clear vein-alteration associations recognised in this thesis may be due to the nature of the sample suite, most of which is affected by sericitic alteration. It is likely that Campbell et al. (2020) had more comprehensive understandings of alteration distribution that allowed associations to be defined, owing to their utilisation of three-dimensional models (e.g., Figure 3.5). Nevertheless, as most of the samples studied in this thesis exhibit sericitic alteration, it is suggested that sericitic alteration is widespread and pervasive at Iron Cap, and that vein-alteration associations are not particularly useful for the differentiation of vein generations. One similarity to the study of Campbell et al. (2020) is that a propylitic alteration assemblage has not been specifically identified in any samples, although chlorite is variably observed in the potassic and sericitic assemblages.

In summary, there are some key similarities and differences between the vein classifications of Campbell et al. (2020), and those presented in this thesis. The main reasons for discrepancies are likely that the study of Campbell et al. (2020) had aims to provide a descriptive model of the deposit, and does not enter into the detail of the vein characteristics, timing, and genetic process, rather covering the fundamental macroscopic characteristics of the veins. Meanwhile, this thesis has taken a more detailed approach to vein characterisation and classification, applying a range of analytical techniques down to the micro-scale to attain the most precise characterisations and classifications afforded by the sample suite. Equally, however, the study of Campbell et al. (2020) attains a comprehensive understanding of the deposit characteristics as a whole, likely utilising all of the Iron Cap drill core (but with a less detailed petrography), which may have provided insights into vein classifications that could not be ascertained in the limited sample suite and deposit knowledge contained in this thesis. Nevertheless, the detailed approach of this thesis also has implications for the understanding of deposit mineralogy, metal de-

portment, and genetic processes (below and Chapter 8) that are not highlighted by the study of Campbell et al. (2020), owing to their more generalised approach.

5.7 Implications for the understanding of Iron Cap

Each occurrence of the eight vein generations described in this chapter has been marked on a three-dimensional model constrained by the sampled drill holes (Figure 5.32). A video that illustrates the three-dimensional aspect is presented in Appendix B. The model shows the spatial distribution of vein generations at Iron Cap, which was utilised during the paragenetic sequencing of vein generations outlined in Section 5.5, and the construction of Figure 5.30.

Figure 5.32 and Appendix B allow an assessment to be made of the apparent abundance and distribution of vein generations present at Iron Cap. It should again be noted (as in Section 5.3) that the sample suite analysed in this thesis is limited by the number of samples collected, the location of the collected samples, and the sampling method (Ap-

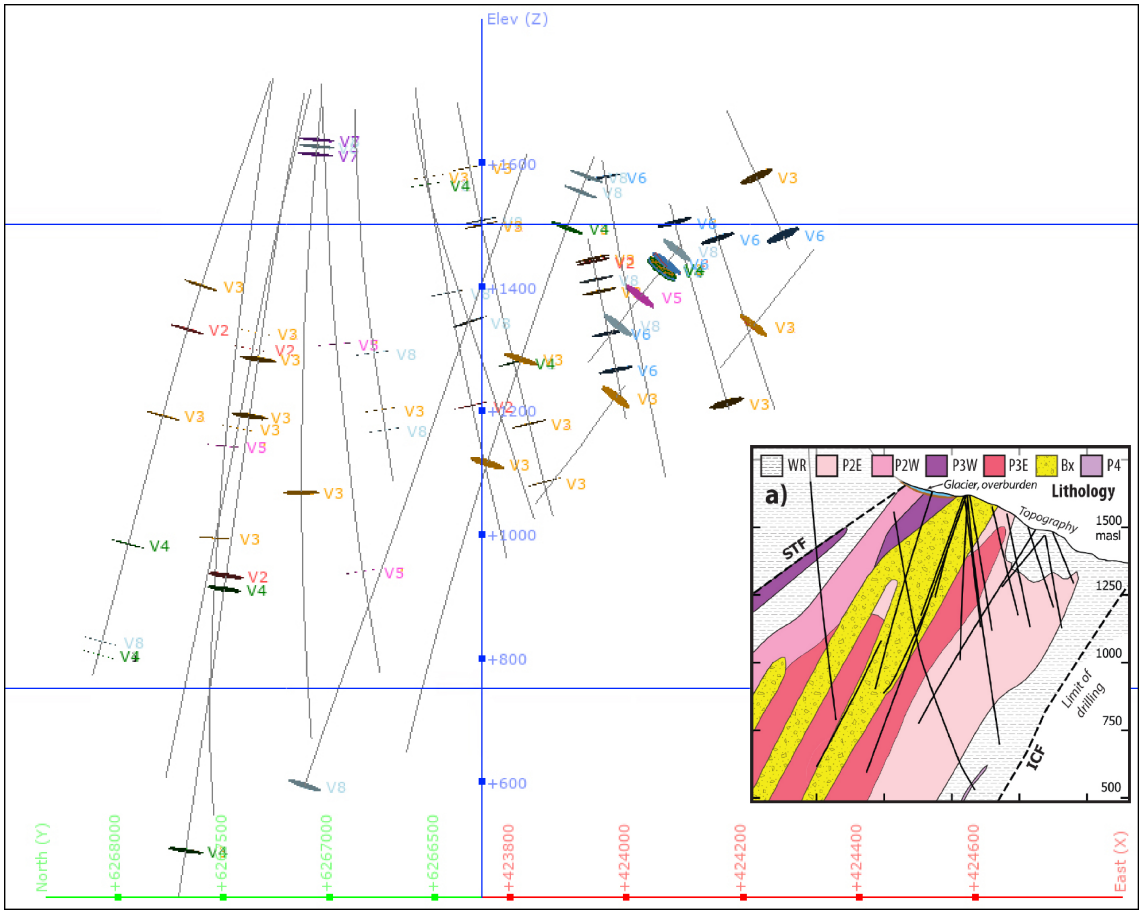

Figure 5.32. Distribution of vein generations within the sampled drill holes at Iron Cap, based on the sample suite collected. This field of view looks N-NE, and is similar to that of Figure 3.5, from Campbell et al. (2020) (Figure 3.5A is inset for reference). A video illustrating the three-dimensional distribution is presented in Appendix B.

Table 5.3
Abundance and vertical distribution of vein generations within the sampled drill holes at Iron Cap, based on the sample suite collected.

	V1	V2	V3	V4	V5	V6	V7	V8
No.	2	15	43	11	5	10	3	20
Min depth (m)	970	38	24	48	109	26	73	11
Max depth (m)	970	798	1252	1252	791	224	97	970

pendix A). Therefore, the assessments presented below may not be applicable throughout Iron Cap. Nevertheless, Figure 5.32 and Appendix B show that V2, V3, V4, V6, and V8 veins are observed in numerous different drill holes, illustrating their apparent widespread lateral distribution. However, V6 veins appear to be specifically concentrated in drill holes towards the SE end of the deposit; they are not observed in samples from the drill holes of the 2017 program, which are situated further towards the NW (cf. Appendix A).

The abundance and vertical distribution of the vein generations are summarised in Table 5.3, to complement to visual illustration of Figure 5.32. This highlights the fact that veins of the V3 generation are the most commonly observed within the sample suite, and may therefore be the most common vein generation at Iron Cap. Meanwhile, V1 veins are constrained to depth, and V6 and V7 veins are only observed at shallow levels, indicating that these vein generations in particular may have genetic links to depth (e.g., proximity to a causative intrusion; Sillitoe, 2010), as noted in Section 5.5.

Knowledge of the abundance and distribution of vein generations is additionally useful because it may help to explain the variation in deposit characteristics, such as the distribution of ore minerals. In particular, comparisons to deposit-scale models and maps, such as those presented by Campbell et al. (2020) may highlight associations between vein generations and lithologies, Au and Cu grades, alteration assemblages, and/or quartz vein volumes (Figure 3.5). Another aspect, which is relevant to this thesis, is that vein abundance and distribution may help to elucidate the distribution of trace elements at Iron Cap, because certain trace elements may be enriched in specific ore minerals and veins (cf. Chapter 4). This means that the presence of a vein could speak to the enrichment of trace elements within the local rock mass. These aspects are considered further in Chapter 8, where the understanding of Iron Cap with regards to vein and ore formation processes, the conditions of vein formation, and the development of Iron Cap as a resource are also discussed.

5.8 Sample selection for LA-ICP-MS

A suite of samples were selected for LA-ICP-MS, in order to carry out compositional analyses of the ore minerals contained within the vein generations at Iron Cap (Table 5.4). Vein samples of V2-V7 were selected for analysis, as these vein generations contain ore minerals. V1 and V8 veins lack ore minerals and were therefore not selected for analysis.

There were some limitations imposed on the sample selection process. Firstly, sample selection was constrained to the first batch of samples collected from Iron Cap, as the second batch had not undergone petrographic study when preparations for LA-ICP-MS were made (Appendix A). Similarly, not all samples from the first batch had been characterised, limiting the selection of samples to those from the first batch that had been characterised. There was also a specific time period booked for LA-ICP-MS work (5 days) at an external facility, which limited the number of samples that were feasible to analyse within the given timeframe. Finally, at the time of sample selection, it was expected that additional LA-ICP-MS analyses would be carried out to generate a comprehensive dataset of ore mineral compositions from a wider and more representative sample set. However, there were unforeseen limitations imposed on additional analytical work, meaning that only the one period of LA-ICP-MS analysis was carried out. This was owing to breakdown of the LA-ICP-MS instrumentation at the University of Leeds, followed by lack of access due to pandemic lockdowns and lab closures.

Despite the limitations noted above, a suite of samples were selected to meet specific criteria. Representation of the different mineralised vein generations, and the ore minerals they contained, was the main criteria for sample selection. Therefore, each vein generation from V2-V7 had at least one sample chosen for LA-ICP-MS. A larger number of vein samples were selected for veins that are more abundant in the sample suite; hence, V3 is the most well-represented, followed by V2, V4, V5 and V6, and finally V7 (Table 5.4). The selection of specific samples from each vein generation was largely based on the adequate presence of the major and minor ore minerals that could be analysed by LA-ICP-MS (i.e., crystals were large enough, and there were enough different occurrences), and the confidence in the vein classifications at that point in the petrographic study. For example, sample IC72-798 is a type example of a V2 vein (Figure 5.6A); other vein samples sometimes exhibit features that meant there was some ambiguity in vein classification (as the petrographic study was still ongoing), and the vein classifications were not as well-constrained at that point in the study as they are now. In addition to these criteria, there were efforts made during sample selection to represent vein occurrences from different parts of the deposit (i.e., different depths and/or drill holes), or that

Table 5.4
Vein samples and ore minerals selected for LA-ICP-MS. A total of 13 samples were selected for analysis. Note that some samples contain more than one vein generation.

Vein samples	Py	Ccp	Gn	Tnt-Ttr	Sp	Apy
V2						
IC65-430	–	X	–	–	–	–
IC70-402	X	X	X	X	–	–
IC70-429	X	X	X	–	–	–
IC72-798	X	X	X	X	–	–
V3						
IC33-030-1	X	–	–	–	–	–
IC59-033-1	X	X	X	–	X	–
IC65-430	X	X	X	–	–	–
IC70-402	X	X	X	X	–	–
IC73-518	X	X	X	X	–	–
V4						
IC65-430	–	X	–	–	–	–
IC71-784	–	X	X	–	–	–
IC71-970-2	–	X	X	–	–	–
V5						
IC63-791	–	X	X	X	–	–
IC69-598	–	X	X	X	–	–
V6						
IC33-030-1	–	X	X	X	X	–
IC37-157-2	X	X	X	–	X	–
V7						
IC66-073	X	–	–	–	–	X

differed slightly in their characteristics to other veins of the same generation – primarily with regard to ore mineralogy, where some minor or trace minerals are not always present in a given vein generation. Similarly, for the purposes of attaining the maximum number of LA-ICP-MS analyses within a limited timeframe, the few samples containing more than one vein occurrence (e.g., IC65-430) were prioritised, in order to reduce time spent switching samples, and to address questions around chemical similarity in cross-cutting veins.

Within each vein sample, the ore minerals that were selected for analysis depended on the ore mineralogy of the vein occurrence. Where present, pyrite, chalcopyrite, galena, tennantite-tetrahedrite, sphalerite, and arsenopyrite were designated for LA-ICP-MS. As mentioned in Chapter 4, these ore minerals were primarily chosen owing to their major or minor occurrence in the ore mineral assemblage of the vein generations at Iron Cap. Pyrite and chalcopyrite are the most abundant ore minerals at Iron Cap, and in porphyry deposits in general, and were therefore prioritised. Chalcopyrite and galena both occur

in V2-V6, and so were deemed to be best suited to track changes in composition between these vein generations. However, galena is a trace ore mineral in most vein generations, and its generally small grain size meant that meaningful analysis by LA-ICP-MS could be compromised by the particle size relative to the laser spot size. Pyrite, tennantite-tetrahedrite, sphalerite, and arsenopyrite have a more sporadic occurrence throughout the vein generations, but nevertheless were thought to constitute important hosts for trace elements in the veins where they occur as major or minor constituents.

5.9 Summary

The detailed petrographic study of the drill core sample suite collected from Iron Cap has resulted in the identification of eight discrete vein generations. Each vein generation has been characterised and placed in a paragenetic sequence that constrains their relative timing of emplacement, with the earliest vein generation V1, and the latest vein generation V8. The characteristics of the vein generations are summarised in Table 5.4.

The new vein classifications variably map onto those previously classified at Iron Cap by Campbell et al. (2020). Similarities are noted between: previously-classified A- and B-veins, and V2 veins; previously-classified magnetite veins, and V1 veins; previously-classified polymetallic veins, and V6 veins; previously-classified D-veins, and V3 veins; and previously-classified post-mineral veins, and V4, V5, and V8 veins.

Lastly, to meet the aims of this thesis, a suite of vein samples were selected for trace element analysis by LA-ICP-MS, primarily based on the ore minerals present in each vein generation. It is now possible to discuss the approach and results of the LA-ICP-MS analysis within the framework of the vein generations classified here.

6 Ore mineral compositions

6.1 Introduction

The aim of this chapter is to characterise ore minerals across the vein generations in terms of their major and trace element content. Ore mineral compositions aid in understanding the concentration and distribution of trace elements within Iron Cap, and have the potential to elucidate the characteristics of the hydrothermal fluids that formed the veins.

This chapter first outlines the selection criteria by which ore minerals were chosen to go forward to major and trace element analysis (Section 6.2). The major element characterisation of ore minerals by EMPA and SEM-EDX is then presented, alongside the implications of major element mineral compositions for the subsequent LA-ICP-MS analyses (Section 6.3). Next, the reduced LA-ICP-MS data is presented, starting with spot data for each ore mineral (Section 6.4). Each of these subsections records:

- The trace elements hosted by the ore mineral in question;
- The concentrations of each trace element within the ore mineral;
- The frequency of occurrence of each trace element within the ore mineral;
- The profile trace classifications for each trace element within the ore mineral;
- Correlations between trace elements within the ore mineral;
- Differences or similarities between vein generations hosting the same ore mineral.

Map data for pyrite is then presented (Section 6.4). Finally, all the compositional data is collectively considered (Section 6.6), to assess the implications for trace element deportment within and between vein generations.

6.2 Selection of ore minerals for major and trace element analysis

Sample selection for LA-ICP-MS has previously been discussed in Section 5.8. This section describes the selection of analytical targets from within the samples chosen (Table 6.1). The timing of target selection relative to elemental characterisation was as follows:

1. Selection of analytical targets;
2. Major element characterisation by EMPA;
3. Trace element characterisation by LA-ICP-MS, coupled with the selection and analysis of additional targets;

4. Major element characterisation by EMPA and SEM-EDX.

The timings of major element characterisation by EMPA and SEM-EDX are explained in Section 6.3.

Analytical targets selected prior to major and trace element characterisation were chosen by marking points (each labelled with a unique identification code) on thin section BSE scans acquired during earlier petrographic analyses by SEM-EDX (i.e., Chapter 5). The number of targets chosen was constrained in the first instance by the time available for LA-ICP-MS (5 days), and the number of spots deemed feasible to analyse within this timeframe after consultation with the laboratory technician. Accordingly, 250 analytical targets were chosen for spot analyses by LA-ICP-MS. Approximately 5 targets per ore mineral per sample were selected, which varied slightly (typically ± 1 spot) depending on the abundance of mineral particles in the sample, and the size of mineral particles in relation to the laser spot size (10 µm). Mineral particles $<$10 µm in diameter were not selected, being too small for analysis. Analytical targets were spaced throughout each sample and the contained veins to evaluate heterogeneity in ore mineral compositions within the sampled vein area.

Additional analytical targets were selected during LA-ICP-MS, when it became clear that the 250 spots previously selected would be easily analysed within the time available. As such, the total number of spot analyses increased to 428 (Table 6.1). These additional spots were chosen while operating the LA-ICP-MS system, and given different identification codes to those previously selected. The selection criteria was the same as that outlined above for analytical targets chosen prior to major and trace element characterisation.

Six pyrite particles were also selected forthe acquisition of trace element maps by LA-ICP-MS (Table 6.1). These were chosen as analytical targets because they exhibit zonations (identified by previous petrographic work; Chapter 5), and are of an appreciable size ($\sim$250 µm diameter) to return a relatively high-resolution image. Pyrite particles from different vein generations were represented in the selected targets.

6.3 Ore mineral characterisation by EMPA and SEM-EDX

The analytical targets selected for trace element characterisation by LA-ICP-MS were also characterised in terms of their major elements by EMPA (Table 6.2) and SEM-EDX (Table 6.3), using the methodologies described in Appendix A. Major element characterisation is necessary for the reduction of raw LA-ICP-MS data as isotope intensity counts, to element concentrations in ppm. Section 6.4.1 specifically addresses the LA-ICP-MS data reduction process.

Table 6.1
The number of LA-ICP-MS analyses per vein generation, sample and mineral type. Sub-totals of analyses for each vein generation are shown, with total analyses per mineral at the bottom of the table. A total of 428 spot and 6 map analyses were completed.

Vein samples	Py	Py maps	Ccp	Gn	Tnt-Ttr	Sp	Apy
V2							
IC65-430	–	–	10	–	–	–	–
IC70-402	8	–	10	4	10	–	–
IC70-429	12	1	12	2	–	–	–
IC72-798	12	–	12	4	12	–	–
Sub-total	32	1	44	10	22	–	–
V3							
IC33-030-1	10	–	–	–	–	–	–
IC59-033-1	10	1	12	5	–	6	–
IC65-430	10	1	12	2	–	–	–
IC70-402	4	–	2	1	2	–	–
IC73-518	10	1	10	4	12	–	–
Sub-total	44	3	36	12	14	6	–
V4							
IC65-430	–	–	10	–	–	–	–
IC71-784	–	–	12	4	–	–	–
IC71-970-2	–	–	10	3	–	–	–
Sub-total	–	–	32	7	–	–	–
V5							
IC63-791	–	–	7	1	13	–	–
IC69-598	–	–	16	5	16	–	–
Sub-total	–	–	23	6	29	–	–
V6							
IC33-030-1	–	–	7	12	10	10	–
IC37-157-2	10	1	10	12	–	10	–
Sub-total	10	1	17	24	10	20	–
V7							
IC66-073	10	1	–	–	–	–	20
Total	96	6	152	59	75	26	20

As noted in Section 6.2, major element characterisation by EMPA took place before and after LA-ICP-MS, while major element characterisation by SEM-EDX took place after LA-ICP-MS. This was owing to the fixed timeslot for LA-ICP-MS, which meant that there was insufficient time available prior to LA-ICP-MS to undertake the complete major element characterisation of selected targets by EMPA/SEM-EDX. The analytical targets characterised by EMPA prior to LA-ICP-MS were: galena particles that may be destroyed during LA-ICP-MS owing to their small size (all galena data in Table 6.2), and the pyrite and chalcopyrite particles from three vein samples.

The remainder of the analytical targets were characterised by EMPA or SEM-EDX af-

Table 6.2

Summary of ore mineral EMPA data. Elements that were not analysed for in a specific ore mineral are marked 'n.a.', while elements below detection limits are marked '–'. Yellow text highlights the values used for reduction of the LA-ICP-MS data. Bracketed numbers indicate the number of analyses per mineral and vein generation.

All data in wt.%	S	Fe	Co	Ni	Cu	As	Se	Ag	Pb	Bi	Total
Pyrite (41)											
Mean	53.41	47.53	0.02	0.03	0.15	0.56	n.a.	n.a.	0.17	n.a.	101.48
Median	53.46	47.59	0.02	0.02	0.03	0.13	n.a.	n.a.	0.16	n.a.	101.58
Std. Dev.	0.57	0.53	0.01	0.02	0.17	0.72	n.a.	n.a.	0.06	n.a.	0.70
V2 mean (6)	53.31	47.19	–	0.02	0.17	0.02	n.a.	n.a.	0.23	n.a.	100.88
V3 mean (15)	53.40	47.55	0.02	0.05	0.16	0.72	n.a.	n.a.	0.19	n.a.	101.57
V6 mean (10)	53.72	47.77	–	0.02	0.02	0.04	n.a.	n.a.	0.14	n.a.	101.64
V7 mean (10)	53.19	47.46	0.02	0.02	0.25	0.77	n.a.	n.a.	0.14	n.a.	101.57
Chalcopyrite (58)											
Mean	34.41	30.37	0.02	0.02	34.42	0.04	n.a.	n.a.	0.11	n.a.	99.32
Median	34.52	30.59	0.01	0.01	34.5	0.04	n.a.	n.a.	0.10	n.a.	99.54
Std. Dev.	0.44	0.76	0.01	0.01	0.96	0.04	n.a.	n.a.	0.05	n.a.	1.68
V2 mean (16)	34.14	29.88	0.02	0.02	34.93	0.04	n.a.	n.a.	0.10	n.a.	99.06
V3 mean (17)	34.55	30.71	0.02	0.02	34.24	0.05	n.a.	n.a.	0.13	n.a.	99.64
V4 mean (15)	34.52	30.54	0.01	0.01	34.31	0.06	n.a.	n.a.	0.12	n.a.	99.49
V6 mean (10)	34.44	30.30	0.01	0.01	34.11	0.03	n.a.	n.a.	0.10	n.a.	98.96
Galena (34)											
Mean	11.11	n.a.	n.a.	n.a.	n.a.	n.a.	4.80	0.25	82.14	0.48	98.77
Median	12.40	n.a.	n.a.	n.a.	n.a.	n.a.	1.33	0.18	83.46	0.34	99.49
Std. Dev.	2.60	n.a.	n.a.	n.a.	n.a.	n.a.	5.88	0.39	4.20	0.67	2.16
V2 mean (7)	8.88	n.a.	n.a.	n.a.	n.a.	n.a.	9.35	0.07	79.58	0.19	98.08
V3 mean (8)	12.30	n.a.	n.a.	n.a.	n.a.	n.a.	1.90	0.24	82.06	0.44	96.94
V4 mean (5)	6.81	n.a.	n.a.	n.a.	n.a.	n.a.	15.11	0.98	74.92	1.72	99.54
V5 mean (4)	12.57	n.a.	n.a.	n.a.	n.a.	n.a.	1.48	0.03	85.61	0.06	99.75
V6 mean (10)	13.27	n.a.	n.a.	n.a.	n.a.	n.a.	0.10	0.10	86.22	0.25	99.94

(continued on next page)

Table 6.2
(continued)

All data in wt.%	S	Fe	Co	Ni	Cu	As	Se	Ag	Pb	Bi	Total
Arsenopyrite (20 – V7 only)											
Mean	19.73	34.71	0.03	0.07	0.07	45.95	n.a.	n.a.	0.08	n.a.	100.57
Median	18.92	34.50	0.02	0.02	0.06	46.52	n.a.	n.a.	0.07	n.a.	100.73
Std. Dev.	2.15	0.80	0.03	0.07	0.06	3.60	n.a.	n.a.	0.05	n.a.	1.33

Table 6.3

Summary of tennantite-tetrahedrite and sphalerite SEM-EDX data. Yellow text highlights the Zn value used for reduction of the sphalerite LA-ICP-MS data; tennantite-tetrahedrite data was reduced using the Cu value of each individual mineral occurrence. Bracketed numbers indicate the number of analyses per mineral and vein generation.

All data in wt.%	S	Fe	Cu	Zn	As	Ag	Cd	Sb	Bi	Total
Tennantite-tetrahedrite (72)										
Mean	28.4	2.4	40.2	5.7	14.0	1.1	0.3	11.4	–	102.5
Median	28.7	2.3	40.7	5.8	16.2	1.1	0.3	8.1	–	102.5
Std. Dev.	0.9	1.3	1.5	1.1	5.4	0.5	0.0	7.3	–	1.4
V2 mean (22)	27.9	2.3	40.4	5.5	11.0	–	–	15.6	–	102.7
V3 mean (11)	28.5	4.0	38.8	5.1	14.1	0.8	–	11.3	–	102.4
V5 mean (29)	29.2	2.4	41.5	5.7	18.8	0.4	0.3	4.7	–	102.4
V6 mean (10)	27.3	0.9	38.0	6.9	6.7	1.5	–	21.5	–	102.8
Sphalerite (27)										
Mean	34.6	0.6	0.6	64.0	–	–	1.0	–	1.4	100.5
Median	34.7	0.4	0.5	64.6	–	–	1.0	–	1.4	101.0
Std. Dev.	0.3	0.4	0.3	1.8	–	–	0.2	–	0.0	1.9
V3 mean (7)	34.6	0.9	0.9	63.8	–	–	1.3	–	–	100.9
V6 mean (20)	34.6	0.4	0.5	64.1	–	–	0.9	–	1.4	100.3

ter LA-ICP-MS had been completed. Pyrite, chalcopyrite, and arsenopyrite present in three vein samples were analysed by EMPA. Access limitations owing to the pandemic meant that not all ore minerals could be analysed by EMPA, and the remaining ore minerals were therefore analysed by SEM-EDX. Nevertheless, the LA-ICP-MS laboratory manager confirmed that SEM-EDX data would be sufficient for reduction of the LA-ICP-MS data (S. McClenaghan, pers. comm., 2020). Tennantite-tetrahedrite and sphalerite (Table 6.3), and the remaining pyrite, chalcopyrite, and galena particles not characterised by EMPA were characterised by SEM-EDX. The pyrite, chalcopyrite, and galena SEM-EDX data were not used for reduction of the LA-ICP-MS data, and are therefore presented in Appendix A.

There are some limitations to the EMPA and SEM-EDX data, in terms of their comparability to the LA-ICP-MS data. Major element data was collected from the same ore mineral particles that underwent trace element analysis. Spots for LA-ICP-MS were aligned on the same points that were previously analysed by EMPA; however, there was spot misalignment between ablation pits and the EMPA/SEM-EDX analysis carried out after LA-ICP-MS. This was because the spots for EMPA/SEM-EDX analysis were in many cases placed adjacent to ablation pits to avoid sputtered ore mineral ejecta that often surrounds ablation pits. The ejecta were avoided as they may not represent the composition of the spot site, potentially originating from a greater depth within the mineral. However, even in ideal scenarios where spots are aligned between LA-ICP-MS and EMPA/SEM-EDX, comparable analysis of the same material volume is not possible, because LA-ICP-MS ablates a pit both wider and deeper than the spot analyses of EMPA/SEM-EDX. Therefore, there is necessarily a degree of uncertainty as to the equivalence of analytical spots of LA-ICP-MS and EMPA/SEM-EDX.

The SEM-EDX data in particular may also be limited by its accuracy. Major element data collected by SEM-EDX has some advantages over the EMPA data, because the elements do not have to be pre-determined prior to quantification, meaning that all elements present above lower limits of detection are quantified. However, SEM-EDX analysis works with higher limits of detection than EMPA, meaning that the concentration data is likely to be less accurate than the EMPA data. Despite this, the totals for sphalerite in Table 6.3 are close to 100 wt.%, indicating that the major element characterisation is accurate. On the other hand, the data for tennantite-tetrahedrite is consistently above 100 wt.%, suggesting that there may have been issues with calibration during SEM-EDX analysis of these particles. Nevertheless, the totals remain within a reasonable field of accuracy (<103 wt.%).

The EMPA and SEM-EDX data highlight some compositional variations in the ore

minerals from the Iron Cap vein generations. In particular, galena often hosts weight percent amounts of Se, and in some cases, the Se-enriched Pb-S minerals can be classified as clausthalite (PbSe) rather than galena, because they have atomic Se:S ratios >1 (Figure 6.1A). The highest concentrations of Se are observed in V4 galena-clausthalite, with mean Se concentrations of 15.11 wt.%; clausthalite is only identified in V4 vein samples. Galena from V2 also contains elevated Se, with a mean of 9.35 wt.% Se. Meanwhile, V3 and V5 galena exhibit similar mean Se concentrations of 1.9 wt.% and 1.48 wt.% Se, respectively. Galena from V6 is the most Se-poor, hosting mean concentrations <0.097 wt.% Se. Figure 6.1A shows that Se and S in galena-clausthalite exhibit a strong negative correlation, while Figure 6.1B shows that Ag and Bi are also present in galena, and that these elements exhibit a strong positive correlation.

Pyrite, chalcopyrite, and arsenopyrite show little variation in their major element compositions; only As is variably enriched in pyrite from V3 and V7. Meanwhile, the SEM-EDX data shows that the composition of tennantite-tetrahedrite varies between veins, principally in terms of As and Sb, but also to a lesser extent in Fe, Cu, Zn, and Ag (Table 6.3). Figure 6.2 illustrates that the Fe:Zn ratio and As:Sb ratio of tennantite-tetrahedrite varies between veins, but that both element pairs are negatively correlated. In Figure 6.2A, V2 tennantite-tetrahedrite spans the entire range of Zn contents, in two groups; one around 1 apfu Fe and Zn, and the other around 0.3 apfu Fe and 1.7 apfu Zn. Meanwhile, V3 tennantite-tetrahedrite is generally more Fe-rich, and deviates from the negative correlation line. Both V5 and V6 tennantite-tetrahedrite form constrained

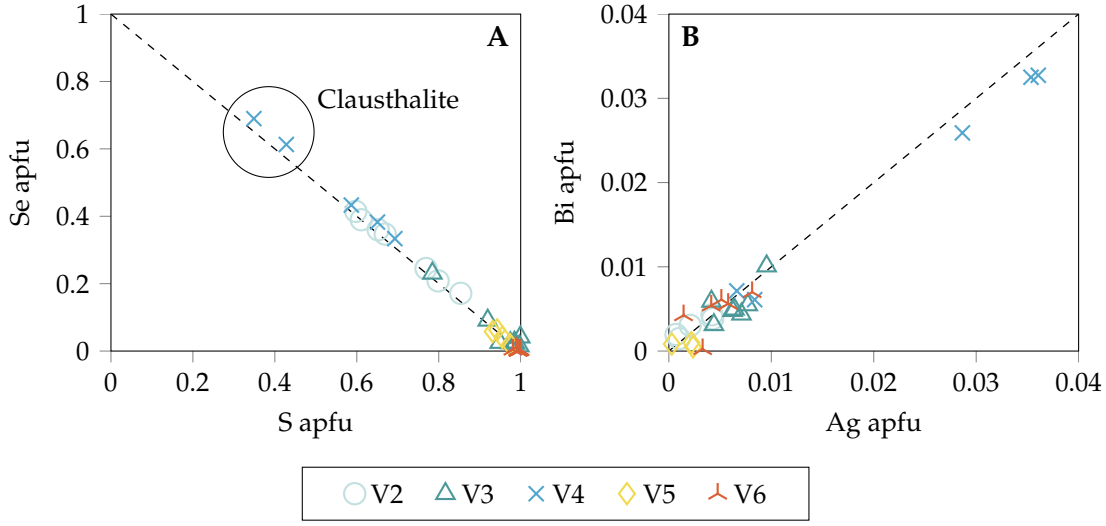

Figure 6.1. Co-variation of selected elements in galena, from EMPA data converted to atoms per formula unit (apfu), with S vs. Se in A, and Ag vs. Bi in B. Dashed lines represent perfect negative correlations (A) and positive correlations (B). The black circle in A highlights the two V4 occurrences of clausthalite, which are so classified because they have a higher atomic proportion of Se than S (i.e., >0.5 apfu Se).

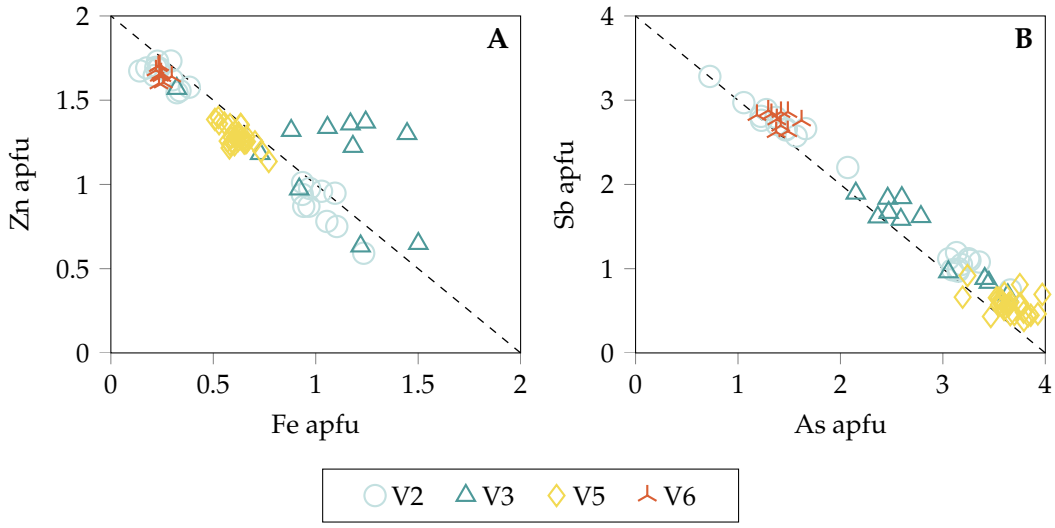

Figure 6.2. Co-variation of selected elements in tennantite-tetrahedrite, from SEM data converted to apfu, with Fe vs. Zn in A, and As vs. Sb in B. Dashed lines represent perfect negative correlations. In B, tennantite can be classified at ≥2 apfu As, while tetrahedrite can be classifed at ≥2 apfu Sb.

groups centred on 0.7 apfu Fe and 1.3 apfu Zn, and 0.3 apfu Fe and 1.7 apfu Zn, respectively.

In Figure 6.2B, V5 tennantite-tetrahedrite is shown to be the most As-rich and Sb-poor, with V6 tennantite-tetrahedrite Sb-rich and As-poor. Tennantite-tetrahedrite from V2 and V3 vary between ∼0.5-3.5 apfu As and Sb, with V2 tennantite-tetrahedrite forming two main groups; one As-rich and one Sb-rich. V3 tennantite-tetrahedrite is mostly concentrated around 2.5 apfu As and 1.7 apfu Sb. Table 6.3 shows that Ag is most enriched in tennantite-tetrahedrite from V3 and V6 veins; V2 tennantite-tetrahedrite lacks Ag, while V5 tennantite-tetrahedrite exhibits a lower mean value than V3 and V6. Conversely, Cu has lower mean values in tennantite-tetrahedrite from V3 and V6, than V2 and V5. The SEM-EDX data also shows that sphalerite hosts Fe, Cu and Cd, with V3 sphalerite exhibiting higher mean values for all of these elements than V6 sphalerite (Table 6.3).

6.4 LA-ICP-MS spot data

The LA-ICP-MS analytical process is described in full in Appendix A.

6.4.1 Spot data reduction

The LA-ICP-MS data was reduced from its raw form as isotope intensity counts, to element concentrations in ppm. Owing to software limitations, the data reduction process was carried out by the laboratory technician from the Raw Materials Characterisation Laboratory of Trinity College Dublin, where the LA-ICP-MS analysis took place. Ele-

ments below detection limits were automatically excluded from the reduced dataset.

During data reduction, the laboratory technician deemed it necessary to reject 120 spot analyses for the reasons outlined below, meaning that only 308 out of 428 spot analyses were successfully reduced (Table 6.4). Spot analyses of pyrite were rejected if the Fe channel dropped abruptly during the time interval of a single analysis, or when the standards used indicated that there was a sensitivity problem over the course of a run (i.e., multiple spot analyses). Application of these quality control criteria meant that 32 pyrite spot analyses were rejected, and that none of the data from pyrite particles in V2 vein sample IC70-429, and V3 vein sample IC65-430 were successfully reduced, following problems of standard acquisition during these runs. Chalcopyrite analyses were rejected when prominent signal spikes of As or Pb were present, because these indicate that large inclusions containing these elements (e.g., tennantite-tetrahedrite and galena) were also ablated. While 38 chalcopyrite analyses were rejected, all vein samples containing chalcopyrite had at least some data successfully reduced. Almost half the galena analyses (27) were rejected, owing an abrupt drop in the Pb channel during the acquisition of an individual analysis. This may be attributed to the small size of the galena particles in many of the vein samples; complete ablation of galena followed by ablation of the surrounding matrix was likely during the analysis. Similarly, tennantite-tetrahedrite, sphalerite, and arsenopyrite analyses were rejected when the major element channels (Cu, Zn, and Fe, respectively) dropped abruptly, again likely related to the small size and total ablation of the particles, meaning that 13 tennantite-tetrahedrite, 7 sphalerite, and 3 arsenopyrite analyses were rejected from the reduced data.

The analyses that were not rejected were reduced using the median values of major elements from the EMPA or SEM-EDX data, or individual major element values for each ore mineral particle. Pyrite, chalcopyrite, galena and arsenopyrite analyses were reduced using the median values of Fe (pyrite, chalcopyrite, arsenopyrite) or Pb (galena), from the EMPA data of each respective ore mineral (yellow text in Table 6.2). Tennantite-tetrahedrite data were reduced using the Cu value of each individual mineral particle from the SEM-EDX data, while sphalerite data were reduced using the median Zn value from the SEM-EDX data (yellow text in Table 6.3).

Ideally, the data for all minerals would have been reduced using the same methodology as for tennantite-tetrahedrite, because the use of individual major element compositions for each particle means that major element variations between particles are accounted for. On the contrary, the use of a median value means that major element compositional variations between individual particles are not well accounted for. Furthermore, the pyrite, chalcopyrite, and galena median values do not include major element data

Table 6.4
The number of reduced LA-ICP-MS analyses per vein generation, sample and mineral type. Sub-totals of analyses for each vein generation are shown, with total analyses per mineral at the bottom of the table. A total of 308 spot and 6 map analyses were reduced.

Vein samples	Py	Py maps	Ccp	Gn	Tnt-Ttr	Sp	Apy
V2							
IC65-430	–	–	8	–	–	–	–
IC70-402	8	–	10	1	10	–	–
IC70-429	–	1	11	–	–	–	–
IC72-798	10	–	12	1	12	–	–
Sub-total	18	1	41	2	22	–	–
V3							
IC33-030-1	9	–	–	–	–	–	–
IC59-033-1	9	1	12	1	–	2	–
IC65-430	–	1	6	2	–	–	–
IC70-402	4	–	2	–	2	–	–
IC73-518	9	1	2	2	5	–	–
Sub-total	31	3	22	5	7	2	–
V4							
IC65-430	–	–	10	–	–	–	–
IC71-784	–	–	9	2	–	–	–
IC71-970-2	–	–	9	1	–	–	–
Sub-total	–	–	28	3	–	–	–
V5							
IC63-791	–	–	6	–	10	–	–
IC69-598	–	–	4	–	16	–	–
Sub-total	–	–	10	–	26	–	–
V6							
IC33-030-1	–	–	4	11	7	9	–
IC37-157-2	9	1	9	11	–	8	–
Sub-total	9	1	13	22	7	17	–
V7							
IC66-073	6	1	–	–	–	–	17
Total	64	6	114	32	62	19	17

collected by SEM-EDX, meaning that not all mineral particles in the vein sample suite are represented, and the median values may not be applicable to the whole dataset. In particular, additional pyrite from V2 and V3 vein samples (55 particles), and chalcopyrite (96) and galena (24) from vein samples of V2-V6 are not included in the calculation of the median major element values, because these data were collected by SEM-EDX. Similarly, EMPA data for the LA-ICP-MS analyses that were excluded from the reduction process were still included in the calculation of the median major element values. The above factors highlight the fact that median values may not be representative of the major element compositions of each mineral particle; this has implications for the accuracy of the

LA-ICP-MS data (below). However, Table 6.2 shows that only marginal variations ($<\pm1$ wt.%) are evident between the mean major element values of different vein generations in terms of pyrite, chalcopyrite, sphalerite, and arsenopyrite; thus there are unlikely to be major accuracy implications for the data of these minerals. Meanwhile, galena is more challenging, as it shows large variations (in excess of ±8 wt.%) in terms of its Pb content, as discussed below.

Reduction of the raw LA-ICP-MS data was carried out using Iolite software and the Trace_Elements Data Reduction Scheme (DRS). Limits of detection were calculated using the method of Pettke et al. (2012). Essentially, the DRS calculates the concentration of an unknown element using the following equation:

$$\text{Concentration (ppm)} = \frac{E_i}{N_i}\,\text{sample} \times \frac{E_c}{N_c}\,\text{standard} \times N_c\,\text{sample}$$

Where E_i is the intensity of an unknown element (in cps), N_i is the intensity of the normalisation element (in cps), E_c is the concentration of an unknown element (in ppm), and N_c is the concentration of the normalisation element (in ppm). For example, when calculating the concentration of Cu in pyrite, the equation would be used as follows:

$$\text{Cu concentration} = \frac{1500\,\text{cps Cu}}{700000\,\text{cps Fe}} \times \frac{134000\,\text{ppm Cu}}{156000\,\text{ppm Fe}} \times 475900\,\text{ppm Fe} = 875\,\text{ppm}$$

This is a simplification of the DRS, which also includes additional features such as baseline subtraction to improve the accuracy of the reduced data. Nevertheless, the above equations show that, when using a median value, all analyses of the same mineral are corrected to the same normalisation element value (e.g., all pyrite was corrected to 47.59 wt.% Fe). If the value of the normalisation element is not accurate, trace element concentrations may be over- or under-corrected, depending on the difference between the actual and provided value of the normalisation element.

In particular, galena particles show large variations from the median Pb value used for normalisation. The galena with lower-than-median weight percent of Pb in the EMPA data also have high Se contents (e.g., V4 galena in Table 6.2). This is because the relative atomic mass of Se ($\sim$78) is much greater than that of S ($\sim$32), meaning that substituting one atom of S for one of Se increases the overall weight of the galena, and means that the weight percent of Pb decreases in turn, even though the number of Pb atoms has not changed. Therefore, reducing the LA-ICP-MS data of Se-rich galena using a value of Pb that is higher than the actual value of Pb in the galena crystal means that the trace element concentrations are likely to have been over-corrected to higher values. On the contrary, galena with higher-than-median Pb values in the EMPA data (e.g., V6 galena in

Table 6.2) are likely to have been under-corrected, and so are likely to exhibit lower trace element concentrations.

This is also true for the other ore minerals that with major element compositions that vary from the median value used for normalisation, although only galena varies to such a degree owing to its Se content. This emphasises the importance of reducing the LA-ICP-MS data using representative major element data, ideally using individual major element data for each particle, as noted above. Indeed, re-processing of the raw data using individual major element data for each particle would yield more accurate results, but time and software access limitations preclude the possibility for this thesis.

6.4.2 Reduced spot data

The reduced LA-ICP-MS spot data is summarised in Table 6.5 and discussed throughout the following sections. Median values are preferred over mean values owing to the limited number of LA-ICP-MS analyses for each ore mineral, and the general skew in the mean values to higher concentrations (i.e., means are regularly greater than medians), due to outliers and ranges in concentration over multiple orders of magnitude. The median values for each trace element in each ore mineral from the different vein generations are reported in the following sections, while the mean values are recorded in Table 6.5.

A qualitative assessment of the raw LA-ICP-MS data was also carried out. Each trace element identified in each mineral particle was categorised based on the shape of the ablation profile, to provide an indication of the mode of occurrence of each trace element. The different categories and their definitions are outlined in Table 6.6, while example profiles that correspond to each category are illustrated in Figure 6.3. Most studies that utilise LA-ICP-MS analysis carry out a similar qualitative assessment (e.g., Cook et al., 2011; George et al., 2015, 2018a), designating profile traces as smooth/flat or spiky, which are invoked to indicate that an element is present as lattice incorporations, or as discrete inclusions, respectively. Spiky profiles are regularly excluded from datasets, because they are not interpreted to represent the composition of the target mineral; however, this can lead to a loss of information, as some trace elements might only be present as inclusions, and therefore not detected in datasets if all spiky profiles are excluded.

This thesis assigns additional profile trace classifications in an effort to generate a more comprehensive and quantitative dataset that can be utilised to more accurately describe the occurrence of trace elements within ore minerals. While this qualitative assessment does not provide conclusive proof of trace element hosting as lattice incorporations and/or discrete inclusions, it may be used to highlight which elements are more likely to be present as one or the other. Together with the concentration data, the ablation profile

Table 6.5

Summary of ore mineral LA-ICP-MS data. Bracketed numbers indicate the number of analyses per mineral and vein generation. Mean lower limits of detection (LOD) are provided for each ore mineral. Elements not analysed, or those not above minimum detection limits are marked '–', while 'n.a.' indicates data is not applicable (i.e., element used for normalisation).

All data in ppm	V	Mn	Fe	Co	Ni	Cu	Zn	Ga	Ge	As	Se	Mo	Ag	Cd	In	Sb	Sn	Te	W	Au	Hg	Tl	Pb	Bi
Pyrite (64)																								
Max	58.00	–	n.a.	8750.00	147.00	6400.00	270.00	31.00	13.00	55100.00	1720.00	2.52	77.00	–	–	3120.00	17.60	36.30	8.00	83.60	83.10	–	1220.00	72.00
Min	2.50	–	n.a.	0.48	7.30	2.80	25.00	1.10	1.59	6.60	2.50	0.66	0.31	–	–	0.64	3.70	1.50	0.32	0.27	1.29	–	0.07	0.07
No.	2	–	n.a.	47	20	55	11	4	7	47	54	6	27	–	–	32	23	31	16	16	9	–	53	38
Mean	30.25	–	n.a.	389.70	31.64	678.74	106.54	9.60	4.31	5774.04	328.23	1.57	8.37	–	–	321.27	8.10	9.28	1.29	9.89	31.95	–	70.95	5.42
Median	30.25	–	n.a.	32.00	19.55	35.00	51.00	3.15	3.50	508.00	193.50	1.54	4.11	–	–	13.90	7.40	6.80	0.78	1.15	7.80	–	6.40	0.41
Std. Dev.	27.75	–	n.a.	1430.72	31.85	1623.91	84.89	12.40	3.64	11349.07	371.00	0.72	14.47	–	–	712.49	3.97	9.22	1.79	22.18	33.81	–	185.78	12.56
V2 mean (18)	–	–	n.a.	20.87	41.50	1919.54	137.60	–	–	120.43	582.39	0.83	7.41	–	–	25.99	7.47	8.77	0.79	0.75	1.29	–	36.00	14.24
V3 mean (31)	–	–	n.a.	746.28	29.68	86.45	101.98	1.70	4.97	6714.38	255.73	1.85	6.14	–	–	523.77	8.38	6.61	2.46	27.11	46.97	–	110.75	1.43
V6 mean (9)	–	–	n.a.	17.20	9.80	4.67	–	–	–	1037.88	110.31	–	2.67	–	–	–	8.73	18.87	–	5.14	–	–	41.15	7.92
V7 mean (6)	30.25	–	n.a.	8.81	–	57.33	38.00	17.50	3.43	14610.00	37.03	1.15	27.12	–	–	190.45	6.85	3.50	1.12	1.07	2.25	–	38.03	0.23
Mean LOD	2.38	–	n.a.	0.63	7.87	4.31	24.67	1.45	1.93	8.39	8.73	2.41	0.61	5.53	–	0.80	5.77	2.07	0.52	0.59	1.14	–	0.62	0.09
Chalcopyrite (114)																								
Max	–	–	n.a.	550.00	–	442000.00	142.00	264.00	13.50	144.00	831.00	81.00	252.00	–	47.80	37.30	134.00	10.50	–	6.10	7.10	–	242.00	16.40
Min	–	–	n.a.	1.90	–	305000.00	48.00	7.90	2.80	16.50	17.10	1.30	1.34	–	0.78	1.55	13.20	6.10	–	1.38	4.00	–	0.94	0.16
No.	–	–	n.a.	3	–	114	27	8	6	8	109	3	90	–	114	34	30	2	–	5	5	–	93	56
Mean	–	–	n.a.	185.47	–	397140.35	79.93	51.03	7.70	62.94	226.17	28.27	61.72	–	9.30	10.04	30.13	8.30	–	3.16	4.94	–	12.70	2.15
Median	–	–	n.a.	4.50	–	400500.00	81.00	12.00	8.00	61.50	124.00	2.50	47.10	–	6.60	5.65	21.95	8.30	–	2.84	4.70	–	4.90	1.22
Std. Dev.	–	–	n.a.	257.77	–	20719.46	19.56	82.01	3.81	36.64	188.84	37.29	54.11	–	9.23	10.92	22.60	2.20	–	1.66	1.14	–	28.18	2.85
V2 mean (41)	–	–	n.a.	–	–	399195.12	63.86	–	12.10	–	272.75	41.15	54.63	–	8.47	10.52	30.66	6.10	–	2.37	–	–	11.50	2.07
V3 mean (22)	–	–	n.a.	550.00	–	393227.27	76.20	9.55	–	62.50	117.50	–	44.25	–	8.58	11.84	26.98	10.50	–	6.10	–	–	21.12	2.18
V4 mean (28)	–	–	n.a.	1.90	–	397250.00	94.18	9.10	2.80	25.00	361.11	–	89.43	–	3.77	5.03	–	–	–	–	4.94	–	5.39	2.70
V5 mean (10)	–	–	n.a.	4.50	–	382200.00	–	–	–	84.25	88.78	–	19.95	–	13.55	13.86	30.38	–	–	2.49	–	–	22.89	1.27
V6 mean (13)	–	–	n.a.	–	–	408538.46	73.50	76.00	6.40	16.50	24.78	2.50	68.54	–	21.76	8.78	–	–	–	–	–	–	10.97	1.53
Mean LOD	–	–	n.a.	2.64	40.98	22.51	80.93	4.29	9.24	29.69	31.10	2.33	2.33	18.17	0.30	2.48	16.34	11.46	–	2.15	5.81	–	1.63	0.56
Galena (32)																								
Max	–	–	–	37.00	66.00	11900.00	3800.00	24.00	6.10	750.00	500000.00	–	32900.00	183.00	0.43	183.00	2520.00	8300.00	–	20.10	22.50	–	n.a.	67400.00
Min	–	–	–	0.30	10.00	0.92	4.90	0.16	0.27	0.90	865.00	–	132.00	1.80	0.02	1.20	1.36	2.60	–	0.11	0.47	–	n.a.	54.00
No.	–	–	–	8	6	30	13	9	13	14	32	–	32	31	6	32	31	32	–	18	15	–	n.a.	32
Mean	–	–	–	11.87	35.83	627.35	392.61	3.65	1.00	68.17	51131.78	–	2882.68	51.83	0.17	60.23	169.92	577.92	–	1.79	4.46	–	n.a.	5728.68
Median	–	–	–	1.85	30.00	12.75	34.00	1.41	0.53	5.25	2735.00	–	2275.00	49.10	0.13	10.35	8.30	25.30	–	0.31	2.70	–	n.a.	4535.00
Std. Dev.	–	–	–	14.49	22.27	2216.25	1017.18	7.21	1.49	189.92	121495.26	–	5672.63	32.41	0.14	67.38	515.44	1740.29	–	4.52	5.33	–	n.a.	11618.12
V2 mean (2)	–	–	–	–	20.00	477.35	41.00	–	–	41.00	153500.00	–	671.50	1.80	–	8.45	891.00	3463.50	–	1.84	3.35	–	n.a.	1589.00
V3 mean (5)	–	–	–	–	–	28.44	47.35	–	0.58	376.85	16126.00	–	1778.00	50.96	–	29.04	31.17	90.10	–	0.68	11.69	–	n.a.	3542.60
V4 mean (3)	–	–	–	11.03	10.00	4033.33	1000.00	12.80	2.42	59.00	400333.33	–	15153.33	27.03	0.26	4.40	1068.43	3532.33	–	7.34	6.40	–	n.a.	30063.33
V6 mean (22)	–	–	–	12.38	46.25	281.18	440.91	1.03	0.56	10.07	2163.05	–	1661.49	57.68	0.13	79.64	7.07	23.59	–	0.46	2.20	–	n.a.	3283.49
Mean LOD	–	–	–	0.31	6.21	2.22	10.12	0.49	3.95	6.77	4.26	–	0.17	1.35	0.02	0.87	1.08	0.65	–	0.17	0.97	–	n.a.	0.06

(continued on next page)

Table 6.5

(continued)

All data in ppm	V	Mn	Fe	Co	Ni	Cu	Zn	Ga	Ge	As	Se	Mo	Ag	Cd	In	Sb	Sn	Te	W	Au	Hg	Tl	Pb	Bi
Tennantite-tetrahedrite (62)																								
Max	–	–	40000.00	82.10	–	n.a.	121400.00	–	1.91	383000.00	1490.00	–	12670.00	5100.00	76.80	284000.00	1110.00	2780.00	–	1.25	2780.00	–	1240.00	14360.00
Min	–	–	4900.00	3.50	–	n.a.	42200.00	–	1.31	73800.00	35.60	–	30.60	114.00	1.37	17330.00	6.00	3.90	–	1.25	212.00	–	0.41	0.65
No.	–	–	62	23	–	n.a.	62	–	2	62	61	–	62	62	62	62	59	61	–	1	62	–	37	62
Mean	–	–	19087.26	39.33	–	n.a.	85941.94	–	1.61	199587.10	590.67	–	2827.52	2201.39	10.67	122969.84	146.85	361.63	–	1.25	867.58	–	55.24	622.15
Median	–	–	20050.00	38.40	–	n.a.	87500.00	–	1.61	229500.00	423.00	–	1775.00	2325.00	4.65	91300.00	47.50	120.00	–	1.25	791.50	–	8.70	247.00
Std. Dev.	–	–	10024.59	20.10	–	n.a.	20066.85	–	0.30	81685.08	409.20	–	3332.12	1206.43	12.92	85977.74	239.26	600.83	–	0.00	460.81	–	199.49	1871.24
V2 mean (22)	–	–	18964.55	44.63	–	n.a.	87413.64	–	–	153727.27	1075.50	–	808.79	1185.32	17.90	177118.18	303.39	774.23	–	1.25	969.64	–	21.59	1227.59
V3 mean (7)	–	–	25997.14	–	–	n.a.	72771.43	–	1.61	191142.86	356.57	–	4117.44	2982.71	5.80	111071.43	70.77	193.81	–	–	853.00	–	31.53	1079.81
V5 mean (26)	–	–	20596.92	–	–	n.a.	84603.85	–	–	267115.38	367.15	–	1928.88	2452.31	7.84	48116.54	51.99	123.86	–	–	910.42	–	13.26	152.89
V6 mean (7)	–	–	6955.71	4.03	–	n.a.	99457.14	–	–	101342.86	54.68	–	11220.00	3681.43	3.28	242714.29	41.12	81.91	–	–	402.29	–	244.67	4.64
Mean LOD	–	–	269.50	2.10	35.65	n.a.	65.94	6.29	7.45	189.83	24.49	–	1.43	9.31	0.18	5.98	10.23	2.81	–	1.54	7.17	–	2.90	0.24
Sphalerite (19)																								
Max	–	155.00	3520.00	54.20	–	1210.00	n.a.	349.00	7.50	36.00	105.00	–	66.00	10030.00	88.90	118.00	3.30	–	–	2.20	168.00	0.37	30000.00	2.39
Min	–	49.00	792.00	1.27	–	13.90	n.a.	0.47	1.17	4.50	5.30	–	0.94	5850.00	9.90	1.40	2.90	–	–	0.75	35.00	0.13	1.65	0.11
No.	–	18	19	6	–	19	n.a.	13	6	12	15	–	19	19	19	15	3	–	–	2	19	10	19	10
Mean	–	87.00	1860.42	18.71	–	453.42	n.a.	42.54	2.74	15.63	24.55	–	21.02	7851.58	34.87	26.12	3.07	–	–	1.48	82.91	0.23	1696.07	0.79
Median	–	79.50	1420.00	1.60	–	361.00	n.a.	3.83	2.05	17.40	11.60	–	15.60	7930.00	33.30	12.80	3.00	–	–	1.48	75.10	0.17	22.00	0.70
Std. Dev.	–	27.25	958.79	24.36	–	385.56	n.a.	92.62	2.18	9.32	31.65	–	18.60	1344.22	21.14	32.38	0.17	–	–	0.73	45.41	0.09	6682.92	0.63
V3 mean (2)	–	49.00	1520.00	53.15	–	577.50	n.a.	0.54	7.50	19.00	103.50	–	10.65	9545.00	10.15	2.10	2.90	–	–	2.20	166.50	0.27	5.65	0.70
V6 mean (17)	–	89.24	1900.47	1.49	–	438.82	n.a.	46.04	1.79	15.32	12.40	–	22.24	7652.35	37.78	29.82	3.15	–	–	0.75	73.08	0.22	1894.94	0.82
Mean LOD	–	28.00	97.95	1.08	11.81	3.21	n.a.	0.37	1.30	5.41	5.37	–	0.38	6.52	0.06	0.81	2.42	–	–	0.59	1.10	0.15	0.38	0.07
Arsenopyrite (17 – V7 only)																								
Max	279.00	–	n.a.	280.00	230.00	1400.00	142.00	–	–	1630000.00	710.00	160.00	106.00	41.00	–	109000.00	371.00	1010.00	–	960.00	32.00	–	576.00	7.00
Min	9.40	–	n.a.	13.60	23.00	149.00	49.00	–	–	247000.00	74.00	1.70	2.79	41.00	–	2450.00	11.60	9.00	–	3.90	8.70	–	97.00	0.44
No.	10	–	n.a.	15	13	17	3	–	–	17	12	6	15	1	–	17	12	15	–	17	7	–	16	11
Mean	50.22	–	n.a.	88.99	94.17	809.12	84.00	–	–	919235.29	279.33	28.83	24.71	41.00	–	26162.35	99.05	192.54	–	169.38	20.09	–	214.19	2.02
Median	17.15	–	n.a.	69.00	70.00	860.00	61.00	–	–	865000.00	199.50	2.65	16.90	41.00	–	21300.00	77.50	92.00	–	64.00	17.10	–	174.00	1.48
Std. Dev.	78.50	–	n.a.	78.12	57.42	391.15	41.30	–	–	342608.08	203.79	58.66	24.79	0.00	–	28463.30	93.45	256.68	–	244.10	8.56	–	116.67	1.76
Mean LOD	10.70	–	n.a.	8.06	54.71	14.41	74.06	–	–	1326.47	147.35	3.20	4.31	17.23	–	5.54	16.45	70.88	–	9.43	42.97	–	51.05	1.18

Table 6.6
Definition of LA-ICP-MS profile trace classifications.

Profile trace	Definition
Smooth and matched	Smooth profile correlated to a key element's profile (element used for normalisation, e.g., Fe in pyrite).
Smooth and unmatched	Smooth profile de-correlated (partially or wholly) to a key element's profile. Generally has a signal over most of the interval, otherwise classed as spiky.
Spiky and similar	Spiky profile, but some parts match a key element's profile, and a signal is present throughout most of the interval
Spiky	Spiky profile throughout, unmatched to a key elements profile
Singular spikes	A sudden spike in the profile, typically with other associated elements spiking too.
Unmatched	Profile antithetic to that of a key elements profile.

assessment allows a greater understanding of trace element deportment within the ore mineral suite. The profile trace classifications for each trace element in each of the ore minerals are presented throughout the following sections, while there is discussion of the implication of these classifications in Chapter 8.

The trace element data is also reported in the following sections, primarily as summary boxplots of concentrations. These boxplots include all data, regardless of the profile trace classifications. This is due to the fact that these are interpretive assignments, and may not accurately represent the hosting mechansm of a trace element within an ore mineral. If the trace element data for LA-ICP-MS analyses classified as unmatched, singular spikes, and potentially spiky, were excluded from the dataset there would be a shift in the statistics displayed in boxplots. However, it is deemed unlikely that there would be major changes in the reported maximums, minimums, means, ranges, and interquartile ranges for most trace elements of significance (i.e., those that are present well above detection limits). This is because most of the elements with high proportions of spiky, or singular spike, profile classifications are close to the lower limits of detection, whereas the remaining elements with high proportions of spiky and similar, smooth and unmatched, or smooth and matched profile classifications are measured at concentrations well above the lower limits of detection – the statistics for these latter elements would be relatively unchanged with exclusion of the spikier profiles. Furthermore, during the data reduction process, analyses were excluded from the dataset when prominent signal spikes of other elements were observed (Section 6.4.1), meaning that further exclusion of data is not required to remove the obvious influence of inclusions on trace element concentrations.

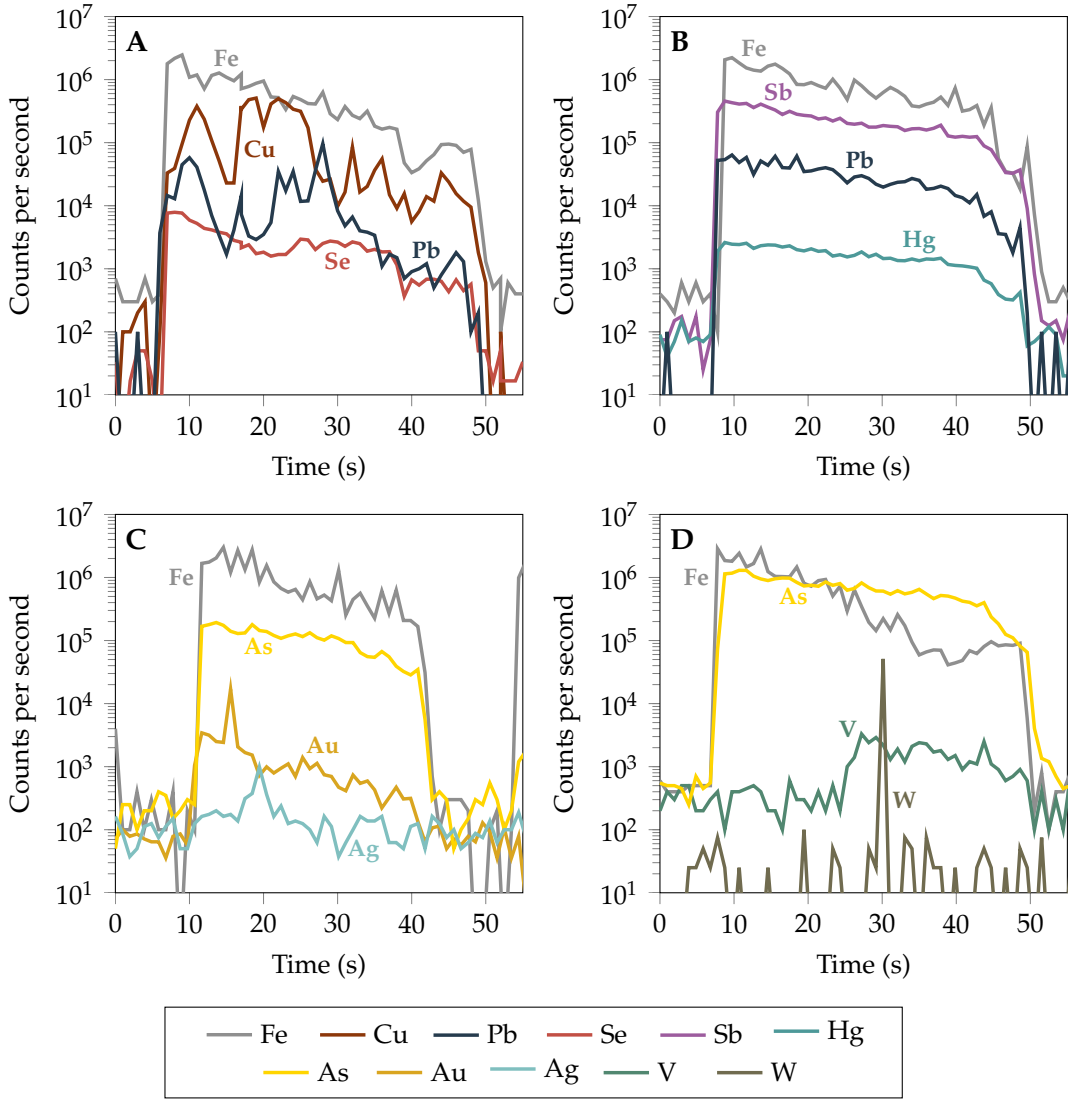

Figure 6.3. Example LA-ICP-MS profiles for pyrite, illustrating the different profile classifications. A) V2 pyrite crystal from sample IC72-798, showing a smooth and unmatched trace for Se, and a spiky trace for Cu and Pb. B) V3 pyrite crystal from sample IC73-518, showing a smooth and matched trace for Sb and Hg, and a spiky and similar trace for Pb. C) V6 pyrite crystal from sample IC37-157-2, showing a smooth and unmatched trace for As, a spiky and similar trace for Au, and a trace of singular spikes for Ag (one spike above the background at 20 s). D) V7 pyrite crystal from sample IC66-073, showing a smooth and matched trace for As, an unmatched trace for V, and a trace of singular spikes for W (one spike above background at 30 s); the second half of the profile (~25 s onwards) corresponds to arsenopyrite rather than pyrite.

6.4.3 Pyrite

A total of 64 pyrite analyses from V2, V3, V6, and V7 vein samples were reduced. The trace element concentrations recorded in pyrite are summarised in Figure 6.4. In terms of median trace element concentrations, As and Se are the most enriched in pyrite, at approximately 500 ppm and 200 ppm, respectively. The remaining trace elements have median concentrations <100 ppm, with V, Co, Ni, Cu, Zn, and Sb between 10-100 ppm, although V is only present in two pyrite particles. Gallium, Ge, Mo, Ag, Sn, Te, W, Au,

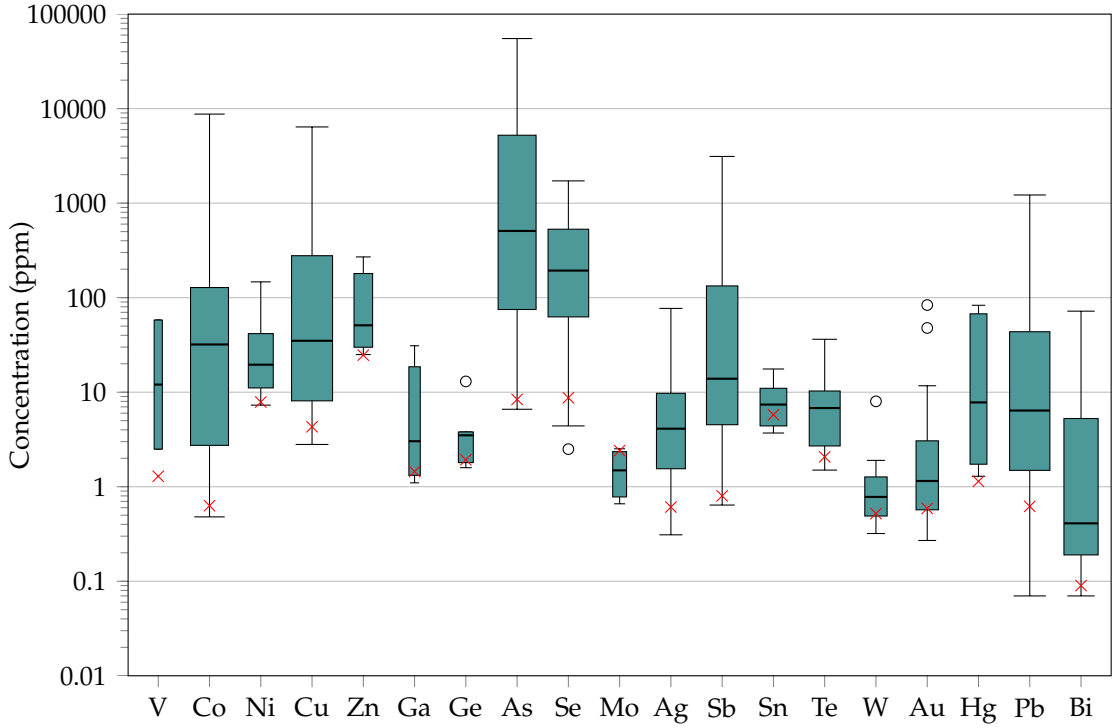

Figure 6.4. Variable width boxplot of trace elements in pyrite, measured by LA-ICP-MS. The boxplot illustrates the range of concentrations for each trace element (black lines with ticks), the interquartile range (IQR) that represents the middle 50% of the data (coloured boxes), and the median value of the dataset (horizontal black lines within the blue boxes). Box width is indicative of the number of pyrite samples containing the trace element, i.e. V has the minimum sample size of 2, while Cu has the maximum sample size of 55. Open circles represent outliers in the data, which are classified as more than 1.5 times the IQR above the upper quartile, or below the lower quartile, and are calculated in logarithmic space rather than by absolute values. A logarithmic outlier calculation results in fewer outliers classified at higher values, and more outliers classified at lower values, compared to outlier calculations using absolute values. Red crosses are mean lower limits of detection; no data below detection limits is shown.

Hg, Pb and Bi all exhibit median concentrations <10 ppm. While median values illustrate the general enrichment of trace elements, the wide range in concentrations for many of the trace elements shows that they are not consistent throughout the pyrite particles analysed. In particular, As is sometimes enriched to weight percent levels, while Co, Cu, Se, Sb and Pb can exceed 1000 ppm. Nickel and Zn are occasionally measured at concentrations >100 ppm, while V, Ga, Ge, Mo, Ag, Sn, Te, W, Au, Hg, and Bi are only present at concentrations <100 ppm. Only Zn is always present above 10 ppm where detected, while all other trace elements are measured at concentrations <10 ppm; however, this is attributed to the relative detection limits of Zn and other elements in pyrite (Table 6.5).

Figure 6.4 also shows that Co, Cu, As, Se, and Pb are detected in the majority of the pyrite particles analysed, represented by the wide box widths. Meanwhile, Ni, Ag, Sb, Sn, Te, and Bi are less frequently detected, although are still present in more than a third

of the pyrite particles. The rarest trace elements detected in pyrite are V, Zn, Ga, Ge, Mo, W, Au, and Hg, which are all present in less than a third of pyrite particles, down to only two particles in the case of V. Cadmium was not detected in any pyrite particles. Thallium was analysed for, and detected in some pyrite particles, but this data was not quantified owing to the absence of Tl in the standard used for data reduction.

Figure 6.5 highlights trends in the hosting of trace elements in pyrite from different vein generations. In particular, Co, Cu, As, Se, Ag, Sn, Te, Au, Pb, and Bi are shown to be present in pyrite from all the vein generations analysed. Nickel is largely present in V2 and V3 pyrite, with one occurrence in V6 pyrite. Meanwhile, Zn, Mo, Sb, W, and Hg are absent from V6 pyrite, but present in pyrite from V2, V3 and V7. Gallium and Ge are exclusively hosted by V3 and V7 pyrite.

Selenium concentrations decrease from V2 to V3 to V6 to V7, when considering the median values and IQRs (Figure 6.5). The same parameters show that As increases from V2 to V6 to V7; V3 pyrite is an exception to the trend, hosting almost the entire range of As concentrations. Other trace elements do not exhibit such clear trends, although minor decreases are observed for Zn from V2 to V3 to V7, and Ag from V2 to V3 to V6 (and to V7 when considering median values). Pyrite from V2 is more enriched in Cu than pyrite from the other vein generations, while V3 pyrite is more enriched in Co and Hg. Antimony is similarly enriched in V3 and V7 pyrite, but less concentrated in V2 pyrite. Tin and Te are present at similar concentrations in pyrite from all the vein generations analysed, although V6 pyrite hosts slightly higher concentrations of Te. Gold is most enriched in V3 and V6 pyrite, compared to V2 and V7 pyrite. Meanwhile, the ranges and IQRs for Pb in pyrite from the different vein generations overlap considerably, although the median values for V2 and V6 are an order of magnitude lower than those for V3 and V7. Finally, Bi is most enriched in pyrite from V2 and V6, with lower concentrations more common in V3 and V7 pyrite.

Classification of the LA-ICP-MS profile traces for each trace element in pyrite shows that Co, Ni, As, and Se exhibit a high proportion of smooth and matched, and smooth and unmatched profile traces (Figure 6.6). Smooth (matched or unmatched) profile traces are also observed for Ag, Sb, and Hg in approximately a third of the pyrite particles where they are detected. Meanwhile, Cu, Zn, Te, Au and Pb exhibit low proportions ($\leq$12%) of smooth and matched and/or smooth and unmatched profile traces. Spiky and similar profile traces are observed for the aforementioned elements that exhibit smooth traces (minus Cu), and Mo, Sn, and Bi, while spiky profile traces are dominant for Cu, Zn, Ge, Mo, Sn, Te, Au, Pb, and Bi. Meanwhile, V and Ga profile traces are wholly or largely classified as singular spikes or unmatched. Copper, Zn, Ge, Mo, Ag, Sb, Sn, Te, W, Au,

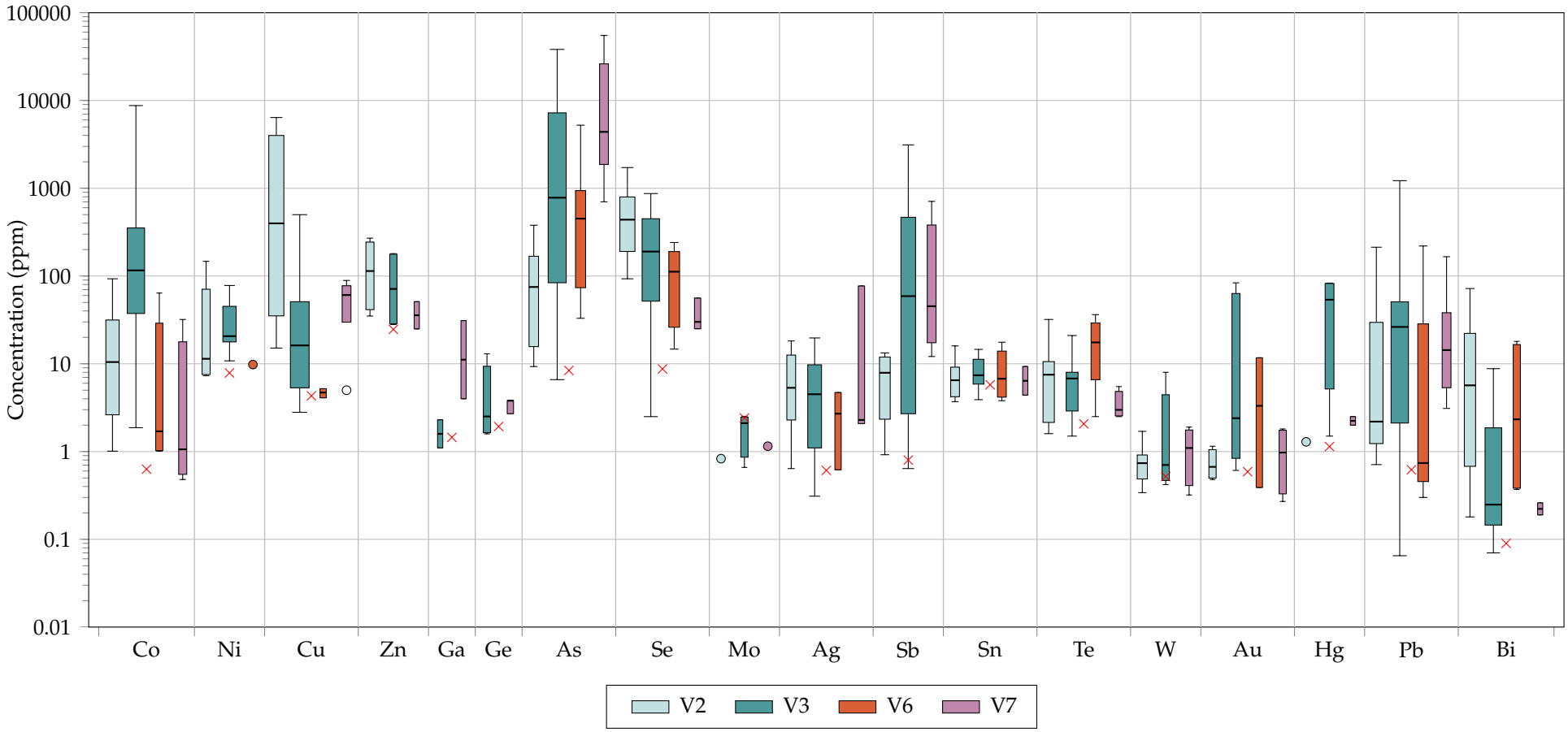

Figure 6.5. Variable width boxplot of trace element concentrations in pyrite from different vein generations, measured by LA-ICP-MS. Box width is indicative of the number of pyrite samples containing the trace element, out of a maximum of 28 (Cu in V3 pyrite). Filled circles represent sample sizes of 1 (e.g., Ni in V6 pyrite). Open circles represent outliers in the data, which are classified as in Figure 6.4. Red crosses are mean lower limits of detection; no data below detection limits is shown. Vanadium is not shown because it is only present in V7 pyrite.

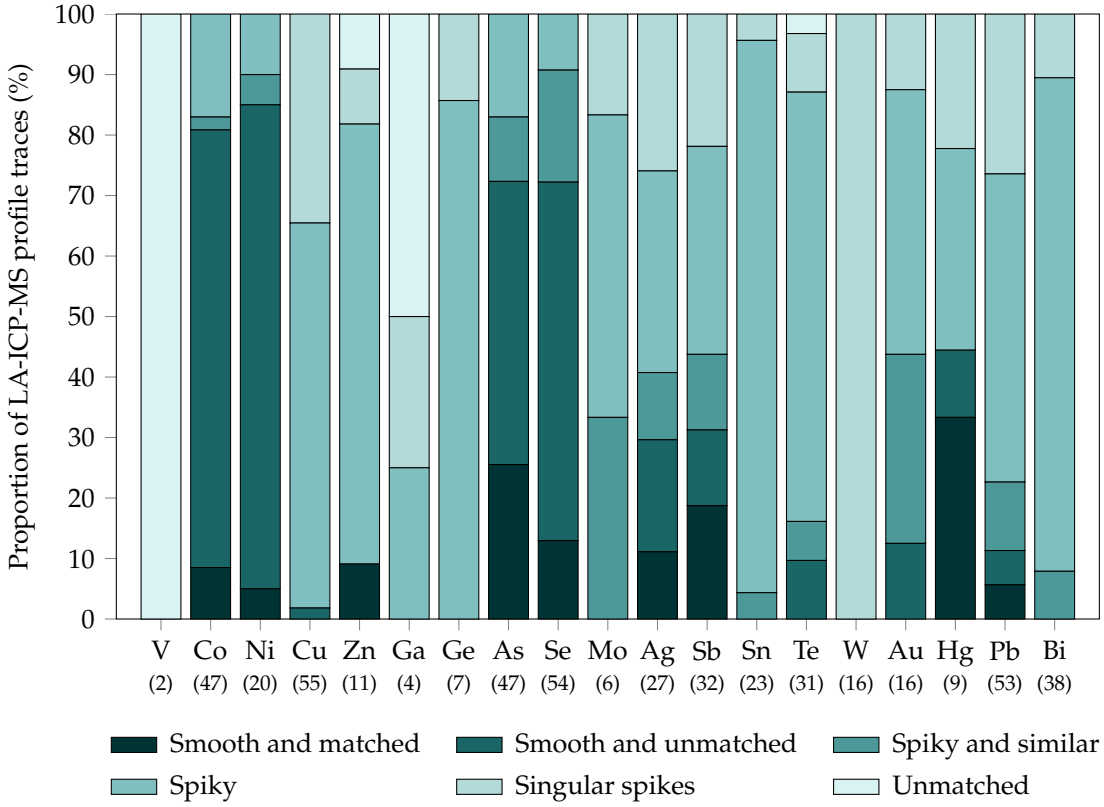

Figure 6.6. Proportion of LA-ICP-MS profile traces exhibited for each trace element in the pyrite particles analysed. Definitions of profile traces are in Table 6.6. Bracketed numbers show the total number of pyrite analyses each element occurs in, out of a maximum of 64.

Hg, Pb and Bi also exhibit traces of singular spikes, while Zn, Ga, and Te have some profile traces that are unmatched.

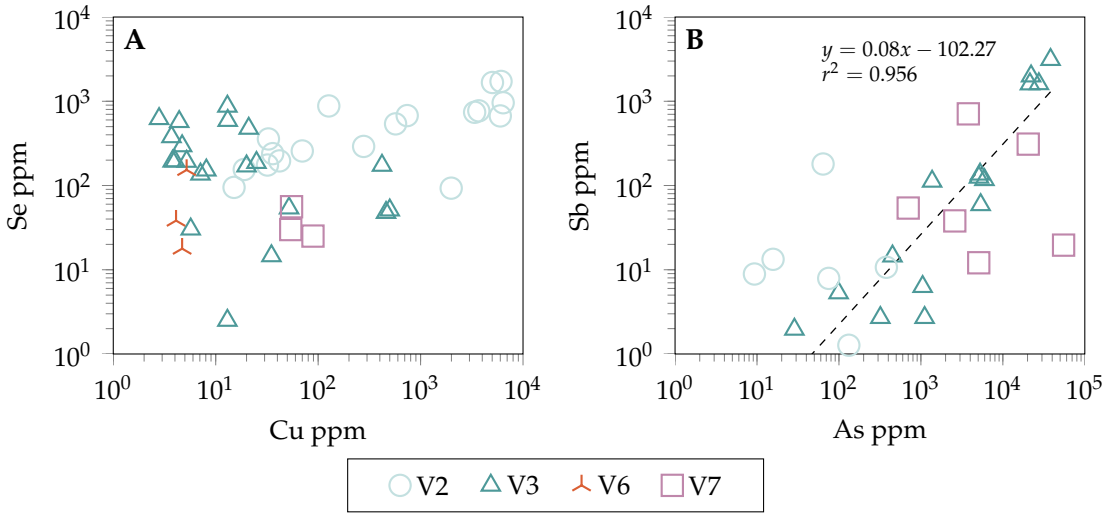

Figure 6.7. Logarithmic bivariate plots of Cu vs. Se (A), and As vs. Sb (B) in pyrite. A linear regression trendline (dashed black line) is fit to the V3 pyrite in B, with the equation describing the slope of line, and the coefficient of determination (r^2) describing the variation in As with respect to Sb. For example, a value of $r^2 = 0.956$ for pyrite from V3 means that 95.6% of the variance in As can be explained by the variance in Sb.

A bivariate analysis shows that there are few correlations between trace elements in pyrite, and the different vein generations are not clearly differentiated based on trace element correlations. Nevertheless, there are correlations observed in some V2 pyrite in terms of Cu and Se, and in V3 pyrite in terms of As and Sb (Figure 6.7). The correlation coefficient (r) for Cu and Se in pyrite from V2 is $r = 0.75$, and for As and Sb in pyrite from V3, $r = 0.98$.

6.4.4 Chalcopyrite

A total of 114 chalcopyrite analyses from V2-V7 vein samples were reduced. The trace element concentrations recorded in chalcopyrite are summarised in Figure 6.8. In general, chalcopyrite does not host high concentrations of most trace elements. The only trace element with a median value >100 ppm is Se. Zinc, Ga, As, Ag, and Sn have median values between 10-100 ppm, while Co, Ge, Mo, In, Sb, Te, Au, Hg, Pb, and Bi all have median values <10 ppm. The ranges (and outliers) show that Co, Zn, Ga, As, Se, Ag, Sn and Pb may all occur above 100 ppm, with Se reaching the highest concentrations. Meanwhile, Ge, Mo, In, Sb, Te, Au, and Bi only reach concentrations between 10-100 ppm, with Hg always present below 10 ppm. Conversely, Zn, As, Se, and Sn are always present above 10 ppm, owing to their relative limits of detection compared to the other trace elements (Table 6.5).

Box widths in Figure 6.8 show that In is detected in all the chalcopyrite particles analysed, while Se, Ag, Pb, and to a lesser extent Bi, are detected in the majority of analyses. Zinc, Sb, and Sn are detected in approximately a quarter of chalcopyrite analyses, while

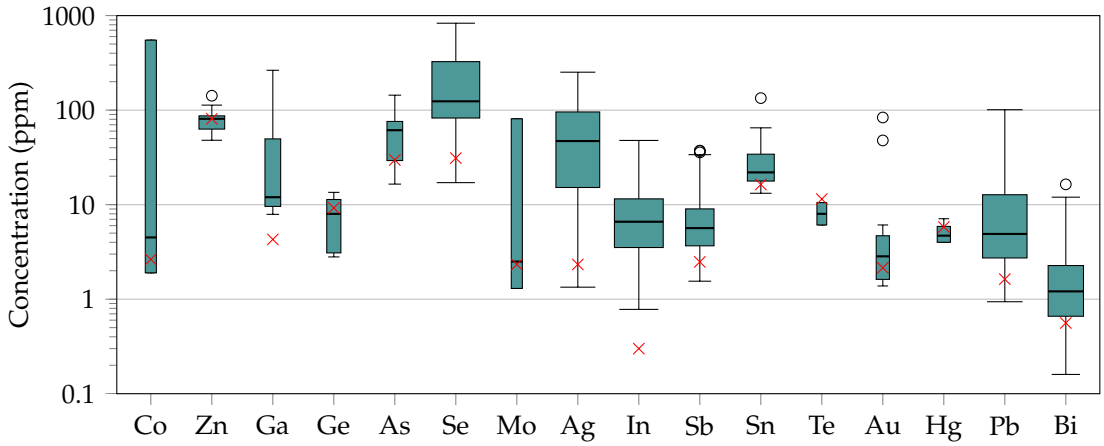

Figure 6.8. Variable width boxplot of elements in chalcopyrite, measured by LA-ICP-MS. Box width is relative to the number of chalcopyrite particles containing the element, out of a maximum of 114 (e.g., In), to a minimum of 2 (e.g., Te). Open circles represent outliers in the data, which are classified as in Figure 6.4. Red crosses are mean lower limits of detection; no data below detection limits is shown.

Co, Ga, Ge, As, Mo, Te, Au, and Hg are recognised in less than 10 chalcopyrite particles. Nickel and Cd were not detected in any chalcopyrite analyses. The high limits of detection for Ni, Zn, As, Se, Cd and Sn may have contributed to a lack of detection of these trace elements in some chalcopyrite particles. As with pyrite, Tl was analysed for and detected in some chalcopyrite particles, but the raw data was not reduced due to a lack of standardisation.

In a summary of trace element concentrations in chalcopyrite by vein generation, Figure 6.9 shows that only Zn, Se, Ag, In, Sb, Sn, Pb, and Bi are present in enough samples to allow informative comparisons between veins. The clearest trend in trace element concentrations in chalcopyrite is shown by the median values and IQRs of In, where concentrations decrease from V2 to V3 to V4, then increase from V4 to V5 to V6. The inverse of this trend is shown by Zn, although no Zn is detected in V5 chalcopyrite. Selenium is most enriched in V2 and V4, while V3 and V5 chalcopyrite host lower concentrations, and V6 chalcopyrite hosts the least Se. A similar, but less clear trend, is observed for Ag, where V2 and V4 are somewhat comparable (although V4 extends to higher Ag contents, and V2 to lower), and V3 and V5 have similar median values, but V3 chalcopyrite hosts a larger range of Ag concentrations. In terms of Sb contents, V3 and V5 are again comparable, with larger IQRs and generally higher concentrations of Sb than V2, V4, and V6. Tin is absent from the analysis of V4 and V6 chalcopyrite, and most frequently detected in V2 chalcopyrite, although present at comparable concentrations in V2, V3, and V5. Chalcopyrite from V5 and V6 exhibits higher median values for Pb than chalcopyrite from V2-V4, although there is significant overlap in the ranges of Pb from all veins. Conversely, the median values of Bi are comparable between all vein generations, but the ranges for V2-V4 chalcopyrite extend to higher Bi contents than V5 and V6 chalcopyrite.

Classification of the LA-ICP-MS profile traces for each trace element in chalcopyrite shows that few trace elements exhibit smooth and matched/unmatched profile traces (Figure 6.6). The major elements (i.e., Cu, Fe) were also recognised to produce relatively spiky traces; the reasons and implications for this are discussed in Chapter 8. Gallium is the only trace element that sometimes exhibits smooth and matched profiles, and Ag the only element that sometimes exhibits smooth and unmatched profiles. Both these trace elements, along with Se, Mo, In, Sb, Sn, Au, Pb, and Bi, also exhibit spiky and similar profiles. The highest proportions of the aforementioned profiles are classified for Ag and In (>80%), followed by Ga and Se (>60%), and Sn (>40%). Cobalt, Zn, Ge, As, Te, and Hg are dominated by profiles classified as spiky, singular spikes, and/or unmatched.

Bivariate analyses of trace elements in chalcopyrite reveal relationships between Se and In, and Se and Ag, that allow differentiation of chalcopyrite from different vein gen-

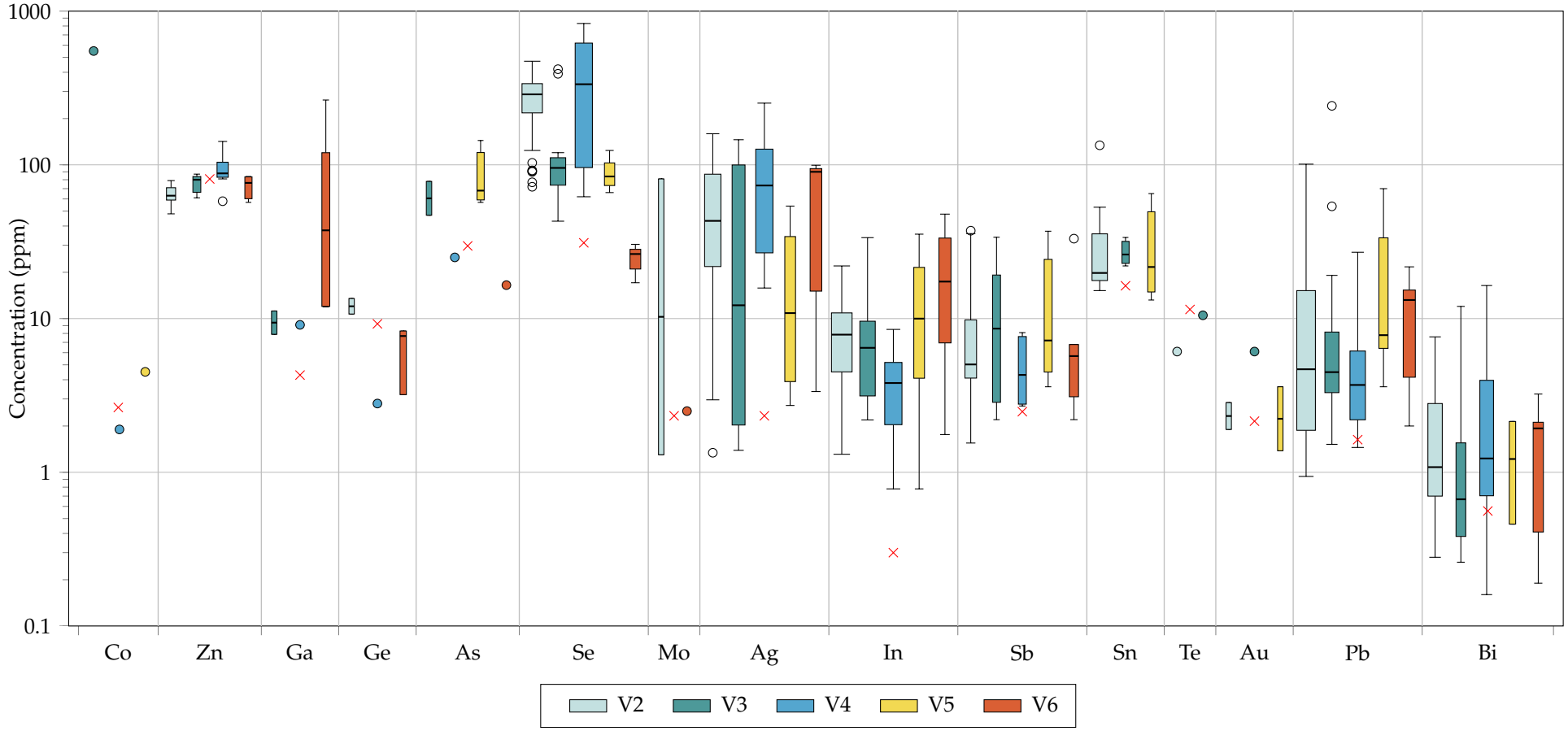

Figure 6.9. Variable width boxplot of trace element concentrations in chalcopyrite from different vein generations, measured by LA-ICP-MS. Box width is relative to the number of chalcopyrite samples containing the trace element, out of a maximum of 41 (In in V2 chalcopyrite). Filled circles represent sample sizes of 1 (e.g., Co in V3-V5 chalcopyrite). Open circles represent outliers in the data, which are classified as in Figure 6.4. Copper and Hg are not shown; the latter because it is only present in V4 chalcopyrite. Red crosses are mean lower limits of detection; no data below detection limits is shown.

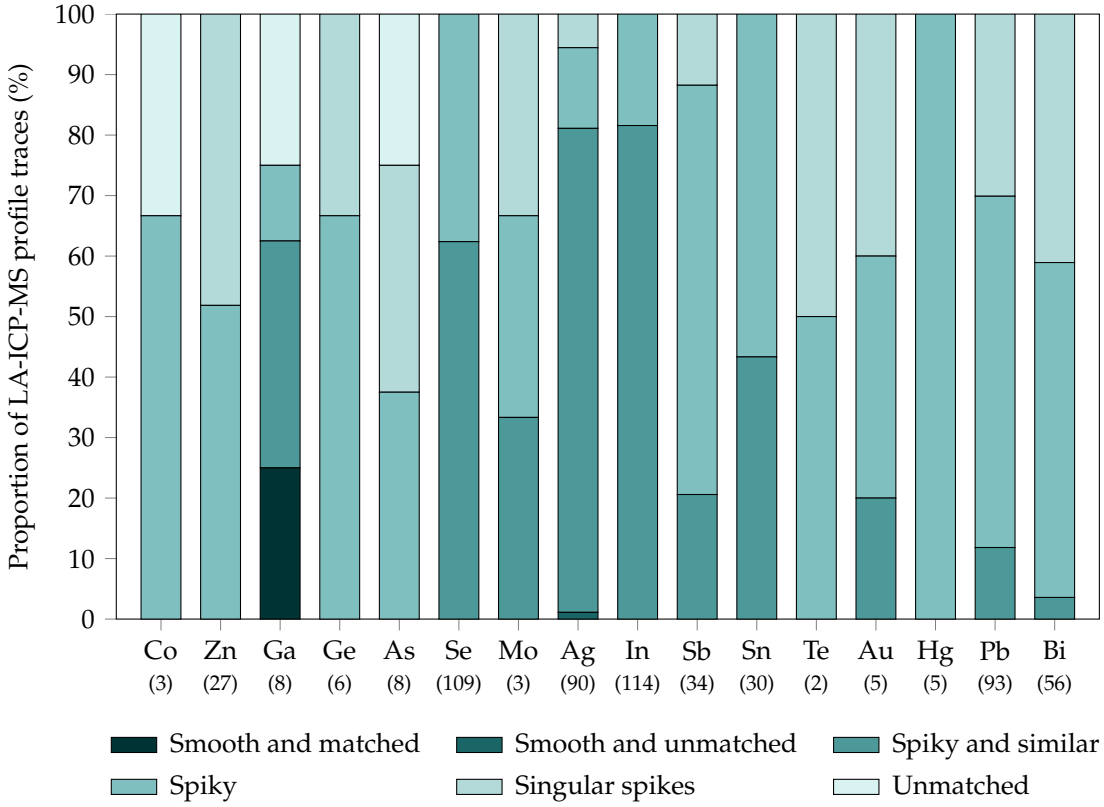

Figure 6.10. Proportion of LA-ICP-MS profile traces exhibited for each element in the chalcopyrite particles analysed. Definitions of profile traces are in Table 6.6. Bracketed numbers show the total number of chalcopyrite analyses each element occurs in, out of a maximum of 114.

erations (Figure 6.11). Chalcopyrite from V4 hosts the highest concentrations of Se or Ag, with low concentrations of In; a negative correlation between Se and Ag is observed. Conversely, chalcopyrite from V5 and V6 hosts the highest concentrations of In, and consistent, low concentrations of Se (V6 less than V5), with low Ag. Chalcopyrite from V2 is differentiated because it hosts moderate enrichments of Se and In, with moderate to low Ag. Finally, V3 chalcopyrite exhibits low concentrations of Se and In, with moderate to low Ag contents, although two V3 chalcopyrite particles host high concentrations of Se and In; these are from sample IC70-402, where a V3 vein cross-cuts a V2 vein. In Figure 6.11B, there is a negative correlation ($r = -0.83$) between Se and Ag in V4 chalcopyrite.

6.4.5 Galena

A total of 32 galena analyses from V2, V3, V4, and V6 vein samples were reduced. The trace element concentrations recorded in galena are summarised in Figure 6.12. Bismuth, Se, and Ag, are enriched in galena, exhibiting median values in excess of 4500 ppm, 2700 ppm, and 2200 ppm, respectively. Other trace elements are present at lower average concentrations, with median values between 10-100 ppm for Ni, Cu, Zn, Cd, Sb, and Te, median values between 1-10 ppm for Co, Ga, and Hg, and median values between 0.1-1

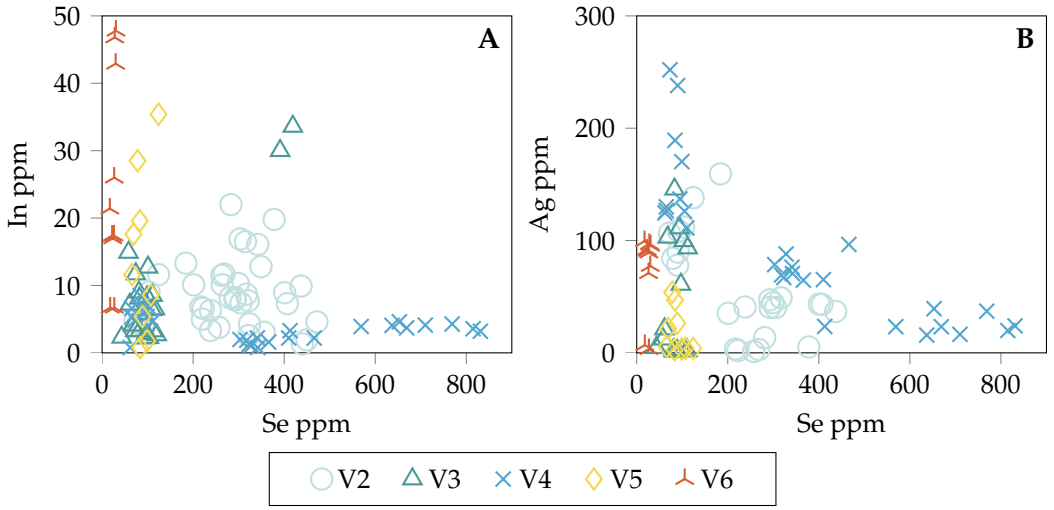

Figure 6.11. Bivariate plots of Se vs. In (A) and Se vs. Ag (B) in chalcopyrite.

ppm for Ge, In, and Au.

The ranges and IQRs of trace elements in galena are highly variable. In line with their high median values, Bi, Se, and Ag, are occasionally present at weight percent levels, and are usually present at concentrations >100 ppm; only Bi is measured at concentrations

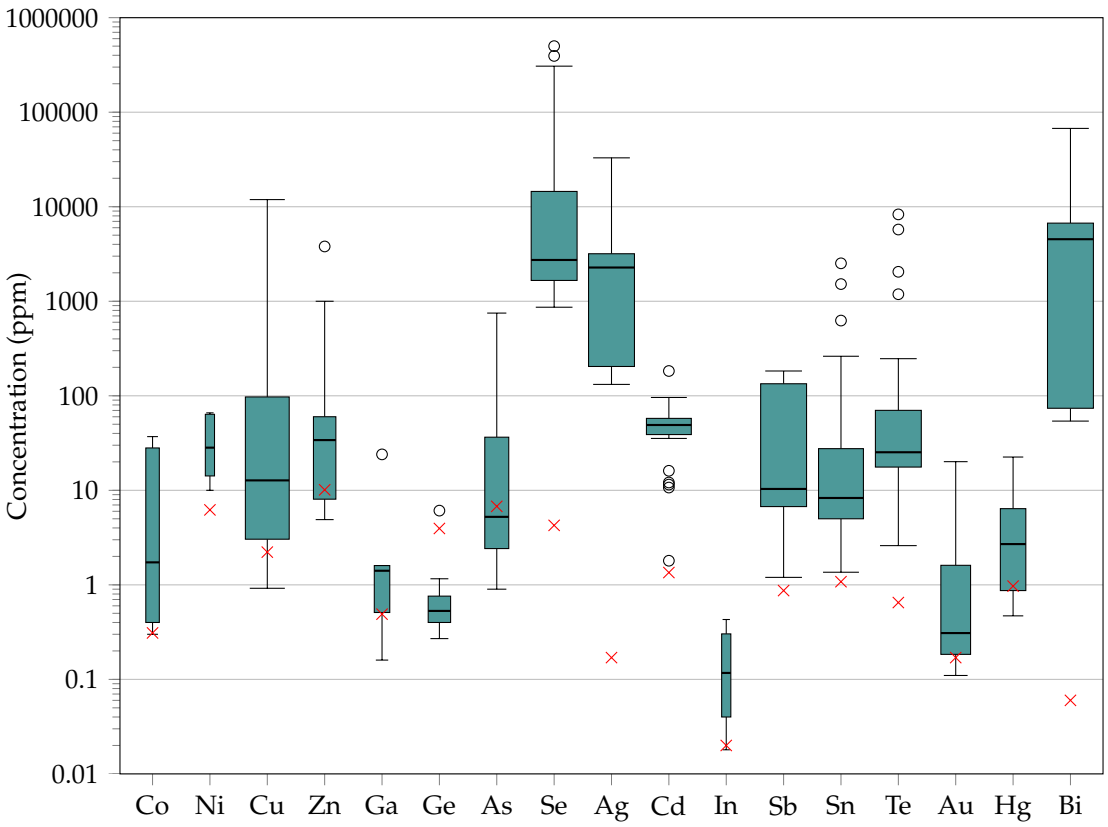

Figure 6.12. Variable width boxplot of elements in galena, measured by LA-ICP-MS. Box width is relative to the number of galena particles containing the element, out of a maximum of 32 (e.g., Se). Open circles represent outliers in the data, which are classified as in Figure 6.4. Red crosses are mean lower limits of detection; no data below detection limits is shown.

<100 ppm. In particular, Se is always present at concentrations >850 ppm. Copper also rarely reaches weight percent concentrations, while outliers for Zn, Sn, and Te are measured at concentrations >1000 ppm. Arsenic, Cd and Sb are recorded at maximum values (or outliers in the case of Cd) of between 100-1000 ppm, while Co, Ni, Ga, Au and Hg can similarly reach concentrations between 10-100 ppm. Only Ge has a maximum value between 1-10 ppm, while only In has a maximum between 0.1-1 ppm. Minimum values for all trace elements apart from Se, Ag, and Bi are below 10 ppm, likely corresponding to their lower limits of detection; for example, In is detected down to 0.02 ppm, but also has the lowest lower limit of detection (Table 6.5).

Wide box widths for Se, Ag, Sb, Te, and Bi in Figure 6.12 correspond to the detection of these trace elements in all galena particles analysed. Copper, Cd, and Sn are also present in the majority of analyses. Conversely, Zn, Ge, As, Au, and Hg are detected in less than half of the galena particles, while Co, Ni, Ga, and In are detected in less than a third. As with pyrite and chalcopyrite, Tl was analysed for and detected in some galena particles, but the raw data was not reduced.

There are differences in trace element concentrations in galena from different vein generations, as illustrated in Figure 6.13. Selenium concentrations vary the most between vein generations, with the highest Se concentrations in V4 galena, followed by galena from V2, then V3, with V6 galena hosting the lowest Se concentrations. Near-identical trends are recognised for Ag and Bi, with the highest concentrations of these trace elements in V4 galena, and decreasing in terms of median concentrations from V3 to V2/V6 (Ag is more enriched in V2 than V6, while Bi is more enriched in V6 than V2). However, there is overlap in the IQRs of V2, V3, and V6 in terms of Ag and Bi concentrations. Nevertheless, the above trends (i.e., Se concentrations, similarity between Ag and Bi concentrations) align with those recognised in the EMPA data (Section 6.3). Antimony increases from V2 to V3, decreases from V3 to V4, and increases from V4 to V6, with V6 galena hosting the highest concentrations of Sb.

Copper, Sn and Te exhibit similar trends, whereby the median values and IQRs of these trace elements are higher in V2 and V4, lower in V3, and are at the lowest concentrations in V6. Gold also follows a similar trend, although there is more overlap in Au concentrations in V3 and V6 galena. Conversely, Cd is most concentrated in V3 and V6 galena, but there is overlap of the IQRs of V3, V6, and V4 galena, and only one analysis of V2 galena that contains the lowest Cd concentrations. Arsenic appears to be least enriched in V6 galena, while V2-V4 galena hosts similar concentrations. A caveat of the galena data presented here is that there are a limited number of reduced analyses, particularly for V2, V3, and V4 galena (Table 6.4), meaning that there may be greater variation

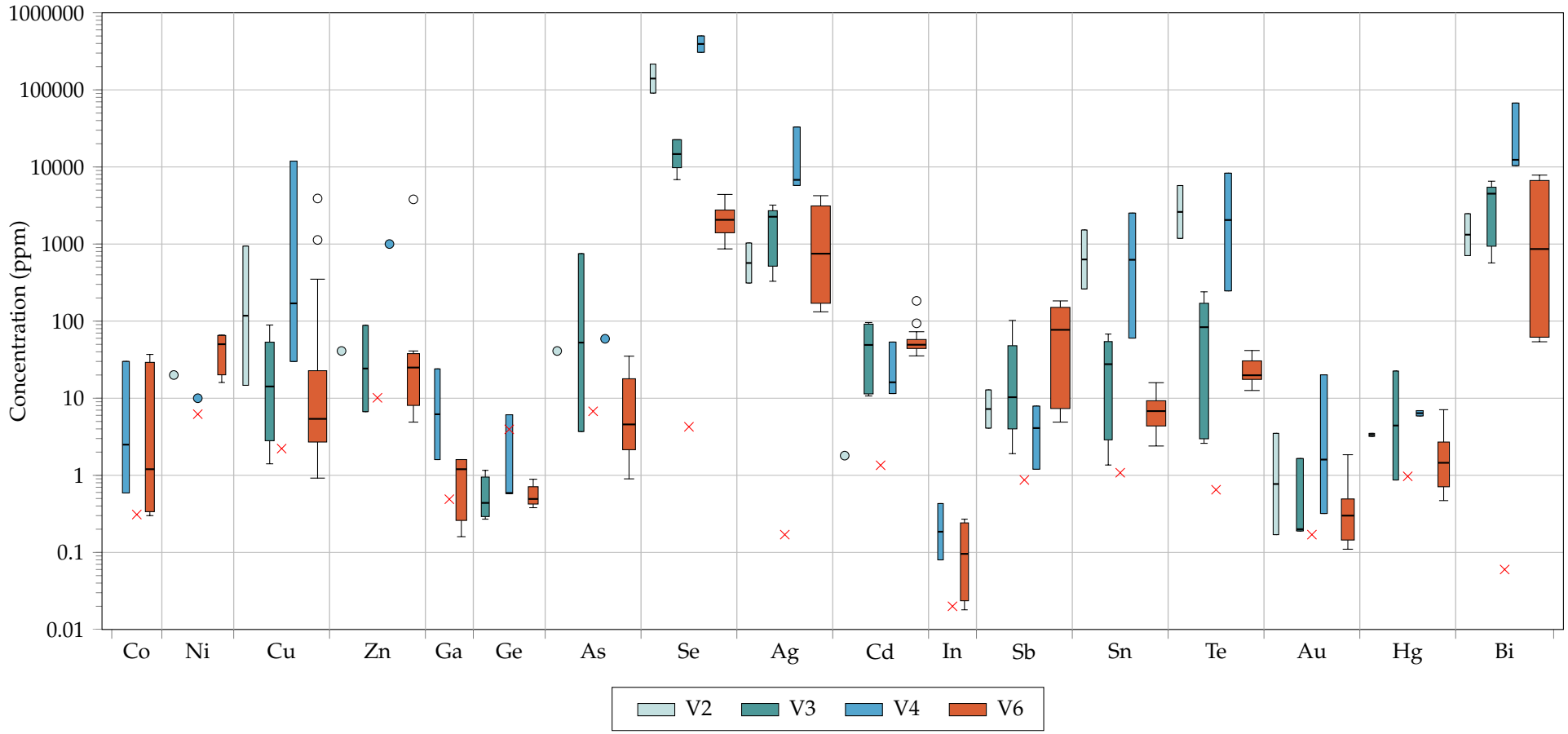

Figure 6.13. Variable width boxplot of trace element concentrations in galena from different vein generations, measured by LA-ICP-MS. Box width is relative to the number of galena samples containing the trace element, out of a maximum of 22 (e.g., Se in V6 galena). Filled circles represent sample sizes of 1 (e.g., Ni in V2 and V3 galena). Open circles represent outliers in the data, which are classified as in Figure 6.4. Red crosses are mean lower limits of detection; no data below detection limits is shown.

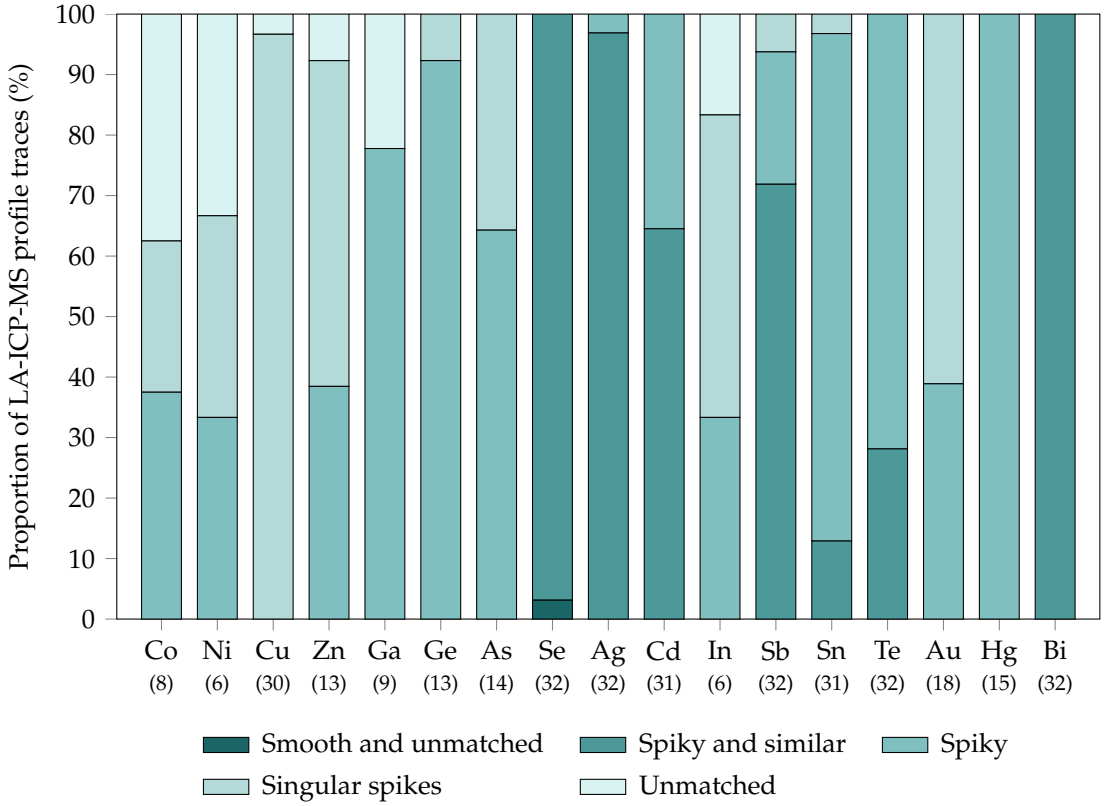

Figure 6.14. Proportion of LA-ICP-MS profile traces exhibited for each element in the galena particles analysed. Definitions of profile traces are in Table 6.6. Bracketed numbers show the total number of galena analyses each element occurs in, out of a maximum of 32.

in trace element concentrations than is recorded in the reduced data. Similarly, as noted in Section 6.4.1, the galena data is subject to error owing to the use of a median Pb value for data reduction that is not well mathced to the actual Pb content of all galena particles analysed.

Profile classifications for trace elements in galena (Figure 6.14) show that, like chalcopyrite, few trace elements produce smooth intensity signals. Selenium, Ag, Cd, Sb, and Bi exhibit high proportions (>60%) of spiky and similar profiles, while Se also exhibits a low proportion of smooth and unmatched profile traces. Tin and Te also display spiky and similar profiles, although less frequently (<30%), with the remainder of their profiles classified as spiky, or rarely singular spikes (for Sn). In addition to Sn and Te, a high proportion (>60%) of profiles are classified as spiky for Ga, Ge, As, and Hg, while a lower proportion (<40%) of spiky profiles are classified for Co, Ni, Zn, In, and Au; these may indicate some lattice hosting given the generally spiky nature of element profiles during LA-ICP-MS of galena. Traces of singular spikes, or those classified as unmatched, are recognised in at least a third of Co, Ni, Cu, Zn, As, In, and Au profiles.

Both Ag and Bi, and Sn and Te, are strongly correlated in galena, as shown in Figure 6.15. There are two distinct groups in Figure 6.15A, the first defining a strong positive

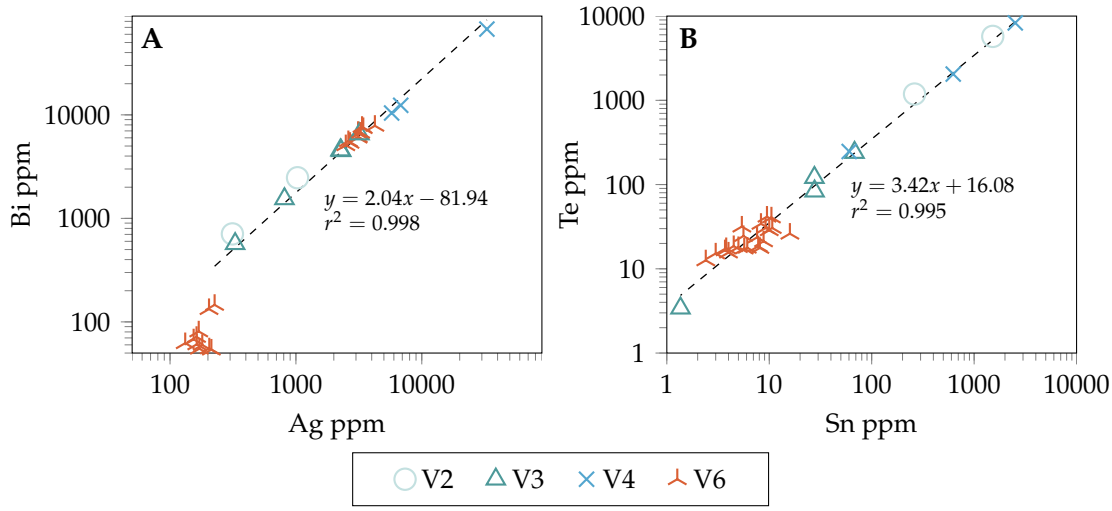

Figure 6.15. Logarithmic bivariate plots of Ag vs. Bi (A) and Sn vs. Te (B) in galena. Dashed black lines are linear regression trendlines for the data; however, the cluster of V6 galena with low Ag and Bi concentrations in A are not included in the trendline calculation, because they deviate below the line calculated for the other galena crystals.

correlation ($r = 1$) between Ag and Bi, and the second consisting of V6 galena that exhibits low Ag and Bi concentrations with no clear correlation. Figure 6.15B shows that Sn and Te are consistently positively correlated ($r = 1$), although there is some deviation around the trendline, particularly in V6 galena.

6.4.6 Tennantite-tetrahedrite

A total of 62 tennantite-tetrahedrite analyses from V2, V3, V5, and V6 vein samples were reduced; the element concentrations are summarised in Figure 6.16. As major elements, Fe, Zn, As, and Sb are the most enriched, although there is variety in their concentrations. In particular, As and Sb have median values of approximately 23 wt.% and 9 wt.%, respectively, and IQRs of 15 wt.% and 24 wt.%, respectively.

In terms of trace elements, tennantite-tetrahedrite is most enriched in Cd and Ag, with median values in excess of 2300 ppm and 1700 ppm, respectively. Relatively high median concentrations (>100 ppm) for Hg, Se, Bi, and Te are also observed. Cobalt and Sn have median values between 10-100 ppm, while Ge, In, and Pb have median values between 1-10 ppm. Only one analysis detected Au in tennantite-tetrahedrite, at a concentration of <2 ppm. Silver occasionally reaches weight percent levels, while Se, Cd, Sn, Te, Hg, Pb, and Bi are sometimes observed at concentrations >1000 ppm. Conversely, Co and In are present at concentrations <100 ppm, while Ge is present at concentrations <10 ppm. Aside from the major elements, only Cd and Hg are always present at concentrations >100 ppm.

Box widths in Figure 6.16 also show that Ag, Cd, In, Hg, and Bi are detected in all

analyses of tennantite-tetrahedrite, in addition to the major elements (i.e., Fe, Zn, Sb, As). Similarly, Se and Te are present in all but one of the tennantite-tetrahedrite particles analysed, while Sn is present in all but three. Cobalt is detected in approximately a third of analyses, while Ge is only detected in two; as above, Au is only detected once. Nickel and Ga were not detected in any analyses. As with pyrite, chalcopyrite, and galena, Tl was analysed for and detected in some tennantite-tetrahedrite particles, but the raw data was not reduced.

Element concentrations in tennantite-tetrahedrite vary between vein generations (Figure 6.17). In terms of the major elements, differences are evident between tennantite-tetrahedrite from V5 and V6; the former hosting higher concentrations of Fe and As, and lower concentrations of Sb, compared to the latter. An increase in the median values of As and a decrease in the median values and IQRs of Sb is also evident from V2 to V3 to V5. Cobalt is in the majority of tennantite-tetrahedrite from V2, but at low concentrations and frequency in V6, and absent from V3 and V5. A trend in Se concentrations is observed, with tennantite-tetrahedrite from V2 hosting the highest concentrations, V3 and V5 exhibiting comparable concentrations (although the median of V5 is higher), and V6 tennantite-tetrahedrite with the lowest concentrations. The inverse is true for Ag, al-

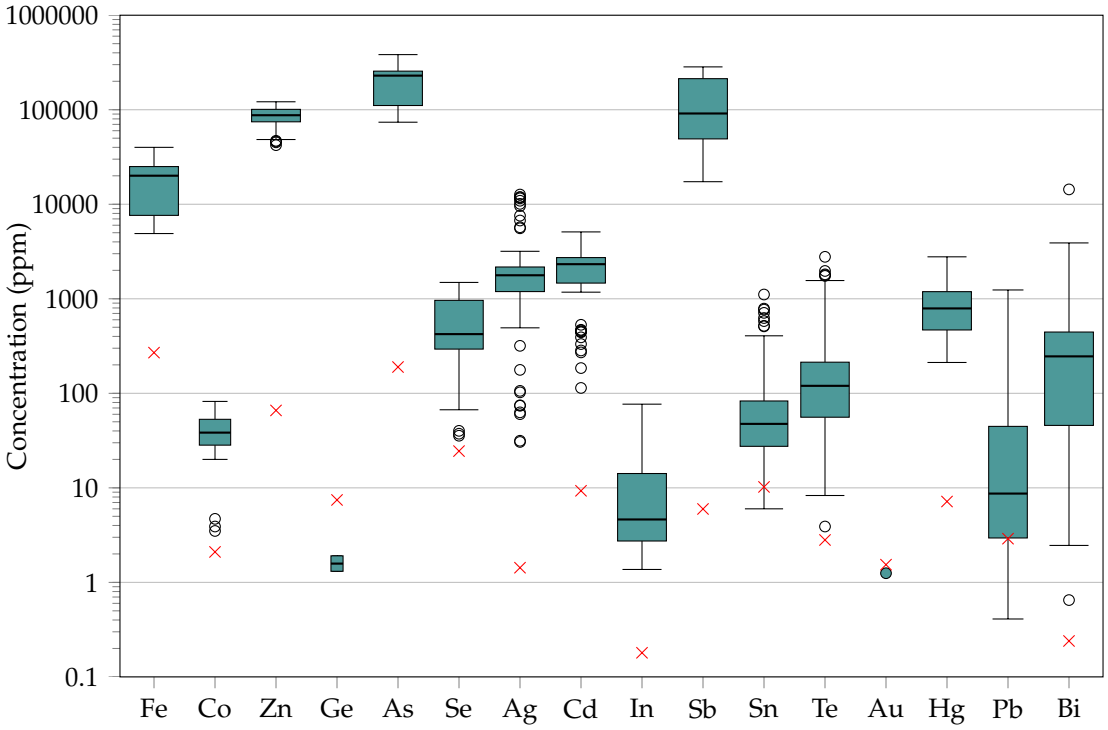

Figure 6.16. Variable width boxplot of elements in tennantite-tetrahedrite, measured by LA-ICP-MS. Box width is relative to the number of tennantite-tetrahedrite particles containing the element, out of a maximum of 62 (e.g., Fe); Filled circles represent a sample size of 1 (e.g., Au). Open circles represent outliers in the data, which are classified as in Figure 6.4. Red crosses are mean lower limits of detection; no data below detection limits is shown.

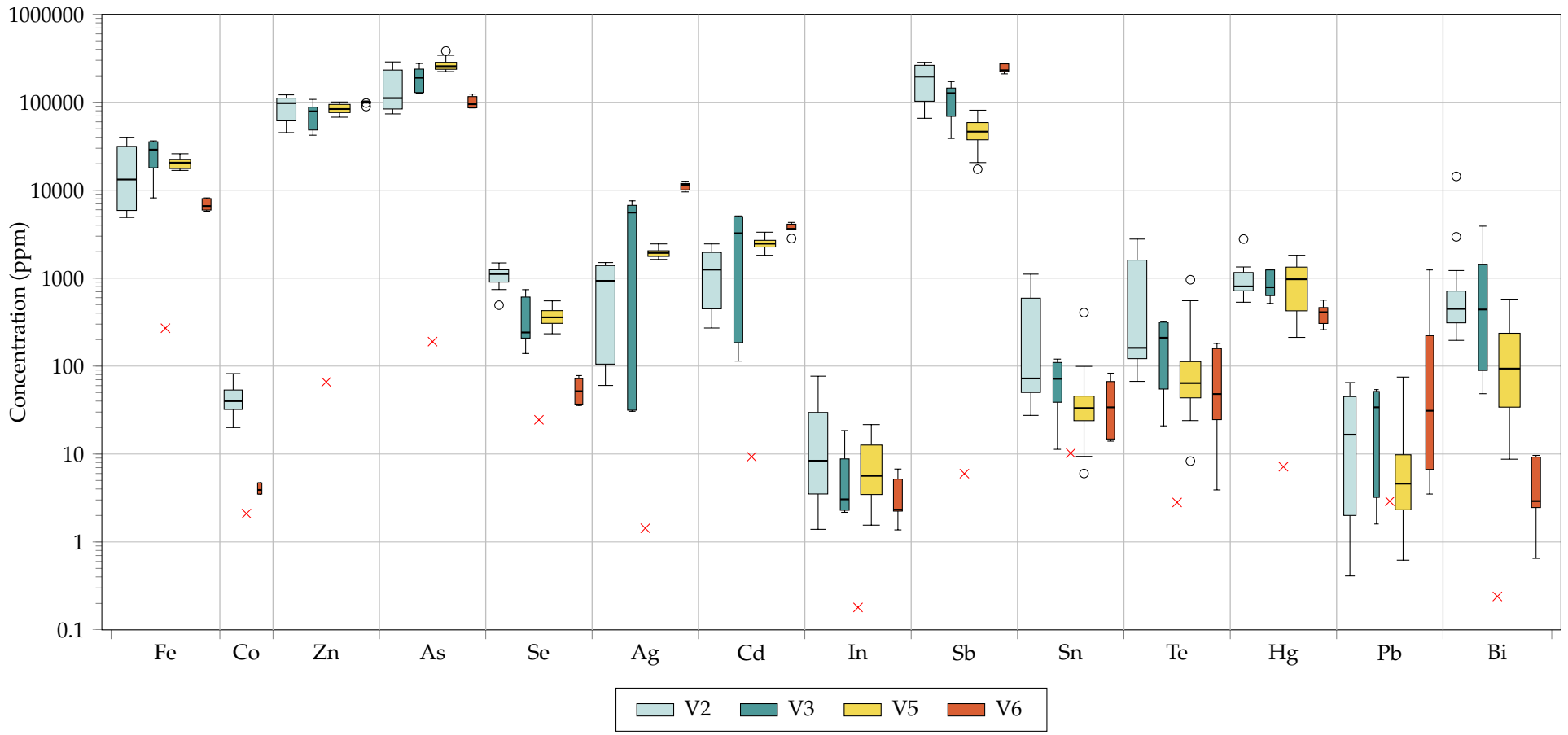

Figure 6.17. Variable width boxplot of trace element concentrations in tennantite-tetrahedrite from different vein generations, measured by LA-ICP-MS. Box width is relative to the number of tennantite-tetrahedrite samples containing the trace element, out of a maximum of 26 (e.g., Fe in V5 tennantite-tetrahedrite). Open circles represent outliers in the data, which are classified as in Figure 6.4. Red crosses are mean lower limits of detection; no data below detection limits is shown. Germanium and Au are not shown because they are only present in V3 and V2 tennantite-tetrahedrite, respectively.

though the IQR of V3 tennantite-tetrahedrite overlaps the IQRs of V2, as well as V5. Cadmium exhibits a similar trend, with the lowest concentrations (based on median values and IQRs) in V2, increasing to V5 and to V6, while the IQR of V3 tennantite-tetrahedrite overlaps the IQRs of V2, V5, and V6, although the median of V3 tennantite-tetrahedrite is comparable to that of V6. Tennantite-tetrahedrite from V2 and V5 is generally more enriched in In than that from V3 and V6, with V2 tennantite-tetrahedrite hosting the highest concentrations. Tin and Te exhibit near-identical trends, with the IQR of V2 tennantite-tetrahedrite at higher concentrations of both trace elements, decreasing to V3, with V5 and V6 at comparable concentrations. However, the median values of Sn and Te in tennantite-tetrahedrite are comparable between V2 and V3 at higher concentrations, and comparable between V5 and V6 at lower concentrations. Mercury and Pb are also similar between vein generations; V6 is more variable, however, with a lower IQR and median for Hg and a higher IQR for Pb, compared to the other vein generations. Finally, Bi is most depleted in V6 tennantite-tetrahedrite, increasing to V5, and again to V2/V3, where similar concentrations are recorded.

Analysis of LA-ICP-MS profiles of trace elements in tennantite-tetrahedrite shows that, similar to chalcopyrite and galena, no trace elements produce smooth intensity sig-

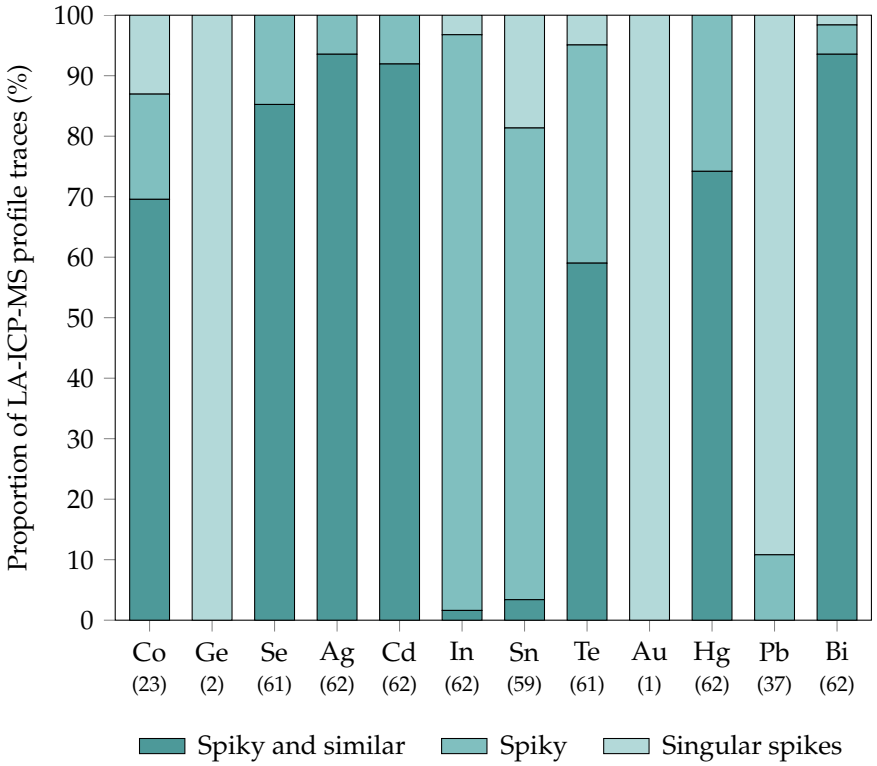

Figure 6.18. Proportion of LA-ICP-MS profile traces exhibited for each trace element in the tennantite-tetrahedrite particles analysed. Major elements (Fe, Zn, As, and Sb) are not shown. Definitions of profile traces are in Table 6.6. Bracketed numbers show the total number of tennantite-tetrahedrite analyses each trace element occurs in, out of a maximum of 62.

nals (Figure 6.18). Selenium, Ag, Cd, and Bi exhibit the highest proportions (>85%) of spiky and similar profiles, with Co, Te, and Hg exhibiting slightly lower proportions (59-75%). Indium and Sn have low proportions (<5%) of spiky and similar profiles, with remaining profiles dominantly classified as spiky. In contrast, Ge, Au, and Pb are characterised by profiles classified as singular spikes.

Bivariate analyses show that there is co-variation in element pairs in tennantite-tetrahedrite (Figure 6.19). Two discrete positive correlations are recognised between Ag and Sb in Figure 6.19A, denoted by a dashed black linear regression trendline ($r = 0.98$), and the second denoted by a solid black trendline ($r = 0.93$). Similarly positive correlations are shown between Ag and Cd in Figure 6.19B ($r = 0.73$) and between Sn and Te in Figure 6.19D ($r = 1$). Conversely, a weak negative correlation is apparent between Ag and Se in C ($r = -0.61$). The two V3 tennantite-tetrahedrite crystals in the clusters of V2 analyses in Figure 6.19A, B, and C are from sample IC70-402, where a V3 vein cross-cuts a V2 vein

Distinction of tennantite-tetrahedrite from different vein generations is also possible

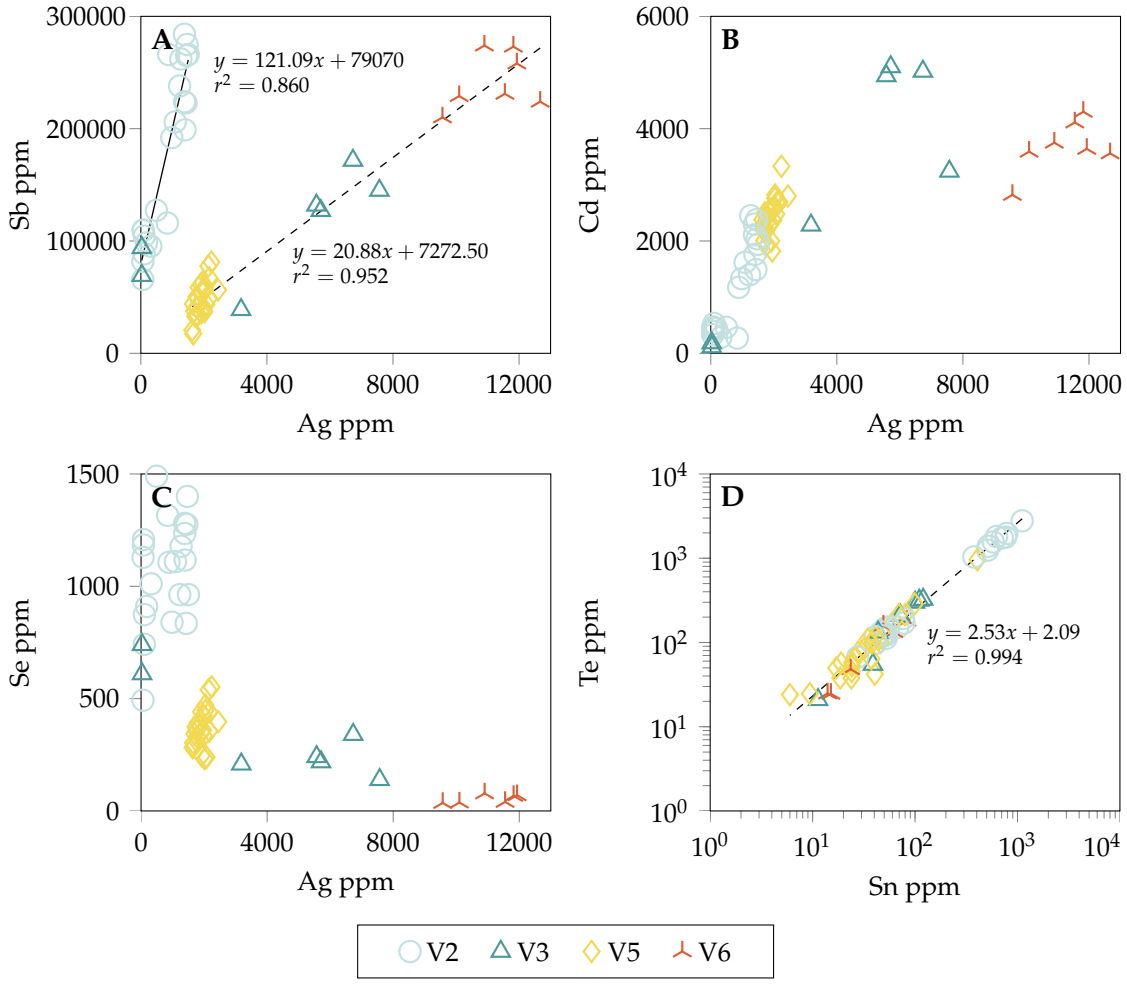

Figure 6.19. Bivariate plots of selected elements in tennantite-tetrahedrite, with Ag vs. Sb in A, Ag vs. Cd in B, Ag vs. Se in C, and Sn vs. Te in D. Note that D uses a logarithmic scale. Dashed and solid black lines are linear regression trendlines.

from these plots, when considering concentrations of Ag, Sb, Cd, and Se. In particular, V2 tennantite-tetrahedrite is low-Ag and forms a discrete positive correlation trend with Sb (high) and Cd (low), while also exhibiting high Se. Meanwhile, V3 tennantite-tetrahedrite exhibits moderate concentrations of Ag and Sb, with high Cd, and low Se; exceptions are the two V3 analyses that lie within the clusters of V2 tennantite-tetrahedrite. In comparison, V5 tennantite-tetrahedrite forms a tight cluster around 2000 ppm Ag, with the lowest Sb contents, and continues the positive trend between Ag and Cd in V2 tennantite-tetrahedrite to higher values; Se concentrations are moderate, between V2 and V3. Finally, V6 tennantite-tetrahedrite is characterised by the highest Ag and Sb contents, with moderate-high Cd that deviates below the positive trend between Ag and Cd defined by tennantite-tetrahedrite from V2, V3 and V5. Meanwhile, the lowest Se contents are found in V6 tennantite-tetrahedrite.

6.4.7 Sphalerite

A total of 19 sphalerite analyses from V3 and V6 vein samples were reduced. The trace element concentrations recorded in sphalerite are summarised in Figure 6.20. Cadmium is the most enriched trace element in sphalerite, with a median value approaching 8000 ppm. Iron and Cu are also enriched, with median values of approximately 1400 ppm and

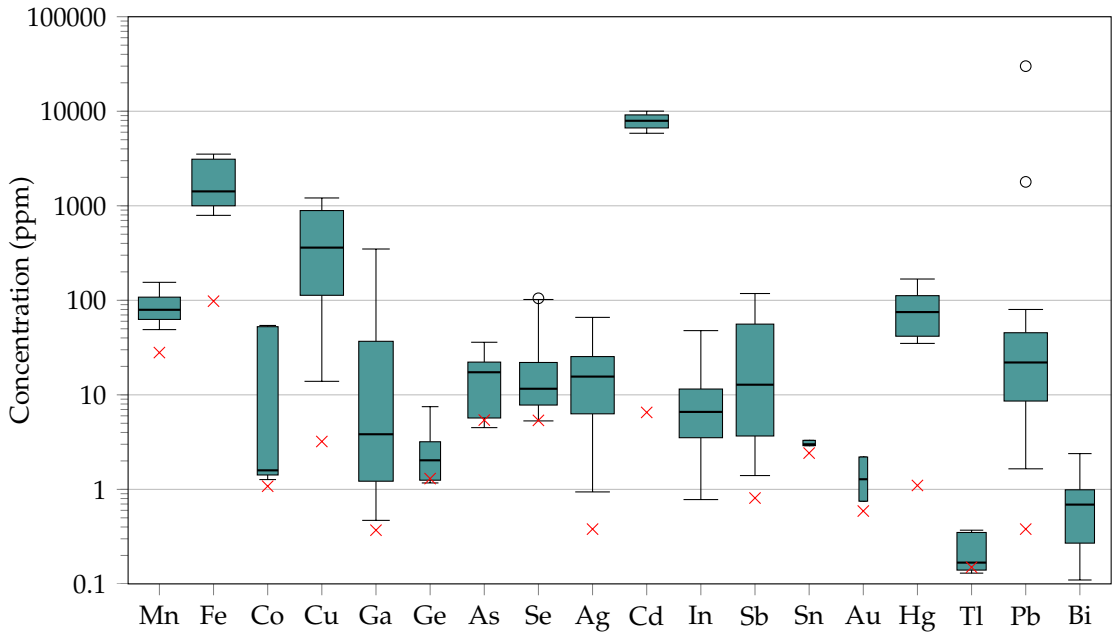

Figure 6.20. Variable width boxplot of elements in sphalerite, measured by LA-ICP-MS. Box width is relative to the number of sphalerite particles containing the element, out of a maximum of 19 (e.g., Fe). Open circles represent outliers in the data, which are classified as in Figure 6.4. Red crosses are mean lower limits of detection; no data below detection limits is shown. The mean lower detection limit for Bi (0.086 ppm) is not shown.

350 ppm, respectively. A range of other trace elements are present, with median values of <100 ppm. Manganese, As, Se, Ag, Sb, Hg, and Pb have median concentrations between 10-100 ppm, while Co, Ga, Ge, In, Sn, and Au have median concentrations between 1-10 ppm, and Tl and Bi have median concentrations <1 ppm.

The range in element concentrations in Figure 6.20 shows that Cd is the only element recorded at concentrations >1 wt.% ppm (although rarely), and is always present at concentrations >5800 ppm. Meanwhile, maximum concentrations of Fe and Cu are recorded around 3500 ppm and 1200 ppm, respectively. Iron is always present at concentrations >750 ppm, while Cu concentrations down to approximately 10 ppm are recorded. Of the other trace elements, Mn, Ga, Se, Sb, and Hg sometimes occur at concentrations >100 ppm, while Co, As, Ag, In, and Pb exhibit maximum concentrations between 10-100 ppm, and Ge, Sn, Au, Tl, and Bi are all present at concentrations <10 ppm. The box widths show that Fe, Cu, Ag, Cd, In, Hg, and Pb are detected in all sphalerite analyses. Manganese, Ga, As, Se, Sb, Tl, and Bi are present in more than half the analyses, while Co, Ge, Sn, and Au are less frequently detected. Nickel was not detected in any analyses.

Figure 6.21 shows that reliable comparisons between vein generations are not possible with the sphalerite LA-ICP-MS data, because only two analyses from V3 were reduced, with the remainder (17) from V6. Nevertheless, the two V3 analyses provide an initial insight into the trace element content of V3 sphalerite. Most of the V3 analyses fall within the trace element ranges of V6 sphalerite, apart from Mn, In, and Sb, where the V3 analyses are recorded at lower concentrations than the range for V6, and Co, Ge, Se, and Hg, where the V3 analyses are recorded at higher concentrations than the range for V6. Gold is only present in one analyses of V3 sphalerite, and one of V6, with the higher concentrations in V3.

Analysis of LA-ICP-MS profiles for the trace elements in sphalerite shows that only Cd exhibits wholly smooth profile traces (Figure 6.22). One Hg profile is classified as smooth and matched, while the remainder are largely spiky and similar. The majority of In profiles are classified as spiky and similar, while Fe, Co, Ga, Se, and Ag exhibit lower proportions (<37%) of this profile classification. Spiky profiles are dominant for Mn, Fe, Co, As, Ag, Pb, and Bi, while profiles of singular spikes are dominant (>50%) for Cu, Ge, Se, Sb, Au, and Tl; Ga, As, Ag, Sb, Pb, and Bi also exhibit these profiles to a lesser degree (up to 33%). Unmatched profile traces are recongised for Fe, Ga, Ag, Sb, and Pb.

There are no apparent clear correlations recognised between trace element pairs in sphalerite, but this may be a consequence of the small dataset. Weak positive correlations ($r = 0.74$) are identified between Fe and In, and Se and Hg, as illustrated in Figure 6.23, but more data is required to confirm these relationships. As mentioned, the lack of data

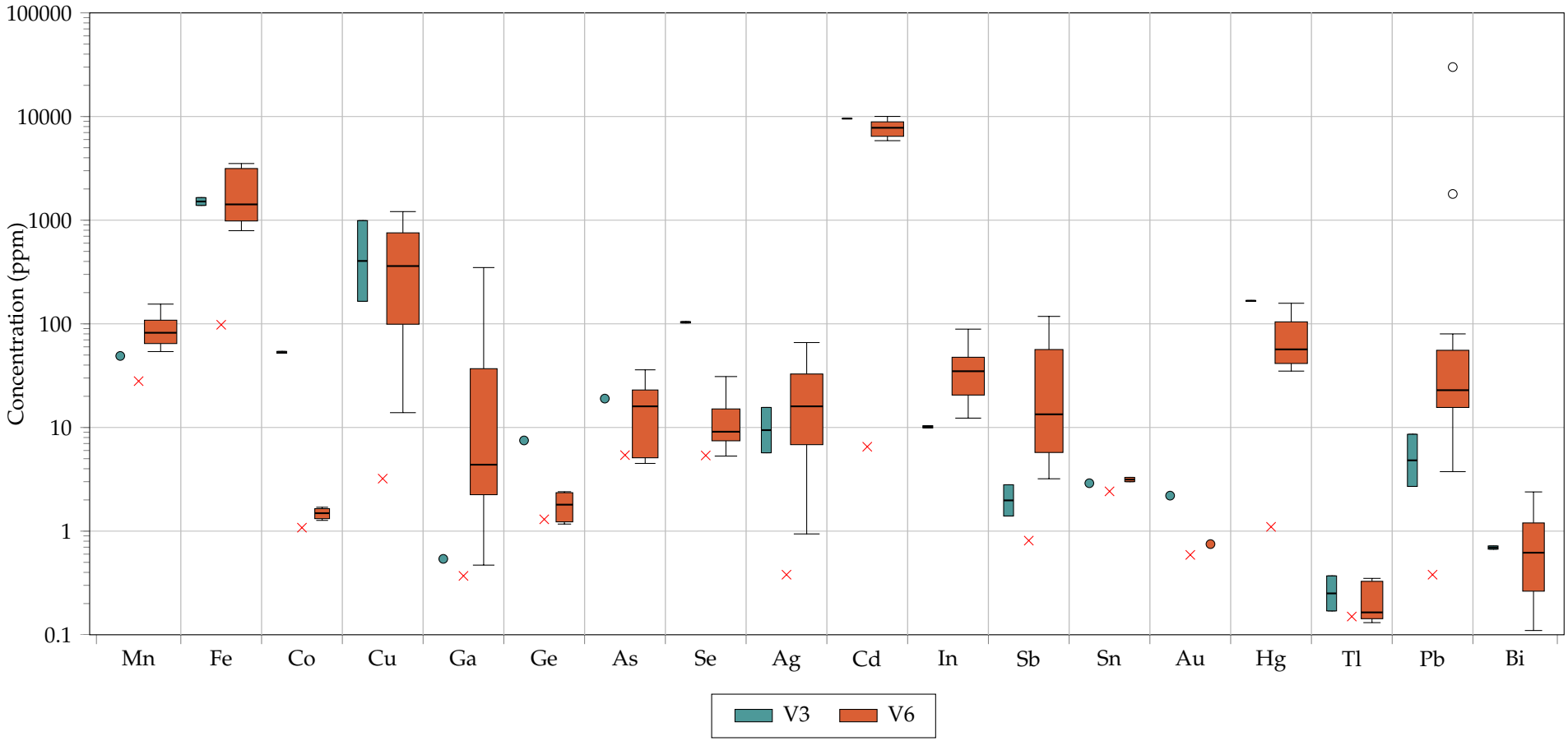

Figure 6.21. Variable width boxplot of trace element concentrations in sphalerite from different vein generations, measured by LA-ICP-MS. Box width is relative to the number of sphalerite particles containing the trace element, out of a maximum of 17 (e.g., Mn in V6 sphalerite). Only 2 analyses of V3 sphalerite were reduced. Filled circles represent sample sizes of 1 (e.g., Mn in V3 sphalerite). Open circles represent outliers in the data, which are classified as in Figure 6.4. Red crosses are mean lower limits of detection; no data below detection limits is shown. The mean lower detection limit for Bi (0.086 ppm) is not shown.

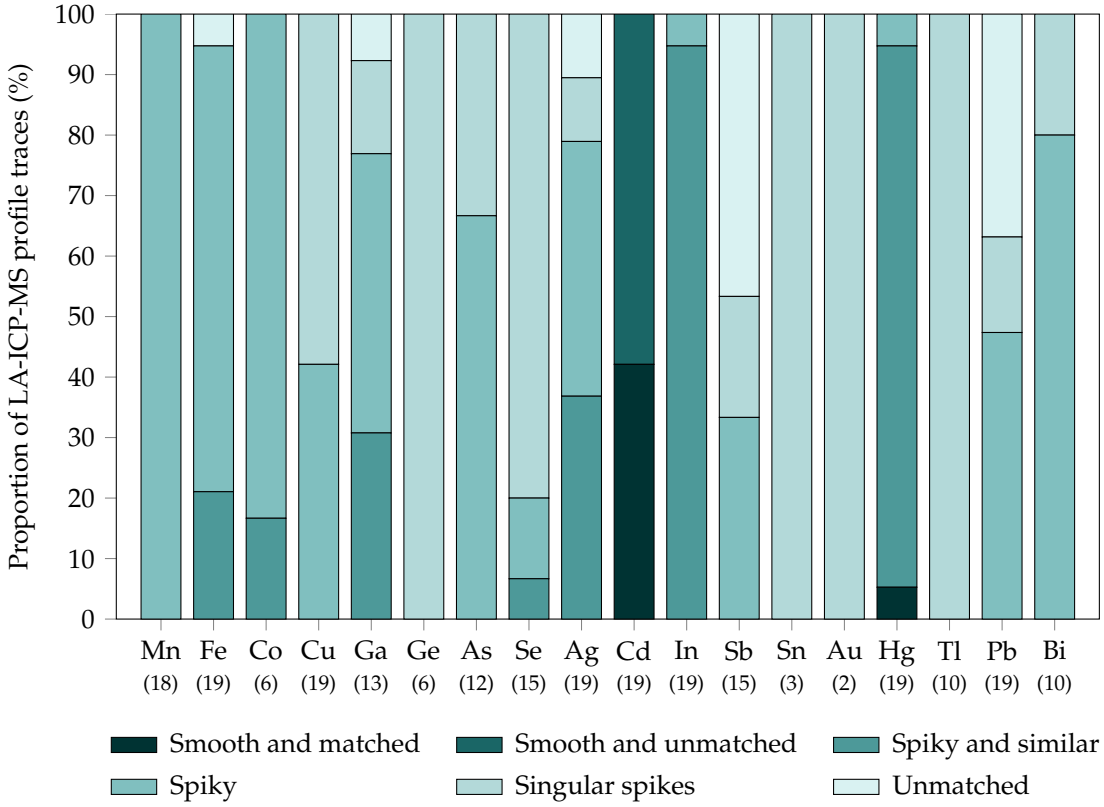

Figure 6.22. Proportion of LA-ICP-MS profile traces exhibited for each trace element in the sphalerite particles analysed. Definitions of profile traces are in Table 6.6. Bracketed numbers show the total number of sphalerite analyses each element occurs in, out of a maximum of 19.

means that sphalerite from V3 and V6 cannot be reliably characterised, although Figure 6.23B shows that the two V3 sphalerite particles analysed contain higher concentrations of Se and Hg than V6 sphalerite.

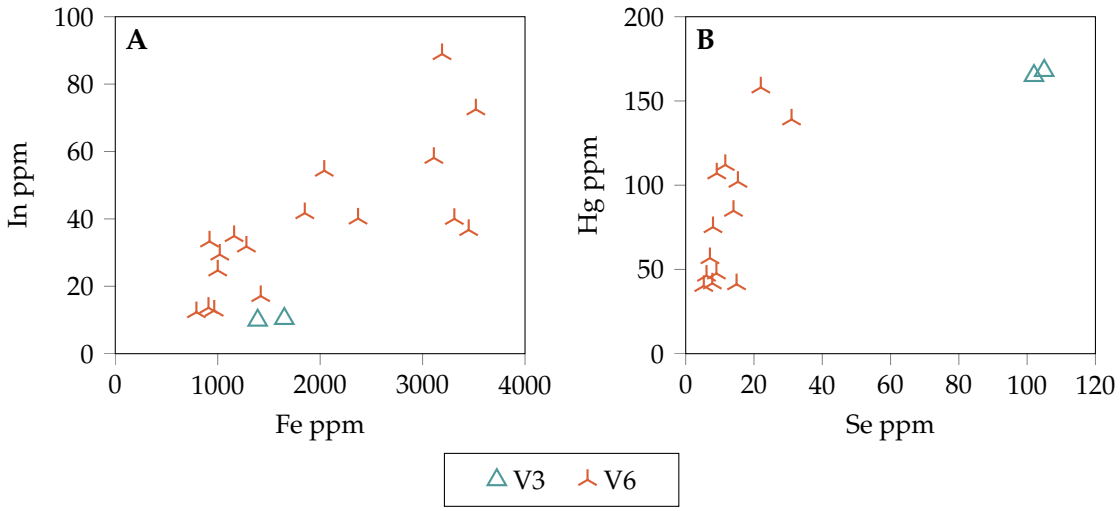

Figure 6.23. Bivariate plots of Fe vs. In (A) and Se vs. Hg (B) in sphalerite.

6.4.8 Arsenopyrite

A total of 17 arsenopyrite analyses from V7 vein samples were reduced. The trace element concentrations recorded in arsenopyrite are summarised in Figure 6.24. Antimony is by far the most enriched trace element in arsenopyrite, with a median value in excess of 2 wt.%, ranging up to a maximum of >10 wt.%.

Copper, Se, and Pb have median values between 100-1000 ppm, while V, Co, Ni, Zn, Ag, Sn, Te, Au, and Hg are present with median concentrations between 10-100 ppm. Cadmium is only detected in one analysis, at 41 ppm, while Mo and Bi have median concentrations <10 ppm. Only Sb is always present at concentrations >1000 ppm, although Cu and Te reach maximum concentrations above this threshold. Of the remaining trace elements, V, Co, Ni, Zn, Se, Ag, Sn, Au, and Pb exhibit maximum concentrations between 100-1000 ppm, with Au and Se reaching the highest values. The box widths in Figure 6.24 show that only Cu, Sb, and Au are detected in all analyses, while Co, Ni, Se, Ag, Sn, Te, and Pb are present in ≥12 analyses. Vanadium and Bi are detected in 10 and 11 analyses, respectively, while Zn, Mo, Cd, Hg, and Bi are present in ≤7 analyses. As with pyrite,

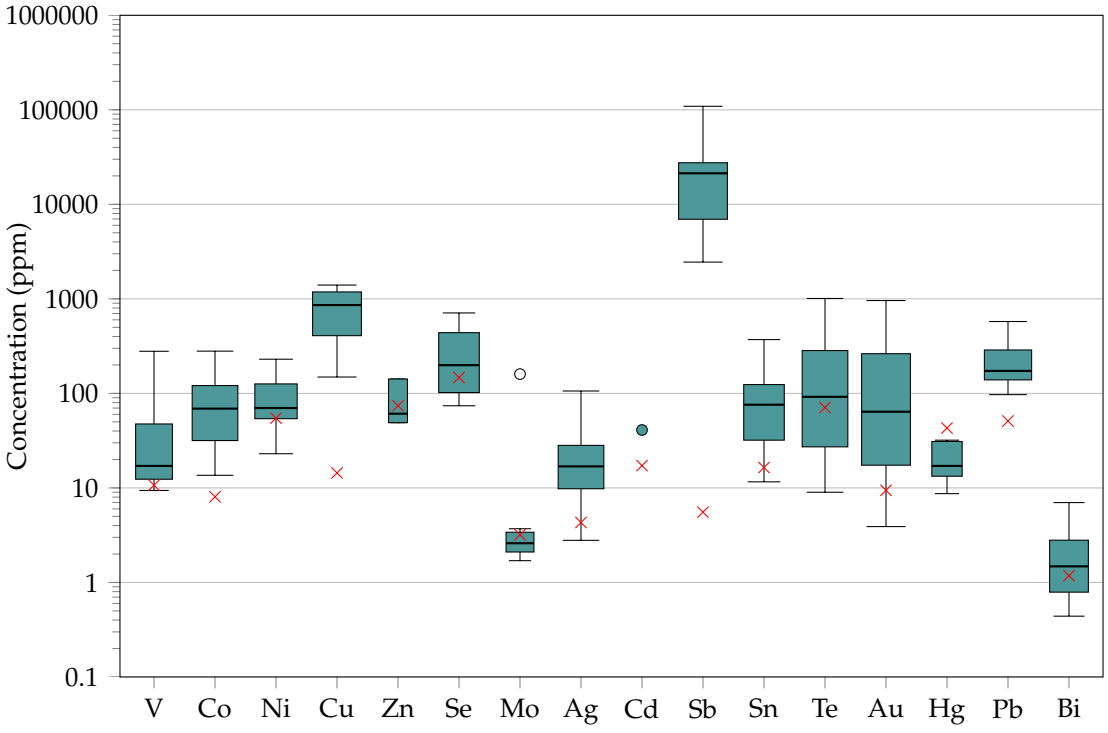

Figure 6.24. Variable width boxplot of trace elements in arsenopyrite, measured by LA-ICP-MS. Box width is relative to the number of arsenopyrite crystals containing the trace element, out of a maximum of 17 (e.g., Cu). Filled circles represent a sample size of 1 (e.g., Cd). Open circles represent outliers in the data, which are classified as in Figure 6.4. Arsenic has not been included, given the inaccuracy of recorded values (in some cases exceeding 100 wt.%). Red crosses are mean lower limits of detection; no data below detection limits is shown.

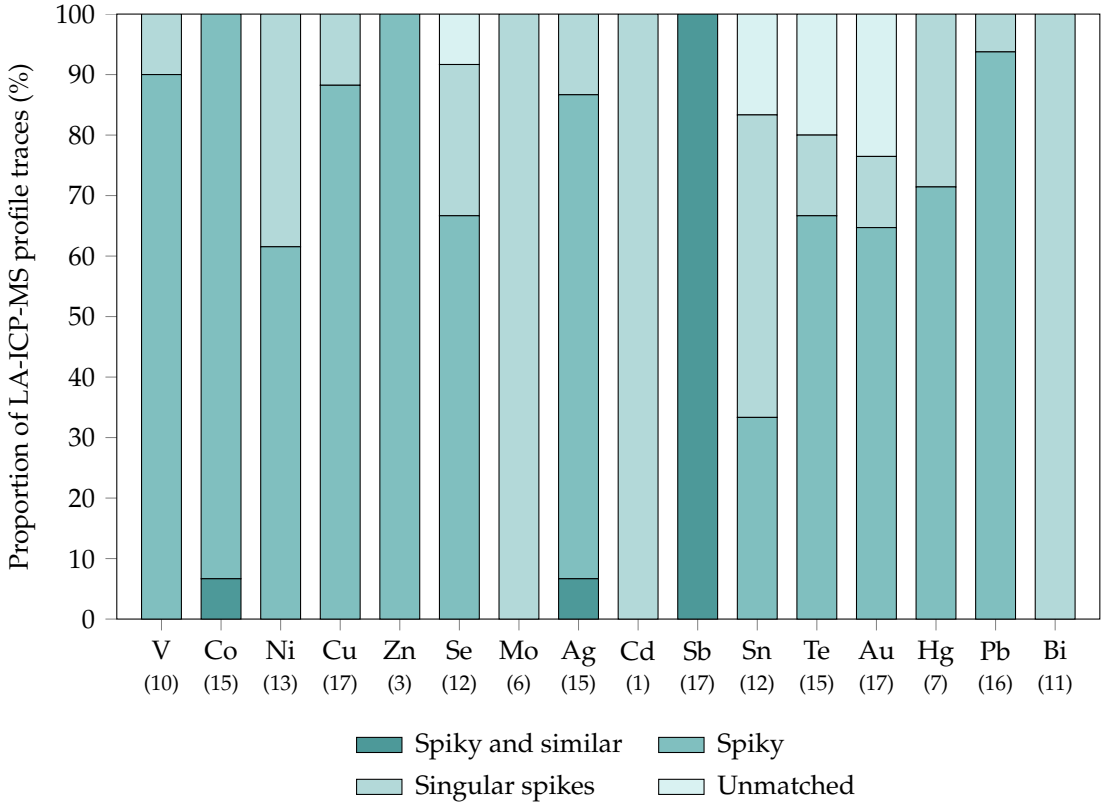

Figure 6.25. Proportion of LA-ICP-MS profile traces exhibited for each trace element in the arsenopyrite particles analysed. Definitions of profile traces are in Table 6.6. Bracketed numbers show the total number of arsenopyrite analyses each trace element occurs in, out of a maximum of 17.

chalcopyrite, galena, and tennantite-tetrahedrite, Tl was analysed for and detected in some arsenopyrite particles, but the raw data was not reduced.

Analysis of LA-ICP-MS profiles of trace elements in arsenopyrite shows that, similar to chalcopyrite, galena, and tennantite-tetrahedrite no trace elements produce smooth intensity signals (Figure 6.25). Antimony is the only trace element that has profiles wholly classified as spiky and similar, while Co and Ag exhibit one profile each classified as spiky and similar. Spiky profiles are classified for the majority (>60%) of V, Co, Ni, Cu, Zn, Se, Ag, Te, Au, Hg, and Pb traces. Singular spikes are wholly classified for Mo, Cd, and Bi, while unmatched profiles are classified for <30% of Se, Sn, Te, and Au.

Despite the limited number of analyses, two correlations are recognised in the trace element data for arsenopyrite (Figure 6.26), with Au positively correlating with Te ($r = 0.98$), and Sn positively correlating with Te ($r = 1$). However, there is some variation in Figure 6.26A, with Au and Te deviating around the trendline, particularly at lower concentrations. Meanwhile, Figure 6.26B shows that Sn and Te are more consistently correlated, with less deviation around the trendline.

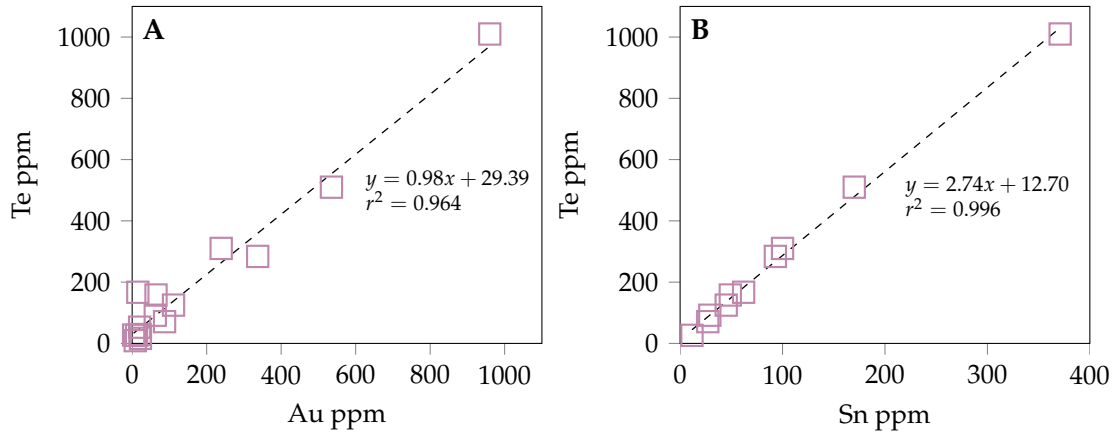

Figure 6.26. Bivariate plots of Au vs. Te (A) and Sn vs. Te (B) in V7 arsenopyrite. Dashed black lines are linear regression trendlines.

6.5 LA-ICP-MS map data

The LA-ICP-MS analytical process is described in full in Appendix A.6.

6.5.1 Map data reduction

The data for six pyrite particles were reduced to generate trace element maps for pyrite from V2 (1), V3 (3), V6 (1), and V7 (1) vein samples. To produce quantitative maps, the raw LA-ICP-MS data as intensity counts was reduced in Iolite using the median value of Fe in pyrite from the EMPA data (Table 6.2). When exporting the trace element maps, concentration scale limits (in ppm) were selected to best illustrate the distribution of a trace element within a pyrite crystal; scale maxima do not necessarily correspond to the highest concentrations recorded. Meanwhile, lower concentrations of trace elements may not be well respresented in the map images, depending on the maximum scale limit used. For example, a scale limit of 10000 ppm highlights changes in concentration in terms of 1000s ppm, but smaller-scale variations and lower concentrations (i.e., 10s-100s ppm) are not well represented. This is a limitation of trace element map presentation, and the fact that different trace elements are present at different concentrations that require appropriate scale limits. To represent smaller-scale variations and lower concentrations, a logarithmic output scale could be used, although this is not possible in Iolite. Alternatively, a second sequence of map images could be generated using lower scale limits to represent smaller-scale variations and lower element concentrations.

After exporting the reduced maps, non-pyrite minerals (i.e., surrounding ore minerals and gangue) were masked out of the images, because these minerals do not have similar Fe contents to pyrite, and are therefore not accurately quantified in terms of their trace elements when reducing the data for pyrite. Masks were created in Adobe Photoshop,

based on the Fe counts per second (cps) maps. The selective colour function was used to select blue and cyan colours, which correspond to low Fe contents (roughly less than half the Fe cps recorded for pyrite), and these areas were coloured black to mask non-pyrite areas of the trace element maps. In the following subsections, the Fe cps map of each pyrite particle is presented, along with a BSE image, to show that only non-pyrite minerals (i.e., blue and cyan in Fe cps maps) were masked out. This masking approach is similar to that used by Franchini et al. (2015), for the presentation of quantitative pyrite maps.

6.5.2 V2 pyrite

Trace element maps for the one V2 pyrite particle analysed are presented in Figure 6.27. These maps show that none of the trace elements are homogeneously distributed within the pyrite. Cobalt, Ni, As, and Se appear to be the most widely distributed, although their patterns of distribution are different. Cobalt and Ni are highest in select regions of the pyrite crystal; the highest Ni concentrations in three discrete areas of the pyrite core also correspond to elevated Se, and moderate As. However, the highest As concentrations are adjacent to the highest Ni concentrations, and correlate with elevated levels of Au and Pb, as well as Se. The highest Co concentrations do not correlate with elevated levels of other trace elements. When Co and Ni are present at lower concentrations (i.e., light blue colours), they define linear patterns, separated by regions that lack both elements.

Arsenic is largely concentrated in the three discrete areas in the core of the pyrite, with lower concentrations of As surrounding these areas, some of which correspond to elevated Se. Lower concentrations of As towards the rim of the pyrite define linear patterns, with large areas between core and rim lacking As. Meanwhile, Se is present throughout the pyrite crystal. As mentioned, some higher Se concentrations correspond to elevated levels of Ni, As, Au, and Pb, while additional areas of higher Se towards the top of the map do not correlate to elevated levels of other trace elements. Silver, Sb, and Hg are rarely present, with discrete areas that are elevated in Ag and Sb. The highest Ag correlates to the highest Pb contents, and also overlaps with Au. Copper is largely present at high concentrations as discrete spots, or defining linear patterns along the rim of the pyrite that likely correspond to chalcopyrite rather than pyrite.

6.5.3 V3 pyrite

Three pyrite particles from V3 veins were analysed to produce the trace element maps shown in Figure 6.28, 6.29, and 6.30.

The V3 pyrite from sample IC65-430 (Figure 6.28) is compositionally heterogeneous

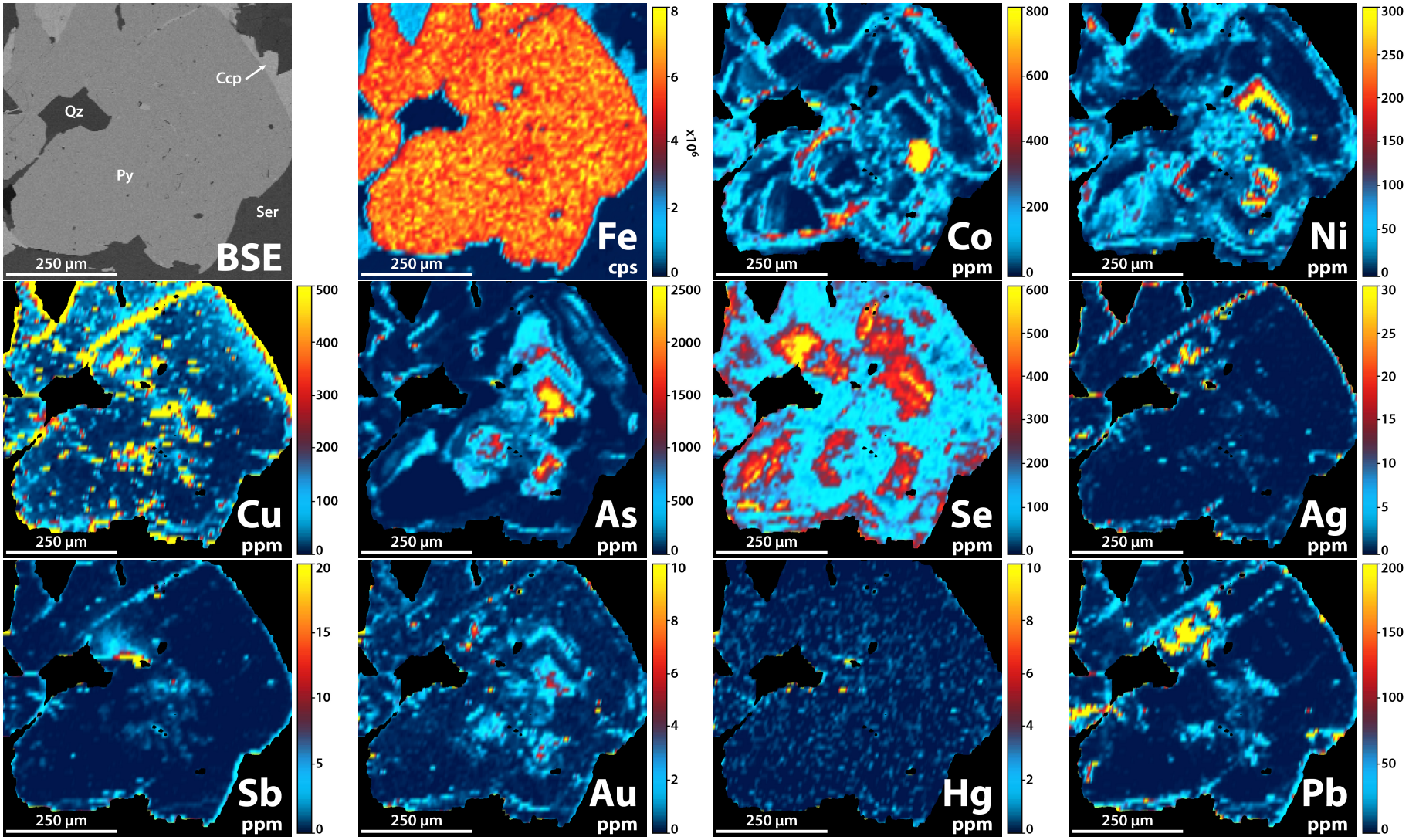

Figure 6.27. Trace element maps of a V2 pyrite crystal from sample IC70-429. A BSE image of the pyrite crystal is also shown.

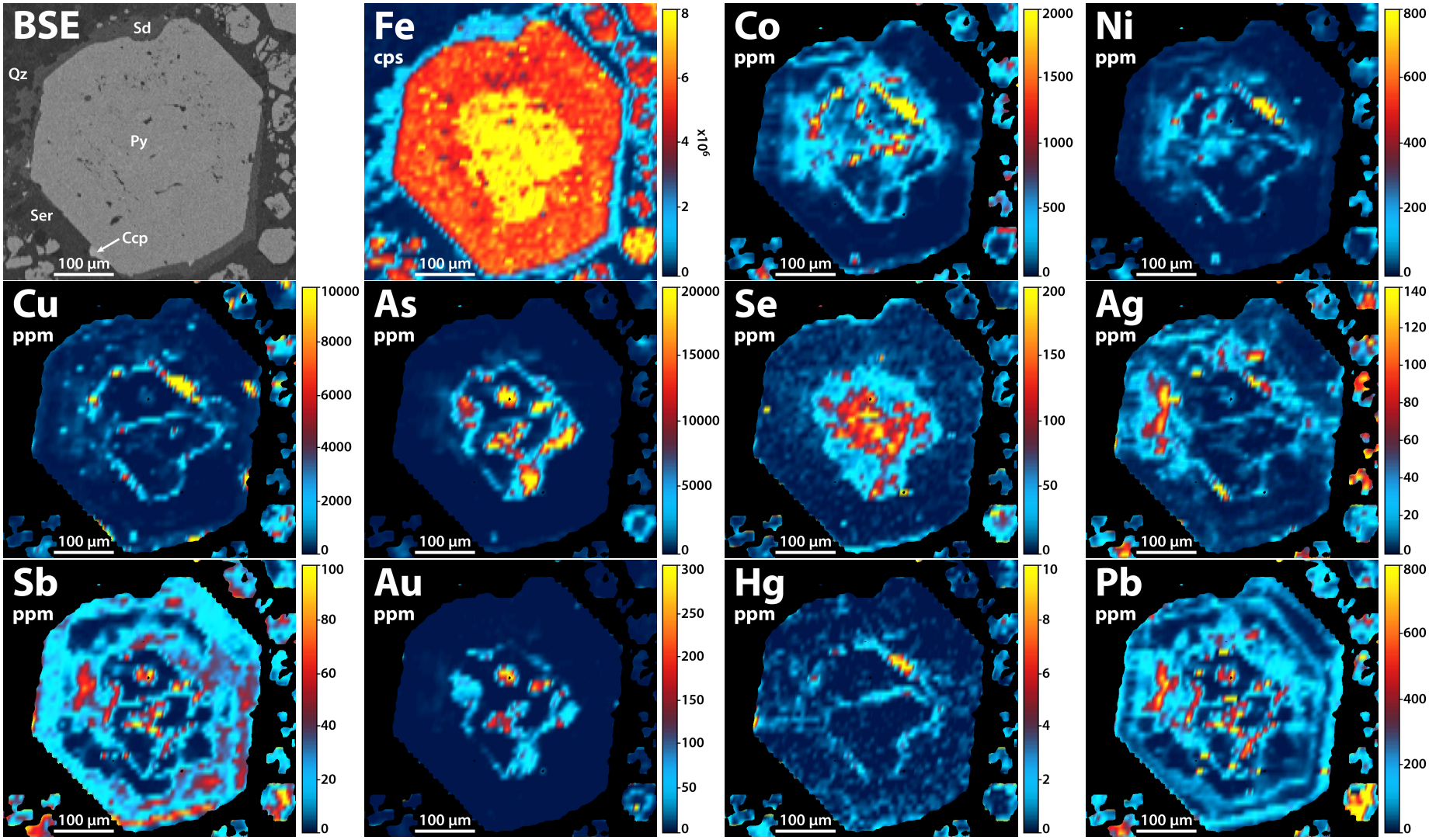

Figure 6.28. Trace element maps of a V3 pyrite crystal from sample IC65-430. A BSE image of the pyrite crystal is also shown.

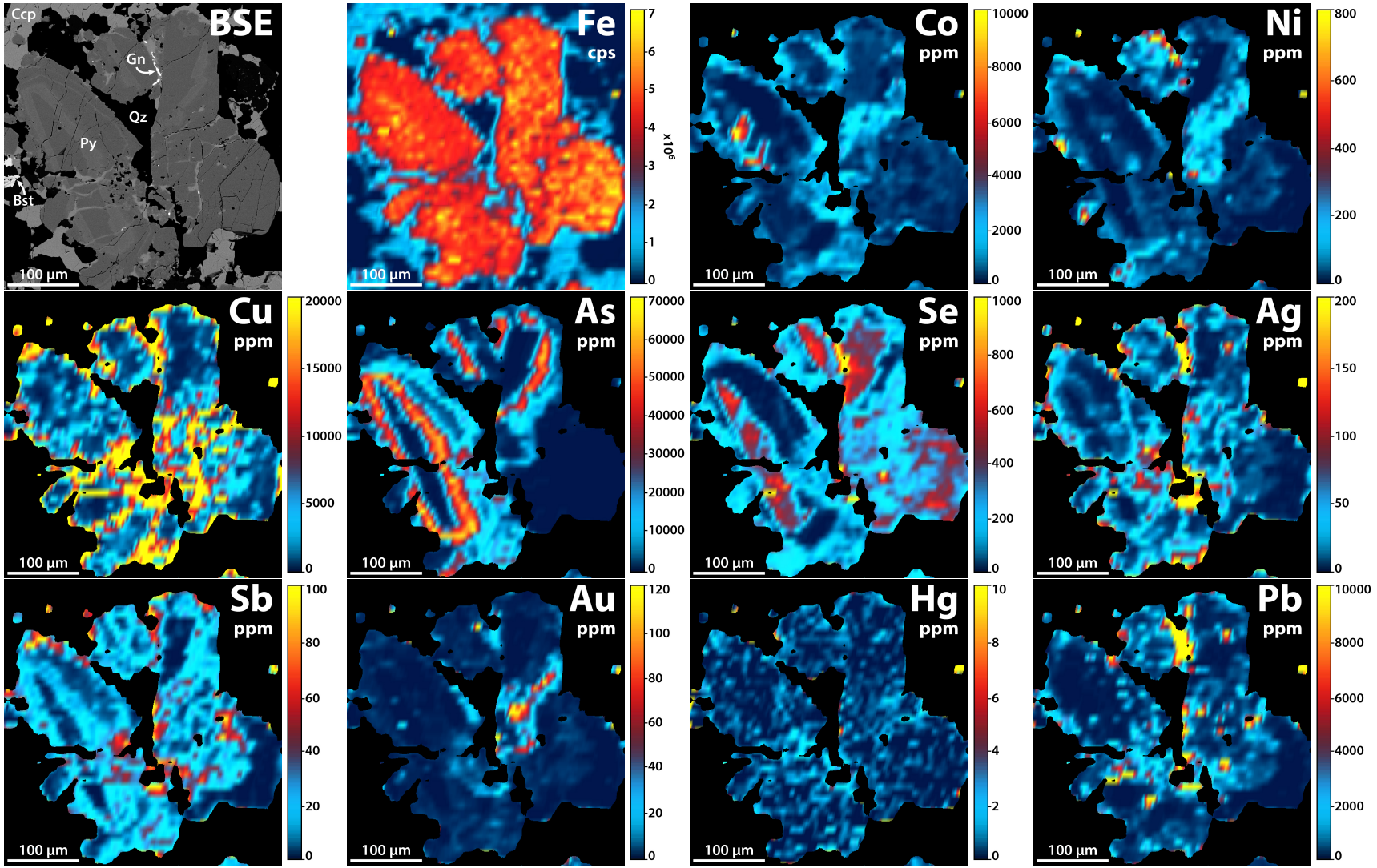

Figure 6.29. Trace element maps of a V3 pyrite crystal from sample IC59-033-1. A BSE image of the pyrite crystal is also shown.

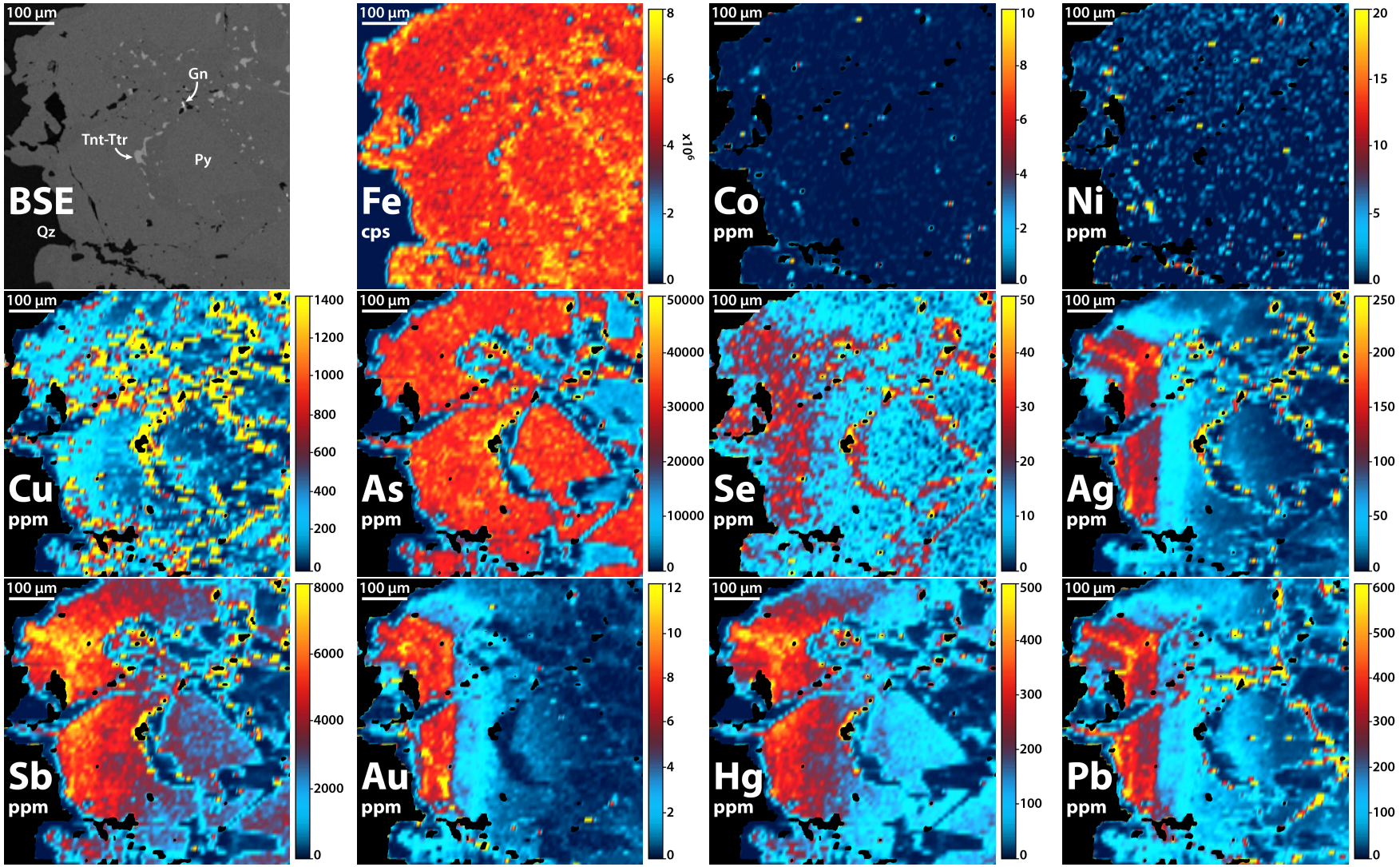

Figure 6.30. Trace element maps of a V3 pyrite crystal from sample IC73-518. A BSE image of the pyrite crystal is also shown.

with respect to Fe, with a core elevated in Fe and a comparatively Fe-depleted rim. The core region is also elevated in all the other trace elements analysed for, to varying degrees. However, Se is the only trace element present at elevated levels throughout the core, with the highest concentrations towards the centre. Arsenic and Au exhibit similar patterns of elevation in discrete areas of the core zone, some of which also correspond to high concentrations of Sb and Pb; Sb and Pb are correlated throughout the core. Nickel, Cu, Ag, and Hg share similar patterns of elevation in the core zone, defining a linear pattern of lower concentrations that outline and cut through the centre of the core zone, and an area of higher concentrations at the top-right edge of the core zone. Cobalt also shares a similar pattern of elevation, although is it present throughout more of the core zone than Ni, Cu, Ag and Hg.

Outside of the core, Co, Ni, Cu, As, Se, Au, and Hg are predominantly present at low concentrations, if at all (i.e., dark blue colours; Figure 6.28). Meanwhile, Ag is more elevated, particularly to the left side of the core, where Co, Sb, and Pb are also present. Elsewhere in the pyrite rim, Sb and Pb are similarly present at low concentrations, with fluctuations in concentration defining a euhedral crystal shape (most clearly seen in the Pb map). A series of smaller pyrite particles also surround the larger pyrite, and these share similar characteristics to the larger pyrite, although they are not uniform. One smaller pyrite particle in the bottom right corner of the image corresponds to the core of the larger pyrite, with elevated Fe, Cu, As, Se, Sb, Au, and Pb, while the remainder of the smaller pyrite particles are more representative of the rim of the larger pyrite, with elevated Ag, Sb, and Pb, and variable Co, Ni, and Cu.

Figure 6.29 shows a V3 pyrite from sample IC59-033-1. Arsenic is highly elevated (i.e., >5 wt.%) in distinctive elongate zones in the pyrite, which correspond to the light-grey parts in the BSE image of pyrite; the darker-grey parts seemingly lack As. Although not present in great quantities, Sb also shares a similar pattern of elevation to As. Meanwhile, Se exhibits an antithetic pattern of elevation compared to As and Sb. Elevated Cu is present in patchy regions of the pyrite particles; these likely correspond to chalcopyrite, which is observed in the BSE image to cross-cut and infill fractures in the pyrite. Elevations of both Pb and Ag correspond to the presence of galena in cracks in the pyrite, although lower concentrations of these elements (particularly Ag) are distributed throughout the pyrite similarly to Sb. Gold is elevated in a discrete region in the middle of the right-side section of pyrite, corresponding to the presence of low As, Co, and Ni; Sb and Se are also present but do not differentiate the Au-rich region. In the left-side section of pyrite, Co is elevated in two regions that correspond to lower concentrations of Se.

Compared to the V3 pyrite in Figure 6.28, the V3 pyrite in Figure 6.29 contains higher

concentrations of As, Se, and Co, with similar concentrations of Ni, Ag, Sb, Au and Hg. Common features include the association between As and Au, the independent distribution of Se, and the similar (but not identical) distribution of Co and Ni. A major difference is the shape of the two pyrites, and the differences in their trace element distributions; i.e., the V3 pyrite in Figure 6.28 has a distinctive core and rim, while the V3 pyrite in Figure 6.29 has a more complex form, with more variable elevations and depletions.

The final V3 pyrite analysed lacks widespread Co and Ni, and is particularly more enriched in Sb and Hg than the previous V3 pyrite particles (Figure 6.30). Differences in Fe content are also observed; elevated Fe defines a network-like pattern that corresponds to a darker grey colour in the BSE image, where inclusions of other ore minerals (particularly tennantite-tetrahedrite) are abundant. This network-like pattern is also evident in the other trace element maps, where depletions of As, Sb, Au, Hg, and Pb are observed. Patchy elevations of Cu, Se, Ag, Sb, and Pb are also present in the network-like region, which may correspond to the presence of tennantite-tetrahedrite, rather than pyrite. Outside the network-like pattern, the larger segments of pyrite are elevated in As, and variably elevated in Se, Ag, Sb, Au, Hg, and Pb. These latter trace elements are present at high concentrations in a linear band to the left side of the pyrite segments, and decrease gradually towards the right. Where As is present at lower concentrations (i.e., light blue colours) in the pyrite segments, only Se is also present at low concentrations; Ag, Sb, Au, Hg, and Pb are absent.

In summary, the trace element maps illustrate that the deportment of trace elements is not consistent in V3 pyrite particles. Each pyrite form shows different trace element concentrations; i.e., euhedral crystals show differences between core and rim (Figure 6.28), elongate particles exhibit zones (Figure 6.29), and more massive particles show differences between crystal segments and a fracture-like network (Figure 6.30). The concentration of trace elements also varies: As is always elevated up to weight percent levels; Co and Ni are enriched up to at least 100s ppm in two of the three V3 pyrite particles, but absent from the third; Se is present in all three. Conversely, Sb and Hg are enriched (100s-1000s ppm) in one of the three V3 pyrite particles, but otherwise absent or present at low concentrations (i.e., $\leq$100 ppm). Gold is present in all three pyrite particles, but concentrations vary between 10s-100s ppm. Silver is similarly ubiquitous, but is always enriched up to 100s ppm. The distribution of Cu and Pb is often patchy, suggestive of inclusions of chalcopyrite or tennantite-tetrahedrite (Cu), or galena (Pb), although Pb is more evenly distributed, up to 100s ppm, in two of the three V3 pyrite particles. Correlations between trace elements vary between the three pyrite particles, but some associations are consistent, in particular, Au is always elevated where As is elevated, and Co

and Ni are similarly distributed.

6.5.4 V6 pyrite

Trace element maps for the one V6 pyrite analysed are presented in Figure 6.31. Gradational differences in Fe (cps) from top to bottom are a result of changes in the detection of Fe over the course of the mapping run, and do not reflect changes in the Fe content of the pyrite crystal.

The V6 pyrite exhibits multiple concentric zones, most clearly depicted in the Co, As, and Se maps. Elevations in these three trace elements characterise the different zones, with Co elevations correlating to a lack of As and Se, As elevations correlating to a lack of Co and Se, and Se elevations correlating to a lack of As and Co; only in the outermost zone where As is most elevated is Se also present at low concentrations. Gold is also observed is in this zone, on the right side of the pyrite. Nickel is detected in the Co-rich zone, but it is only present at very low concentrations. Copper, Ag, Sb, Au, and Pb predominantly have a patchy distribution that does not correlate well with the zones defined by Co, As, and Se. These elements tend to be most elevated in the outermost zone on the right side of the pyrite, or in the As-rich zone in the pyrite core. The highest Cu and Pb concentrations at the top of the trace element maps correlate to the galena and tennantite-tetrahedrite fracture infill, with Ag, Au, and Sb also being present in this fracture. Similarly, the tennantite-tetrahedrite inclusion in pyrite in the BSE image correlates to the elevated Hg concentrations, visible around the edge of the black mask; Hg is otherwise absent from the pyrite. The inclusion of tennantite-tetrahedrite (black pixels) is located on the inner edge of the Se-rich zone.

6.5.5 V7 pyrite

Trace element maps for the one V7 pyrite analysed are presented in Figure 6.32. There are distinct variations in trace element concentrations throughout this pyrite, from core to rim. The core is predominantly elevated in Ni, Sb, Hg, and Pb, with Co, Cu, Se, and Ag also present. Moving outwards from the core, As is elevated in rounded concentric zones, with concentrations varying from high to low depending on the zone. The rounded zones are also evident in the Co, Cu, Ag, Sb, and Au maps (and less so in Ni and Pb maps) where these trace elements are present at low concentrations in specific zones. Selenium is elevated in the rim of the pyrite, surrounding the concentric zones, while Co is most elevated on the outermost margins. Inclusions of arsenopyrite observed in the BSE image correspond to high concentrations of As, Se, and Au, with low concentrations of Cu, Ag, Sb, Hg, and Pb.

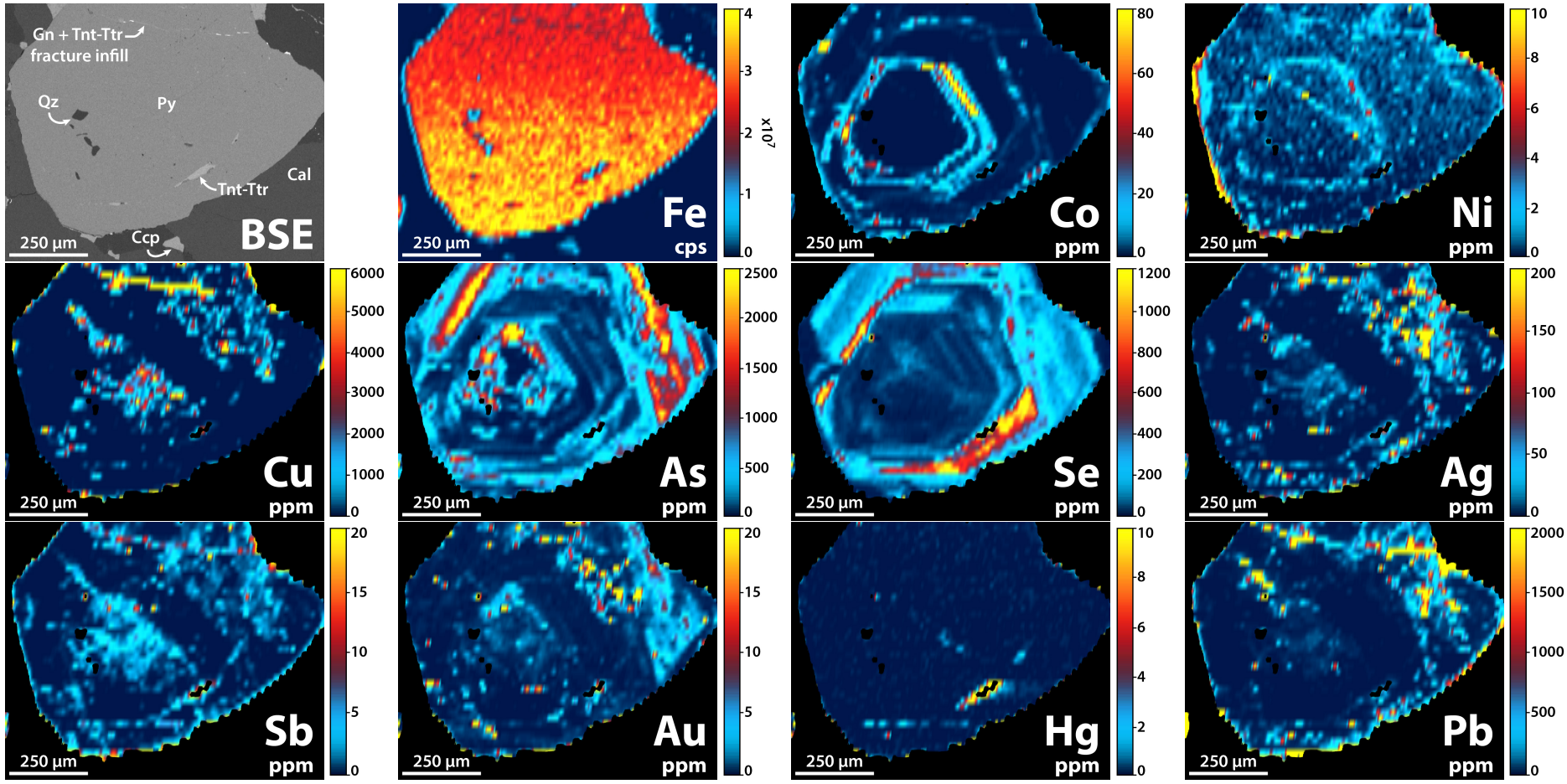

Figure 6.31. Trace element maps of a V6 pyrite crystal from sample IC37-157-2. A BSE image of the pyrite crystal is also shown.

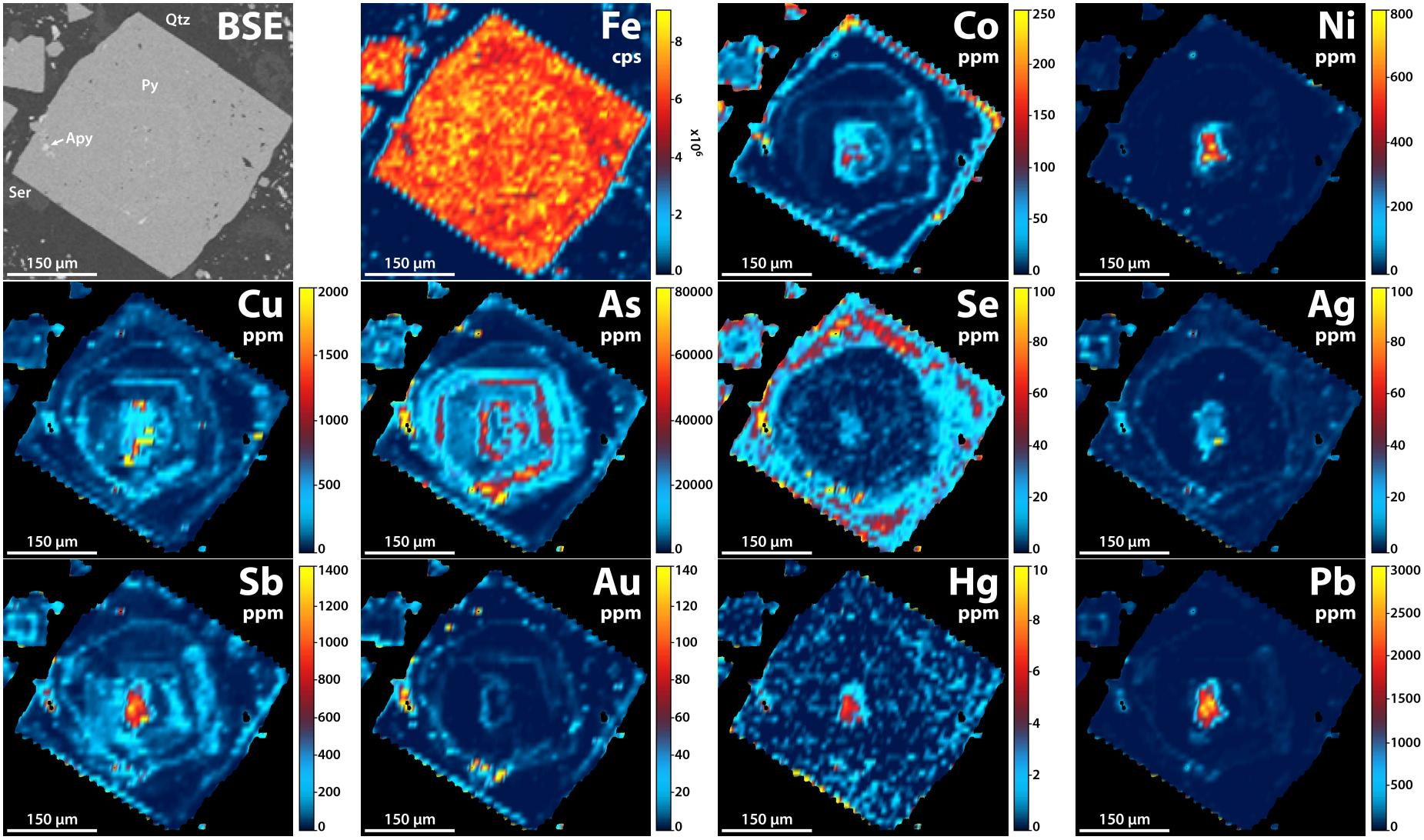

Figure 6.32. Trace element maps of a V7 pyrite crystal from sample IC66-073. A BSE image of the pyrite crystal is also shown.

6.6 Trace element deportment

The LA-ICP-MS data shows that trace elements are not consistently distributed throughout the vein samples from Iron Cap, with differences recognised in the concentration of trace elements in different ore minerals, and the same ore minerals from different vein generations. This section compiles the previously reported LA-ICP-MS data to improve the understanding of where certain trace elements may be found.

Figure 6.33 compares the concentrations of trace elements recorded in the different ore minerals. This boxplot illustrates the differential partitioning of trace elements between different ore minerals, providing an indication of where specific trace elements are most concentrated. In particular, Figure 6.33 shows that, after arsenopyrite and tennantite-tetrahedrite, As is most concentrated in pyrite. Selenium tends to be enriched to concentrations of >100 ppm in all ore minerals apart from sphalerite, but is most concentrated in galena. Silver is most concentrated in galena and tennantite-tetrahedrite, while Cd is most concentrated in tennantite-tetrahedrite and sphalerite. After tennantite-tetrahedrite, Sb is most concentrated in arsenopyrite. Tin and Te exhibit similar levels of enrichment (generally <100 ppm) in all ore minerals apart from sphalerite (Te was not analysed for in sphalerite), with particularly elevated concentrations of these elements detected in galena, tennantite-tetrahedrite and arsenopyrite. Gold is most concentrated in arsenopyrite, while Hg is most concentrated in tennantite-tetrahedrite. Lastly, Bi is most concentrated in galena and tennantite-tetrahedrite.

As evidenced throughout this chapter, there are variations in these trends depending on the vein generation or sample in question, meaning that Figure 6.33 and associated text only constitute a generalised summary of trace element deportment. This is explored further below, and also in Chapter 8, where ore mineral proportions are also taken into account to determine the deportment of trace elements, and the importance of specific ore minerals as trace element hosts. Nevertheless, a benefit of the data presented here is that it provides information relevant to the development of Iron Cap in an economic sense; this is also discussed in Chapter 8.

Variations in the concentration of selected trace elements between vein generations are summarised in Table 6.7, highlighting that specific veins appear to be enriched in certain trace elements. In particular, Co appears to be most concentrated in V3 veins, where pyrite, chalcopyrite, and sphalerite host the highest concentrations relative to the same ore minerals in other vein generations. Selenium appears to be most concentrated in V4 veins, where galena and chalcopyrite host the highest concentrations relative to the same ore minerals in other vein generations. However, the most Se-enriched pyrite

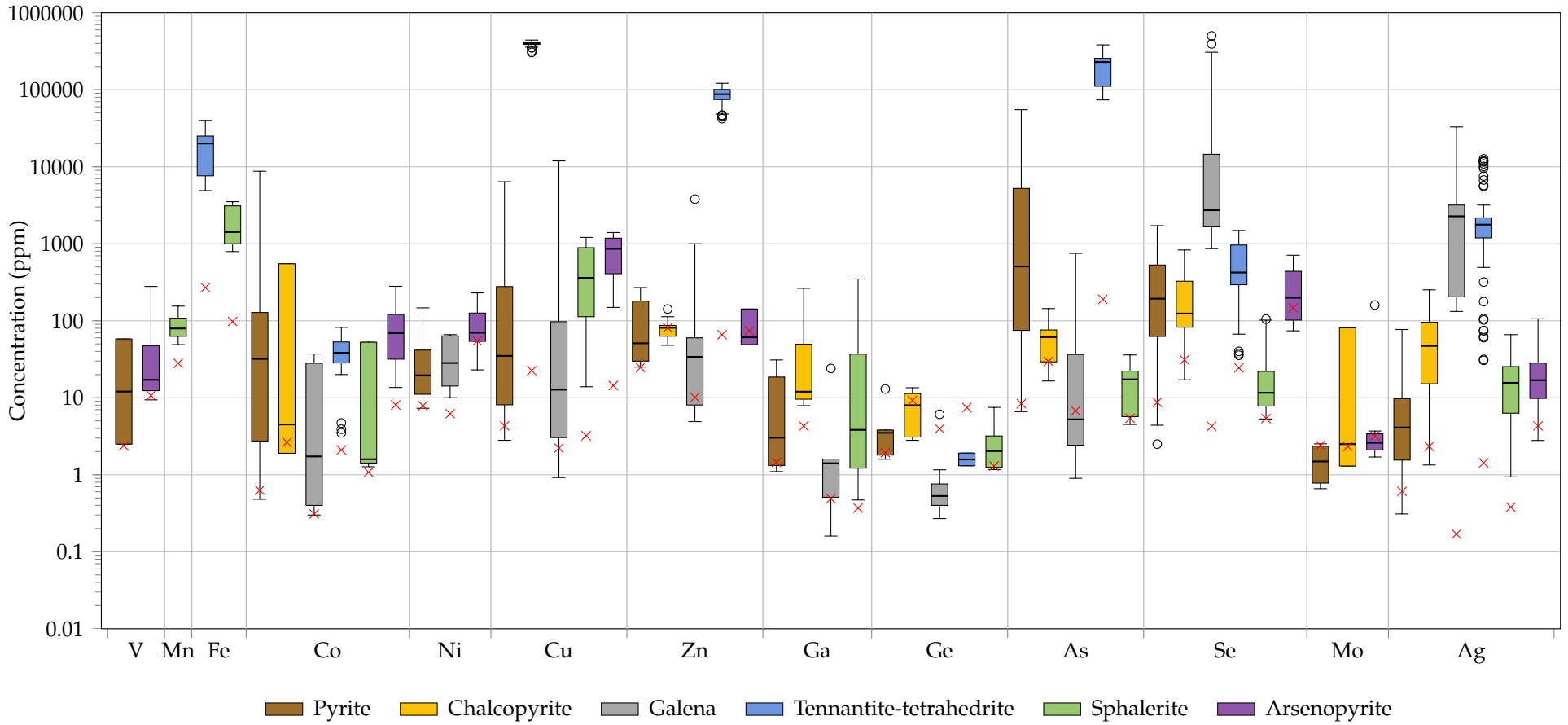

Figure 6.33. Boxplot of trace element concentrations in the ore minerals analysed by LA-ICP-MS. Filled circles represent sample sizes of 1 (e.g., Cd in arsenopyrite). Open circles represent outliers in the data, which are classified as in Figure 6.4. Red crosses are mean lower limits of detection; no data below detection limits is shown. Major elements used for normalisation are not shown; Fe in pyrite, chalcopyrite, and arsenopyrite, Cu in tennantite-tetrahedrite, Zn in sphalerite, and Pb in galena. Arsenic in arsenopyrite is not shown because of the inaccuracy of measured concentrations, in some cases exceeding 100 wt.%. *(continued on next page)*

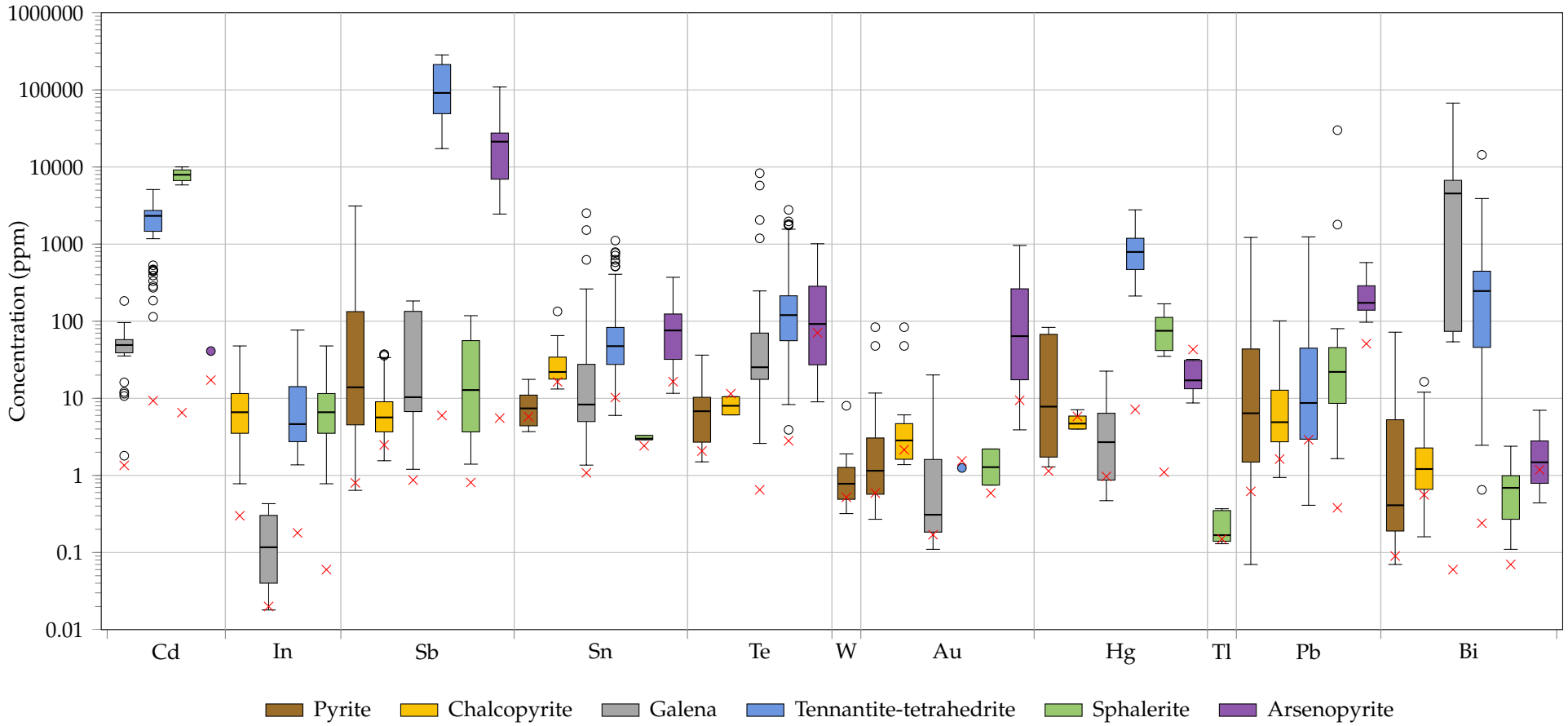

Figure 6.33. *(continued)*

Table 6.7

Median concentrations of selected trace elements in the ore minerals from different vein generations. Number of analyses are in brackets.

All data in ppm	Co	Ni	As	Se	Ag	Cd	In	Sb	Sn	Te	Au	Hg	Bi
V2													
Pyrite (18)	12	11	75	448	6	–	–	8	7	8	1	1	6
Chalcopyrite (41)	–	–	–	288	43	–	8	5	20	6	2	–	1
Galena (2)	–	20	41	154000	672	2	–	8	891	3460	2	3	1590
Tnt-ttr (22)	40	–	112000	1110	933	1250	9	196000	73	162	1	805	448
V3													
Pyrite (31)	746	30	6710	256	6	–	–	524	8	7	27	47	1
Chalcopyrite (22)	550	–	63	96	12	–	6	9	26	11	6	–	1
Galena (5)	–	–	377	14700	2260	49	–	10	28	84	<1	12	4500
Tnt-ttr (7)	–	–	190000	241	5570	3240	3	127000	72	210	–	787	440
Sphalerite (2)	53	–	19	104	11	9550	10	2	3	–	2	167	1
V4													
Chalcopyrite (28)	2	–	25	335	73	–	4	4	–	–	–	5	1
Galena (3)	3	10	59	394000	6800	16	<1	4	625	2050	2	6	12370
V5													
Chalcopyrite (10)	5	–	68	84	14	–	10	7	22	–	2	–	1
Tnt-ttr (26)	–	–	257000	358	1940	2470	6	46500	33	64	–	975	94
V6													
Pyrite (9)	17	10	1040	110	3	–	–	–	9	19	5	–	8
Chalcopyrite (13)	–	–	17	26	90	–	17	6	–	–	–	–	2
Galena (22)	1	52	5	2070	1360	49	<1	78	7	20	<1	2	2618
Tnt-ttr (7)	4	–	95100	54	11600	3640	2	231000	36	48	–	410	3
Sphalerite (17)	1	–	16	9	16	7790	35	13	3	–	1	57	1
V7													
Pyrite (6)	9	–	14600	37	27	–	–	190	7	4	1	2	<1
Arsenopyrite (17)	69	70	865000	200	17	41	–	21300	78	92	64	17	1

and tennantite-tetrahedrite are in V2 veins, while the most Se-enriched sphalerite is in V3 veins. V6 veins appear to be the most Ag-rich in terms of chalcopyrite and tennantite-tetrahedrite, while galena is most enriched in Ag in V4 veins. V3 and V6 veins appear to be more enriched in Cd, compared to V2, V4, and V7 veins, while V6 veins also appear to be the most In-rich. These observations are discussed in Chapter 8.

In summary, the ore minerals from different vein generations exhibit distinct trace element compositions. These may be utilised to quantitatively describe the distribution of trace elements in the sample suite from Iron Cap. The ore mineral compositions may be further utilised to elucidate the characteristics of the hydrothermal fluids that formed each vein generation. These topics are explored in the following chapters.

7 Modelling trace element partitioning

7.1 Introduction

Determining whether trace elements are lattice-hosted or present as discrete inclusions within ore minerals is a key aspect of many trace element studies (e.g., Cook et al., 2011; George et al., 2015; Grant et al., 2018; Rivas-Romero et al., 2021), because the mode of trace element incorporation has implications for the conditions of ore mineral crystallisation (e.g., Reich et al., 2005; Wu et al., 2021). Trace elements that are incorporated into the lattice of an ore mineral are intrinsically linked to the hydrothermal fluid via the partition coefficient (K_D):

$$K_D = \frac{\text{concentration in ore mineral}}{\text{concentration in hydrothermal fluid}} \quad (1)$$

Therefore, changes in the concentration of lattice-hosted trace elements in an ore mineral may help elucidate changes in the characteristics of hydrothermal fluid. Discrete inclusions are still important to consider, but are not controlled by a K_D in their present state, as they are not substituted for elements in the lattice. Furthermore, inclusions may not necessarily be direct precipitates of the hydrothermal fluid at the time of ore mineral crystallisation, because inclusions can also form prior to, or after, crystallisation of the host mineral (cf. Section 4.4).

This chapter aims to utilise the fundamental relationship between the composition of an ore mineral and a hydrothermal fluid (equation (1)) in a model based on lattice strain theory, to assess the compatibility of certain trace elements in the lattice of selected ore minerals. The relative K_Ds of lattice-hosted trace elements will also be determined, which may have implications for the understanding of hydrothermal fluid characteristics. Out of the ore minerals analysed by LA-ICP-MS, only pyrite is considered, because:

1. It has a relatively simple mineral formula and structure (Bowles et al., 2011), at least in comparison to chalcopyrite and tennantite-tetraehdrite (cf. Gibbs et al., 2007; George et al., 2017), meaning that it is relatively simple to model;

2. There is trace element data (both spot and map) available for pyrite across vein generations (in comparison to sphalerite and arsenopyrite; Chapter 6), which is important to be able to utilise the model for interpreting hydrothermal fluid evolution;

3. Other ore minerals (i.e., galena) are likely to contain lattice-hosted trace elements owing largely to coupled substitutions (e.g., George et al., 2015), which are not able to be considered in the simple model of this thesis;

4. Pyrite is one of the most common ore minerals in many ore deposit types (e.g., orogenic gold, VMS, porphyry, and epithermal; Sillitoe, 2010; Cook et al., 2013; Hannington et al., 2014), and is the most commonly studied ore mineral in the context of trace elements (e.g. Reich et al., 2005; Franchini et al., 2015; Keith et al., 2016; Steadman et al., 2021), thus the outcomes of the modelling are likely to be more widely applicable than for the other ore minerals analysed by LA-ICP-MS.

This chapter is stuctured to first outline the rationale underpinning the modelling approach (Section 7.2). Next, the theoretical model is explained (Section 7.3), and the model for trace elements in pyrite is presented (Section 7.4). The modelling approach is then evaluated, and the implications of the modelling are layed out (Section 7.5); these are discussed in greater detail in the following chapter.

7.2 Modelling rationale

Most studies that attempt to discriminate between lattice-hosted and inclusion-hosted trace elements in ore minerals are based on the classification of LA-ICP-MS profiles traces as spiky, or smooth/flat, which are interpreted to represent inclusions, and lattice-hosting, respectively (e.g., Cook et al., 2011; George et al., 2015; Grant et al., 2018; Rivas-Romero et al., 2021). However, such interpretations are limited by the spatial resolution of LA-ICP-MS analyses, because spot sizes are typically on the scale of tens of microns, and the compositional data are a result of ablating a volume of material, meaning that distinguishing between lattice-hosted trace elements and inclusion particles approximately $<$10 µm in size based on profile traces is not possible (e.g., Wu et al., 2019). Lattice-hosting may also be inferred based on the correlation of trace element concentrations with major element concentrations; for example, a 1:1 negative correlation (in terms of apfu) between As and S in pyrite is suggestive of lattice incorporation of As^-, substituting for S^{2-} (Roman et al., 2019). Similarly, positive correlations between trace elements may be indicative of lattice-hosting owing to coupled substitutions; for example, George et al. (2018a) identified a positive correlation between Tl + Cu + Ag and Sb in pyrite, and proposed that this could indicate a coupled substitution: $(Tl^+, Cu^+, Ag^+) + Sb^{3+} \longleftrightarrow 2\,Fe^{2+}$.

In the context of ore formation, few studies have attempted to investigate the incorporation of trace elements in ore minerals in greater depth (e.g., Wu et al., 2019; Fougerouse et al., 2021), meaning that there is much more to be learned. Nevertheless, experimental work on solid solutions highlights that some trace elements may be present as direct lattice substitutions in pyrite; for example, pyrite forms solid solutions with vaesite (NiS_2) and cattierite (CoS_2), indicating that Ni^{2+} and Co^{2+} can readily substitute for Fe^{2+} (Bowles et al., 2011). Meanwhile, George et al. (2018b) compared the ionic radii of Fe and Cu in

chalcopyrite with the ionic radii of trace elements detected by LA-ICP-MS in chalcopyrite. They found that Ni^{2+}, Co^{2+}, Zn^{2+}, In^{3+}, and Sn^{4+} could theoretically substitute for Cu^{+}, Cu_2^{+}, Fe^{2+}, and/or Fe^{3+} in chalcopyrite, given the similarities in ionic radii, although they concluded that trace element incorporation mechanisms were poorly understood. This research project has sought to apply a model that is better able understand the incorporation of trace elements into ore minerals, applying the concepts of lattice strain theory summarised in Section 4.4.

Blundy and Wood (1994) developed a lattice strain model to quantitatively predict trace element K_Ds between silicate minerals and co-existing melts, where the size and elasticity of the crystal lattice sites, and the size and charge of the substituent ions are key parameters. By utilising pre-determined K_D data for a cation site, their model can be used to predict the K_Ds of other trace element cations of similar charge into the cation site (Blundy and Wood, 1994). This makes it possible to assess the compatibility of cations in a lattice site, and therefore interpret changes in mineral compositions with respect to element K_Ds. Such an approach has not yet been applied to sulphide minerals precipitated from hydrothermal fluids.

More recently, van Hinsberg et al. (2010) utilised the model of Blundy and Wood (1994) to assess mineral-fluid element partitioning. They conducted partitioning experiments involving fluorite in aqueous solutions to test if a lattice strain model could accurately describe experimentally-determined partitioning behaviour, in agreement with Blundy and Wood (1994) for mineral-melt experiments. Importantly, van Hinsberg et al. (2010) noted that element speciation in the fluid had an impact on partitioning behaviour, but that these effects can be accounted for when the speciation of an element in the hydrothermal fluid of interest is known from other sources (e.g., fluid inclusions or experimental studies). Alternatively, if element speciation is not known, it is often possible to model cations of similar charge, because their speciation is often similar (van Hinsberg et al., 2010).

Both Blundy and Wood (1994) and van Hinsberg et al. (2010) utilised experiments conducted at relevant physicochemical conditions to determine K_Ds and assess element partitioning. Experimental data is not available for the ore minerals considered in this thesis, particularly for natural samples under porphyry ore-forming conditions. However, there is data for trace elements in pyrite from active seafloor hydrothermal systems, where the composition of hydrothermal fluids have also been recorded (Grant et al., 2018). Although not ideal, this data can be used to calculate trace element K_Ds, which can then be used to constrain a lattice strain model for pyrite. As the understanding of trace element incorporation in ore minerals is currently not well understood, particularly

in terms of K_Ds, such a model constitutes an attempt to improve this understanding, and gain insights to the processes that may be taking place.

One aspect of mineral-melt/fluid partitioning calculations that warrants further discussion in regard to porphyry systems is the assumption of equilibrium conditions. Porphyry deposits often exhibit evidence of disequilibrium between minerals and hydrothermal fluids; this is commonly exemplified by mineral textures (e.g., an abundance of porosity and/or mineral inclusions) that suggest rapid crystallisation took place (e.g., Roman et al., 2019). Other evidence comes from trace element studies, where pyrite maps show that mineral growth followed non-concentric patterns, and/or that trace elements not expected to be incorporated in the pyrite lattice are enriched due to disequilbrium precipitation (e.g., Sykora et al., 2018; Steadman et al., 2021). While it is evident that disequilibrium conditions often occur within porphyry systems, it remains necesssary to assume equilibrium for the purposes of modelling trace element partitioning, because it is not feasible to account for all possible influences within a simple model. However, it should be noted that where mineral textures and/or trace element signatures suggest disequilibrium precipitation has taken place, that any outcomes of partitioning calculations that assume equilibrium conditions should be considered with caution.

7.3 Lattice strain model

The lattice strain model of Blundy and Wood (1994) describes a quantitative relationship between the elastic properties of a crystal lattice site and the behaviour of trace elements partitioning into that site, using the equation:

$$K_D = D_o \exp\left(\frac{-4\pi E_{\mathrm{M}} N_A \left(\frac{r_o}{2}\left(r_i - r_o\right)^2 + \frac{1}{3}\left(r_i - r_o\right)^3\right)}{RT}\right) \tag{2}$$

where r_o is the optimum ionic radius for the lattice site of interest, r_i is the radius of the substituent ion, E_{M} is the Young's modulus of the lattice site of interest, N_A is Avogadro's number, R is the gas constant, T is temperature in °K, and D_o is the strain-compensated K_D for a fictive ion with a radius of r_o. Calculating K_Ds using equation (2) for a range of r_i values and plotting the data on a graph generates a parabola that describes the relationship between K_D and ionic radius in a crystal lattice site, which is dependent upon E_{M} and T, as illustrated in Figure 7.1.

Ion size is an important variable, because the value for r_o controls how well matched substituent ions (i.e., r_i) are to the lattice site. Similar values for r_o and r_i mean that substituent ions (of similar charge) should have little trouble entering the lattice site,

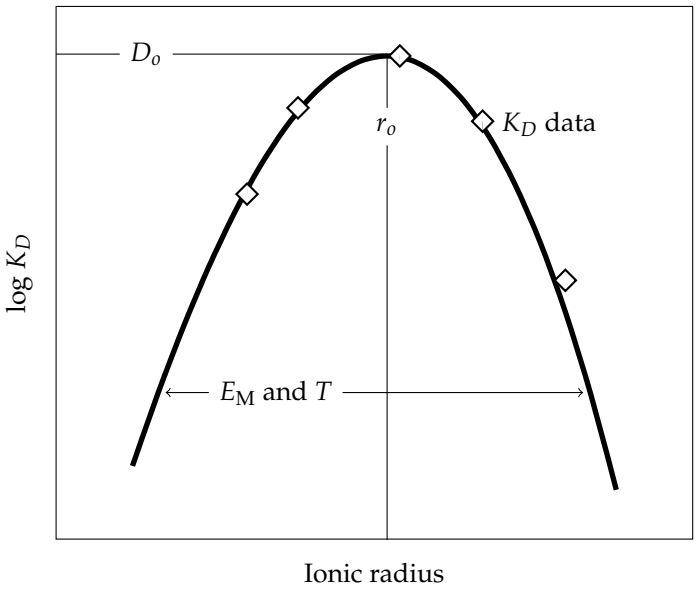

Figure 7.1. Illustration of the lattice strain model (modified from Blundy and Wood, 2003). The parabola is drawn from a series of data points (not shown) calculated using equation (2), with different values for r_i. Ions with radii that fall on the apex of the parabola have the highest K_Ds, and are most readily substituted into the crystal lattice site, because they fit with the least strain. The width of the parabola is dependent upon E_M for a given T; with lower E_M leading to a wider parabola, and higher E_M leading to a tighter parabola. When T increases, the parabola widens, and when T decreases, the parabola tightens. Pre-determined K_D data (diamond symbols) is required to constrain the parabola to r_o and D_o, which fix the location of the parabola on the x and y axis, respectively. However, it is possible to generate a purely theoretical parabola for a given T, without constraints from K_D data, and assuming that r_o is equal to the ionic radius of the substituted ion. In this case, the parabola will be unconstrained in terms of D_o, meaning that only relative K_Ds can be generated.

while any deviation of r_i from r_o requires consideration of the elastic properties of the crystal to assess whether substitution may occur. The Young's modulus (E_M) is a measure of the elastic response of the site to lattice strain (Blundy and Wood, 1994); in other words, it is the stiffness of the bonds of the lattice site. Sites with lower E_M have bonds that are more elastic and respond to lower degrees of stress than sites with higher E_M, which have stiffer bonds that respond to higher degrees of stress. This means that sites with lower E_M can more readily accomodate ions that are not well-matched in terms of size (i.e., are smaller or larger), because they require lower degress of stress to induce the strain necessary to fit mismatched ions. In comparison, sites with higher E_M require higher degrees of stress to induce the strain necessary to accomodate the same ions. Temperature is inversely proportional to E_M because bonds get stiffer as T decreases, which mimics the effect of increasing E_M at a constant T. However, Blundy and Wood (1994) note that E_M is relatively insensitive to changes in T, meaning that a single value for E_M can be used to model partitioning at different T conditions.

The model of Blundy and Wood (1994) is based on the treatment of substituent ions as point defects in a crystal lattice, therefore only accounting for changes in the composition of a crystal on a single ion basis. This simplification allows the determination of a set of K_Ds for a lattice site in a pure crystal; complications would arise when considering further compositional changes above that of a single ion, because K_Ds are often sensitive to crystal composition (Blundy and Wood, 2003). This is owing to the fact that the lattice properties of the crystal change as ions are substituted, meaning that the properties considered for a lattice site in a pure crystal would no longer be applicable (Blundy and Wood, 2003). Coupled substitutions thus cannot be modelled using equation (2), because they involve two separate ions of differing charge entering two separate lattice sites. The two substituent ions may not sit on adjacent sites and the lattice strain may not simply be the sum of that generated by the two substitutions (Blundy and Wood, 2003). It is therefore too complex a process to consider using the simple model.

However, it is possible to consider direct substitution of ions of differing charge into the lattice site of interest. From their experimental data, Blundy and Wood (1994) show that E_M varies linearly with ion charge, such that E_M can be supplemented by $\frac{z_i}{z_o}$ in equation (2) to generate data for ions of differing charge, where z_o is the optimum charge at the site of interest, and z_i is the charge of the substituent ion:

$$K_D = D_o \exp\left(\frac{-4\pi E_\mathrm{M} \frac{z_i}{z_o} N_A \left(\frac{r_o}{2}\left(r_i - r_o\right)^2 + \frac{1}{3}\left(r_i - r_o\right)^3\right)}{RT}\right) \tag{3}$$

The parabola in Figure 7.1 thus tightens with increasing charge. Blundy and Wood (1994) also show that K_D varies with the degree of charge mismatch, whereby ions with higher charge mismatch have lower K_Ds than ions that are matched in terms of charge. This is also evident in the mineral-fluid experiments of van Hinsberg et al. (2010), who show that, for the substitution of Ca^{2+} in fluorite, substituent 2+ ions generate a parabola with a higher peak K_D than the parabolae for substituent 1+ and 3+ ions. For similar degrees of charge mismatch in different directions (i.e., 1+ vs. 3+ ions into a 2+ site), Blundy and Wood (2003) note that there is no simple generalisation that can be applied, contrary to the third rule of Goldschmidt, which states that the higher charged ion will be preferentially incorporated (Goldschmidt, 1937). Further research has shown that ions of zero charge can also be modelled, although the dependence of K_Ds on charge mismatch holds true, such that for the substitution of Ca^{2+}, K_Ds for substituent ions generally follow the charge order: $2+ > 3+ \approx 1+ > 4+ \geq 0+$ (Wood and Blundy, 2001). It is not possible to use equation (3) to model the substitution of ions of zero charge, but this is not an issue for this thesis, as ions of this nature are noble gasses, which are not recorded in the trace

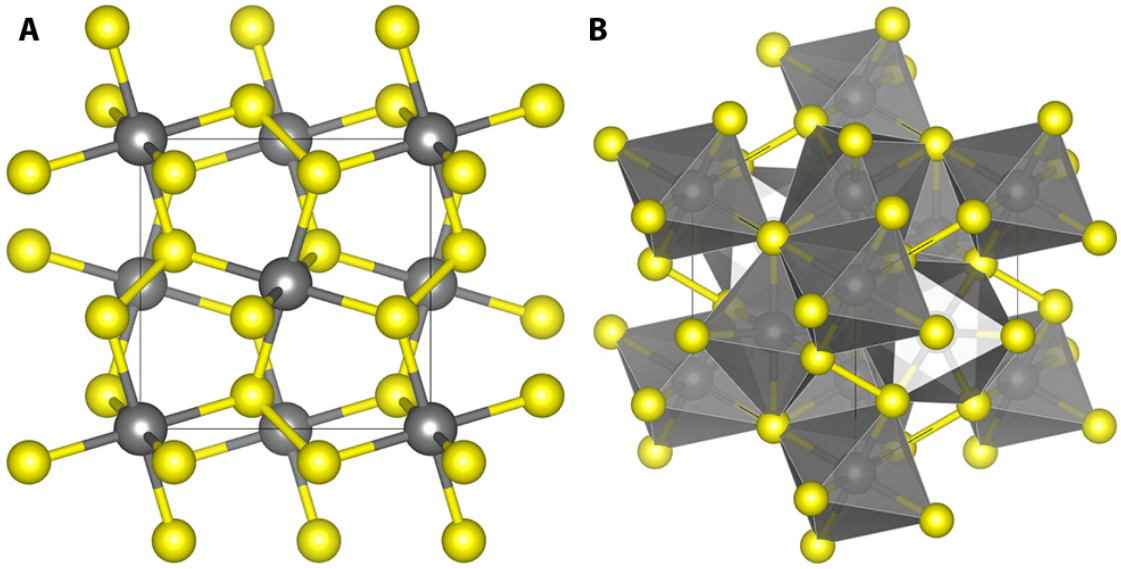

Figure 7.2. Crystal structure of pyrite, showing relationships between Fe atoms and S_2 dimers (A), and FeS_6 octahedra (B). Sulphur atoms are in yellow, and Fe atoms are in grey; polyhedra are also in grey because they house Fe atoms. Images modified from Wikimedia (2020); these were created using structural data from Bayliss (1977).

element data for ore minerals (Chapter 4 and 6).

With equation (3) it is possible to model the partitioning behaviour of a range of trace elements between ore minerals and hydrothermal fluids. Ionic radii for trace elements in various valence states and structural configurations (i.e., coordination numbers) are readily available (Shannon, 1976). However, modification of these values is likely necessary because ore minerals are not all simple ionic structures (e.g., Gibbs et al., 2007). The remaining input parameters required for the calculation of K_Ds are E_M for the ore mineral of interest, and empirically constrained K_D data for trace elements between the ore mineral and hydrothermal fluid, in order to constrain the generated parabola in terms of D_o and r_o. The selection of these parameters in the case of pyrite is dicussed below.

7.4 Trace element partitioning in pyrite

Pyrite (FeS_2) is of the cubic crystal system, with a primitive cubic lattice in octahedral coordination, meaning that each Fe atom interacts with six S atoms (coordination number = 6) forming FeS_6 octahedra (Bowles et al., 2011). Unlike some other cubic sulphides that exhibit simple NaCl crystal structures (e.g., galena), pyrite has a crystal structure that is more complex and densely-packed owing to the accomodation of an additional S atom per metal atom (Bowles et al., 2011). This is illustrated in Figure 7.2, where S_2 dimers link together a framework of corner-sharing FeS_6 octahedra (Gibbs et al., 2007). Notably, Figure 7.2B shows that the pyrite crystal structure is distorted and non-ideal, because the FeS_6 octahedra are not all in the same orientation.

The interatomic distance (i.e., bond length) of Fe–S bonds in pyrite is 2.26 Å, as determined from measurements in a crystal diffraction study of synthetic pyrite (Brostigen and Kjekshus, 1969). This value is inconsistent with the Fe–S bond lengths derived from the sum of Fe and S effective ionic radii data of Shannon (1976). Simply adding the radii of low-spin, octahedrally coordinated Fe^{2+} (0.61 Å), and octahedrally-coordinated S^{2-} (1.84 Å), yields a Fe–S bond length of 2.45 Å, which is ∼8% larger than the experimentally-derived value. This discrepancy can be explained by the Fe–S bonds in pyrite being partially covalent. The data from Shannon (1976) is derived from measurements of ion-O bond lengths, minus the atomic radius of octahedrally-coordinated O^{2-} (1.40 Å), to generate an effective ionic radius for the ion of interest. However, O has a higher electronegativity (3.44) than S (2.58). A lower electronegativity leads to an increase in the covalency of a bond, and the shortening of a bond; therefore, Fe–S bonds are more covalent, and exhibit shorter bond lengths, than Fe–O bonds (Shannon, 1976; Gibbs et al., 2017). Utilising the data from Shannon (1976) for lattice strain modelling of pyrite therefore requires atomic radii to be adjusted for a degree of covalency.

Adjustment of the effective ionic radii of Shannon (1976) is achieved by calculating the degree of covalency, using the equation:

$$r_a = r_e\,(1 - C) + (r_c \times C) \tag{4}$$

where r_a is the adjusted ionic radii, r_e is the effective ionic radii (from Shannon, 1976), C is the degree of covalency, and r_c is the covalent radii (from Pyykkö and Atsumi, 2009). For Fe–S bonds in pyrite, the value of C was adjusted such that $r_a(\text{Fe}) + r_a(\text{S}) = 2.26$ Å, the experimentally-derived Fe–S bond length. A 0.73 degree of covalency was required to achieve this, resulting in values of $r_a(\text{Fe}) = 1.01$ Å and $r_a(\text{S}) = 1.25$ Å. This equates to the Fe–S bonds in pyrite being 73% covalent and 27% ionic. The radii of each cation considered for substitution on the Fe^{2+} site in pyrite was similarly adjusted using equation (4), and using the same degree of covalency. A limitation of this approach is that, as noted above, not all ions have the same electronegativity, and thus the degree of covalency may vary between ions.

Table 7.1 summarises the ions (and their various ionic radii) considered for modelling in terms of what could plausibly subititute into pyrite. Ions were chosen based on the presence of the elements in the LA-ICP-MS data (Section 6.4.3), and the typical oxidation state of the elements in hydrothermal fluids (of porphyry systems, where possible; references in Table 7.1). For modelling ion substitution into the Fe^{2+} site in pyrite, only 1+, 2+, and 3+ ions are considered, because, as noted above, ions with greater degrees of

Table 7.1
Ionic radii (r_e, r_c, and r_a) for the ions modelled. Ion choice is based on the typical oxidation state of an element in hydrothermal fluids, derived from the references listed. Values of r_e and r_c are from Shannon (1976) and Pyykkö and Atsumi (2009), respectively.

Ions	r_e (Å)	r_c (Å)	r_a (Å)	Reference of oxidation state
2+ ions				
Co^{2+}	0.65	1.11	0.99	Migdisov et al. (2011)
Ni^{2+}	0.69	1.10	0.99	Liu et al. (2012)
Cu^{2+}	0.73	1.12	1.01	Kouzmanov and Pokrovski (2012)
Mn^{2+}	0.67	1.19	1.05	Suleimenov and Seward (2000)
Zn^{2+}	0.74	1.18	1.06	Kouzmanov and Pokrovski (2012)
Cd^{2+}	0.95	1.36	1.25	Bazarkina et al. (2010)
Hg^{2+}	1.02	1.33	1.25	Barnes and Seward (1997)
Pb^{2+}	1.19	1.44	1.37	Kouzmanov and Pokrovski (2012)
1+ ions				
Cu^{+}	0.77	1.12	1.03	Kouzmanov and Pokrovski (2012)
Ag^{+}	1.15	1.28	1.24	Kouzmanov and Pokrovski (2012)
Au^{+}	1.37	1.24	1.28	Kouzmanov and Pokrovski (2012)
Tl^{+}	1.50	1.44	1.46	Bebie et al. (1998)
3+ ions				
As^{3+}	0.58	1.21	1.04	Kouzmanov and Pokrovski (2012)
Ga^{3+}	0.62	1.24	1.07	Wood and Samson (2006)
Sb^{3+}	0.76	1.40	1.23	Kouzmanov and Pokrovski (2012)
In^{3+}	0.80	1.42	1.25	Wood and Samson (2006)
Bi^{3+}	1.03	1.51	1.38	Tooth et al. (2013)

charge mismatch (i.e., $>\pm 1$) have lower K_Ds, and are thus unlikely to be hosted in great quantities as direct substitutions.

Determining the Young's modulus (E) of pyrite, in particular that of the Fe^{2+} site (E_M), first requires calculation or determination of the bulk modulus, K, which is related to E through the expression:

$$E = 3K\,(1 - 2v) \tag{5}$$

where v is Poisson's ratio, a measure of the compressiblity of a material in a direction perpendicular to the direction of applied stress (Fossen, 2010). As in the study of Blundy and Wood (1994), it is assumed that the mineral behaves as a perfect Poisson's solid, where $v = 0.25$.

The K of pyrite has been empirically determined from experiments and computational studies; a value of 1470 kbar is utilised here (Banjara et al., 2018). Inputting K into equation (5) yields a E of 2205 kbar for pyrite. This value, when converted to pascals, may be used in equation (3) to generate K_D data for pyrite; however, it has been shown that K for a crystal is not necessarily the same as K for an individual polyhedra (Hazen and Finger, 1979). Blundy and Wood (1994) therefore suggest utilising the K-volume rela-

tionship proposed by Hazen and Finger (1979) to estimate the polyhedral bulk modulus, K_p, for the site of interest:

$$K_p = \frac{7.5\left(S^2 Z_c Z_a\right)}{d^3} \tag{6}$$

where S^2 is an empirical term for the relative ionicity of the bond (0.40 for sulphides; Hazen and Finger, 1979), Z_c is the charge of the cation, Z_a is the charge of the anion, and d is the mean cation-anion separation. In minerals such as pyrite, which only have a single cation-anion bond to consider, d is equal to the cation–anion bond length (i.e., Fe–S). In the context of the lattice strain model, this means that when considering substitutions on the Fe^{2+} site, there is an assumption that r_o is equal to the ionic radius of Fe^{2+} for the calculation of K_p. Nevertheless, inputting the known parameters for pyrite into equation (6) gives:

$$K_p = \frac{7.5\left(0.40 \times 2 \times 2\right)}{2.26^3} = 1039.58 \text{ kbar} \tag{7}$$

which is ∼41% lower than K for the pyrite crystal (1470 kbar; Banjara et al., 2018). Calculating for E_{M} in equation (5) gives 1559.36 kbar, which again is ∼41% lower than E for the pyrite crystal. This would suggest that the FeS_6 octahedra in pyrite are able to accomodate more lattice strain than the pyrite crystal as a whole.

However, equation (6) only provides an *estimate* of K_p. To accurately calculate K_p, an accurate value for the K-volume relationship (expressed as $K_p(d^3)/S^2 Z_c Z_a = 7.5 \pm 0.2$; Hazen and Finger, 1979) is required. From the polyhedra considered in their study, Hazen and Finger (1979) show that, depending on the mineral in question, this value can vary from <2.6 to 12.0 (5.4 to 7.8 for sulphides). This means that calculating for K_p using equation (6) is only accurate when the K-volume relationship value for the mineral is close to 7.5, otherwise there can be a wide deviation in K_p from the true value. Hazen and Finger (1979) do not provide data for Fe–S polyhedra, thus the "correct" value for the K-volume relationship is not fully constrained. Blundy and Wood (1994) also show from their experimental data that, for plagioclase and pyroxene, E_{M} is similar in magnitude to E for the bulk crystal, implying that the elastic properties of the large cation sites in these minerals (as opposed to the relatively rigid Si-O framework) dominantly control the elastic properties of the mineral. It may be a similar case for pyrite, which is wholly composed of FeS_6 octahedra; yet, the distorted nature of the pyrite structure and the arrangement of the octahedra, and the links between them (Figure 7.2B) implies that there may be variations between E_{M} and E, because E_{M} accounts only for an individual octahedra, while E additionally accounts for the arrangement of the octahedra (Hazen and Finger, 1979). Owing to the uncertainty around the true value for the lattice site E_{M} in the FeS_6 octahedra, both the experimental value of E for the pyrite crystal (2205 kbar),

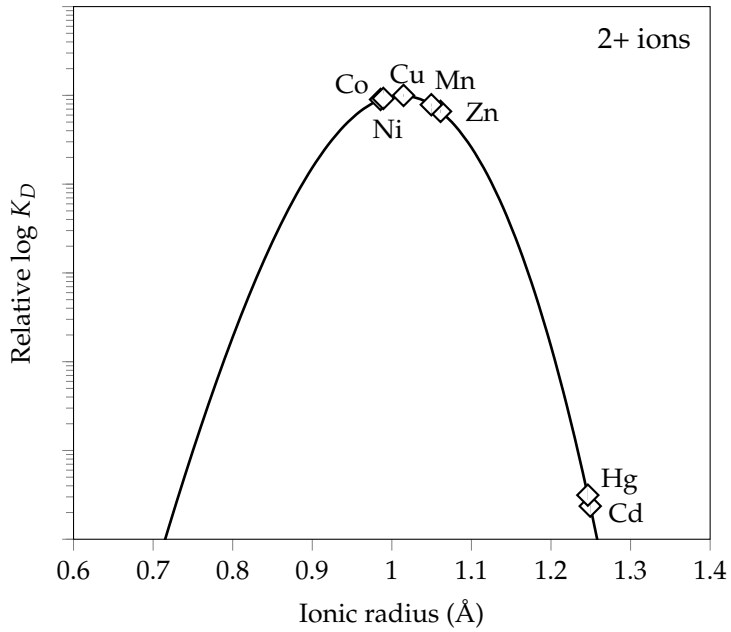

Figure 7.3. Relative K_D plot of 2+ ion substitution into the Fe^{2+} site in pyrite at 350°C. Note that this is not yet a fully functioning model, and is shown for illustrative purposes.

and the calculated value of E_M (1559.36 kbar), were taken forward for calculation and evaluation again natural data to assess which value is more appropriate for modelling trace element partitioning in pyrite.

A theoretical parabola for 2+ ion substitution into the Fe^{2+} site in pyrite is shown in Figure 7.3, to illustrate the construction of a lattice strain model using equation (3). This is not a fully functioning model at this stage, because E, D_o, and r_o are unconstrained without natural K_D data. A value of 2205 kbar for E was used for this illustration, and it is assumed that r_o is equal to the r_a of Fe^{2+} (1.01 Å). Meanwhile, an arbitrary value for D_o was used to illustrate relative K_Ds at a temperature of 350°C (chosen to represent possible ore-forming conditions in porphyry deposits, cf. Chapter 2). The ions were positioned on the parabola in line with their ionic radii (r_a).

This illustrative parabola shows that some ions lie on the parabola near its apex, indicating that these cations should have relatively high K_Ds into pyrite, under the parameters outlined above. Similar plots for the substitution of 1+ and 3+ ions into the Fe^{2+} site in pyrite are shown in Figure 7.4, illustrating that the 1+ parabola is wider, and the 3+ parabola is tighter, compared to the 2+ parabola. The relationship between the 1+, 2+, and 3+ parabolae in terms of D_o is unknown at this stage, although the 1+ and 3+ parabola are likely to have D_o lower than the 2+ parabola, as mentioned in Section 7.3.

Temperature variations do not adversely affect K_Ds for ions near the apex of the parabola (i.e., those with the highest K_Ds). However, for ions that lie on the limbs of the parabola, lower temperatures result in lower K_Ds because the parabola tightens (i.e.,

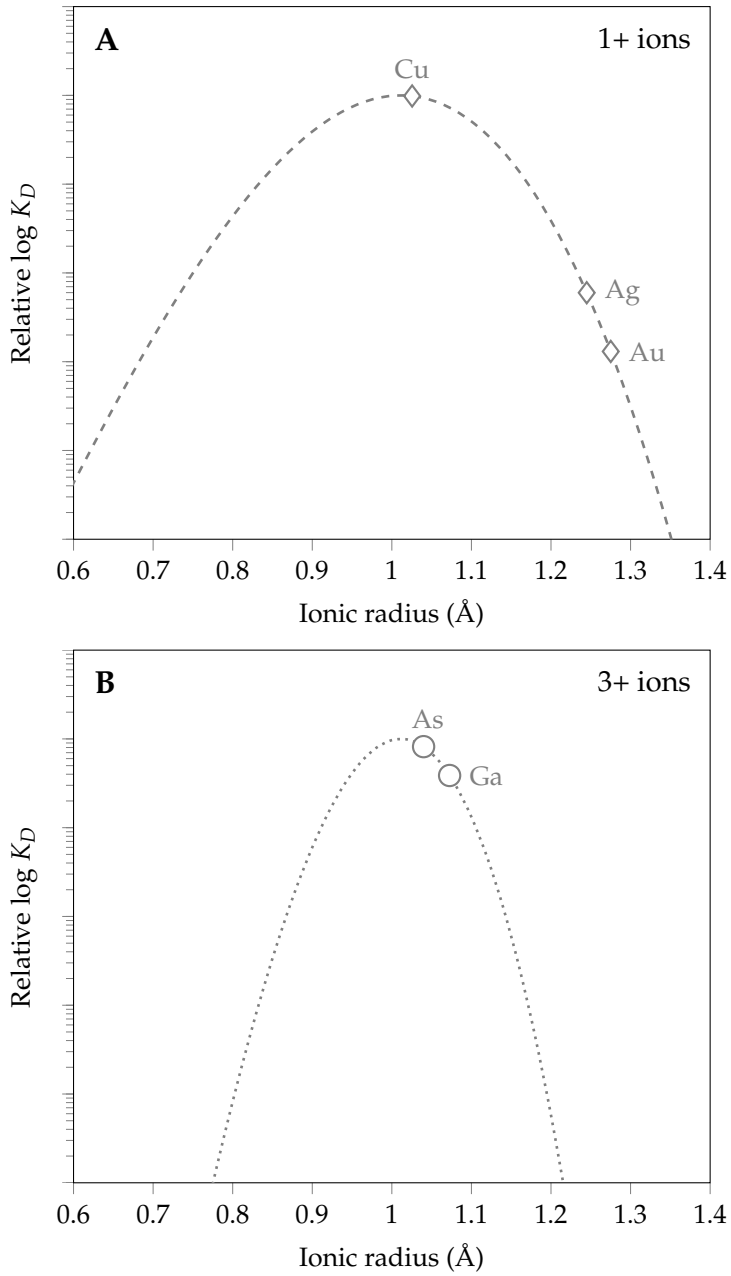

Figure 7.4. Relative K_D plots of 1+ (A) and 3+ (B) ion substitution into the Fe^{2+} site in pyrite at 350°C. The graphs are constructed as in Figure 7.3.

bonds effectively become stiffer), whereas higher temperatures result in higher K_Ds because the parabola widens (i.e., bonds effectively become more elastic). This is illustrated in the case of Hg^{2+} in Figure 7.5, where the K_D for Hg^{2+} at 200°C is approximately two orders of magnitude lower than the K_D for Hg^{2+} at 500°C. Comparatively, the K_D for Co^{2+} is relatively static, and does not vary markedly between 200 to 500°C (Figure 7.5). Variations in K_D induced by temperature changes are thus more prominent the more the radius of the substituting ion departs from r_o.

The next step is to constrain the shape and position of the parabolae calculated for Figure 7.3 and 7.4 in terms of E, D_o and r_o, by utilising empirical measurements of K_Ds

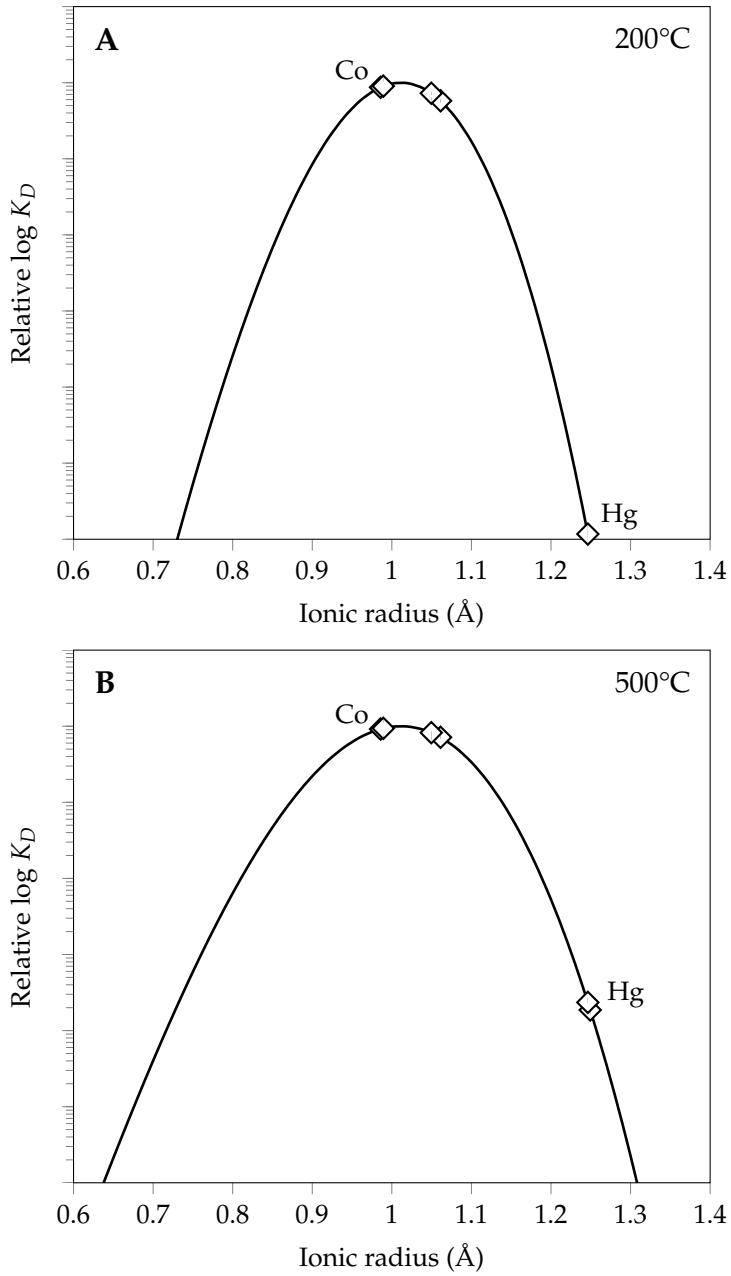

Figure 7.5. Relative K_D plots of 2+ ions at 200 °C and 500 °C, illustrating the effect of temperature changes. The graphs are constructed as in Figure 7.3.

from natural systems. Presently, there are no published studies of porphyry deposits that include both pyrite trace element compositions and hydrothermal fluid compositions. However, there *are* compositional data available for pyrite and vent fluids from active seafloor hydrothermal systems, such as the Trans-Atlantic Geotraverse (TAG) deposit on the Mid-Atlantic Ridge (Grant et al., 2018).

Grant et al. (2018) present LA-ICP-MS data for pyrite from various locations throughout the TAG deposit, and estimate the minimum concentrations of trace elements in the hydrothermal fluids based on mass balance calculations using the mean composition of pyrite. They compare their calculated concentrations in the fluid with an average of vent

fluid measurements from TAG. This data can be utilised to calculate K_Ds for the elements available by using equation (1), where the concentration in pyrite is the mean of the LA-ICP-MS data of Grant et al. (2018), and the concentration in the hydrothermal fluid is the mean of measurements from vent fluids (from the references in Table 10 of Grant et al., 2018). The limitations of using the Grant et al. (2018) data to calculate K_Ds, and the reliability of the calculated K_Ds, are discussed in Chapter 8.

The calculated K_Ds for the available elements have been utilised to constrain the shape and position of the previously-constructed parabola (Figure 7.6). The mean T of the vent fluid measurements utilised by Grant et al. (2018), 328°C, was used to construct the model, because this is the temperature at which partitioning between pyrite and fluid appears to have occurred. The parabola for the 2+ ions was adjusted by altering E (using either 2205 kbar, or 1559.36 kbar), r_o, and D_o, such that it passes through the K_D data (Figure 7.6A). However, it is clear that the ions are not all aligned and cannot all lie on the parabola; therefore, the parabola was adjusted to pass through as many data points as possible.

The experimentally-determined value of E for the bulk crystal (2205 kbar), instead of the calculated value of E_M for the lattice site (1559.36 kbar), was used to best fit the parabola through the data points. This justifies the use of E, and validates the approach of Blundy and Wood (1994), showing that E in pyrite is likely to be equal to E_M, and that calculation of E_M for the Fe^{2+} site in pyrite using equation 7 is not particularly accurate. Adjustment of the position of the parabola to fit the data was achieved by using a value of 6000 for D_o, and a value of 0.92 Å for r_o in Figure 7.6A. This shows that r_o is not equal to the r_a of Fe^{2+} (1.01 Å), as was assumed in the construction of the illustrative parabola in Figure 7.3 and 7.4. Similar adjustment of the 1+ and 3+ parabola was required in Figure 7.6B; however, owing to the spread of data, these parabolae can only pass through one data point each, meaning that D_o and r_o are poorly constrained for the 1+ and 3+ ions. The now-constrained value of E (2205 kbar), along with values for D_o of 50 for the 1+ ions, and 10000 for the 3+ ions, were used to fit the respective parabola through data points.

The position of the 1+ and 3+ parabolae on the x axis was fixed by an r_o of 0.92 Å, the value determined from the 2+ parabola. This r_o value was used because it is the only value of r_o that has been constrained by the empirical K_D data. Furthermore, the r_o of a lattice site is not expected to change dramatically with the substitution of ions of differing charge (e.g., Blundy and Wood, 1994; van Hinsberg et al., 2010), although there are likely to be minor differences, because of the difference in the effective electronegativity of the ion-S bond with charge (Gibbs et al., 2017). For example, 1+ ions generally exhibit lower

electronegativities because of their decreased charge relative to 2+ ions, meaning that the radius of the S ion in 1+ ion-S bonds will generally be smaller than in 2+ ion-S bonds (Gibbs et al., 2017). This would lead to the r_o for the 1+ ions being larger than the r_o for 2+ ions, as shown in the experiments of Blundy and Wood (1994) and van Hinsberg et al. (2010). However, the relatively high degree of covalency accounted for in the pyrite model (73%) strongly negates this effect, leading to the r_a of the 1+, 2+, and 3+ ions being relatively comparable, compared to the differences in r_e between these ions (Table 7.1). This means that the r_o for substituent 2+ ions is likely to be relatively simililar to the r_o

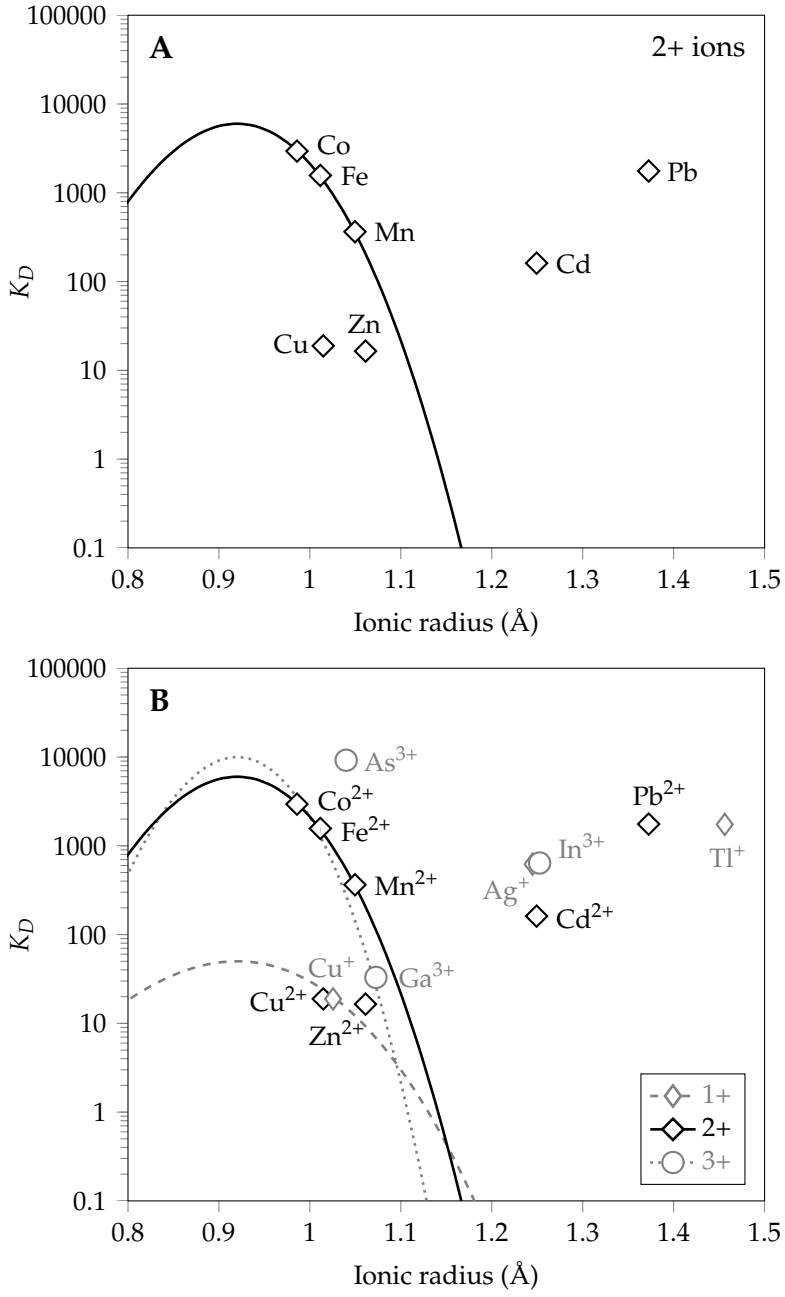

Figure 7.6. Trace element K_D plots for ion substitution into the Fe^{2+} site in pyrite, constrained by natural K_D data calculated from Grant et al. (2018), where T = 328°C. The 2+ parabola is the most well-constrained (A), whereas the 1+ and 3+ parabola (B) pass through only one data point each.

for substituent 1+ and 3+ ions in pyrite.

With a 2+ parabola constrained by the natural K_D data calculated from Grant et al. (2018), it is now possible to quantitatively predict K_Ds for 2+ ion substitution into pyrite at various T conditions. This is explored in Chapter 8, with regards to the LA-ICP-MS data collected from Iron Cap.

7.5 Assessment and implications of the model

This section assesses the viability of the lattice strain model for pyrite presented in Section 7.4, and outlines some of the implications of the modelling work completed. Further discussion of the model and its implications can be found in Chapter 8.

The 2+ parabola constructed for ion substitution in pyrite (Figure 7.6A) passes through multiple points of natural K_D data, suggesting that the model is able to explain the presence of at least some of the elements measured in pyrite by Grant et al. (2018). Ions that are lattice-hosted in the Fe^{2+} site owing to direct substitutions should lie on the parabola. Ions that do not lie on the parabola are likely not to be wholly lattice-hosted, with the possible presence of discrete inclusions, coupled substitutions, and/or different ions.

It is reasonable that Fe^{2+} should have a relatively high K_D and lie on the parabola in Figure 7.6A, because it effectively defines the pyrite lattice. A relatively high K_D for Co^{2+} into pyrite is also reflected in the constraining natural data of Grant et al. (2018). The presence of Co^{2+} on the parabola in the constrained model suggests that it is lattice-hosted owing to direct substitutions for Fe^{2+}. This is a reasonable assumption, owing to the fact that pyrite can form solid solutions with cattierite (CoS_2; Bowles et al., 2011). Similarly, Mn^{2+} is predicted to have a relatively high K_D for pyrite, and also lies on the parabola in the constrained model. Manganese is not commonly detected in trace element studies of pyrite from porphyry deposits (cf. Section 4.3.1); however, there is a pyrite-structured Mn-mineral, hauerite (MnS_2; Bowles et al., 2011), which indicates that Mn^{2+} could be accomodated into a pyrite structure. Therefore, when Mn^{2+} is available in a hydrothermal fluid, it is likely to have relatively high K_Ds for pyrite and be lattice-hosted in the Fe^{2+} site. This could explain the elevated Mn concentrations in pyrite from the sedimentary-hosted gold deposit at Sukhoi Log, Russia (Large et al., 2007).

That Fe^{2+} and two of the 2+ ions closest to the peak of the parabola in the theoretical model (Figure 7.3) should lie on the parabola in the constrained model using natural data provides an indication that the parabola for the 2+ ions is viable. One of the key outcomes of the modelling is that the "ideal" r_o for the Fe^{2+} site in pyrite appears to be *smaller* than the ionic radius of Fe^{2+}, meaning that Co^{2+} actually has a higher K_D into pyrite than Fe^{2+}, and therefore that Co will be selectively enriched into the solid phase during pyrite

formation, relative to the hydrothermal fluid. A caveat to this interpretation is that other factors may be involved in the incorporation of Co in the pyrite lattice; in particular, the presence of competing ions, and the concentration of ligands that facilitate the transport of Co in the hydrothermal fluid, and the crystallisation of other Co-bearing minerals. For example, one vein-free sample from Iron Cap contains multiple grains of Fe-bearing cobaltite (CoAsS); it could be interpreted that the hydrothermal fluids that interacted with the wall rock in this sample were particularly Co-rich, such that instead of forming pyrite, Co and As were enriched enough to form cobaltite.

In Figure 7.6A, both Cd^{2+} and Pb^{2+} have relatively high apparent K_Ds, but they lie multiple orders of magnitude above the parabola. Grant et al. (2018) note the presence of both galena ($\pm$ Pb-bearing sulphosalts) and sphalerite inclusions in pyrite in their study of the TAG deposit, while analysis of sphalerite records common Cd-enrichment (mean 307.1 ppm; Grant et al., 2018). It is thus likely that Cd^{2+} and Pb^{2+} are largely present in the TAG pyrite as discrete inclusions of sphalerite and galena ($\pm$ Pb-bearing sulphosalts), respectively, which would align with their higher-than-expected K_Ds. The model for the 2+ ions is thus able to discriminate between trace elements that are truly lattice-hosted (Co, Mn), and those that may be present in other states (e.g., as discrete inclusions), such as Pb or Cd.

Both Zn^{2+} and Cu^{2+} lie *below* the parabola in Figure 7.6A. Unlike Fe^{2+}, Co^{2+}, and Mn^{2+}, Zn^{2+} has a filled d-orbital, which causes it to be more polarisable, and thus have a more covalent bond with S than the other 2+ ions on the parabola (Shannon, 1976; Blundy and Wood, 1994). This means that Zn^{2+} is likely to have a larger r_a than calculated, as the degree of covalency used to calculate r_a for the ions in Table 7.1 (73%) may be underestimated in the case of Zn^{2+}. This would mean that, in Figure 7.6A, Zn^{2+} should plot more to the right, and possibly intersect the parabola to show that it is lattice-hosted in pyrite. Another option is that Zn^{2+} has a different speciation in the hydrothermal fluids from TAG than the other 2+ ions on the parabola (e.g., van Hinsberg et al., 2010). However, this may be an unlikely option, as the speciation of these cations in hydrothermal fluids is often similar (e.g., as chloride or hydrogen sulphide complexes; Kouzmanov and Pokrovski, 2012). On the other hand, it is likely that Cu^{2+} is not present in pyrite as a 2+ ion, given the fact that it lies multiple orders of magnitude below the parabola; it should have a K_D of at least a similar magnitude to Fe^{2+} if it were incorporated into the pyrite lattice.

While the model for the 2+ ions appears to be viable and useful, the 1+ and 3+ parabolae in Figure 7.6B are poorly constrained, as they only pass through one data point each. This means that prediction of substitution for these ions is not possible without large de-

grees of uncertainty. However, for the 1+ and 3+ ions that have high K_Ds, comparable to, or greater than the K_D for Fe^{2+} on the 2+ parabola (i.e., Tl^{+} and As^{3+}), it can be implied that these ions are likely not present as lattice substitutions, because charge mismatched ions should have lower K_Ds than charge matched ions that lie near the peak of a parabola (Blundy and Wood, 1994). Indeed, an elevated K_D for As^{3+} could be explained by the fact that As^{2-} substitution may also occur in the S^{2-} site in pyrite (e.g., Bowles et al., 2011). It is also notable that all the 1+ and 3+ ions considered in both the theoretical and constrained model have larger ionic radii than both r_o and Fe^{2+}. This makes the possibility of coupled substitutions into two Fe^{2+} sites in pyrite unlikely (i.e., $2\,Fe^{2+} \longleftrightarrow 1^{+}$ ion + 3^{+} ion), as the accomodation of two ions of mismatched charge that are both larger than r_o would require high degrees of lattice strain, and hence relatively low K_Ds would be expected for the coupled substitution in question.

7.6 Summary

A lattice strain model has been constructed to predict element partitioning into the Fe^{2+} site in pyrite, accounting for the elastic properties of the lattice site, the radius of the substituting ion relative to the optimum radius of the lattice site, the charge of the substituting ion relative to the optimum charge of the lattice site, and temperature. A theoretical model was first constructed to show that Co^{2+}, Cu^{2+}, Ni^{2+}, Mn^{2+}, and Zn^{2+} should have relatively high K_Ds into pyrite, while Cu^{+}, and As^{3+} and Ga^{3+} should have the highest K_Ds of the 1+ and 3+ ions, respectively. Temperature is shown to affect K_Ds when ions are not well matched to the lattice site in terms of ionic radius, otherwise K_Ds are relatively insensitive to temperature.

To more accurately constrain the model in terms of the optimum site radius, and predict quantitative K_Ds, natural K_D data for pyrite was calculated from compositions of pyrite and vent fluids from the TAG deposit (Grant et al., 2018). The previously constructed theoretical model has been aligned using natural K_D data. The constrained model indicates that, in pyrite from the TAG deposit, Co and Mn are lattice-hosted as 2+ ions via substitution into the Fe^{2+} site. Meanwhile, Pb and Cd are likely present as discrete inclusions in the pyrite, consistent with descriptions by Grant et al. (2018).

A key finding is that the model shows that the optimum radius of the Fe^{2+} site in pyrite is smaller than the radius of Fe^{2+}. Accordingly, Co exhibits a higher K_D for pyrite than Fe, meaning that pyrite preferentially acquires Co such that a hydrothermal fluid precipitating pyrite will never become saturated in Co. Therefore, seperate Co phases will not precipitate from fluids precipitating pyrite. Furthermore, coupled substitutions involving 1+ and 3+ ions are unlikely to occur in pyrite, owing to the ionic radii of these

ions being larger than the optiumum radius of the Fe^{2+} site. These findings are discussed in the context of Iron Cap in the following chapter, where quantitative prediction of K_Ds for 2+ ions into pyrite is now possible.

8 Discussion

8.1 Introduction

This chapter collectively utilises the previous work of this thesis to address the aims of the research presented in Chapter 1. To this end, Section 8.2 considers the vein and ore formation processes in the context of the petrographical work presented in Chapter 5. Section 8.3 discusses the use of trace elements as indicators of hydrothermal fluid evolution, utilising the compositional data for ore minerals presented in Chapter 6, and the modelling work presented in Chapter 7. The nature of hydrothermal fluid evolution at Iron Cap is then discussed (Section 8.4) in the context of the data presented in this thesis. Finally, the implications of the research for the development of Iron Cap are presented in Section 8.5.

8.2 Vein and ore formation processes

The petrographic study (Chapter 5) has identified numerous features that are indicative of certain vein and ore formation processes. This section discusses these features, and interprets the associated formation processes. The petrographic work has also been interpreted to generate a paragenesis of minerals within the vein generations at Iron Cap (Figure 8.1), which is also discussed in this section.

8.2.1 Insights from gangue mineral textures

Cathodoluminescence shows that the quartz in the vein generations from Iron Cap is often weakly-luminescent in dark blue-green to black colours. This is evident in V3, V5, V6, V7, and variably in V4 (Figure 5.8, 5.15, 5.20, 5.23 and 5.27). The V2 vein generation is an exception, because it hosts two discrete generations of quartz: Q1 (bright blue luminescent), and Q2 (dark blue-green to black luminescent; Figure 5.7). The Q1 quartz is barren and constitutes the majority of the vein volume, while Q2 quartz hosts ore minerals (Figure 5.8) and exhibits mineral textures that indicate co-crystallisation. In particular,

Figure 8.1. *(next page)* Paragenesis for selected minerals in the vein generations at Iron Cap. Line width is proportional to estimated abundance; thick lines are for major minerals (>10% in terms of vein volume), medium lines are for minor minerals (2-10%), and thin lines are for trace minerals (<2%). Dashed lines indicate that a mineral is not always present. Modification processes (i.e., recrystallisation, replacement, remobilisation; discussed in text) are marked in red. Text labels indicate dominant ore minerals relations; letters stand for crystallisation with, or as inclusions in, quartz (Q), pyrite (P), chalcopyrite (C), tennantite-tetrahedrite (T), and arsenopyrite (A).

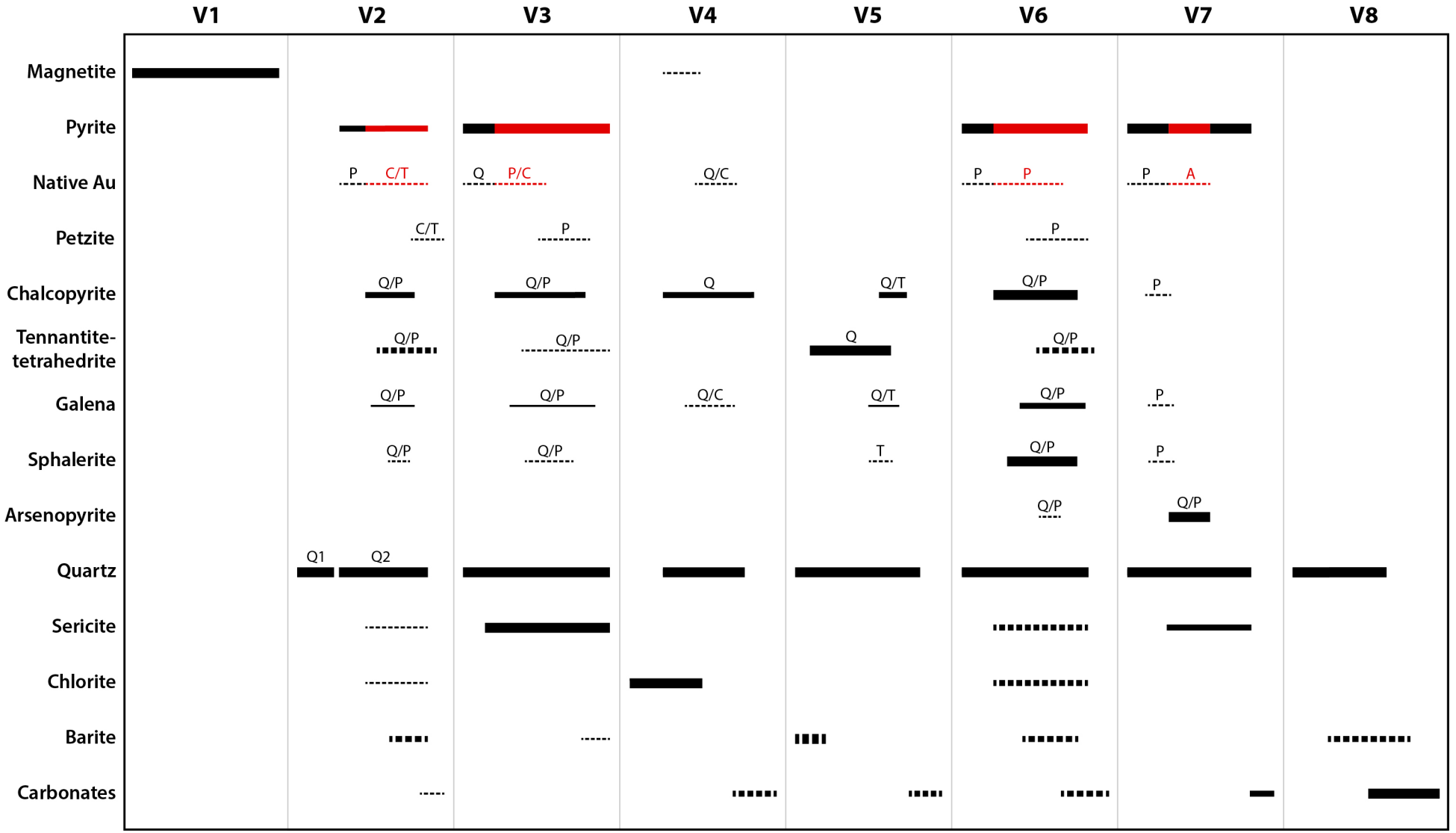
V1
V2
V3
V4
V5
V6
V7
V8
Magnetite
Pyrite
Native Au
Petzite
Chalcopyrite
Tennantite-tetrahedrite
Galena
Sphalerite
Arsenopyrite
Quartz
Sericite
Chlorite
Barite
Carbonates
P
C/T
Q
P/C
Q/C
P
A
Q/P
Q
Q/T
T
Q1
Q2

formation of 120° triple junction grain boundaries indicates equilibrium crystallisation (Figure 5.9D; George et al., 2016). Moreover, growth of Q2 quartz from the boundaries of Q1 quartz (Figure 5.8A), and the growth of ore minerals around quartz crystals (Figure 5.9A, D, F) also suggests that Q2 precipitation commenced prior to ore mineral deposition, while the growth of Q2 quartz in cracks in pyrite and around pyrite crystals (Figure 5.9) further shows that Q2 quartz precipitation continued during sulphide deposition.

The cross-cutting and infilling nature of Q2 quartz within Q1 quartz indicates that at least two discrete stages of vein formation occurred, with Q2 representing the later stage. The embayment of Q1 grain boundaries and primary growth zones (most clearly seen in Figure 5.7D) suggests that infiltration of the later Q2-precipitating fluids may have been facilitated by the dissolution of Q1 quartz. Similar textures indicating quartz dissolution have been recorded in other porphyry deposits (e.g., Bingham, USA; Oyu Tolgoi, Mongolia; Elatsite, Bulgaria; Altar, Argentina; Landtwing et al., 2005; Müller et al., 2010; Stefanova et al., 2014; Maydagán et al., 2015), and quartz solubility calculations for the hydrothermal fluids of porphyry systems have been utilised to show that fields of retrograde quartz solubility can occur at certain conditions (Monecke et al., 2018). Direct comparisons can be drawn to the Altar deposit, Argentina, where A-veins contain an early quartz generation that is strongly-luminescent in CL and sometimes exhibits dissolution textures, followed by a later quartz generation that is weakly-luminescent and hosts the ore, similar to the characteristics of Q1 and Q2 quartz, respectively, in V2 veins at Iron Cap (Maydagán et al., 2015).

As the ore minerals in V2 veins are hosted in Q2 quartz, dissolution of quartz also appears to have facilitated ore precipitation. The central suture and/or crackled texture of V2 veins (defined by Q2-stage ore and gangue minerals) can be explained by quartz dissolution, where the variance in this texture is likely dependent upon the flow paths utilised by the quartz-dissolving fluids, such as along Q1 grain boundaries. However, the co-crystallisation of Q2 quartz with the ore minerals indicates that conditions of retrograde quartz solubility were not prevalent at the time of ore mineral precipitation. Therefore, retrograde quartz solubility may have only served to create fluid flow paths within the Q1 quartz for the later fluids precipitating Q2 quartz and ore.

The Q2 quartz of V2 veins is comparable to the weakly-luminescent quartz of V3-V7 veins. The weakly-luminescent quartz in these veins is similarly cogenetic with the ore minerals, principally evidenced by ore minerals demarkating quartz crystal boundaries (e.g., Figure 5.12F, 5.16A, 5.21B, 5.24E), quartz growing in pyrite cracks and/or around pyrite (e.g., Figure 5.12C, 5.12A, 5.28A), and ore minerals including quartz (e.g., Figure 5.12D, 5.16E, 5.21C, 5.24E, 5.28D). The similarity in CL characteristics of vein quartz be-

tween generations, and the fact that most ore minerals are hosted in weakly-luminescent quartz, suggests that vein and ore formation processes and/or the conditions of vein and ore formation may have been similar across generations.

One anomalous V5 sample (IC01-109) that is hosted at shallow depths by hornfels (compared to other V5 veins, which are present at more intermediate depths with igneous host rocks) also shows some evidence of quartz dissolution. In particular, one vein in this sample exhibits quartz that is zoned with bright blue luminescence (Figure 5.19C). It is interpreted that this was a barren quartz vein (possibly local to the hornfels), that was re-opened by a V5 vein, as the tennantite-tetrahedrite is hosted by weakly-luminescent quartz, and there is embayment and cross-cutting of the bright blue-luminescent quartz by the weakly-luminescent quartz and tenanntite-tetrahedrite (Figure 5.19C). Further evidence to support this theory comes from other V5 veins in the same sample, which dominantly exhibit the weakly-luminescent quartz characteristic of most V5 veins; however, these veins also host embayed clasts of bright blue quartz (Figure 5.19D), which again may have originated from a pre-existing quartz vein. These textures suggest that V5 vein formation in this sample may have been facilitated by quartz dissolution. However, this theory cannot be confidently extrapolated to other V5 veins, because there is a lack of textural evidence to support quartz dissolution in other V5 vein samples. Indeed, there is no further textural evidence of quartz dissolution within the V3-V7 vein generations, likely owing to the lack of multiple quartz generations; only V2 veins consistently host more than one quartz generation within a single vein occurrence. Therefore, only V2 vein formation can be attributed to quartz dissolution processes, based on the mineral textures reported in Chapter 5.

V4 veins are unique at Iron Cap in that quartz has variable CL characteristics that appear to correlate to the presence or absence/low abundance of chlorite. Some V4 veins host chlorite and have quartz that appears black in CL, while other V4 veins that lack the presence or abundance of chlorite host quartz that luminesces in bright blue to dark blue-green colours (Figure 5.15). It could be that these are two un-related vein types that show similarities in characteristics, but formed via different processes, where chlorite is precipitated in one vein type but not (or less so) in the other. Alternatively, it could be that chlorite affects the CL characteristics of quartz in V4 veins, as outlined below.

When present in V4 veins, chlorite is interpreted to have begun precipitating earliest (Figure 8.1), as quartz ($\pm$ chalcopyrite) is commonly observed to cross-cut chlorite (Figure 5.16C), be hosted within chlorite masses (Figure 5.16A), or grow around chlorite crystals (Figure 5.16F). Later fluids precipitating quartz in V4 veins may have dissolved chlorite, evidenced by the textures of quartz in chlorite in Figure 5.16C. This would lead to the

fluids becoming more enriched in the elements present in the chlorite, such as Al and Fe. Therefore, in V4 veins with little or no pre-existing chlorite, significant enrichment of chlorite-hosted elements in the quartz-precipitating fluids would not be expected, whereas in V4 veins that are chlorite-rich, the quartz-precipitating fluids would be more likely to become enriched in the chlorite-hosted elements. During the later precipitation of quartz, the elements liberated during chlorite dissolution may have become incorporated as trace elements in the quartz lattice, thus affecting the CL response (Frelinger et al., 2015). In a study of the Grasberg deposit, Indonesia, Baline (2007) showed that weakly-luminescent quartz was elevated in Fe compared to stongly-luminescent quartz, suggesting that Fe can supress the CL response of quartz. Similarly, Rusk et al. (2008) showed that increases in Al content correlated with a decrease in luminescence intensity in quartz from the Butte deposit, USA. However, enrichment of Al in quartz may also correlate to an increased CL response, and there appears to be no systematic relationship recorded for Al and Fe as CL activators (Frelinger et al., 2015). Therefore, it remains to be proven whether all V4 veins are genetically related, with the presence or absence of chlorite affecting the CL response of quartz, or whether or not all the veins classified as V4 are genetically alike, having formed via different processes that led to the presence or absence of chlorite.

Quartz in V6 veins luminesces in dark blue-green colours and shows evidence of brecciation, with crystal fragments of varying sizes making up much of the vein quartz (Figure 5.23). Ore minerals are associated with the darkest blue (almost black) quartz, which does not show brecciation textures like the more lumnescent quartz; however, this may simply be because it is difficult to observe textures in weakly luminescent quartz. Nevertheless, the darkest blue quartz and associated ore minerals tend to infill pockets in the more luminescent, brecciated quartz, sometimes forming interconnected networks (e.g., Figure 5.23A). These textures suggest that the darkest blue luminescent quartz and ore minerals may have been introduced to V6 veins during or after brecciation, with fluid flow occurring between the clasts of more luminescent quartz. However, one particularly large pyrite crystal ($\sim$1 cm width) in one V6 vein sample (middle-top of Figure 5.22C), hosts clasts of brecciated quartz (beneath the NL label in Figure 5.23B), but only in part of the crystal; the boundary between relatively clean pyrite and quartz inclusion-rich pyrite is observed in Figure 5.25B. This suggests that pyrite was present prior to brecciation, and continued to crystallise during and after brecciation. Brecciation of early vein quartz by later fluids is also observed in the Oyu Tolgoi deposit, Mongolia (Müller et al., 2010), and breccia textures are recorded in E-veins from the Rosario deposit, Chile (Masterman et al., 2005); E-veins have some comparable characteristics to V6 veins (Table 2.2; Section

5.5).

Carbonate minerals (typically calcite) are dominantly present in the later generations of ore-bearing veins at Iron Cap (V6 and V7); they are also occassionally present in earlier vein generations (V2, V4, V5). Carbonates are interpreted to be paragenetically late in all cases, as they cross-cut other gangue minerals (quartz and/or chlorite; Figure 5.14A, 5.16A and F, 5.26B, 5.28A), fill porosity between quartz crystals (Figure 5.16B and E, 5.20A, 5.22C), and/or grow around pyrite crystals (Figure 5.24A and B, 5.28A and C). However, ore minerals other than pyrite are occasionally hosted by, or co-occur with, carbonate minerals in V4 and V6 veins (Figure 5.16B, 5.24A), suggesting that carbonate precipitation commenced during the later stages of ore mineral precipitation in these veins.

Sulphate minerals are not often observed in the vein generations at Iron Cap. Indeed, only barite is present as a major constituent in V5 veins (variably present), where it occurs as large masses cross-cut by quartz and tennantite-tetrahedrite (Figure 5.24A), or as inclusions in both quartz and tennantite-tetrahedrite (Figure5.24A, B). These textures suggest that the fluids precipitating tennantite-tetrahedrite in V5 veins were paragenetically later than those that precipitated barite.

A range of gangue minerals (thorite, K-feldspar, plagioclase, sericite, and chlorite) are present within V1 vein margins, but do not appear to be related to V1 vein formation, suggesting that this vein generation has experienced post-precipitation modification. Indeed, the diffuse, irregular form of V1 veins is suggestive of formation in a ductile regime, where veins may be subject to deformation prior to cooling of the rock mass to temperatures below the ductile-brittle transition (Sillitoe, 2010). Nevertheless, current mineral textures indicate that the magnetite of V1 veins post-dates or pre-dates the majority of the gangue minerals. This is shown where thorite is surrounded by magnetite (Figure 5.3), with thorite exhibiting euhedral crystal forms, indicating that thorite crystallised prior to magnetite; thorite is typically an accessory mineral in felsic igneous rocks (Best, 2003), and has been noted as an accessory mineral in the causative intrusions of other porphyry deposits (e.g., Skouries, Greece; Kroll et al., 2002). Magnetite also sometimes grows around K-feldspar and plagioclase (Figure 5.5A), suggesting that these minerals were present in the host rock prior to magnetite precipitation. Futhermore, sericite is most concentrated where magnetite is brecciated and of smaller grain sizes (Figure 5.4), suggesting that sericitic alteration has subsequently occurred along the V1 vein to brecciate and disperse the magnetite crystals so that they now reside within sericite. Sericite in the V1 vein margin also truncates or overprints cross-cutting V4 veins, supporting this theory.

One gangue mineral, rutile, is interpreted to be associated with V1 vein formation, because magnetite-rutile intergrowths are observed (Figure 5.3). However, magnetite grows around the magnetite-rutile intergrowths, indicating that the V1 magnetite crystals were precipitated later than the intergrowths. The intergrowths exhibit symplectite-like textures, suggesting that they may have formed due to the exsolution of magnetite and rutile from pre-existing ilmenite (Tan et al., 2015, 2022), which implies that ilmenite was present prior to magnetite introduction. If this theory is correct, it is likely that exsolution occurred during vein formation, given the lack of these textures in the host rock, and the requirement for destabilisation of ilmenite owing to a change in conditions; Tan et al. (2022) state that this is promoted by fluids. Therefore, rutile is not interpreted to have been directly precipitated from the hydrothermal fluids that precipitated the magnetite, but is nevertheless included in the V1 assemblage because it likely formed owing to the breakdown of ilmenite during V1 vein formation.

8.2.2 Insights from ore mineral textures

Pyrite, where present in the vein generations at Iron Cap (Figure 8.1), appears to have begun crystallising earlier than other ore minerals. This is principally evidenced by the growth of other ore minerals around pyrite crystals, and/or within cracks in pyrite (Figure 5.9, 5.12, 5.24, 5.28). Chalcopyrite, tennantite-tetrahedrite, galena, and sphalerite ($\pm$ other minor and trace ore minerals; Table 5.1) are interpreted to be co-crystallised after initial pyrite precipitation, where these ore minerals are present (Figure 8.1), because of their similar occurrence in relation to pyrite, and the fact that they occasionally exhibit 120° triple junction grain boundaries (also with quartz; Figure 5.9D and 5.24). Chalcopyrite "disease" in sphalerite from V6 veins is also a possible indicator of co-crystallisation (Figure 5.24B; Govindarao et al., 2018); indeed, where galena is present adjacent to the chalcopyrite within sphalerite, 120° triple junction grain boundaries are often observed. In V4 and V5 veins, which lack pyrite, co-crystallisation of chalcopyrite $\pm$ galena (V4), and tennantite-tetrahedrite, chalcopyrite, galena $\pm$ trace ore minerals (V5) is interpreted owing to the similar occurrence of these ore minerals within quartz (Figure 5.16 and 5.21). Therefore, in veins that contain pyrite in addition to other ore minerals, there are multiple stages of ore formation (Figure 8.1).

Modification of pyrite is widely evident in V2, V3, V6 and V7 veins, and likely occurred during the precipitation of the other ore minerals. This is because pyrite crystals are often annealed into larger masses (Figure 5.9C, 5.12C, 5.24E), trapping inclusions of other ore minerals (and quartz). Furthermore, porosity generation in pyrite coupled with the presence of other ore minerals as inclusions (Figure 5.9F, 5.13B) is in-

dicative of coupled dissolution-reprecipitation processes, whereby later fluids begin to dissolve the pyrite, generating porosity, and allowing the precipitation of other ore minerals in the pore space to form inclusions (Putnis, 2009). In some cases, it is evident that coupled dissolution-reprecipitation processes have progressed further to partially replace pyrite crystals. For example, Figure 5.10A shows the pseudomorphic replacement of pyrite by chalcopyrite, tennantite-tetrahedrite and quartz, while Figure 5.24D shows the pseudomorphic replacement of pyrite by chalcopyrite and galena. However, non-pseduomorphic replacement of pyrite is more commonly evident, where pyrite crystals are surrounded by chalcopyrite, and exhibit more rounded forms and diffuse crystal boundaries (Figure 5.9D and 5.12D), or host chalcopyrite in fractures with diffuse margins (Figure 5.10B and 5.12F) that were likely generated by the coupled dissolution of pyrite and precipitation of chalcopyrite. Pyrite replacement is most widespread in V7 veins, where arsenopyrite has replaced pyrite along linear planes within crystals (Figure 5.28A), regularly destroying the original crystal forms (Figure 5.28B, D).

Some ore mineral textures illustrate that pyrite crystallisation was not limited to the early stages of vein formation, and that pyrite occasionally co-crystallised with other ore minerals, or indeed crystallised after other ore minerals. Co-crystallisation of some pyrite crystals with other ore minerals is particularly apparent in V6 veins, with the formation of 120° triple junction grain boundaries, and the presence of rounded inclusions in non-porous pyrite (Figure 5.24A). Pyrite in V3 veins also exhibits multiple generations; Figure 5.12A shows an early As-rich pyrite overgrown by a more As-depleted pyrite that is intergrown with tennantite-tetrahedrite and galena, while Figure 5.12C shows galena inclusions constrained to a specific pyrite zone, indicating that pyrite crystallisation continued after the precipitation of galena. Some inclusions retain relatively euhedral crystal forms that suggest pyrite grew around them (hence post-dating them), such as the hessite inclusions in the core of the pyrite in Figure 5.24C, and the arsenopyrite inclusions in the lower right pyrite in Figure 5.28C.

The above discussion shows that the formation of pyrite in the vein generations of Iron Cap is complex, likely involving multiple stages of crystallisation and modification, with different pyrite crystals (even in the same vein generation) having different formation processes; the crystallisation of pyrite during vein formation is further discussed in Section 8.3.3. Pyrite stability may have been transient during vein formation, evidenced by the variable extent of coupled dissolution-reprecipitation processes (Putnis, 2009), and the multiple stages of pyrite crystallisation. In contrast, the formation of chalcopyrite, tennantite-tetrahedrite, galena, sphalerite, and arsenopyrite ($\pm$ other trace ore minerals) appears to be relatively constrained to a discrete time period in each vein generation,

with little evidence to suggest modification or additional stages of crystallisation took place.

Gold-bearing minerals (native Au and petzite) in the vein generations at Iron Cap warrant separate discussion, as their formation processes appear to be somewhat different to other ore minerals. In veins that contain pyrite, native Au and petzite are principally present as inclusions in pyrite (Figure 5.10A, B, 5.13C, D, 5.25, 5.29B), included in vein quartz (Figure 5.13A), with other ore minerals in cracks in pyrite (Figure 5.13B), or as inclusions in other ore minerals (arsenopyrite in V7; Figure 5.29A). Gold hosted as inclusions in pyrite is interpreted to be secondary, generated by annealing of pyrite crystals, or coupled dissolution-reprecipitation processes (Putnis, 2009). The former is evidenced by the co-crystallisation of other ore minerals in irregular-shaped inclusions (e.g., Figure 5.25C), while the latter is evidenced by post-precipitation porosity in the pyrite, and the co-occurrence of other ore minerals as inclusions in the same pyrite crystals (e.g., Figure 5.13D). Comparable Au in pyrite textures are reported and similarly interpreted by Sung et al. (2009) at the Sunrise Dam Archaean gold deposit. Ultimately, the common co-occurrence of inclusion-hosted Au with other ore minerals within pyrite suggests a post-pyrite crystallisation introduction, given that pyrite crystallisation is texturally evidenced to pre-date the crystallisation of other ore minerals (Figure 8.1). The native Au hosted as inclusions in arsenopyrite in V7 veins is interpreted to be synchronous with arsenopyrite crystallisation, as the arsenopyrite lacks porosity, and the Au inclusions are constrained to specific compositional zones within the arsenopyrite (Figure 5.29A), constraining the timing of their precipitation.

In contrast to the interpretation above, it is equally possible that Au was also, or alternatively, introduced during initial pyrite precipitation, as "invisible Au" (i.e., lattice-hosted, or as nanoparticles) in pyrite (e.g., Cook and Chryssoulis, 1990; Fougerouse et al., 2021). Later fluids dissolving and replacing the pyrite may have dissolved invisible Au, liberating it from pyrite for precipitation as native Au and petzite inclusions within the pore space in pyrite (e.g., Fougerouse et al., 2016a), or as native Au grains and petzite associated with later ore minerals and quartz. Indeed, native Au inclusions tend to be observed in pyrite crystals that have experienced extensive coupled dissolution-reprecipitation (e.g., Figure 5.10A, B, 5.29B), suggesting that remobilisation and upgrading of Au may be an important process at Iron Cap.

Further indications of Au remobilisation come from the occurrence of native Au with petzite in V2 veins, which occur within hessite, either surrounding pyrite in chalcopyrite, or in tennantite-tetrahedrite (Figure 5.10C, D). The hessite that hosts the Au exhibits concave boundaries, while smaller, droplet-shaped inclusions of hessite are observed in

chalcopyrite or tennantite-tetrahedrite, oriented towards the corners of the larger crystals. Furthermore, native Au is hosted in the core of the hessite inclusions, surrounded by petzite. These textures are consistent with those generated by the crystallisation of a melt phase, which wets grain boundaries (e.g., Frost et al., 2002; Voudouris et al., 2013; Hastie et al., 2020). Low melting-point chalcophile elements (including Au, Ag, Te, Hg, Sb, and Bi) have previously been proposed to form melts in orogenic Au deposits (e.g., Frost et al., 2002; Voudouris et al., 2013; Hastie et al., 2020), where they may be fluid-mediated, meaning that they are molten during hydrothermal fluid flow and are therefore able to scavenge metals during ore formation, prior to melt crystallisation (Tooth et al., 2008, 2011). It is therefore interpreted that a Au-Ag-Te melt was active during V2 vein formation at Iron Cap, migrating along chalcopyrite and tennantite-tetrahedrite grain boundaries, with hessite crystallising first, followed by petzite and finally native Au. The post-chalcopyrite-tennantite-tetrahedrite timing of the melt phase could be explained by the experimental work of Cabri (1965), which shows that Au-Ag-Te melts can exist at temperatures as low as 335°C, slightly lower than the temperature ranges typically invoked for ore formation by hydrothermal fluids in porphyry systems (e.g., 425-350°C; Landtwing et al., 2005, Section 2.5).

It is possible that Au-Ag-Te melts at Iron Cap were derived from the coupled dissolution-reprecipitation processes affecting early pyrite. The melts may have been generated as Au was liberated from the early pyrite, remaining molten during ore formation and scavenging Au present in the fluid, which itself may have been liberated from the early pyrite, or introduced later. Similar theories are proposed by Hastie et al. (2020) for the formation of orogenic Au deposits from Abitibi, Canada, where it is thought that early Au-bearing pyrite was affected by coupled dissolution-reprecipitation processes, releasing the Au to form melts composed of low melting-point chalcophile elements. Meanwhile, from experiments that involve the replacement of pyrrhotite by magnetite, Tooth et al. (2011) show that interface-coupled dissolution-reprecipitation processes (where dissolution of the parent mineral is closely coupled with the precipitation of the product) promote the formation of polymetallic melts, and their precipitation as inclusions. Petzite and hessite, and rarely native Au and hessite, co-occur in inclusions in pyrite from V3 and V6 veins (Figure 5.13D, 5.25A, B), which may indicate that Au-Ag-Te melts were also involved in the formation of these vein generations. Furthermore, Au in V6 veins is only observed as inclusions in pyrite, implying that interface-coupled dissolution-reprecipitation processes may have been dominant in remobilising and concentrating Au.

Gold in V4 veins only occurs as native Au, hosted by quartz and chalcopyrite (Figure 5.17); it is thus interpreted to be co-genetic with these minerals. V5 veins conspicously

lack Au, and instead host a AgHg alloy within tennantite-tetrahedrite (Figure 5.21), indicating that Au was absent from the hydrothermal fluids.

8.2.3 Similarities in vein formation

The relative timing of vein formation has been discussed in Section 5.5. This section specifically considers whether there is evidence to suggest that there are similarities in the timing of formation of different vein generations at Iron Cap, as there are few cross-cutting relationships observed, and some vein generations exhibit similar characteristics.

The common occurrence of weakly-luminescent quartz in V2-V7 veins implies that quartz may have been precipitated from hydrothermal fluids with similar characteristics in order to impart the similar CL charactersitics, or may have resulted from similar vein formation processes. In a study of quartz solubility, Monecke et al. (2018) show that only late D and E veins in porphyry systems tend to exhibit dark colours in CL, which may indicate that the weakly-luminescent quartz in the veins at Iron Cap is associated with the later stages of hydrothermal fluid evolution. Indeed, the bright blue-luminescent Q1 quartz in V2 veins pre-dates the weakly-luminescent Q2 quartz, indicating that weakly-luminescent quartz is associated with later-stage fluid flow in V2 veins. As ore minerals are principally associated with weakly-luminescent quartz in V2-V7 veins, it could also be that ore deposition at Iron Cap occurred relatively late in the evolution of the hydrothermal system. This would agree with other porphyry deposit studies that suggest ore deposition post-dates the formation of early A- and B-veins (e.g., Pudack et al., 2009; Stefanova et al., 2014; Tsuruoka, 2017).

Alteration assemblages may provide a timing constraint, as sericitic alteration is a later-stage product of a porphyry hydrothermal system than potassic alteration (e.g., Seedorff et al., 2005; Sillitoe, 2010). Sericite and other wall rock gangue minerals are occasionally observed in the crackled-texture of V2 veins, while the ore minerals contained within V2 veins can be observed disseminated in the groundmass surrounding the veins (e.g., Figure 5.9E). This may indicate that sericitic alteration occurred after the precipitation of Q1 quartz, and during, or after, the precipitation of Q2 quartz and ore minerals. This provides evidence to support the theory that weakly-luminescent quartz and ore deposition in V2 veins occurred relatively late in system evolution. V3 veins always host sericite, suggesting that they may also have been synchronous with sericitic alteration and associated with the later stages of system evolution. If both V2 (Q2-phase) and V3 veins are associated with sericitic alteration, it would be expected that later vein generations are also associated with sericitic alteration, unless there is a perturbation of typical alteration sequences. V4 veins are an exception, because they are sometimes hosted

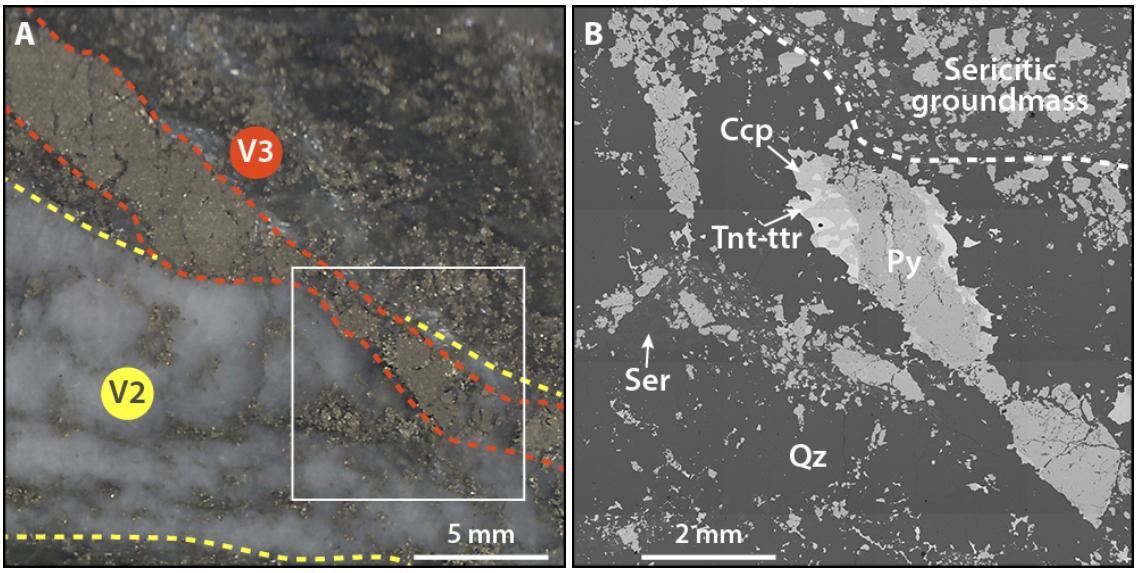

Figure 8.2. V2 and V3 vein relationships in sample IC70-402. V3 cross-cuts V2 in A (also seen in CL), while in B, SEM (BSE mode) imaging shows that chalcopyrite and tennantite-tetrahedrite, which may be related to V2, are grown around V3 pyrite. The white box in A roughly marks the outline of the SEM (BSE mode) image in B.

within potassic-altered rocks at depth, indicating that they are not genetically linked to sericitic alteration, and therefore that the fluids responsible for V4 formation were likely not capable of generating sericitic alteration.

There are strong similarities between the Q2-phase of V2 veins and V3 veins in terms of mineralogy and mineral textures (cf. Section 5.4.2 and 5.4.3), and in terms of mineral paragenesis (Figure 8.1). In one sample, a V3 vein cross-cuts a V2 vein (Figure 8.2A), but both the pyrite of the V3 vein, and the ore minerals in the crackled-texture infill of V2, are hosted by weakly-luminescent quartz, meaning that there is no clear distinction between the veins in CL. It is also difficult to distinguish between the veins in BSE, although the V3 vein hosts larger crystals of pyrite (Figure 8.2B). The similarity in characteristics between the V2 vein Q2-phase and V3 veins, and the difficulties distinguishing between the two in Figure 8.2), could indicate that the V2 vein Q2-phase and V3 veins are one and the same, forming from similar fluids. The lack of V2 and V3 interaction elsewhere in sample suite means that a cogenetic relationship between V2 and V3 ore mineral introduction cannot be proven, but it equally cannot be ruled out on the basis of observed interaction.

There are also similarities between V3 and V7 veins, in that they are both dominated by pyrite, and exhibit similar morphologies. It has already been noted in Section 5.5 that V7 veins may constitute peripheral mineralisation, owing to their apparent restriction to a local, near-surface part of the deposit. However, it could be that V7 veins are a peripheral, As-rich variation of V3 veins.

8.3 Trace elements as indicators of hydrothermal fluid evolution

The trace element data collected during this research project (Chapter 6) has implications for the incorporation mechanisms of trace elements in the analysed ore minerals, and may be utilised to characterise the trace element signature of the vein generations sampled from Iron Cap. Furthermore, the data highlights that there are also trace element variations within vein generations. When utilising lattice strain models (Chapter 7), it may be possible to provide insights to the causes behind trace element variations within vein generations. Collectively, these data may provide indications of the characteristics of the hydrothermal fluids that precipitated the ore minerals, and thus be used as indicators of hydrothermal fluid evolution. This section discusses these topics.

8.3.1 Trace element incorporation in the analysed ore minerals

As noted in Chapter 4 and 7, determining whether trace elements are present as lattice incorporations and/or as discrete inclusions is important in the context of this thesis, because the concentration of lattice-hosted trace elements may be directly linked to changes in the hydrothermal fluid. The ore mineral composition data presented in Chapter 6 allows interpretations to be made of the mode of occurrence of different trace elements within the ore minerals analysed by LA-ICP-MS. This section therefore assesses this data to determine which trace elements are likely to be present as lattice incorporations and/or as discrete inclusions in the ore minerals analysed.

Qualitative analysis of LA-ICP-MS profile traces is commonly utilised in trace element studies to provide indications of the incorporation of trace elements (e.g., Large et al., 2009; Cook et al., 2011; Reich et al., 2013; George et al., 2015; Tardani et al., 2017; George et al., 2018a; Grant et al., 2018; Rottier et al., 2018; Roman et al., 2019; Benites et al., 2021). A similar analysis has been employed in Chapter 6, where profile traces for each element in an ore mineral have been classified into one of six categories. These classifications are again described in Table 8.1, where the implications of each classification are also interpreted.

One aspect of these classifications that merits further discussion is the behaviour of the ore mineral during ablation. In particular, only pyrite regularly produced smooth profile traces for elements during LA-ICP-MS, whereas chalcopyrite, galena, tennantite-tetrahedrite, sphalerite, and arsenopyrite regularly produced relatively spiky traces, even for major elements (e.g., Cu and Fe in chalcopyrite; Section 6.4.2). It is possible that the lack of smooth traces is a result of the different ablation characteristics of these sulphides compared to pyrite. Gilbert et al. (2014) investigated the ablation properties of sulphide

Table 8.1
Interpretation of LA-ICP-MS profile trace classifications.

Profile trace	Definition	Interpretation
Smooth and matched	Smooth profile correlated to a key element's profile (element used for normalisation, e.g., Fe in pyrite).	Homogeneous lattice incorporation of an element, and uniform distribution relative to the key element.
Smooth and unmatched	Smooth profile de-correlated (partially or wholly) to a key element's profile. Generally has a signal over most of the interval, otherwise classed as spiky.	Heterogeneous lattice incorporation of an element (e.g., zonations).
Spiky and similar	Spiky profile, but some parts match a key element's profile, and a signal is present throughout most of the interval	Some lattice incorporation of an element, either zonations or lattice-hosting plus inclusions. When concentrations of an element are close to detection limits, a spiky and similar profile may represent homoegenous lattice incorporation of the element, because a low signal intensity makes achieving a smooth profile unlikely. The behaviour of the ore mineral during ablation may also result in a spiky and similar profile, instead of a smooth profile, for lattice-hosted trace elements (see text).
Spiky	Spiky profile throughout, unmatched to a key elements profile	Element is present either as numerous inclusions, or as lattice incorporations plus inclusions. As above, low signal intensities and ore mineral behaviour during ablation may also result in spiky profiles.
Singular spikes	A sudden spike in the profile, typically with other associated elements spiking too.	Element is present as discrete inclusions.
Unmatched	Profile antithetic to that of a key elements profile.	Element is not contained within the host mineral. Likely caused by ablation of another mineral particle, adjecent to, or included within, the host mineral.

minerals by characterising the shape of ablation craters, and the composition and morphology of the sputtered ejecta around the ablation site to show that pyrite is efficiently ablated, whereas other sulphide minerals (including chalcopyrite, tetrahedrite, and sphalerite) experience some melting during ablation. These differences in ablation efficiency may explain the production of fewer smooth intensity signals for sulphides other than pyrite, whereby melt particles of these sulphides, rather than individual atoms, are more likely to be analysed by the ICP-MS (Gilbert et al., 2014). In the absence of smooth traces, spiky and similar profiles are thus likely to be most indicative of lattice-hosted trace elements in chalcopyrite, galena, tennantite-tetrahedrite, sphalerite, and arsenopyrite.

The profile trace classifications have been utilised to interpret the dominant mode of occurrence of trace elements in the analysed ore minerals (Table 8.2). This shows that Co, Ni, As, and Se appear to be dominantly lattice-hosted in pyrite. In chalcopyrite, Ga, Se, Ag, and In appear to be dominantly present as lattice incorporations, while the same is true for Se, Ag, Cd, Sb, and Bi in galena. Tennantite-tetrahedrite appears to host the widest variety of trace elements as dominant lattice incorporations: Co, Se, Ag, Cd, Hg, and Bi. In contrast, sphalerite only appears to host Cd, In, and Hg as dominant lattice incorporations, while only Sb appears to be dominantly lattice-hosted in arsenopyrite.

Some of the more uncommonly detected trace elements present at low concentrations, close to detection limits, may incorrectly appear to be dominantly present as inclusions (or mixed incorporation) within the ore minerals, owing to the classification of spiky and similar profiles, spiky profiles, or traces of singular spikes. This is because the low concentration of an element, close to detection limits, produces these profile traces during LA-ICP-MS, even if the element is lattice-hosted, meaning that it is not possible to determine incorporation mechanisms. This may mean that the interpretations of incorporation mechanisms for the following elements that are detected commonly at low concentrations, close to detection limits, are incorrect:

- Zn, Ga, Ge, Mo, Sn, W, and Bi in pyrite;
- Co, Zn, Ge, Mo, Sb, Sn, Te, Au, Hg, and Bi in chalcopyrite;
- Co, Ga, Ge, As, Au, and Hg in galena;
- Ge and Au in tennantite-tetrahedrite;
- Co, Ge, Se, Sn, Au, Tl, and Bi in sphalerite;
- V, Ni, Zn, Se, Mo, Hg, and Bi in arsenopyrite.

Nevertheless, the low concentrations of these elements shows that, even if they are lattice-hosted, they are not major components of the host minerals, and thus have a limited use

Table 8.2

Dominant occurrence of trace elements in the ore minerals analysed, based on the interpretation of LA-ICP-MS profile traces. Lattice-hosting (LH) is classified when an element collectively exhibits >60% of smooth and matched, smooth and unmatched, and/or spiky and similar profile traces. Inclusions (I) are classified when an element exhibits <10% of these profile traces; i.e., >90% of spiky, singular spikes, and/or unmatched profile traces. Mixed incorporation (M), lattice-hosting and/or inclusions, is classified when an element exhibits between 60-10% of smooth and matched, smooth and unmatched, and/or spiky and similar profile traces. Elements not analysed for, or not present above detection limits, are marked '–'.

	V	Mn	Fe	Co	Ni	Cu	Zn	Ga	Ge	As	Se	Mo	Ag	Cd	In	Sb	Sn	Te	W	Au	Hg	Tl	Pb	Bi
Pyrite	I	–	–	LH	LH	I	I	I	I	LH	LH	M	M	–	–	M	I	M	I	M	M	–	M	I
Chlacopyrite	–	–	–	I	–	–	I	LH	I	I	LH	M	LH	–	LH	M	M	I	–	M	I	–	M	I
Galena	–	–	–	I	I	I	I	I	I	I	LH	–	LH	LH	I	LH	M	M	–	I	I	–	–	LH
Tennantite-tetrahedrite	–	–	–	LH	–	–	–	–	I	–	LH	–	LH	LH	I	–	I	M	–	I	LH	–	I	LH
Sphalerite	–	I	M	M	–	I	–	M	I	I	I	–	M	LH	LH	I	I	–	–	I	LH	I	I	I
Arsenopyrite	I	–	–	I	I	I	I	–	–	–	I	I	I	I	–	LH	I	I	–	I	I	–	I	I

in being utilised to elucidate the conditions of the hydrothermal fluids. However, their apparent absence as lattice incorporations may in some cases be used to indicate the prevailing conditions of the hydrothermal fluids during ore formation, as discussed in Section 8.4.

It is possible to consolidate the interpretations of trace element incorporation mechanisms presented in Table 8.2 by assessing the bivariate plots of elements in different ore minerals from Chapter 6. A positive correlation is recognised between Cu and Se in V2 pyrite (Figure 6.7A), which may be indicative of Se-bearing chalcopyrite and/or tennantite-tetrahedrite inclusions. Tennantite-tetrahedrite may be more likely for the higher Cu and Se data points in Figure 6.7A, because the Se contents of V2 tennantite-tetrahedrite (often >1000 ppm) are comparable with these, whereas V2 chalcopyrite has lower Se contents (often <400 ppm), and may therefore be attributed to the lower Cu and Se data points. This could support the interpretation that Cu in pyrite may be regularly attributed to inclusions of other minerals, and may also explain why a minority of Se profiles in pyrite are classified as spiky and similar, or spiky (Figure 6.6). On a similar note, Figure 6.7B shows a positive correlation between As and Sb in V3 pyrite. This is attributed to inclusions of tennantite-tetrahedrite, because the four V3 pyrite particles with the highest Sb and As also contain the highest Hg concentrations (>50 ppm); Hg is preferentially concentrated in tennantite-tetrahedrite in V2 (Table 6.7). This could support the interpretation that As, Sb, and Hg sometimes occur as inclusions in pyrite (Table 8.2).

Major element analysis of galena shows that Se and S are negatively correlated (Figure 6.1A), suggesting that Se occurs in galena as lattice substitutions for S (i.e., galena-clausthalite solid solution; Liu and Chang, 1994). In contrast, Ag and Bi exhibit a strong positive correlation (Figure 6.1B), suggesting that coupled substitution of these elements occurs in the galena lattice (e.g., George et al., 2015); the same trend is recognised in the trace element data (Figure 6.15). However, there is variation around the trendline in Figure 6.1A, suggesting that some Ag and Bi may not be present as coupled substitutions in galena. Figure 6.15A also indicates this, because the trendline has a negative intercept value, implying that Ag incorporation without Bi may occur, and the slope of the line (2.04) is slightly greater than the ratio of the relative atomic mass of Bi and Ag (1.97), suggesting that Bi, with the higher relative atomic mass, may be incorporated without Ag. A cluster of V6 galena particles below the trendline in Figure 6.15 could also suggest that the incorporation of Ag without Bi may occur. However, Figure 8.3 shows that addition of Bi and Sb aligns these V6 galena particles with the trendline, indicating that the coupled subsitition $Ag^{+} + (Bi, Sb)^{3+} \longleftrightarrow 2\,Pb^{2+}$ is in effect (e.g., George et al., 2015). A caveat of this is that Sb has a lower relative atomic mass (∼121) compared to Bi (∼209), meaning

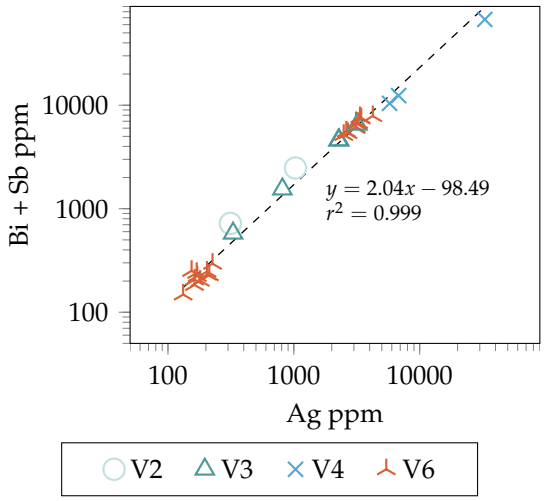

Figure 8.3. Logarithmic bivariate plot illustrating coupled substitutions in galena. The dashed black line is a linear regression trendline.

that it would be expected for the V6 galena particles with higher Sb to plot above the trendline in order to be fully accounted for by a coupled substitution. As it stands, it appears likely that these V6 galena particles also separately incorporate Ag (i.e., not as a coupled substitution). Nevertheless, this discussion highlights that Sb is likely to dominantly occur as lattice incorporations in galena, in similarity to Se, Ag, and Bi, which agrees with the interpretations in Table 8.2.

The positive correlation recognised between Sb and Ag in tennantite-tetrahedrite (Figure 6.19A) shows that Ag is likely present as lattice incorporations, and is more compatible in tennantite-tetrahedrite elevated in Sb, consistent with observations from the Rio Blanco porphyry deposit, Chile (Crespo et al., 2020). However, there are two trends in Figure 6.19A; the steeper trend defined largely by V2 tennantite-tetrahedrite may indicate that there is a further control on Ag incorporation. Figure 6.19C shows that V2 tennantite-tetrahedrite is also enriched in Se relative to tennantite-tetrahedrite from other vein generations, and that there is a negative correlation (although weak) between Se and Ag, meaning that the incorporation of Se may hinder the incorporation of Ag, and that the two are unlikely to be co-enriched. This would suggest that Se is incorporated into the tennantite-tetrahedrite lattice. A positive correlation is also recognised between Ag and Cd in tennantite-tetrahedrite (Figure 6.19B), meaning that Cd is likely to be present as lattice incorporations, because it appears to be co-enriched with Ag, which has already been suggested to occur in the lattice. These interpretations correlate with those in Table 8.2.

A ~1:1 positive correlation is identified between Au and Te in arsenopyrite (Figure 6.26A), although there is a spread of data points around the trendline. This may suggest that these trace elements dominantly co-occur as inclusions of Au-Te-bearing particles,

with increasing concentrations of both trace elements correlating to the ablation of larger proportions of inclusions within arsenopyrite. The positive correlations recognised between Sn and Te in arsenopyrite (Figure 6.26B), galena (Figure 6.15B), and tennantite-tetrahedrite (Figure 6.19D) could corroborate this interpretation, because a similar Sn-Te correlation in multiple minerals suggests that Sn and Te dominantly occur as inclusions. In arsenopyrite, elevated Au contents also correlate to elevated Sn contents, but there is a weaker correlation between Au and Sn, than between Au and Te; nevertheless, the association between Au and Sn, where Sn is likely present as inclusions, suggests that Au is also likely to be present as inclusions. Ratios between Sn and Te in arsenopyrite, galena, and tennantite-tetrahedrite are all ∼1:3, providing further indications that these elements occur as inclusions, with the ratio of Sn:Te perhaps reflecting the stoichiometry of the inclusion particles. The interpretation that Au, Sn, and Te dominantly occur as inclusions in arsenopyrite aligns with that in Table 8.2; however, Sn and/or Te sometimes exhibit spiky and similar profile traces in galena and tennantite-tetrahedrite, which has lead to the interpretation that Sn may be lattice-hosted in galena, and Te lattice-hosted in both galena and tennantite-tetrahedrite. This could be explained by the homogeneous distribution of Sn-Te inclusions in these minerals, although this cannot be confirmed in the present study. Finally, the bivariate plots for chalcopyrite and sphalerite do not aid in elucidating trace element incorporation, but may nevertheless provide indications of hydrothermal fluid characteristics, as discussed in Section 8.3.2.

Further indications of incorporation mechanisms can be gained from the qualitative analysis of LA-ICP-MS maps, in terms of the distribution patterns of trace elements (e.g., Large et al., 2009; Kouhestani et al., 2017; Steadman et al., 2021). The maps of pyrite in Section 6.5 show that, in general, Co, Ni, As, Se most often appear (i.e., in the majority of maps) to be homogeneously distributed within a crystal or zone, suggesting lattice incorporation of these elements. On the contrary, Cu, Ag, and Hg, most often appear as discrete spots of elevated concentrations, indicative of inclusions, although homogeneous distribution of Cu in multiple zones is uniquely observed in Figure 6.32, and homogeneous distribution of Ag and Hg in multiple zones is uniquely observed in Figure 6.30. Antimony, Au, and Pb are mixed, with homogeneous distributions and discrete spots both observed in multiple maps. These observations agree with the classification of incorporation mechanisms of these elements in pyrite from Table 8.2. The lattice-strain modelling introduced in Chapter 7 also has implications for understanding trace element incorporation in pyrite; this is discussed in Section 8.3.2.

The interpretations of trace element incorporation based on empirical observations (Table 8.2) are largely compitable with the interpretations of trace element incorporation

from previous studies. In pyrite, Co, Ni, Cu, As, Se, Mo, Ag, Sb, Te, Au, and Pb are interpreted to potentially occur as lattice incorporations (Chouinard et al., 2005b; Reich et al., 2005; Deditius et al., 2009, 2011; Reich et al., 2013; Keith et al., 2016, 2018; Grant et al., 2018; Meng et al., 2020), with Co, Ni, As, and Se proposed to be the most common incorporations (Keith et al., 2016). This is in alignment with the interpretations in Table 8.2, although the presence of Hg as a lattice-hosted element in pyrite has, to the author's knowledge, not previously been recorded.

Studies of trace elements in chalcopyrite have suggested that Co, Zn, Ga, As, Se, Ag, In, Sn, and Pb may occur as lattice incorporations (Cook et al., 2009; Maslennikov et al., 2009; Carvalho et al., 2018; Grant et al., 2018; George et al., 2018b). Meanwhile, galena is interpreted to be able to incorporate Cu, Se, Ag, Cd, Sb, Te, Hg, and Bi into the mineral lattice (Liu and Chang, 1994; George et al., 2015), and tennantite-tetrahedrite is interpreted to be able to incorporate Co, Se, Ag, Cd, Te, Hg, Pb and Bi (George et al., 2017; Crespo et al., 2020). In the case of sphalerite, Mn, Fe, Co, Ga, Ge, As, Cd, In, Sn, and Hg are interpreted to sometimes occur as lattice incorporations (Cook et al., 2009; Lockington et al., 2014; Frenzel et al., 2016), while for arsenopyrite, only Au has been measured and interpreted to be occasionally lattice-hosted (Cook and Chryssoulis, 1990; Reich et al., 2005; Deditius et al., 2014). This summary of trace element hosting from the literature indicates that the interpretations of lattice incorporations in Table 8.2 are within reason.

8.3.2 Trace element variations between vein generations

To further investigate trace element deportment, and specifically the partitioning of trace elements between ore minerals, comparisons can be made of the concentrations of lattice-hosted elements in the ore minerals across vein generations. Figure 8.4 shows this for Se, where it is apparent that galena, where present, is always the most enriched in Se. Pyrite has a wide range in Se, and where present, overlaps the ranges of tennantite-tetrahedrite and chalcopyrite. This can be explained by the fact that pyrite crystals are compositionally heterogeneous, and therefore spot analyses are not necessarily representative of the bulk composition of each crystal, shown in the LA-ICP-MS trace element maps in Section 6.5. Furthermore, pyrite is interpreted to have a more complex formation history than other ore minerals, with crystallisation commencing prior to that of the other ore minerals (Section 8.2.2). This would mean that, if pyrite is not co-crystallised, its concentration of trace elements should not reflect trends in partitioning between ore minerals, as noted by George et al. (2016) and George et al. (2017) in their studies of trace element partitioning between co-crystallised ore minerals. Therefore, the data for pyrite is not reliable in

terms of assessing element partitioning between ore minerals, and is thus not considered further. After galena, tennantite-tetrahedrite, and then chalcopyrite, are consistently the next most Se-rich, suggesting that Se follows a partitioning trend of: galena > tennantite-tetrahedrite > chalcopyrite. It is unclear whether sphalerite and arsenopyrite in the vein generations incorporate Se into the lattice (Section 8.3.1), thus the Se content of these minerals are not considered in the context of partitioning trends. Nevertheless, the partitioning trend outlined above appears to be compatible with the trends identified by George et al. (2016) and George et al. (2017).

A relationship between the Se concentration in ore minerals and the temperature of hydrothermal fluids has been determined from studies of VMS deposits, whereby higher temperatures have been linked to the elevated Se contents in ore, specifically pyrite and chalcopyrite (Auclair et al., 1987; Maslennikov et al., 2009). Contrastingly, Keith et al. (2018) identified an antithetic relationship between the Se content of pyrite, and fluid temperature, based on the trace element analyses of pyrite from different ore deposits. However, Keith et al. (2018) did not detect Se at concentrations of >100 ppm in pyrite from porphyry deposits, which casts doubt on the applicability of this relationship in

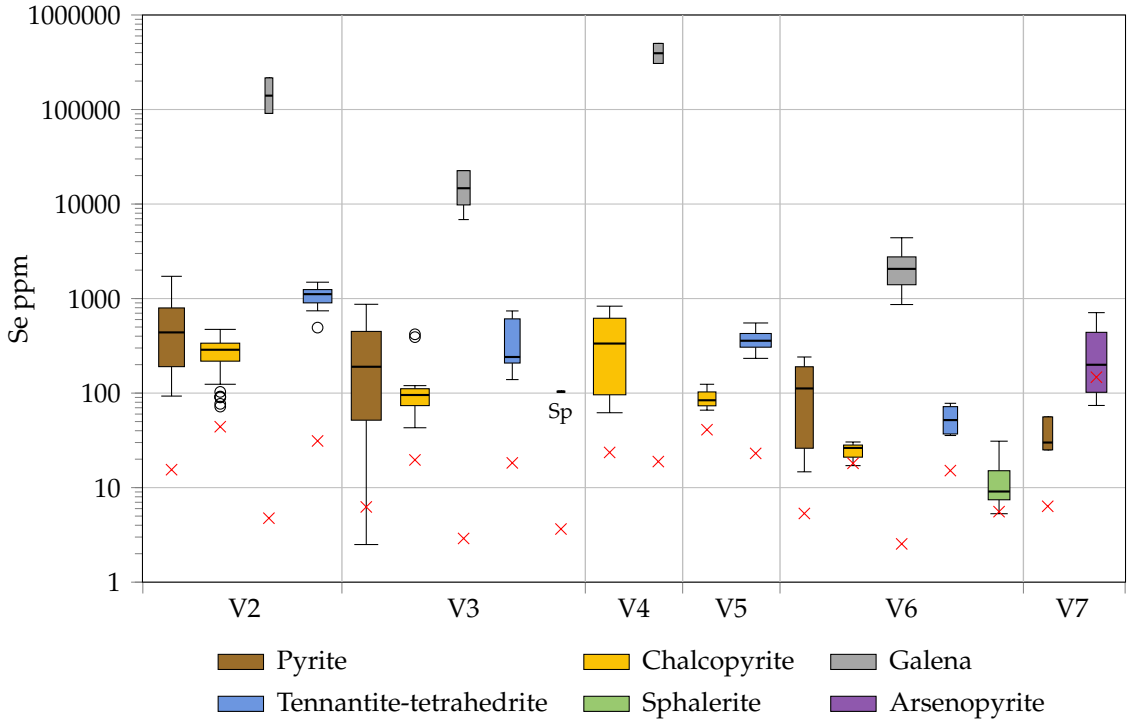

Figure 8.4. Variable width boxplot of Se in the ore minerals analysed by LA-ICP-MS. Box width is relative to the number of samples containing Se (e.g., V2 chalcopyrite has the highest sample count of 40, while V3 sphalerite has the lowest sample count of 2; this also accounts for the very short box length, with 2 samples of similar Se concentration). Open circles represent outliers in the data, which are classified as in Figure 6.4. Red crosses are mean lower limits of detection; no data below detection limits is shown.

porphyry systems, as the concentrations of Se in pyrite from Iron Cap reach a maximum of in excess of 1700 ppm, with a median of ∼200 ppm (Section 6.4.3). Indeed, it would be expected for higher temperatures to increase the partitioning of Se into pyrite (in terms of K_D), and all ore minerals for that matter, given that increases in temperatures theoretically encourage ion substitution, as shown in Section 7.4 (e.g., Figure 7.5). An alternate theory is that the Se concentration in pyrite is controlled by the S/Se ratio of the fluid, as illustrated by the numerical simulations of Huston et al. (1995), which were applied to explain the formation of VMS deposits.

Given that, in theory, the concentration of an element in a mineral is a product of equation (1), the changes in Se concentration in the same ore minerals over different vein generations (Figure 8.4) are likely to correspond to changes in the hydrothermal fluid, be that conditional changes (i.e., temperature), and/or changes in fluid chemistry (i.e., Se/S ratios). For the reasons noted above, it could be suggested that higher Se concentrations in the ore minerals signify either higher hydrothermal fluid temperatures, or an increased effective concentration of Se in the fluid. Thus, Figure 8.4 shows that the highest fluid temperatures, or the most effectively Se-rich fluids are likely to have been prevalent during the formation of V4 veins, which hosts the most Se-rich galena and chalcopyrite. In turn, this implies a decreasing trend from V4 > V2 > V3/V5 > V6.

There are differences in the proportional concentration of Se partitioned into each ore mineral between different vein generations (Table 8.3), which may further elucidate the controls on Se concentrations in the ore minerals. The variation in the Se proportions in pyrite and sphalerite across vein generations could be explained by the factors noted above (timing of crystallisation, lack of data), thus not reflecting partitioning trends. However, the differences in Se partitioning between chalcopyrite, galena, and tennantite-tetrahedrite require further consideration. The galena LA-ICP-MS data is possibly subject to a degree of error, particularly for Se-rich galena (Section 6.4.1), which could partly explain the apparent differences in the proportion of Se partitioned into galena across vein generations. However, the differences in the proportion of Se partitioned into tenanntite-tetrahedrite cannot be attributed to similar causes. There is a trend whereby the highest proportions of Se in galena and tennantite-tetrahedrite occur in the same vein (V2), with decreasing proportions of Se in both minerals occurring in the V3, and then V6.

If the conditions of ore formation in these veins were the same, it would be expected for the magnitude of partitioning trends to be relatively similar, because K_Ds are relatively constant under constant conditions (Chapter 7). In other words, changes solely in the effective concentration of Se in the fluid would not be expected to induce changes in the proportion of Se partitioned into each ore mineral. Therefore, to explain the vari-

Table 8.3
Median concentrations of Se from ore minerals of V2-V6, proportional to the Se concentrations in chalcopyrite, which is ubiquitous throughout these vein generations. Values reported to a maximum of 3 significant figures.

	V2	V3	V4	V5	V6
Chalcopyrite	1.00	1.00	1.00	1.00	1.00
Pyrite	1.53	1.99	–	–	4.26
Galena	487	154	1180	–	78.4
Tennantite-tetrahedrite	3.87	2.52	–	4.26	1.97
Sphalerite	–	1.08	–	–	0.35

ance in the proportional concentration of Se noted above, it is suggested that there were changes in the conditions of ore formation; principally temperature. Higher temperatures appear to increase the proportion of Se partitioned into galena, relative to the proportion of Se partitioned into tennantite-tetrahedrite and chalcopyrite. Furthermore, the proportion of Se partitioned into tennantite-tetrahedrite would likely increase relative to that partitioned into chalcopyrite at higher temperatures. This indicates that the changes in Se concentration between vein generations are likely, at least in part, due to changes in temperature.

Silver is the only other trace element that appears to be lattice-hosted in the majority of co-crystallised ore minerals (Table 8.2), and detected in all vein generations (Table 6.33). It may thus be useful for assessing partitioning trends and variations between vein generations, as illustrated in Figure 8.5. There is overlap in the ranges and IQRs of Ag for the co-crystallised ore minerals (chalcopyrite, galena, tennantite-tetrahedrite, and sphalerite), indicating that, unlike Se, there is not a definitive partitioning trend; Ag concentrations appear to vary by as much as two orders of magnitude within the same ore minerals of a vein generation. Nevertheless, it appears that in V5 and V6 veins, tennantite-tetrahedrite hosts the highest concentrations of Ag; this is also true when considering the median values for V2 and V3 veins. Galena is generally the secondmost Ag-rich mineral, although again there is overlap with the range in tennantite-tetrahedrite in V2 and V3 veins. Chalcopyrite and then sphalerite complete the partitioning trend, although there is overlap in the ranges of Ag in these minerals; the median values for chalcopyrite are higher than those for sphalerite. Sphalerite may also largely host Ag as inclusions (Table 8.2), meaning that it cannot be reliably assessed in terms of Ag partitioning; therefore, only galena, tennantite-tetrahedrite and chalcopyrite are considered further. The lack of clarity in partitioning trends is also reflected in the concentrations of Ag in the ore minerals between vein generations. In general, the ore minerals of V4 veins appear to be the most Ag-rich, followed by those in V6, V3, V5, and then V2 veins.

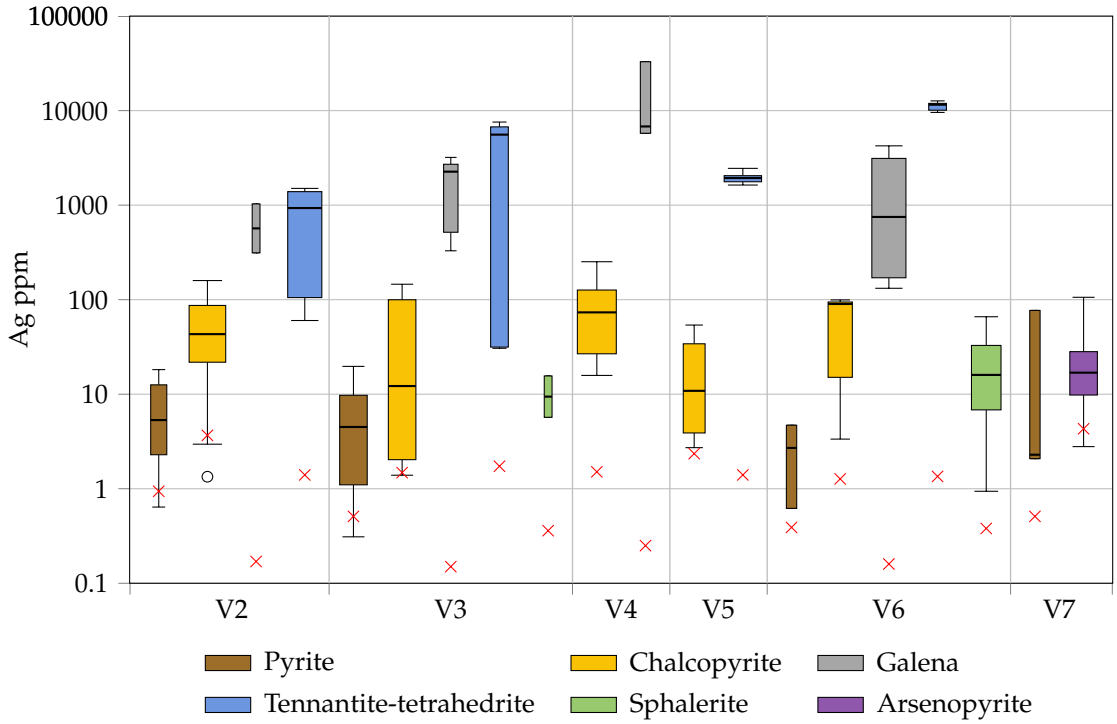

Figure 8.5. Variable width boxplot of Ag in the ore minerals analysed by LA-ICP-MS. Box width is relative to the number of samples containing Ag, out of a maximum of 28 (V4 chalcopyrite). Open circles represent outliers in the data, which are classified as in Figure 6.4. Red crosses are mean lower limits of detection; no data below detection limits is shown.

George et al. (2017) recognised that Ag is preferentially partitioned into tennantite-tetrahedrite over galena, which is generally observed in Figure 8.5. However, the fact that Ag partitioning appears to be less consistent than Se partitioning requires further explanation. George et al. (2016) and George et al. (2017) argued that if partitioning trends are not consistent, it means that the ore minerals did not co-crystallise. However, further interrogation of the trace element data highlights that these inconsistencies may be due to variations within vein generations; the trace element data for individual vein samples more clearly exhibits partitioning trends. Indeed, the only overlaps in Ag concentration between different ore minerals in the same samples are in two V2 samples (IC72-798, IC70-402), where one galena particle in each sample exhibits Ag contents within the range for tennantite-tetrahedrite. The fact that only one galena analysis was successfully reduced in each of these samples means that the accuracy of the galena trace element data cannot be assessed. Furthermore, the high Se contents of these V2 galena particles (∼20 wt.% Se in IC72-798, and ∼9 wt.% Se in IC70-402) could mean that the trace element data (i.e., Ag concentrations) may be over-corrected to higher values, as noted above, and in Section 6.4.1. This would indicate that the overlap in Ag concentrations between galena and tennante-tetrahedrite in these samples may be due to analytical inaccuracies.

Therefore, it appears that there may be a consistent partitioning trend for Ag, whereby

higher Ag contents occur in tennnantite-tetrahedrite > galena > chalcopyrite, although this is not always clearly observed when collectively considering the Ag concentrations in ore minerals from the same vein generation (Figure 8.5). The fact that the trend is not always clearly observed could suggest that the changes in Ag concentration in the ore minerals of different vein generations may be dominantly related to changes in the effective concentration of Ag in the hydrothermal fluid, rather than changes in K_Ds (i.e., due to temperature changes), because significant changes in K_Ds between veins of the same generation would likely require considerable temperature changes (e.g., Section 7.4). Such changes would not be expected between veins of the same generation because mineralogical, textural, or morphological changes would likely be evident (e.g., Sillitoe, 2010; Monecke et al., 2018).

In alignment with this theory, Pal'yanova (2008) utilised physico-chemical modelling of aqueous sulphide-chloride solutions in pyritic ore, to assess the behaviour of Ag in hydrothermal fluids at conditions comparable to those in porphyry systems. Their work showed that, between 300-400°C, the concentration of Ag is highest in acidic, high chloride solutions, compared to more alkaline or chloride-poor solutions. In turn, this implies that for veins with generally lower Ag concentrations in ore minerals (i.e., V2), the hydrothermal fluids are likely to have been more alkaline, or chloride-poor, whereas for veins with generally higher Ag concentrations in ore minerals (i.e., V4, V6), the hydrothermal fluids are likely to have been more acidic, or chloride-rich. Pal'yanova (2008) also interpreted that porphyry fluids evolve to become more Ag-enriched, owing largely to the tendency of later porphyry fluids to be more acidic and chloride-poor than earlier fluids (e.g., Section 2.5; Sillitoe, 2010; Reed et al., 2013). Therefore, it could be interpreted that the vein generations containing the most Ag-enriched ore minerals correspond to formation by fluids later in the evolution of the hydrothermal system. The later enrichment of Ag is also evidenced in porphyry deposits elsewhere, where metal zoning patterns show that Ag tends to be concentrated in more peripheral mineralisation, which corresponds to the later stages of hydrothermal fluid evolution (e.g., Sillitoe, 2010; Kouzmanov and Pokrovski, 2012).

Differences in trace element deportment between vein generations are also evidenced by bivariate plots; in particular, those for chalcopyrite (Figure 6.11). In V4, V5, V6, and most of V3 veins, Se and In show no correlation in chalcopyrite, implying that the controls on the lattice incorporation of Se and In into chalcopyrite are not the same. Increases in Se may be attributed to increases in temperature, as noted above. Therefore, increases in In may be alternatively controlled by fluid chemistry (i.e., the effective concentration of In the hydrothermal fluids). The co-elevation of Se and In in V2 chalcopyrite might then be

attributed to the co-occurrence of favourable conditions for both Se and In incorporation; the lack of a correlation between Se and In in V2 chalcopyrite suggests that there is no control in terms of crystal lattice compatiblity (i.e., no coupled substitution of Se and In occurs).

The two V3 chalcopyrite particles with elevated Se and In are located in sample IC70-402, where a V3 vein cross-cuts a V2 vein (Figure 8.2). The fact that the composition of these chalcopyrite particles does not align with the composition of other V3 chalcopyrite particles, suggests that there may be local controls affecting Se and In incorporation in this sample. Indeed, the elevated concentrations of Se and In relative to V2 chalcopyrite, which the V3 vein cross-cuts, suggests that zone refining may have occurred, whereby some of the Se and In the V2 chalcopyrite was liberated during V3 vein formation, enriching these elements in the hydrothermal fluid for incorporation into V3 chalcopyrite. This provides evidence to suggest that V3 veins post-date V2 veins, and that the two are unlikely to have formed at the same time (cf. Section 8.2.3).

Similar zone refining processes have been proposed to explain elevated trace element contents in later generations of pyrite of the TAG deposit on the Mid-Atlantic Ridge (Grant et al., 2018), highlighting that the trace element content of ore minerals may be affected by modification processes. This has relevance to the interpretation of trace elements in ore minerals, particularly in V2, V3, V6, and V7 veins, where pyrite appears to have experienced coupled dissolution-reprecipitation (Section 8.2.2). In these veins, it is possible that the trace element content of the later ore minerals may not be directly representative of the hydrothermal fluids, because some trace elements may have been concentrated in the earlier pyrite, and then liberated during dissolution to become in enriched in the later fluids precipitating the other ore minerals.

Nevertheless, this section shows that there are distinct differences between the trace element content of different vein generations in terms of their bulk concentrations, and in terms of the concentrations of trace elements in specific ore minerals. These differences are most likely to represent differences in the hydrothermal fluids during ore formation, in terms of conditional changes and/or changes in fluid chemistry.

8.3.3 Trace element variations within vein generations

The trace element maps of pyrite presented in Section 6.5 illustrate that, even within vein generations, there can be major fluctuations in the concentration of certain trace elements hosted in ore minerals. These maps are interpreted below to identify different stages of pyrite formation, and to provide insights into the variation in trace element incorporation in pyrite over the course of the formation of a single vein. The lattice strain

models presented in Chapter 7 are then utilised to explore the implications of these trace element variations in terms of the characteristics of the hydrothermal fluids during vein formation.

Each pyrite particle mapped by LA-ICP-MS is interpreted to be composed of multiple generations, as shown below. These generations are assigned based on general trends in the trace element maps, to enable the discussion of the evolution of trace elements in pyrite. Although the assigned generations are likely to represent different stages of pyrite growth, there are also evidently different stages of growth recorded within generations. The assigned generations are thus intended to represent the most significant changes in pyrite characteristics and growth.

8.3.3.1 V2 pyrite

The V2 pyrite particle in Figure 6.27 is interpreted to be composed of three generations of pyrite, as shown in Figure 8.6. The earliest generation, Py1, is located in the core of the particle, and characterised by variable elevations in Ni, As, Se, and Au. The three particles of Py1 surrounding the Py2 label in Figure 8.6 exhibit zones of elevated As and Au, antithetic to zones of elevated Ni and Se (± minor Co). The compositional zones in these regions reflect primary precipitation (i.e., growth zones; e.g., Sykora et al., 2018; Steadman et al., 2021). The remaining Py1 particle to the top left is elevated in Se, perhaps reflecting a later growth zone in Py1 that is depleted in Ni, As, and Au. The irregular shape of Py1 particles, coupled with the non-concentric zoning (i.e., termination of growth zones at particle boundaries), suggests that original crystals of Py1 have been

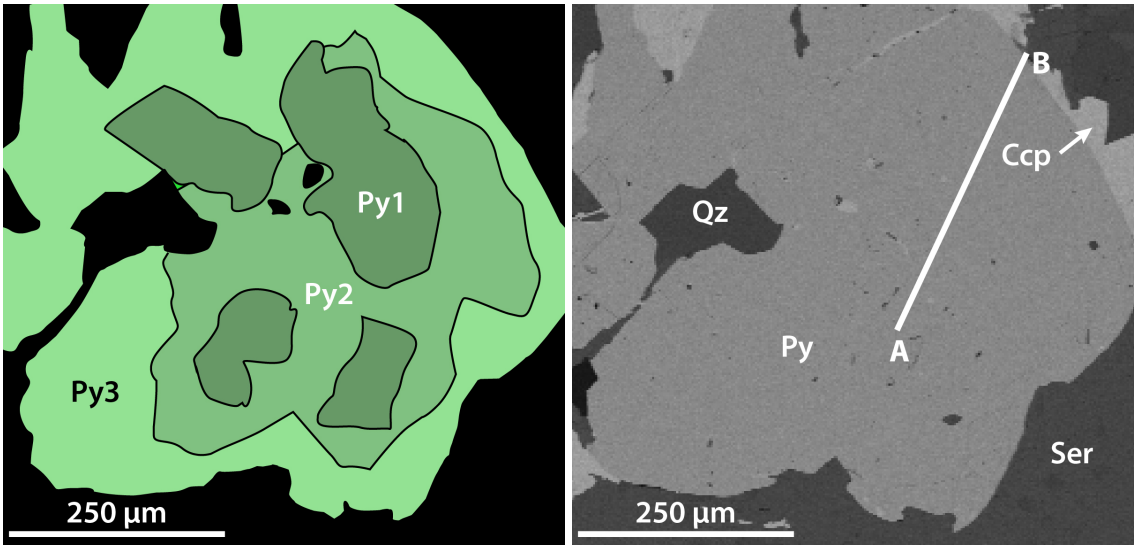

Figure 8.6. Interpreted pyrite generations in a V2 pyrite from sample IC70-429, based on trace element maps in Figure 6.27. A BSE image is also shown for reference, with an A to B line travese marked.

broken up and later intergrown and amalgamated by Py2/3. Elevated Co, and variably Ni, define Py1 crystal faces preserved from crystal growth, supporting this theory.

Brecciation, recrystallisation, or dissolution processes, may have effected the breaking up of Py1. Coupled dissolution-reprecipitation processes (e.g., Putnis, 2009) might be evidenced by the elevation of Pb and Cu ($\pm$ Ag, Sb) in Py1, which are interpreted to correspond to inclusions, owing to their spotty distribution. Furthermore, the core of Py2, which likely corresponds to the earliest pyrite growth after Py1, contains moderate elevations in all the trace elements analysed (apart from Hg), possibly indicating liberation of these elements from Py1 for precipitation in Py2. Lower concentrations of Se principally characterise Py2, while Co and Ni are variably elevated. Meanwhile, Py3 is characterised by elevated Se, Co, and Ni. These later pyrite generations do not display clear growth zoning, which may further indicate that they formed by modification processes (e.g., annealing, recrystallisation), rather than by primary precipitation from a hydrothermal fluid.

A traverse of the V2 pyrite particle (from A to B; Figure 8.6) has been created by exporting the LA-ICP-MS map images in greyscale, importing these into ImageJ software, and then extracting a line traverse in terms of the colour of each pixel out of 255, where 0 is black, and 255 is white. Pixel values in terms of colour were then converted back to concentration by multiplying the pixel value by the concentration (in ppm) over 255. The line traverse is shown in Figure 8.7, where it is apparent that there are few co-elevations between trace elements. Only Au, where present, is co-elevated with As, indicating that there is a relationship between the incorporation of these elements into pyrite. Indeed, it is well-known that As enhances the incorporation of Au in pyrite, either as inclusions (nanoparticles), or as lattice incorporations (e.g., Reich et al., 2005, 2013; Deditius et al., 2014). This relationship maybe used to infer the chemistry of the hydrothermal fluids, as Deditius et al. (2014) compared porphyry fluid compositions (e.g., from fluid inclusions) with pyrite trace element data to show that Au/As ratios in pyrite from porphyry deposits "correspond reasonably" with the Au/As signature of the hydrothermal fluids.

In Figure 8.7, Se concentrations appear to be relatively consistent throughout, varying only on a scale of 100s ppm (up to $\sim$600 ppm). This suggests that the factors influencing the incorporation of Se (e.g., temperature; Section 8.3.2) did not change markedly during the crystallisation of this pyrite particle, although there are subtle changes between pyrite generations; Py1 is more elevated in Se than Py2/3. On the contrary, Co, Ni, and As fluctuate over several orders of magnitude, suggesting that the factors influencing the incorporation of these elements varied more significantly than for Se. Cobalt and Ni are co-elevated in discrete regions of all three pyrite crystals (e.g., in the centre of the Py1

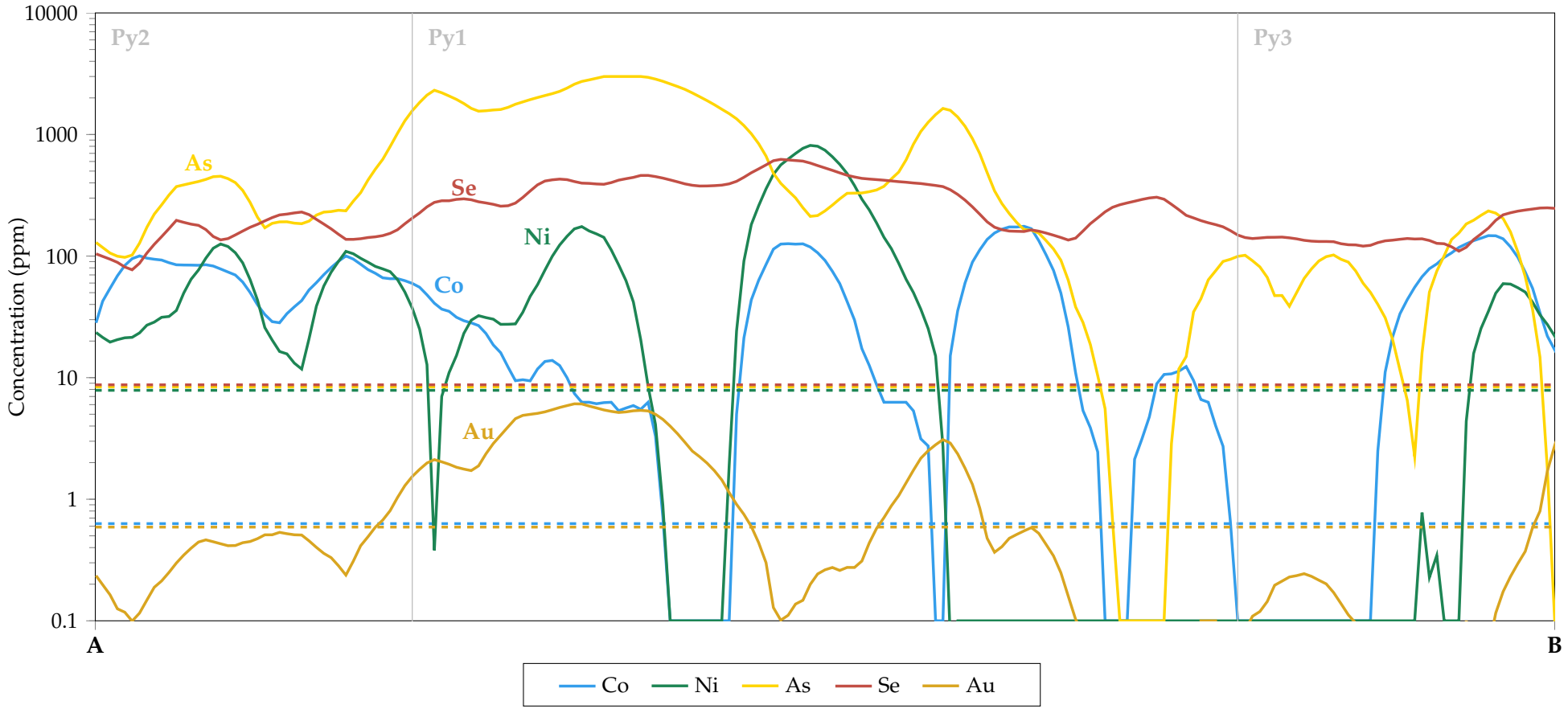

Figure 8.7. Line traverse of the V2 pyrite particle from sample IC70-429, based on the trace element data from LA-ICP-MS mapping. The location of the A to B traverse is marked in Figure 8.6. Dashed lines are approximate lower limits of detection.

traverse), but this relationship is not always observed.

8.3.3.2 V3 pyrite: IC65-430

The V3 pyrite particle in Figure 6.28 exhibits at least three generations of pyrite (Figure 8.8). Py1 is mostly elevated throughout in Fe and Se, whereas As and Au are co-correlated in discrete regions. The discrete regions are also variably elevated in Sb and Pb, which appear to be lattice-hosted in Py2 and Py3, and define the boundary between these two generations. This may suggest that Sb and Pb are also lattice hosted in Py1; therefore, the discrete enrichment zone of As, Au, Sb, and Pb in Py1 may represent discrete pyrite particles that were amalgamated in a similar process to the V2 Py1 (Figure 8.6). However, the fact that Fe and Se are mostly elevated throughout Py1 complicates this theory. Alternatively, the enriched regions of As and Au (±Sb, Pb) may have formed due to sector zoning (e.g., Chouinard et al., 2005b; Sykora et al., 2018), while Fe and Se were enriched throughout. It is unclear why Py1 appears to be elevated in Fe; this might be expected if Py2/3 were elevated (i.e., to weight percent levels) in trace elements, such that the intensity of the Fe signal was lower compared to Py1. However, this is not the case for the trace elements mapped. The fact that the BSE image shows no distinction between Py1 and Py2/3 in terms of relative atomic mass, may suggest that the apparent increase in Fe in Py1 is caused by difference in the structure of the mineral; perhaps Py1 is marcasite instead of pyrite.

The anhedral form of Py1 indicates that it may have been affected by modification processes prior to the precipitation of Py2. The distribution of Cu and Hg (± Co, Ni, Ag, Sb, Pb) is interpreted to represent post-Py1 infiltration and the earliest precipitation

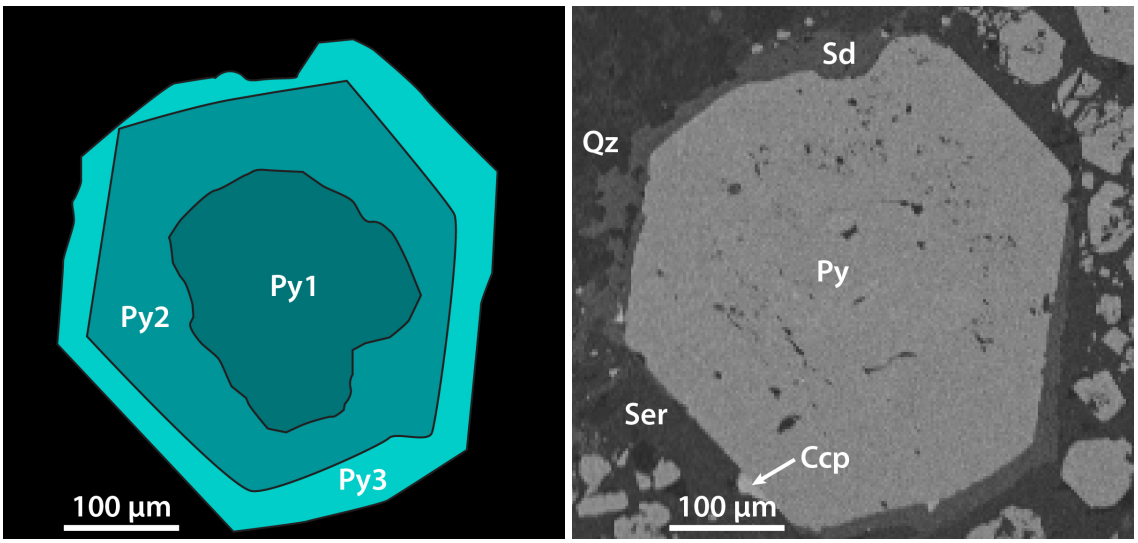

Figure 8.8. Interpreted pyrite generations in a V3 pyrite from sample IC65-430, based on trace element maps in Figure 6.28. A BSE image is also shown for reference.

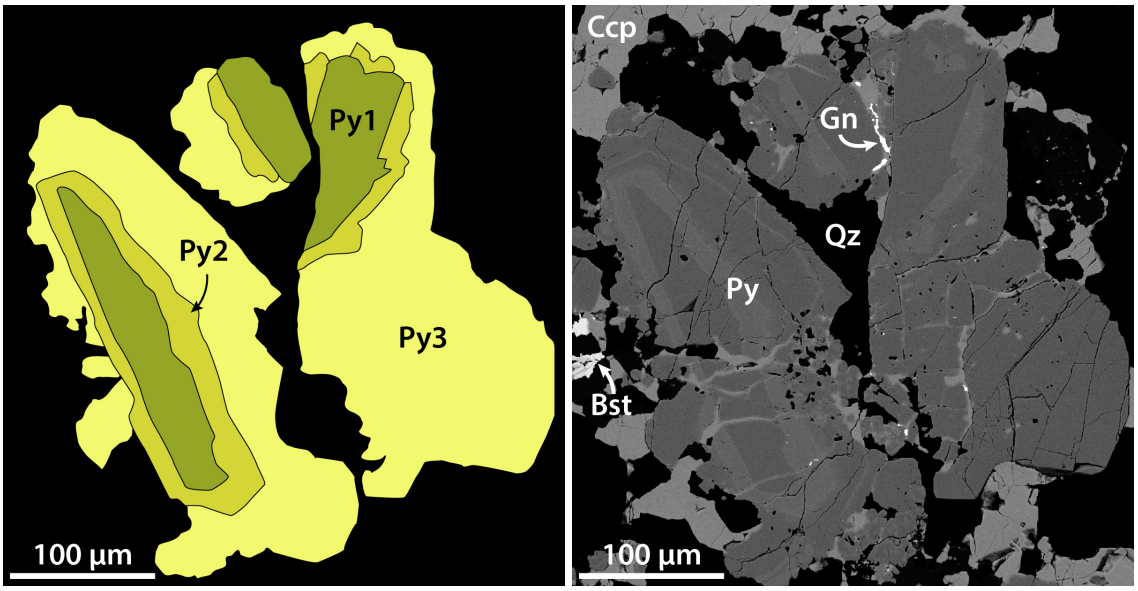

Figure 8.9. Interpreted pyrite generations in a V3 pyrite from sample IC59-033-1, based on trace element maps in Figure 6.29. A BSE image is also shown for reference.

of Py2. Py2 is elevated in Co, Ni, Ag, Sb, and Pb, although the distribution of these elements again suggests that sector zoning may have occurred. On the other hand, Py2 is porous, suggesting that it was affected by dissolution (e.g., Putnis, 2009), which could have caused the irregular distribution of trace elements. However, the fact that the porosity is largely constrained to Py2, and not abundant in Py3, may alternatively indicate that porosity was generated during primary precipitation (Deditius et al., 2011), perhaps by rapid precipitation due to phase seperation (Roman et al., 2019). The relatively euhedral shape of Py2 and Py3 (moderately elevated in Sb and Pb) suggests that later modification processes did not alter these generations of pyrite.

Adjacent to the large pyrite particle there are numerous smaller particles with trace element signatures comparable to Py1 (elevated Fe, As, Se, Sb, Au, and Pb) and Py2 (elevated Ag, and moderate Co, Sb, and Pb), suggesting either that this pyrite has been brecciated, or that they each represent primary particles of Py1 and Py2. The concentric zoning in As and Au in the Py1 particle in the bottom right of the map indicates that the latter scenario might be more plausible.

8.3.3.3 V3 pyrite: IC59-033-1

At least three generations of pyrite are interpreted to be present in the V3 pyrite particles in Figure 6.29, as shown in Figure 8.9. Concentric zoning is evident, suggestive of primary growth. Py1 is elevated in Se, with elevations of Co antithetic to Se, while Py2 is primarily elevated in As, with moderate elevations of Sb also observed. Concentric zoning continues in Py3, but is more variable, with Co, Ni, As, Se, Ag, Sb, and Au elevated

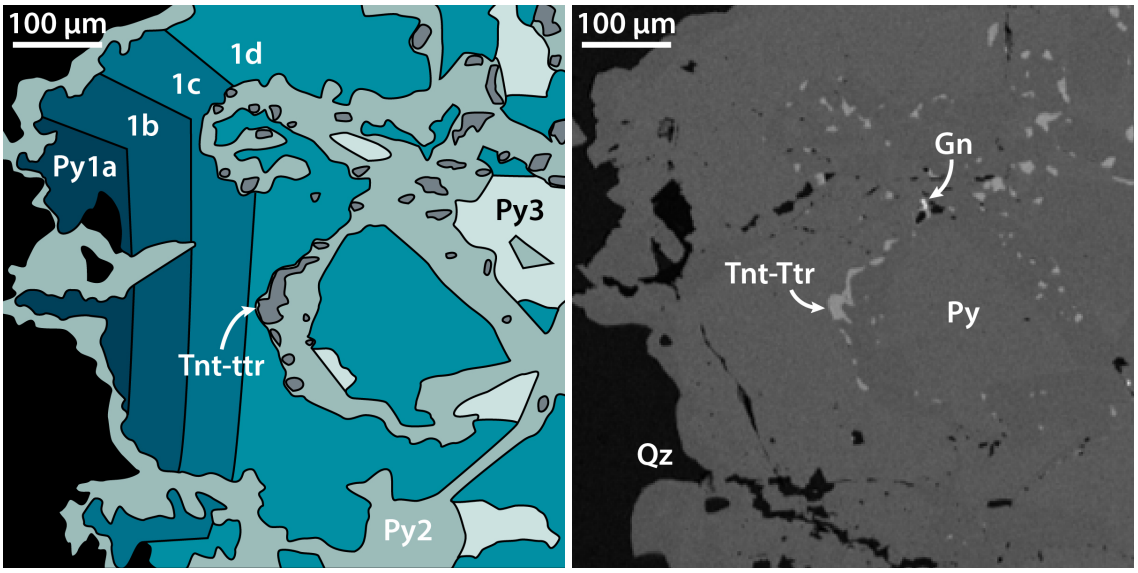

Figure 8.10. Interpreted pyrite generations in a V3 pyrite from sample IC73-518, based on trace element maps in Figure 6.30. A BSE image is also shown for reference.

in various regions. The antithetic elevation of Se and As suggests that the controls on the incorporation of these trace elements in pyrite are not the same; the same could be said of Se and Co.

The distribution of Cu and Pb is interpreted to represent chalcopyrite and galena, respectively; elevations of Se, Ag, and Sb may also correspond to these minerals (cf. Section 6.4.4 and 6.4.5). Extensive dissolution-reprecipitation is evidenced by the cross-cutting of primary growth zones by chalcopyrite, and the brecciated nature of much of Py3, and indeed the Py1/2 regions to the right side of the image. This constrains the timing of modification to post-Py3. It may also indicate that the chalcopyrite and galena scavenged the trace elements liberated from the pyrite.

8.3.3.4 V3 pyrite: IC73-518

The V3 pyrite particle mapped in Figure 6.30 is interpreted to have three overarching generations of pyrite, although the earliest has been subdivided into four further generations (Figure 8.10). This is because Py1 exhibits different compositional zones suggestive of primary deposition; Py1a is elevated in Sb and Hg, Py1b is elevated in Se, Ag, Sb, Au, Hg, and Pb, while Py1c is elevated in the same trace elements as Py1b, but to a lesser degree. Lastly, Py1d is elevated in the same trace elements as Py1b/c, but at lower concentrations, which receed outwards from the margin of Py1c. Py1 is interpreted to represent an original, and relatively euhedral, pyrite crystal that formed in an environment with fluctuating physical and/or chemical conditions, resulting in the zonations. The co-elevations and -depletions in Py1 suggest that the environment of crystallisation

either enhanced or inhibited trace element incorporation in general, with no apparent discrimination between different trace elements. However, As appears to be homogeneously elevated throughout all of Py1, suggesting that its incorporation was not linked to the factors controlling the incorporation of other trace elements.

Rapid crystallisation could be invoked to explain the incorporation of trace elements in Py1, leading to more disordered crystal structures, and allowing the incorporation of trace elements that might not otherwise be incorporated in the lattice (Steadman et al., 2021). Indeed, Hg has not, to the author's knowledge, been recorded as a lattice-hosted trace element in pyrite; its distribution in Figure 6.30 would suggest it is lattice-hosted. Other elements, such as Ag, Sb, and Pb, are also not commonly present as lattice incorporations (Section 8.3.1), implying that the conditions of crystallisation enhanced their incorporation. Rapid crystallisation is typically related to lower temperatures, or processes such as phase separation, or fluid mixing (Roman et al., 2019; Steadman et al., 2021). Both Co and Ni are essentially absent from Py1 (and Py2/3), which could be linked to formation at lower temperatures, because numerous studies have recognised an association between the elevation of Co and Ni in pyrite, and higher temperatures of ore formation (e.g., porphyry vs. epithermal pyrite; Maydagán et al., 2013; Franchini et al., 2015; Sykora et al., 2018; Steadman et al., 2021).

After the precipitation of Py1, coupled dissolution-reprecipitation processes are interpreted to have occurred, based on the anhedral form of Py1 particles, and the network-like texture of Py2, which also hosts inclusions of tennantite-tetrahedrite and galena, and exhibits porosity. The Py2 generation is depleted in all the trace elements analysed, with spotty elevations of Fe, Cu, Se, Ag, Sb, Hg, and Pb interpreted to represent the distribution of tennantite-tetrahedrite and galena. The lack of trace elements in Py2 could be explained by the preferential partitioning of the trace elements liberated from Py1 into other ore minerals, rather than incorporation into Py2. Py3, which is only moderately elevated in As, is interpreted to have crystallised last, because it is also trace element-poor, and hosts an inclusion of Py2 on the right side of the map. Py3 also lacks inclusions of tennantite-tetrahedrite and galena, suggesting that it post-dates the formation of these ore minerals.

8.3.3.5 V6 pyrite

Unlike the previous pyrite particles discussed, the V6 pyrite in Figure 6.31 is not interpreted to have experienced post-precipitation modification. Primary growth zones (Figure 8.11) are evidenced by the concentric fluctuation of trace elements; in particular, Co, As, and Se. These three elements also appear to be antithetically elevated; indeed, this

is exemplified by the line traverse in Figure 8.12. However, the traverse also shows that there is evidently some co-elevation of As, Se, and Co in Py3-5, meaning that there is variation between the controls on incorporation of these elements. Py1 also contains Cu, Ag, Sb, and Au (± Pb) as spotty distributions, interpreted to reflect inclusions.

Sector zoning could have contributed to the differences in elevation within Py4 in terms of Se, and in Py5 in terms of As, whereby different crystal faces of the pyrite accomodate different trace elements (or concentrations of trace elements), owing to their different atomic arrangements (Chouinard et al., 2005b; Wu et al., 2019; Hastie et al., 2020). This type of zoning is attributed to rapid crystallisation (Chouinard et al., 2005b; Wu et al., 2019; Hastie et al., 2020), suggesting that Py4/5 grew faster than the earlier generations of pyrite. Rapid crystallisation may also have enhanced the incorporation of Au, which is predominantly elevated in Py5, and appears to be mostly lattice-hosted, owing to its relatively homogeneous distribution, similar to As; correlation between As and Au in Py5 is evident in Figure 8.12. Furthermore, the abundance of inclusions of Cu, Ag, Sb, Au, and Pb in Py4/5, evidenced by their spotty distribution, could also be explained by rapid growth (e.g., Roman et al., 2019). As noted in Section 8.3.3.4, rapid crystallisation is typically related to lower temperatures, or processes like phase separation or fluid mixing (Roman et al., 2019; Steadman et al., 2021), meaning that Py4/5 could be related such conditions or processes. The presence of tennantite-tetrahedrite inclusions, grown along the margins of Py3, also suggests that Py4/5 formed under different circumstances than Py1-3, which lack these inclusions.

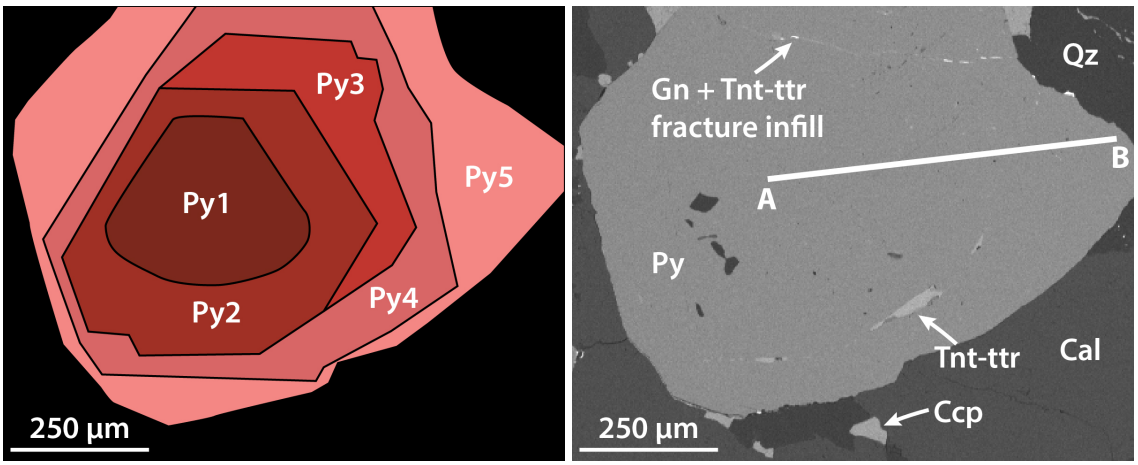

Figure 8.11. Interpreted pyrite generations in a V6 pyrite from sample IC37-157-2, based on trace element maps in Figure 6.31. A BSE image is also shown for reference, with an A to B line travese marked.

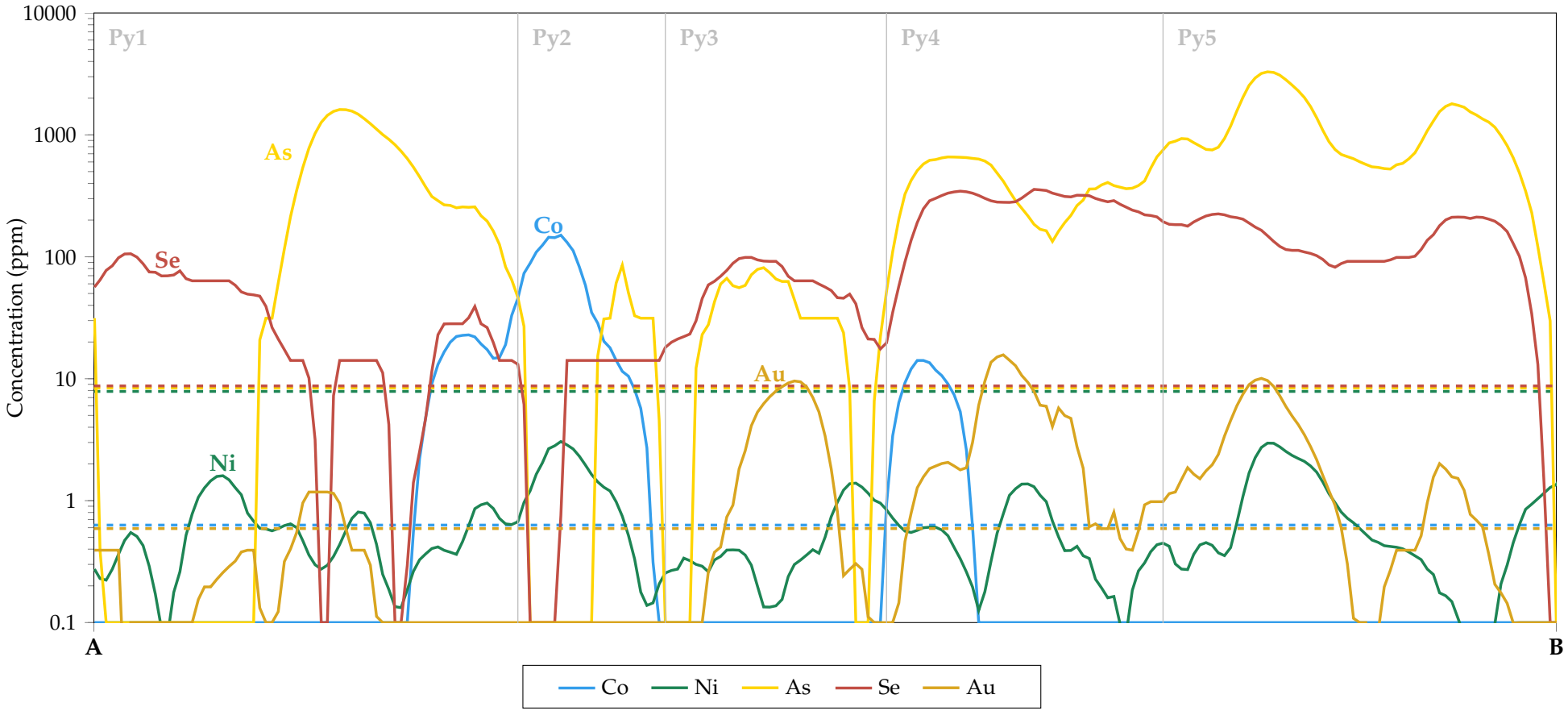

Figure 8.12. Line traverse of the V6 pyrite particle from sample IC37-157-2, based on the trace element data from LA-ICP-MS mapping. The location of the A to B traverse is marked in Figure 8.11. Dashed lines are approximate lower limits of detection.

8.3.3.6 *V7 pyrite*

Primary growth zones also characterise the V7 pyrite in Figure 6.32, as interpreted in Figure 8.13. The earliest pyrite generation in the core, Py1, is elevated in Co, Ni, Cu, Ag, Sb, Hg, and Pb, with moderate Se. The remaining generations are defined largely by varying concentrations of Co, Cu, As, Se, and Sb, as illustrated in the line traverse in Figure 8.14. In particular, As, Cu, and Au elevations are correlated in Py2, Py4, and Py6, indicating a similar control on incorporation. However, the ratios of As:Cu:Au vary between these generations, suggesting that Py2, Py4, and Py6 did not form from hydrothermal fluids with the same characteristics.

Copper is not interpreted to dominantly occur as a lattice-hosted element in pyrite in the samples from Iron Cap (e.g., Table 8.2), but its distribution in Figure 6.32, and its correlation with As and Au, suggests otherwise. Reich et al. (2013) interpreted that Cu is lattice-hosted in pyrite from the Dexing deposit, China, although they noted an antithetic relationship between As and Cu, suggesting that the chemistry of the hydrothermal fluids (i.e., Cu-rich or As-rich) controlled the precipitation of alternating Cu-rich and As-rich zones in pyrite. On the other hand, Wu et al. (2019) utilised nanoscale secondary ion mass spectrometry and atom probe tomography to show that As, Cu, and Au may be co-elevated in pyrite owing to crystal growth rate controls that generate As-Cu-Au-rich sector zones (cf. Section 8.3.3.5). Sector zoning is not clearly observed in Figure 6.32, implying that the chemistry of the hydrothermal fluids (i.e., As- and Cu-rich) may be a more likely control on the co-elevation of these elements in Py2, Py4, and Py6. Relative

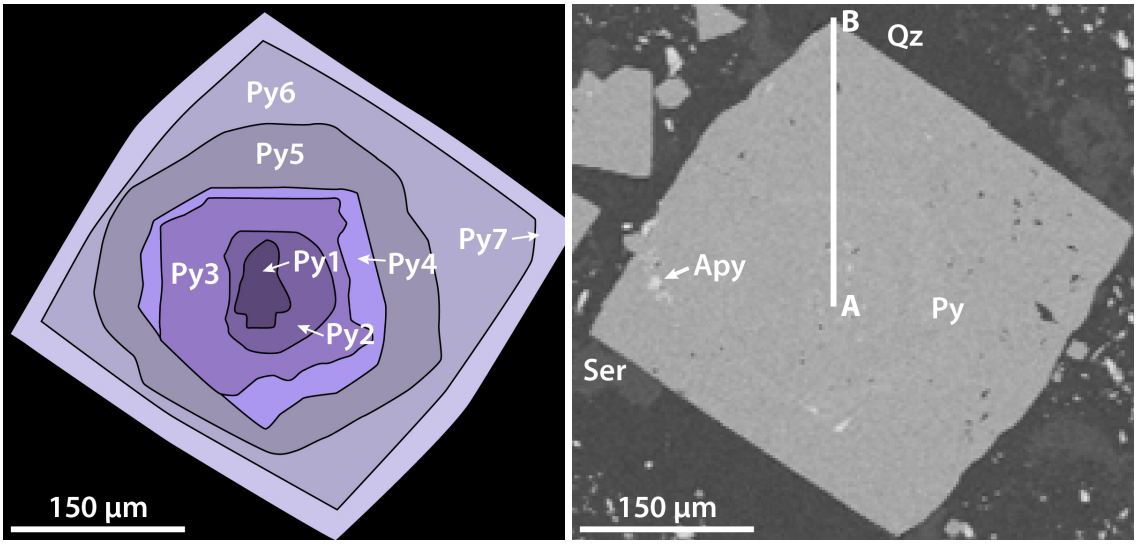

Figure 8.13. Interpreted pyrite generations in a V7 pyrite from sample IC66-073, based on trace element maps in Figure 6.32. A BSE image is also shown for reference, with an A to B line travese marked.

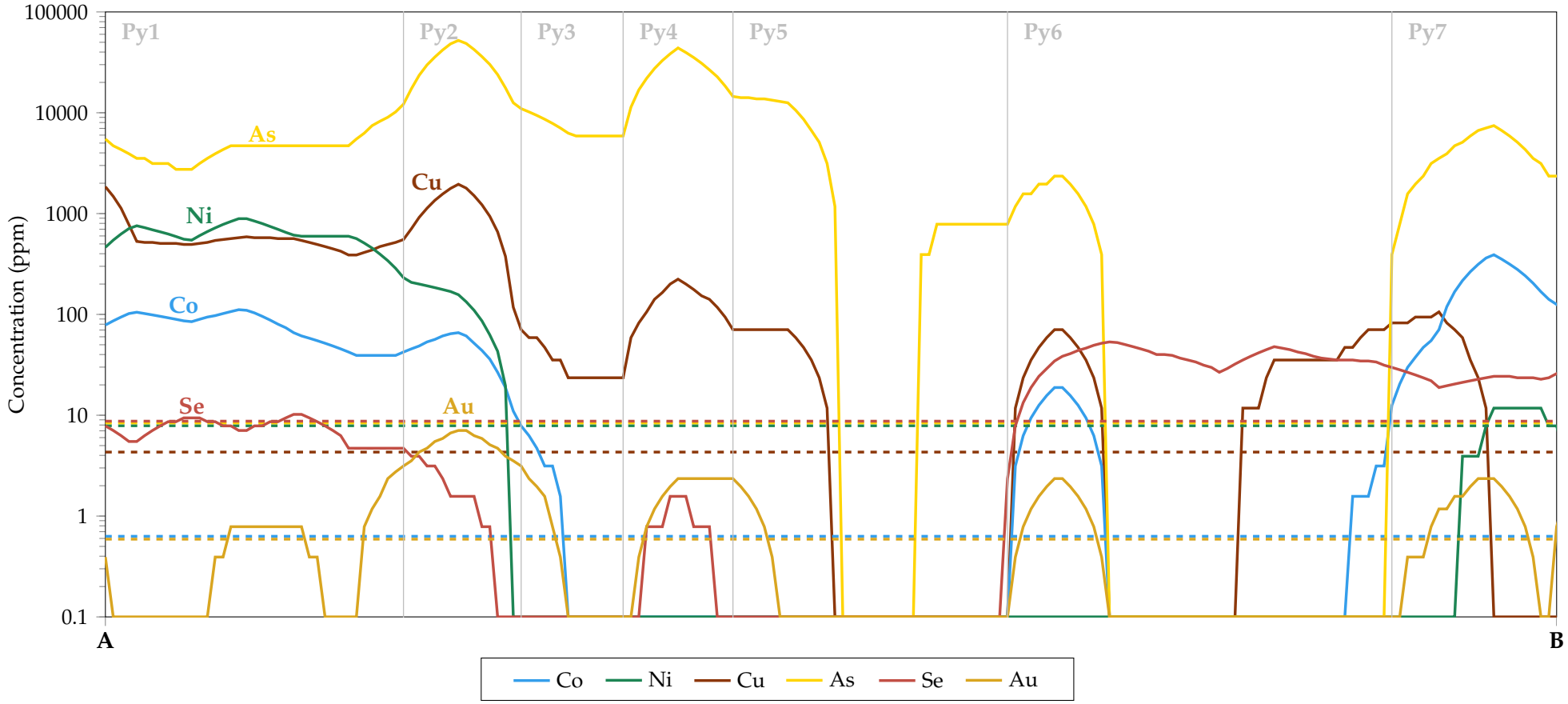

Figure 8.14. Line traverse of the V7 pyrite particle from sample IC66-073, based on the trace element data from LA-ICP-MS mapping. The location of the A to B traverse is marked in Figure 8.13. Dashed lines are approximate lower limits of detection.

depletions of these elements in the fluid during the precipitation of Py3, and parts of Py5/6 could also be suggested.

The co-elevation of multiple trace elements in Py1, and their depletion outwards into Py2/3 (apart from As and Cu), indicates that the earliest pyrite crystallisation event was particularly favourable for the incorporation of trace elements. As noted in Section 8.3.3.2, this may be due to rapid crystallisation, since elements that are not usually interpreted to be lattice-hosted (Ag, Sb, Hg, and Pb) are elevated. Equally, it could be due to the chemistry of the hydrothermal fluids, as both As and Cu are elevated (Figure 8.14).

There is a distinct change in the morphology of the pyrite between Py5 and Py6, transitioning from anhedral to euhedral. Porosity and arsenopyrite inclusions are also evident in Py6/7, while Se is elevated. Together, this indicates that the conditions of crystallisation have changed (i.e., the characteristics of the hydrothermal fluid). Selenium is not subject to the same fluctuations in concentration as other elements (Figure 8.14); its consistent elevation in Py5/6 further supports a conditional control (i.e., temperature) for the incorporation of Se in pyrite.

8.3.3.7 Utilising the lattice strain model for pyrite

The lattice strain model developed for pyrite in Chapter 7 can be utilised to further investigate the controls on trace element incorporation, and provide insights to the characteristics of the hydrothermal fluids during the formation of pyrite from the Iron Cap vein samples. The 2+ parabola constrained by K_D data calculated from the study of Grant et al. (2018) has been modified to predict the K_Ds of trace elements in pyrite at temperatures relevant to porphyry ore formation (Figure 8.15). A change in temperature is the only modification made to the 2+ parabola, compared to Figure 7.6, with the 2+ ions plotted on the parabola in line with their ionic radii (r_a; Table 7.1); Cu^{2+} is not included as it has previously been shown that Cu is unlikely to be lattice-hosted as a 2+ ion in pyrite (Chapter 7).

The graphs show that, of the 2+ ions modelled, only Co, Ni, Mn, and Zn have relatively high K_Ds and would be expected to substitute into the Fe^{2+} site in pyrite at concentrations greater than ~1/10000th the concentration of Fe (~10s ppm). Therefore, the other elements that were modelled and predominantly occur as 2+ ions (Cd, Hg, and Pb), are most likely to be present in pyrite as inclusions, because they are not visible in Figure 8.15 as their K_Ds are extremely low (i.e., <0.1). Cadmium was not detected in the pyrite from Iron Cap by LA-ICP-MS, but both Hg and Pb were detected at concentrations up to 100s-1000s ppm (Section 6.4.3), and interpreted to be present as both inclusions and lattice incorporations, based on the LA-ICP-MS data (Section 8.3.1). This suggests that,

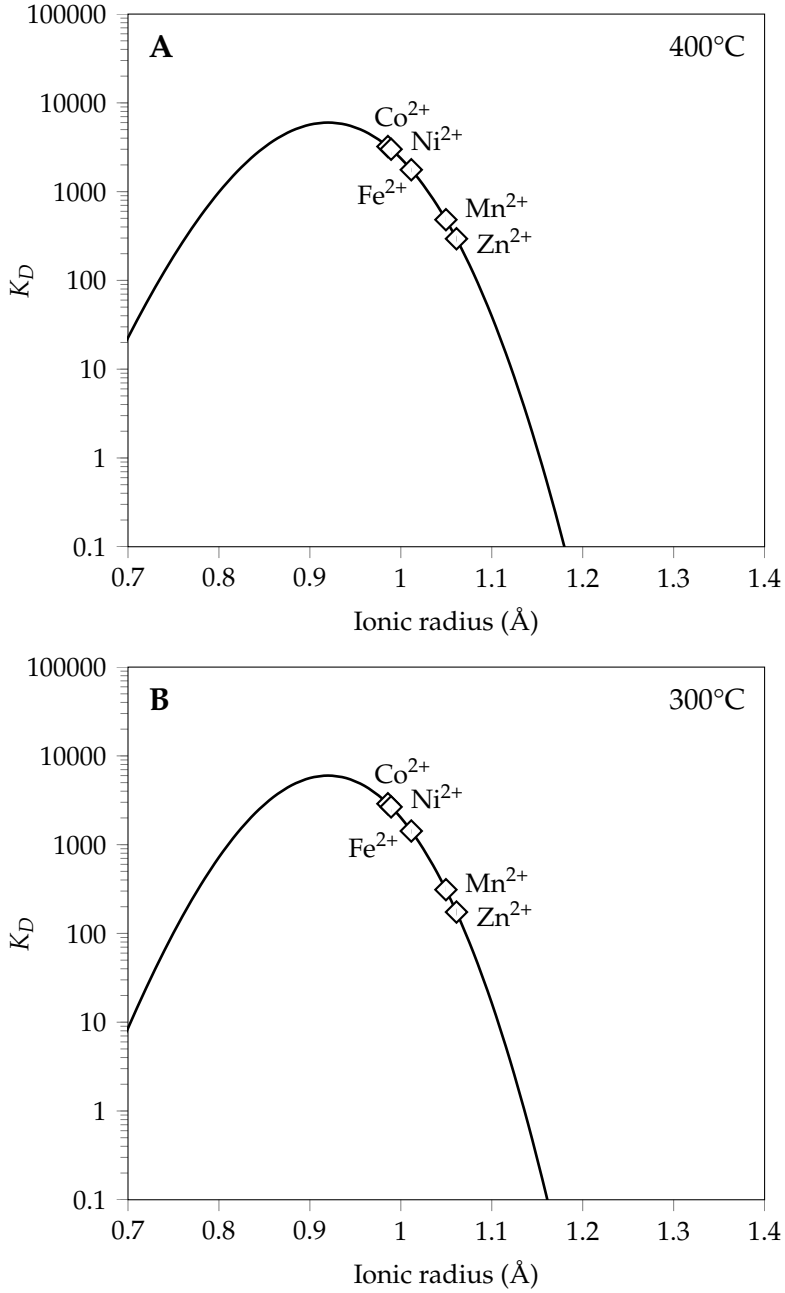

Figure 8.15. Trace element K_D plots for 2+ ion substitution into the Fe^{2+} site in pyrite, where T = 400°C (A), and 300°C (B).

even though they might appear to be lattice-hosted owing to a homogeneous distribution (e.g., in a LA-ICP-MS profile trace, or map/zone), it is most likely that they are nevertheless present as inclusions of a size too small to be distinguished by interpretation of LA-ICP-MS data (i.e., <10 µm). It should be noted that this model does not take into account kinetic processes (e.g., adsorption, rates of crystallisation), which could lead to the apparent lattice-hosting of trace elements with low K_Ds, as discussed in the previous sections.

Figure 8.15 also shows that, as demonstrated in Chapter 7, there is a neglibile variation in the predicted K_Ds of trace elements into pyrite with temperature, for ions that lie near

the apex of the parabola (i.e., have the highest K_Ds). Therefore, even if the approximate temperatures used to predict the K_Ds of Co, Ni, Mn, and Zn into pyrite are not absolutely accurate, the error induced by calculating at a different temperature is relatively minor. Only for the ions not visible owing to their low K_Ds (Cd, Pb, Hg) would K_Ds increase more signficantly in line with increases in temperature.

One addition to the 2+ parabola that was not quantified by the natural K_D data of Grant et al. (2018) is Ni^{2+}, which is shown to have a predicted K_D for pyrite higher than that of Fe^{2+}. This suggests that, like Co, Ni will be preferentially enriched into pyrite whenever it is present in a hydrothermal fluid precipitating pyrite. The concentrations of Co and Ni in pyrite can therefore be used to calculate the effective concentration of these elements in the hydrothermal fluid. Calculating for the concentration of the hydrothermal fluid in equation (1), using the concentration data of pyrite generations from map traverses presented in the previous sections, generates traverses that record the effective concentration of Co and Ni in the hydrothermal fluids during the precipitation of different pyrite crystals (Figure 8.16). The traverses were calculated using the K_Ds of Co and Ni at 400°C (Figure 8.16A), and at 300°C (Figure 8.16B, C), to approximate the temperature of ore formation of V2 veins, and V6/V7 veins, respectively; although, as noted, temperature variations do not adversely affect K_Ds for Co and Ni.

The Co and Ni traverses mirror the shape of those for the pyrite crystals, because the concentrations of Co and Ni in pyrite directly reflect the effective concentrations of Co and Ni in the hydrothermal fluids. Furthermore, as the K_Ds of Co and Ni are relatively insensitive to temperature, the ratio of Co:Ni in pyrite effectively records the Co:Ni ratio of the hydrothermal fluids. Figure 8.16 shows that the effective concentrations of Co and Ni in the hydrothermal fluids vary wildly, over mutiple orders of magnitude. Furthermore, the traverses show that Co:Ni ratios are not consistent, suggesting that there are different controls on the effective concentration of Co and Ni in the hydrothermal fluids, and that different pyrite generations formed from hydrothermal fluids with different Co:Ni ratios. For example, during the precipitation of the V7 pyrite (Figure 8.16C), the hydrothermal fluids were first Ni-Co-rich with relatively lower Co concentrations (Py1-2), before both Co and Ni became depleted (Py3-5). Cobalt then became enriched again briefly in Py6, then was depleted until becoming enriched in the fluids precipitating Py7. Nickel concentrations remained low from Py3-6, only rising near approximate detection limits in Py7, at concentrations roughly 2 orders of magnitude less than Co. The implications of these changes in fluid characteristics during vein formation are discussed in Section 8.4.2.

These are some limitations to the lattice strain model, and thus the calculated fluid

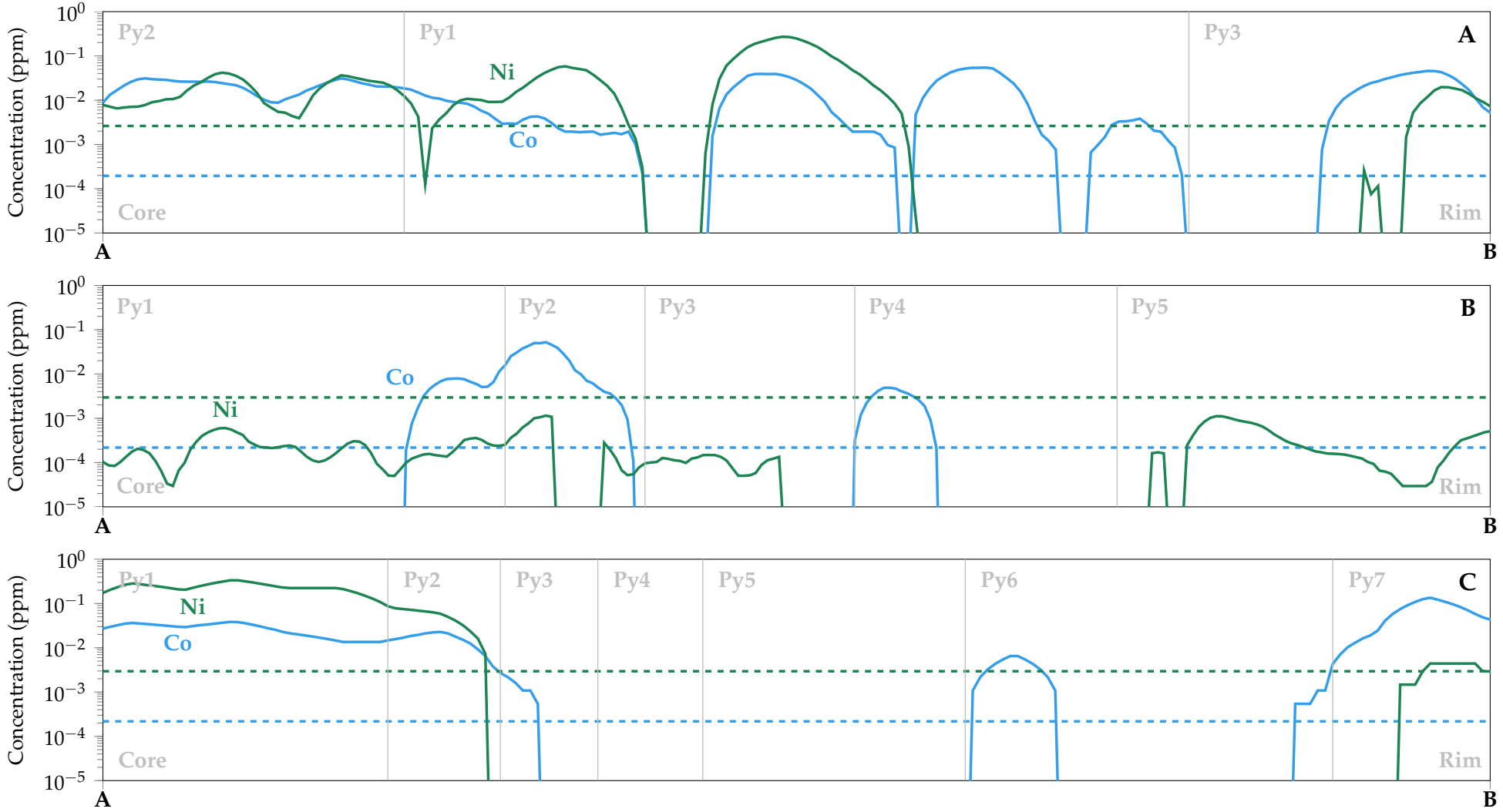

Figure 8.16. Effective concentrations of Co and Ni in the hydrothermal fluids precipitating the V2 (A), V6 (B), and V7 (C) pyrite crystals mapped by LA-ICP-MS. Dashed lines are approximate lower limits of detection.

compositions, owing to the reliability of the natural K_D data calculated from the study of Grant et al. (2018). In particular, although the pyrite and fluid compositions are from the same deposit, they are not from co-existing pyrite and fluid. Fluid compositions and temperatures are an average of vent fluid measurements, while the pyrite compositions are an average from samples obtained throughout the TAG deposit (Grant et al., 2018). This means that the K_D data calculated constitutes an average of the TAG deposit, and may not reflect the actual paritioning behaviour of trace elements in a hydrothermal fluid precipitating a pyrite crystal. Similarly, the apparent K_Ds reflect the partitioning behaviour of trace elements in the fluids from TAG, which are not the same as porphyry fluids (cf. Kouzmanov and Pokrovski, 2012); for example, owing to the lower pressures of ore formation, and the potential for mixing with seawater (Hannington et al., 2014). The ideal scenario would be to constrain the model using experimentally-derived K_D data for trace elements between pyrite and porphyry-like fluids. Despite these limitations, the model appears to work within reason, and has provided valuable insights to the characteristics of the hydrothermal fluids during vein formation at Iron Cap.

8.4 Hydrothermal fluid evolution at Iron Cap

The previous sections have illustrated that there are differences in the characteristics of the hydrothermal fluids that formed different vein generations, and that the characteristics of the hydrothermal fluids changed during vein formation. This section therefore aims to elucidate the possible conditions that may have been prevalent, and the evolutionary processes that may have taken place, during the formation of Iron Cap.

8.4.1 Hydrothermal fluid evolution between the formation of vein generations

This section discusses the evolution of hydrothermal fluids between vein generations, with aims to advance the previously constructed genetic model of Iron Cap in Section 3.6. A temporal sequence of fluid evolution is discussed below, based on the timing relations of vein generations (i.e., V1 early, to V8 late). In reality, it is possible that different vein generations formed at similar times in different parts of the hydrothermal system (e.g., Figure 2.9); however, the limited sample suite utilised in this research project does not permit a comprehensive understanding of the spatial evolution of the hydrothermal fluids. Nevertheless, in some cases it is possible to infer the spatial aspects of hydrothermal fluid evolution, based on the distribution of vein samples, as illustrated in Figure 5.32 and Appendix B.

The V1 vein generation at Iron Cap likely formed at high temperatures early in system evolution, owing to the apparent restriction of V1 veins to the deep, potassic-altered

parts of the deposit. The lack of quartz and sulphide minerals further supports this, suggesting that temperatures were in excess of 500-600°C (Kouzmanov and Pokrovski, 2012; Monecke et al., 2018). Their discontinuous, irregular form also indicates vein formation ocurred in a ductile regime at temperatures of >350-500°C (Sillitoe, 2010; Fournier, 1999; Monecke et al., 2018). The similarity of V1 veins to early porphyry M-veins in other deposits complies with these interpretations (Arancibia and Clark, 1996; Sillitoe, 2010) .

V2 veins are the earliest veins to host ore minerals, but they formed over at least two distinct stages; the first characterised by barren quartz, and the second by the introduction of ore minerals with minor quartz (Section 8.2). At the high temperatures of V1 vein formation, quartz solubility decreases with decreasing temperature (Monecke et al., 2018), suggesting that such a change may have occurred to induce the precipitation of quartz in V2 veins, instead of magnetite. Dissolution of Q1 quartz is interpreted to have occurred to generate flow paths for the later fluids precipitating ore minerals and minor Q2 quartz (Section 8.2), which may have occurred at relatively low temperatures (e.g., ∼375-450°C; Monecke et al., 2018). Ore mineral precipitation from porphyry fluids is often similarly attributed to reductions in temperature, to around <400°C (e.g., Kouzmanov and Pokrovski, 2012; Hurtig et al., 2021). The relatively high Se contents of the ore minerals in V2 veins may further suggest that the temperatures of ore formation were relatively high (Section 8.3.2), while the existence of a Au-Ag-Te melt phase late in the paragenesis indicates that temperatures remained above 335°C during vein formation (Cabri, 1965). Lastly, the similarity of V2 veins to A- and/or B-veins in other porphyry deposits (e.g., Landtwing et al., 2005; Maydagán et al., 2015) indicates that relatively high temperatures of formation are within reason.

The comparability between V2 (Q2-phase) and V3 veins in terms of mineralogy could indicate that they formed from similar fluids under similar conditions. However, there are differences in trace element deportment between these veins, suggesting that there were likely some differences. In particular, Se is present at lower concentrations in V3 ore minerals compared to V2 ore minerals, which could relate to a drop in temperature between V2 and V3 veins (Section 8.3.2). Equally, the common presence of sericite in V3 veins suggests that the hydrothermal fluids were more acidic than the V1/V2 vein-forming fluids, likely owing to the disproportionation of SO_2 to H_2S below 400°C (e.g., Seedorff et al., 2005; Kouzmanov and Pokrovski, 2012; Reed et al., 2013).

Unlike V3 veins, V4 veins are not directly associated with sericite, and are also found in potassic-altered rocks, suggesting that the vein-forming fluids were not acidic enough to generate sericitic alteration. The galena and chalcopyrite of V4 veins also host the highest Se contents compared to the same ore minerals in other vein generations, implying

that the temperatures of vein formation were paradoxically higher than preceeding veins (Section 8.3.2). Meanwhile, the elevated Ag contents of these minerals could indicate that the V4 fluids were chloride-rich (Pal'yanova, 2008; Hurtig et al., 2021). The lack of pyrite in V4 veins is particularly notable, which could again be attributed to higher temperatures. This is chiefly because quartz-chalcopyrite veins in porphyry deposits are typically classified as A-veins, which are formed from high temperature fluids (e.g., Gustafson and Hunt, 1975; Sillitoe, 2010). The wavy form of many V4 veins similarly indicates that vein formation could have occurred at relatively high temperatures in a ductile regime (i.e., >350-500°C; Sillitoe, 2010; Fournier, 1999; Monecke et al., 2018).

V4 veins host chlorite, which is not commonly reported as a vein constituent in porphyry deposits, rather tending to form as an alteration product of biotite during propylitic alteration (e.g., Seedorff et al., 2005; Sillitoe, 2010). However, chlorite-bearing veins are noted in some deposits. For example, Muntean and Einaudi (2000) described narrow, discontinuous garnet-chlorite-magnetite veins from the Verde porphyry Au deposit, Chile, with the veins locally containing sulphides, including chalcopyrite and galena. Muntean and Einaudi (2000) interpreted that these veins formed during the early, high temperature stages of hydrothermal activity, owing to the observation that they are cross-cut by Au-bearing banded veins and intrusive breccias, and are absent in the later intrusives. The presence of chlorite in V4 veins could therefore support the theory that the vein-forming fluids were of a high temperature, perhaps owing to the emplacement of a later intrusion that raised the temperature of the hydrothermal system. There are multiple syn-mineralisation intrusive phases at Iron Cap (Campbell et al., 2020), which could support this interpretation; however, assessment of the cross-cutting relationships between vein generations and intrusions would be necessary to substantiate this.

The Se concentrations in tennantite-tetrahedrite and chalcopyrite from V5 veins are comparable to those of V3 veins, indicating similar hydrothermal fluid temperatures. Lower temperatures compared to V1, V2, and V4 veins could be supported by the fact that tennantite-tetrahedrite is the dominant ore mineral; this is commonly associated with later-stage E-veins in porphyry deposits, where formation is attributed to fluids at lower temperatures of ∼300°C or less (e.g., Masterman et al., 2005; Maydagán et al., 2015). Furthermore, the apparent absence of Au in V5 veins suggests that the hydrothermal fluids were lacking in Au.

V6 veins appear to be restricted to shallow depths, indicating that they are late-stage, and thus likely a lower temperature product of the hydrothermal system. This is supported by the fact that the ore minerals of V6 veins are the most depleted in Se compared to the ore minerals of other veins. Lower temperatures could also be evidenced by the

decimeter-scale width and linear margins of V6 veins, indicating that they formed in a brittle, hydrostatic regime (i.e., <350-500°C; Sillitoe, 2010; Fournier, 1999; Monecke et al., 2018). The enrichment of base metal sulphides and sulphosalts further supports the interpretation that fluids were of a lower temperature, as the abundance of sphalerite and galena in particular is likely to be related to reductions in temperature (Kouzmanov and Pokrovski, 2012). Meanwhile, the acidic nature of the fluids is evidenced by the common presence of sericitic alteration halos, a feature attributed to late-stage veins in porphyry deposits (e.g., Gustafson and Hunt, 1975; Sillitoe, 2010).

The apparent localisation of V7 veins to a specific, shallow part of Iron Cap suggests that these veins may be a peripheral respresentation of the hydrothermal system, perhaps forming from low temperature, acidic fluids, owing to the association with strong sericitic alteration. Finally, V8 veins may represent the last, low temperature stages of fluid flow related to the hydrothermal system (e.g., Stefanova et al., 2014).

8.4.2 Hydrothermal fluid evolution during vein formation

The trace element analysis of ore minerals has highlighted that fluid characteristics change during the formation of individual veins. This is principally evidenced by the variation in the trace element composition of pyrite, as discussed in Section 8.3.3. This section discusses the possible changes in the hydrothermal fluids during vein formation.

Fluctuations in trace element concentrations, coupled with the variation of trace element ratios between different pyrite generations within a crystal strongly suggest that a hydrothermal fluid with constant characteristics cannot be responsible for the formation of a given vein. This is best illustrated by the concentrations of Co and Ni in pyrite, which have been shown to represent the effective concentrations of Co and Ni in the fluid. The variation in Co/Ni ratios in Figure 8.16 shows that fluid chemistry is regularly changing during the precipitation of a pyrite crystal. Moreover, the abruptness of the variations in Co and Ni indicate that there were sudden, and sometimes repetitive changes in the fluid (e.g., Co in Py1 of Figure 8.16A), which are unlikely to be caused by gradual processes such as cooling or fluid-rock interaction. Therefore, it is most probable that multiple different fluids are responsible for the changing Co/Ni ratios, and thus the changes in the composition of growth zones in pyrite.

Fluid mixing is one scenario that could explain the fluctuations in chemistry during vein formation. For example, in Py1/2 of Figure 8.16B, the concentrations of Co and Ni appear to be independently controlled, which could be explained by the initial presence of a relatively Ni-rich, Co-depleted fluid that was later mixed with a separate and relatively Co-rich, Ni-depleted fluid near the Py1/2 boundary. Fluid mixing could occur

when a vein-forming fluid is mixed with later fluid pulses with different compositions that periodically invade the site of vein formation. Such processes have been proposed to explain decoupling of As and Cu in pyrite zones, where As-rich or Cu-rich vapours are thought to have been intermittently introduced to mix with the pyrite-forming fluid (Deditius et al., 2009; Reich et al., 2013). Alternatively, variation in fluid flow paths could cause fluid mixing, whereby two (or more) separate flow paths converge. This could be evidenced by the interconnected networks that porphyry veins tend to form (e.g., Figure 5.6, 5.11, and 5.14).

Vein re-opening may also cause fluctuations in fluid chemistry, with separate fluids introduced at different points in time, as per crack-seal vein formation models (e.g., Best, 2003; Mernagh et al., 2020). Weis et al. (2012) used numerical modelling to propose that hydrothermal fluids migrate outwards from a causative porphyry intrusion via overpressure-permeability waves, possibly leading to multiple vein re-opening events as different fluids move through the same rock mass previously occupied by different fluids. Vein re-opening is also empirically evidenced in porphyry deposits, usually by different quartz generations (e.g., Redmond et al., 2004; Rottier and Casanova, 2020). However, it could be that it is a more frequent process than is suggested by such textural features, leading to regular inputs of different fluids, which could in turn explain the variability in trace element concentrations in growth zones in pyrite.

Phase separation may play a role in facilitating the production of fluids with different compositions, with different elements preferentially partitioning into a vapour phase relative to a co-exisiting hypersaline liquid, or vice versa (e.g., Heinrich, 2005; Williams-Jones and Heinrich, 2005; Zajacz et al., 2017). A number of other parameters may also lead to differences in trace element concentrations between separate fluids, such as temperature, pressure, salinity, pH, fO_2, and ligand availability (e.g., Kouzmanov and Pokrovski, 2012; Bodnar et al., 2013; Hurtig et al., 2021). Experimental studies have shown that both Co and Ni are primary transported as chloride complexes in aqueous fluids, but that the solubility of Ni under variable temperatures and pressures is considerably lower than that of Co (Migdisov et al., 2011; Liu et al., 2012). This suggests that temperature and pressure variations alone are unlikely to control the variations in the effective concentrations of Co and Ni in the hydrothermal fluids forming pyrite, because Ni would always be present in the fluids at concentrations lower than Co, which is not observed in Figure 8.16. Furthermore, as Co and Ni are similarly transported, it is unlikely that they would be differentially partitioned between vapour and hypersaline liquid during phase separation. Indeed, the partitioning behaviour of other base metals that have high affinities for Cl (i.e., Fe, Zn, Pb) is reported to be similar (Pokrovski et al., 2008).

Other processes that could be invoked to explain Co and Ni variations are changes in the composition of the starting fluids (i.e., at the point of exsolution from a magma), and fluid-rock interaction. Changes in Co and Ni concentrations in the starting fluids may be primarily dependent on the behaviour of Cl, owing to their aqueous mobility as chloride complexes (Migdisov et al., 2011; Liu et al., 2012). As a comparative, experimental studies have shown that the effective partitioning of Cu (as a chloride complex) into the fluids exsolved from a magma is linked to that of Cl (i.e., salinity; Tattitch et al., 2021). Monte Carlo simulations have further been utilised to show that the salinity of the fluids depends primarily on the concentrations of Cl in the magma, which increase throughout differentiation (Tattitch et al., 2021). This could mean that the different Co and Ni concentrations in the hydrothermal fluids relate to the exsolution of fluids at different points in time from a causative intrusion. Furthermore, the changing composition of the magma through time could lead to variable Co/Ni ratios, which in turn would be reflected in different hydrothermal fluids.

Differing degrees of fluid-rock interaction could also affect the concentrations of Co and Ni in different fluids. When considering a starting fluid of a constant composition, and stable temperature and pressure conditions, the degree of fluid-rock interaction is primarily dependent on the nature of the wall rock (i.e., its composition, and whether or not it has already been altered), and the fluid to rock ratio (e.g., Seedorff et al., 2005; Reed et al., 2013). This illustrates that it would be expected for two different fluids experiencing different flow paths, or even the same flow paths at different times, to exhibit different compositions, because they will have passed through wall rocks of a different nature, and/or have interacted with different volumes of rock. In particular, variable Co/Ni ratios could be effected by variable degrees of Co and/or Ni scavenging from the wall rocks (e.g., Fougerouse et al., 2016b).

Remobilisation of trace elements may also lead to variable fluid compositions, whereby dissolution of a previously-precipitated ore mineral enriches the fluid in the mineral components (i.e., zone refining; e.g., George et al., 2018a). For example, Py2 in Figure 8.16A may have formed via coupled dissolution-reprecipitation of Py1, exemplified not only by textural features, but also by the comparable Ni concentrations, and the more elevated Co concentrations (Section 8.3.3.1). This would mean that the effective Co and Ni concentrations in the Py2-forming fluid would have been inherited from Py1, and thus not be representative of the primary fluid. Dissolution-reprecipitation of pyrite is widely recognised in the Iron Cap veins, which could suggest that remobilisation is an influential process in affecting fluid compositions during vein formation. However, as the dissolution of a mineral is likely required for remobilisation to occur, conditional changes that

affect the stability of a mineral phase in a fluid must also occur (Putnis, 2009).

This section shows that a given vein is likely a product of multiple different fluids. In turn, a given vein exhibits a geochemical signature that respresents an average of the different fluids that formed the vein. This illustrates that porphyry hydrothermal systems are chaotic and complex, and that interpretations of fluid evolution on a deposit scale (e.g., between vein generations; Section 8.4.1) do not provide a complete picture this complexity. Furthermore, it has been demonstrated that trace element studies, and specifically trace element maps of pyrite, have utility for elucidating the changes in hydrothermal fluids during vein formation.

8.5 Implications for the development of Iron Cap

The petrographic work of this thesis has lead to the classification of eight vein generations, which exhibit some differences to previous vein classifications at Iron Cap (Table 5.2). This indicates that it may be useful to revisit the vein classification schemes currently in place at Iron Cap, for the reasons outlined below.

The detailed mineralogy of the vein generations classified in this thesis has been recorded (Table 5.1), providing an indication of the relative importance of different veins as hosts for ore. In addition, each vein generation has been characterised in terms its Au occurrences, illustrating that not all veins are Au-bearing, and that there is variation in the hosting of native Au and/or petzite. These Au phases are regularly $<10\,\mu m$ in size and most often observed as inclusions in pyrite, or within cracks in pyrite. However, they are also observed to occur as inclusions in other ore minerals, and can be hosted within vein quartz. This information could have implications for the approaches to Au recovery. Meanwhile, the trace element analysis of ore mineral assemblages has been utilised to determine the trace element signature of different vein generations, and also to describe the deportment of specific trace elements; both within vein generations (e.g., Figure 8.4), and within the sample suite as a whole (Figure 6.33). These results highlight that not all Iron Cap ore is geochemically similar, and that there are trends between veins and ore minerals.

The above information could be utilised to improve the understanding of ore and trace element distributions, by integrating it into a three-dimensional model of vein occurrences, such as that presented in Section 5.7. The model in Section 5.7 not only illustrates that some vein generations (i.e., V3) are observed more frequently in the sample suite collected than other veins, perhaps reflecting their proportions in the deposit, but also that some vein generations (e.g., V6) may be restricted to certain parts of the deposit. Knowledge of vein abundances and distributions could be used to predict where certain

trace elements are elevated within the deposit. Alternatively, the geochemical signatures of different vein generations might be able to be recognised in bulk assay data from drill core, potentially constituting a new approach to mapping and classifying vein occurrences. However, this latter approach would require detailed development and testing to ensure effectiveness.

An understanding of the geochemical heterogeneity of the Iron Cap veins could also come in useful when assessing mineral processing and metallurgical approaches; in particular, it may be helpful to incorporate samples of different vein generations when conducting additional assessments, to consolidate the findings presented in the current prefeasibility study (Threlkeld et al., 2020). Nevertheless, previous tests have shown that flotation concentrates from Iron Cap may incur smelter penalties for As, Sb, and Hg ($\pm$Pb), while Se is also elevated to an average of 255 ppm (Threlkeld et al., 2020). The elevation of these elements could be explained by the petrographic and geochemical work presented in this thesis. In particular, aside from arsenopyrite and tennantite-tetrahedrite, the latter of which is most As-rich in V5 veins, pyrite may have contributed to the elevations in As, since As can reach up to weight percent levels in pyrite from V3 and V7 veins. Tennantite-tetrahedrite and arsenopyrite are also likely to have contributed to elevations in Sb, with Sb most enriched in V2/V6 tennantite-tetrahedrite, and commonly present at weight percent levels (sometimes exceeding 10 wt.%) in arsenopyrite. On the other hand, it is likely that tennantite-tetrahedrite is the primary cause of elevated Hg, although pyrite from V3 veins may also have contributed Hg. Selenium is more varied, with the elevations in the flotation concentrates likely dependent upon the vein generation(s) tested; the ore of V2 veins is most Se-rich, followed by V4 veins and then V6 veins. However, galena tends to be the primary host of Se, despite its low abundance, meaning that a relatively high proportion of Se in the concentrates likely came from galena.

Inclusions of trace elements within ore minerals may also be useful to consider. Indeed, the common presence of Pb (probably galena) as inclusions in all ore minerals analysed by LA-ICP-MS in this thesis could explain the elevations in Pb in one of the test flotation concentrates (Threlkeld et al., 2020), even though galena does not tend to be commonly observed macroscopically. However, it is equally possible that V6 veins, which have a high proportion of galena ($\sim$25%) in the ore, were included in the composite sample tested. Nevertheless, aside from the trace element signature of vein generations, consideration of inclusion-hosted trace elements may be beneficial, such as the common presence of Sn-Te inclusions in galena, tennantite-tetrahedrite, and arsenopyrite. Of particular note is the detection of Au as inclusions in all ore minerals analysed by LA-ICP-MS, suggesting that the occurrence of Au is more variable than suggested by

petrographic study, which may be useful to take into account when conducting further tests of Au recovery.

8.6 Implications for porphyry exploration models

Many of the findings relevant for Iron Cap (Section 8.5) may be considered in the context of developing of porphyry exploration models in general. However, there are some specific aspects that could have greater implications for porphyry exploration models. In particular, the recognition of Au remobilisation via Au-Ag-Te melt phases at Iron Cap may be an important aspect to consider when developing exploration models for other deposits; upgrading or depletion of Au in specific vein generations may have implications for the hosting of Au (e.g., within pyrite, or not), and/or the concentration of Au within veins. The trace element analysis of Iron Cap ore minerals also reveals that Au occurs within all ore minerals, either as inclusions, or lattice incorporations, and that arsenopyrite is a particularly common host for Au as Au-Te inclusions in late-stage veins. This information may be useful to consider when determining Au distribution within porphyry veins.

The recognition that different vein generations exhibit discrete geochemical signatures is of particular relevance for porphyry exploration elsewhere. Enrichments and/or depletions of certain trace elements within ore minerals, such as Se or Ag, may indicate proximity to specific porphyry ore zones, and indeed support the placement of veins within paragenetic sequences. Further investigation of trace element enrichments and depletions may be used to asses hydrothermal fluid characteristics; Se may relate to temperatures of ore formation, while Ag may indicate pH or salinity.

Lastly, lattice strain models for pyrite show that Co and Ni have higher partition coefficients into pyrite than Fe, thus Co/Ni ratios in pyrite reflect the Co/Ni ratios of the hydrothermal fluids. Therefore, enrichments of Co and Ni in porphyry pyrite are likely to indicate a closer proximity to the fluid source than Co-Ni-poor pyrite, whereby earlier pyrite extracts the Co and Ni available in the hydrothermal fluids, meaning that later pyrite precipitates from fluids that are Co-Ni-poor. Determining Co/Ni ratios of pyrite from different veins may thus be useful for understanding the sequence of vein generations. Furthermore, the recognition of oscillating Co/Ni ratios during the formation of specific pyrite crystals at Iron Cap shows that porphyry veins form via multiple different fluids with contrasting characteristics, and that porphyry systems are inherently chaotic. This means that exploration models should allow for a degree of variability in characteristics between deposits, and indeed within deposits. Regardless, there are trace element trends (e.g., in terms of Se or Ag) that may be recognised, and useful, despite the chaotic

nature of porphyry systems.

9 Conclusions

This thesis has examined the trace element contents of ore minerals from successive vein generations to investigate variations in hydrothermal fluid characteristics throughout the formation of the Au-rich porphyry deposit of Iron Cap. This chapter summarises the key findings of the research, and provides recommendations for future work.

9.1 Vein generations at Iron Cap

The detailed petrographical analyses of drill core samples from Iron Cap has lead to the characterisation of eight vein generations, each of which has been temporally constrained to reflect a discrete stage in the evolution of the hydrothermal system. Differences are recognised between current and previous vein classifications (Campbell et al., 2020), progressing the understanding of the different stages of hydrothermal fluid evolution, and expanding the knowledge of mineral assemblages and occurrences.

A mineral paragenesis shows that most veins form over multiple stages, consisting of primary deposition and/or secondary modification. In particular, the earliest economically mineralised veins (V2) are formed by the initial precipitation of barren quartz, which is then partially dissolved to create flow paths for later fluids precipitating ore minerals. These veins show similarities to typical porphyry A/B-veins, supporting the multi-stage vein formation models proposed for such veins by other researchers (e.g., Landtwing et al., 2005; Maydagán et al., 2015; Monecke et al., 2018).

However, the interpretation at Iron Cap is that Au in these veins was partly remobilised from its initial residence in pyrite via dissolution-reprecipitation mechanisms, leading to the production of a Au-Ag-Te melt phase that remained molten until after the latest stages of ore mineral precipitation. Other vein generations at Iron Cap may have also experienced these processes of Au upgrading, owing to the widespread evidence of pyrite modification, and the co-existence of native Au, petzite and/or hessite. The associated occurrence of dissolution-reprecipitation mechanisms and Au-bearing melts has been recognised in orogenic gold systems (Hastie et al., 2020), but has not previously been attributed to porphyry ore formation.

Interpretations of hydrothermal fluid conditions highlight that there may have been a perturbation of a typical thermal evolution from hot to cold over the lifetime of the hydrothermal system, with V4 quartz-chalcopyrite-chlorite veins possibly representing a spike in temperature owing to the emplacement of a later intrusion. The Iron Cap hydrothermal system had not been investigated prior to this research project, meaning that these findings aid in the understanding of deposit formation, both locally, and more

widely for Au-rich porphyry deposits in general.

9.2 Deportment of trace elements

Trace element analysis of pyrite, chalcopyrite, galena, tennantite-tetrahedrite, sphalerite and arsenopyrite from different vein generations by LA-ICP-MS shows that there is heterogeneity in the concentrations of specific trace elements between ore minerals, and between veins. However, Se is often enriched (>100 ppm) in all ore minerals analysed. Other key enrichments are: As in pyrite, Ag and Bi in galena, Ag, Cd, Hg, and Bi in tennantite-tetrahedrite, Fe and Cd in sphalerite, and Sb in arsenopyrite. This thesis contains the first record of trace elements in arsenopyrite over and above that of Au, and the first record of trace elements in sphalerite (via LA-ICP-MS) from a porphyry deposit.

The mode of occurrence of specific trace elements has been interpreted from LA-ICP-MS profile traces and maps, and bivariate plots of spot data, to show that the following trace elements are likely to occur as lattice incorporations:

- Pyrite: Co, Ni, As, Se (± Mo, Ag, Sb, Te, Au, Hg, Pb);
- Chalcopyrite: Ga, Se, Ag (± Mo, Sb, Sn, Au, Pb);
- Galena: Se, Ag, Cd, Sb, Bi (± Sn, Te);
- Tennantite-tetrahedrite: Co, Se, Ag, Cd, Hg, Bi (± Te);
- Sphalerite: Cd, In, Hg (± Fe, Co, Ga, Ag);
- Arsenopyrite: Sb.

Gold is detected in all the ore minerals, either as lattice incorporations, and/or as inclusions; arsenopyrite appears to be a particularly common host for Au as Au-Te inclusions. These findings largely align with those of previous trace element studies, although the presence of Hg in pyrite as a lattice incorporation has not previously been recognised.

Trace element data has been examined to illuminate the trace element signature of different vein generations, showing that different veins may be distinguished by concentrations of specific trace elements. This information could be used to predict trace element distributions at Iron Cap, by use of a vein distribution model, or alternatively to map vein occurrences from bulk assay data. It also shows that specific ore minerals are the primary hosts for certain trace elements; for example, galena accounts for the majority of Se, despite its low abundance.

Trace element partitioning trends are also recognised, both between ore minerals and between veins. In particular, Se exhibits a consistent partitioning trend in the order galena

> tennantite-tetrahedrite > chalcopyrite, although there are systematic variations in Se concentrations between vein generations that may relate to the temperatures of ore formation. Similarly, the common detection of Ag in the ore mineral suite has allowed the recognition of a partitioning trend in the order tennantite-tetrahedrite > galena > chalcopyrite, where variations in Ag concentrations between vein generations could represent changes in the pH or salinity of the ore-forming fluids.

9.3 Trace element partitioning in pyrite

Trace element maps illustrate that pyrite is compositionally heterogeneous, and that trace element concentrations vary abruptly between different generations of pyrite within the same crystal; no two trace elements are consistently correlated. This shows that spot analyses of pyrite are not necessarily representative of the bulk composition of a crystal. Furthermore, the maps highlight that there is considerable complexity to pyrite formation and modification, which cannot be fully explained by previous research.

A lattice strain model for pyrite has been constructed to elucidate the causes behind some of the variations observed. The model shows that, at typical porphyry temperatures, only Co, Ni, Mn, and Zn are likely to substitute into the Fe^{2+} site in the pyrite lattice to elevated concentrations (i.e., >10 ppm). This confirms the lattice-hosting of Co and Ni in pyrite, as interpreted from the spot data, and shows that enrichments of other 2+ ions in pyrite (e.g., Pb, Hg) are probably due to other incorporation mechanisms (e.g., inclusions). The model also shows that coupled substitutions involving 1+ and 3+ ions are unlikely to occur in pyrite, because the radii of these ions are larger than optimum ionic radius for the Fe^{2+} site.

The key finding of the model is that the optimum ionic radius for the Fe^{2+} site in pyrite is actually smaller than the ionic radius of Fe^{2+}, meaning that Co and Ni have higher partition coefficients into pyrite than Fe. In turn, this means that pyrite will preferentially incorporate Co and Ni whenever it is present in a hydrothermal fluid. This information can be used to explain the common Co-Ni-rich signature of early porphyry pyrite compared to later porphyry/epithermal pyrite (Maydagán et al., 2013; Franchini et al., 2015; Sykora et al., 2018; Steadman et al., 2021), whereby the earlier pyrite efficiently extracts the Co and Ni available in the hydrothermal fluids, such that later fluids and pyrite are Co-Ni-depleted. There are also implications for the formation of Co deposits, because Co will never become saturated in hydrothermal fluids precipitating pyrite, and thus separate Co phases will not precipitate.

The effective concentrations of Co and Ni in the hydrothermal fluids that precipitated different pyrite crystals at Iron Cap have been calculated, given that the partitioning of

Co and Ni into pyrite is controlled only by external parameters; Co/Ni ratios in pyrite directly reflect Co/Ni ratios in the hydrothermal fluids. Examination of traverses through different pyrite crystals shows that the effective concentrations of Co and Ni in the hydrothermal fluids vary wildly, which means that pyrite formation cannot be attributed to a hydrothermal fluid of a single composition. Therefore, multiple different fluids with contrasting characteristics must have been involved in the formation of a single pyrite crystal, and thus a vein. This shows that fluid evolution in porphyry systems is inherently more chaotic and complex than expressed in deposit-scale models, with vein formation likely involving numerous episodes of fluid pulsing, fluid mixing, and/or vein re-opening to generate the trace element heterogeneity recorded in pyrite crystals. The geochemical signature of a vein thus represents an average of the different fluids that formed the vein. However, there are trends noted between different vein generations at Iron Cap (e.g., in terms of Se and Ag), meaning that there must have been systematic changes (e.g., in terms of temperature) between the different fluid packages that formed different vein generations.

These findings show that pyrite effectively records the presence and characteristics of different hydrothermal fluids, and that with application of the lattice strain model utilised in this thesis, it is possible to gain insights to the chemistry of the fluids that formed any given pyrite crystal. This is widely applicable to a range of different hydrothermal mineral deposits, because pyrite is so ubiquitous.

9.4 Recommendations for future work

The utility of studying trace elements to elucidate hydrothermal fluid characteristics and evolution has been demonstrated in this thesis. However, there are ways in which future studies could enhance understanding. The lattice strain model for pyrite has been constrained using partition coefficients calculated using averages of natural data from a seafloor hydrothermal system. To better constrain the model, and improve its applicability for porphyry deposits in particular, it would be beneficial to calculate partition coefficients from trace element data of pyrite from a porphyry deposit, coupled with compositional data of apparent co-existing fluids gained by LA-ICP-MS of fluid inclusions. Alternatively, an experimental study of trace element partitioning between pyrite and porphyry-like fluids would help to improve the understanding of trace element partitioning in pyrite.

The lattice strain model for pyrite could also be adapted to predict trace element partitioning on the S site; for example, for Se, Te, and As. This could have implications for the understanding of Au incorporation into pyrite, because As and Au concentrations in

pyrite are often positively correlated (Reich et al., 2005). Similarly, it may help to elucidate the relationship between Se concentrations and temperature, as proposed by other researchers (Auclair et al., 1987; Maslennikov et al., 2009; Keith et al., 2018), and in this thesis. Further adaptations to the model may be made to predict trace element partitioning into galena and chalcopyrite. These minerals are more complex to consider, because coupled substitutions would have to be accomodated in the galena model (e.g., George et al., 2015), while chalcopyrite has multiple cation sites, and its valence state remains uncertain (Gibbs et al., 2007; George et al., 2018a). Nevertheless, the findings of these models could have specific implications for the characteristics of the hydrothermal fluids directly precipitating primary ore minerals.

In the case of Iron Cap, further study of vein generations is required to advance the genetic model, owing to the limited number of studies currently completed on the deposit. Integration of the approaches of this thesis and the study of Campbell et al. (2020) would be particularly beneficial, whereby detailed petrography and trace element geochemistry could be combined with deposit-scale logging and mapping to generate a more comprehensive picture of deposit genesis. Additional approches that could further elucidate genetic process at Iron Cap may include the use of fluid inclusions, studied by LA-ICP-MS, and with specific isotope analyses to reveal fluid compositions and sources. Such studies could be applied to ore minerals like sphalerite in the vein generations of Iron Cap, to determine whether the fluids forming different veins had different sources. Fluid temperatures at Iron Cap are also currently uncertain – pinning down specific temperatures of ore formation would serve to refine the partition coefficient data determined for elements in pyrite. Fluid inclusions could be analysed by microthermometry to provide temperature estimates, while trace elements in quartz (e.g., Ti) could be determined by LA-ICP-MS to serve a similar purpose.

On a wider scale, comparative studies of trace elements in the ore minerals of porphyry vein generations would determine whether this approach has use in other systems, and whether it can be expanded to develop indicator minerals/elements that might be more widely utilised during exploration.

References

Alldrick, D.J., 1993, Geology and metallogeny of the Stewart mining camp, northwestern British Columbia: British Columbia Geological Survey Bulletin, v. 85, 105 p.

Andikagumi, H., Macpherson, C.G., and McCaffrey, K.J., 2020, Upper Plate Stress Controls the Distribution of Mariana Arc Volcanoes: Journal of Geophysical Research: Solid Earth, v. 125, p. 1–27.

Annen, C., Blundy, J.D., and Sparks, R.S., 2006, The genesis of intermediate and silicic magmas in deep crustal hot zones: Journal of Petrology, v. 47, no. 3, p. 505–539.

Arancibia, O.N., and Clark, A.H., 1996, Early magnetite-amphibole-plagioclase alteration-mineralization in the Island Copper porphyry copper-gold-molybdenum deposit, British Columbia: Economic Geology, v. 91, p. 402–438.

Archibald, S., Migdisov, A., and Williams-Jones, A.E., 2001, The stability of Au-chloride complexes in water vapor at elevated temperatures and pressures: Geochimica et Cosmochimica Acta, v. 65, no. 23, p. 4413–4423.

Auclair, G., Fouquet, Y., and Bohn, M., 1987, Distribution of Selenium in High-Temperature Hydrothermal Sulfide Deposits at 13° North, East Pacific Rise: The Canadian Mineralogist, v. 25, no. 4, p. 577–587.

Audetat, A., and Simon, A.C., 2012, Magmatic Controls on Porphyry Copper Genesis: SEG Special Publication 16, p. 553–572.

Augustin, J., and Gaboury, D., 2019, Multi-stage and multi-sourced fluid and gold in the formation of orogenic gold deposits in the world-class Mana district of Burkina Faso – Revealed by LA-ICP-MS analysis of pyrites and arsenopyrites: Ore Geology Reviews, v. 104, p. 495–521.

Ayres, R., Ayres, L., and Råde, I., 2003, The Life Cycle of Copper; its Co-Products and By-Products: 1st edn., Dordrecht, Springer, 265 p.

Baker, T., Bickford, D., Juras, S., Lewis, P., Oztas, Y., Ross, K., Tukac, A., Rabayrol, F., Miskovic, A., Friedman, R., Creaser, R.A., and Spikings, R., 2016, Chapter 3: The Geology of the Kişladağ Porphyry Gold Deposit, Turkey: Economic Geology Special Publication 19, p. 57–83.

Baline, L.M., 2007, Hydrothermal fluids and Cu–Au mineralization of the Deep Grasberg Porphyry Deposit, Papua, Indonesia: Ph.D. thesis, University of Texas, 268 p.

Banjara, D., Malozovsky, Y., Franklin, L.S., and Bagayoko, D., 2018, First-principles studies of electronic, transport and bulk properties of pyrite FeS_2: AIP Advances, v. 8, p. 1–12.

Barnes, H.L., and Seward, T.M., 1997, Geothermal systems and mercury deposits, *in* Barnes, H.L., ed., Geochemistry of hydrothermal ore deposits: 3rd edn., New York, Wiley, p. 699–736.

Bayliss, P., 1977, Crystal structure refinement of a weakly anisotropic pyrite: American Mineralogist, v. 62, p. 1168–1172.

Bazarkina, E.F., Pokrovski, G.S., Zotov, A.V., and Hazemann, J.L., 2010, Structure and stability of cadmium chloride complexes in hydrothermal fluids: Chemical Geology, v. 276, p. 1–17.

Bebie, J., Seward, T.M., and Hovey, J.K., 1998, Spectrophotometric determination of the stability of thallium (I) chloride complexes in aqueous solution up to 200°C: Geochimica et Cosmochimica Acta, v. 62, no. 9, p. 1643–1651.

BEIS, 2022, Resilience for the Future: The United Kingdom's Critical Minerals Strategy, 46 p.

Benites, D., Torró, L., Vallance, J., Laurent, O., Valverde, P.E., Kouzmanov, K., Chelle-Michou, C., and Fontboté, L., 2021, Distribution of indium, germanium, gallium and other minor and trace elements in polymetallic ores from a porphyry system: The Morococha district, Peru: Ore Geology Reviews, v. 136, p. 1–25.

Bente, K., and Doering, T., 1993, Solid-state diffusion in sphalerites: an experimental verification of the "chalcopyrite disease": European Journal of Mineralogy, v. 5, p. 465–478.

Best, M.G., 2003, Igneous and Metamorphic Petrology: 2nd edn., Blackwell Science, 729 p.

Bethke, P.M., and Barton, P.B., 1971, Distribution of some minor elements between coexisting sulfide minerals: Economic Geology, v. 66, p. 140–163.

Bissig, T., and Cooke, D.R., 2014, Introduction to the Special Issue Devoted to Alkalic Porphyry Cu-Au and Epithermal Au Deposits: Economic Geology, v. 109, p. 819–825.

Blundy, J., and Wood, B., 1994, Prediction of crystal-melt partition coefficients from elastic moduli: Nature, v. 372, p. 452–454.

Blundy, J., and Wood, B., 2003, Partitioning of trace elements between crystals and melts: Earth and Planetary Science Letters, v. 210, p. 383–397.

Blundy, J., Mavrogenes, J., Tattitch, B., Sparks, S., and Gilmer, A., 2015, Generation of porphyry copper deposits by gas-brine reaction in volcanic arcs: Nature Geoscience, v. 8, p. 235–240.

Blundy, J., Afanasyev, A., Tattitch, B., Sparks, S., Melnik, O., Utkin, I., and Rust, A., 2021, The economic potential of metalliferous sub-volcanic brines: Royal Society Open Science, v. 8, p. 1–28.

Bodnar, R.J., Lecumberri-Sanchez, P., Moncada, D., and Steele-MacInnis, M., 2013, Fluid Inclusions in Hydrothermal Ore Deposits, *in* Holland, H.D., and Turekian, K.K., eds., Treatise on Geochemistry: 2nd edn., v.13, Oxford, Elsevier Ltd., p. 119–142.

Botcharnikov, R.E., Linnen, R.L., Wilke, M., Holtz, F., Jugo, P.J., and Berndt, J., 2011, High gold concentrations in sulphide-bearing magma under oxidizing conditions: Nature Geoscience, v. 4, p. 112–115.

Botcharnikov, R.E., Holtz, F., Mungall, J.E., Beermann, O., Linnen, R.L., and Garbe-Schönberg, D., 2013, Behavior of gold in a magma at sulfide-sulfate transition: Revisited: American Mineralogist, v. 98, p. 1459–1464.

Bowles, J.F.W., Howie, R.A., Vaughan, D.J., and Zussman, J., 2011, Rock-forming Minerals: Volume 5A: Non-Silicates: Oxides, Hydroxides and Sulphides: 2nd edn., Geological Society of London, 920 p.

Brostigen, G., and Kjekshus, A., 1969, Redetermined Crystal Structure of FeS_2 (Pyrite): Acta Chem. Scand., v. 23, no. 6, p. 2186–2188.

Bureau, H., and Keppler, H., 1999, Complete miscibility between silicate melts and hydrous fluids in the upper mantle: Experimental evidence and geochemical implications: Earth and Planetary Science Letters, v. 165, p. 187–196.

Burnham, W.C., 1979, Magmas and Hydrothermal Fluids, *in* Barnes, H.L., ed., Geochemistry of hydrothermal ore deposits: 2nd edn., New York, Wiley, p. 71–136.

Cabri, L.J., 1965, Phase relations in the Au-Ag-Te system and their mineralogical significance: Economic Geology, v. 60, no. 8, p. 1569–1606.

Campbell, M.E., and Dilles, J.H., 2017, Magmatic History of the Kerr-Sulphurets-Mitchell Copper-Gold Porphyry District, Northwestern British Columbia (NTS 104B): Geoscience BC Summary of Activities 2016, Geoscience BC, Report 2017-1, p. 233–244.

Campbell, M.E., Savell, M., Dodd, T., and Dilles, J.H., 2020, The Iron Cap deposit –A new giant gold-copper porphyry deposit in the Early Jurassic Sulphurets porphyry district: Canadian Institute of Mining, Metallurgy and Petroleum, Special Volume 57, p. 422-435.

Carvalho, J.R.S., Relvas, J.M.R.S., Pinto, A.M.M., Frenzel, M., Krause, J., Gutzmer, J., Pacheco, N., Fonseca, R., Santos, S., Caetano, P., Reis, T., and Gonçalves, M., 2018, Indium and selenium distribution in the Neves-Corvo deposit, Iberian Pyrite Belt, Portugal: Mineralogical Magazine, v. 82, p. 5–41.

Cashman, K.V., Sparks, R.S.J., and Blundy, J.D., 2017, Vertically extensive and unstable magmatic systems: A unified view of igneous processes: Science, v. 355, p. 1–9.

Chelle-Michou, C., Rottier, B., Caricchi, L., and Simpson, G., 2017, Tempo of magma degassing and the genesis of porphyry copper deposits: Scientific Reports, v. 7, p. 1–12.

Chen, K., Tang, M., Lee, C.T.A., Wang, Z., Zou, Z., Hu, Z., and Liu, Y., 2020, Sulfide-bearing cumulates in deep continental arcs: The missing copper reservoir: Earth and Planetary Science Letters, v. 531, p. 1–10.

Chiaradia, M., 2014, Copper enrichment in arc magmas controlled by overriding plate thickness: Nature Geoscience, v. 7, p. 43–46.

Chiaradia, M., 2020, Gold endowments of porphyry deposits controlled by precipitation efficiency: Nature Communications, v. 11, p. 1-10.

Chiaradia, M., and Caricchi, L., 2017, Stochastic modelling of deep magmatic controls on porphyry copper deposit endowment: Scientific Reports, v. 7, p. 1–11.

Chiaradia, M., and Caricchi, L., 2022, Supergiant porphyry copper deposits are failed large eruptions: Communications Earth & Environment, v. 3, no. 107, p. 1–9.

Chiaradia, M., Schaltegger, U., Spikings, R., Wotzlaw, J.F., and Ovtcharova, M., 2013, How accurately can we date the duration of magmatic-hydrothermal events in porphyry systems?-An invited paper: Economic Geology, v. 108, no. 4, p. 565–584.

Chouinard, A., Paquette, J., and Williams-Jones, A.E., 2005a, Crystallographic controls on trace-element incorporation in Auriferous pyrite from the Pascua epithermal high-sulfidation deposit, Chile-Argentina: Canadian Mineralogist, v. 43, p. 951–963.

Chouinard, A., Williams-Jones, A.E., Leonardson, R.W., Hodgson, C.J., Silva, P., Téllez, C., Vega, J., and Rojas, F., 2005b, Geology and genesis of the multistage high-sulfidation

epithermal Pascua Au-Ag-Cu deposit, Chile and Argentina: Economic Geology, v. 100, p. 463–490.

Cioacă, M.E., Munteanu, M., Qi, L., and Costin, G., 2014, Trace element concentrations in porphyry copper deposits from Metaliferi Mountains, Romania: A reconnaissance study: Ore Geology Reviews, v. 63, p. 22–39.

Cline, J.S., and Bodnar, R.J., 1991, Can Economic Porphyry Copper Mineralization be Generated by a Typical Calc-Alkline Melt?: Journal of Geophysical Research, v. 96, p. 8113–8126.

Cook, N.J., and Chryssoulis, S.L., 1990, Concentrations of "Invisible Gold" in the common sulphides: Canadian Mineralogist, v. 28, p. 1–16.

Cook, N.J., Ciobanu, C.L., Pring, A., Skinner, W., Shimizu, M., Danyushevsky, L., Saini-Eidukat, B., and Melcher, F., 2009, Trace and minor elements in sphalerite: A LA-ICPMS study: Geochimica et Cosmochimica Acta, v. 73, p. 4761–4791.

Cook, N.J., Ciobanu, C.L., Danyushevsky, L.V., and Gilbert, S., 2011, Minor and trace elements in bornite and associated Cu-(Fe)-sulfides: A LA-ICP-MS study: Geochimica et Cosmochimica Acta, v. 75, p. 6473–6496.

Cook, N.J., Ciobanu, C.L., Meria, D., Silcock, D., and Wade, B., 2013, Arsenopyrite-pyrite association in an orogenic gold ore: Tracing mineralization history from textures and trace elements: Economic Geology, v. 108, no. 6, p. 1273–1283.

Cook, N., Ciobanu, C., George, L., Zhu, Z.Y., Wade, B., and Ehrig, K., 2016, Trace Element Analysis of Minerals in Magmatic-Hydrothermal Ores by Laser Ablation Inductively-Coupled Plasma Mass Spectrometry: Approaches and Opportunities: Minerals, v. 6, p. 1–34.

Cooke, D.R., Hollings, P., Wilkinson, J.J., and Tosdal, R.M., 2014, Geochemistry of Porphyry Deposits, *in* Holland, H.D., and Turekian, K.K., eds., Treatise on Geochemistry: 2nd edn., v.13, Oxford, Elsevier Ltd., p. 357–381.

Cooke, D.R., Hollings, P., and Walshe, J., 2005, Giant Porphyry Deposits: Characteristics, Distribution, and Tectonic Controls: Economic Geology, v. 100, no. 5, p. 801–818.

Cooke, D.R., Wilkinson, J.J., Baker, M., Agnew, P., Phillips, J., Chang, Z., Chen, H., Wilkinson, C.C., Inglis, S., Hollings, P., Zhang, L., Gemmell, J.B., White, N.C., Danyushevsky, L., and Martin, H., 2020, Using Mineral Chemistry to Aid Exploration: A Case Study

from the Resolution Porphyry Cu-Mo Deposit, Arizona: Economic Geology, v. 115, no. 4, p. 813–840.

Corbett, G., 2002, Epithermal gold for explorationists: AIG Journal – Applied geoscientific practice and research in Australia, Paper 2002-01, p. 1–26.

Corbett, T.M., and Leach, G.J., 1998, Southwest Pacific Rim Gold-Copper Systems: Structure, Alteration, and Mineralization: SEG Special Publication No. 6, 247 p.

Crespo, J., Reich, M., Barra, F., Verdugo, J.J., Martínez, C., Leisen, M., Romero, R., Morata, D., and Marquardt, C., 2020, Occurrence and Distribution of Silver in the World-Class Río Blanco Porphyry Cu-Mo Deposit, Central Chile: Economic Geology, v. 115, no. 8, p. 1619–1644.

Deditius, A.P., Utsunomiya, S., Ewig, R.C., Chryssoulis, S.L., Venter, D., and Kesler, S.E., 2009, Decoupled geochemical behavior of As and Cu in hydrothermal systems: Geology, v. 37, no. 8, p. 707–710.

Deditius, A.P., Utsunomiya, S., Reich, M., Kesler, S.E., Ewing, R.C., Hough, R., and Walshe, J., 2011, Trace metal nanoparticles in pyrite: Ore Geology Reviews, v. 42, p. 32–46.

Deditius, A.P., Reich, M., Kesler, S.E., Utsunomiya, S., Chryssoulis, S.L., Walshe, J., and Ewing, R.C., 2014, The coupled geochemistry of Au and As in pyrite from hydrothermal ore deposits: Geochimica et Cosmochimica Acta, v. 140, p. 644–670.

Deditius, A.P., Reich, M., Large, R., and Deditius, A.P., 2017, New advances in trace element geochemistry of ore minerals and accessory phases: Ore Geology Reviews, v. 81, p. 1215–1217.

Defant, M.J., and Drummond, M.S., 1990, Derivation of some modern arc magmas by melting of young subducted lithosphere: Nature, v. 347, p. 662–665.

Del Real, I., Reich, M., Simon, A.C., Deditius, A., Barra, F., Rodríguez-Mustafa, M.A., Thompson, J.F.H., and Roberts, M.P., 2021, Formation of giant iron oxide-copper-gold deposits by superimposed, episodic hydrothermal pulses: Communications Earth & Environment, v. 2, no. 192, p. 1–9.

Ditson, G.M., Wells, R.C., and Bridge, D.J., 1995, Kerr: The geology and evolution of a deformed porphyry copper-gold deposit, northwestern British Columbia: Canadian Institute of Mining, Metallurgy and Petroleum, Special Volume 46, p. 509–523.

Dostal, J., 2017, Rare earth element deposits of alkaline igneous rocks: Resources, v. 6, p. 1–12.

Edmonds, M., and Woods, A.W., 2018, Exsolved volatiles in magma reservoirs: Journal of Volcanology and Geothermal Research, v. 368, p. 13–30.

Einaudi, M.T., Hedenquist, J.W., and Esra Inan, E., 2003, Sulfidation State of Fluids in Active and Extinct Hydrothermal Systems: Transitions from Porphyry to Epithermal Environments: SEG Special Publication no. 10, p. 285–313.

Febbo, G.E., Kennedy, L.A., Savell, M., Creaser, R.A., and Friedman, R.M., 2015, Geology of the Mitchell Au-Cu-Ag-Mo porphyry deposit, northwestern British Columbia, Canada: British Columbia Ministry of Energy and Mines British Columbia Geological Survey Paper 2015–1, p. 59–86.

Febbo, G.E., Kennedy, L.A., Nelson, J.L., Savell, M.J., Campbell, M.E., Creaser, R.A., Friedman, R.M., van Straaten, B.I., and Stein, H.J., 2019, The Evolution and Structural Modification of the Supergiant Mitchell Au-Cu Porphyry, Northwestern British Columbia: Economic Geology, v. 114, no. 2, p. 303–324.

Fekete, S., Weis, P., Driesner, T., Bouvier, A.S., Baumgartner, L., and Heinrich, C.A., 2016, Contrasting hydrological processes of meteoric water incursion during magmatic–hydrothermal ore deposition: An oxygen isotope study by ion microprobe: Earth and Planetary Science Letters, v. 451, p. 263–271.

Fossen, H., 2010, Structural Geology: Cambridge University Press, 362 p.

Fougerouse, D., Micklethwaite, S., Tomkins, A.G., Mei, Y., Kilburn, M., Guagliardo, P., Fisher, L.A., Halfpenny, A., Gee, M., Paterson, D., and Howard, D.L., 2016a, Gold remobilisation and formation of high grade ore shoots driven by dissolution-reprecipitation replacement and Ni substitution into auriferous arsenopyrite: Geochimica et Cosmochimica Acta, v. 178, p. 143–159.

Fougerouse, D., Reddy, S.M., Saxey, D.W., Rickard, W.D., Van Riessen, A., and Micklethwaite, S., 2016b, Nanoscale gold clusters in arsenopyrite controlled by growth rate not concentration: Evidence from atom probe microscopy: American Mineralogist, v. 101, no. 8, p. 1916–1919.

Fougerouse, D., Reddy, S.M., Aylmore, M., Yang, L., Guagliardo, P., Saxey, D.W., Rickard, W.D., and Timms, N., 2021, A new kind of invisible gold in pyrite hosted in deformation-related dislocations: Geology, v. 49, no. 10, p. 1225–1229.

Fournier, R.O., 1999, Hydrothermal processes related to movement of fluid from plastic into brittle rock in the magmatic-epithermal environment: Economic Geology, v. 94, p. 1193–1211.

Franchini, M., McFarlane, C., Maydagán, L., Reich, M., Lentz, D.R., Meinert, L., and Bouhier, V., 2015, Trace metals in pyrite and marcasite from the Agua Rica porphyry-high sulfidation epithermal deposit, Catamarca, Argentina: Textural features and metal zoning at the porphyry to epithermal transition: Ore Geology Reviews, v. 66, p. 366–387.

Frelinger, S.N., Ledvina, M.D., Kyle, J.R., and Zhao, D., 2015, Scanning electron microscopy cathodoluminescence of quartz: Principles, techniques and applications in ore geology: Ore Geology Reviews, v. 65, p. 840–852.

Frenzel, M., Cook, N.J., Ciobanu, C.L., Slattery, A.D., Wade, B.P., Gilbert, S., Ehrig, K., Burisch, M., Verdugo-Ihl, M.R., and Voudouris, P., 2020, Halogens in hydrothermal sphalerite record origin of ore-forming fluids: Geology, v. 48, no. 8, p. 766–770.

Frenzel, M., Hirsch, T., and Gutzmer, J., 2016, Gallium, germanium, indium, and other trace and minor elements in sphalerite as a function of deposit type - A meta-analysis: Ore Geology Reviews, v. 76, p. 52–78.

Frost, B.R., Mavrogenes, J.A., and Tomkins, A.G., 2002, Partial melting of sulfide ore deposits during medium- and high-grade metamorphism: Canadian Mineralogist, v. 40, p. 1–18.

George, L., Cook, N.J., Cristiana, C., and Wade, B.P., 2015, Trace and minor elements in galena: A reconnaissance LA-ICP-MS study: American Mineralogist, v. 100, p. 548–569.

George, L.L., Cook, N.J., and Ciobanu, C.L., 2016, Partitioning of trace elements in co-crystallized sphalerite-galena-chalcopyrite hydrothermal ores: Ore Geology Reviews, v. 77, p. 97–116.

George, L., Cook, N., and Ciobanu, C., 2017, Minor and Trace Elements in Natural Tetrahedrite-Tennantite: Effects on Element Partitioning among Base Metal Sulphides: Minerals, v. 7, no. 2, p. 17.

George, L.L., Biagioni, C., D'Orazio, M., and Cook, N.J., 2018a, Textural and trace element evolution of pyrite during greenschist facies metamorphic recrystallization in the southern Apuan Alps (Tuscany, Italy): Influence on the formation of Tl-rich sulfosalt melt: Ore Geology Reviews, v. 102, p. 59–105.

George, L.L., Cook, N.J., Crowe, B.B.P., and Ciobanu, C.L., 2018b, Trace elements in hydrothermal chalcopyrite: Mineralogical Magazine, v. 82, p. 59–88.

Gibbs, G.V., Cox, D.F., Rosso, K.M., Ross, N.L., Downs, R.T., and Spackman, M.A., 2007, Theoretical electron density distributions for Fe- and Cu-sulfide earth materials: A connection between bond length, bond critical point properties, local energy densities, and bonded interactions: Journal of Physical Chemistry B, v. 111, no. 8, p. 1923–1931.

Gibbs, G.V., Ross, N.L., and Cox, D.F., 2017, Sulfide bonded atomic radii: Physics and Chemistry of Minerals, v. 44, no. 8, p. 561–566.

Gilbert, S.E., Danyushevsky, L.V., Goemann, K., and Death, D., 2014, Fractionation of sulphur relative to iron during laser ablation-ICP-MS analyses of sulphide minerals: Implications for quantification: Journal of Analytical Atomic Spectrometry, v. 29, no. 6, p. 1024–1033.

Goldschmidt, V.M., 1937, The principles of distribution of chemical elements in minerals and rocks: Journal of the Chemistry Society, v. 140, p. 655–673.

Götze, J., 2012, Application of cathodoluminescence microscopy and spectroscopy in geosciences: Microscopy and Microanalysis, v. 18, no. 6, p. 1270–1284.

Govindarao, B., Pruseth, K.L., and Mishra, B., 2018, Sulfide partial melting and chalcopyrite disease: An experimental study: American Mineralogist, v. 103, no. 8, p. 1200–1207.

Grant, H.L., Hannington, M.D., Petersen, S., Frische, M., and Fuchs, S.H., 2018, Constraints on the behavior of trace elements in the actively-forming TAG deposit, Mid-Atlantic Ridge, based on LA-ICP-MS analyses of pyrite: Chemical Geology, v. 498, p. 45–71.

Gregory, M.J., Lang, J.R., Gilbert, S., and Hoal, K.O., 2013, Geometallurgy of the Pebble porphyry copper-gold-molybdenum deposit, Alaska: Implications for gold distribution and paragenesis: Economic Geology, v. 108, no. 3, p. 463–482.

Grondahl, C., and Zajacz, Z., 2017, Magmatic controls on the genesis of porphyry Cu–Mo–Au deposits: The Bingham Canyon example: Earth and Planetary Science Letters, v. 480, p. 53–65.

Gustafson, L.B., and Hunt, J.P., 1975, The Porphyry Copper Deposit at El Salvador, Chile: Economic Geology, v. 70, no. 5, p. 857–912.

Gustafson, L.B., and Quiroga, J.G., 1995, Patterns of Mineralization and Alteration below the Porphyry Copper Orebody at El Salvador, Chile: Economic Geology, v. 90, p. 2–16.

Hannington, M.D., 2014, Volcanogenic Massive Sulfide Deposits: *in* Holland, H.D., and Turekian, K.K., eds., Treatise on Geochemistry: 2nd edn., v.13, Oxford, Elsevier Ltd., p. 463–485.

Hastie, E.C.G., Kontak, D.J., and Lafrance, B., 2020, Gold Remobilization: Insights from Gold Deposits in the Archean Swayze Greenstone Belt, Abitibi Subprovince, Canada: Economic Geology, v. 115, no. 2, p. 241–277.

Hastie, E.C.G., Schindler, M., Kontak, D.J., and Lafrance, B., 2021, Transport and coarsening of gold nanoparticles in an orogenic deposit by dissolution–reprecipitation and Ostwald ripening: Communications Earth & Environment, v. 2, no. 57, p. 1–9.

Hazen, R.M., and Finger, L.W., 1979, Bulk Modulus-Volume Relationship for Cation-Anion Polyhedra: Journal of Geophysical Research, v. 84, p. 6723–6728.

Hedenquist, J.W., and Lowenstern, J.B., 1994, The role of magmas in the formation of hydrothermal ore deposits: Nature, v. 370, p. 519–527.

Hedenquist, J.W., Arribas, A., and Reynolds, T.J., 1998, Evolution of an intrusion-centered hydrothermal system: Far Southeast-Lepanto porphyry and epithermal Cu-Au deposits, Philippines: Economic Geology, v. 93, no. 4, p. 373–404.

Heinrich, C.A., 2005, The physical and chemical evolution of low-salinity magmatic fluids at the porphyry to epithermal transition: A thermodynamic study: Mineralium Deposita, v. 39, no. 8, p. 864–889.

Heinrich, C.A., Ryan, C.G., Mernagh, T.P., and Eadington, P.J., 1992, Segregation of ore metals between magmatic brine and vapor; a fluid inclusion study using PIXE microanalysis: Economic Geology, v. 87, no. 6, p. 1566–1583.

Henley, R.W., and McNabb, A., 1978, Magmatic vapor plumes and ground-water interaction in porphyry copper emplacement: Economic Geology, v. 73, no. 1, p. 1–18.

Hildreth, W., and Moorbath, S., 1988, Crustal contributions to arc magmatism in the Andes of Central Chile: Contributions to Mineralogy and Petrology, v. 98, no. 4, p. 455–489.

Holwell, D.A., Fiorentini, M., McDonald, I., Lu, Y., Giuliani, A., Smith, D.J., Keith, M., and Locmelis, M., 2019, A metasomatized lithospheric mantle control on the metallogenic signature of post-subduction magmatism: Nature Communications, v. 10, no. 3511, p. 1–10.

Hou, Z., Yang, Z., Lu, Y., Kemp, A., Zheng, Y., Li, Q., Tang, J., Yang, Z., and Duan, L., 2015, A genetic linkage between subduction- and collision-related porphyry Cu deposits in continental collision zones: Geology, v. 43, no. 3, p. 247–250.

Hurtig, N.C., and Williams-Jones, A.E., 2014, An experimental study of the transport of gold through hydration of AuCl in aqueous vapour and vapour-like fluids: Geochimica et Cosmochimica Acta, v. 127, p. 305–325.

Hurtig, N.C., Migdisov, A.A., and Williams-Jones, A.E., 2021, Are Vapor-Like Fluids Viable Ore Fluids for Cu-Au-Mo Porphyry Ore Formation?: Economic Geology, v. 116, no. 7, p. 1599–1624.

Huston, D.L., Sie, S.H., Suter, G.F., Cooke, D.R., and Both, R.A., 1995, Trace Elements in Sulfide Minerals from Eastern Australian Volcanic-Hosted Massive Sulfide Deposits: Economic Geology, v. 90, p. 1167–1196.

Jebrak, M., 1997, Hydrothermal breccias in vein-type ore deposits: A review of mechanisms, morphology and size distribution: Ore Geology Reviews, v. 12, p. 111–134.

Jenkin, G., Graham, H., Smith, D., Khan, R., Abbott, A., and Harris, R., 2019, Gold and critical element recovery with environmentally benign Deep Eutectic Solvnets, *in* Proceedings of the 15th SGA biennial meeting: p. 1512–1515.

Jenner, F.E., O'Neill, H.S.C., Arculus, R.J., and Mavrogenes, J.A., 2010, The magnetite crisis in the evolution of arc-related magmas and the initial concentration of Au, Ag and Cu: Journal of Petrology, v. 51, no. 12, p. 2445–2464.

Jensen, K.R., Campos, E., Wilkinson, J.J., Wilkinson, C.C., Kearsley, A., Miranda-Díaz, G., and Véliz, W., 2022, Hydrothermal fluid evolution in the Escondida porphyry copper deposit, northern Chile: evidence from SEM-CL imaging of quartz veins and LA-ICP-MS of fluid inclusions: Mineralium Deposita, v. 57, p. 279–300.

Jugo, P.J., Wilke, M., and Botcharnikov, R.E., 2010, Sulfur K-edge XANES analysis of natural and synthetic basaltic glasses: Implications for S speciation and S content as function of oxygen fugacity: Geochimica et Cosmochimica Acta, v. 74, no. 20, p. 5926–5938.

Keith, M., Häckel, F., Haase, K.M., Schwarz-Schampera, U., and Klemd, R., 2016, Trace element systematics of pyrite from submarine hydrothermal vents: Ore Geology Reviews, v. 72, p. 728–745.

Keith, M., Smith, D.J., Jenkin, G.R., Holwell, D.A., and Dye, M.D., 2018, A review of Te and Se systematics in hydrothermal pyrite from precious metal deposits: Insights into ore-forming processes: Ore Geology Reviews, v. 96, p. 269–282.

Keith, M., Smith, D.J., Doyle, K., Holwell, D.A., Jenkin, G.R., Barry, T.L., Becker, J., and Rampe, J., 2020, Pyrite chemistry: A new window into Au-Te ore-forming processes in alkaline epithermal districts, Cripple Creek, Colorado: Geochimica et Cosmochimica Acta, v. 274, p. 172–191.

Keith, M., Haase, K.M., Häckel, F., Schwarz-Schampera, U., Klemd, R., Hannington, M., Strauss, H., McConachy, T., and Anderson, M., 2021, Trace element fractionation and precipitation in submarine back-arc hydrothermal systems, Nifonea caldera, New Hebrides subduction zone: Ore Geology Reviews, v. 135, p. 1–19.

Kelley, K.A., and Cottrell, E., 2009, Water and the oxidation state of subduction zone magmas: Science, v. 325, p. 605–607.

Kelley, K. D., Eppinger, R. G., Lang, J., Smith, S. M., and Fey, D. L., 2011, Porphyry Cu indicator minerals in till as an exploration tool: example from the giant Pebble porphyry Cu-Au-Mo deposit, Alaska, USA: Geochemistry: Exploration, Environment, Analysis, v. 11, p. 321–334.

Kessel, R., Schmidt, M.W., Ulmer, P., and Pettke, T., 2005, Trace element signature of subduction-zone fluids, melts and supercritical liquids at 120-180 km depth: Nature, v. 437, p. 724–727.

Kirkham, R., and Margolis, J., 1995, Overview of the Sulphurets area, northwestern British Columbia: Canadian Institute of Mining, Metallurgy and Petroleum, Special Volume 46, p. 473–483.

Koděra, P., Heinrich, C.A., Wälle, M., and Lexa, J., 2014, Magmatic salt melt and vapor: Extreme fluids forming porphyry gold deposits in shallow subvolcanic settings: Geology, v. 42, no. 6, p. 495–498.

Kouhestani, H., Ghaderi, M., Large, R.R., and Zaw, K., 2017, Texture and chemistry of pyrite at Chah Zard epithermal gold–silver deposit, Iran: Ore Geology Reviews, v. 84, p. 80–101.

Kouzmanov, K., and Pokrovski, G.S., 2012, Hydrothermal Controls on Metal Distribution in Porphyry Cu (-Mo-Au) Systems: SEG Special Publication 16, p. 573–618.

Kroll, T., Müller, D., Seifert, T., Herzig, P.M., and Schneider, A., 2002, Petrology and geochemistry of the shoshonite-hosted Skouries porphyry Cu-Au deposit, Chalkidiki, Greece: Mineralium Deposita, v. 37, p. 137–144.

Landtwing, M.R., Pettke, T., Halter, W.E., Heinrich, C.A., Redmond, P.B., Einaudi, M.T., and Kunze, K., 2005, Copper deposition during quartz dissolution by cooling magmatic-hydrothermal fluids: The Bingham porphyry: Earth and Planetary Science Letters, v. 235, p. 229–243.

Landtwing, M.R., Furrer, C., Redmond, P.B., Pettke, T., Guillong, M., and Heinrich, C.A., 2010, The Bingham Canyon porphyry Cu-Mo-Au deposit. III. Zoned copper-gold ore deposition by magmatic vapor expansion: Economic Geology, v. 105, no. 1, p. 91–118.

Lang, J.R., Lueck, B., Mortensen, J.K., Russell, J.K., Stanley, C.R., and Thompson, J.F., 1995a, Triassic-Jurassic silica-undersaturated and silica-saturated alkalic intrusions in the Cordillera of British Columbia: Implications for arc magmatism: Geology, v. 23, no. 5, p. 451–454.

Lang, J.R., Stanley, C.R., and Thompson, J.F.H., 1995b, Porphyry Copper-Gold Deposits Related to Alkalic Igneous Rocks in the Triassic-Jurassic Arc Terranes of British Columbia: Arizona Geological Society Digest 20, p. 219–236.

Large, R.R., Maslennikov, V.V., Robert, F., Danyushevsky, L.V., and Chang, Z., 2007, Multistage sedimentary and metamorphic origin of pyrite and gold in the Giant Sukhoi log deposit, Lena Gold Province, Russia: Economic Geology, v. 102, no. 7, p. 1233–1267.

Large, R.R., Danyushevsky, L., Hollit, C., Maslennikov, V., Meffre, S., Gilbert, S., Bull, S., Scott, R., Emsbo, P., Thomas, H., Singh, B., and Foster, J., 2009, Gold and Trace Element Zonation in Pyrite Using a Laser Imaging Technique: Implications for the Timing of Gold in Orogenic and Carlin-Style Sediment-Hosted Deposits: Economic Geology, v. 104, no. 5, p. 635–668.

Large, S.J., Bakker, E.Y., Weis, P., Wälle, M., Ressel, M., and Heinrich, C.A., 2016, Trace elements in fluid inclusions of sediment-hosted gold deposits indicate a magmatic-hydrothermal origin of the Carlin ore trend: Geology, v. 44, no. 12, p. 1015–1018.

Lee, C.T.A., and Tang, M., 2020, How to make porphyry copper deposits: Earth and Planetary Science Letters, v. 529, p. 1–11.

Lee, C.T.A., Luffi, P., Le Roux, V., Dasgupta, R., Albaréde, F., and Leeman, W.P., 2010, The redox state of arc mantle using Zn/Fe systematics: Nature, v. 468, p. 681–685.

Lee, C.T.A., Luffi, P., Chin, E.J., Bouchet, R., Dasgupta, R., Morton, D.M., Le Roux, V., Yin, Q.Z., and Jin, D., 2012, Copper Systematics in Arc Magmas: Science, v. 335, p. 64–66.

Lee, C.T.A., Lee, T.C., and Wu, C.T., 2014, Modeling the compositional evolution of recharging, evacuating, and fractionating (REFC) magma chambers: Implications for differentiation of arc magmas: Geochimica et Cosmochimica Acta, v. 143, p. 8–22.

Lerchbaumer, L., and Audétat, A., 2012, High Cu concentrations in vapor-type fluid inclusions: An artifact?: Geochimica et Cosmochimica Acta, v. 88, p. 255–274.

Li, Y., and Audétat, A., 2012, Partitioning of V, Mn, Co, Ni, Cu, Zn, As, Mo, Ag, Sn, Sb, W, Au, Pb, and Bi between sulfide phases and hydrous basanite melt at upper mantle conditions: Earth and Planetary Science Letters, v. 355-356, p. 327–340.

Li, Y., Feng, L., Kiseeva, E.S., Gao, Z., Guo, H., Du, Z., Wang, F., and Shi, L., 2019, An essential role for sulfur in sulfide-silicate melt partitioning of gold and magmatic gold transport at subduction settings: Earth and Planetary Science Letters, v. 528, p. 1–12.

Li, Y., Audétat, A., Liu, Z., and Wang, F., 2021, Chalcophile element partitioning between Cu-rich sulfide phases and silicate melt and implications for the formation of Earth's continental crust: Geochimica et Cosmochimica Acta, v. 302, p. 61–82.

Lipson, R., 2014, The Promise and Perils of Porphyry Deposits in the Future of Gold Production: SEG Newsletter, v. 98, p. 1, 14–21.

Liu, H., and Chang, L.L.Y., 1994, Phase relations in the system PbS-PbSe-PbTe: Mineralogical Magazine, v. 58, p. 567–578.

Liu, W., Migdisov, A., and Williams-Jones, A., 2012, The stability of aqueous nickel(II) chloride complexes in hydrothermal solutions: Results of UV-Visible spectroscopic experiments: Geochimica et Cosmochimica Acta, v. 94, p. 276–290.

Lockington, J.A., Cook, N.J., and Ciobanu, C.L., 2014, Trace and minor elements in sphalerite from metamorphosed sulphide deposits: Mineralogy and Petrology, v. 108, no. 6, p. 873–890.

Logan, J.M., and Mihalynuk, M.G., 2014, Tectonic Controls on Early Mesozoic Paired Alkaline Porphyry Deposit Belts (Cu-Au ± Ag-Pt-Pd-Mo) Within the Canadian Cordillera: Economic Geology, v. 109, p. 827–858.

Loucks, R.R., 2014, Distinctive composition of copper-ore-forming arc magmas: Australian Journal of Earth Sciences, v. 61, p. 5–16.

Marks, M.A., Hettmann, K., Schilling, J., Frost, B.R., and Markl, G., 2011, The mineralogical diversity of alkaline igneous rocks: Critical factors for the transition from miaskitic to agpaitic phase assemblages: Journal of Petrology, v. 52, no. 3, p. 439–455.

Martin, A.J., Keith, M., McDonald, I., Haase, K.M., McFall, K.A., Klemd, R., and MacLeod, C.J., 2019, Trace element systematics and ore-forming processes in mafic VMS deposits: Evidence from the Troodos ophiolite, Cyprus: Ore Geology Reviews, v. 106, p. 205–225.

Maslennikov, V.V., Maslennikova, S.P., Large, R.R., and Danyushevsky, L.V., 2009, Study of Trace Element Zonation in Vent Chimneys from the Silurian Yaman-Kasy Volcanic-Hosted Massive Sulfide Deposit (Southern Urals, Russia) Using Laser Ablation-Inductively Coupled Plasma Mass Spectrometry (LA-ICPMS): Economic Geology, v. 104, no. 8, p. 1111–1141.

Masterman, G.J., Cooke, D.R., Berry, R.F., Walshe, J.L., Lee, A.W., and Clark, A.H., 2005, Fluid chemistry, structural setting, and emplacement history of the Rosario Cu-Mo porphyry and Cu-Ag-Au epithermal veins, Collahuasi district, northern Chile: Economic Geology, v. 100, no. 5, p. 835–862.

Maydagán, L., Franchini, M., Lentz, D., Pons, J., and McFarlane, C., 2013, Sulfide composition and isotopic signature of the Altar Cu-Au deposit, Argentina: Constraints on the evolution of the porphyry-epithermal system: Canadian Mineralogist, v. 51, p. 813–840.

Maydagán, L., Franchini, M., Chiaradia, M., Dilles, J., and Rey, R., 2014, The Altar porphyry Cu-(Au-Mo) deposit (Argentina): A complex magmatic-hydrothermal system with evidence of recharge processes: Economic Geology, v. 109, no. 3, p. 621–641.

Maydagán, L., Franchini, M., Rusk, B., Lentz, D.R., McFarlane, C., Impiccini, A., Ríos, F.J., and Rey, R., 2015, Porphyry to epithermal transition in the altar Cu-(Au-Mo) deposit, Argentina, studied by cathodoluminescence, LA-ICP-MS, and fluid inclusion analysis: Economic Geology, v. 110, no. 4, p. 889–923.

Meffre, S., Large, R.R., Steadman, J.A., Gregory, D.D., Stepanov, A.S., Kamenetsky, V.S., Ehrig, K., and Scott, R.J., 2016, Multi-stage enrichment processes for large gold-bearing ore deposits: Ore Geology Reviews, v. 76, p. 268–279.

Meng, X., Li, X., Chu, F., Zhu, J., Lei, J., Li, Z., Wang, H., Chen, L., and Zhu, Z., 2020, Trace element and sulfur isotope compositions for pyrite across the mineralization zones of

a sulfide chimney from the East Pacific Rise (1-2°S): Ore Geology Reviews, v. 116, p. 2–15.

Mernagh, T.P., Leys, C., and Henley, R.W., 2020, Fluid inclusion systematics in porphyry copper deposits: The super-giant Grasberg deposit, Indonesia, as a case study: Ore Geology Reviews, v. 123, no. April, p. 103,570.

Micko, J., Tosdal, R.M., Bissig, T., Chamberlain, C.M., and Simpson, K.A., 2014, Hydrothermal Alteration and Mineralization of the Galore Creek Alkalic Cu-Au Porphyry Deposit, Northwestern British Columbia, Canada: Economic Geology, v. 109, p. 891–914.

Migdisov, A.A., Zezin, D., and Williams-Jones, A.E., 2011, An experimental study of Cobalt (II) complexation in Cl^- and H_2S^- bearing hydrothermal solutions: Geochimica et Cosmochimica Acta, v. 75, no. 14, p. 4065–4079.

MINING.com, 2021, RANKED: World's top 10 gold projects: https://www.mining.com/featured-article/ranked-worlds-top-10-gold-projects/ (accessed August 2021).

Mishra, B.P., Pati, P., Dora, M.L., Baswani, S.R., Meshram, T., Shareef, M., Pattanayak, R.S., Suryavanshi, H., Mishra, M., and Raza, M.A., 2021, Trace-element systematics and isotopic characteristics of sphalerite-pyrite from volcanogenic massive sulfide deposits of Betul belt, central Indian Tectonic Zone: Insight of ore genesis to exploration: Ore Geology Reviews, v. 134, p. 1–25.

Monecke, T., Monecke, J., Reynolds, T.J., Tsuruoka, S., Bennett, M.M., Skewes, W.B., and Palin, R.M., 2018, Quartz Solubility in the H2O-NaCl System: A Framework for Understanding Vein Formation in Porphyry Copper Deposits: Economic Geology, v. 113, no. 5, p. 1007–1046.

Müller, A., Herrington, R., Armstrong, R., Seltmann, R., Kirwin, D.J., Stenina, N.G., and Kronz, A., 2010, Trace elements and cathodoluminescence of quartz in stockwork veins of Mongolian porphyry-style deposits: Mineralium Deposita, v. 45, no. 7, p. 707–727.

Mungall, J.E., 2002, Roasting the mantle: Slab melting and the genesis of major Au and Au-rich Cu deposits: Geology, v. 30, no. 10, p. 915–918.

Muntean, J.L., and Einaudi, M.T., 2000, Porphyry gold deposits of the Refugio district, Maricunga belt, Northern Chile: Economic Geology, v. 95, no. 7, p. 1445–1472.

Muntean, J.L., Cline, J.S., Simon, A.C., and Longo, A.A., 2011, Magmatic-hydrothermal origin of Nevada's Carlin-type gold deposits: Nature Geoscience, v. 4, no. 2, p. 122–127.

Murakami, H., Seo, J.H., and Heinrich, C.A., 2010, The relation between Cu/Au ratio and formation depth of porphyry-style Cu-Au ± Mo deposits: Mineralium Deposita, v. 45, p. 11–21.

Nadeau, O., Williams-Jones, A.E., and Stix, J., 2010, Sulphide magma as a source of metals in arc-related magmatic hydrothermal ore fluids: Nature Geoscience, v. 3, no. 7, p. 501–506.

Nelson, J., and Colpron, M., 2007, Tectonics and metallogeny of the British Columbia, Yukon and Alaskan Cordillera, 1.8 Ga to the present, *in* Goodfellow, W.D., ed., Mineral deposits of Canada: A synthesis of major deposit-types, district metallogeny, the evolution of geological provinces, and exploration methods: Geological association of Canada, mineral deposits division: Special Publication No. 5, p. 755–791.

Nelson, J., and Kyba, J., 2014, Structural and stratigraphic control of porphyry and related mineralization in the Treaty Glacier – KSM – Brucejack – Stewart trend of western Stikinia, *in* Geological fieldwork 2013, British Columbia Ministry Of Energy and Mines, British Columbia Geological Survey Paper 2014-1, p. 111–140.

Nelson, J.L., Colpron, M., and Israel, S., 2013, The Cordillera of British Columbia, Yukon, and Alaska: Tectonics and Metallogeny: Economic Geology Special Publication 17, p. 53–109.

Nelson, J., Waldron, J., van Straaten, B., Zagorevski, A., and Rees, C., 2018, Revised stratigraphy of the Hazelton Group in the Iskut River region, northwestern British Columbia: Geological Fieldwork 2017, British Columbia Ministry Of Energy and Mines, British Columbia Geological Survey Paper 2018-1, p. 15–38.

O'Neill, H.S.C., and Mavrogenes, J.A., 2002, The sulfide capacity and the sulfur content at sulfide saturation of silicate melts at 1400°C and 1 bar: Journal of Petrology, v. 43, no. 6, p. 1049–1087.

Palacios, C., Hérail, G., Townley, B., Maksaev, V., Sepúlveda, F., de Parseval, P., Rivas, P., Lahsen, A., and Parada, M.A., 2001, The composition of gold in the Cerro Casale gold-rich porphyry deposit, Maricunga Belt, Northern Chile: Canadian Mineralogist, v. 39, p. 907–915.

Pal'yanova, G., 2008, Physicochemical modeling of the coupled behavior of gold and silver in hydrothermal processes: Gold fineness, Au/Ag ratios and their possible implications: Chemical Geology, v. 255, p. 399–413.

Park, J.W., Campbell, I.H., Malaviarachchi, S.P., Cocker, H., Hao, H., and Kay, S.M., 2019, Chalcophile element fertility and the formation of porphyry Cu ± Au deposits: Mineralium Deposita, v. 54, no. 5, p. 657–670.

Park, J.W., Campbell, I.H., Chiaradia, M., Hao, H., and Lee, C.T., 2021, Crustal magmatic controls on the formation of porphyry copper deposits: Nature Reviews Earth and Environment, v. 2, no. 8, p. 542–557.

Parmigiani, A., Faroughi, S., Huber, C., Bachmann, O., and Su, Y., 2016, Bubble accumulation and its role in the evolution of magma reservoirs in the upper crust: Nature, v. 532, p. 492–495.

Pašava, J., Svojtka, M., Veselovský, F., Ďurišová, J., Ackerman, L., Pour, O., Drábek, M., Halodová, P., and Haluzová, E., 2016, Laser ablation ICPMS study of trace element chemistry in molybdenite coupled with scanning electron microscopy (SEM) – An important tool for identification of different types of mineralization: Ore Geology Reviews, v. 72, p. 874–895.

Pettke, T., Oberli, F., Audétat, A., Guillong, M., Simon, A.C., Hanley, J.J., and Klemm, L.M., 2012, Recent developments in element concentration and isotope ratio analysis of individual fluid inclusions by laser ablation single and multiple collector ICP-MS: Ore Geology Reviews, v. 44, p. 10–38.

Pokrovski, G.S., Borisova, A.Y., and Harrichoury, J.C., 2008, The effect of sulfur on vapor-liquid fractionation of metals in hydrothermal systems: Earth and Planetary Science Letters, v. 266, p. 345–362.

Porter, J.P., Schroeder, K., and Austin, G., 2012, Geology of the Bingham Canyon Porphyry Cu-Mo-Au Deposit, Utah: SEG Special Publication no. 16, p. 127–146.

Pudack, C., Halter, W.E., Heinrich, C.A., and Pettke, T., 2009, Evolution of magmatic vapor to gold-rich epithermal liquid: The porphyry to epithermal transition at Nevados de Famatina, Northwest Argentina: Economic Geology, v. 104, no. 4, p. 449-477.

Putnis, A., 2009, Mineral replacement reactions: Reviews in Mineralogy and Geochemistry, v. 70, p. 87–124.

Pyykkö, P., and Atsumi, M., 2009, Molecular single-bond covalent radii for elements 1-118: Chemistry – A European Journal, v. 15, p. 186–197.

Redmond, P.B., Einaudi, M.T., Inan, E.E., Landtwing, M.R., and Heinrich, C.A., 2004, Copper deposition by fluid cooling in intrusion-centered systems: New insights from the Bingham porphyry ore deposit, Utah: Geology, v. 32, no. 3, p. 217–220.

Reed, M.H., and Palandri, J., 2006, Sulfide mineral precipitation from hydrothermal fluids: Reviews in Mineralogy and Geochemistry, v. 61, p. 609–631.

Reed, M., Rusk, B., and Palandri, J., 2013, The Butte magmatic-hydrothermal system: One fluid yields all alteration and veins: Economic Geology, v. 108, no. 6, p. 1379–1396.

Reich, M., Kesler, S.E., Utsunomiya, S., Palenik, C.S., Chryssoulis, S.L., and Ewing, R.C., 2005, Solubility of gold in arsenian pyrite: Geochimica et Cosmochimica Acta, v. 69, no. 11, p. 2781–2796.

Reich, M., Deditius, A., Chryssoulis, S., Li, J.W., Ma, C.Q., Parada, M.A., Barra, F., and Mittermayr, F., 2013, Pyrite as a record of hydrothermal fluid evolution in a porphyry copper system: A SIMS/EMPA trace element study: Geochimica et Cosmochimica Acta, v. 104, p. 42–62.

Richards, J.P., 2009, Postsubduction porphyry Cu-Au and epithermal Au deposits: Products of remelting of subduction-modified lithosphere: Geology, v. 37, no. 3, p. 247–250.

Richards, J.P., 2011, Magmatic to hydrothermal metal fluxes in convergent and collided margins: Ore Geology Reviews, v. 40, p. 1–26.

Richards, J.P., 2013, Giant ore deposits formed by optimal alignments and combinations of geological processes: Nature Geoscience, v. 6, p. 911–916.

Richards, J.P., 2015, The oxidation state, and sulfur and Cu contents of arc magmas: Implications for metallogeny: Lithos, v. 233, p. 27–45.

Richards, J.P., 2018, A shake-up in the porphyry world?: Economic Geology, v. 113, no. 6, p. 1225–1233.

Richards, J.P., Boyce, A.J., and Pringle, M.S., 2001, Geologic evolution of the Escondida area, northern Chile: A model for spatial and temporal localization of porphyry Cu mineralization: Economic Geology, v. 96, no. 2, p. 271–305.

Rivas-Romero, C., Reich, M., Barra, F., Gregory, D., and Pichott, S., 2021, The Relation between Trace Element Composition of Cu-(Fe) Sulfides and Hydrothermal Alteration

in a Porphyry Copper Deposit: Insights from the Chuquicamata Underground Mine, Chile: Minerals, v. 11, p. 1–29.

Roedder, E., 1971, Fluid inclusion studies on the porphyry-type ore deposits at Bingham, Utah, Butte, Montana, and Climax, Colorado: Economic Geology, v. 66, no. 1, p. 98–118.

Roman, N., Reich, M., Leisen, M., Morata, D., Barra, F., and Deditius, A.P., 2019, Geochemical and micro-textural fingerprints of boiling in pyrite: Geochimica et Cosmochimica Acta, v. 246, p. 60–85.

Rosset, S., 2017, Evolution of Hydrothermal Alteration and Mineralization at the Deformed Kerr and Deep Kerr Cu-Au Porphyry Deposits, Northwestern British Columbia, Canada: Masters Thesis, University of British Columbia, 919 p.

Rottier, B., and Casanova, V., 2020, Trace element composition of quartz from porphyry systems: a tracer of the mineralizing fluid evolution: Mineralium Deposita, v. 56, p. 843–862.

Rottier, B., Kouzmanov, K., Casanova, V., Wälle, M., and Fontboté, L., 2018, Cyclic Dilution of Magmatic Metal-Rich Hypersaline Fluids by Magmatic Low-Salinity Fluid: A Major Process Generating the Giant Epithermal Polymetallic Deposit of Cerro de Pasco, Peru: Economic Geology, v. 113, no. 4, p. 825–856.

Rusk, B.G., Reed, M.H., Dilles, J.H., Klemm, L.M., and Heinrich, C.A., 2004, Compositions of magmatic hydrothermal fluids determined by LA-ICP-MS of fluid inclusions from the porphyry copper-molybdenum deposit at Butte, MT: Chemical Geology, v. 210, p. 173–199.

Rusk, B.G., Reed, M.H., and Dilles, J.H., 2008, Fluid Inclusion Evidence for Magmatic-Hydrothermal Fluid Evolution in the Porphyry Copper-Molybdenum Deposit at Butte, Montana: Economic Geology, v. 103, no. 2, p. 307–334.

Salomon de Friedberg, H., and Robinson, T., 2015, Tackling Impurities in Copper Concentrates: https://www.teck.com/media/Tackling-Impurities-in-Copper-Concentrates.pdf (accessed February 2022).

Saunders, J.A., Hofstra, A.H., Goldfarb, R.J., and Reed, M.H., 2014, Geochemistry of Hydrothermal Gold Deposits, *in* Holland, H.D., and Turekian, K.K., eds., Treatise on Geochemistry: 2nd edn., v. 13, Oxford, Elsevier Ltd., p. 383–424.

Savage, K.S., Tingle, T.N., O'Day, P.A., Waychunas, G.A., and Bird, D.K., 2000, Arsenic

speciation in pyrite and secondary weathering phases, Mother Lode Gold District, Tuolumne County, California: Applied Geochemistry, v. 15, no. 8, p. 1219–1244.

Savell, M., and Threlkeld, W.E., 2013, The KSM Project – A Cluster of Porphyry Related, Deformed and Dismembered Au-Cu-Mo Deposits Displaying a Transition from Deep Porphyry to Shallow Vein Environments: https://seabridgegold.net/pdf/geology/KSM_Geology_update_Sep_2013.pdf (accessed November 2020).

Schöpa, A., Annen, C., Dilles, J.H., Sparks, R.S.J., and Blundy, J.D., 2017, Magma Emplacement Rates and Porphyry Copper Deposits: Thermal Modeling of the Yerington Batholith, Nevada: Economic Geology, v. 112, no. 7, p. 1653–1672.

Schulz, K., DeYoung, J., Jr., Seal, R.R., I., and Bradley, D., eds., 2017, Critical Mineral Resources of the United States - Economic and Environmental Geology and Prospects for Future Supply: U.S. Geological Survey Professional Paper 1802, 797 p.

Seabridge Gold, 2020a, KSM (Kerr-Sulphurets-Mitchell): Exploration: https://seabridgegold.net/ksm_explore.php (accessed November 2020).

Seabridge Gold, 2020b, KSM (Kerr-Sulphurets-Mitchell): Geology: https://seabridgegold.net/ksm_geology.php (accessed November 2020).

Seedorff, E., Dilles, J.H., Proffett, Jr., J.M., Einaudi, M.T., Zurcher, L., Stavast, W.J.A., Johnson, D.A., and Barton, M.D., 2005, Porphyry Deposits: Characteristics and Origin of Hypogene Features: Economic Geology 100th Anniversary Volume, p. 251–298.

Seo, J.H., Guillong, M., and Heinrich, C.A., 2009, The role of sulfur in the formation of magmatic-hydrothermal copper-gold deposits: Earth and Planetary Science Letters, v. 282, p. 323–328.

Seward, T.M., Williams-Jones, A.E., and Migdisov, A.A., 2014, The Chemistry of Metal Transport and Deposition by Ore-Forming Hydrothermal Fluids, *in in* Holland, H.D., and Turekian, K.K., eds., Treatise on Geochemistry: 2nd edn., v. 13, Oxford, Elsevier Ltd., p. 29–57.

Shannon, R.D., 1976, Revised effective ionic radii and systematic studies of interatomic distances in halides and chalcogenides: Acta Crystallographica, v. 32, p. 751–767.

Sharman, E.R., Taylor, B.E., Minarik, W.G., Dubé, B., and Wing, B.A., 2015, Sulfur isotope and trace element data from ore sulfides in the Noranda district (Abitibi, Canada):

Implications for volcanogenic massive sulfide deposit genesis: Mineralium Deposita, v. 50, no. 5, p. 591–606.

Shore, M., and Fowler, A.D., 1996, Oscillatory Zoning in Minerals: A Common Phenomenon: The Canadian Mineralogist, v. 34, p. 1111–1126.

Sillitoe, R.H., 1972, A Plate Tectonic Model for the Origin Porphyry Copper Deposits: Economic Geology, v. 67, p. 184–197.

Sillitoe, R.H., 1979, Some thoughts on gold-rich porphyry copper deposits: Mineralium Deposita, v. 14, no. 2, p. 161–174.

Sillitoe, R.H., 1985, Ore-related Breccias in Volcanoplutonic arcs: Economic Geology, v. 80, no. 6, p. 1467–1514.

Sillitoe, R.H., 2000, Gold-Rich Porphyry Deposits: Descriptive and Genetic Models and Their Role in Exploration and Discovery: SEG Reviews, v. 13, p. 315–345.

Sillitoe, R.H., 2010, Porphyry copper systems: Economic Geology, v. 105, no. 1, p. 3–41.

Simmons, S.F., White, N.C., and John, D.A., 2005, Geological Characteristics of Epithermal Precious and Base Metal Deposits: Economic Geology 100th Anniversary Volume, p. 485–522.

Simmons, S.F., Brown, K.L., and Tutolo, B.M., 2016, Hydrothermal transport of Ag, Au, Cu, Pb, Te, Zn, and other metals and metalloids in New Zealand geothermal systems: Spatial Patterns, Fluid-mineral equilibria, and implications for epithermal mineralization: Economic Geology, v. 111, no. 3, p. 589–618.

Singer, D.A., 1995, World class base and precious metal deposits – a quantitative analysis: Economic Geology, v. 90, no. 1, p. 88–104.

Singer, D.A., Berger, V.I., and Moring, B.C., 2008, Porphyry Copper Deposits of the World: Database And Grade and Tonnage: USGS, 45 p.

Spencer, C.J., Roberts, N.M., and Santosh, M., 2017, Growth, destruction, and preservation of Earth's continental crust: Earth-Science Reviews, v. 172, p. 87–106.

Steadman, J.A., Large, R.R., Olin, P.H., Danyushevsky, L.V., Meffre, S., Huston, D., Fabris, A., Lisitsin, V., and Wells, T., 2021, Pyrite trace element behavior in magmatic-hydrothermal environments: An LA-ICPMS imaging study: Ore Geology Reviews, v. 128, p. 1–20.

Stefanova, E., Driesner, T., Zajacz, Z., Heinrich, C.A., Petrov, P., and Vasilev, Z., 2014, Melt and fluid inclusions in hydrothermal veins: The magmatic to hydrothermal evolution of the Elatsite porphyry Cu-Au deposit, Bulgaria: Economic Geology, v. 109, no. 5, p. 1359–1381.

Stefánsson, A., and Seward, T.M., 2003, Stability of chloridogold(I) complexes in aqueous solutions from 300 to 600°C and from 500 to 1800 bar: Geochimica et Cosmochimica Acta, v. 67, no. 23, p. 4559–4576.

Suleimenov, O.M., and Seward, T.M., 2000, Spectrophotometric measurements of metal complex formation at high temperatures: The stability of Mn(II) chloride species: Chemical Geology, v. 167, p. 177–192.

Sun, W., Zhang, H., Ling, M.X., Ding, X., Chung, S.L., Zhou, J., Yang, X.Y., and Fan, W., 2011, The genetic association of adakites and Cu-Au ore deposits: International Geology Review, v. 53, p. 691–703.

Sun, W., Huang, R., Li, H., Hu, Y., Zhang, C., Sun, S., Zhang, L., Ding, X., Li, C., Zartman, R.E., and Ling, M., 2015, Porphyry deposits and oxidized magmas: Ore Geology Reviews, v. 65, p. 97–131.

Sun, W., Wang, J., Zhang, L., chan Zhang, C., Li, H., Ling, M., Ding, X., Li, C., and Liang, H., 2017, The formation of porphyry copper deposits: Acta Geochimica, v. 36, no. 1, p. 9–15.

Sung, Y.H., Brugger, J., Ciobanu, C.L., Pring, A., Skinner, W., and Nugus, M., 2009, Invisible gold in arsenian pyrite and arsenopyrite from a multistage Archaean gold deposit: Sunrise Dam, Eastern Goldfields Province, Western Australia: Mineralium Deposita, v. 44, p. 765–791.

Sykora, S., Cooke, D.R., Meffre, S., Stephanov, A.S., Gardner, K., Scott, R., Selley, D., and Harris, A.C., 2018, Evolution of Pyrite Trace Element Compositions from Porphyry-Style and Epithermal Conditions at the Lihir Gold Deposit: Implications for Ore Genesis and Mineral Processing: Economic Geology, v. 113, no. 1, p. 193–208.

Tan, W., Wang, C.Y., He, H., Xing, C., Liang, X., and Dong, H., 2015, Magnetite-rutile symplectite derived from ilmenite-hematite solid solution in the Xinjie Fe-Ti oxide-bearing, mafic-ultramafic layered intrusion (SW China): American Mineralogist, v. 100, no. 10, p. 2348–2351.

Tan, W., Wang, C.Y., Reddy, S.M., He, H., Xian, H., and Xing, C., 2022, Magnetite-rutile symplectite in ilmenite records magma hydration in layered intrusions: American Mineralogist, v. 107, no. 3, p. 395–404.

Tardani, D., Reich, M., Deditius, A.P., Chryssoulis, S., Sánchez-Alfaro, P., Wrage, J., and Roberts, M.P., 2017, Copper–arsenic decoupling in an active geothermal system: A link between pyrite and fluid composition: Geochimica et Cosmochimica Acta, v. 204, p. 179–204.

Tattitch, B., Chelle-Michou, C., Blundy, J., and Loucks, R.R., 2021, Chemical feedbacks during magma degassing control chlorine partitioning and metal extraction in volcanic arcs: Nature Communications, v. 12, no. 1774, p. 1–11.

Threlkeld, W.E., Ghaffari, H., Huang, J., Gray, J.H., Hammett, R., Masson, B., Kinakin, D., Lechner, M.J., Parkinson, J.G., Schmidt, R., Brazier, N., Hanson, K., and Keylock, A., 2020, KSM (Kerr-Sulphurets-Mitchell) Prefeasibility Study and Preliminary Economic Assessment Update: National Instrument 43-101 Technical Report, 672 p.

Thybo, H., and Artemieva, I.M., 2013, Moho and magmatic underplating in continental lithosphere: Tectonophysics, v. 609, p. 605–619.

Tombe, S.P., Richards, J.P., Greig, C.J., Board, W.S., Creaser, R.A., Muehlenbachs, K.A., Larson, P.B., Dufrane, S.A., and Spell, T., 2018, Origin of the high-grade Early Jurassic Brucejack epithermal Au-Ag deposits, Sulphurets Mining Camp, northwestern British Columbia: Ore Geology Reviews, v. 95, p. 480–517.

Tooth, B., Brugger, J., Ciobanu, C., and Liu, W., 2008, Modeling of gold scavenging by bismuth melts coexisting with hydrothermal fluids: Geology, v. 36, no. 10, p. 815–818.

Tooth, B., Ciobanu, C.L., Green, L., O'Neill, B., and Brugger, J., 2011, Bi-melt formation and gold scavenging from hydrothermal fluids: An experimental study: Geochimica et Cosmochimica Acta, v. 75, p. 5423–5443.

Tooth, B., Etschmann, B., Pokrovski, G.S., Testemale, D., Hazemann, J.L., Grundler, P.V., and Brugger, J., 2013, Bismuth speciation in hydrothermal fluids: An X-ray absorption spectroscopy and solubility study: Geochimica et Cosmochimica Acta, v. 101, p. 156–172.

Tsuruoka, S., 2017, The evolution of hydrothermal fluids from the deep porphyry environment to the shallow epithermal environment: Ph.D. thesis, Colorado School of Mines, 182 p.

Ulrich, T., Kamber, B.S., Jugo, P.J., and Tinkham, D.K., 2009, Imaging element-distribution patterns in minerals by Laser Ablation-Inductively Coupled Plasma-Mass spectrometry (LA-ICP-MS): Canadian Mineralogist, v. 47, no. 5, p. 1001–1012.

USGS, 2022, Selenium: Mineral Commodity Summaries, 2 p.

van Hinsberg, V.J., Migdisov, A.A., and Williams-Jones, A.E., 2010, Reading the mineral record of fluid composition from element partitioning: Geology, v. 38, no. 9, p. 847–850.

Vila, T., Sillitoe, R.H., Betzhold, J., and Viteri, E., 1991, The porphyry gold deposit at Marte, northern Chile: Economic Geology, v. 86, no. 6, p. 1271–1286.

Voudouris, P.C., Spry, P.G., Mavrogonatos, C., Sakellaris, G.A., Bristol, S.K., Melfos, V., and Fornadel, A.P., 2013, Bismuthinite derivatives, lillianite homologues, and bismuth sulfotellurides as indicators of gold mineralization in the Stanos shear-zone related deposit, Chalkidiki, Northern Greece: Canadian Mineralogist, v. 51, no. 1, p. 119–142.

Wallace, P.J., 2005, Volatiles in subduction zone magmas: Concentrations and fluxes based on melt inclusion and volcanic gas data: Journal of Volcanology and Geothermal Research, v. 140, p. 217–240.

Wang, B., Zhou, T.F., Fan, Y., Chen, J., Liu, Y.N., and Chen, Y., 2020, Breccia, hydrothermal alteration and structural geology of the Huangtun porphyry Au-Cu deposit in the Middle-Lower Yangtze Metallogenic Belt, eastern China: Ore Geology Reviews, v. 120, p. 103,414.

Weis, P., Driesner, T., and Heinrich, C.A., 2012, Porphyry-copper ore shells form at stable pressure-temperature fronts within dynamic fluid plumes: Science, v. 338, p. 1613–1616.

Whitney, D.L., and Evans, B.W., 2010, Abbreviations for names of rock-forming minerals: American Mineralogist, v. 95, no. 1, p. 185–187.

Wikimedia, 2020, Pyrite crystal structure: https://commons.wikimedia.org/wiki/User:Ra%27ike/Gallery#Cubic (accessed May 2022).

Wilkinson, J.J., 2001, Fluid inclusions in hydrothermal ore deposits: Lithos, v. 55, p. 229–272.

Wilkinson, J.J., 2013, Triggers for the formation of porphyry ore deposits in magmatic arcs: Nature Geoscience, v. 6, no. 11, p. 917–925.

Wilkinson, J.J., Chang, Z., Cooke, D.R., Baker, M.J., Wilkinson, C.C., Inglis, S., Chen, H., and Gemmell, B.J., 2015, The chlorite proximitor: A new tool for detecting porphyry ore deposits: Journal of Geochemical Exploration, v. 152, p. 10–26.

Williams-Jones, A.E., and Heinrich, C.A., 2005, Vapor Transport of Metals and the Formation of Magmatic-Hydrothermal Ore Deposits: Economic Geology 100th Anniversary Volume, p. 1287–1312.

Williams-Jones, A.E., Bowell, R.J., and Migdisov, A.A., 2009, Gold in Solution: Elements, v. 5, no. 5, p. 281–287.

Williamson, B.J., Herrington, R.J., and Morris, A., 2016, Porphyry copper enrichment linked to excess aluminium in plagioclase: Nature Geoscience, v. 9., p. 237–241.

Wilson, A.J., 2003, The geology, genesis and exploration context of the Cadia gold-copper porphyry deposits, New South Wales, Australia: Ph.D. thesis, Universtiy of Tasmania, 316 p.

Wilson, A.J., Cooke, D.R., Stein, H.J., Fanning, C.M., Holliday, J.R., and Tedder, I.J., 2007, U-Pb and Re-Os geochronologic evidence for two alkalic porphyry ore-forming events in the Cadia District, New South Wales, Australia: Economic Geology, v. 102, no. 1, p. 3–26.

Wood, B.J., and Blundy, J.D., 2001, The effect of cation charge on crystal-melt partitioning of trace elements: Earth and Planetary Science Letters, v. 188, p. 59–71.

Wood, S.A., and Samson, I.M., 2006, The aqueous geochemistry of gallium, germanium, indium and scandium: Ore Geology Reviews, v. 28, p. 57–102.

Wu, Y.F., Fougerouse, D., Evans, K., Reddy, S.M., Saxey, D.W., Guagliardo, P., and Li, J.W., 2019, Gold, arsenic, and copper zoning in pyrite: A record of fluid chemistry and growth kinetics: Geology, v. 47, no. 7, p. 641–644.

Wu, Y.F., Evans, K., Hu, S.Y., Fougerouse, D., Fisher, L.A., Fisher, L.A., Guagliardo, P., and Li, J.W., 2021, Decoupling of Au and As during rapid pyrite crystallization: Geology, v. 49, no. 7, p. 827–831.

Zajacz, Z., Seo, J.H., Candela, P.A., Piccoli, P.M., and Tossell, J.A., 2011, The solubility of copper in high-temperature magmatic vapors: A quest for the significance of various chloride and sulfide complexes: Geochimica et Cosmochimica Acta, v. 75, no. 10, p. 2811–2827.

Zajacz, Z., Candela, P.A., Piccoli, P.M., Wälle, M., and Sanchez-Valle, C., 2012, Gold and copper in volatile saturated mafic to intermediate magmas: Solubilities, partitioning, and implications for ore deposit formation: Geochimica et Cosmochimica Acta, v. 91, p. 140–159.

Zajacz, Z., Candela, P.A., and Piccoli, P.M., 2017, The partitioning of Cu, Au and Mo between liquid and vapor at magmatic temperatures and its implications for the genesis of magmatic-hydrothermal ore deposits: Geochimica et Cosmochimica Acta, v. 207, p. 81–101.

Zhang, B., Li, N., ping Shu, S., Wang, W., Yu, J., Chen, X., Ye, T., and Chen, Y.J., 2017, Textural and compositional evolution of Au-hosting Fe-S-As minerals at the Axi epithermal gold deposit, Western Tianshan, NW China: Ore Geology Reviews, v. 100, p. 31–50.

Zimmer, M.M., Plank, T., Hauri, E.H., Yogodzinski, G.M., Stelling, P., Larsen, J., Singer, B., Jicha, B., Mandeville, C., and Nye, C.J., 2010, The role of water in generating the calc-alkaline trend: New volatile data for Aleutian magmas and a new tholeiitic index: Journal of Petrology, v. 51, no. 12, p. 2411–2444.

Appendix A – Methodology and analytical procedures

A.1 Introduction

Table A.1 lists the drill core samples collected during this research project, and the preparation and analytical procedures applied to each sample. The following sections expand on the methdology of these procedures and the rationale for selecting and implementing each method.

A.2 Sample selection and collection

The collection of drill core was planned in as much detail as possible, in order to acquire the most appropriate sample set for conducting research on this project. Selection of samples was limited by the authors knowledge of Iron Cap, given the lack of previous research on Iron Cap published at the commencement of the research project. However, data was provided by Seabridge Gold to enable sample selection prior to site visits. Explained in further detail below are the processes and rationale for the selection of drill core samples, and the collection procedures employed in the field. Site visits to KSM for sample collection took place in June 2018 (6 sampling days) and September 2019 (5 sampling days).

The KSM deposits have undergone an extensive drill program, which began in 2005.

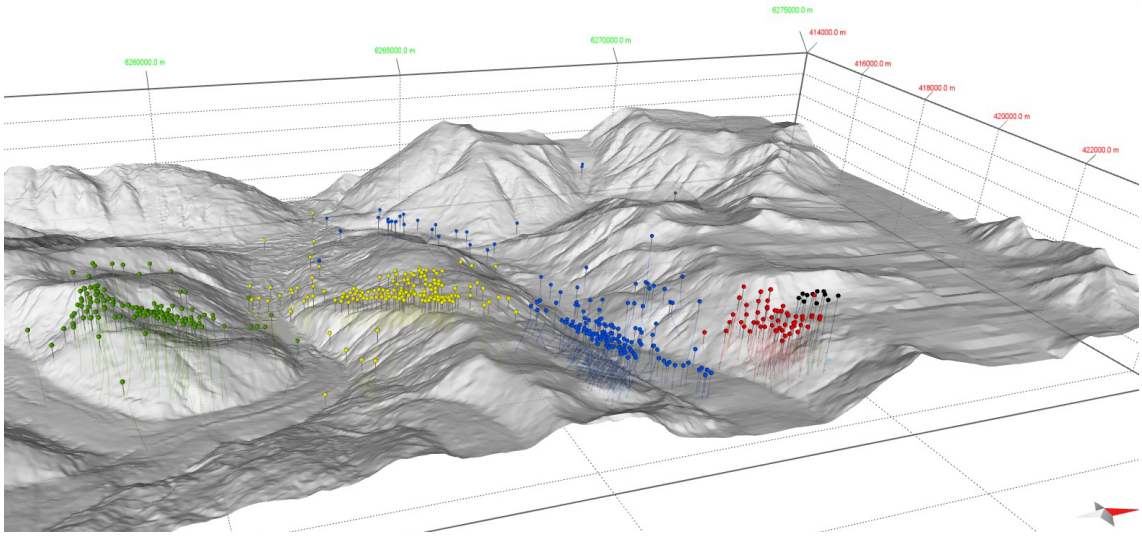

Figure A.1. Drill holes in the KSM district on a digital elevation model, viewed from E-SE. Data for drill collar locations, hole depths, and orientations was supplied by Seabridge Gold. The pins are coloured to the target deposit: green, Kerr; yellow, Sulphurets; blue, Mitchell; and red, Iron Cap. Black pins are also Iron Cap, marking the latest (2017) drill program that data was received for. Each grid square is 2 by 5 km, with the E-W scale (labelled in red text) on a 2 km spacing, and the N-S scale (labelled in green text) on a 5 km spacing.

Table A.1

List of samples collected from Iron Cap (IC) drill core, and the preparation and analytical procedures applied to each. Sample numbers were assigned by combining drill hole number and the interval depth (from–to). Those with an additional -1 or -2 indicate that more than one thin section was created from a single core sample. Seabridge Gold drill holes are named following the format: Deposit-Year-Hole number. The total number of thin sections created and samples analysed by each method is shown at the bottom of the table. TS — Thin section.

Sample number	Drill hole	From (m)	To (m)	TS	SEM BSE-EDX	SEM CL	EMPA	LA-ICP-MS
IC01-011	IC-05-01	11.8	11.9	–	–	–	–	–
IC01-039	IC-05-01	39.3	39.6	X	X	X	–	–
IC01-048	IC-05-01	48.3	48.6	–	–	–	–	–
IC01-052	IC-05-01	52.0	52.3	X	X	X	–	–
IC01-054	IC-05-01	54.5	54.7	X	X	–	–	–
IC01-109	IC-05-01	109.0	109.4	X	X	–	–	–
IC01-170	IC-05-01	169.8	170.1	–	–	–	–	–
IC02-160	IC-05-02	160.4	160.6	X	X	–	–	–
IC05-024	IC-05-05	24.0	24.3	X	X	X	–	–
IC06-053	IC-10-06	53.8	54.0	X	X	–	–	–
IC11-026	IC-10-11	26.7	27.0	X	X	X	–	–
IC33-030-1	IC-10-033	30.2	30.5	X	X	X	X	X
IC33-030-2	IC-10-033	30.2	30.5	X	X	–	–	–
IC33-144	IC-10-033	144.1	144.4	–	–	–	–	–
IC33-170	IC-10-033	170.2	170.4	–	–	–	–	–
IC33-338	IC-10-033	338.6	338.9	–	–	–	–	–
IC37-033	IC-10-037	33.5	33.7	X	–	–	–	–
IC37-038	IC-10-037	38.3	38.6	X	X	X	–	–
IC37-067	IC-10-037	67.8	68.1	X	X	–	–	–
IC37-088	IC-10-037	88.0	88.4	X	X	–	–	–
IC37-157-1	IC-10-037	157.4	157.7	X	X	X	–	–
IC37-157-2	IC-10-037	157.4	157.7	X	X	X	X	X
IC37-218	IC-10-037	218.1	218.5	X	X	–	–	–
IC43-118	IC-10-043	118.0	118.3	X	X	X	–	–
IC43-224	IC-10-043	224.7	225.0	X	X	X	–	–
IC51-1085	IC-13-051	1085.6	1085.9	–	–	–	–	–
IC59-033-1	IC-14-059	33.5	34.0	X	X	X	X	X
IC59-033-2	IC-14-059	33.5	34.0	X	X	–	–	–
IC59-060	IC-14-059	60.5	60.8	X	X	–	–	–
IC59-123	IC-14-059	123.3	123.7	X	X	X	–	–
IC59-351	IC-14-059	351.0	351.2	–	–	–	–	–
IC59-530	IC-14-059	530.5	530.8	–	–	–	–	–
IC63-421-1	IC-17-063	421.4	421.6	X	X	–	–	–
IC63-421-2	IC-17-063	421.4	421.6	X	–	–	–	–
IC63-791	IC-17-063	791.0	791.2	X	X	X	X	X
IC64-144	IC-17-064	144.5	144.7	–	–	–	–	–
IC64-156	IC-17-064	156.4	156.7	X	X	X	–	–
IC64-335	IC-17-064	335.1	335.4	–	–	–	–	–
IC64-521	IC-17-064	521.0	521.4	X	X	X	–	–
IC65-106	IC-17-065	106.4	106.6	X	X	–	–	–
IC65-194	IC-17-065	194.0	194.3	–	–	–	–	–
IC65-201	IC-17-065	201.3	201.6	–	–	–	–	–
IC65-430	IC-17-065	430.2	430.3	X	X	X	X	X
IC65-430-2	IC-17-065	430.2	430.3	X	X	X	–	–
IC65-532	IC-17-065	532.7	532.9	X	X	–	–	–

(continued on next page)

Table A.1
(continued)

Sample number	Drill hole	From (m)	To (m)	TS	SEM BSE-EDX	SEM CL	EMPA	LA-ICP-MS
IC65-629	IC-17-065	629.7	630.0	X	–	–	–	–
IC66-073	IC-17-066	73.4	73.6	X	X	X	X	X
IC66-084	IC-17-066	84.3	84.6	X	X	–	–	–
IC66-097-1	IC-17-066	97.5	97.7	X	X	–	–	–
IC66-097-2	IC-17-066	97.5	97.7	X	X	–	–	–
IC66-647	IC-17-066	647.0	647.3	–	–	–	–	–
IC67-116	IC-17-067	116.3	116.5	–	–	–	–	–
IC67-130	IC-17-067	130.1	130.2	X	–	–	–	–
IC67-233	IC-17-067	233.0	233.3	–	–	–	–	–
IC67-350	IC-17-067	350.8	351.1	X	X	–	–	–
IC69-383	IC-17-069	383.4	383.7	–	–	–	–	–
IC69-598	IC-17-069	598.9	599.1	X	X	X	X	X
IC69-748	IC-17-069	748.6	748.8	–	–	–	–	–
IC70-402	IC-17-070	402.6	402.8	X	X	X	X	X
IC70-429	IC-17-070	429.9	430.2	X	X	X	X	X
IC70-560	IC-17-070	560.2	560.4	X	X	X	–	–
IC71-350	IC-17-071	349.8	350.2	–	–	–	–	–
IC71-424	IC-17-071	424.4	424.6	X	X	–	–	–
IC71-570	IC-17-071	569.7	570.1	X	X	X	–	–
IC71-784	IC-17-071	785.1	785.3	X	X	X	X	X
IC71-948	IC-17-071	948.3	948.6	X	X	–	–	–
IC71-970-1	IC-17-071	970.2	970.5	X	X	X	–	–
IC71-970-2	IC-17-071	970.2	970.5	X	X	X	X	X
IC72-1252	IC-17-072	1251.8	1252.1	X	X	–	–	–
IC72-441	IC-17-072	441.2	441.6	–	–	–	–	–
IC72-506	IC-17-072	506.4	506.7	–	–	–	–	–
IC72-535	IC-17-072	535.2	535.5	–	–	–	–	–
IC72-798	IC-17-072	798.8	799.0	X	X	X	X	X
IC72-821	IC-17-072	821.0	821.1	–	–	–	–	–
IC73-393	IC-17-073	393.2	393.6	–	–	–	–	–
IC73-485	IC-17-073	485.7	485.9	–	–	–	–	–
IC73-518	IC-17-073	519.0	519.4	X	X	–	X	X
			Total	52	48	27	13	13

As of 2017, more than 650 holes had been drilled in the district (Figure A.1). Selection of drill core samples for this research was informed by multiple criteria, and limited in the first instance by the data supplied by Seabridge Gold prior to fieldwork. For sample selection in June 2018, core logs and assays for the 2017 drill program were provided, which primarily targets the deep, porphyry-style mineralisation. The selection of core samples during this period was therefore focussed on these 11 drill holes (black pins in Figure A.1). MOVE and ioGAS software were utilised to assess the distribution of drill holes, and features down-hole. The following criteria were used to inform sample selection from this dataset, ordered by priority:

- Elements of interest from assays – Au, Cu, Pb, Zn, Sb, As, Se, Hg, Sb, Bi, Ag concen-

trations were investigated, and the samples chosen contained one or more of these at different levels of abundance; for example, both Au-rich samples with high Se, and Au-rich samples with low Se were selected (high and low values being relative to the range of concentrations present in the assays).

- Vein abundance and style – Assays record the abundance of veins within the interval, while the style of veining is simply noted in core logs as young or old A, B, or D veins. High vein abundance intervals were preferred to ensure representation of veins in the sample, while the variety of Seabridge Gold-classified A, B and D veins were also covered in the sample suite.
- Alteration style – The chosen sample suite covered the range of potassic, phyllic and propylitic alteration styles described in the core logs.
- Host intrusions or units – To ensure representation of vein style variation between units (if present), the sample suite was, where possible, chosen to include core from the majority of host intrusions and units.
- Hole depth – Samples from shallow to deep depths were chosen, but as this drill program targeted the deep porphyry, proportionally more samples were taken from depths greater than 250 m.
- Hole distribution – Samples from each of the 11 drill holes were chosen, to ensure representation of lateral variations, if present.

While this desk study highlighted target intervals, selection of samples on site sometimes varied marginally from these intervals following visual inspection of the core, in order to obtain samples containing veins of interest. A total of 31 samples were collected using information provided by the desk study (Table A.1). An additional 10 samples were chosen purely on visual inspection of core, where a particularly interesting vein was present — typically when the vein was not yet observed in the current samples, or when the vein contained an abundance of ore minerals. In addition to the 41 samples chosen from the 2017 drill core, a further 20 samples were selected from pre-2017 drill core when on site. Due to the time constraints during the sampling period, Seabridge Gold provided basic Cu-Au grade models on site to highlight drill holes of potential interest, the core of which was then visually inspected. The main aim for this sampling was to obtain as many different mineralised veins as possible, prioritising those not observed in the 2017 drill core. Alteration style, host unit, hole depth, and hole distribution were also taken into account.

A second visit to KSM in September 2019 provided an opportunity to collect additional core samples. The aim for this core sampling campaign was to target the near-surface portion of the deposit, which potentially exhibits more later-stage mineralisation.

Prior to the visit, Seabridge Gold provided photos of select core intervals from 20 different drill holes. These images informed the selection of 9 core samples, each of which contained a vein of interest.

The process of collecting samples from core boxes on site was consistent between both site visits. Drill core was inspected as half-core, and then taken to the cutting shed, where Seabridge Gold employees cut each sample in half lengthways. One part was chosen as a sample, and the other returned to the appropriate core box. The quarter-core samples were then labelled with marker pen and placed in plastic bags, which were also labelled with tags. Photographs of the quarter-core sample, the half-core sample, and the full core box containing each sample were also taken to record surrounding features and ensure that samples were not later misidentified. In total, 70 drill core samples were collected (Table A.1).

Selection bias was introduced when sampling core, both with samples informed by the desk study, and with those based primarily on visual inspection. The reasoning for this is the nature of the study, in which vein samples are required, containing elevated concentrations of one or more element of interest. A purely random sampling approach would not prove to be useful for these purposes, as veins can be sparse in many core intervals, and trace element concentrations vary markedly. The selection bias was therefore warranted to obtain samples enabling the undertaking of the study, but mitigated where possible by choosing samples within the range of each criterion listed above (e.g., both Au-rich and Au-poor samples were selected, not solely Au-rich samples).

A.3 Sample preparation

All samples were visually inspected at the macro scale, to determine whether polished thin sections should be made. Thin sections were necessary in order to be able to generate a detailed description of each vein sample using micro-analytical techniques, and thus provide a precise classification of each vein generation present in the sample suite. Furthermore, thin sections were required for trace element analytical work by LA-ICP-MS. The presence of mineralised veins was the primary criteria for thin section creation, with the representation of different vein types (determined by macroscopic study) necessary to meet the aims of this thesis. Some samples containing mineralised veins were not made into thin sections, because similar vein types were already chosen for thin section creation, and there was a limit to the number of thin sections that could reasonably be analysed within the timeframe of the project. Nevertheless, all samples were scanned at a high resolution to record their features, and to inform later descriptions of vein features and the classification of vein generations.

A total of 52 vein samples were made into polished thin sections at the University of Leeds. Regions designated for thin section creation were marked on rock samples using permanent marker, labelled, and given to the laboratory technician, who made the sections. Most regions were of a size of approximately 2 x 3 cm. The crafting process involved cutting down the sample to a thin block of the desired region, fixing the block to a glass slide using epoxy resin, cutting the block down to a 1 mm thickness, and finally grinding and polishing the block until the desired thickness of ∼30 µm was achieved.

A.4 Scanning electron microscopy

The majority of detailed petrographic work on thin sections was carried out using SEM, in order to precisely characterise the vein samples in terms of their mineralogy and textural features. Prior to SEM work, each sample was analysed by transmitted and reflected light microscopy to record the basic mineralogy, and highlight features that warranted further investigation during SEM. Thin sections to be analysed by SEM were first coated with a thin (∼5-20 nm) carbon coating in order to achieve proper conductivity during analysis, and prevent charging at high vacuum conditions (Frelinger et al., 2015). All SEM was carried out at the University of Leeds Electron Microscopy and Spectroscopy Centre using a Tescan VEGA3 XM.

A.4.1 BSE-EDX

SEM Back-Scattered Electron (BSE) imagery and Energy Dispersive X-ray (EDX) spectroscopy are key analytical techniques in petrographic work, allowing the high-resolution imaging of micron-scale mineral occurrences and textural features, coupled with the elemental analysis and chemical characterisation of minerals for accurate identification. As such, these analytical techniques were employed extensively throughout this research project, to build a database of the minerals present in the vein samples, and their various modes of occurrence. Similarly, textural features present in the vein samples were necessary to record, as these inform the construction of a paragenetic sequence, and the interpretation of vein and ore formation conditions. Elemental analysis by EDX was carried out using an Oxford Instruments X-max 150 detector with Aztec energy software.

Each thin section analysed by BSE-EDX (n. 48; Table A.1) was first mapped at a high resolution in BSE; each map was made up of multiple images stitched together, with each image having a view field of 2.5 x 2.5 mm, and saved at a resolution of 1024 x 1024 pixels. These maps were used to provide an overview of textural features, mineral proportions, and mineral distributions, and also provided a means by which to efficiently navigate around a thin section, and to mark on sites of EDX analyses for future reference.

Thin sections were investigated visually by BSE, and EDX spot analysis was employed to provide semi-quantitative data to identify mineral phases. Sites of EDX analysis were imaged and described, noting the minerals present, the occurrences of minerals and key textural information; each site was typically made up of multiple EDX analyses of different minerals. The number of sites per thin section depended on the variation in vein mineralogy and features, with more uniform samples, or those with few features of interest typically having <10 sites, whereas more heterogeneous, mineralogically and texturally complex samples typically had >20 sites. Following analysis, labelled BSE images and the semi-quantitative EDX data for each site was exported. Site descriptions were tabulated in Excel to provide a mineralogical database. A total of 48 thin sections were analysed by BSE-EDX, with more than 750 sites (each of which includes multiple spot analyses) analysed over the course of the project.

Additional EDX analyses by SEM were carried out to generate quantitative compositional data for the ore minerals analysed by LA-ICP-MS, as presented in Table 6.3 and A.2. This data was collected for the purposes of reduction of the LA-ICP-MS data; however, only the SEM-EDX data for tennantite-tetrahedrite and sphalerite was used, as outlined in Section 6.3. Pyrite, chalcopyrite, galena, and arsenopyrite LA-ICP-MS data was reduced using EMPA data, meaning that the data presented in Table A.2 was not used.

Quantitative SEM-EDX data was acquired with the aid of a Co standard, and consistent analytical settings. Aztec software was used to calibrate to the Co standard. A beam intensity of 15 kV was used to maintain a count rate of ∼30000 and a dead time of ∼30%, while the acquire settings were based on reaching 2000000 counts; each analysis took approximately one minute. Analyses were carried out by focussing on a target mineral at a high magnification, setting the analytical distance to 15 mm, and then commencing the spot analysis. Re-calibration with the Co standard was completed every 1 hour, using the same analytical process and settings. The stoichiometry of target minerals was checked to ensure accuracy of the data.

A.4.2 Cathodoluminescence

Cathodoluminescence is commonly employed in petrographic studies to discriminate between different generations of vein quartz; quartz reveals unique textures in SEM-CL that may also illuminate genetic processes (e.g., Götze, 2012; Stefanova et al., 2014; Maydagán et al., 2015; Frelinger et al., 2015). Luminescence intensity in quartz is dependent on the density of defects, such as structural imperfections (e.g., site vacancies, fluid inclusions), or impurities (i.e., trace elements), each of which may inhibit or encourage luminescence (Frelinger et al., 2015). Other minerals, such as carbonates, also luminesce under CL

Table A.2

Summary of pyrite, chalcopyrite, and galena SEM-EDX data. Elements that were not detected during analysis are marked 'n.d.'. Bracketed numbers indicate the number of analyses per mineral and vein generation.

All data in wt.%	S	Fe	Co	Cu	Zn	As	Se	Ag	Sb	Te	Pb	Bi	Total
Pyrite (55)													
Mean	56.1	46.4	n.d.	0.4	n.d.	1.3	n.d.	n.d.	0.1	n.d.	n.d.	n.d.	102.7
Median	56.2	46.4	n.d.	0.4	n.d.	1.5	n.d.	n.d.	0.1	n.d.	n.d.	n.d.	102.8
V2 mean (26)	56.3	46.5	n.d.	0.4	n.d.	n.d.	n.d.	n.d.	n.d.	n.d.	n.d.	n.d.	102.9
V3 mean (29)	56	46.2	n.d.	n.d.	n.d.	1.3	n.d.	n.d.	0.1	n.d.	n.d.	n.d.	102.5
Chalcopyrite (96)													
Mean	36.5	30.1	0.2	33.6	0.3	0.5	n.d.	0.4	n.d.	n.d.	n.d.	n.d.	100.3
Median	36.7	30.3	0.2	33.7	0.3	0.3	n.d.	0.4	n.d.	n.d.	n.d.	n.d.	100.5
V2 mean (28)	36.8	30.4	n.d.	33.7	n.d.	n.d.	n.d.	n.d.	n.d.	n.d.	n.d.	n.d.	100.9
V3 mean (22)	36.5	30.2	0.2	33.4	n.d.	n.d.	n.d.	n.d.	n.d.	n.d.	n.d.	n.d.	100.2
V4 mean (17)	37	30.6	n.d.	33.9	n.d.	n.d.	n.d.	n.d.	n.d.	n.d.	n.d.	n.d.	101.5
V5 mean (22)	35.5	29.1	n.d.	33.6	0.3	0.5	n.d.	0.4	n.d.	n.d.	n.d.	n.d.	98.5
V6 mean (7)	36.7	30.2	n.d.	33.6	n.d.	n.d.	n.d.	n.d.	n.d.	n.d.	n.d.	n.d.	100.5
Galena (24)													
Mean	12.3	0.4	n.d.	1.6	0.5	2.3	4.7	n.d.	n.d.	0.2	90.6	3.4	105.9
Median	13.2	0.3	n.d.	0.8	0.5	2.3	1.9	n.d.	n.d.	0.2	91.7	3.4	105.7
V2 mean (1)	11.4	n.d.	n.d.	n.d.	n.d.	n.d.	2.8	n.d.	n.d.	0.2	86.3	n.d.	100.7
V3 mean (4)	12.2	0.7	n.d.	0.6	n.d.	n.d.	1.6	n.d.	n.d.	n.d.	89.5	n.d.	104.1
V4 mean (2)	4.6	n.d.	n.d.	n.d.	n.d.	n.d.	16.9	n.d.	n.d.	n.d.	83.5	n.d.	105.1
V5 mean (2)	13.4	0.2	n.d.	3.8	0.5	2.3	1.9	n.d.	n.d.	n.d.	91.8	n.d.	113.8
V6 mean (15)	13.3	0.4	n.d.	0.5	0.5	n.d.	0.3	n.d.	n.d.	n.d.	92	3.4	105.7

(Frelinger et al., 2015), but quartz tends to be the target mineral in porphyry deposits because of the common abundance of vein quartz co-existing with ore minerals (e.g., Sillitoe, 2010). Analysis of vein samples by SEM-CL was crucial for this research project, to characterise the quartz of different veins and recognise similarities or differences between vein quartz that could aid in the classification of vein generations, and the interpretation of genetic processes.

Of the thin sections analyed by BSE-EDX, only around half (n. 27) were subsequently analysed by SEM-CL (Table A.1), owing to the time required to complete a full thin section scan. The analyses were carried out prior to EMPA and LA-ICP-MS. Thin sections were selected for SEM-CL to meet the aim of discriminating and characterising different vein generations; therefore, a suite of samples with different vein types were chosen. Samples with higher proportions of vein quartz were prioritised, and those with higher proportions of carbonates were avoided where possible, as carbonates luminesce more strongly than quartz and can obscure the CL response of adjacent quartz crystals owing to streaking in the resulting CL image (Frelinger et al., 2015). Full thin section scans were completed for all the samples analysed by SEM-CL, using the methodology below. The Tescan VEGA3 XM at the Univeristy of Leeds is outfitted with a colour CL system, allowing the production of coloured CL scans, as opposed to monochromatic.

The analytical process began with focussing on a thin section at a high magnfication to ensure that CL images would be clear. The in-built image snapper function on the Tescan software was used to select the area/s to be mapped, and the desired resolution of individual output images, which was set to 1024 x 1024 pixels. Output images were later stiched together to generate a full thin section scan, using an overlap of 20%. Prior to commencing a scan, the magnification was set to a view field of approximately 1.3 x 1.3 mm per image; this setting was adjusted marginally when setting up different scans to alter the acquire time to within the available timeframe (usually $\sim$16 hours), as the acquire time was also dependent on the size of the mapped area. Two full section scans were able to be completed in the timeframe available for each session, with approximately 8 hours per scan. The scan speed was set to slow (5 out of 6) to allow ample time for quartz to luminesce and produce a high resolution image, as luminescence intensity is time-dependent (Frelinger et al., 2015). The beam intensity was set to a high value of 18-20 kV to ensure that the CL detector recieved a strong signal to produce clear images. After images were acquired, the inbuilt Tescan software was used to stitch together the output images as a full section scan with the maximum resolution possible (20000 pixels on the longest side).

As noted in Section A.4.1, BSE maps were acquired for all thin sections analysed by

SEM, using a similar methodology to that described above, but with faster scan speeds for scan times of ∼6 minutes, rather than 8 hours. Regardless, BSE scans are of a sufficiently high resolution, and were compiled with CL scans in Adobe Photoshop to create composite BSE-CL images. These images were useful for identifying where ore minerals were located on the CL scans, as ore minerals are non-luminescent in CL, and show up black. Relationships between quartz generations and ore minerals could then be investigated. The composite images were created by overlaying CL scans with BSE maps, changing the opacity of the BSE layer such that both maps were visible, and aligning the two images as accurately as possible. The contrast and brightness of BSE maps and/or CL scans was sometimes increased to ensure that both layers were adequately visible.

A.5 Electron microprobe analysis

Quantitative characterisation of ore minerals by EMPA was carried out for the purposes of LA-ICP-MS data reduction. As noted in Chapter 6, not all ore minerals were able to be analysed by EMPA; only some pyrite, chalcopyrite, and arsenopyrite particles, and all galena particles. The ore minerals chosen for analysis can be difficult to characterise by EMPA, because their compositions may vary between particles (e.g., Chapter 4). Therefore, the elements that were deemed most likely to be present in the ore minerals were analysed for, informed by the petrographic study and a review of the literature (Chapter 4). Analysis totals were checked to ensure that they were close to 100 wt.% (within ±3 wt.%), meaning that other major elements were unlikely to be missed, and adjacent mineral particles were not included in the analyses. The stoichiometry of minerals was also checked to confirm this. To complete the analyses within a reasonable timeframe and with acceptable precision, which depend partly on the count time per element, a limited suite of elements were selected to analyse for in each ore mineral. Pyrite, chalcopyrite, and arsenopyrite were analysed in the same runs, using the same element suite; galena was analysed separately, with a different element suite.

All EMPA was carried out at the University of Leeds Electron Microscopy and Spectroscopy Centre using a JEOL JXA8230 electron microprobe analyser. Analyses were completed using an accelerating voltage of 20kV, a beam current of 50nA, and a count time of 20 seconds for each element. Elements and X-ray lines used for analysis were:

- Pyrite, chalcopyrite, and arsenopyrite: Fe (Kα), S (Kα), Cu (Kα), As (Lα), Co (Kα), Ni (Kα), Pb (Mα);
- Galena: Pb (Lα), S (Kα), Bi (Mα), Ag (Lα), Se (Lα).

The standards used for calibration were:

- Pyrite, chalcopyrite, and arsenopyrite: $CuFeS_2$ (Fe, S, Cu), InAs (As), Co metal (Co), Ni metal (Ni), PbS (Pb);
- Galena: PbS (Pb, S), Ag_2Te (Ag), Bi metal (Bi), Se metal (Se).

Standards were analysed 3-4 times at the start of each analytical session, and the standards data was checked to ensure that variance between the analyses was below 1%, ensuring precise data collection. Accuracy was ensured by choice of appropriate standards (reducing the impact of matrix mismatch, although this was accounted for in the software), and the careful selection of background signals such that peak magnitude was correctly determined. Standard deviations of the EMPA data are shown in Table 6.2.

A.6 Laser ablation-inductively coupled plasma-mass spectrometry

The determination of trace elements in ore minerals is commonly achieved using LA-ICP-MS (e.g., Cook et al., 2009; Maydagán et al., 2015; George et al., 2015, 2018a; Steadman et al., 2021), owing to the ability of this technique to, in-situ, rapidly analyse for a wide range of different elements, and to detect and quantify element concentrations down to ppb levels (Cook et al., 2016; Deditius et al., 2017). These are the main reasons that LA-ICP-MS was chosen as the primary analytical method for this research project. The basic approach of LA-ICP-MS is as follows (e.g., Ulrich et al., 2009; Cook et al., 2016):

1. A sample is loaded into an analysis chamber that is continuously purged by a carrier gas;
2. A high energy laser beam is used to ablate a small area of material;
3. The ablated material is transferred by the carrier gas, through a tube, and then into the plasma of an ICP-MS unit;
4. The plasma (ICP) converts the material into ions that are then measured by the MS;
5. The MS separates ions by their mass to charge ratio, and records the signal intensity of different ions;
6. Ion intensities are converted to element concentrations through a data reduction process that correlates to a known value of a major element in the sample.

Analysis of selected samples by LA-ICP-MS was undertaken at the Raw Materials Characterisation Laboratory of Trinity College Dublin over a period of 5 days in February 2020. Trace element concentrations of the selected ore minerals were determined using a Teledyne Photon Machines Analyte G2 Excimer LA system, equipped with a 193 nm

ATLEX 300 ArF excimer laser and a HelEx II active two-volume ablation cell sample chamber. The LA system was coupled to a Thermo Scientific iCAP-Qc ICP-MS. Iolite software was used to set up the analyses, and to control the system.

Polished thin sections were cleaned with an alcohol solution prior to loading into the sample chamber, which could hold up to 4 thin sections. Seperate analysis runs were created for each ore mineral/group of ore minerals, in order of: pyrite (3 runs), chalcopyrite (4 runs), sphalerite (1 run), tennantite-tetrahedrite and galena (3 runs), and arsenopyrite (1 run). Separation of the ore minerals allowed for the selection of different element lists and associated dwell times, while also reducing the likelihood of cross-contamination between ore minerals, as enriched elements ablated from one ore mineral may reside in the connecting tube to the ICP-MS for some time (several days or more) and contaminate later analyses (Cook et al., 2016). For this reason, the tennantite-tetrahedrite and galena, and arsenopyrite runs were scheduled after pyrite, chalcopyrite and sphalerite, due to the high concentration of As and/or Sb and/or Pb in the tennantite-tetrahedrite, galena and arsenopyrite relative to the trace levels of these elements in pyrite, chalcopyrite and sphalerite.

A series of standard reference materials (SRMs) were loaded and analysed with each run: NIST 612 glass (for external calibration), MASS1 (for data reduction of all except sphalerite), MUL (for data reduction of sphalerite), and UQAC (secondary, for external calibration). Each SRM was analysed (using the specific run settings) twice at the start of the run, before the analysis of ore minerals, and twice at the end of the run, after the analysis of ore minerals. During one particularly long run (over 45 minutes), the SRMs were also analysed twice in the middle of the run. Helium was used as a carrier gas for the ablated material. Periods of background collection were scheduled between each spot analysis, to ensure that signal overlaps between different analyses were suitably reduced.

The isotopes analysed for are recorded in Table A.3. Dwell times were adjusted based on test ablations on similar surrounding material to the sites of interest. These tests highlighted which isotopes were present, and the signals they produced in the ICP-MS. Dwell times were then adjusted depending on if the signal was subjectively weak or strong, with the aim being to have the shortest possbile dwell time for each spot analysis (i.e. $<$1 second), while still recording the presence of trace elements. Longer dwell times are less accurate in recording the composition of a small volume of mineral, as more material is required to be ablated for the ICP-MS to measure each element for a longer time. They also run the risk of missing mineral micro-inclusions, as these could be completely ablated before the ICP-MS comes round to measuring the elements present in the inclusion.

The analytical settings for spot analyses were as follows: circular spot, spot size of

Table A.3
Element isotopes analysed for in each ore mineral during LA-ICP-MS, and the dwell times for the respective isotopes. Total dwell times for a single spot analysis of a specific ore mineral are calculated at the bottom of the table.

	Dwell time (s)					
Isotope	Py	Py maps	Ccp	Tnt-Ttr and Gn	Sp	Apy
^{34}S	0.01	0.005	0.015	0.01	0.01	0.005
^{51}V	0.01	n.a.	n.a.	n.a.	n.a.	0.01
^{55}Mn	n.a.	n.a.	n.a.	n.a.	0.01	n.a.
^{57}Fe	0.01	0.002	0.015	0.01	0.01	0.005
^{59}Co	0.06	0.02	0.03	0.03	0.03	0.04
^{60}Ni	0.07	0.03	0.03	0.03	0.03	0.05
^{63}Cu	0.01	0.005	0.01	0.004	0.01	0.01
^{66}Zn	0.01	n.a.	0.01	0.01	0.01	0.01
^{69}Ga	0.03	n.a.	0.04	0.03	0.05	n.a.
^{73}Ge	0.03	n.a.	0.04	0.03	0.07	n.a.
^{75}As	0.02	0.02	0.01	0.02	0.02	0.001
^{77}Se	0.06	0.03	0.04	0.05	0.04	0.05
^{95}Mo	0.04	n.a.	0.03	n.a.	n.a.	0.04
^{107}Ag	0.08	0.03	0.095	0.05	0.08	0.06
^{112}Cd	0.01	n.a.	0.01	0.01	0.01	0.01
^{113}In	n.a.	n.a.	0.01	0.01	0.03	n.a.
^{115}In	n.a.	n.a.	0.01	0.01	0.03	n.a.
^{121}Sb	0.04	0.04	0.04	0.04	0.04	0.02
^{124}Sn	0.01	n.a.	0.02	0.02	0.06	0.02
^{125}Te	0.04	n.a.	0.01	0.06	n.a.	0.06
^{182}W	0.04	n.a.	n.a.	n.a.	n.a.	n.a.
^{197}Au	0.14	0.06	0.12	0.06	0.06	0.07
^{199}Hg	0.1	0.05	0.04	0.05	0.1	0.05
^{205}Tl	0.04	n.a.	0.04	0.06	0.03	0.04
^{208}Pb	0.01	0.005	0.015	0.001	0.01	0.01
^{209}Bi	0.07	n.a.	0.01	0.04	0.06	0.05
Total	0.94	0.297	0.69	0.635	0.8	0.611

n.a. indicates an isotope was not analysed.

15 µm, fluence of 1 J/cm^3, laser repetition rate of 6 (per second), and a total shot count of 250. This yielded a total analysis time of ∼40 seconds per spot. Map analyses were carried out by ablating sequential line traverses of an area. The analytical settings for the majority of map analyses of were: square spot, spot size of 10 µm, fluence of 1 J/cm^3, laser repetition rate of 40, and a scan velocity of 15. The analytical settings for the map analysis of the larger V6 pyrite differed slightly, with a spot size of 20 µm, laser repetition rate of 40, and a scan velocity of 23. Time of completion of map analyses varied depending on the size of the area mapped.

Following data acquistion, the data was reduced from its raw form as isotope inten-

sity counts, to element concentrations in ppm. The data reduction processes are described in Chapter 6.

Appendix B – Video of vein distributions at Iron Cap

The video file can be found in the digital appendices. Note that the video (and each new panel) begins looking N-NE, prior to rotation, the same orientation as Figure 5.32.